

ference

NBS  
Publi-  
cations



A111103 056369

# NBS SPECIAL PUBLICATION 567

U.S. DEPARTMENT OF COMMERCE / National Bureau of Standards

## Accuracy in Powder Diffraction

C  
00  
577  
o.567  
980

## NATIONAL BUREAU OF STANDARDS

The National Bureau of Standards<sup>1</sup> was established by an act of Congress on March 3, 1901. The Bureau's overall goal is to strengthen and advance the Nation's science and technology and facilitate their effective application for public benefit. To this end, the Bureau conducts research and provides: (1) a basis for the Nation's physical measurement system, (2) scientific and technological services for industry and government, (3) a technical basis for equity in trade, and (4) technical services to promote public safety. The Bureau's technical work is performed by the National Measurement Laboratory, the National Engineering Laboratory, and the Institute for Computer Sciences and Technology.

**THE NATIONAL MEASUREMENT LABORATORY** provides the national system of physical and chemical and materials measurement; coordinates the system with measurement systems of other nations and furnishes essential services leading to accurate and uniform physical and chemical measurement throughout the Nation's scientific community, industry, and commerce; conducts materials research leading to improved methods of measurement, standards, and data on the properties of materials needed by industry, commerce, educational institutions, and Government; provides advisory and research services to other Government agencies; develops, produces, and distributes Standard Reference Materials; and provides calibration services. The Laboratory consists of the following centers:

Absolute Physical Quantities<sup>2</sup> — Radiation Research — Thermodynamics and Molecular Science — Analytical Chemistry — Materials Science.

**THE NATIONAL ENGINEERING LABORATORY** provides technology and technical services to the public and private sectors to address national needs and to solve national problems; conducts research in engineering and applied science in support of these efforts; builds and maintains competence in the necessary disciplines required to carry out this research and technical service; develops engineering data and measurement capabilities; provides engineering measurement traceability services; develops test methods and proposes engineering standards and code changes; develops and proposes new engineering practices; and develops and improves mechanisms to transfer results of its research to the ultimate user. The Laboratory consists of the following centers:

Applied Mathematics — Electronics and Electrical Engineering<sup>2</sup> — Mechanical Engineering and Process Technology<sup>2</sup> — Building Technology — Fire Research — Consumer Product Technology — Field Methods.

**THE INSTITUTE FOR COMPUTER SCIENCES AND TECHNOLOGY** conducts research and provides scientific and technical services to aid Federal agencies in the selection, acquisition, application, and use of computer technology to improve effectiveness and economy in Government operations in accordance with Public Law 89-306 (40 U.S.C. 759), relevant Executive Orders, and other directives; carries out this mission by managing the Federal Information Processing Standards Program, developing Federal ADP standards guidelines, and managing Federal participation in ADP voluntary standardization activities; provides scientific and technological advisory services and assistance to Federal agencies; and provides the technical foundation for computer-related policies of the Federal Government. The Institute consists of the following centers:

Programming Science and Technology — Computer Systems Engineering.

<sup>1</sup>Headquarters and Laboratories at Gaithersburg, MD, unless otherwise noted; mailing address Washington, DC 20234.

<sup>2</sup>Some divisions within the center are located at Boulder, CO 80303.

APR 21 1980  
not acc - Ref  
QC100  
. U57  
no. 567  
1980

# Accuracy in Powder Diffraction

---

Proceedings of a Symposium on Accuracy in Powder Diffraction  
Held at the National Bureau of Standards  
Gaithersburg, Maryland  
June 11-15, 1979

Edited by:

S. Block  
C. R. Hubbard

Center for Materials Science  
National Measurement Laboratory  
National Bureau of Standards  
Washington, D.C. 20234

Sponsored by:

International Union of Crystallography  
5 Abbey Square  
Chester, CHI 2HU, England

Chemistry Division  
National Research Council of Canada  
Ottawa, Canada K1A0R6

National Measurement Laboratory  
National Bureau of Standards  
Washington, D.C. 20234



*Special publication*

---

U.S. DEPARTMENT OF COMMERCE, Philip M. Klutznick, Secretary

Luther H. Hodges, Jr., Deputy Secretary

Jordan J. Baruch, Assistant Secretary for Science and Technology

5. NATIONAL BUREAU OF STANDARDS, Ernest Ambler, Director

Issued February 1980

Library of Congress Catalog Card Number: 80-600010

**National Bureau of Standards Special Publication 567**

Nat. Bur. Stand. (U.S.), Spec. Publ. 567, 553 pages (Feb. 1980)

CODEN: XNBSAV

U.S. GOVERNMENT PRINTING OFFICE

WASHINGTON: 1980

---

For sale by the Superintendent of Documents, U.S. Government Printing Office, Washington, D.C. 20402  
Stock No. 003-003-02153-9

(Add 25 percent additional for other than U.S. mailing).

## Preface

The symposium on Accuracy in Powder Diffraction was held to meet the deep and widespread need to assess the current position of powder diffraction including both the fundamentals underlying the accuracy attainable in the entire measurement and analysis system as well as new developments in techniques and applications. The last international meeting on powder diffraction was in Stockholm, Sweden, in June 1959. In the past two decades there have been great developments in materials science. Parallel with this has been a renewed and enlarged interest in x-ray powder diffraction both for materials analysis and characterization. The applications range from stress determinations to quantitative analysis to structural determination from line shape.

The symposium was cosponsored by the International Union of Crystallography, the Chemistry Division of the National Research Council of Canada, and the National Bureau of Standards. The organizing committee had an advisory board representing seven countries. There were 115 attendees from 17 different countries.

These proceedings include most of the invited talks (two were not available at the time of publication), extended abstracts or papers from selected contributions and abstracts of all remaining papers. Pertinent discussion of the papers is also included. It is hoped that these proceedings will serve not only as a record of the symposium, but as a source book for the latest knowledge in this increasingly important field.

S. Block and C. Hubbard  
Editors

### Disclaimer:

Certain trade names and company products are identified in order to adequately specify the experimental procedure. In no case does such identification imply recommendation or endorsement by the National Bureau of Standards, nor does it imply that the products are necessarily the best available for the purpose. Views expressed by the various authors are their own and do not necessarily represent those of the National Bureau of Standards.

## Acknowledgments

The editors wish to thank the advisory committee and other members of the organizing committee as well as the participants in the symposium. Special thanks are due to the arrangements committee for their assistance and the publication committee for producing the proceedings.

## Committees

### ORGANIZING

- S. Block, National Bureau of Standards, Chairman
- L. Calvert, National Research Council of Canada
- J. B. Cohen, Northwestern University
- C. R. Hubbard, National Bureau of Standards
- P. Suortti, University of Helsinki, Finland

### ADVISORY

- W. G. Bronger, Inst. f. Anorganische Chemie, West Germany
- M. Cernohorsky, J. E. Purkyne University, Czechoslovakia
- A. J. Guinier, Universite Paris SUD, France
- S. Hosoya, University of Tokyo, Japan
- G. B. Mitra, Indian Inst. of Techn., India
- W. Parrish, IBM, San Jose, CA, USA
- T. M. Sabine, New South Wales Inst. of Techn., Australia

### ARRANGEMENTS

- D. Appleman, Smithsonian Institution
- R. B. Johnson, NBS
- J. A. Lorden, NBS
- R. F. Martin, NBS
- B. A. Myers, NBS
- K. Stang, NBS

### PROCEEDINGS PUBLICATION

- J. Bartlett, NBS
- B. Myers, NBS
- E. Ring, NBS

## Table of Contents

Preface . . . . .	iii
Acknowledgments . . . . .	iv
Welcome . . . . .	x
I. TOTAL PATTERN	
Chairperson, L. Calvert	
COMPONENTS OF THE TOTAL X-RAY SCATTERING (Invited Paper) . . . . .	1
P. Suortti	
NEUTRON DIFFRACTION -- THE TOTAL POWDER PATTERN	
(Invited Paper) . . . . .	21
T. M. Sabine	
SYNCHROTRON RADIATION AND ENERGY-DISPERSIVE DIFFRACTION	
(Invited Paper) . . . . .	33
B. Buras	
ACCURACY IN X-RAY WAVELENGTHS (Invited Paper) . . . . .	55
R. Deslattes, A. Hening, and E. G. Kessler, Jr.	
NEGLECTED CONSIDERATIONS FOR INTENSITY MEASUREMENT	
(Invited Paper) . . . . .	73
L. D. Jennings	
II. INSTRUMENTATION AND AUTOMATION	
Chairperson, Floyd Mauer	
POSITION-SENSITIVE DETECTORS FOR POWDER DIFFRACTOMETRY	
(Invited, Abstract only) . . . . .	85
R. W. Hendricks, M. K. Kopp, and A. H. Narten	
DETERMINATION OF THE SPECTRAL INTENSITY OF THE INCIDENT	
BEAM IN ENERGY DISPERSIVE X-RAY DIFFRACTION (Abstract) . . . . .	87
R. Uno and J. Ishigaki	
TIME-OF-FLIGHT NEUTRON POWDER DIFFRACTION AT PRESSURES TO	
35 KILOBARS (Abstract) . . . . .	89
J. D. Jorgensen	
POWDER--A COMPUTING SYSTEM FOR X-RAY POWDER DIFFRACTION	
CALCULATIONS (Abstract) . . . . .	91
B. C. Osgood and R. L. Snyder	
THRESHOLD LEVEL DETERMINATIONS FROM DIGITAL X-RAY POWDER	
DIFFRACTION PATTERNS (Abstract) . . . . .	93
C. Mallory and R. L. Snyder	

### III. PROFILE FITTING

Chairperson, J. Rush

ACCURACY OF THE PROFILE FITTING METHOD FOR X-RAY POLYCRYSTALLINE DIFFRACTOMETRY (Invited Paper) . . . . .	95
W. Parrish and T. C. Huang	
PROFILE REFINEMENT OF NEUTRON POWDER DIFFRACTION PATTERNS (Invited Paper) . . . . .	111
A. W. Hewat	
STRUCTURAL ANALYSIS FROM X-RAY POWDER DIFFRACTION PATTERNS WITH THE RIETVELD METHOD (Invited Paper) . . . . .	143
R. A. Young	
A NEW PATTERN FITTING STRUCTURE REFINEMENT PROGRAM FOR X-RAY POWDER DATA (Abstract) . . . . .	165
Ch. Baerlocher and A. Hepp	
THE DETERMINATION OF STRUCTURAL PARAMETERS AND THEIR STANDARD DEVIATIONS FROM POWDER DIFFRACTION PATTERNS (Paper) . . . . .	167
M. J. Cooper, M. Sakata, and K. D. Rouse	
STRUCTURAL REFINEMENT OF NEUTRON AND X-RAY DATA BY THE RIETVELD METHOD: APPLICATION TO $Al_2O_3$ and $BiVO_4$ (Paper) . . . . .	189
D. E. Cox, A. R. Moodenbaugh, A. W. Sleight and H.-Y. Chen	
TEMPERATURE DEPENDENCE OF THE ATOMIC THERMAL DISPLACEMENTS IN $UO_2$ : A TEST CASE FOR THE RIETVELD PROFILE REFINEMENT METHOD (Paper) . . . . .	203
A. Albinati, M. J. Cooper, K. D. Rouse, M. W. Thomas, and B. T. M. Willis	
STUDIES OF THERMAL MOTION USING CONSTRAINED PROFILE ANALYSIS (Abstract) . . . . .	211
E. Prince, C. S. Choi and S. F. Trevino	

### IV. ANALYSIS OF PEAK SHAPE

Chairperson, P. Suortti

ACCURACY OF CRYSTALLITE SIZE AND STRAIN VALUES FROM X-RAY DIFFRACTION LINE PROFILES USING FOURIER SERIES (Invited Paper) . . . . .	213
R. Delhez, Th.H. de Keijser, and E. J. Mittemeijer	
ACCURACY OF CRYSTALLITE SIZE AND STRAIN DETERMINED FROM THE INTEGRAL BREADTH OF POWDER DIFFRACTION LINES (Invited Paper) . . . . .	255
J. I. Langford	
DETERMINATION OF COMPOSITIONAL VARIATIONS BY X-RAY DIFFRACTION LINE PROFILE ANALYSIS (Invited Paper) . . . . .	271
E. J. Mittemeijer and R. Delhez	

STRUCTURES FROM POWDER DATA: DATA SAMPLING, REFINEMENT AND ACCURACY (Paper) . . . . .	315
W. J. Mortier	

V. LATTICE PARAMETERS AND INDEXING

    Chairperson, Marlene Morris

ACCURACY IN METHODS OF LATTICE-PARAMETER MEASUREMENT (Invited Paper) . . . . .	325
--	-----

    A. J. C. Wilson

SOME STATISTICAL ASPECTS OF LATTICE PARAMETER EVALUATION (Invited Paper) . . . . .	353
--	-----

    J. Mandel

DATA ACCURACY FOR POWDER INDEXING (Invited Paper) . . . . .	361
---	-----

    R. Shirley

SUCCESSIVE DICHOTOMY METHOD FOR INDEXING POWDER PATTERNS (Abstract) . . . . .	383
---	-----

    D. Louer

THE DETERMINATION OF THE PRECISE LATTICE PARAMETER OF A DIFFUSE MINOR PHASE IN A DILUTE BINARY URANIUM ALLOY (Abstract) . . . . .	385
---	-----

    D. A. Carpenter and C. M. Davenport

PRECISION GUINIER X-RAY POWDER DIFFRACTION DATA (Abstract) . . . . .	387
--	-----

    J. W. Edmonds

A SIMPLE GRAPHICAL METHOD FOR OBTAINING REASONABLY ACCURATE CELL DIMENSIONS FROM X-RAY POWDER PHOTOGRAPHS OF HEXAGONAL AND TETRAGONAL MINERALS (Abstract) . . . . .	391
---	-----

    E. E. Fejer

THE RELIABILITY OF POWDER INDEXING PROCEDURES (Paper) . . . . .	393
---	-----

    A. D. Mighell and J. K. Stalick

X-RAY POWDER DIFFRACTION IDENTIFICATION OF CRYSTAL PHASES WITH SUPERIMPOSED LINES BY THEIR SELECTIVE CRYSTALLIZATION (Abstract) . . . . .	405
---	-----

    I. Mayer, I. Gedalia and B. Laufer

COMPARISON BETWEEN DEBYE-SCHERRER, TRANSMISSION AND REFLECTION MEASURING MODES (Abstract) . . . . .	407
---	-----

    E. Woelfel

VI. APPLICATIONS

SESSION I. Chairperson, M. Kuriyama

STATISTICAL ANALYSIS OF THE MEASUREMENT OF GRAIN AND  
PARTICLE SIZE WITH X-RAYS (Invited, Abstract only) . . . . . 409

J. Hilliard

ANALYSIS AND TOPOGRAPHY OF LATTICE DEFECTS IN POWDER  
DIFFRACTION PATTERNS (Invited Paper) . . . . . 411

S. Weissmann

DETERMINATION OF PREFRACTURE DAMAGE IN FATIGUED AND STRESS-CORRODED  
MATERIALS BY X-RAY DOUBLE CRYSTAL DIFFRACTOMETRY (Paper) . . . . . 433

R. N. Pangborn, R. Yazici, T. Tsakalokos, S. Weissman and

I. R. Kramer

HIGH RESOLUTION POWDER DIFFRACTION AT ARGONNE'S ZING-P<sup>+</sup> PROTOTYPE  
PULSED NEUTRON SOURCE (Abstract) . . . . . 451

J. D. Jorgensen, F. J. Rotella, and M. H. Mueller

SESSION II. Chairperson, L. Mordfin

STRESS ANALYSIS FROM POWDER DIFFRACTION PATTERNS (Invited Paper) . . . . . 453

J. B. Cohen, H. Dolle, and M. R. James

X-RAY RESIDUAL STRESS EVALUATION BY AN ENERGY DISPERSIVE  
SYSTEM (Paper) . . . . . 479

M. Kuriyama, W. J. Boettinger, and H. E. Burdette

SESSION III. Chairperson, J. B. Cohen

STANDARD REFERENCE MATERIALS FOR QUANTITATIVE ANALYSIS AND  
d-SPACING MEASUREMENT (Invited Paper) . . . . . 489

C. R. Hubbard

STRUCTURAL ANALYSIS FROM GUINIER FILM DATA (Paper) . . . . . 503

P. -E. Werner

OPTIMAL DEGREE OF AUTOMATION IN QUANTITATIVE X-RAY DIFFRACTION PHASE  
ANALYSIS (Abstract) . . . . . 511

A. Griger

VII. FUTURE OPPORTUNITIES IN POWDER DIFFRACTION

Chairperson, S. Block

STANDARDS FOR THE PUBLICATION OF POWDER PATTERNS: THE  
AMERICAN CRYSTALLOGRAPHIC ASSOCIATION SUBCOMMITTEE'S  
FINAL REPORT (Invited Paper) . . . . . 513

L. D. Calvert, J. L. Flippen-Anderson, C. R. Hubbard,

Q. C. Johnson, P. G. Lenhert, M. C. Nickols, W. Parrish,

D. K. Smith, G. S. Smith, R. L. Snyder, and R. A. Young

SUGGESTIONS FOR A QUANTITATIVE EVALUATION OF POWDER PATTERNS (Paper) . . . . .	537
G. Donnay	
X-RAY POWDER DIFFRACTION . . . . .	543
L. D. Calvert	
FUTURE OF POWDER NEUTRON DIFFRACTION . . . . .	547
M. H. Mueller	
JCPDS - INTERNATIONAL CENTER FOR DIFFRACTION DATA: PRESENT AND FUTURE ACTIVITIES . . . . .	551
G. McCarthy and D. K. Smith	

III. POSTERS

DESIGN OF A HIGH-ACCURACY GONIOMETER FOR X-RAY POWDER DIFFRACTOMETRY AT CONTROLLED TEMPERATURE . . . . .	557
J. F. Berar, G. Calvarin, J. Chevreul, M. Gramond and D. Weigel	
THE EFFECT OF TWINNING ON PARTICLE SIZE BROADENING IN SOME OXIDES DERIVED BY DEHYDRATION REACTION . . . . .	559
F. Watari	
LIST OF PARTICIPANTS . . . . .	565

ABSTRACT

The proceeding of the Symposium on Accuracy in Powder Diffraction presents the papers, abstracts and discussions of the symposium held at the NBS, Gaithersburg, Maryland on June 11-15, 1979. The symposium was jointly sponsored by the NBS, the National Research Council of Canada and the International Union of Crystallography. These proceedings contain a total of 24 invited and contributed abstracts. Many papers are followed by an edited discussion. The proceedings are divided into the following topics: Total Pattern, Instrumentation and Automation, Profile Fitting, Analysis of Peak Shape, Lattice Parameters and Indexing, Applications, and Future Opportunities in Powder Diffraction.

Key words: Applications; lattice parameters; peak shape; powder diffraction; profile fitting; x-ray neutron.

## WELCOME

John B. Wachtman, Jr.  
Director, Center for Materials Science  
National Bureau of Standards

Good morning and welcome to the National Bureau of Standards. Many of us here have a long and useful contacts with individuals and organizations in the field of powder diffraction. I suspect all of you know of our participation in the Joint Committee for Powder Diffraction and the role of some of our staff members in the publication of CRYSTAL DATA and the Powder Data File. We have a deep concern for accuracy in powder diffraction. Our work includes experimental and theoretical improvements in means for obtaining and analyzing both x-ray and neutron diffraction data. I hope many of you will be able to take the tours on Wednesday of our neutron and x-ray facilities. We also seek to contribute to accuracy in powder diffraction through supplying standard powder for x-ray diffraction.

Because of our measurements and standards mission and our deep involvement in powder diffraction we are very pleased to co-sponsor this Symposium together with the National Research Council of Canada and the International Union of Crystallography.

This Symposium is very timely. There is a resurgence of interest in powder diffraction as evidenced by recent formation by the American Crystallographic Association of a special group in applied crystallography with powder diffraction as one of the major components. Several developments contribute to this resurgence. New experimental developments, including synchrotron radiation and improved detectors, are opening exciting new possibilities. Advances in theory coupled with powerful, on-line computing ability are greatly improving feedback-controlled experiments and analysis of patterns. Availability of microprocessors at reasonable prices is making many of these techniques available for general use. Concern with precise control of phase composition and microstructure is enhancing the role of powder diffraction in quality control. Concern with toxic substances and pollution control places new demands and opens new opportunities for powder diffraction.

As I indicated, we at NBS are very pleased to be co-sponsoring so timely a Symposium. If there is anything which you would like to recommend for the future role of NBS, we would welcome your suggestions.

## COMPONENTS OF THE TOTAL X-RAY SCATTERING

P. Suortti  
University of Helsinki  
Siltavuorenpenger 20 D  
SF-00170 Helsinki 17  
Finland

Separation of the non-Bragg components of scattering is discussed in analytic and synthetic approaches. Various interactions of the x-ray photons with the electrons are considered, and the radiative processes are studied in more detail. The spectrum of the radiation is smeared by the detection system, and the possibilities of separating the elastic or nearly elastic scattering on the basis of energy is discussed. Calculations of TDS and multiple scattering are treated briefly, and the use of the approximative sum rules of kinematical diffraction in connection of an absolute intensity measurement is introduced. The role of the background in the diffraction pattern synthesis by profile fitting is also considered. A few examples of extrapolation of the background level from the separable parts of the Bragg reflections are given with the Voigtian as the profile function. The evaluation of the thermal parameters from the powder diffraction data is considered as a concrete example. The results demonstrate the importance of a correct background separation and a realistic profile function.

### 1. Introduction

The total scattering of (monoenergetic) x-rays from a crystalline sample is a very broad subject, and we have to limit the scope right from the beginning. Our point of view is very practical: we want to separate the elastic part of the total scattering and resolve it to individual reflections. However, it has been demonstrated that this separation is far from trivial, and it cannot be performed accurately without a careful consideration of all the components of scattering.

Absorption and scattering of photons in medium is summarized by the Kramers-Kronig relations. The significance of these relations to our practical goal is that the dispersion

terms of the atomic scattering factors,  $f'$  and  $f''$ , can be evaluated from the attenuation coefficient. The scattering can be divided into resonant and non-resonant parts, and we will summarize briefly the various processes and study how they can be separated from each other.

It is clear that an unambiguous treatment of the total scattering must be based on the analytical approach outlined above. Some parts of this analysis are based on theoretical calculations or independent data which may not be available for the compound being studied. In such a case, the results are synthesized within a phenomenological model of scattering and diffraction, and the results are ultimately justified by internal consistency. The consistency may be artificial, however, and the parameters of the model do not necessarily correspond to the physical quantities they are purported to represent. Test cases, where the analytic and synthetic approaches can be compared, are therefore crucial for a critical appraisal of the reliability of the fitting procedures. We will demonstrate the problems involved by a simple example and suggest improvements to the present day methods.

## 2. Scattering Cross Section

The interaction Hamiltonian between an atomic electron and the radiation field is given by

$$H' = -\frac{e}{mc} \mathbf{A} \cdot \mathbf{p} + \frac{e^2}{2mc^2} \mathbf{A} \cdot \mathbf{A}, \quad (1)$$

where  $\mathbf{p}$  and  $\mathbf{A}$  are operators with the classical analogues of the electron momentum and the vector potential of the radiation field, respectively. The  $\mathbf{A} \cdot \mathbf{p}$  term makes no contribution in first order, but taken twice it gives rise to the resonant scattering, which may be much larger than the contribution of the  $\mathbf{A} \cdot \mathbf{A}$  term. In the resonant scattering, the atomic state  $A$  absorbs the incident photon of energy  $\hbar\omega_1$  and becomes an intermediate state  $I$  and simultaneously or subsequently state  $I$  emits the outgoing photon of energy  $\hbar\omega_2$  and changes into state  $B$ . In the  $\mathbf{A} \cdot \mathbf{A}$  interaction, there is no intermediate state. These processes are illustrated by the space-time diagrams of figure 1.

The resonant scattering consists of fluorescence lines of Lorentzian shape or of resonant Raman scattering, which has a low energy tail due to sharing of energy between the outgoing electron and photon [1-4]<sup>1</sup>. Both components are isotropic and give only a smooth background to the powder diffraction pattern, or can be eliminated altogether by energy discrimination.

<sup>1</sup>Figures in brackets indicate the literature references at the end of this paper.

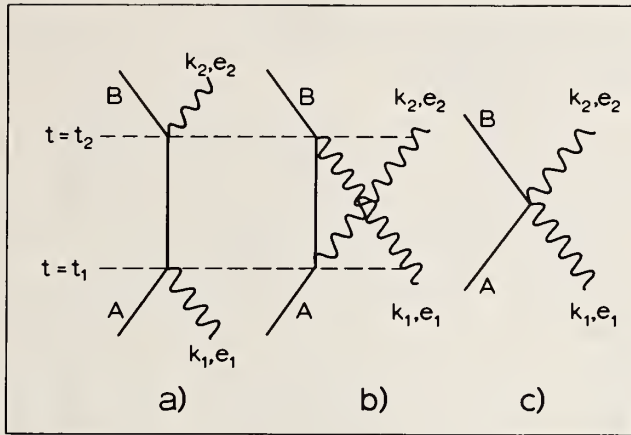


Figure 1. Space-time diagrams for scattering of photons by atomic electrons. In the resonant scattering (a and b) an intermediate state prevails between  $t_1$  and  $t_2$  and c represents non-resonant scattering. The wave-vector and the (unit) polarization vector of the incident photon are given by  $k_1$  and  $e_1$ , and those of the scattered photon by  $k_2$  and  $e_2$ .

The non-resonant part can be written as

$$\begin{aligned} \frac{d^2\sigma}{d\omega_2 d\Omega} &= r_e^2 \left( \frac{\omega_2}{\omega_1} \right) (e_1 \cdot e_2)^2 \sum_{AB} |\langle B | e^{ik \cdot r} | A \rangle|^2 \delta(E_B - E_A - \hbar\omega) \\ &= r_e^2 \left( \frac{\omega_2}{\omega_1} \right) (e_1 \cdot e_2)^2 S(\underline{k}, \omega), \end{aligned} \quad (2)$$

where  $r_e$  is the electron scattering length,  $\omega = \omega_1 - \omega_2$ ,  $\underline{k} = \underline{k}_1 - \underline{k}_2$ , and  $S(\underline{k}, \omega)$  is the dynamic scattering factor [5]. In the energy region of  $\hbar\omega \cong 10$  keV, the various scattering processes are characterized by the entity accepting the momentum and energy transfers,  $\underline{k}$  and  $\Delta\varepsilon = \hbar\omega$ . For Bragg and disorder scattering  $\underline{k}$  is absorbed by the average lattice and  $\Delta\varepsilon \cong 0$ ; in the thermal diffuse scattering (TDS) the interaction is with the vibrating atoms, and  $\Delta\varepsilon$  is from 0 to 0.1 eV; in the plasmon scattering collectives of electrons are involved and  $\Delta\varepsilon \cong 10$  eV; and finally, in the Compton scattering  $\underline{k}$  is carried by one electron with an energy change of order 10 to  $10^2$  eV. The energy spectrum of the various processes is illustrated in figure 2. For completeness, also the resonant contributions are included.

### 3. Spectral Analysis

In most cases, the subject of interest is the unmodified (Bragg + disorder) part of the scattering, and the foremost practical problem of powder diffraction is the separation of

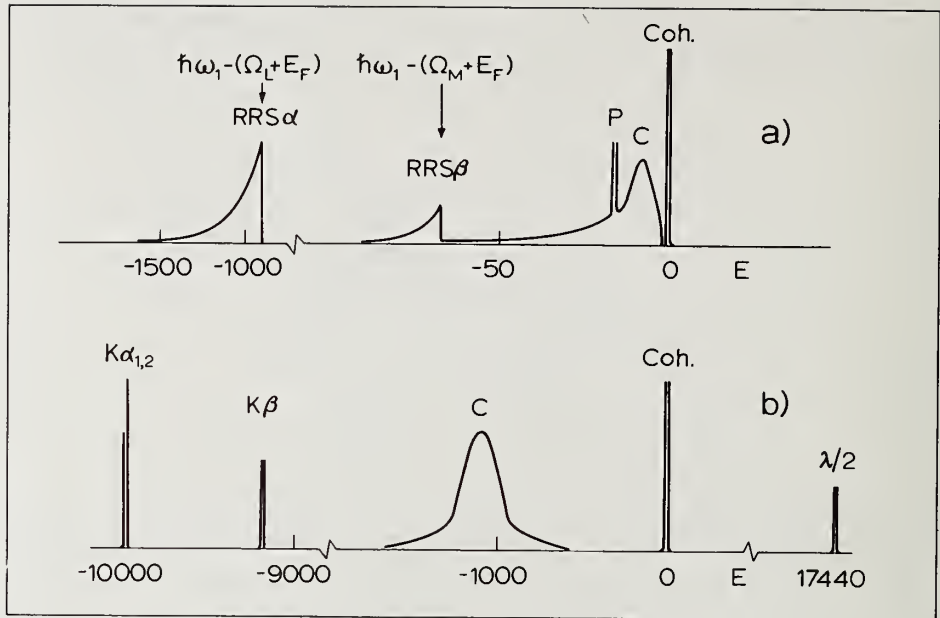


Figure 2. Spectra of the radiation scattered by a mono-atomic sample: a corresponds approximately to scattering of  $\text{CuK}\alpha$  from Ni at  $2\theta = 20^\circ$  and b to scattering of  $\text{MoK}\alpha$  from Ni at  $2\theta = 150^\circ$ . Coherent scattering (Bragg, disorder, TDS) is denoted by Coh, Compton by C, plasmon by P,  $\text{RRS}\alpha$  and  $\text{RRS}\beta$  signify the  $(1s,2p)$ ,  $(1s,3p)$  contributions to the resonant Raman scattering, respectively,  $\lambda/2$  the coherent scattering of the half-wavelength, and  $K\alpha$  plus  $K\beta$  the specimen fluorescence. The energies are in eV.

this part from the rest, from the background. We will start with considering the possibilities of making this separation on the basis of the energy shifts of the background components.

It is possible to separate the elastic scattering from the TDS and other inelastic scattering by means of the Mössbauer effect [6-8]. The available intensity from the  $\gamma$ -ray sources (usually the 14.4 keV line of  $^{57}\text{Co}$ ) is rather low, and the technique has been applied only to measurements of single crystal reflections. The background level (TDS + Compton) in the recent measurements has been typically of order 1 count/s, which would probably be sufficient for an absolute determination of the background intensity over the whole measuring range.

The spectra of figure 2 are convoluted by the detector resolution function, and the cases of the scintillation counter and the semiconductor detector (SCD) are illustrated in figure 3. The scintillation counter is barely able to reject the  $\lambda/2$  component or low energy fluorescence, but it has other advantages such as low price, reliability, and large effective area. At large incident energies and scattering angles, the SCD's separate the

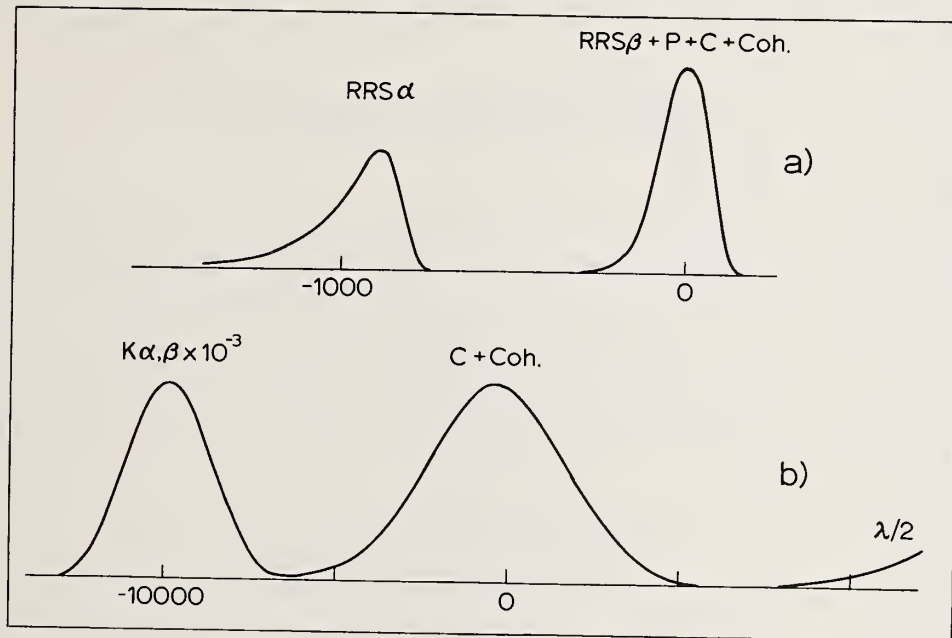


Figure 3. The spectra of figure 2 as convoluted by the detector resolution function; in a by that of an SCD and in b by that of a scintillation counter. The intensity ratios correspond to background scattering.

Compton contribution completely from the elastic peak, and this is utilized in the Compton profile measurements. Also at the crystallographic energies of order 10 keV some degree of separation is possible at large scattering angles, where the energy shift becomes a few hundreds of eV [9]. This is very important in studies of liquid or disordered structures.

The resolving power of a crystal monochromator placed in the diffracted beam is typically a few tens of eV, comparable to the energy difference between  $K\alpha_1$  and  $K\alpha_2$  of the commonly used radiations. This is not sufficient for separation of the TDS and plasmon or Compton scattering at low angles, but the rest of the background is effectively eliminated. Accordingly, this construction has become increasingly popular in the recent years. The drawback of the diffracted beam monochromators is their non-uniform response. Most of the commonly used monochromators are mosaic crystals, and the reflectivity may vary much from point to point, see figure 4. On the other hand, elastic bending of nearly perfect crystals (Ge, Si, quartz) results in monochromators with large areas of uniform sensitivity. The reflecting range of a perfect crystal is very narrow but the peak intensity high, and with proper dimensions very effective constructions are possible [10,11]. Much of the renewed interest in monochromators is due to the increasing use of synchrotron radiation, which will open up new avenues also for the powder method [12,13].

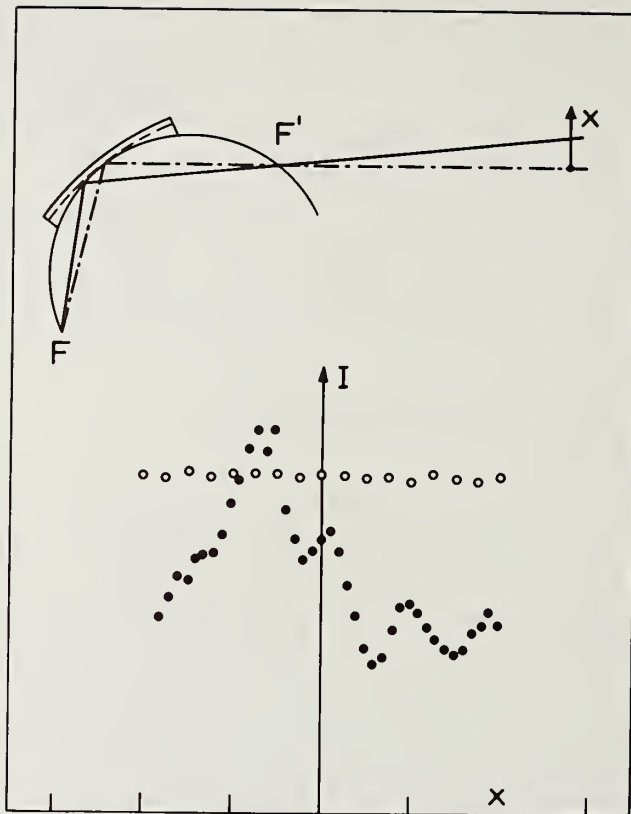


Figure 4. Reflectivity of bent crystal monochromators along a line of the crystal face in the diffracting plane: graphite (00.2) (●) and quartz (10.1) (○). The diameter of the pinhole beam has been of order 0.1 mm.

#### 4. Elastic and Nearly Elastic Scattering

##### 4.1. Kinematical theory

The preceding discussion implied that in practice the coherent part of the scattering Bragg, disorder and thermal diffuse, is detected together. Their separation is based on differences in the angular behavior, which, in turn, is derived from a model for diffraction from the powder sample. In the following, we will consider the general properties of these components and the practical possibilities of separating them.

The coherent scattering from a modulated structure can be divided into two parts: that from the average structure,  $I_1(k)$ , and that from the distortions,  $I_2(k)$ . In the kinematic approximation of diffraction [14], in electron units,

$$I_1(k) = |\overline{F(k)}|^2 \sum_{m=0}^{\infty} v(r_m) e^{ik \cdot r_m} = \frac{|F(k)|^2}{V V_c} |S(k - k_{hk1})|^2 \quad (3a)$$

$$I_2(k) = \sum_{m=0}^{\infty} \phi_m(k) v(r_m) e^{ik \cdot r_m} = \frac{|S(k)|^2}{V} * I_2'(k), \quad (3b)$$

where  $r_{\tilde{m}}$  is the separation between two unit cells,  $V$  is the volume of the crystal, and  $V_c$  that of the average unit cell. The structure factor of the average crystal,  $F(\tilde{k})$ , and that of the modulation,  $\phi_m(\tilde{k})$ , are defined by

$$F_n(\tilde{k}) = \overline{F(\tilde{k})} + \phi_n(\tilde{k}) ; \quad \phi_m(\tilde{k}) = \overline{\phi_n \phi_{n+m}} . \quad (4)$$

$V(\tilde{r})$  is the autocorrelation function of  $s(\tilde{r})$ , the shape function of the crystal, and  $S(\tilde{k})$  is the Fourier transform of  $s(\tilde{r})$ . The Bragg reflections are centered at  $k_{\text{hkl}}$ , and their profile is given by  $S(\tilde{k})$ . It is worth noting that the diffuse scattering from an infinite crystal,  $I_2^1(\tilde{k})$ , is convoluted by the same profile function  $S(\tilde{k})$ . Also, the effects of varying  $k_1$  and  $k_2$  (beam divergences) can be included in  $S(\tilde{k})$ .

In general, the coefficients  $\phi_m$  of the Fourier series expansion of  $I_2^1(\tilde{k})$  are functions of  $\tilde{k}$

$$I_2^1(\tilde{k}) = \sum_{m=0}^{\infty} \phi_m(\tilde{k}) e^{i\tilde{k} \cdot \tilde{r}_m} , \quad (5)$$

which means that  $I_2^1(\tilde{k})$  is only quasi-periodic in  $\tilde{k}$ . Suppose, however, that we can find a function  $\Psi(\tilde{k})$  such that  $I_2^1(\tilde{k}) = I_2^1(\tilde{k})/\Psi(\tilde{k})$  is periodic in  $\tilde{k}$ . If there are essentially different contributions to  $I_2^1(\tilde{k})$ , division to a few terms may be useful;  $I_{2j}^1(\tilde{k})/\Psi_j(\tilde{k})$ , so that the functions  $\Psi_j(\tilde{k})$  would be smooth. For instance, these could account for the contributions of different vibration modes to the total TDS. The Fourier coefficients  $\phi_m^1$  which are independent of  $\tilde{k}$  are

$$\phi_m^1 = \frac{V_c}{(2\pi)^3} \int_{V_c^*} I_2^1(\tilde{k}) e^{-i\tilde{k} \cdot \tilde{r}_m} d^3\tilde{k} , \quad (6)$$

and

$$\phi_m(\tilde{k}) = \Psi(\tilde{k}) \phi_m^1 , \quad (7)$$

where the integration is over the reciprocal unit cell  $V_c^* = (2\pi)^3/V_c$ . The first term in the series (6) is

$$\phi_0(\tilde{k}) = \Psi(\tilde{k}) \frac{V_c}{(2\pi)^3} \int_{V_c^*} I_2^1(\tilde{k}) d^3\tilde{k} , \quad (8)$$

and if the average value of  $I_2''(\underline{k})$  is normalized to unity,

$$\phi_0(\underline{k}) = F_n(\underline{k})F_n(\underline{k}) - F(\underline{k}) F(\underline{k}) = \Psi(\underline{k}) . \quad (9)$$

In the following, we will exclude substitutional disorder, and accordingly for thermal motion and homogeneous strains

$$\phi_0(\underline{k}) = \overline{|F(\underline{k})|^2} - |F(\underline{k})|^2 . \quad (10)$$

In this case, the diffuse intensity from a disordered structure consists of a periodic function  $I_2''(\underline{k})$  modulated by  $\phi_0(\underline{k})$ , which covers the variation of the structure factor from one reciprocal unit cell to another. For the TDS, the relevant parameters of  $\phi_0(\underline{k})$  are the amplitude ratios of the various vibration modes: for a specific example see [15].

The integral value of a Bragg reflection  $hkl$  is

$$\frac{1}{(2\pi)^3} \int_{V_c^*} I_1(\underline{k}) d^3k = \frac{1}{V_c} \overline{|F(\underline{k}_{hkl})|^2} . \quad (11)$$

An approximation for the diffuse scattering is obtained by taking  $\phi_0(\underline{k})$  at  $\underline{k}_{hkl}$ ,

$$\frac{1}{(2\pi)^3} \int_{V_c^*} I_2'(\underline{k}) d^3k = \frac{1}{V_c} \overline{|F(\underline{k}_{hkl})|^2} - \frac{1}{V_c} |F(\underline{k}_{hkl})|^2 . \quad (12)$$

This indicates that the Bragg plus diffuse scattering approximately equals to the scattering from the undistorted structure (cf. [16]).

#### 4.2. Powder TDS and multiple scattering

It is rather difficult to describe the scattering from static distortions without some specific model, whereas the features of the TDS are common to all crystalline solids. In the harmonic approximation, the first order term of  $I_2''(\underline{k})$  is proportional to  $E_j(\underline{q})\omega_j^{-2}(\underline{q})$ , where  $E_j(\underline{q})$  is the energy of the mode of angular frequency  $\omega_j(\underline{q})$  and wave-vector  $\underline{q}$ . For a crystal with  $n$  atoms in the primitive unit cell, three of the branches  $j$  are acoustic with  $\omega_A(\underline{q}=0) = 0$ , and  $3(n-1)$  are optic with  $\omega_0(\underline{q}=0) \neq 0$ . The acoustic vibrations make the TDS to peak at the reciprocal lattice points, while the contribution from the optic modes varies slowly with  $\underline{q}$ , as well as that from the processes where two or more phonons are involved.

The spherical averaging which takes place in powder diffraction is illustrated in figure 5. This smooths  $I_2''(\underline{k})$  appreciably, but the peaks at  $\underline{k}_{hkl}$  persist. The number of the reciprocal lattice points that contribute to  $I_2''(\underline{k})$  increases with  $\underline{k}$ , and the peaking part of  $I_2''(\underline{k})$  becomes less pronounced; also the increase of the multi-phonon processes has a similar effect. Figure 6 shows the result of a calculation for a mono-atomic fcc crystal. In the

general case of many atoms per cell, this would represent only the fluctuating part of  $I_2''(k)$ , which lies on the top of the smooth contributions to  $I_2''(k)$ . The average value,  $I_2''(k) = 1$ , is also shown in the figure.

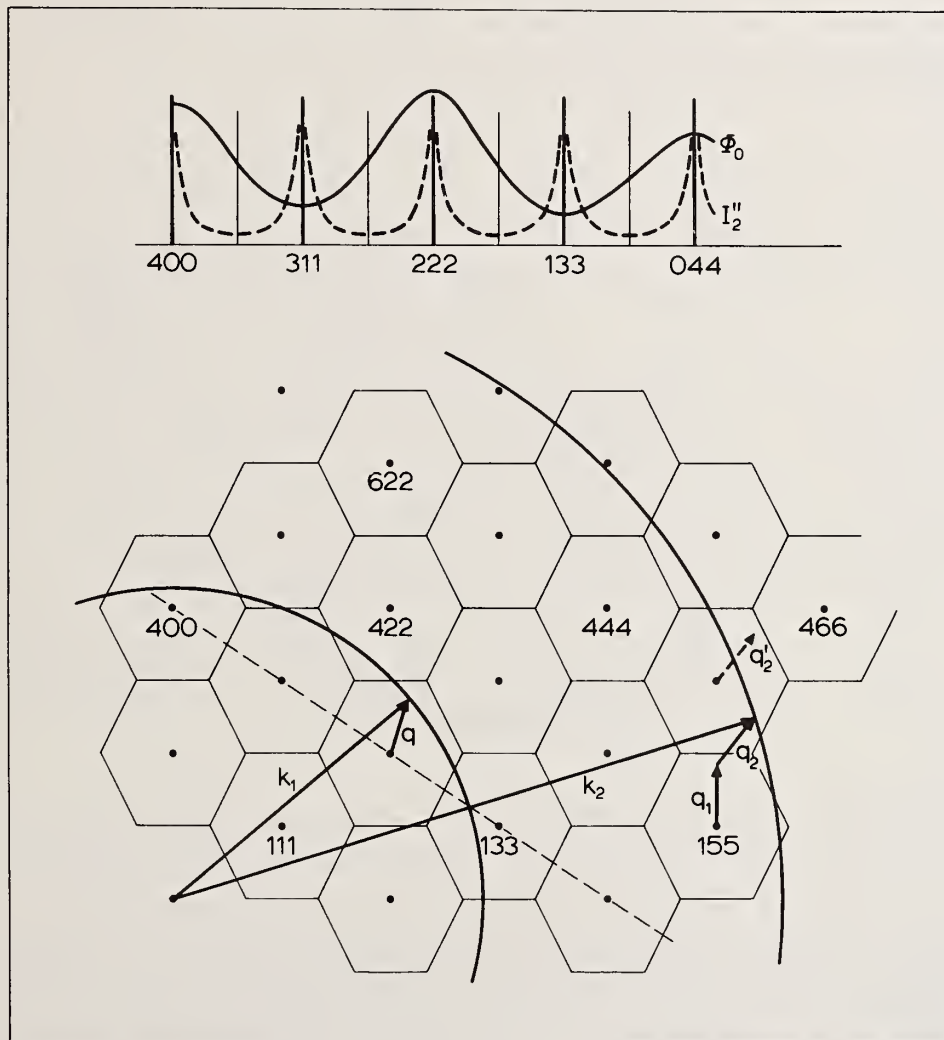


Figure 5. (011) plane in the reciprocal lattice of the fcc crystal. The Brillouin zones are marked with thin lines. Powder averaging is indicated by the circles of radii  $k_1$  and  $k_2$ . Vector  $q$  shows one-phonon TDS at  $k_1$  and  $q_1 + q_2$  a two-phonon contribution at  $k_2$ . The insert shows schematically the TDS functions for an NaCl-type crystal along the broken line.

For the general behavior of  $I_2''(k)$  also the spherical average of  $\phi_0(k)$  is to be calculated. The result is the Debye equation for the difference of scattering of one distorted unit cell from that of one perfect cell,

$$\phi_0(k) = \sum_j^n \sum_i^n f_j(k) f_i(k) \{1 - e^{-M_j - M_i}\} \frac{\text{sinkr}}{kr}, \quad (13)$$

9

where  $f$  is the atomic scattering factor,  $M$  the Debye-Waller factor, and  $r = r_j - r_i$ . At large values of  $k$ , the terms  $i \neq j$  become small, and

$$\phi_0(k) \rightarrow \sum_j f_j^2(k) \{1 - e^{-2M_j}\}, \quad (14)$$

which approximates the average value of  $I_2'(k)$ .

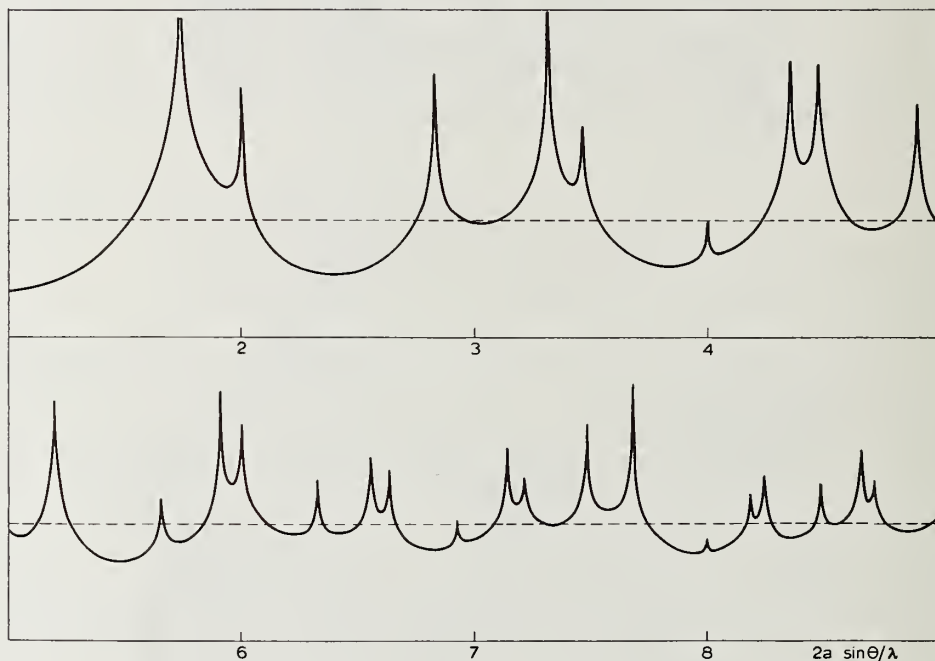


Figure 6. The powder TDS,  $I_2''(k)$  from acoustic phonons for the fcc structure. The parameters are those of Ni. The broken line indicates the average value.  $I_2''(k)$  is singular at the reciprocal points, but the peaks are rounded off by the convolution with the instrument function.

Now we will turn to the practical problem of separating the background from the Bragg reflections. Suppose that all other components but the TDS have been subtracted by energy analysis or by calculation from independently known scattering cross sections. This latter approach requires an absolute measurement of the scattered intensity, and this is supposed to be the case also in the following analysis.

The Bragg reflections lay on the top of an intensity distribution exemplified in figure 6, although the sharp peaks are rounded off due to limited resolution. It is clear that some fraction of the TDS peaks is counted with the Bragg intensity, if a straight background line is assumed. On the other hand, the tails of the reflections may extend a few degrees to both sides of the peaks and they begin to overlap even at moderate values of

hkl. Therefore, the real problem of background subtraction is often that of finding the correct level of the background, and to this end the average  $I_2'(k)$  suffices.

Utilization of eq. (13) or (14) requires a knowledge of the thermal vibration parameters,  $B_j = M_j/(\sin\theta/\lambda)^2$ , but in a typical case they are among the parameters to be determined from the powder pattern.  $\phi_0(k)$  can be determined at small or intermediate angles and extrapolated to the large angles, but the problem is that  $f_j(k)\exp(-M_j)$  is a function of both  $k$  and  $j$ . At high enough temperatures  $E_j(q) \cong k_B T$ , and the average  $B$  is proportional to  $T$  in the harmonic approximation. Accordingly, measurements at two temperatures would yield the correct separation between the TDS and Bragg scattering. This method has been used for determination of the  $B$ -values with good results [17]. However, many important cases are excluded because of large anharmonic effects or phase transitions. Perhaps, the best experimental method for finding the background level is a measurement on a well crystallized powder sample. Here, the limiting factor is the instrumental broadening of the Bragg reflections.

The correction for the included TDS is based on a calculation of the scattering from the acoustic phonons. The minimum information for the calculation is an approximate knowledge of the elastic constants. The sharp maxima at the Bragg peak positions are rounded off by the convolution with the profile function. An estimate for the fractional correction to the integrated Bragg reflection is given by the Chipman-Paskin formula [18], which is valid for well separated reflections. A formula which may be applied to crystals with more than one atom in the primitive unit cell is given by [19];

$$\alpha = \frac{8\pi k_B T}{\rho} \frac{\Delta(2\theta)\cos\theta}{\lambda v_t^2} \frac{\sin\theta}{\lambda^2}, \quad (15)$$

where  $\Delta(2\theta)$  is the width of the scan in rad,  $\rho$  is the density of the diffracting material, and  $v_t$  the average velocity of the transverse long-wavelength acoustic phonons. To give an idea of the magnitude of the correction we substitute typical values as  $k_B T \cong 4.10^{-23}$  J,  $\rho \cong 4.10^3$  kgm<sup>-3</sup>,  $v_t \cong 2.10^3$  ms<sup>-1</sup>,  $\Delta(2\theta)\cos\theta \cong 0.05$ ,  $\lambda \cong 1.5$  Å. This results in  $\alpha \cong 0.2$  Å<sup>2</sup>  $(\sin\theta/\lambda)^2$ . This is of the same form as the temperature factor,  $M$ , and if the TDS correction is ignored, the average  $B$ -value would be too small by about  $0.1$  Å<sup>2</sup> in the present example.

The above calculation was for the case where the reflections could be separated completely from the background, and the included TDS was the peak above the straight background line. The use of the average TDS as the background may compensate the correction for the TDS to a large extent. This is illustrated in figure 7. This compensating effect occurs when the reflections are wider than the TDS peaks above the average value. Evidently, this balancing becomes exact when the overlap of the peaks is large enough to make  $I_1(k) + I_2(k)$  everywhere larger than the average TDS. However, sharing of intensity between the reflections is not usually correct, particularly when strong and weak reflections are next to each other. The neutron case is more favorable, as phonons which are faster than the neutrons do not contribute to the TDS peak.

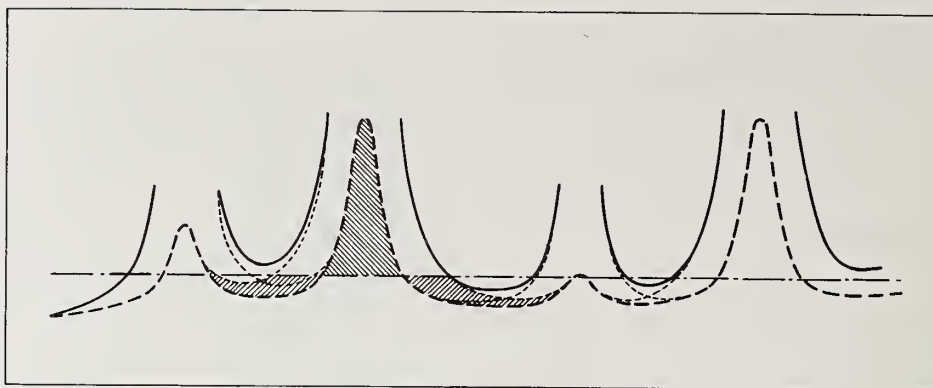


Figure 7. Separation of the background and correction for the included TDS. Total scattering is marked by the solid line, TDS by the broken line, and resolving to individual reflections by the dotted line. The partial compensation of the included TDS by the tails of the reflection below the average background line (-.-) is indicated by shading.

The x-ray photons that are scattered more than once in the sample cause another contribution to the observed radiation. In case that most of the scattering is only slightly modified, the calculation is reduced to a geometrical problem, where the single scattering is used as input [20]. Typically, there are small peaks plus a smooth contribution, which can be ignored in most cases. However, if the absorption coefficient is small and the sample large, the contribution to the total scattering may be large enough to deserve a detailed calculation.

The analytical approach to the total x-ray scattering is used very seldom, although in many cases data is available for a complete calculation. It has been demonstrated that the x-ray scattering can be resolved to identified components without a remainder through an energy analysis and with sufficient knowledge of the lattice dynamics of the crystal [21]. From the practical point of view, an important result of this analysis is that the actual widths of the reflections are very large, typically of the order of  $5^\circ$  in  $2\theta$ . More fundamentally, comparison of the reflection profiles and the integrated intensities reveals deviations from the predictions of the kinematical theory.

The analysis of the background even in the simplest form where only the average TDS is calculated requires a knowledge of the absolute scale of the intensity. It can be estimated on the basis of the kinematical theory, but it is far more preferable to determine the scale experimentally. The primary flux of the x-ray photons can be measured with a set of calibrated foils [22], or with a reference scatterer, such as the standard Ni sample for  $\text{CuK}\alpha$  radiation [21].

## 5. Powder Pattern Synthesis

In the synthetic methods, the profiles of the Bragg reflections are "known," and the reflections are separated from the background and from each other by the least squares

fitting of the superposition of these profiles to the experimental pattern. This method was first applied to the neutron diffraction patterns [23,24], and in recent years several studies of x-ray case have been published [25-27]. Typically, the output includes cell dimensions, atomic positions, and anisotropic thermal vibration parameters. The main problems of the method are separation of the background and finding the correct profile function, and some of the results are very sensitive to the choices made.

### 5.1. Separation of background

Profile fitting presumes that the Bragg peaks are superimposed on a constant or slowly varying background. We have seen that the actual background is not smooth, and so the fitted pattern is always affected by the TDS to some extent. The peaking part of the TDS is included in the profile function, and part of the correction for the TDS is taken care by the use of the average TDS as the background level. However, the integrated intensity of an individual reflection may be in error by an amount comparable with  $\alpha$  from eq. (15).

In the actual fitting procedures, the background is determined at a few scattering angles on the basis of visual examination of the pattern, and linear interpolation is used between these points. The selected background level depends on the assumed profile of the powder reflections; for instance, if a Gaussian profile is assumed, the background level should be found at a distance of 1.5 to 2 times the FWHM from the peak. The relation between the background level and the profile function can be made explicit by including the background level in the parameters to be refined [28].

The correct background level can be found if the behavior of the tails of the reflections is known. The particle size effects are specific to the sample, but in many cases even the tails of the reflections are determined by the instrumental factors. In such a case, the profile function for a given instrument can be extrapolated from a few carefully studied test cases.

### 5.2. Profile function

The actual profile can be found only through the analytic approach described earlier. Various functions have been compared with the experimental powder profiles [29-32], but sufficient attention to the separation of the tails from the background has not been paid. Scattering of  $\text{CuK}\alpha$  radiation from Ni powder was analyzed very carefully in order to give an example of the possibilities of the powder method [21]. The various components were subtracted from the total one by one, and at the end only the Bragg reflections were left on a small residual background of amorphous scattering. This data can be used for an analysis of the profile functions without the ambiguity arising from the unknown background level. Also the scattering of 1.51 Å neutrons from the same powder was measured and the background was determined on the basis of the x-ray profiles. Furthermore, the x-ray profiles were deconvoluted by the instrument function in order to reveal the effects of particle size and strain. A few examples are shown in figure 8.

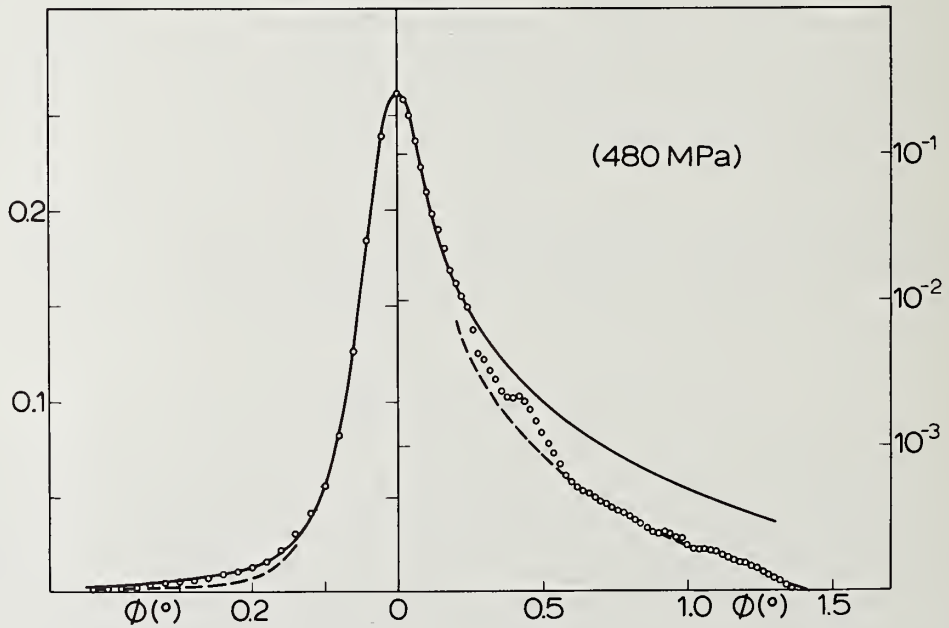
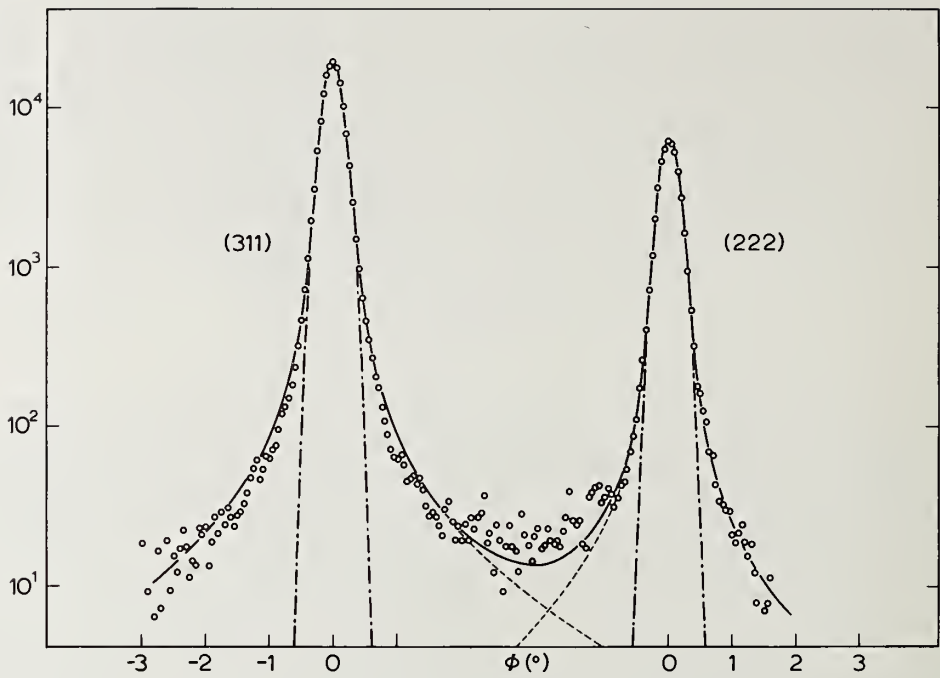


Figure 8. Neutron and x-ray reflections from Ni powder on arbitrary scales. In the neutron case reflections 311 and 222 are shown in the logarithmic scale, the full line is the Voigtian fit, where the individual contributions are shown by the dotted lines, and the dash-dotted line is the Gaussian fit. The symmetrized x-ray reflection 111 from a sample pressed at 480 MPa is shown in linear and logarithmic scales. The full line is the Voigtian fit and the broken line the Lorentzian fitted to the  $L^{-1}\phi^{-2}$  tail of the reflection.

The peak part of the reflection profile is broadened by the lattice strains, but this broadening may be masked by the instrumental factors. In practice, convolution of the various effects results in a shape that can be approximated by a Gaussian. According to the kinematical theory the tails of the reflections fall off as  $L^{-1}\phi^{-2}$ , where  $L$  is a characteristic dimension of the crystallites and  $\phi = \Delta(2\theta)$  is the angular distance from the center of the reflection. Also the effects of the other factors may extend to this region. Inclusion of the TDS above a straight background line affects the tails, and at least in neutron diffractometry the instrumental effects are seen in the tails, too. This gradual change from the Gaussian peak to a long, Lorentzian type tail is covered by the Voigtian, which is the convolution of the Gaussian and the Lorentzian [33,34]. The examples of figure 8 demonstrate that a very close fit is achieved down to an intensity level of  $10^{-2}$  to  $10^{-3}$  times the peak intensity, and that the improvement over the customarily used Gaussian is clear in the tails of the reflections. The deviations in the x-ray case show, however, that strain and particle size effects cannot be simultaneously parametrized by the Voigtian. The tail is of form  $L^{-2}\phi^{-2}$  with  $L = 1000 \text{ \AA}$ , and the shape between  $0.1^\circ$  and  $0.5^\circ$  is mostly due to strains. The crystallites are understood to be about  $1000 \text{ \AA}$  diameter but appreciably strained at the same time.

The good description of the neutron diffraction profiles of Ni encouraged us to study a number of other cases, although a similar analysis of the background was not possible. The parameters that determine the Voigtian, the FWHM and the integral width, turned out to be typical to the instrument used (fig. 9). At least in this case, it looks feasible to use the Voigtian as the profile function and even to include the background level in the parameters being refined, although the convergence of such a procedure must be studied carefully. In any case, it is obvious that the improved profile function will make the sharing of intensity between the reflections much more correct, particularly when strong and weak reflections are closely spaced.

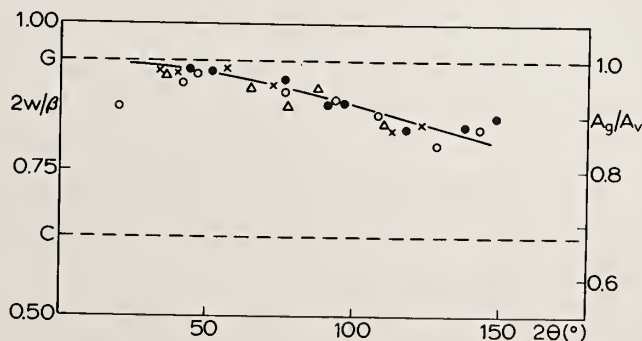


Figure 9. The ratio of the FWHM to the integral width,  $2w/\beta$ , of powder reflections measured with  $1.38 \text{ \AA}$  to  $1.91 \text{ \AA}$  neutrons from various compounds. The broken lines indicated by G and C show the values of  $2w/\beta$  for a pure Gaussian and a pure Cauchy (Lorentzian) profile, respectively.  $A_g/A_v$  is the ratio of the area under the Gaussian to that under the Voigtian, when the peaks and FWHM's coincide. The solid line is a fit of form  $A_g/A_v = \exp(-2\Delta B \sin^2 \theta / \lambda^2)$  to the filled dots measured for Ni.

## 6. Thermal Motion Parameters

The reduction of the Bragg intensity with the increasing temperature can be related to the vibration amplitudes of the atoms through the harmonic approximation. The integrated counts of a reflection in the ideal powder approximation is

$$n_{hkl} = n_0 r_e^2 \frac{\psi K_{pol} \lambda^3 p_{hkl}}{8\pi V_c^2 \sin^2 \theta_{hkl} \sin^2 \theta_{hkl}} A_{hkl} |\overline{F_{hkl}}|^2, \quad (16)$$

where  $n_0$  is the incident photon (neutron) flux,  $\psi$  the planar angle intercepted by the slit height,  $K_{pol}$  the polarization factor, and  $p_{hkl}$  the multiplicity. The absorption factor  $A_{hkl}$  depends on the geometry and

$$\overline{F_{hkl}} = \sum_j (f_j + f'_j + if''_j) \exp\{-\sum \beta_{\mu\nu} h_\mu h_\nu\}, \quad (17)$$

where  $h_\mu$  is used for the Miller indices  $h, k, l$ . In the neutron case  $r_e$  is substituted by unity, and  $f_j$  by  $b_j$ , the nuclear scattering length. In the following, we will study a cubic metal with one atom per the primitive unit cell, and so  $\beta_{\mu\nu} = \beta \cdot \delta_{\mu\nu} = B/4a^2$ , where  $a$  is the lattice constant.

The thermal parameter  $B$  can be determined from an absolute measurement of  $n_{hkl}$  provided that  $f$  (or  $b$ ) is known, or  $B$  can be evaluated from a comparison of the relative values of many integrated reflections. In the case of Ni, we can compare the results obtained by different methods. These include absolute x-ray measurements on ten different samples and three types of analysis of relative neutron measurements from the same powder.

The x-ray intensities are affected by the specimen granularity, preferred orientation and primary extinction. The effects of the first two could be corrected experimentally, and extinction-free values could be extrapolated from the measurements on different samples. The background was separated through the analysis described earlier. Although large, the correction for anomalous dispersion,  $f'$ , is known accurately from the interferometric measurements [35]. The specimen effects are negligible in the neutron case, and the only problem is the separation of the background. There is no need for the TDS correction as almost all phonons are faster than the 1.51 Å neutrons. The reflections were integrated point by point and from the fitted profile functions. The actual fit was made only with the Gaussian and the difference to the Voigtian was estimated from the ratio of the integral values,  $A_g/A_v$ , taken from figure 9.

The results of table 1 show that a careful analysis of the background leads to a good consistency of the x-ray and neutron values. Also the agreement with the theoretical and most of the other experimental values is close. The remarkable features are the failure of the Gaussian fit and the success of the Voigtian. This difference is due to the tails of the reflections, because the same background was assumed.

Table 1. The harmonic thermal motion parameter, B, for Ni.

Method	B ( $\text{\AA}^2$ )	
powder, 1.542 $\text{\AA}$ x-rays	$0.34 \pm 0.02$	present, absolute f-values
1.51 $\text{\AA}$ neutrons	$0.34 \pm 0.02$	present, relative b-values
	0.46	present, Gaussian fit
	0.32	present, Voigtian fit
calculation, force constant model	0.381	Barron and Smith [36], from phonon dispersion data
powder, 0.709 $\text{\AA}$ x-rays	0.386	Paakkari [17], two temperatures
powder, 0.709 $\text{\AA}$ x-rays	0.37	Inkinen and Suortti [37], relative f-values
powder, 0.8 to 1.5 $\text{\AA}$ neutrons	0.426	Cooper and Taylor [38]
powder, neutrons, TOF	0.34	Windsor and Sinclair [39]

## 7. Discussion

The preceding chapters have centered on the problem of separating the Bragg scattering from the other radiation recorded by the detector. An exhaustive analysis is feasible only in the simplest cases, but these may serve as indispensable reference points for studies of complicated compounds. It has been found that the actual widths of the powder reflections are typically several degrees, and so the real problem is finding the correct background level. Quite little information is needed for an approximate calculation of this level if the absolute scale of intensity is determined. It is emphasized that it is very little additional effort to obtain absolute values rather than accurate relative values. From the synthetic point of view, it may be possible to find profile functions which are correct enough to allow separation of the tails of the reflections from the background. Again, the results of this approach must be tested in cases where also the analytic approach is possible.

When the reliability of the integrated Bragg reflections improves, the problem becomes that of conversion of the scattering power to physically meaningful parameters. The Bragg scattering is affected by departures from the conditions of the ideal powder sample, which is assumed in the derivation of eq. (16). The powder particles of the actual sample are not independent and randomly oriented, and they do not consist of small perfect crystallites. There are correction methods for the effects of granularity and preferred orientation, although they require tedious subsidiary measurements. On the other hand, there is no adequate diffraction theory for a sample where the crystallites are large enough to cause primary extinction and are strained at the same time, and which contains also amorphous material between the crystallites. The effects of these deviations are seen in the x-ray profile of figure 8, and they have been analyzed more thoroughly elsewhere [21]. In a

typical case, the F-values obtained by a straightforward application of eq. (16) may be in error by several percent. Considering the other limitations of the powder method, this may not be much, but even at the moment powder data is used for evaluating values of physical parameters which are sensitive to errors in F. It is hoped that some of the present activity with the practical aspects of powder diffractometry will be directed to the fundamental problems of the method.

---

The author wishes to thank Dr. L. D. Jennings for many years of collaboration and for putting forward many of the ideas presented in this paper.

#### References

- [1] Eisenberger, P., Platzman, P. M., and Winick, H., Phys. Rev. B13, 2377-2380 (1976).
- [2] Eisenberger, P., Platzman, P. M., and Winick, H., Phys. Rev. Letters, 36, 623-626 (1976).
- [3] Bannett, Y. B., Rapaport, D. C., and Freund, I., Phys. Rev. A16, 2011-2021 (1977).
- [4] Suortti, P., Phys. Stat. Solidi. (b) 91, 657-666 (1979).
- [5] Eisenberger, P. and Platzman, P. M., Phys. Rev. A2, 415-423 (1970).
- [6] O'Connor, D. A. and Butt, N. M., Phys. Lett. 7, 233-235 (1963).
- [7] Albanese, G. and Ghezzi, C., Phys. Rev. B8, 1315-1323 (1973).
- [8] Bärnighausen, E., J. Appl. Cryst. 11, 221-228 (1978).
- [9] Paakkari, T. and Suortti, P., Phys. Rev. B9, 1756-1761 (1974).
- [10] Berreman, D. W., Rev. Sci. Instrum. 26, 1048-1054 (1955).
- [11] Berreman, D. W., Stamatoff, J., and Kennedy, S. J., Appl. Optics, 16, 2081-2085 (1977).
- [12] Hastings, J. B., Kincaid, B. M., and Eisenberger, P., Nucl. Instr. Methods, 152, 167-177 (1978).
- [13] Lemonnier, M., Fourme, R., Rousseaux, F., and Kahn, R., Nucl. Instr. Methods, 152, 173-177 (1978).
- [14] Guinier, A., X-ray Diffraction (W. H. Freeman, San Francisco, 1963).
- [15] Smith, T., in Phonons in Perfect Lattices and in Lattices with Point Imperfections, R. W. H. Stevenson, ed., chap. 6, (Oliver and Boyd, Edinburgh, 1966), pp. 161-169.
- [16] LaFleur, P. L. G. M., Acta Cryst. A26, 674-678 (1970).
- [17] Paakkari, T., Acta Cryst. A30, 83-86 (1974).
- [18] Chipman, D. R. and Paskin, A., J. Appl. Phys. 30, 1998-2001 (1959).
- [19] Haav, A. A., Peljo, E., and Surotti, P., Phys. Stat. Solidi. (b) 80, 255-264 (1977).
- [20] Suortti, P., Phys. Fenn. 10, 161-166 (1975).
- [21] Suortti, P. and Jennings, L. D., Acta Cryst. A33, 1012-1027 (1977).
- [22] Chipman, D. R., Acta Cryst. A25, 209-214 (1969).
- [23] Rietveld, H. M., J. Appl. Cryst. 2, 65-71 (1969).

- [24] Hewat, A. W., J. Phys. C 6, 2559-2572 (1973).
- [25] Werner, P.-E., Ark. Kem. 31, 505-511 (1970).
- [26] Young, R. A., Mackie, P. E., and Von Dreele, R. B., J. Appl. Cryst. 10, 262-269 (1977).
- [27] Ayers, G. L., Huang, T. C., and Parrish, W., J. Appl. Cryst. 11, 229-233 (1978).
- [28] Sabine, T. M. and Clarke, P. J., J. Appl. Cryst. 10, 277-280 (1977).
- [29] Malmros, G. and Thomas, J. O., J. Appl. Cryst. 10, 7-11 (1977).
- [30] Hall, M. M., Veeraraghavan, V. G., Rubin, H., and Winchell, P. G., J. Appl. Cryst. 10, 66-68 (1977).
- [31] Rondot, D. and Mignot, J., J. Appl. Cryst. 10, 84-90 (1977).
- [32] Khattak, C. P. and Cox, D. E., J. Appl. Cryst. 10, 405-411 (1977).
- [33] Langford, J. I., J. Appl. Cryst. 11, 10-14 (1978).
- [34] Suortti, P., Ahtee, M., and Unonius, L., J. Appl. Cryst. 12, in press (1979).
- [35] Bonse, U. and Materlik, G., Z. Physik, B24, 189-191 (1976).
- [36] Barron, T. H. and Smith, T., J. Phys. Chem. Solids, 27, 1951-1952 (1966).
- [37] Inkinen, O. and Suortti, P., Ann. Acad. Sci. Fenn. A VI, 147 (1964).
- [38] Cooper, M. J. and Taylor, R. I., Acta Cryst. A25, 714-715 (1969).
- [39] Windsor, C. G. and Sinclair, R. N., Acta Cryst. A32, 395-409 (1976).

#### Discussion

Question (Kuriyama): Regarding the flux conservation within a reciprocal unit cell when diffuse scattering exists, I believe that statement holds only for small momentum transfers within a reciprocal unit cell.

Response (Suortti): Yes, this is consistent with replacing the structure factor, of the disorder scattering by its value at the center of the Brillouin zone in the approximate formula of the conservation of scattering.

Comment (Langford, Mittemeijer, and DeKeijser): For Dr. Suortti's paper it is shown that a Voigt function may provide a significant improvement in profile fitting, as compared to the functions formerly used. Also this function incidently does not provide a complete description of the tails of the profile in case of pure size broadening. Thus from the "Voigt" tail an erroneous value for the crystallite size is obtained. We would like to remark that if a quick estimate of size and strain values is to be obtained from line breadths, then the method using Voigt functions (J. I. Langford, this conference) can give valuable results, since the size-strain parameters are not solely obtained from the tails of the profiles. However, if the detailed shape of the profile is taken into account (e.g. as in the Fourier and Variance methods) any assumption on the shape of the profile is avoided.

Response (Suortti): The author agrees that the bulk of the information of size and strain of the powder crystallites is contained in the intense part of the reflection. However,

the use of the tails of the reflections has some advantages. First, that part is not critically affected by the inaccuracies of the deconvolution procedures. Second, the size effect can be isolated from the tails of the reflection without any assumptions of the type of the strain, and this is a very concrete measure of the mosaic crystal model, namely the average thickness of the diffracting crystallites. A fuller discussion of this aspect is given in reference [21].

Comment (Kuriyama): In your characterization of the background scattering, you have identified x-ray Raman scattering as resonant Raman. I would like to remind you, however, that there is a Raman scattering which does not require the resonant conditions: that is the Raman scattering caused by the  $A^2$  interaction term in the Hamiltonian.

Response (Suortti): It is true that there is also a Raman scattering contribution to the non-resonant scattering. However, this is very small, and has been neglected in the present study. The resonant Raman scattering arises from the  $\bar{A} \cdot \bar{p}$  interaction taken twice, and it increases rapidly when the resonant condition is approached from below going over to fluorescence at the absorption edge.

## NEUTRON DIFFRACTION--THE TOTAL POWDER PATTERN

T. M. Sabine

Institute of New South Wales of Technology

P. O. Box 123

Broadway, New South Wales

Australia 2007

### 1. Introduction

Neutrons are of particular use in the study of solids, liquids and gases because of the following basic properties:

- (i) The thermal neutron wavelength is comparable to the interatomic spacing. Hence, there will be pronounced interference effects when neutrons are scattered by condensed atomic systems;
- (ii) The change in neutron energy from inelastic processes involving the creation and annihilation of excitations in condensed matter are of the order of the incident neutron energy;
- (iii) The neutron has a magnetic moment. This gives it a unique value in probing the magnetic structure and magnetic dynamics of atomic systems;
- (iv) The neutron is a neutral particle. Because of this it can penetrate deeply into matter;
- (v) Neutrons are a gentle wind, compared with the strong breeze of x-rays and the raging gale of electrons, in causing radiation damage in the systems under investigation.

As an experimental science, neutron diffraction started seriously in 1950 when neutron beam fluxes of about  $10^{12}$  n cm<sup>-2</sup> sec<sup>-1</sup> became available. The theoretical basis had been laid by Halpern and Johnson [1]<sup>1</sup>, Weinstock [2], and Cassels [3].

The difficulty of obtaining quantitative information from single crystals due to the breakdown of the kinematical approximation in crystals sufficiently large for appreciable scattering to occur was noticed by the earliest workers [4]. To overcome these extinction effects Wollan and Shull [5] constructed a powder diffractometer. Powder methods gave accurate data for simple compounds, however the problem of overlap between closely spaced reflections precluded study of materials with large unit cells or low symmetry.

---

<sup>1</sup>Figures in brackets indicate the literature references at the end of this paper.

Many workers interested in the application of neutron diffraction to chemical compounds tried to reduce extinction effects or to correct for them. Early work was carried out by Bacon and Lowde [6] and Petersen and Levy [7].

These studies showed that the effects of extinction could be reduced by destroying the perfection of the crystal. Quenching or irradiation damage were favoured techniques [8]. The unfortunate result of these treatments is the introduction of dislocations, point defects and defect clusters, all of which produce appreciable diffraction effects and require explanation in a proper discussion of the structure.

Zachariasen [9] treated extinction in terms of a crystal containing perfect crystal blocks of a certain size and separated by a certain degree of misorientation. His equations were soon incorporated into the least squares refinement procedure with provision for anisotropic block sizes and anisotropic mosaic distribution [10]. Coppens and Sabine [11] used these equations in a refinement of the structure of oxalic acid dihydrate, however, in a direct examination of the same material by Lang topography [12], the dislocation density was found to be orders of magnitude less than that predicted by the results of the Zachariasen treatment. While these discrepancies exist there must be doubt about this solution to the extinction problem.

The powder method continued to be developed slowly, but its use was largely limited to magnetic systems. Studies of the optics of powder diffractometers were made by Cagliotti, Paoletti and Ricci [13] and by Sabine and Browne [14].

Rietveld [15] made a significant improvement in methods of analysis by realising that powder profiles closely followed a Gaussian form. He calculated the ordinates of the Bragg profiles and refined them against the observed pattern. This method, particularly after the development of high resolution neutron diffractometers [16], led to the satisfactory refinement of data from a large number of inorganic compounds [17] with accuracies in positional parameters comparable with those found from single crystal work.

Agreement for thermal parameters was far less satisfactory [18] and a treatment in which all the neutrons scattered by the specimen could be included in the refinement was given by Sabine and Clarke [19].

Development of the appropriate expressions for calculation of the ordinate of a powder pattern is the subject of this paper.

## 2. The Total Neutron Powder Pattern

### 2.1. Bragg scattering

In this analysis it will be assumed that a conventional two-axis powder diffractometer is being used. The monochromatic neutron beam is of sufficient size to completely bathe the specimen. The pattern is scanned by a counter which is fitted with a narrow slit. Typically, this slit subtends ten to twenty minutes of arc at the specimen position. The diffractometer arm moves in small steps of  $2\theta$  under the control of a monitor counter placed in the incident beam. The time spent at each  $2\theta$  position is  $t$ .

The total number of neutrons diffracted into a length  $h$  of the Debye-Scherrer ring, under these experimental conditions, is [20,21]

$$P = \frac{\phi_0 \lambda^3 h V \rho_c j N_c^2 F^2 e^{-2M}}{8\pi R \rho \sin \theta \sin 2\theta}$$

(a glossary of terms is given in table 1) .

To determine the ordinate of the profile at any point we will assume, following Lovelock [15], that the profile of a reflection is obtained by convoluting the above expression with a Gaussian broadening function of area unity. Because of the Maxwellian distribution of neutron velocities in the reactor moderator and the Gaussian distribution of mosaic blocks in the monochromator and the specimen, the profile is accurately Gaussian. The full width at half maximum intensity is given by

$$B = U \tan^2 \theta + V \tan \theta + W$$

where  $U, V, W$  are constants for a given experimental arrangement. The profile for Bragg scattering is then

$$I(2\theta) = \frac{\phi_0 \lambda^3 h V \rho_c j N_c^2 F^2 e^{-2M}}{8\pi R \rho \sin \theta \sin 2\theta} \frac{2}{B} \left( \frac{\ln 2}{\pi} \right)^{1/2} \exp \frac{4 \ln 2}{B^2} (2\theta_i - 2\theta)^2 .$$

$2\theta_i$  is the Bragg position for the  $i$ th reflection. It is assumed for the moment that there is no overlap between reflection profiles.

In an experiment the ordinate of the profile is measured by recording the number of neutrons received by the counter through a slit of width  $w$  in time  $t$ .

Then the Bragg component is given by

$$y_1(2\theta) = t \int_{2\theta - w/2R}^{2\theta + w/2R} I(2\theta) d(2\theta)$$

Using the approximation

$$\int_{x - \frac{\Delta x}{2}}^{x + \frac{\Delta x}{2}} a e^{-px^2} dx = a \Delta x e^{-px^2}$$

Table 1. Glossary of Terms

F	Structure factor per unit cell
$e^{-2M}$	Debye-Waller factor for intensities
b	Coherent scattering length
j	Multiplicity
$\lambda$	Wavelength
V	Specimen volume
$\rho'$	Measured density
$\rho$	Theoretical density
$V_c$	Unit-cell volume
$N_c$	Number of unit cells per unit volume
$\phi_0$	Incident flux (neutrons $m^{-2}s^{-1}$ )
h	Height of counter slit
w	Width of counter slit
s	Step size in $2\theta$
R	Specimen-to-counter distance
t	Time spent for each step
B	Full width at one-half maximum intensity
$y(2\theta)$	The number of neutrons recorded in the counter in time t
$C_i$	Site occupation factor for ith site
$f_i$	The magnetic form factor of the ith atom
$S_i$	The spin of the ith atom
$\Sigma$	Total cross section per unit cell

we obtain

$$y_1(2\theta) = \frac{\phi_0 \lambda^3 h w V \rho' j N_c^2 F^2 e^{-2M} a [\exp(-p x^2)] t}{8 \pi R^2 \rho \sin \theta \sin 2\theta}$$

where

$$a = \frac{2}{B} \left( \frac{\ln 2}{\pi} \right)^{\frac{1}{2}}$$

$$p = \frac{4 \ln 2}{B^2}$$

## 2.2. Diffuse scattering

If we assume  $\Sigma_D$  is the diffuse scattering cross-section per unit cell the number of neutrons received by the counter in time t will be

$$y_2(2\theta) = \frac{\Phi_0 h \omega t N_c V \rho'}{4\pi R^2 \rho} .$$

he total neutron count is then

$$y(2\theta) = \frac{\Phi_0 h \omega t N_c \rho' V}{4\pi R^2 \rho} \left\{ \frac{N_c \lambda^3 j F^2 e^{-2M}}{2 \sin \theta \sin 2\theta} a e^{-px^2} + \Sigma_D \right\} .$$

uperimposed on this count is the experimental background.

Measurement of all the quantities in front of the bracket will enable the data to be put on an absolute scale. In general we will put

$$K = \frac{\Phi_0 h \omega t N_c \rho' V}{4\pi R^2 \rho} .$$

### 2.3. Magnetic Bragg scattering

Scattering from ordered magnetic ions in the crystal is included through the magnetic structure factor which is given by [22]

$$F(\underline{k}) = \sum_j p_j(\underline{k}) \exp 2\pi i \underline{k} \cdot \underline{r}_j [\hat{t}_x(\hat{n}_j \times \hat{t})]$$

$$p_j(\underline{k}) = \frac{e^2 \gamma}{mc^2} \langle S_j \rangle f_j(\underline{k}) .$$

$\langle S_j \rangle$  is the average magnetic moment on the  $j$ th site,  $f_j(\underline{k})$  is the magnetic form factor of this atom,  $\hat{n}_j$  is a unit vector parallel to the direction of the  $j$ th spin,  $\hat{t}$  is a unit vector parallel to the scattering vector. When unpolarized neutrons are used there are no cross terms between nuclear and magnetic scattering and the intensities add. For polarized neutrons the structure factors add.

### 3. Evaluation of $\Sigma_D$

In a system exhibiting long range order, the diffuse scattering arises because of deviations from the average structure. These deviations can be compositional fluctuations (both chemical and isotopic composition) or random displacements from lattice points, or

### 3.1. Atomic short range order

The intensity scattered in the reciprocal lattice direction  $\vec{k}$  ( $k = \frac{2 \sin \theta}{\lambda}$ ) is given by

$$I(\vec{k}) = \sum_0^{N-1} \sum_0^{N-1} b_j b_{j'}^* \exp 2\pi i \vec{k} \cdot \vec{r}_j - \vec{r}_{j'}$$

where  $N$  is the total number of atoms in the crystal.

Following Wilson [23] we put

$$j' = j + m$$

hence

$$I(k) = \sum_{-(N-1)}^{N-1} (N-m) J_m \exp 2\pi i \vec{k} \cdot \vec{r}_m$$

where  $J_m$  is the average value of the structure factor product for sites separated by the vector  $\vec{r}_m$ .

To evaluate this average we consider a disordered AB alloy with concentration  $C_A$  of A and  $C_B$  of B. Set  $P_m^{AA}$  as the probability that  $\vec{r}_m$  joins two A sites,  $P_m^{AB}$  ( $= P_m^{BA}$ ) the probability that it joins an A site and a B site, and  $P_m^{BB}$  the probability that it joins two B sites then

$$J_m = b_A^2 P_m^{AA} + 2b_A b_B P_m^{AB} + b_B^2 P_m^{BB}$$

In terms of the Cowley [24] short range order parameters,  $\alpha_m$ , these probabilities become

$$P_m^{AA} = C_A(C_A + \alpha_m C_B),$$

$$P_m^{AB} = C_A C_B (1 - \alpha_m),$$

$$P_m^{BB} = C_B(C_B + \alpha_m C_A)$$

hence

$$J_m = (C_A b_A + C_B b_B)^2 + C_A C_B (b_A - b_B)^2 \alpha_m$$

Substituting back gives

$$I(\vec{k}) = (C_A b_A + C_B b_B)^2 \sum_{m=0}^{N-1} (N-m) \exp 2\pi i \vec{k} \cdot \vec{r}_m$$

$$+ C_A C_B (b_A - b_B)^2 \sum_{m=0}^{N-1} (N-m) \alpha_m \exp 2\pi i \vec{k} \cdot \vec{r}_m .$$

For large values of N the first term becomes Bragg scattering from the average lattice.  $\alpha_m$  will be non zero only for small values of m, the second term represents diffuse scattering and can be written

$$I(\vec{k}) = N C_A C_B (b_A - b_B)^2 \sum_m \alpha_m \exp 2\pi i \vec{k} \cdot \vec{r}_m .$$

For a powder pattern we must average over all directions of  $\vec{k}$  and obtain

$$I_D = N C_A C_B (b_A - b_B)^2 \sum_{m=1}^{\infty} c_m \alpha_m \frac{\sin 2\pi k r_m}{2\pi k r_m}$$

where  $c_m$  is the number of atoms in the mth shell and  $r_m$  is its radius. Hence

$$\sum_{SRO} = 4\pi I_D$$

where N is the number of atoms in the unit cell.

The cross-sections for several components of the pattern can be deduced from this expression.

### 3.2. Incoherent scattering

If  $b_1$  is the scattering length associated with the 1th isotope and spin state, then the contribution from incoherent scattering becomes ( $\alpha_0=1, \alpha_m=0$ )

$$\Sigma_{\text{incoh}} = 4\pi \left\{ \langle b_1^2 \rangle - \langle b_1 \rangle^2 \right\} .$$

### 3.3. Partial site occupancy

For systems with incomplete site occupancy

$$C_A = C_i \quad b_A = b; \quad C_B = (1-C); \quad b_B = 0$$

where  $C_i$  is the site occupancy factor chosen so that for  $C_i = 1$  all sites in all unit cells are occupied. Then

$$\Sigma_{\text{disorder}} = 4\pi \sum_{i=1}^n C_i(1-C_i) b_i$$

where  $n$  is the number of atoms in the unit cell.

This expression assumes that there is no correlation between vacant sites. If there is clustering of either vacancies or occupied sites modulated diffuse scattering of the form

$$\Sigma_{\text{disorder}} = 4\pi b^2 c(1-c) \sum_m \alpha_m c_m \frac{\sin 2\pi k r_m}{2\pi k r_m}$$

will appear for each atomic species. The cross sections will simply add if the ordering of each species is independent but, in general, cross terms could be expected.

### 3.4. Magnetic diffuse scattering

The treatment for systems in which the magnetic moment varies from site to site follows the treatment of composition fluctuations.

Assuming that the magnetic system is collinear and parallel to the  $z$  axis

$$I(k) = (1 - \tau_z^2) \sum_j \sum_{j'} p_j(k) p_{j'}(k) \exp 2\pi i k \cdot r_j - r_{j'}$$

Defining an AB alloy with  $C_A$  atoms of magnetic scattering factor  $p_A$  and  $C_B$  with scattering factor  $p_B$  a Bragg term containing the average scattering factor is obtained and the diffuse scattering is given by

$$\begin{aligned} \Sigma_{\text{Diffuse}}^{\text{magnetic}} &= 4\pi(1 - \tau_z^2) C_A C_B (p_A(k) - p_B(k)) \\ &\times \sum_m c_m \alpha_m \frac{\sin 2\pi k r_m}{2\pi k r_m} \end{aligned}$$

The first term reduces to the expression used by Shull and Wilkinson [25]. Marshall [26] has introduced short range order parameters to describe the perturbation of the moments on B atoms which are close neighbours of atoms of type A. These parameters are equivalent to  $\alpha_m$ .

### 3.5. Paramagnetic scattering

The appropriate cross-section is

$$\Sigma_{\text{para}} = \frac{8\pi}{3} \left( \frac{e^2 \gamma}{mc^2} \right)^2 \sum_{j=1}^n S_j (S_j + 1) f_j^2(k)$$

$j$  labels the magnetically active atoms in the unit cell.

### 3.6. Displacement disorder

The formalism of this problem is similar to that of the composition fluctuation problem. An atom can be displaced from a lattice site by a defect in the unit cell or by a large discrepancy in atomic size. Detailed calculations have been given by Warren, Averbach and Roberts [27] and by Borie [28,29].

These calculations lead to the expression

$$\Sigma_{\text{SE}} = 4\pi C_A C_B (b_A - b_B)^2 \left\{ \sum_m \alpha_m c_m \frac{\sin 2\pi k r_m}{2\pi k r_m} - \sum_m d_m \beta_m \left( \frac{\sin 2\pi k r_m}{2\pi k r_m} - \cos 2\pi k r_m \right) \right\}$$

where  $\alpha_m$  is the short range order coefficient and  $\beta_m$  the size effect coefficient.

### 3.7. Thermal diffuse scattering

At any temperature the intensity removed from the Bragg peaks by the Debye-Waller factor reappears as in elastic scattering in the diffuse background.

The simplest approximation to this term is based on the assumption that the atoms vibrate independently. With this assumption

$$\Sigma_{\text{TDS}} = \sum_{\text{unit cell}} 4 b_i^2 (1 - e^{-2M_i})$$

For simple structures it is possible to find expressions which recognize the correlation between atomic vibrations. Treatments have been given of correction to integrated intensities for the component of the TDS which peaks at the position of the Bragg peak [30].

Marshall and Lovesey [22] have given expressions in which the elastic and one-phonon terms are treated exactly and the multi-phonon terms approximated. These are not, at present, convenient for calculation, but could form the basis for a detailed treatment of the TDS contribution to the powder pattern.

#### 4. Conclusion

Expressions have been given for scattering mechanisms which contribute to the total powder pattern. Inclusion of these removes the necessity for a subjective estimate of the background.

Those quantities which are the result of local deviations from the average structure are included in the refinement process through their contributions to both the Bragg scattering and the diffuse scattering. A constraint that the total scattering is conserved can then be applied.

#### References

- [1] Halpern, O. and Johnson, M. H., On the magnetic scattering of neutrons, *Phys. Rev.* 35, 890-923 (1939).
- [2] Weinstock, R., The inelastic scattering of slow neutrons, *Phys. Rev.* 65, 1-20 (1944).
- [3] Cassels, J. M., The scattering of neutrons by crystals, *Prog. Nucl. Phys.* 1, 185-215 (1950).
- [4] Fermi, E. and Marshall, L., Interference phenomena of slow neutrons, *Phys. Rev.* 71, 666-677 (1947).
- [5] Wollan, E. O. and Shull, C. G., The diffraction of neutrons by crystalline powders, *Phys. Rev.* 73, 830-841 (1948).
- [6] Bacon, G. E. and Lowde, R. D., Secondary extinction and neutron crystallography, *Acta. Cryst.* 1, 303-314 (1948).
- [7] Peterson, S. W. and Levy, H. A., The use of single-crystal neutron-diffraction data for crystal-structure determination, *J. Chem. Phys.* 19, 1416-1418 (1951).
- [8] Sanger, P. L., An experimental determination of the ionic state of MgO by single-crystal methods, *Acta. Cryst. A* 25, 694-702 (1969).
- [9] Zachariasen, W. H., A general theory of x-ray diffraction in crystals, *Acta. Cryst.* 23, 558-564 (1967).
- [10] Coppens, P. and Hamilton, W. C., Anisotropic extinction corrections in the Zachariasen approximation, *Acta. Cryst. A* 26, 71-83 (1970).
- [11] Coppens, P. and Sabine, T. M., Neutron diffraction study of hydrogen bonding and thermal motion in deuterated  $\alpha$  and  $\beta$  oxalic acid dihydrate, *Acta. Cryst. B* 25, 2442-2451 (1969).

- [12] Michell, D., Smith, A. P., and Sabine, T. M., The dislocation arrangement in  $\alpha$ -oxalic acid dihydrate, *Acta. Cryst. B* 25, 2458-2460 (1969).
- [13] Caglioti, G., Paoletti, A., and Ricci, F. P., On resolution and luminosity of a neutron powder spectrometer, *Nucl. Instr.* 3, 223 (1958).
- [14] Sabine, T. M. and Browne, J. D., A geometrical consideration in the design of neutron powder spectrometers, *Acta. Cryst.* 16, 435-436 (1963).
- [15] Rietveld, H. M., A profile refinement method for nuclear and magnetic structures, *J. Appl. Cryst.* 2, 65-71 (1969).
- [16] Hewat, A. W., Design for a conventional high resolution neutron powder diffractometer, *Nucl. Instr. Methods*, 127, 361-379 (1975).
- [17] Cheetham, A. K. and Taylor, J. C., Profile analysis of neutron powder data, *J. Solid State Chem.* 21, 253-275 (1977).
- [18] Andresen, A. F., Hewat, A. W., and Sabine, T. M., The reliability of neutron powder profile refinement, *J. Appl. Cryst.* (in press).
- [19] Sabine, T. M. and Clarke, P. J., Powder neutron diffraction - refinement of the total pattern, *J. Appl. Cryst.* 10, 277-280 (1977).
- [20] Bacon, G. E., Neutron Diffraction (Oxford University Press, 1962).
- [21] Warren, B. E., X-ray Diffraction (Addison-Wesley, Mass., 1969).
- [22] Marshall, W. and Lovesey, S. W., Theory of Thermal Neutron Scattering (Oxford University Press, 1971).
- [23] Wilson, A. J. C., Imperfections in the structure of cobalt. II Mathematical treatment of proposed structure, *Proc. Roy. Soc. A* 180, 277-285 (1942).
- [24] Cowley, J. M., An approximate theory of order in alloys, *Phys. Rev.* 77, 669-675 (1950).
- [25] Shull, C. G. and Wilkinson, M. K., Neutron diffraction studies of the magnetic structures of alloys of transition elements, *Phys. Rev.* 97, 304-310 (1955).
- [6] Marshall, W., Neutron elastic diffuse scattering from mixed magnetic systems, *J. Phys. C* 1, 88-101 (1968).
- [7] Warren, B. E., Averbach, B. L., and Roberts, B. W., Atomic size effects in the x-ray scattering by alloys, *J. Appl. Phys.* 22, 1493-1496 (1951).
- [8] Borie, B., X-ray diffraction effects of atomic size in alloys, *Acta. Cryst.* 10, 89-96 (1957).
- [9] Borie, B., X-ray diffraction effects of atomic size in alloys II, *Acta. Cryst.* 12, 280-282 (1959).
- [10] Willis, B. T. M. and Pryor, A. W., Thermal Vibrations in Crystallography (Cambridge University Press, 1975).

#### Discussion

Question (Thomas): Have you included the effect of TDS which peaks under the Bragg peaks your MgO data?

Response (Sabine): No, in the approximation I used at present TDS is a smooth function of  $\sin \theta/\lambda$ . I am preparing an expression for TDS which contains components peaking under Bragg positions.

Comment (Ladell): The shape of a diffraction profile, whether Gaussian or Lorentzian, can be determined experimentally by using samples which have high preferred orientation. In this case, it is possible to see Lorentzian character in the profile stretching over many degrees.

Response (Sabine): This may be true in the x-ray case in which the Lorentzian profile of the spectral line, which is a consequence of the nature of x-ray production, dominates the distribution. However, for neutrons, we have a Maxwellian distribution in the moderator followed by Gaussian mosaic block distributions in the monochromator and specimen. From the central limit theorem, the final profile is fairly accurately Gaussian.

## SYNCHROTRON RADIATION AND ENERGY-DISPERSIVE DIFFRACTION

B. Buras

Physics Laboratory II, University of Copenhagen  
Universitetsparken 5, DK-2100 Copenhagen, and  
Risø National Laboratory, DK-4000 Roskilde  
Denmark

X-ray energy-dispersive diffraction utilizes white radiation; in this method the scattering angle is fixed during a measurement, a semiconductor detector performs an energy (wavelength) analysis of the diffracted x-rays and all reflections are recorded simultaneously. As was demonstrated at DESY (Hamburg, F.R.G.), NINA (Daresbury, U.K.), VEPP-3 (Novosibirsk, U.S.S.R.) and recently also at the storage ring DORIS (Hamburg, F.R.G.), synchrotron radiation with its special features-- particularly a continuous and smooth spectrum extending to short wavelengths, excellent collimation, high intensity, and well-defined polarization--is ideal for this method. In the case of a storage ring, the spectral distribution of the incident radiation can also be calculated from the machine parameters, essential in making quantitative structural analyses.

The paper discusses briefly the following problems, important for structural studies by means of synchrotron radiation and energy-dispersive diffraction: incident spectrum, polarization, large scattering vectors, profile fitting, momentum resolution and precision of interplanar distance measurements, studies of samples in special environments, counting time and counting rate, time-resolved studies, corrections and limitations.

### 1. Introduction

X-ray energy-dispersive diffractometry (XED) invented in the late sixties [1,2]<sup>1</sup> and since then developed and utilized at conventional x-ray sources [3-50], requires a collimated incident beam of a smooth "white" spectrum. Thus, synchrotron

---

<sup>1</sup>Figures in brackets indicate the literature references at the end of this paper.

radiation is the proper x-ray source for this method. Other qualities of synchrotron radiation, such as high intensity and known polarization, make it an almost ideal source, as was recently demonstrated at DESY [51-54], NINA [55-58], VEPP-3 [59] and DORIS [60-61].

This review gives a brief description of the XED method, recalls the characteristic features of synchrotron radiation and discusses the following problems important for powder diffraction by means of synchrotron radiation: incident spectrum, polarization, large scattering vectors, profile fitting, momentum resolution and precision of interplanar distance measurements, studies of samples in special environments, counting time and count-rate, time-resolved studies, corrections and limitations.

The discussion is rather brief and is intended to give only a general picture of the present status of energy-dispersive diffractometry. More details may be found in the quoted papers.

The use of XED for single crystal studies is beyond the scope of this paper. However, references to single crystal work are included in the list of references.

## 2. The Method

Figure 1 shows the principle of the method. A white, collimated x-ray beam is scattered by the powdered sample through a fixed angle  $2\theta_0$  and the wavelength (energy) distribution of the scattered photons is analysed by a semiconductor detector connected to a multichannel pulse height analyser. Each set of crystal lattice planes of spacing  $d_H$  ( $H$  indicates indices of reflection HKL) selects from the incident white spectrum photons of energy  $E_H$  (wavelength  $\lambda_H$ ) fulfilling the Bragg equation

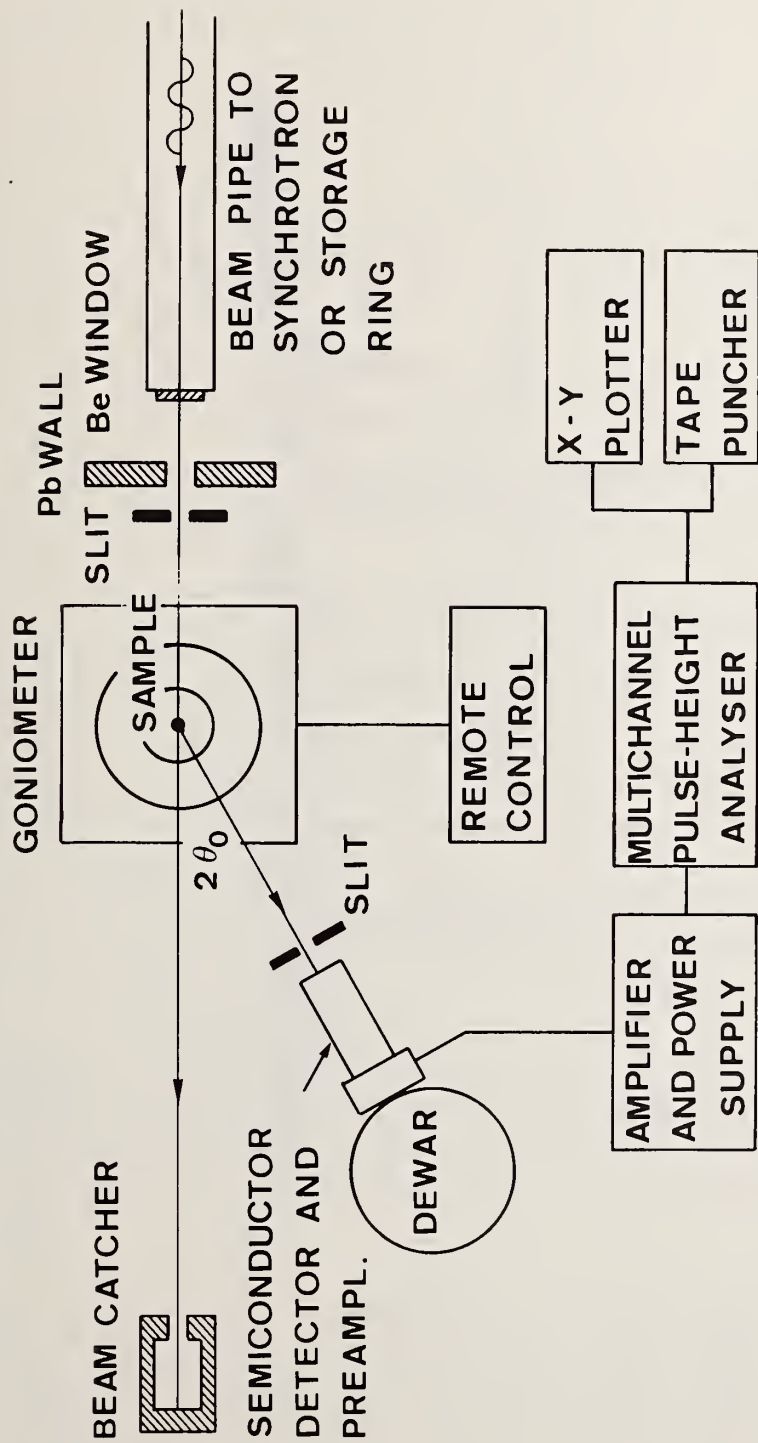
$$2 d_H \sin\theta_0 = \lambda_H(\text{\AA}) = \frac{hc}{E_H} = \frac{12.4 (\text{keV}\cdot\text{\AA})}{E_H} \quad (1)$$

( $h$  is Planck's constant,  $c$  the velocity of light), and reflects them to the detector. Figure 2 shows an example of a pattern measured at DORIS.

The integrated intensity  $I_H$  is given by the formula

$$I_H = C \eta(E) i_0(E) j_H d_H^2 |F_H|^2 \cdot A(E, \theta_0) C_p(\text{kin}) / \sin\theta_0, \quad (2)$$

where  $C$  is a constant,  $\eta(E)$  the detector efficiency,  $i_0(E)$  the incident beam intensity per unit energy range,  $j_H$  the multiplicity factor,  $F_H$  the structure factor including atomic factors,  $A(E, \theta_0)$  the absorption factor, and  $C_p$  the polarization factor. It should be noticed that in order to derive the structure factors from the measured integrated intensities one must know  $i_0(E)$  and  $C_p$ . We return to this point later.



## EXPERIMENTAL SET - UP

Figure 1. The principle of the energy-dispersive and a typical experimental set-up (schematically).

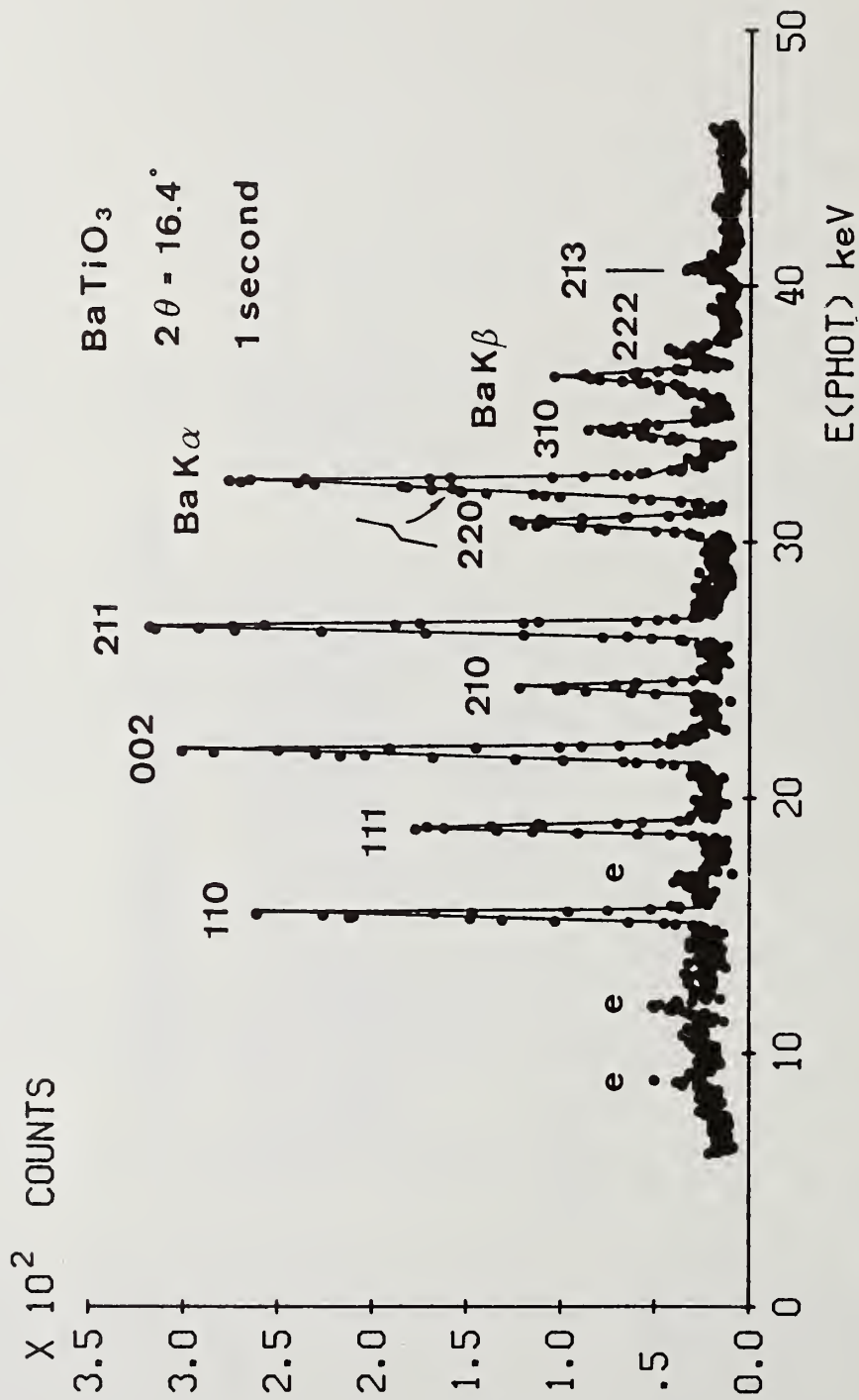


Figure 2. Diffraction pattern from BaTiO<sub>3</sub> powder recorded in 1 s at a scattering angle  $2\theta_0 = 16.4^\circ$  at DORIS (3.7 GeV, 14 mA,  $\lambda_c = 1.34 \text{ \AA}$ ) with an ultra-pure germanium detector (FWHM 150 eV and 485 eV at 5.9 keV and 122 keV, respectively). e = escape peaks.

The main characteristic features of the method, as compared with the x-ray monochromatic beam (angular scan) method, are the following:

- (a) it uses a white beam,
- (b) the scattering angle is fixed during a measurement but can be optimized for each particular experiment,
- (c) the detector is an energy-dispersive one,
- (d) all reflections are recorded simultaneously,
- (e) the exposure time is relatively short (this point is discussed in some detail in Section 4.7).

A white x-ray beam--essential for energy-dispersive diffractometry--can be obtained either from an x-ray tube (Bremsstrahlung) or from a synchrotron radiation source. In the following section the characteristic features of synchrotron radiation are briefly recalled and compared with those of Bremsstrahlung from an x-ray tube.

### 3. Synchrotron Radiation Versus Bremsstrahlung from an X-ray Tube

Synchrotron radiation is emitted by electrons in circular motion with velocities close to that of light. The emitted synchrotron radiation is continuous. Figure 3 shows the spectral distribution of radiation from electrons passing the bending magnets of the National Synchrotron Light Source (NSLS) now under construction in Brookhaven National Laboratory. It extends from infrared (not shown in the figure) to the x-ray region. It can be characterized by the so-called critical wavelength  $\lambda_c$  dividing the spectrum into two halves of equal radiation power. This wavelength is a bit shorter than the one for which the intensity of the spectrum reaches its maximum. In the NSLS  $\lambda_c \approx 2.5 \text{ \AA}$ . By applying a stronger magnetic field locally the radius of curvature becomes smaller and the emitted radiation is shifted toward shorter wavelengths; thus harder x-rays are emitted. This is accomplished by the so-called wigglers. The proposed NSLS wiggler will give  $\lambda_c = 0.6 \text{ \AA}$ . As the rule of thumb, useful intensity can be obtained down to 1/5 of  $\lambda_c$  and thus in the case of the NSLS to  $\sim 0.5 \text{ \AA}$  ( $\sim 25 \text{ keV}$ ) from bending magnets and  $\sim 0.12 \text{ \AA}$  ( $\sim 100 \text{ keV}$ ) from the wiggler. The latter wavelengths are shorter than those from conventional sources.

Synchrotron radiation is emitted tangentially to the orbit with a very small mean angular spread  $\Delta\Psi$  in the plane perpendicular to the orbital plane<sup>2</sup> (fig. 4). This spread is inversely proportional to the electron energy. For 2.5 GeV electrons of the NSLS  $\Delta\Psi$  equals 0.2 millirad  $\approx 42$  seconds of arc for  $\lambda_c$ .  $\Delta\Psi$  decreases slowly with decreasing wavelength.

<sup>2</sup>The spectral brilliance is also much larger, especially at dedicated synchrotron radiation source.

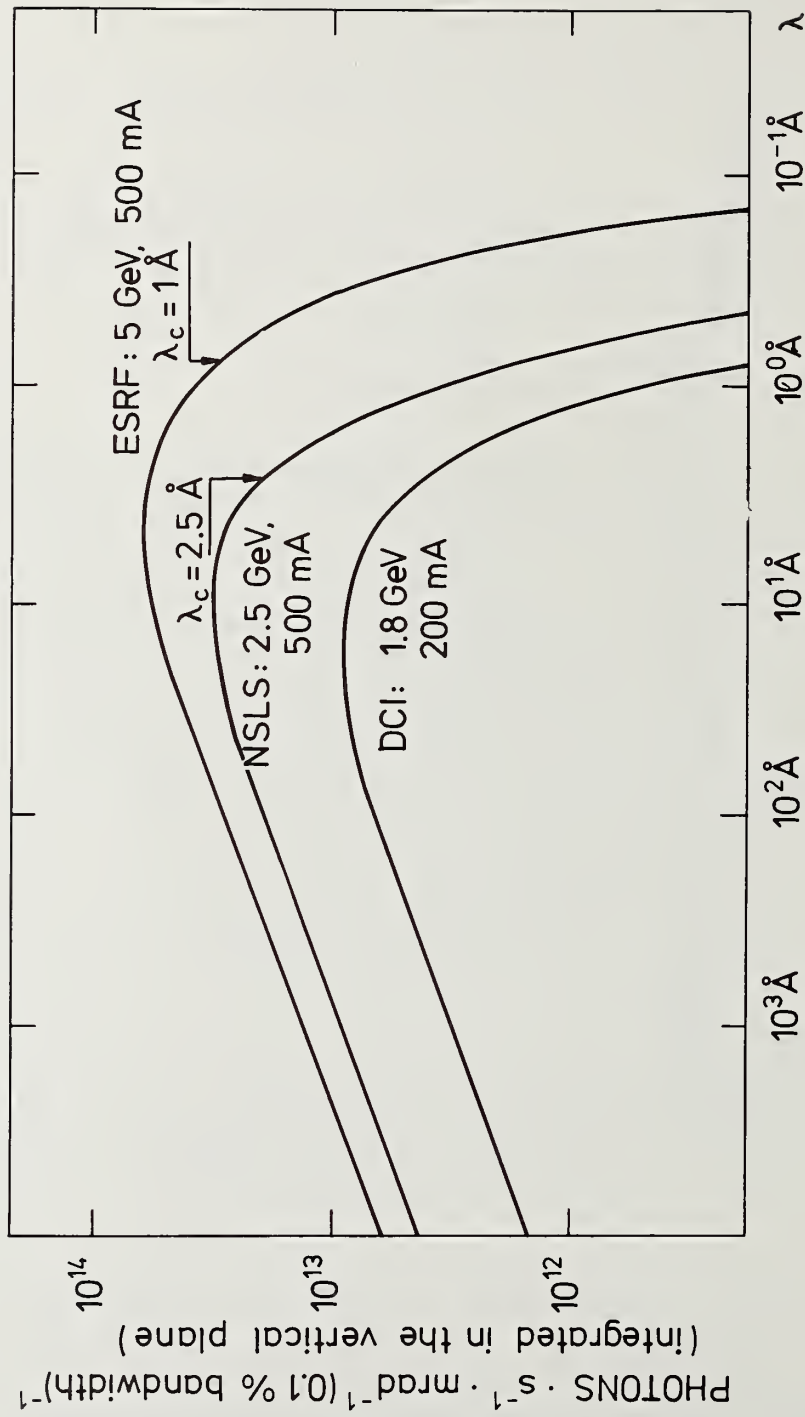


Figure 3. The spectral distributions of radiation emitted from bending magnets. (Photons per second per mrad (horizontal) per 0.1 percent band width (integrated in the vertical plane and time averaged) versus wavelength) from DCI (Orsay, France) already existing, NSLS (Brookhaven, USA) under construction and the European Synchrotron Radiation Facility (ESRF) under discussion.

$$\Delta\psi = \frac{0.5 \text{ MeV}}{E} \quad (E - \text{electron energy})$$

For  $E = 5 \text{ GeV}$

$$\Delta\psi = 10^{-4} \text{ rad} = 0.1 \text{ mrad} = 21''$$

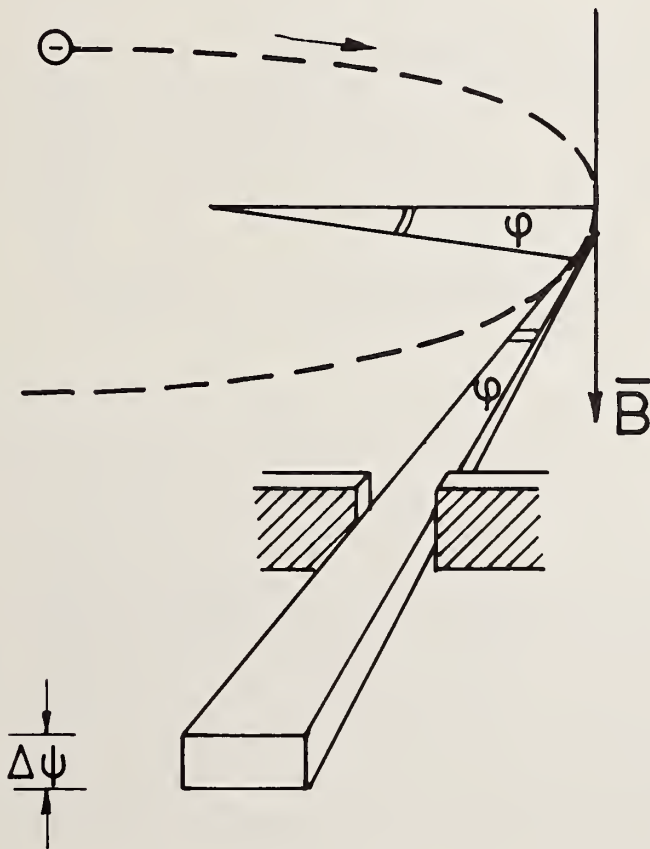


Figure 4. Geometry of emission of synchrotron radiation by electrons in circular motion with velocities close to that of light.  $B$ -bending magnetic field perpendicular to the electron orbit.

Radiation is emitted from the whole orbit within a flat pancake in the plane of the electron orbit. Using a beam definer one cuts from this pancake a small slice and is able to obtain a beam of synchrotron radiation very well collimated both in the vertical and horizontal planes. The radiation is in a very high degree plane-polarized in the plane of the orbit and elliptically out of this plane. For an ideal orbit the radiation would be completely plane-polarized in its plane.

Figure 5 shows a comparison between x-rays from a conventional x-ray generator and those produced by a storage ring. The radiation from the focal spot of the anode is emitted into a half sphere while synchrotron radiation emerges within a small vertical angle, as already discussed (fig. 5a). The intensity of synchrotron radiation from large machines, discussed here, is several orders of magnitude larger than Bremsstrahlung from the most powerful rotating anode tubes (fig. 5b). The comparison between the monochromatic characteristic radiation from an anode and the monochromatic radiation which can be obtained from the continuous synchrotron spectrum (by means of a monochromator) is beyond the scope of this paper. It can be said, however, that in general synchrotron radiation is superior.

The intensity of radiation from an anode is constant in time while from a storage ring it comes out in short pulses, typically of 0.1 - 1 ns length, separated by 2 ns - 1  $\mu$ s (fig. 5c). This is a result of the fact that electrons in a storage ring travel in short bunches few centimeters long. The separation time depends on the number of bunches travelling in the storage ring.

#### 4. The Energy-Dispersive Method at a Storage Ring

##### 4.1. Polarization

As can be seen from eqs. (2) a quantitative structure analysis requires knowledge of the polarization factor; this in turn requires knowledge of the polarization of the incident beam. In the case of conventional sources Bremsstrahlung polarization is dependent on the photon energy and it cannot be calculated. The measurements are difficult, time consuming and rather inaccurate [46]. In the case of synchrotron radiation the polarization of the incident beam is well known and easy to take into account. Because the radiation is in a very high degree plane polarized in the plane of the orbit (which is horizontal), a vertical scattering plane is advantageous. In the case of a horizontal scattering plane the polarization factor decreases from  $2\theta_0 = 0$  or  $180^\circ$  to  $2\theta_0 = 90^\circ$  and becomes very small at  $2\theta_0 = 90^\circ$ . However, for scattering angles smaller than  $30^\circ$  or larger than  $150^\circ$  the loss is smaller than 25 percent and can be in most cases easily tolerated taking into account the high incident intensity.

##### 4.2. The incident spectrum and crystal structure analysis

As already mentioned in Section 2, in order to perform a quantitative structural analysis one must know besides the polarization also the incident spectrum  $i_0(E)$ . In the

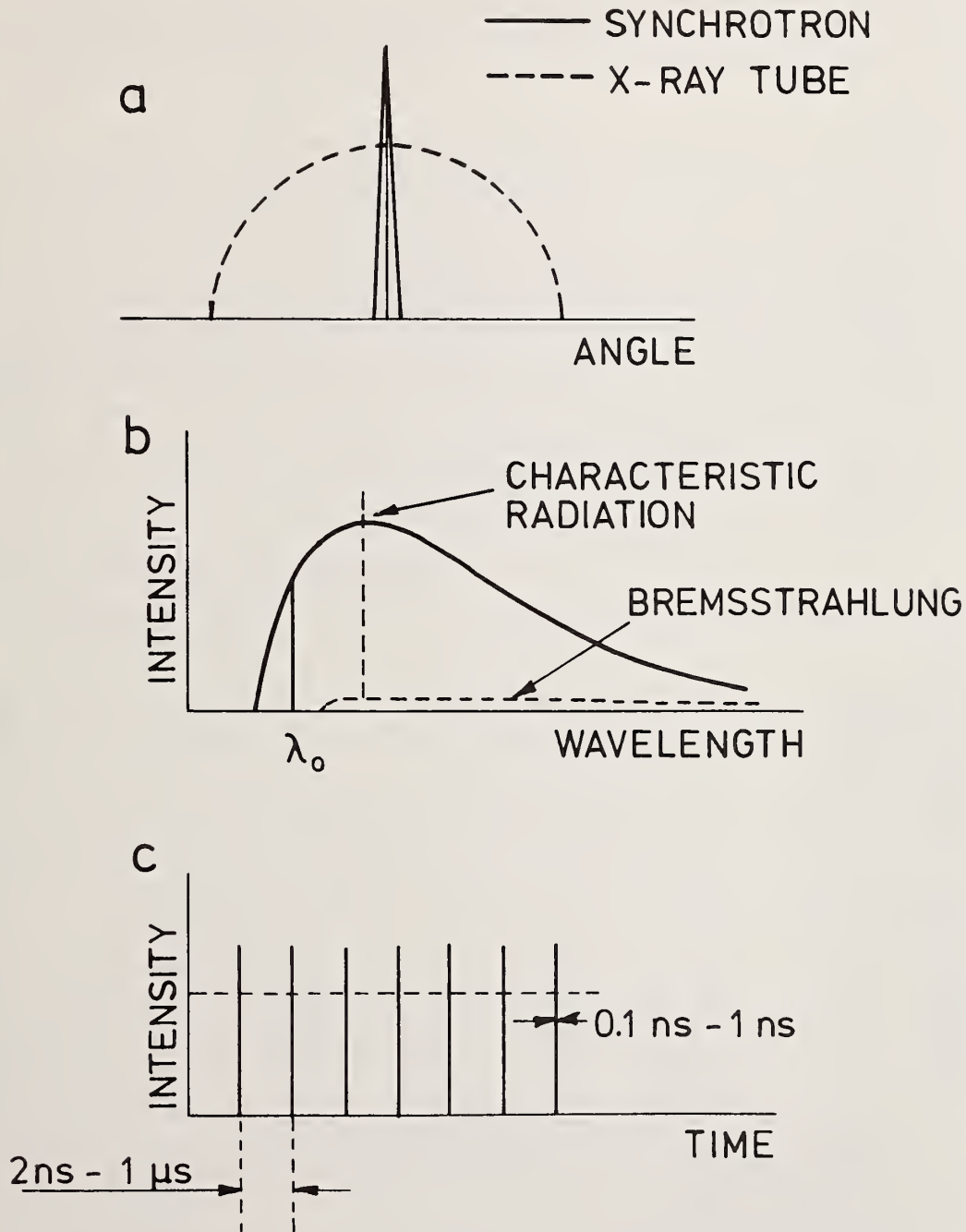


Figure 5. Comparison between x-ray synchrotron radiation and Bremsstrahlung from an x-ray tube.

case of conventional x-ray sources  $i_0(E)$  cannot be calculated. The measurements of  $i_0(E)$  are time consuming and present a source of errors. Nevertheless, it was shown that the determination of structure factors using XED with conventional sources is in principle possible [34]. It was also demonstrated that in the case of a synchrotron (NINA) operating in a dedicated mode a Rietveld type profile fitting procedure (in which both the incident spectrum and the crystal parameters are fitted) can be successfully applied [58].

In the case of a storage ring the situation is much more favourable. It is well known that the spectral distribution of the emitted radiation can be calculated from the machine parameters and it was recently shown that the calculated spectrum (in this case at DORIS in Hamburg) can be used for structural XED studies [61]. For several substances the structural parameters were obtained from the measured integrated intensities or from a Rietveld type profile fitting procedure. The reliability factors were around 0.03 for simple substances (Silicon, Iron) and  $R_{\text{prof}}$  was equal to 0.10 and 0.14 in the case of Urea and Naphthalene, respectively ( $R_{\text{int}}$  was equal to 0.05 and 0.06, respectively). Figure 6 shows, as an example, the results of refinement for Urea.

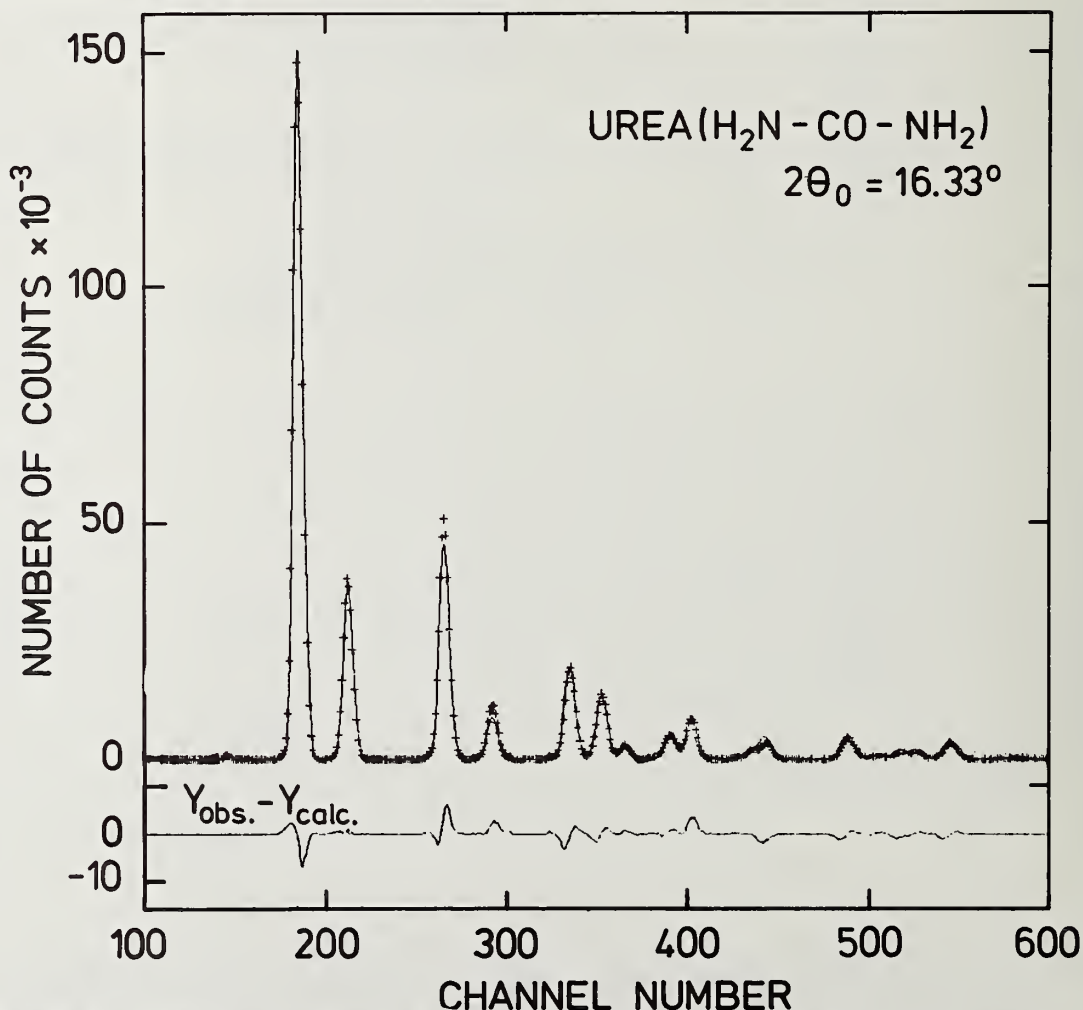


Figure 6. Diffraction pattern of Urea (after background subtraction). Crosses denote the experimental points and the full line the refined profile.

### 4.3. Large scattering vectors

The modulus of the scattering vector  $\vec{Q}$  is given by

$$Q(\text{\AA}^{-1}) = \frac{4\pi}{\lambda} \sin\theta_0 \approx E(\text{keV}) \cdot \sin\theta_0 \quad (3)$$

and thus it increases with the photon energy. For the maximum photon energies to be obtained at the NSLS and quoted in Section 3 one should be able to use scattering vectors as large as  $\sim 25 \text{\AA}^{-1}$  and  $100 \text{\AA}^{-1}$  with radiation from bending magnets and wigglers, respectively. This should be compared with about  $17 \text{\AA}^{-1}$  from a conventional source ( $\text{MoK}\alpha$ ). The importance of measurements at large scattering vector does not need to be advocated, however, one should remember that because of thermal vibrations and the decreasing atomic form factor the scattered intensity decreases with increasing scattering vectors; thus even for intense synchrotron radiation in each case a certain limit exists beyond which large scattering vectors are useless for structural studies.

### 4.4. Momentum resolution and precision of interplanar distances measurements

The momentum resolution is limited by the energy resolution of the detector system and by the collimation used. There is little hope that the energy resolution can be improved beyond 100 eV at 5.9 keV (at present the best detectors have a resolution of ca. 140 eV at 5.9 keV). A major advantage in working with synchrotron radiation is the excellent collimation of the incident beam and its high intensity, which enables small samples to be used as well as fine slit systems and large distances between sample and detector (or fine Soller collimators for large samples). In addition the high intensity secures good statistics.

As a result of the very good collimation, the best resolution is obtained not, as one might think, in backscattering but at small (but not too small) scattering angles [53]. Figure 7 shows the dependence of the FWHM of a diffraction peak ( $\delta d_{\text{FWHM}}$ -measured in the d-interplanar spacing scale) on the scattering angle for different d-spacing and different collimations,  $\Delta\theta_0$ . One notes a pronounced minimum for  $\Delta\theta_0 = 10^{-4}$ , obtainable with synchrotron radiation. However, small scattering angles require high photon energies and this points to the need for hard x-rays. Nevertheless, using the formulas of reference [53] one can in each case find the scattering angle for optimum resolution. It follows also from references [26] and [53] that with XED it is possible to measure interplanar distances with a precision of 0.01 percent.

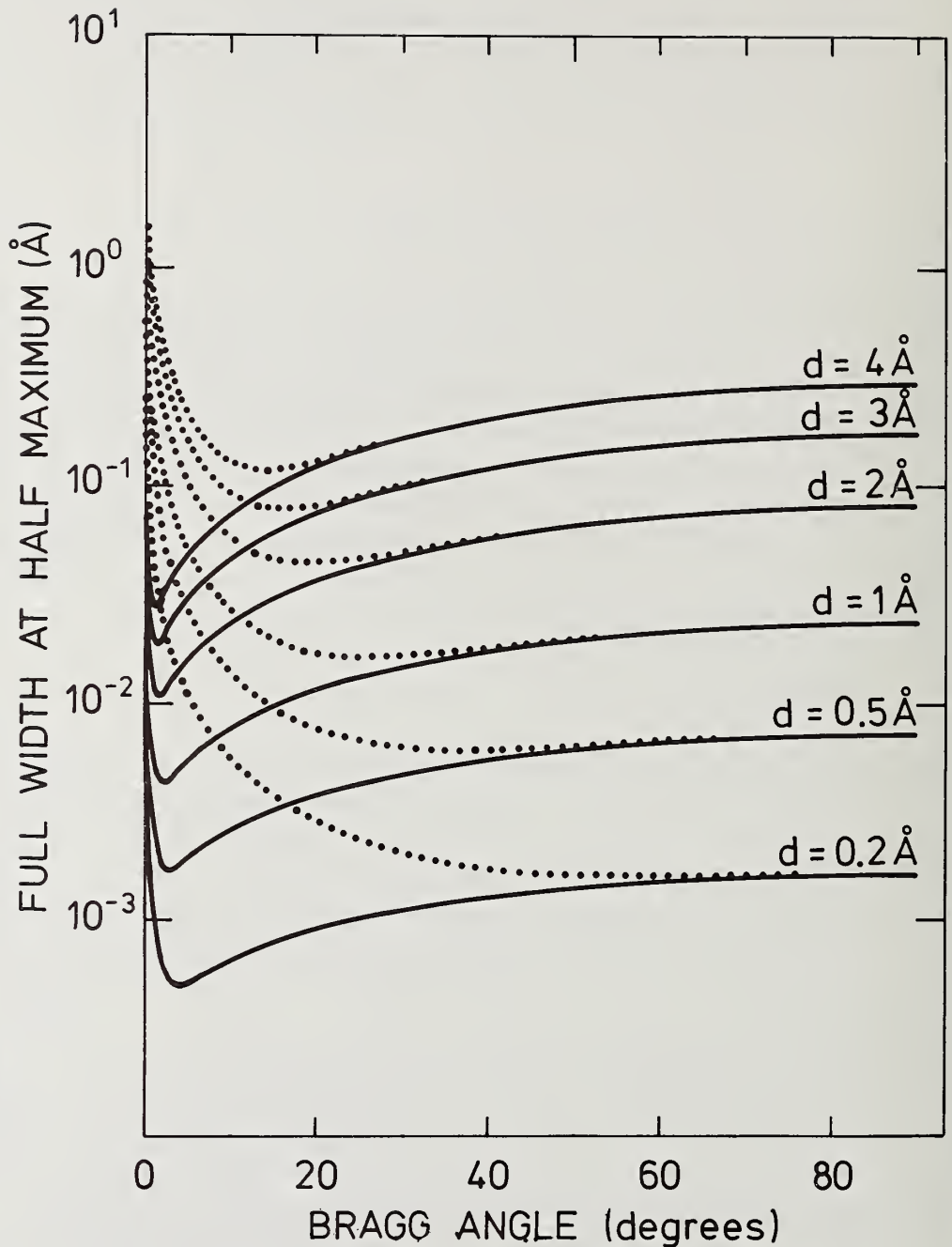


Figure 7. The dependence of  $\delta d_{\text{FWHM}}$  (the FWHM of a diffraction peak measured in the interplanar spacing scale) on the Bragg angle  $\theta_0$  for  $\Delta\theta_0 = 10^{-4}$  rad (full lines) and  $\Delta\theta_0 = 5 \cdot 10^{-3}$  rad (dotted lines) for different interplanar spacings  $d$  using a germanium detector with a resolution of 150 eV and 485 eV at 5.9 keV and 122 keV, respectively [53].

#### 4.5. Fixed scattering angle and high energy photons

These two features taken together facilitate studies of samples in special environments (e.g., high pressure, high and/or low temperatures, etc.) where special windows must be used. The loss of intensity due to absorption is smaller for high-energy photons, and the fixed scattering angle enables the use of no more than two (or even one, if backscattering is used) small windows.

These types of measurements have been already made with XED at conventional sources [4,15,40,50] and some demonstration experiments were performed as well with synchrotron radiation [52,54]. For high-pressure measurements in diamond anvils the sample volume is very small ( $0.01 \text{ mm}^3$  and less), so that it is essential that the incident intensity be very high.

#### 4.6. Simultaneous recording of all reflections

This feature of XED makes the method independent of the decrease of the incident beam intensity (it affects only the statistics), due to the decay of the electron current in the storage ring. Thus, no monitor is necessary.

The simultaneous recording of reflections greatly facilitates also, among others, studies of phase transitions.

#### 4.7. Counting time and count-rate

##### 4.7.1. High count-rate

Because of the simultaneous recording of all reflections and the high incident intensity of synchrotron radiation the counting time is relatively small. Counting times of 1s from powdered samples of a volume of  $0.2 \text{ mm}^3$  measured at DORIS (3.7 GeV, 14 mA,  $\lambda_c = 1.34 \text{ \AA}$ ) working in a single bunch mode were reported [61] (e.g., see fig. 2). A further substantial decrease of the counting time is limited by the present maximum count-rate of semiconductor detectors ( $\sim 10^5$  counts/s). However, even with the present maximum count rate for a single detector energy-dispersive diffractometry offers a possibility of improving the counting statistics and thus decreasing the counting time. Because the scattering angle is fixed one can simultaneously use several detectors placed in a circle and simply sum up the data (fig. 8). Such a system is at present expensive but some simplifications lowering the cost can be already envisaged (e.g., a joint cooling system and/or a multichips detector instead of several detectors). The future may bring some development in this field.

All scattering angles =  $2\theta_0$

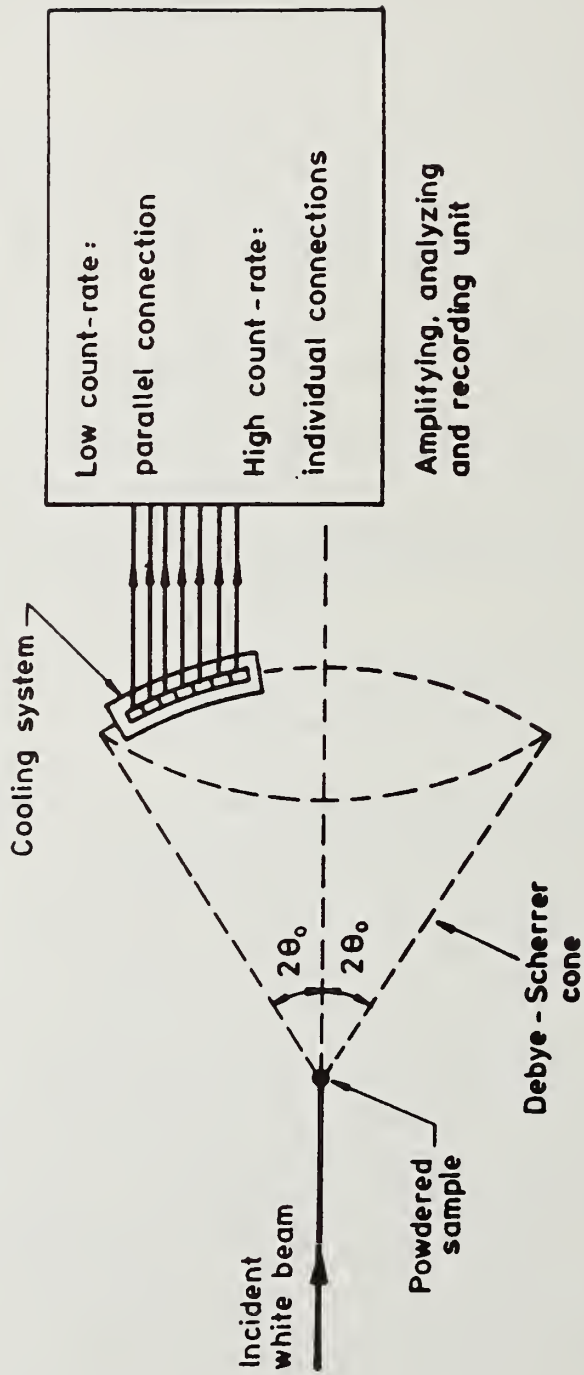


Figure 8. Multidetector system for high and low count-rate utilizing the fixed scattering angle geometry (schematically).

#### 4.7.2. Low count-rate

For very low count-rates one detector (or several detectors in parallel) covering a part or the whole of the Debye-Scherrer ring (cone) can be used (fig. 8). In the case of very small samples (e.g., in a diamond cell) one detector of several centimeters in diameter equipped with a conical collimator might be sufficient [50].

#### 4.8. Time-resolved structural studies

The relatively short counting time, simultaneous recording of all reflections and the possibility of quantitative structure analysis make it possible to collect and analyse data in a few seconds and thus allow structural parameters to be obtained very rapidly. Thus, it seems feasible, for instance, to carry this out semicontinuously with changing temperature and/or pressure and construct a motion picture of the change in crystal structure during a phase transition. This type of time-resolved studies is possible in the time range of few seconds and above. Faster repetitive processes (relaxation times between 10 ns and 1 s depending on the available electronics) can be studied by means of a stroboscopic method. This is illustrated in figure 9 with an example of a repetitively pulsed external electrical field applied synchronously with the x-ray pulse. Thus, XED seems to be a suitable method for studies of transient phenomena in a large range of relaxation times.

#### 4.9. Some other applications

As was already demonstrated at conventional sources, XED can be used for determinative mineralogy [7], Debye-Waller temperature dependence studies [33,44], attenuation coefficients measurements [45], on-stream measurements [17,18], particle size measurements [41] and texture studies [9,23,28,36,49]. In some of these cases the possibility of time-resolved studies, discussed in Section 4.8 is of great importance (e.g., development of texture, annealing of texture, creation of strain). This applies to studies of chemical reactions as well.

#### 4.10. Choice of detectors and bunch mode

The detectors available on the market and tested with synchrotron radiation and XED [51,52,54-58,60,61] are Si(Li) and extra-pure Ge. For low energy photons (below  $\sim 30$  keV) Si(Li) detectors are preferred (with only negligible escape peaks [27] and a low energy absorption edge of Si at 1.84 keV). For higher photon energies Ge detectors are much better because of the higher efficiency at energies above 30 keV. However, escape peaks complicate the diffraction pattern [22], and the presence of the absorption edge at 11.1 keV disturbs the efficiency in this region. In both cases pile-up rejectors should be applied. The pile-up problem deserves a special discussion.

(schematically).

## Time-resolved studies

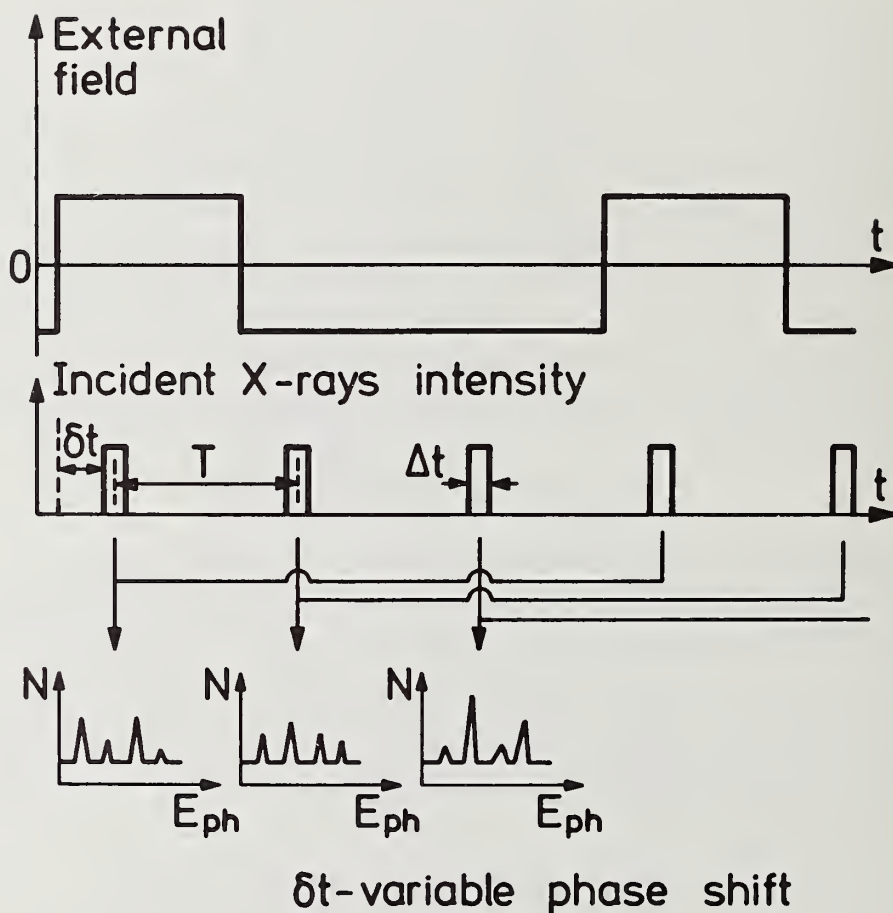


Figure 9. Time-resolved studies by means of a stroboscopic method: by using one (or several counters, as shown in the figure) and changing the phase shift one is able to follow the structure changes induced by the application (or removal) of an external field.

Because of the already mentioned large dead-time of detector systems (ca. 10  $\mu$ s) they record either 0 or 1 photon from each bunch and are "dead" for the next  $\sim$  10  $\mu$ s. Thus, a multibunch mode is better than a single one only when the probability of recording 1 photon from 1 bunch is smaller than unity (as with small samples, fine collimation, high absorption, etc.).

## 5. Summary and Discussion

XED at a storage ring can be used for fast quantitative structure analysis and seems to be especially suitable for phase transition and chemical reaction studies, fast identification of known structures, studies of samples in special environments, liquid and amorphous material studies, determination of textures, and time-resolved studies. Some of these studies could not be made with XED at all or in any case with great difficulty and poor accuracy using conventional sources; some others would need a much longer measuring time if the same precision is to be attained.

In the early days of XED it was thought that some corrections might be much more difficult to apply in the case of a white beam than for a monochromatic one. However, it was shown later that thermal diffuse [33], Compton [35], and absorption [31,34,35,57,58,61] corrections can be applied without special difficulties.

The main disadvantages of XED at present are:

- (a) the fluorescence induced by the white beam obscures the diffraction pattern in some cases, although by a proper choice of the scattering angle the diffraction lines can be shifted to the most convenient position in the pattern;
- (b) the white beam impinges on the sample and this may result in heating it excessively or even in damaging it by radiation;
- (c) the momentum resolution is limited by the energy resolution of the detector system, however, the availability of hard x-rays partly improves the resolution;
- (d) the dead-time of the detector system (of the order of 10  $\mu$ s) limits the counting rate to  $\sim 10^5$  counts/s for one detector.

As concerns the characteristics of synchrotron radiation required by energy-dispersive diffractometry, the importance of hard x-rays should be stressed. It is necessary for obtaining larger scattering vectors, smaller attenuation factors and better momentum resolution.

To sum up: the XED method takes full advantage of the white beam and also utilizes other characteristic features of synchrotron radiation. It is simple to use and relatively fast. It does not provide the accuracy obtainable with sophisticated monochromatic beam methods; however, it has a large number of applications in research and development studies, and in selected areas it has advantages over the monochromatic beam methods.

## References

- [1] Giessen, B. C. and Gordon, G. E., X-ray diffraction: new high speed technique based on x-ray spectroscopy, *Science*, 159, 973-975 (1968).
- [2] Buras, B., Chwaszczewska, J., Szarras, S., and Szmid, Z., Fixed angle scattering/FAS/method for x-ray crystal structure analysis, Institute of Nuclear Research, Warsaw, Report No. 894/II/PS (1968).
- [3] Freud, P. J. and La Mori, P. N., Non-dispersive high pressure high temperature x-ray diffraction analysis, *Trans. Amer. Cryst. Assoc.* 5, 155-162 (1969).
- [4] Freud, P. J. and Sclar, C. B., Apparatus for high-pressure high-temperature x-ray powder diffraction studies, *Rev. Sci. Instr.* 40, 434 (1969).
- [5] Cole, H., Bragg's law and energy sensitive detectors, *J. Appl. Cryst.* 3, 405-6 (1970).
- [6] Chwaszczewska, J., Szarras, S., Szmid, Z., and Szymczak, M., Application of semiconductor detectors in crystal structure investigations, *Phys. Stat. Sol. (a)* 4, 619-626 (1971).
- [7] Ferrel, R. E., Applicability of energy dispersive x-ray powder diffractometry to determinative mineralogy, *Am. Mineral.* 56, 1822-31 (1971).
- [8] Fitzgerald, R. and Gantzel, P., X-ray energy spectrometry in the 0.1-10 Å range, American Society for Testing and Materials, Special Technical Report No. 485 (1971).
- [9] Laine, E. and Lähteenmäki, I., Structure and microstructure study of splat-cooled cadmium, *J. Material Science*, 6, 1418-1421 (1971).
- [10] Buras, B., X-ray spectroscopic methods for crystallographic studies, Physics Laboratory II, University of Copenhagen, Monograph No. 71-08 (1971).
- [11] Reed, S. J. B. and Ware, N. G., The measurements of x-ray peak intensities with a lithium drifted silicon detector by integration over a fixed energy range, *J. Phys. E.: Sci. Instr.* 5, 1112-1114 (1972).
- [12] Lauriat, J. P. and Périó, P., Adaptation d'un ensemble de détection si (Li) á un diffractometre X, *J. Appl. Cryst.* 5, 177-183 (1972).
- [13] Martin, G. W. and Klein, A. S., A complete instrumental system for energy dispersive diffractometry and fluorescence analysis, in *Advances in X-ray Analysis* (Plenum Press, New York, 1972), pp. 254-265.
- [14] Laine, E., Lähteenmäki, I., and Kantola, M., Adaptation of solid state detector in x-ray powder diffractometry, x-ray spectrometry, 1, 93-98 (1972).
- [15] Albritton, L. M. and Margrave, J. L., Polychromatic x-ray diffraction: a rapid and versatile technique for the study of solids under high pressure and high temperature, *High Temperatures - High Pressures*, 4, 13-19 (1972).

- [16] Sparks, C. J. and Gedcke, D. A., Rapid recording of powder diffraction patterns with Si (Li) x-ray energy analysis system: W and Cu targets and error analysis, Advances in X-ray Analysis, Vol. 15 (Plenum Press, New York, 1972), pp. 240-253.
- [17] Nutter, J. C., A non-dispersive on-stream x-ray diffractometer for cement industry, Cement Technology, 55-58 (March/April, 1972).
- [18] Hewitt-Emmett, A., The application of the x-ray diffractometer to process control in cement kilns, Cement Technology, 58-61 (March/April, 1972).
- [19] Buras, B., Staun Olsen, J., Lindegaard Andersen, A., Gerward, L., and Selsmark, B., Energy-dispersive spectroscopic method applied to x-ray diffraction in crystals, Physics Laboratory II, University of Copenhagen, Monograph No. 73 - 12 (1973).
- [20] Kotlicki, A., Boye-Olsen, N., Staun Olsen, J., Mössbauer and x-ray study of proton radiation effects in biotite, Rad. Effects, 28, 1-4 (1976).
- [21] Wilson, A. J. C., Note on the aberration of a fixed-angle energy-dispersive powder diffractometer, J. Appl. Cryst. 6, 230-237 (1973).
- [22] Fukamachi, F., Togawa, S., and Hosoya, S., Escape peaks caused by a Ge (Li) detector in an energy-dispersive diffractometer, J. Appl. Cryst. 6, 297-298 (1973).
- [23] de Ben, H. S. and Broyole, B., Compositional and texture analysis of tantalum thin films by energy-dispersive x-ray analysis, Applied Spectroscopy, 27, 99-102 (1973).
- [24] Laine, E. and Tukia, T., Isotope-excited x-ray fluorescence analysis of binary alloy using energy dispersion, X-ray Spectrometry, 2, 115-119 (1973).
- [25] Hosoya, S. and Fukamachi, T., Rapid determination of polarity sense by an energy-dispersive diffractometer, J. Appl. Cryst. 6, 396-399 (1973).
- [26] Fukamachi, T., Hosoya, S., and Terasaki, O., The precision of interplanar distances measured by an energy-dispersive diffractometer, J. Appl. Cryst. 6, 117-122 (1973).
- [27] Buras, B., Staun Olsen, J., Lindegaard Andersen, A., Gerward, L., and Selsmark, B., Evidence of escape peaks caused by a Si (Li) detector in energy dispersive diffraction, J. Appl. Cryst. 7, 296-297 (1974).
- [28] Szpunar, J., Ojanen, M., and Laine, E., Application of the energy dispersive x-ray diffraction method to texture measurements, Z. f. Metalkunde, 65, 221-226 (1974).
- [29] Laine, E., Lähteenmäki, I., and Hämäläinen, M., Si (Li) semiconductor in angle and energy dispersive x-ray diffractometry, J. Phys. E. Sci. Instr. 7, 951-954 (1974).
- [30] Heilmann, I., Knudsen, J. M., Olsen, N. B., Buras, B., and Staun Olsen, J., Studies of thermal decomposition of  $(\text{NH}_4)_2 \text{Fe}(\text{SO}_4)_2 \cdot 6\text{H}_2\text{O}$ , Solid State Comm. 15, 1481-1484 (1974).
- [31] Buras, B., Staun Olsen, J., Gerward, L., Selsmark, B., and Lindegaard Andersen, A., Energy-dispersive spectroscopic method applied to x-ray diffraction in single crystals, Acta Cryst. A31, 327-333 (1975).
- [32] Buras, B. and Gerward, L., Relations between integrated intensities in crystal diffraction methods for x-rays and neutrons, Acta Cryst. A31, 372-374 (1975).

- [33] Uno, R. and Ishigaki, A., The correction of experimental structure factor for thermal diffuse scattering in the White x-ray diffraction, *Japan J. Appl. Phys.* 14, 291-292 (1975).
- [34] Uno, R. and Ishigaki, A., Determination of structure factors by White x-ray diffraction from a powder sample of GaP, *J. Appl. Cryst.* 8, 578-581 (1975).
- [35] Prober, J. M. and Schultz, J. M., Liquid-structure analysis by energy-scanning x-ray diffraction: mercury, *J. Appl. Cryst.* 8, 405-414 (1975).
- [36] Gerward, L., Lehn, S., and Christiansen, G., Quantitative determination of preferred orientation by energy-dispersive x-ray diffraction, *Texture of Crystalline Solids*, 2, 95-111 (1976).
- [37] Fukamachi, T., Hosoya, S., and Okuniki, M., X-ray intensity measurements on large crystals by energy-dispersive diffractometry. I. Energy dependences of diffraction intensities near the absorption edge, *Acta Cryst.* A32, 104-109 (1976).
- [38] Fukamachi, T., Hosoya, S., and Okuniki, M., X-ray intensity measurements of large crystals by energy-dispersive diffractometry. II. Energy dependences of the friedel pair intensities and their ratio near the absorption edge, *Acta Cryst.* A32, 245-249 (1976).
- [39] Skelton, E. F., Measurement of the temperature dependence of Debye-Waller factors by energy-dispersive methods: application to  $\text{NbCO}_{0.98}$ , *Acta Cryst.* A32, 467-472 (1976).
- [40] Inoue, K., Nakaue, A., and Yagi, Y., Measurement of melting points of Pb up to 90 Kbar by energy dispersive x-ray diffraction technique, Asada Fundamental Research Laboratories, Kobe Steel Ltd., Kobe 657, Japan.
- [41] Gerward, L., Mørup, S., and Topsøe, H., Particle Size and Strain Broadening in energy-dispersive x-ray powder patterns, *J. Appl. Phys.* 47, 822-825 (1976).
- [42] Altee, A., Paakkari, T., and Uno, R., Determination of the structure factors of a LiF powder sample by the energy dispersive x-ray diffraction, Department of Physics, University of Helsinki, Finland.
- [43] Fukamachi, F., Hosoya, S., Kawamura, T., and Okunuki, M., X-ray intensity measurements on large crystals by energy-dispersive diffractometry. III. Fine structures of integrated intensities and anomalous scattering factors near the K absorption edges in GaAs, *Acta Cryst.* A33, 54-58 (1977).
- [44] Skelton, E. F., A new improved method for measuring the temperature dependence of Debye-Waller factors with the use of energy dispersive analysis, Report of NRL Progress (May 1976), pp. 1-11.
- [45] Gerward, L. and Thuesen, G., X-ray attenuation in silicon and germanium in the energy range 26 to 50 keV, *Z. Naturforsch.* 32a, 588-593 (1977).
- [46] Staun Olsen, J., Buras, B., Jensen, T., Alstrup, O., Gerward, L., and Selsmark, B., Influence of polarization of the incident beam on integrated intensities in x-ray energy-dispersive diffractometry, *Acta Cryst.* A34, 84-87 (1978).

- [47] Murata, Y. and Nishikawa, K., The construction of an energy-dispersive x-ray diffractometer for liquids and its application to  $\text{CCl}_4$ , *Bull. Chem. Soc., Japan*, 51, 411-418 (1978).
- [48] Cousins, C. S. G., Gerward, L., and Staun Olsen, J., Multiple diffraction in crystals studied by an x-ray energy-dispersive method, *Phys. Stat. Sol. (a)* 48, 113-119 (1978).
- [49] Szpunar, J. and Gerward, L., Energy-dispersive diffractometry for quantitative determination of texture, Laboratory of Applied Physics III, The Technical University of Denmark, Report No. 20 (1978); Texture of Materials, J. Goldstein and K. Lucke eds. (Springer Verlag, Berlin, 1978), pp. 203-208.
- [50] Holzapfel, W. B., High Pressure Studies Using Energy-Dispersive Diffractometry, private communication.
- [51] Buras, B., Staun Olsen, J., and Gerward, L., X-ray energy dispersive powder diffractometry using synchrotron radiation, *Nucl. Instr. and Meth.* 135, 193-195 (1976).
- [52] Buras, B., Staun Olsen, J., Gerward, L., Will, G., and Hinze, E., X-ray energy-dispersive diffractometry using synchrotron radiation, *J. Appl. Cryst.* 10, 431-438 (1977).
- [53] Buras, B., Niimura, N., and Staun Olsen, J., Optimum resolution in x-ray energy-dispersive diffractometry, *J. Appl. Cryst.* 11, 137-140 (1978).
- [54] Buras, B., Staun Olsen, J., and Gerward, L., White beam, x-ray energy dispersive diffractometry using synchrotron radiation, *Nucl. Instr. and Meth.* 152, 293-296 (1978).
- [55] Bordas, J., Glazer, M., and Munro, I. H., Small-angle scattering experiments on biological materials using synchrotron radiation, *Nature*, 262, 541-545 (1976).
- [56] Bordas, J., Glazer, A. M., Howard, C. J., and Bourdillon, A. J., Energy-dispersive diffraction from polycrystalline materials using synchrotron radiation, *Phil. Mag.* 35, 311-323 (1977).
- [57] Bourdillon, A. J., Glazer, A. M., Hidaka, M., and Bordas, J., High resolution energy-dispersive diffraction using synchrotron radiation, *J. Appl. Cryst.* 11, 684-687 (1978).
- [58] Glazer, A. M., Hidaka, M., and Bordas, J., Energy-dispersive powder profile refinement using synchrotron radiation, *J. Appl. Cryst.* 11, 165-172 (1978).
- [59] Vazina, A. A., Application of synchrotron radiation to x-ray structural studies of biopolymers, in Report of the Wsiesojuznyi Institut Nautchnoi i Technicheskoi Informaciii Akademii Nauk SSSR, M. 8, 242-397 (1976) (in Russian).
- [60] Buras, B., Some Experience with and Future Requirements for Semiconductor Detectors Used for Synchrotron Radiation X-ray Energy-Dispersive Diffractometry, Proceedings of the Workshop on X-ray Instrumentation for Synchrotron Radiation Research, Stanford Linear Accelerator Center. Report No. 78/04 pp. VIII 124-131 (1978).

[61] Buras, B., Gerward, L., Glazer, A. M., Hidaka, M., and Staun Olsen, J., Quantitative structural studies by means of the energy-dispersive method and x-rays from a storage ring, Deutsches Elektronen-Synchrotron DESY Preprint No. SR-79/09 and J. Appl. Cryst. (in press).

#### Discussion

Question (Hewat): Is it fair to conclude that the major limitation of energy dispersive techniques is likely to be counter technology? Firstly, because of the limited resolution possible ( $\Delta d/d \sim 3 \times 10^{-3}$ ), and secondly, because of the limited count rate?

Comment (Buras): At present it is a fair statement. However, as mentioned in Section 4.7 of the paper, there exist some possibilities of improving the count rate.

Comment (Parrish): It would have been interesting to see a comparison for a moderately complicated pattern of a synchrotron-SSD and a scanning diffractometer with monochromator.

Comment (Buras): We are planning to perform this summer such a comparison at DORIS using our triple axis crystal spectrometer.

Question (Uno): How accurate is the absorption factor which you can get in the synchrotron radiation measurement?

Comment (Buras): I am not sure whether I understood your question correctly. I think that accuracy should not depend on whether one uses synchrotron radiation or Bremsstrahlung from a conventional x-ray generator. However, when one applies a profile-fitting procedure one can treat the packing fraction as a fitting parameter.

## ACCURACY IN X-RAY WAVELENGTHS

R. D. Deslattes, A. Henins and E. G. Kessler, Jr.

Center for Absolute Physical Quantities

National Bureau of Standards

Washington, DC 20234

The prominent  $K\alpha_1$  lines most frequently used in precision diffractometry are well known to be afflicted by the proximity of  $K\alpha_2$  radiation, they suffer quite appreciable line widths (none is narrower than 300 ppm) and have substantially asymmetric profiles. On the other hand, these vagaries have not, for most of x-ray history, had as noticeable an effect on final results as has uncertainty in the x-ray scale itself. This situation led very early to introduction of arbitrary "standards" in the x-ray region according to several different conventions leading to a situation where the dominant component of uncertainty for diffraction measurements lay in the conversion factor,  $\lambda$ . Only with the greatest difficulty did the classical ruled grating scheme yield uncertainties in  $\lambda$  below 15-20 ppm.

The past few years have seen a reversal of this situation since, using x-ray and optical interferometry, we can now reckon single crystal periods to near 0.1 ppm. Using other crystal periods derived from these and accurate goniometers, the wavelengths of narrow lines (i.e.,  $\gamma$ -ray transitions) can nowadays be determined to approximately the same accuracy (0.1 ppm). Wavelength values assigned to x-ray lines in this way are thus no longer limited in accuracy by the scale used, but by the characteristics of the lines themselves. This is a subject on which recent work has shed somewhat unexpected light and which carries with it some limitations for crystal measurements (single crystal and powder methods) to which a measure of attention needs to be drawn.

### 1. Introduction

For some years now, we have worked toward an improved knowledge of crystal spacings, x-ray wavelengths and  $\gamma$ -ray wavelengths. These efforts have borne fruit in the fundamental constants area, in tests of theory for normal and exotic atoms and in determination of masses of elementary particles. For the most part the changes in numerical estimates

of x-ray wavelengths and the increased refinement of our results have not had much significance for crystal structure determination. The recent discovery of appreciable fine detail within strong characteristic x-ray lines is probably of even less concern, given effectively low equivalent spectral resolution with which especially powder procedures are carried out.

Nevertheless, it is possibly useful, at times, to attend to the foundations of one's business to be sure they are tidy and robust. It is with this end in mind that we have gathered here a brief summary of the fundamental problems involved together with the new results on profiles and the wavelength scale. There are, in fact, two cases in which the new results may have some practical significance, if one imagines that technical progress continues in structure studies. First, in the comparisons between observed and calculated densities, cell edge dimensions need to be known in terms of the cube root of volume measure (most usually this is expressed as a length and derived from the customary standard but see below). Second, in the area of detailed profile analysis, although a smooth (asymmetric) model suffices at present, it may someday be important to know that this approximation is, in detail, wrong.

## 2. X-ray Wavelength Scales - A Little History

Crystal diffraction measurements, whether carried out for structural or spectroscopic purposes, yield only angles, twice the sines of which are  $\lambda/d$  ratios as was known early in this century from Sir Lawrence Bragg and from Laue's equations. The first good estimate of a macroscopic measure of "d" came in 1912 from Sir William Bragg [1]<sup>1</sup> who equated the mass contained in a unit cell as calculated from atomic measure and from density and (a priori unknown) macroscopic volume. For a hypothetical cubic crystal with cell edge  $a_0$ ,  $n$  molecules per unit cell of average molar mass (molecular weight),  $M$ , Bragg's equation would be:

$$\rho V = \rho a_0^3 = n \frac{M}{N_A} \quad (1)$$

where  $\rho$  is the macroscopic density and  $N_A$  is the Avogadro constant. For an estimate of Bragg made use of the then recently available oil-drop value of the electron's charge,  $e$ , and the already well-known electrochemical Faraday,  $F$ , according to

$$N_A = F/e \quad (2)$$

This approach gave an estimate for the cell edge dimension of rock salt  $a = 2d = 5.62 \times 10^{-8}$  cm. Not long after, Mosely [3] computed a somewhat more accurate value  $d = 2.814 \times 10^{-8}$  cm ( $\sim 1700$  ppm). (Unfortunately, the oil-drop experiment contained a serious systematic error which was to remain undetected for many years and an unknown source of conflict for many more years. An adequate digression on this point would render this report much overlong but it is planned to treat it elsewhere.)

<sup>1</sup>Figures in brackets indicate the literature references at the end of this paper.

As the second decade of this century passed, it became clear that quite accurate  $\lambda/d$  ratios (and evidently  $\lambda'/\lambda$  ratios) were emerging from careful angular measurements of symmetric reflections as suggested in figure 1. Indeed the accuracy of these "tube-spectrometer" measurements was far better than that of Sir William's estimate of the rock-salt cell dimension. The automatic response of a scientific sub-discipline to such a problem, then as now, was to introduce a local unit.

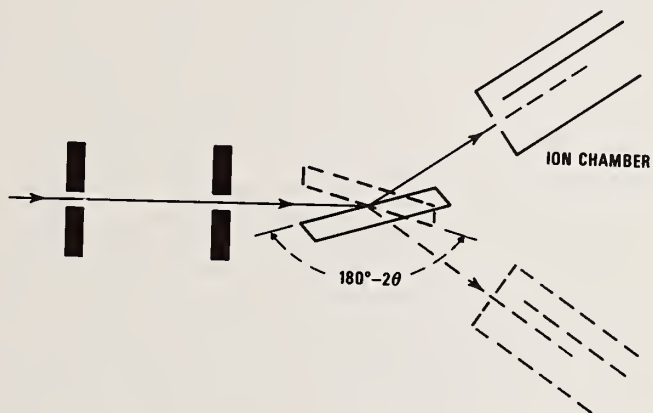


Figure 1. Plan of a "Tube" spectrometer of the sort used in early precision spectroscopic and crystallographic measurements.

In the case at hand of the x-ray spectroscopy/crystal structure business, it was Manne G. Debye [4] (who died, by the way, only last year) who began to use a unit for wavelength nominally  $10^{-11}$  cm and denoted by  $\mu$ . He found calcite to be superior to NaCl and by the time of his 1925 book [5] was advocating fixing the 18 °C grating space of calcite,  $d = 3029.04$  Å. Such a local standard permits succinct exchange of precise information provided only that the local standard is independently reproducible. Unfortunately, as now we know so well, lattice parameters of chemically similar specimens do vary appreciably and such variations have noticeable effects even in the case of such a well behaved natural crystal as calcite.

Clearly, instead of defining a local unit by a crystal dimension, the scale could have been fixed by assigning an exact numerical value to a prominent x-ray line as was, naturally, suggested many times. Resistance to this alternative (at least in principle) seemed to center on the fact that the resolution (or sharpness of definition) of a crystal repeat distance is superior to the fractional widths of x-ray lines; x-ray lines are also troubled by asymmetry and, for the strongest ones, a ubiquitous partner. (As will be seen in the following section, the sharpness of definition possible for the repeating distance of certain crystal dimensions is indeed remarkable while later it will be shown that x-ray lines are rather more sensitive than had been imagined in the past.)

As happens in many areas, standards of practice for the x-ray scale evolved somewhat independently of the "crystal definitions". For convenience and economy of effort, for measurements not of limiting accuracy, conventional values came into use for the wavelengths of

Cu  $K\alpha_1$  and Mo  $K\alpha_1$ . Spectral tables and papers especially in Europe tended to be based on  $\lambda(\text{Mo } K\alpha_1) = 707.831 \text{ xu}$  while papers in the U.S. tended to favor reporting data using  $\lambda(\text{Cu } K\alpha_1) = 1537.400 \text{ xu}$ . That the units so-defined were, in fact, inconsistent was "discovered" by the spectroscopists only in 1964 [6] but was evidently already well-known to crystallographers [7]. To escape the x-unit ambiguity and take the opportunity to eliminate the 0.2 percent offset between the x-unit and the milli Angstrom, Bearden proposed a new, and more consistent, scale [8]. The unit for this scale was denoted by  $\overset{\circ}{\text{A}}^*$  which was chosen in such a way that  $\lambda(\text{W } K\alpha_1) = 0.2090100 \overset{\circ}{\text{A}}^*$ . In reference [8], considerable pains were taken to express previously available data on this more consistent scale. Unfortunately, as will appear below, this scale seems also to suffer a measure of inconsistency. Since crystallographers seldom use W  $K\alpha_1$  radiation it was necessary to wait for a while in order to reach this conclusion in a direct way.

To return to the historical line, it is noted that, shortly after the demonstration of x-ray diffraction by a ruled grating [9], a refined measurement was reported by E. Bäcklin in 1928 [10]. The output datum from this exercise  $\Lambda = \lambda_g/\lambda_s$  represented the ratio of a wavelength as measured on the "grating" scale to the same wavelength as measured on the "Siegbahn" or x-unit scale. By the time of Bäcklin's measurement, a considerable and accurate body of information on x-ray wavelengths and cell dimensions was available. With a value of  $\Lambda$ , this could be then turned to use in determining fundamental physical constants. For example, one could rewrite eq. (1) as a determination of  $N_A$  in terms of a cell volume derived from edge dimensions  $a_x$  (in xu) and  $\Lambda$  as

$$N_A = \frac{nM}{\rho a_x^3 \Lambda^3} \quad (3)$$

Other constants were also available in this way, as, for example,  $h/e$  from the high frequency limit (HFL) of the continuous spectrum where

$$h\nu = hc/\lambda = hc/\lambda_x \Lambda = eV \quad (4)$$

for electrons of energy  $eV$ , with  $V$  the voltage across the x-ray source and  $\lambda = \lambda_x \Lambda$  the wavelength corresponding to the HFL. Unfortunately, the value of " $e$ " derived in this way is in variance with the final result of Millikan's oil drop studies [11]. The Millikan result is widely accepted and strongly held so that Bäcklin's thesis was to begin a debate lasting almost two decades.

Because of its great difficulty and its pivotal role in the controversy, great attention was given to the ruled grating measurement of x-ray lines. J. A. Bearden [12], in particular, made great contributions to the plane grating measurement technology involving

While H. A. Kirkpatrick and J. W. M. DuMond [13] attempted to produce a large, focusing instrument in which the important work of Tyren [14] (who compared calculable hydrogenic spectra with  $A\lambda K\alpha_{1,2}$ ) might be repeated. In all cases, the plan of measurement was to compare  $A\lambda K\alpha_1$  or the peak of the partly resolved doublet with an optical wavelength standard. In the culminating work of the plane grating school, A. Henins was able to report a measure of  $Cu K\alpha_1$  in terms of the  $^{198}Hg$  green line to a claimed accuracy of approximately 10 ppm [15].

At an earlier stage, the weight of cumulative evidence against the oil-drop "e" had become large and the origin of the systematic error (in rotating cylinder air viscosity measurement) had been discovered [16]. At that point, there came a brief "golden age" during which x-ray measurements contributed important and, in some cases, dominant information regarding the fundamental constants. By the sixties, this influence had passed as other methodologies improved toward the few ppm level while x-ray measurements remained burdened with a which stubbornly refused to reach even 10 ppm. (The 10 ppm result noted above came later, at a time when its impact was not large.)

That at the present time, an x-ray method (though not a spectroscopic one) is the dominant source of information on  $N_A$  (at the 1 ppm level), suggests that some new technologies have intervened as indeed they have. These technologies have permitted optical determination of  $\gamma$ -ray lines (which are very sharply defined) with accuracies approaching 0.1 ppm while the following location of characteristic x-ray features to the lesser accuracy ( $\sim 1$  ppm) their larger widths entail.

### 3. New Crystals - New Technology

As one looks at a diagram such as that of figure 1, it appears that an x-ray line can be used to measure a crystal spacing or vice versa but neither can be better known than the other. Since the minimum width of x-ray lines exceeds 300 ppm, there would appear to be a 300 ppm floor on d-measurements and on  $\gamma$ -ray to visible comparisons if they use x-ray intermediate steps. It was clear by the very early sixties that, in response to the needs of semiconductor device technology, crystals of increasing perfection were coming to be available especially in the case of Si. How could one extract the full scientific benefit from these developments in spite of poorly structured characteristic x-ray lines? This question was under active debate in the few remaining x-ray spectroscopy laboratories in the early sixties when the answer became clear in the first beautiful demonstrations of x-ray interferometry by U. Bonse and M. Hart [17].

Early interferometers were cut from single crystal silicon blocks such as indicated in figure 2 for the most primitive LLL (Laue, Laue, Laue) case [18]. These blocks showed atomic-scale Moiré patterns sometimes with appreciable areas of uniform intensity. Best of all, they are substantially achromatic, i.e., the picture seen is rather weakly dependent on x-ray wavelengths. A procedure to determine directly a lattice period (independent of x-ray wavelength values) was evident to all but not necessarily easy to carry out. What had to be done was to provide for motion of the third crystal lamella relative to the first two and determine the motion by optical interferometry with a (visible) wavelength standard. Several

approaches to this problem have been made, three of which were described at a conference held at NBS in 1970 [19]. Numerical results have, thus far, been reported for one of the efforts although progress is evident in the case of two others. In any case, the optical interferometric measurement of the repeat distance in a particular (Si) specimen marks only the first step in a process leading to one or another invariant output. Any assumption that the numerical result can be attributed to crystals other than the object measured involves one in a "generic" approximation which has obviously limited validity and an error structure not easily quantified. The one study so far carried out shows a range of variation of 1 ppm for float zoned samples and 1 ppm for Czochralski material (with a 3 ppm offset) from a small number of distinct sources [20].

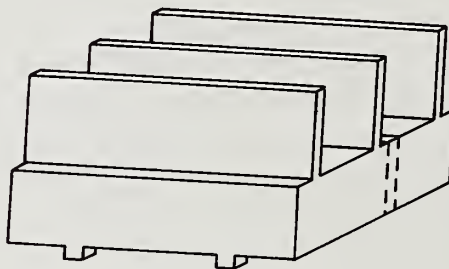


Figure 2. Monolithic symmetric LLL (Laue, Laue, Laue) x-ray Moiré interferometer after U. Bonse and M. Hart [17]. A lattice measurement can be secured by freeing one of the wafers, equipping both it and the pair left with optical mirrors and scanning a common baseline.

The measurement carried out at NBS is shown schematically in figure 3. The optical interferometer is of the hemispherical Fabry-Perot type and the visible standard is a 633 nm  $^3\text{He}^{22}\text{Ne}$  laser stabilized with respect to a saturated absorption feature in molecular iodine, namely the "B" peak in  $^{129}\text{I}_2$  [21]. This particular laser source was measured with respect to both the currently defined wavelength standard ( $^{86}\text{Kr}$ , 606 nm) and the Cs frequency standard. Its numerical value, 632990.079 pm (4 ppb), is consistent with a possible future redefinition of the meter such that  $c = 299792458 \text{ ms}^{-1}$ . It is also closely related to the Balmer  $\alpha$  transition in hydrogen (which is immediately the Rydberg constant,  $R_\infty$ ) hence offering a suitable basis for comparisons with atomic theory, quantum electrodynamics and for fixing masses of elementary particles.

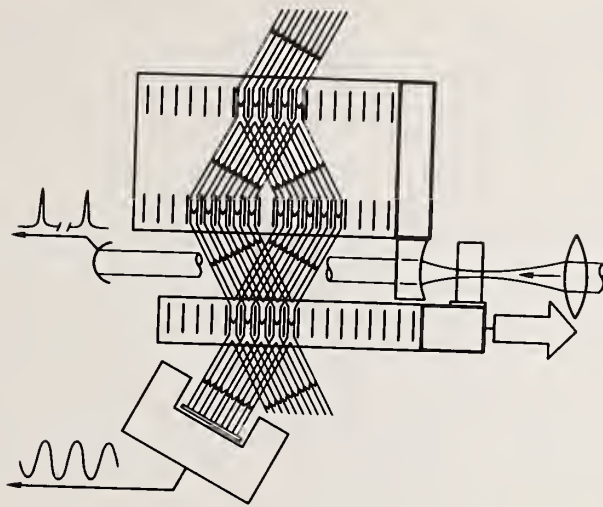


Figure 3. Schematic of combined x-ray and optical interferometers used to determine 220 repeat distance in a Si sample.

The measurement proceeded by successive refinements toward fixing a value for the ratio where  $\lambda$  is the optical wavelength and  $d$  is the 220 repeat distance in our Si specimen (approximately 0.2 nm). This ratio has an integer part and a fractional part which are separately determined. The integer part was determined by scanning to and fro over one or more (300 nm) optical periods while recording the more rapidly varying signal (0.2 nm period) in the x-ray interference channel. The result (which was, of course, known ahead of time) was 1648. The first approximation to the fractional part of the ratio,  $f$ , was obtained by electronically "locking" the system to successive optical fringe maxima and noting the x-ray intensity. With due attention to the circular progression, these intensities could be arranged to give values for the cumulative x-ray phase as a function of optical order number. The values from such curves, averaged for two scan directions, were used as initial approximations to  $f$ . More precise estimates came from runs with larger "steps" covering two or three optical orders between lock points. Finally, we chose pairs of integers,  $m$ ,  $n$ , such that  $f \approx m/n$ . In this case, lock was established only every  $n$  optical orders and the slow change due to the difference,  $f - m/n$ , measured. This procedure gave rather precise results in short times which was helpful in dealing with drifts encountered on the sub-micron scale being measured.

Data from approximately 160 measurements were reasonably well fit by a Gaussian distribution having  $\sigma = 0.5$  ppm which implies for the mean an estimated  $\sigma_m = 0.04$  ppm. Several corrections are needed for systematic effects, namely:  $2.50 \pm 0.01$  ppm due to diffraction shift of the visible light;  $-0.27 \pm 0.03$  ppm because of path curvature of  $1.17 \pm 0.06$  arc sec/200 optical fringes;  $0.34 \pm 0.01$  ppm for specimen compression due to the fact the interferometer measurement was carried out in vacuum while subsequent wavelengths were done at atmospheric pressure. Results for each measurement were corrected back to a

common reference temperature of 25 °C from the measurement temperatures (23.8 °C to 24.4 °C) using  $\alpha = 2.56 \pm 0.03 \text{ ppm K}^{-1}$ . When these corrections are applied and their estimated uncertainties (intended to reflect a 67 percent confidence interval) combined in quadrature with the statistical measurement uncertainty,  $\sigma_m$ , the result is  $d(\text{Si } 220) = 192.01707 \text{ pm}$  (0.1 ppm) at 25 °C or  $a_0 = 543.10628 \text{ pm}$  (0.1 ppm). This result pertains only to the particular piece of Si which was measured.

To progress from one specimen to other specimens and other species, we need procedures by which this single piece of information can be disseminated to other crystals both of the same chemical identity and of different species. Some of these crystals may be useful in themselves, as for example in the case of an Avogadro constant measurement while, for the majority of applications, we require yet another measurement (of diffraction angle) to go to an x-ray or  $\gamma$ -ray wavelength. These processes, namely crystal-to-crystal transfer measurements and diffraction profile measurements are treated in the next two sections.

#### 4. Crystal-to-Crystal Comparisons

To date all of our crystal-to-crystal comparisons have included an implicit transfer in which it is assumed that two specimens from adjacent parts of the same boule have equal unit cells and that the variously available reflections have spacings which are related to the cell edge dimension,  $a_0$ , by  $d_{hkl} = a_0 (h^2 + k^2 + l^2)^{-1/2}$  for the cubic crystals. How good are these assumptions? We have cumulative arguments to the effect that they are not very bad at least down to a few parts in  $10^7$ . As regards uniformity within a boule, we have some worst case limits from the survey mentioned above [20]. In particular, where reference [20] compared crystals obtained from the same source with similar specifications,  $\delta d/d$  appeared to be bounded by 2 in  $10^7$ . Where measurements have been made of the density of sections taken along a single boule, a maximum density change of 0.1 ppm/cm is noted [22]. It would be an extraordinarily worst case hypothesis that the density variation be due entirely to changes in  $a_0$  along the boule. We have demonstrated that the density change between samples is predominantly due to isotopic fractionation and that only a somewhat uncertain but small residue can be due to lattice changes. A reasonable guess is that  $\delta d/d$  likely does not exceed 0.01 ppm/cm.

Questions regarding the reliability of using  $d_{hkl} = a_0 (h^2 + k^2 + l^2)^{-1/2}$  seem addressable in two ways which, though not logically independent, seem to make separate contributions to one's confidence in this matter. The first experimental test asks to what extent are we sure that  $d_{hkl} = d_{lkh} = d_{khl}$ ? More generally, do all triplets,  $hkl$ , for which  $a_0 (h^2 + k^2 + l^2)^{-1/2} = d_0/n$  give equal values for the primitive spacing? As one test of this degeneracy of the 511 and 333 reflections has been verified and we have a substantial body of evidence that different orders of a particular primitive reflection are related by appropriate integers. These results are near the 0.1 ppm level in some cases. In addition, x-ray "polygons" were constructed using four-fold and pseudo six-fold "standards" in a goniometer calibration exercise [23]. The results of these exercises were consistent with "perfect"

four-fold and six-fold symmetry within 0.02 arc sec which, at the Bragg angles used (near 45°) implies effective lattice equality within 0.1 ppm. It is asserted on the basis of the above arguments that equating the results obtained from adjacent parts of the same boule and with equivalent reflections is permissible at the 0.1 ppm level.

Given admissibility of the implicit transfers, how can we make accurate explicit transfers between different crystals of the same species without being limited by the imperfection of x-ray lines? Several modalities are available to this end. Those we have used are related to ones discussed in one form or another by Hart and collaborators as indicated below. One of the schemes applicable to comparison of highly degenerate specimens and not able to handle, as well, cases of rather approximate degeneracy is shown in figure 4. The long crystal shown at A has a grating spacing approximately equal to one of the specimens being compared. When a crystal specimen already characterized as having a repeat distance,  $d_s$ , is placed at the position B, diffraction maxima will be observed as separated by an angle  $\beta_0$ . When the specimen to be calibrated which has a spacing  $d_u$  is placed at B, diffraction maxima, for the symmetric ray-paths shown, will be separated by  $\beta$ . If, with due attention to algebraic sign, we let  $\delta = \beta_0 - \beta$ , then

$$\frac{d_s}{d_u} = \cos(\delta/2) - \sin(\delta/2) \cot\theta \quad (5)$$

where  $\theta$  is the Bragg angle for the first crystal. Evidently knowledge of the x-ray wavelength used is required only for evaluating the  $\cot\theta$  term. Since this term appears multiplied by  $\sin(\delta/2)$ , wavelength information need not be terribly precise provided  $\delta$  is quite small. When such a procedure is applied to equivalent reflections in the same species, the wavelength dependent term is always so small that an extremely crude estimate of the wavelength suffices.

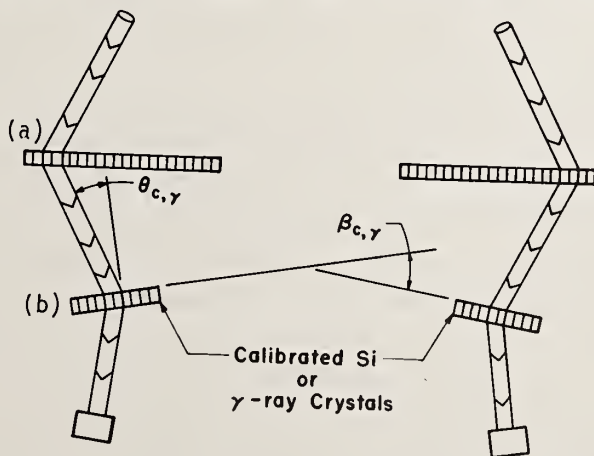


Figure 4. Quasi-non-dispersive arrangement for transfer of crystal calibration.

Unknown sample and standard crystals are alternately placed in position B and the difference,  $\beta$ , between the left and right diffraction paths are measured.

On the other hand, when it is required to compare cell edge dimensions for different crystal species, one must look for near coincidences in order to remain relatively insensitive to x-ray wavelength values. In the main case of interest here, we have made use of the near degeneracy of the 800 reflection in Ge with the 355 reflection in Si, as suggested by Baker and Hart [24]. Since these spacings differ, nominally, by 240 ppm, a wavelength variation good even to 100 ppm would already overwhelm any potential need when due account is taken of the intrinsic widths of x-ray lines.

Altogether there are three regimes in which these "quasi-non-dispersive" transfer measurements can be carried out. In the first, and obviously most desirable, spacing differences are so small, e.g., a few to a few hundred ppm, that the observed profile appears simple and symmetric. In this case one does not need either a good estimate of line shape or a good algorithm for establishing a wavelength scale. In the second case, mismatch is sufficiently large that  $\alpha_1$  and  $\alpha_2$  begin to appear partly resolved. This is a difficult region in which to work because of the required corrections for overlap. The problem can surely be handled by a detailed modeling of the spectrum; up until the present, we have avoided this region and worked, instead in a third regime. For this third mode, mismatch of A and B is sufficient that  $\alpha_1$  and  $\alpha_2$  are clearly resolved though, of course, they appear more closely spaced than in typical single- or double-crystal profiles because of the near cancellation of dispersion. This regime does make some more demands on angle measurement and wavelength information than the others, however it still offers a distinct gain over the fully dispersive case. For example, when one makes a comparison using 1 percent mismatch, there is a 100-fold reduction in the accuracy of angle measurement and of wavelength input data required to generate a targeted output accuracy. One case where this regime was tried involved comparing (440) spacings in Si and Ge where the mismatch is 4 percent. Here the accuracy gain was not quite sufficient to compensate for a relatively poor angle calibration then available for the goniometer in use and limitation of knowledge of the Ag  $K\alpha_1$  radiation used began to become perceptible as we were seeking 0.1 ppm in that particular exercise. Any less stringent requirement would have been easily met.

To summarize this part of the measurement chain, we have transferred spacing information from the interferometrically calibrated Si specimen to all other crystals used in subsequent precision measurements of x-ray and  $\gamma$ -ray lines. These include Si crystals cut for symmetric Laue diffraction using the 220, 400 and 111 reflection and Ge crystals oriented for 400 reflection. As described in the next section, these have been used in measurement of x-ray and  $\gamma$ -ray diffraction profiles having scale errors below the 1 ppm level.

## 5. Double-Crystal Diffraction Measurements

Crystals calibrated as described above can be used for accurate wavelength measurements provided angle measurement facilities are adequate. At accuracy levels suited to work below 1 ppm, the required angle scale needs to be established by an in situ first-principles calibration. Also the scale refinement needed (0.1 arc sec at large angles to well below 0.1 arc sec at small angles) strongly suggests use of interferometric angle measurements.

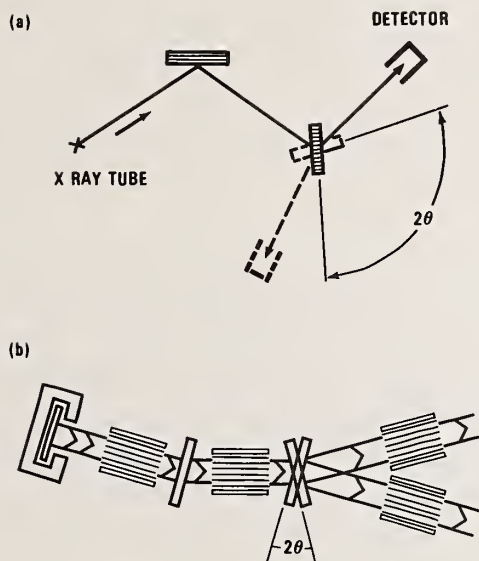


Figure 5. Diagrams of large angle (a) and small angle (b) double crystal diffractometers.

Geometric arrangements of the two instruments used thus far are shown in figure 5.

Figure 5a shows the typical arrangement of a Bearden-Ross instrument [25] which we have used for the  $\text{Cu K}\alpha$  and  $\text{Mo K}\alpha$  measurements. This instrument has a hybrid angle measuring system with a  $\pm 3^\circ$  interferometric goniometer surmounted by a large angle indexer with fairly reproducible  $1^\circ$  stations. The large angle generator was calibrated with respect to a 12-sided optical polygon which, in turn, had been calibrated from first principles. The angle interferometer (resolution limit near 0.01 arc sec) was then calibrated using the indexer to generate up to  $5^\circ$  increments at several points in its range. Because of irreproducibility in the indexer and the several stages required in calibration, this instrumental arrangement was only marginally adequate even for relatively large angle reflections ( $\sim 30^\circ - 50^\circ$ ) with  $\text{Cu K}\alpha$  and  $\text{Mo K}\alpha_{1,2}$  radiation.

The situation of the small-angle instrument [26] indicated in figure 5b was more satisfactory from the point of view of calibration, but it had a very limited angular range of  $5^\circ$ . (This limitation was determined by certain, by now irrelevant, choices made 15 years earlier.) The small angular range could, of course, be entirely covered by interferometric measurement permitting a very satisfactory calibration procedure. In this procedure, all interfacial angles of a 72-sided optical polygon were successively measured by the interferometer; the closure condition, namely that the sum is  $360^\circ$  suffices for the calibration independent of polygon errors. The angle interferometers are, in this case, quite sensitive and easily readable to 0.05 milli arc sec. With the aid of a sensitive autocollimator, such calibration exercises have been carried out over the past four years with individual measurement errors of a few parts in  $10^8$ . The calibration constant changes slowly with time ( $\sim 0.7$

ppm/year) requiring that the value be read from the curve of growth. This appears to have present a limiting accuracy near 0.1 ppm which is entirely satisfactory for the x-ray measurements but limits slightly the  $\gamma$ -ray determinations. Unfortunately, the limited angular range has restricted this instrument's application to only the case of  $W K\alpha_{1,2}$  among the x-ray lines measured. (Still a third instrument with an interferometric range of  $\pm 15^\circ$  has been built [27] and is available to obtain slight improvements in the results to be presented below should these be required.)

Results available thus far for  $Cu K\alpha_1$ ,  $Mo K\alpha_1$ , and  $W K\alpha_1$  are as follows:  $\lambda(Cu K\alpha_1) = 154.05974$  pm (1.0 ppm);  $\lambda(Mo K\alpha_1) = 70.93184$  pm (0.6 ppm);  $\lambda(W K\alpha_1) = 20.901349$  pm (0.9 ppm). Numerical values given for  $Cu K\alpha_1$  and  $Mo K\alpha_1$  differ slightly (0.44 ppm) from those we published in 1974 [28] due to improvements in the lattice parameter measurement and small systematic corrections. If we compare these above data with the three x-ray scale definitions, values for  $\Lambda$  are:  $\Lambda(Cu K\alpha_1 = 1537.400 \text{ xu}) = 1.0020797 \overset{\circ}{\text{A}}/\overset{\circ}{\text{kxu}}$  (1.0 ppm);  $\Lambda(Mo K\alpha_1 = 707.831 \text{ xu}) = 1.0021013 \overset{\circ}{\text{A}}/\overset{\circ}{\text{kxu}}$  (0.6 ppm);  $\Lambda(W K\alpha_1 = 0.2090100 \overset{\circ}{\text{A}}) = 1.0000167 \overset{\circ}{\text{A}}/\overset{\circ}{\text{A}}$  (0.9 ppm). Such conversion factors may be of some utility in interpreting past work, however, we suggest that they are likely to be less needed in the future.

These procedures have also been applied to almost two dozen  $\gamma$ -ray secondary standard lines in the range  $0.06 < E < 1.2$  MeV. Initial results on  $^{198}\text{Au}$  and  $^{192}\text{Ir}$   $\gamma$ -lines [29] have been followed by new measurements on lines from  $^{169}\text{Yb}$  and  $^{170}\text{Tm}$  [30]. All these results have accuracy claims near 0.3 ppm; there are several cases in which satisfactory closure tests have been made among three-level transition groups where  $E_{13} = E_{12} + E_{23}$ .

## 6. Line Shape Refinement

There is one final issue, namely, what are line shapes in detail? Many studies in the past have reported widths and asymmetry indices but there were no really detailed profiles published by the mid-seventies with the high quality crystals by then available. Over 20 years ago Lyman Parratt had developed some qualitative pictures suggesting that all x-ray lines should conceal a detailed infrastructure [31]. There had also been, from time to time, communications reporting observations of some fine scale detail.

In 1976, Sauder, et al. [32] using a tunable arrangement of a high resolution monolithic monochromator [33], studied in detail the profile of  $Cu K\alpha_{1,2}$  with resulting data as shown in figure 6. Calculations on the positions and line strengths for the double vacancy transition arrays corresponding to  $1s2p^6 3d^9 1,3D \rightarrow 1s^2 2p^5 3d^9 1,3P$  and  $1s2p^6 3p^5 1,3P \rightarrow 1s^2 2p^5 1,3SPD$  are also shown in figure 6 along with the result of subtracting Lorentzian doublet components from the raw data. The association between at least the general clumping of the predicted satellite lines and experimental residues appear quite suggestive but some skepticism remains in order. There was, however, other work underway, at the time not known to the U.S. workers which gives striking confirmation of the general picture and offers, in the end, stern warnings regarding the limitation of detailed profile descriptions.

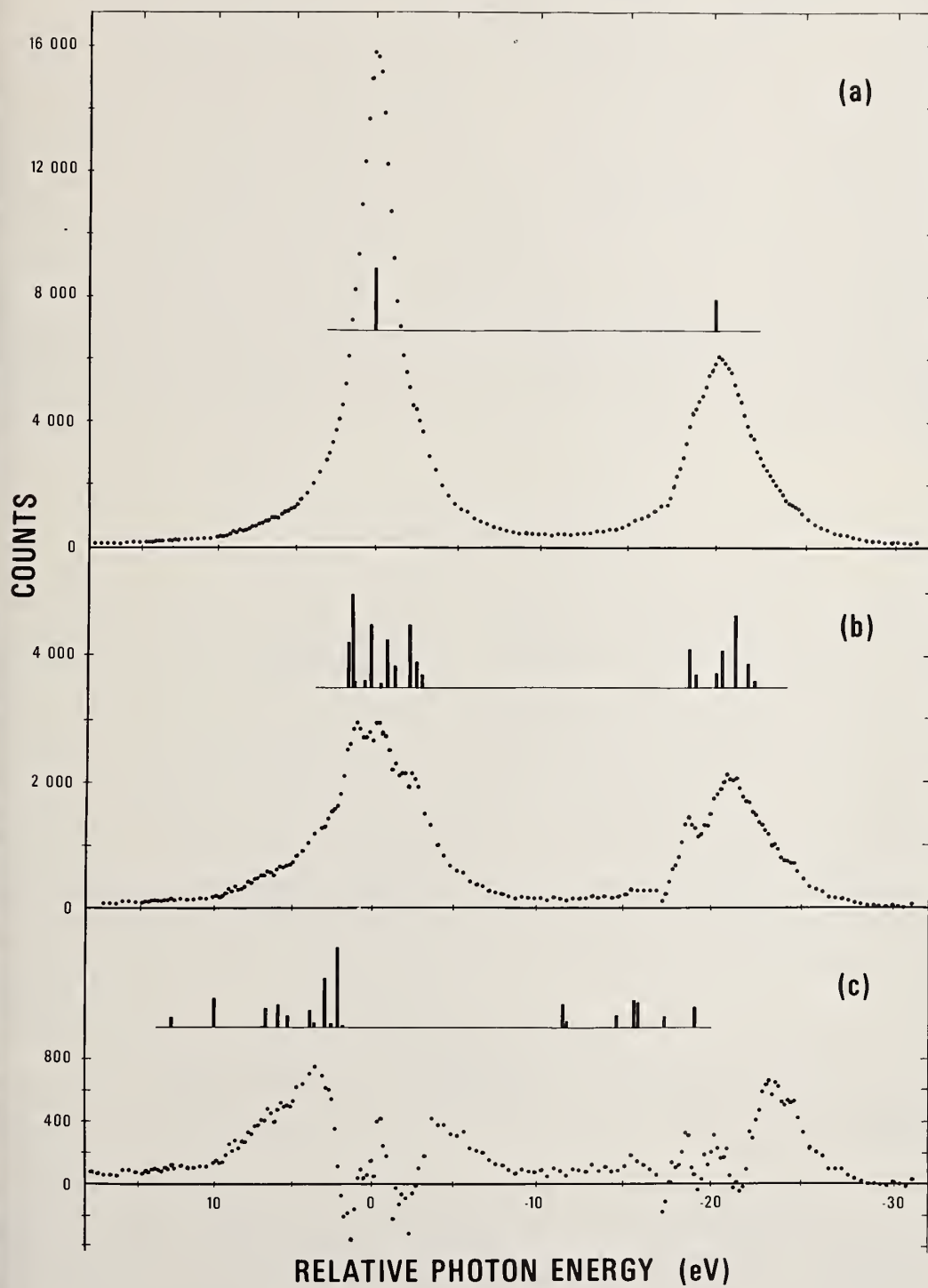


Figure 6. The Cu  $K\alpha_{1,2}$  region as observed, a; spectra resulting from subtracting model distribution, b and c.

Using synchrotron radiation from the electron storage ring at Orsay, Briand, Travennie and Chevallier were studying widths of transition metal lines using near threshold fluorescent excitation [34]. Their instrumentation had far less resolution than that used to obtain figure 6; it was, however, quite adequate to see the remarkable changes in width shown in figure 7. What is happening here is that quite clearly when the incoming photons have energy insufficient for producing a particular double-vacancy initial configuration, the associated satellite array simply disappears. Since these extra transitions are scattered about in some way such as that suggested in figure 6, one sees a narrowing for near threshold excitation. Not only does one have to expect a narrowing but, since the distribution of the satellites has no requirement to be symmetric, shifts must be expected in any smooth property of the profile, e.g., peak location, centroid, etc. Instrumentation used in reference [34] was not quite adequate to show these shifts but their presence seems inevitable. Subsequently, further confirmation [35] of this model has emerged in a detailed study of  $\text{Cu K}\beta_{1,3}$ .

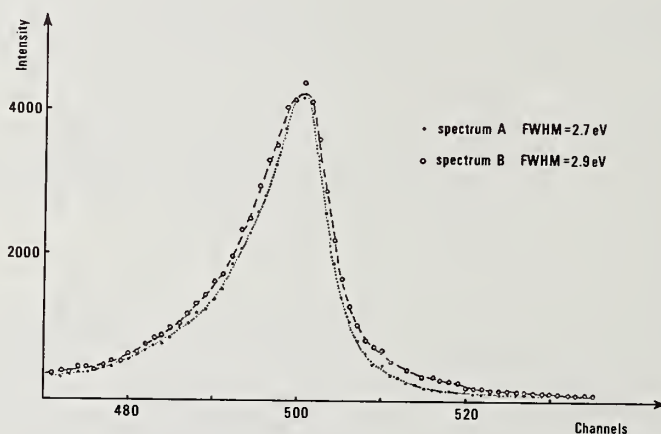


Figure 7. Profile of  $\text{Fe K}\alpha_1$  as obtained very close to single vacancy threshold, A, and with excitation of 500 eV above the single vacancy threshold, B.

What then are the implications of these results for crystallography? As was suggested in the Introduction, nothing in this entire report can be disturbing to crystallography as it is now practiced since there are other, more dominating, sources of error in all current methodologies, especially those using powdered samples. On the other hand, there is at least an aesthetic point in understanding basic limitations and potential sources of confusion. Clearly, no one uses tunable photon excitation of his or her diffraction tube so it remains

to be considered what can be expected from electron bombardment sources. Crudely, the electron excitation behavior with respect to anode voltage represents a complex kinematic averaging of the photon excitation function with necessary allowance for energy loss processes. With constant potential excitation at high tube voltages there is little doubt that, for a clean metal, gross smearing has covered most traces of the above detail. On the other hand, with unfiltered quasi-dc or ac excitation it is clear that the line is changing shape during the time that voltage is near threshold. Surely, this is not a large effect and it occupies a small part of the excitation waveform, but it is there nonetheless. Finally, there is another aspect of this problem which may prove to be a more troublesome one in the end. It is well known that x-ray emission satellites, when they are clearly resolved from their parent transitions, display far greater chemical sensitivity (shifts and intensity changes) than do the diagram lines. It would surely be imprudent to assume that the close-in satellites which are important here have some immunity from this problem. We have, therefore, a mechanism through which aging of the anode in the residual gases of the envelope or its alloying with the cathode and shielding materials may lead, over time, to changes in the shapes and positions of the characteristic lines.

## 8. Summary and Conclusions

An attempt has been made to indicate the state of current knowledge of some of the x-ray lines frequently used in structure studies. The data indicate that a particular profile has features such as peak location which are established at or near the 1 ppm level. It is most desirable that such first-principles determinations be undertaken in at least one or two other laboratories so that the presently available results could be confirmed or challenged.

Certain recently discovered complexities have been recapitulated which tend to make a simple parametrization of the line profiles somewhat suspect. Indeed these complexities are known to point up the existence of a certain level of irreproducibility in the smoothed features of characteristic x-ray lines obtained under different excitation conditions.

At the present time there appears to be no structural methodology that fully utilizes the available accuracy and certainly none is presently troubled by the last mentioned subtle problem areas.

## References

- 1] Bragg, W. H., Proc. Roy. Soc. (London) 88A, 428 (1913); *ibid.* 89A, 246 (1914); 89A, 430 (1914).
- 2] Millikan, R. A., Phys. Rev. 26, 198 (1908); Phil. Mag. 19, 209 (1910).
- 3] Mosely, H. G. S., Phil. Mag. 26, 1024 (1913).
- 4] Siegbahn, M. and Leide, A., Phil. Mag. 38, 647 (1919); Siegbahn, M., Arkiv. Matt. Astron. Fys. 14, Nr. 9 (1919).
- 5] Siegbahn, M., The Spectroscopy of X-rays (Oxford Univ. Press, London, 1925), p. 84.
- 6] Bearden, J. A., Henins, A., Marzolf, J. G., Sauder, W. C., and Thomsen, J. S., Phys. Rev. 135, A899 (1964).

- [7] One of us (R. Deslattes) was given this impression while trying to tell of the then "new" results.
- [8] Bearden, J. A., *Rev. Mod. Phys.* 39, 78 (1967).
- [9] Compton, A. H. and Doan, R. L., *Proc. Natl. Acad. Sci. U.S.* 11, 598 (1925).
- [10] Bäcklin, E., Inaugural dissertation, Uppsala Univ. Arsskrift, 1928; later work is described in *Z. Physik* 93, 450 (1935).
- [11] Millikan, R. A., *Phys. Rev.* 7, 355 (1916).
- [12] Bearden, J. A., *Phys. Rev.* 37, 1210 (1931); 48, 385 (1935).
- [13] Kirkpatrick, H. A., DuMond, S. W. M., and Cohen, E. R., Proceedings of the Third International Conference on Atomic Masses, R. C. Barber, ed. (Univ. of Manitoba Press, Winnipeg, 1965), p. 347.
- [14] Tyrén, F., *Zeits. Physik* 109, 722 (1938).
- [15] Henins, A., in Precision Measurement and Fundamental Constants (D. N. Langenberg and B. N. Taylor, eds.), National Bureau of Standards Special Publication No. 343 (U.S.G.P.O., Washington, D.C., 1971), p. 255.
- [16] This origin for the discrepancy was apparently first suggested by K. Shiba, see discussion by J. S. Thomsen and A. F. Burr, *Am. Jour. Phys.* 36, 803 (1968).
- [17] Bonse, U. and Hart, M., *Appl. Phys. Lett.* 6, 155 (1965); *Z. Phys.* 188, 154 (1965).
- [18] For a review, see U. Bonse and W. Graeff, in X-ray Optics, H.-J. Quesser, ed. (Springer-Verlag, Heidelberg, 1977), p. 93.
- [19] Precision Measurement and Fundamental Constants, D. N. Langenberg and B. N. Taylor, eds., National Bureau of Standards Special Publication No. 343 (U.S.G.P.O., Washington, D.C., 1971).
- [20] Ando, M., Bailey, D., and Hart, M., *Acta. Cryst.* A34, 484 (1978).
- [21] Schweitzer, W. G., Jr., Kessler, E. G., Jr., Deslattes, R. D., Layer, H. P., and Whetstone, J. R., *Appl. Opt.* 12, 2927 (1973).
- [22] Bowman, H. A., Schoonover, R. M., and Carroll, C. L., *J. Res. NBS* 78A, 13 (1974), see especially p. 39, fig. 6.
- [23] This work (unpublished) was carried out with the help of B. Paretzkin.
- [24] Baker, J. F. C. and Hart, M., *Acta. Cryst.* A31, 364 (1975).
- [25] Deslattes, R. D., *Rev. Sci. Inst.* 38, 815 (1967).
- [26] A description of this instrument together with a more thorough description of the entire measurement chain is being prepared.
- [27] This instrument which may, over the next few years cover the range  $0.05 < E < 5$  MeV, was designed and built in collaboration with two scientific visitors, W. Schwitz, University of Fribourg and Swiss National Science Foundation, and L. Jacobs, Assoc., IKS Leuven University and SCK, Mol, Belgium.
- [28] Deslattes, R. D. and Henins, A., *Phys. Rev. Lett.* 31, 972 (1973).
- [29] Kessler, E. G., Deslattes, R. D., Henins, A., and Sauder, W. C., *Phys. Rev. Lett.* 40, 171 (1978). Background and some details can be found elsewhere; see also, R. D. Deslattes in, Proceedings of the International School of Physics "Enrico Fermi" Course LXVIII 12-14 July (1976) (to be published).

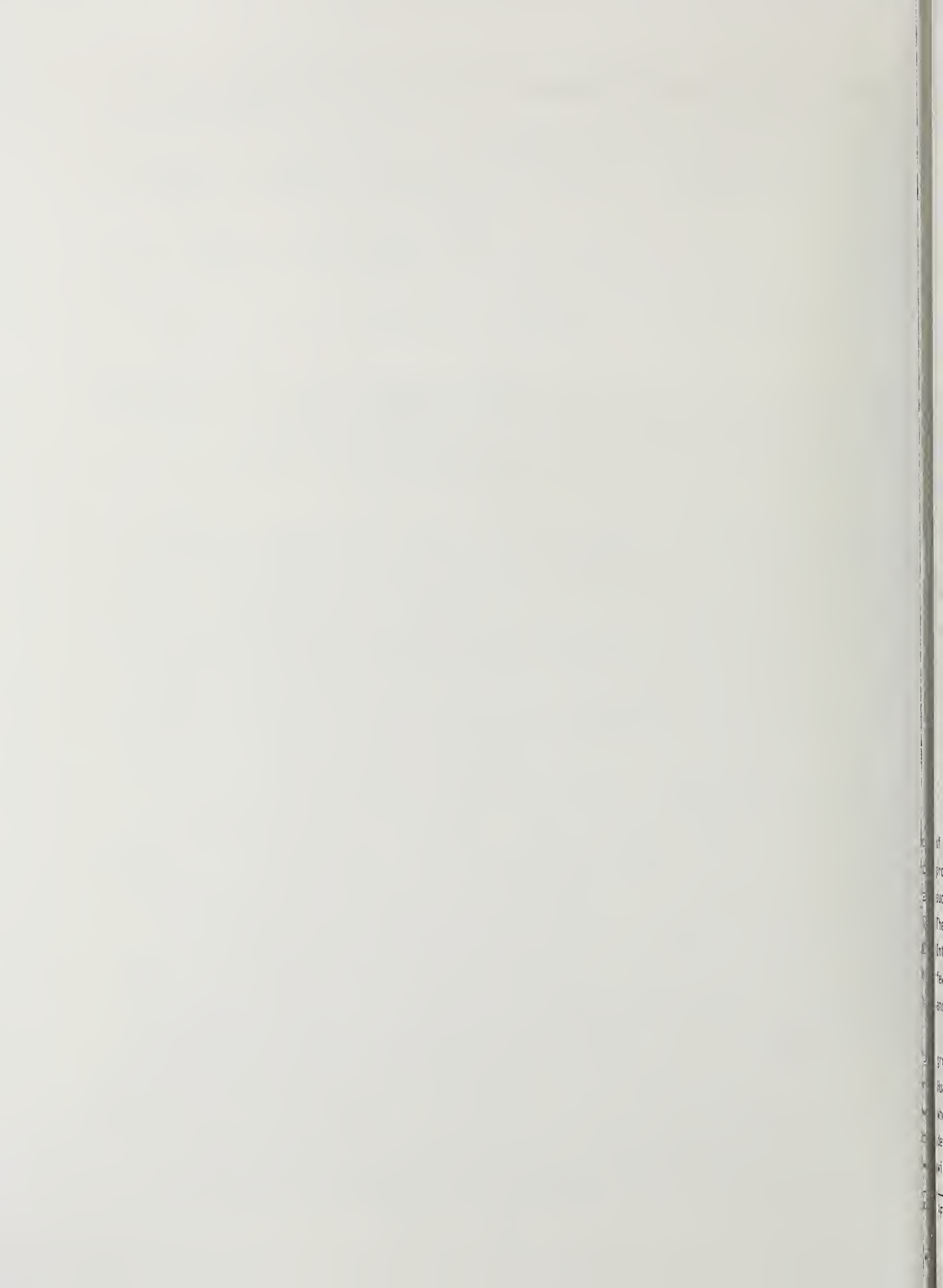
- 0] Kessler, E. G., Jr., Jacobs, L., Schwitz, W., and Deslattes, R. D., Nucl. Instr. and Meth. 160, 435 (1979).
- 1] Parratt, L. G., Rev. Mod. Phys. 31, 616 (1959).
- 2] Sauder, W. C., Huddle, J. R., Wilson, J. D., and LaVilla, R. E., Phys. Lett. 63A, 313 (1977).
- 3] Deslattes, R. D., Appl. Phys. Lett. 12, 133 (1968).
- 4] Chevallier, P., Travennier, M., and Briand, J. P., J. Phys. B 11, L171 (1978).
- 5] LaVilla, R. E., Phys. Rev. A 19, 717 (1979).

#### Discussion

Question (Shirley): Can you please advise us what criterion of line position you used, considering that for example the  $\text{CuK}\alpha_1$  line does not have a very regular shape?

Can you state the wavelength in the form of, for example, medium position at 80 percent maximum intensity, so that the result may be more readily applied?

Response (Deslattes): This is a very good question to which there is not a simple answer especially below 1 ppm. Firstly, the measurements we made on  $\text{CuK}\alpha_1$  and  $\text{MoK}\alpha_1$  were carried out before observation of the internal fine structures mentioned in the text and with insufficient resolution and stability to have seen these features clearly. (In the case of  $\text{W K}\alpha_1$  the linewidth itself may preclude observation of such structures although they are certainly present. The line position criterion was, in each of the above cases, peak location which is given (approximately equivalently) by the asymptotic bisector of the media of chords or formal differentiation of a fitted profile. Discovery of the internal fine structure certainly means that a carefully observed profile would exhibit significant jitter in midpoint location as a function of chord height thereby precluding the realization of a well-defined asymptote. Similarly, no fitting to simple model functions or polynomials of moderate order could exhibit statistical control. Therefore, the formal differentiation algorithm fails also. Thus, all that can be said is that: if one smears the "true" profile adequately, then a convolved result emerges which exhibits the needed properties and its fold has a peak position which is well-defined to a certain extent and is possibly somewhat independent of the details of the smoothing function. This is clearly not a satisfying outcome but is nonetheless what appears to emerge from our best efforts to date. We could, possibly we should, publish some horribly detailed profile (lumps and all) with absolute energy, wavelength or frequency scale and leave it to the user to smooth this as his or her application requires. Remembering that the texture is chemically sensitive and dependent on excitation conditions, we are counseled to moderation in thinking to undertake such an enterprise.



## NEGLECTED CONSIDERATIONS FOR INTENSITY MEASUREMENT

L. D. Jennings  
Army Research Center  
Watertown, MA 02172

Although the primary thrust of powder diffraction is the measurement of the position and shape of the peaks, some applications require accurate intensity measurements. Some considerations and techniques which seem not to be generally appreciated are discussed: (1) the technique of evaluating dead time by measuring the apparent absorption of a single foil as a function of count rate; (2) the role of small angle scattering, for example within an absorbing foil, in this and other connections; (3) the recognition that a typical monochromating crystal displays extreme secondary extinction, thus yielding polarization ratios far from the mosaic value; (4) simple techniques for measuring this polarization ratio using amorphous scattering; and (5) the value of using a wide receiving slit to measure integrated intensities rapidly and with high resolution.

### 1. Introduction

Although most of the discussion at this conference concerns the positions and shapes of powder diffraction peaks, there are also analytical, characterization and structural problems for which intensity information is valuable. With modern photon counting apparatus, such intensities are often available with an apparent accuracy of a fraction of one percent. The actual accuracy is much harder to determine. It was therefore appropriate to conduct an International Powder Intensity Project (under IUCr auspices) [1]<sup>1</sup> some dozen years ago. A few caveats and techniques were developed at that time which may not be generally recognized, and it seems desirable to repeat them here.

Good accuracy requires both reasonable resolution and small and well defined background. Thus, first preference must be given to crystal monochromated radiation. Ayers, Huang, and Parrish [2] have also suggested that standard wavelength dispersive diffractometry, when properly carried out, is more rapid than is energy dispersive or position sensitive detection. I, therefore, will couch the discussion in terms of an ordinary diffractometer with a crystal monochromator. It is often convenient to place the monochromator after the

---

<sup>1</sup>Figures in brackets indicate the literature references at the end of this paper.

sample, to remove fluorescence for example, but, for the highest accuracy, the monochromator must be placed between the source and the sample. I will therefore explicitly consider the latter configuration, though most of the remarks will also apply to other situations.

Rather than merely highlighting a large number of possible considerations, I would prefer to restrict the discussion to just a few points. I hope in that way to give a real appreciation for each one.

## 2. Dead Time

All apparatus which counts individual photons must fail to distinguish pulses which arrive nearly simultaneously. The fraction of the counts lost will depend on the count rate, so some correction must be made, either automatically by the apparatus or in the data reduction step. In any case, the careful experimenter will wish to verify that the correction is accurately made. The usual technique is to compare the expected and measured effect of the insertion of a number of presumably identical absorbing foils. The neglected technique is to make use of a single foil at a number of different count rates.

The usual technique is illustrated in figure 1. An intense beam is attenuated by the successive insertion of nearly identical foils. The apparent count rate is plotted against the number of foils inserted using a semilogarithmic scale. A straight line is fitted to the data at low count rate and a dead time is determined which will bring the points at high count rate up to the line. The procedure has some disadvantages, however. The plot of figure 1 does not readily reveal modest errors or inconsistencies; as shown, a 5 percent effect would scarcely be noticed. Furthermore, there is usually no stated criterion as to how to choose which points are to be fitted with the straight line. Most importantly, the technique does not explicitly take into account the possibility that the foils are not identical.

The neglected technique is much more satisfying and graphic. A master foil is chosen which can conveniently (perhaps automatically) be inserted and removed from the beam. Thus, if the beam is attenuated by foils which are adequately uniform, but whose attenuation factor is otherwise arbitrary, it is possible to plot the apparent absorption of the master foil ( $R$ ) vs the count rate  $N_0$  (with the foil out). Figure 2 shows that such a plot may be represented very closely by the equation  $R = R_t - N_0 \tau (R_t - 1)$ . A little algebra confirms that this result corresponds to the usual dead time formula,  $N_t = N / (1 - N\tau)$ , where  $N_t$  is the true count rate corresponding to the observed count rate  $N$ . Note that the entire derivation relies solely on the assumption that the same foil replaced in the beam in the same way always has the same absorption. There is no question about which points are to be used in the fitting of the line and any discrepancy is clearly visible; 0.1 percent effects can now be seen.

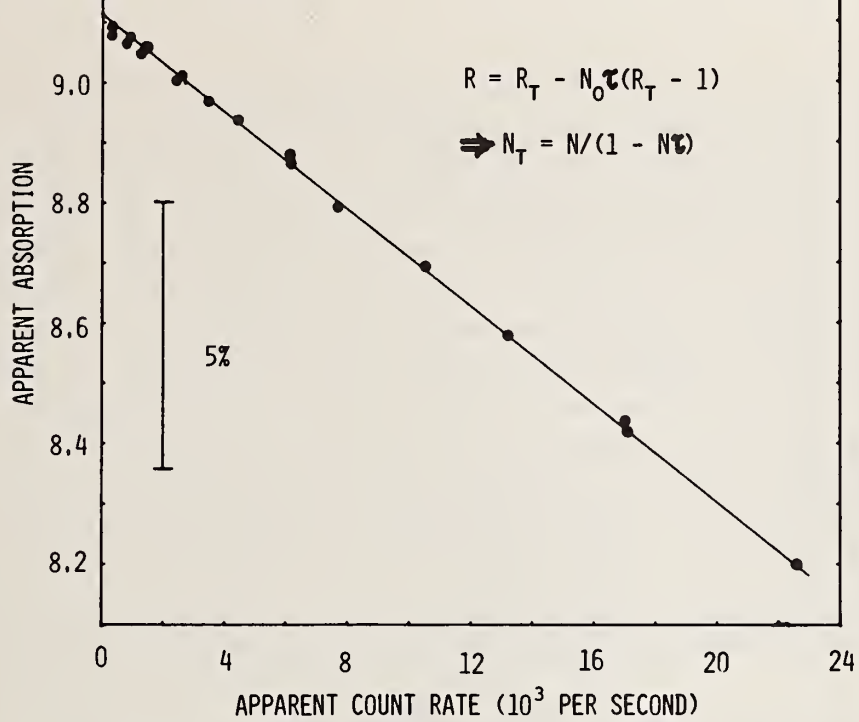


Figure 1. A typical plot of observed count rate vs number of absorbers placed in the beam.

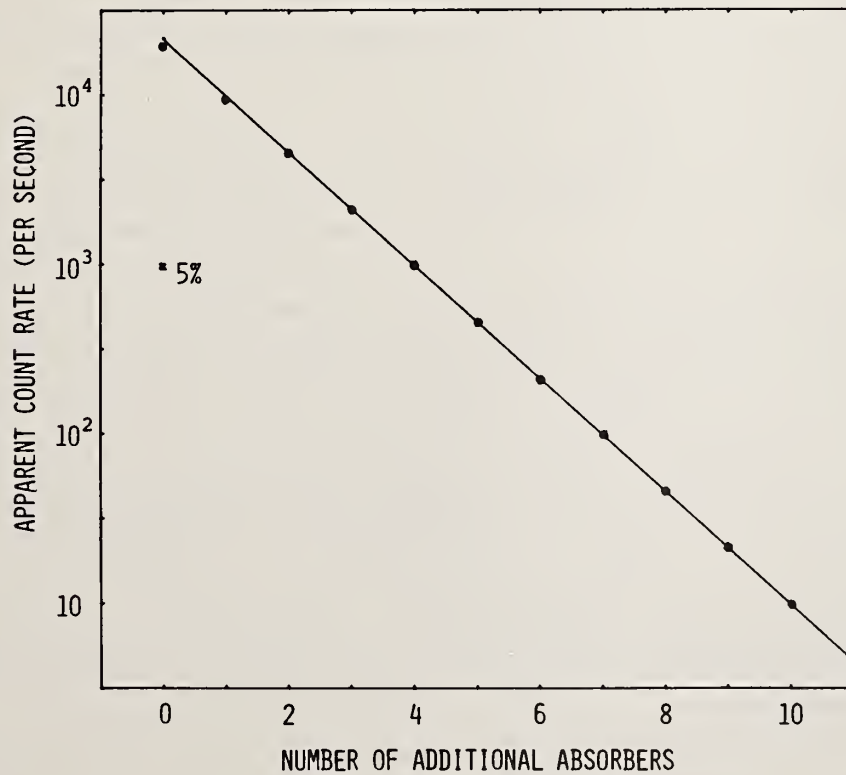


Figure 2. Measured values of apparent absorption of a master foil vs the apparent count rate with the foil removed. The intercept on the y axis is  $R_t$  and the slope is  $\tau(1 - R_t)$ , where  $\tau$  is the dead time.

There are many other issues which need to be considered and also benefits to be derived from having a readily available set of calibrated foils. The choice of foil material is of importance. One has to consider possible beam hardening (the small curvature at low count rate in figure 2 arises partly from beam hardening). For a typical scintillation detector, the entire results depend on the analyzer settings and also perhaps on the beam distribution over the crystal area. Dark counts must of course be taken into consideration. On the other hand, if genuine curvature is found in the plot, it can easily be taken into account by adding a second order term to the dead time formula. In any case, a very accurate value ( $R_t$ ) is obtained for the absorption of the master foil and absorption of other similar foils can be easily obtained by comparison with the master at high count rate. Such values may be used to make measurements on an absolute basis, or help with relative measurements at widely differing count rates. These and other considerations are discussed in more detail in Chipman's paper [3].

In any case, the important thing to remember is that the master foil method is more convenient and more reliable than a method which relies on several foils being identical.

### 3. Small Angle Scattering

There is one aspect of absorbing foils which is especially illustrative. For concreteness, consider the case of a monochromator followed by one or more absorbing foils followed by a small sample. In such a case, one might replace the small sample by an aperture of the same size so as to study the portion of the beam of interest. In this situation, we have often found the apparent absorption of a foil to have an unexpected value. The situation is most marked in the case that the foil is composed of ground powder embedded in plastic (such as is available commercially). The explanation is simple: the monochromator gives rise to a non-uniform beam and the ground powder gives rise to a small angle scattering. Thus, for example, if the sample is in a portion of the beam that is especially intense, the foil will appear to have unusually large absorption.

Although such circumstances are perhaps rather specialized, they have actually arisen in our own work. However, the principle illustrated must always be considered: small angle scattering may sometimes best be thought of as slight broadening of the direct beam; in other situations it is appropriate to think of the small angle scattering as part of the scattering. In this latter case, there is the additional consideration of whether or not the scattering is part of the absorption. This point comes up, for example, if the absorption coefficient is needed in an absolute measurement of a structure factor on a powder. Any measurement of this coefficient which does not have a discussion of angular acceptance of the apparatus is essentially worthless (at least for light elements in powder form where the scattering is appreciable).

In summary, for an accurate experiment, always reflect on whether or not small angle scattering may be a troublesome side effect.

#### 4. Values of the Polarization Ratio

The x-ray reflection from a sample is naturally divided into two components,  $\pi$  with the polarization in the plane of incidence and  $\sigma$  with the polarization normal to the plane of incidence. The remainder of the system may have differing efficiencies for the production or transmission of these two components. The ratio of these two efficiencies is called the polarization ratio,  $K$  [4]. The two most important contributions to polarization ratios differing from unity are polarization arising in the x-ray source and from reflection by a crystal monochromator.

In the typical case where an experiment is performed using line radiation from a tube, account would have to be taken of whether the adjacent bremsstrahlung wavelengths are considered to be part of the background or to be part of the desired beam. In either case, our experience is that line radiation may be considered unpolarized to moderate accuracy. On the other hand, in cases where a crystal monochromator is used, it will be shown that it is essential that the polarization ratio be measured and this measurement will, of course, include any effects arising from the x-ray source.

If the source of x-rays, as viewed from any one point on a monochromating crystal, is substantially uniform over an angular range greater than the mosaic spread of the crystal, then the diffracted power will be proportional to the integrated reflection of that crystal. In this case, there are again two principal polarization directions, and there will be a different integrated reflection for each of these directions. The ratio of these integrated reflections has been called the polarization ratio,  $\alpha$ , by Chandrasekaran [5]. If, in addition to the uniformity condition just mentioned, the source of x-rays is unpolarized, then the polarization ratio defined in this paragraph is identical to that defined in the above paragraph. In the cases that the assumptions are not met, the context makes it clear whether it is  $\alpha$  or  $K$  which is being considered.

It has been assumed by many workers, including Chandrasekaran, that the possible range of  $\alpha$  is from  $\cos^2 2\theta$  to  $\cos 2\theta$ , where  $\theta$  is the Bragg angle. It has also been assumed that the possible range for  $K$  is the same, but that for a highly imperfect monochromating crystal the  $K$  value would be close to the ideally mosaic value,  $\cos^2 2\theta$ . All these assumptions are incorrect. The implications of and reasons for this are discussed below.

Of especial interest in connection with this symposium is the observed range of  $K$ , which enters in an essential way into the polarization factor required to adjust experimental data. For the two most common geometries, an error of  $\Delta$  in  $K$  leads to a fractional error of  $\Delta/(1 + K)$  or  $\Delta/[K(1 + K)]$  in the polarization factor at  $90^\circ$  in comparison to the low angle value. Taking a LiF monochromator at  $\text{CuK}\alpha$  as an example, there are published values of  $K$  ranging from 0.62 to 0.78. There would thus be errors ranging from about 8 percent to about 25 percent if the ideally mosaic value of 0.50 were used instead of the measured value. Note also that some of the measured values are greater than  $\cos 2\theta = 0.71$ .

Because this wide range of K values is not generally appreciated, the Apparatus Commission of the International Union of Crystallography is conducting a survey [6] of measured values. Further information may be obtained from the author who would be very happy if some of the symposium participants were encouraged to perform the necessary experiments.

It is not necessary to understand the physical basis for K values differing so greatly from  $\cos^2 2\theta$  in order to make use of the correct polarization factor. On the other hand, such an understanding may serve as encouragement for making the necessary subsidiary measurements. Consider, then, a very imperfect monochromating crystal with small absorption. Consider also the case that the rocking curve of the crystal is relatively narrow, yet whose width is greater than the angle intercepted by the source of x-rays as viewed from a point on the monochromator. If, in addition, the structure factor is sufficiently large, the kinematic approximation would give far more than total reflection. This is, of course, impossible. The shortcoming in the kinematic approximation is that it does not take account of the diffraction contribution to reduction of the incident beam, an effect referred to as secondary extinction in the present case. In actual fact, for suitably prepared materials, it is possible to achieve the condition that there is very strong secondary extinction (i.e. the power reflected is very much less than that calculated on the kinematic approximation) and yet the  $\sigma$  component of the incident beam is almost totally reflected. In this case, for the  $\pi$  component, the kinematic approximation would give a value smaller by a factor  $\cos^2 2\theta_M$ , with  $\theta_M$  referring to the monochromator. This means that the  $\pi$  component would penetrate farther into the crystal and there would be somewhat more photoelectric absorption of this component. But this is still small in comparison to the portion diffracted so the  $\pi$  component is also almost totally reflected. Therefore, the polarization ratio, under these conditions, is nearly unity.

In actual cases both the geometry and the crystal preparation may not conform to the idealizations discussed above. The general principles do apply, however, and so the thrust of this section is that the polarization ratio may assume a wide range of values, none of which (for a high efficiency monochromator) is close to the kinematic value  $\cos^2 2\theta$ . It is therefore essential that the polarization ratio be measured for work requiring moderate to high accuracy.

## 5. Measurement of the Polarization Ratio

The original impetus for measuring the polarization ratios was the Powder Intensity Project [1] which aspired to the very highest accuracy. Some of the methods used are described in an IUCr sponsored report [7] on accuracy in powder diffraction. For ordinary work, at about 1 percent accuracy, much simpler techniques will suffice. These are described in the appendices to the IUCr polarization ratio survey announcement [6] (available on request from the author) and in the work of LePage, Gabe, and Calvert [8].

The idea is to measure amorphous scattering at  $90^\circ$  in each of the two principal planes. The ratio of these two results gives the polarization ratio directly. The only problem is to ensure that identical solid angles are intercepted by the detector in the two cases. A jig to do this is sketched in figure 3. If the construction permits a full circle rotation of the detector, it is only necessary to put the axis of the jig near the center of the beam and average counts taken at diametrically opposite positions in each of the two principal planes. If such a full circle rotation is not possible, it is then necessary to determine the center of gravity of the beam in each of the two planes so that the effective solid angle can be made the same during the two measurements. This determination may be made by scanning through the beam in each of the planes. Alternatively, the median of the beam power, determined by cutting off half the beam with a stop, may be an adequate approximation to the mean.

The thrust of this section is that it is relatively easy to measure a polarization ratio. I should like to encourage all workers to make such measurements and also submit the results to me as a part of the IUCr survey of polarization ratios.

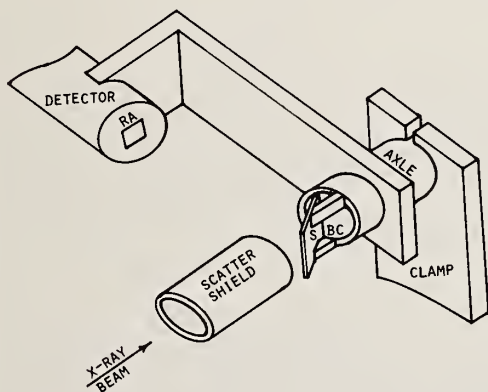


Figure 3. A jig used for measuring the polarization ratio. An amorphous scatterer is designated by S, the beam catcher by BC, and the receiving aperture by RA.

## 6. Use of a Wide Receiving Slit

Figure 4a shows a typical region of a powder scan made with a narrow receiving slit. If the slit were replaced with a somewhat wider slit the count rate would be increased so it would be possible to take the scan of figure 4b somewhat more rapidly and still get the same statistical accuracy. However, it is clear that the scan of figure 4b has poorer resolution. Thus, using the slit of figure 4b, it would be more difficult to separate the intensity belonging to the two different peaks. Because of this situation, it is easy to fall into the error of assuming that a wide slit is inferior to a narrow slit when high accuracy is required. This is not at all the case, as shown by the following example.

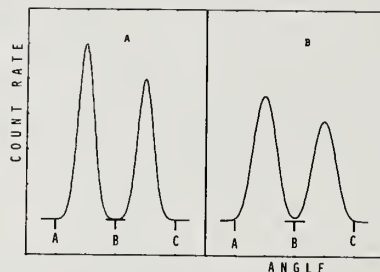


Figure 4. Two typical neighboring peaks in a powder scan. Figure 4a shows the situation with a narrow slit where the received power has dropped to the background level at points A, B, and C. Figure 4b shows the decreased resolution of a somewhat wider slit. A very wide slit, spanning the angular range from point A to point B integrates the peak while giving very well resolved definition of the end points.

Suppose that the problem is to find the relative area of the two peaks in figure 4a as accurately as possible. This might be important in a study of preferred orientation or of relative abundance of two components, for example. The straightforward technique would be to use the same slit that yielded figure 4a and, using either step scanning or continuous scanning techniques, to determine the area between points A and B and also between points B and C. If the wider slit implied by figure 4b were used so as to reduce the time required to get adequate statistical accuracy, it would not be clear as to where to stop scanning the first peak and start scanning the second peak. Suppose, however, that a slit were available whose angular width was just the separation of point A and B. Then, in the not unusual situation that the positions of the peaks were known in advance, it would be possible to place the slit so as to integrate the area from A to B without scanning. Then the slit would be moved so as to integrate the area from B to C, again without scanning. The required information would thus be available directly from a comparison of the two count rates.

It is important to note that in the case described the ends of the "scan" are precisely fixed by the edges of the slit. Thus, the use of the wide slit implies the best possible resolution rather than any loss of resolution. Furthermore, in addition to having the possibility of achieving an accurate value in a short time, the constant count rate allows for a

convenient correction for dead time. Finally, the effect of aberrations (on the integrated reflection) is reduced using the wide slit scheme, as discussed in detail by Suortti and Jennings [9].

Summarizing this section, when intensities rather than peak shapes are required, it is well to consider the use of a slit wide enough to encompass the entire angular range of interest.

## 7. Concluding Remarks

Everything discussed in this paper has been known to me for over a decade and, no doubt, to other workers long before that. I would like to thank the organizers of this symposium for giving me the opportunity to present this old material in the hope that it will give encouragement, even in this day of sophisticated and titillating computer programs, to imaginative consideration of the pedestrian aspects of diffractometry.

## References

- [1] Jennings, L. D., Current status of the I. U. Cr. powder intensity project, Acta Cryst. A25 [1], 217-222 (1969).
- [2] Ayers, G. L., Huang, T. C., and Parrish, W., High-speed x-ray analysis, J. Appl. Cryst. 11 [4], 229-233 (1978).
- [3] Chipman, David R., Conversion of relative intensities to an absolute scale, Acta Cryst. A25 [1], 209-214 (1969).
- [4] Jennings, L. D., Polarization of crystal monochromated x-rays, Acta Cryst. A24 [4], 472-474 (1968).
- [5] Chandrasekaran, K. S., Study of perfection of crystals using polarized x-rays, Acta Cryst. 12, 961-922 (1959).
- [6] International Union of Crystallography, Polarization ratio for x-rays--a survey by the Commission on Crystallographic Apparatus, Acta Cryst. A34 [1], 159-160 (1978).
- [7] Suortti, P. and Jennings, L. D., Accuracy of structure factors from x-ray powder intensity measurements, Acta Cryst. A33 [6], 1012-1027 (1977).
- [8] LePage, Y., Gabe, E. J., and Calvert, L. D., X-ray beam polarization measurements, J. Appl. Cryst. 12 [1], 25-26 (1979).
- [9] Suortti, P. and Jennings, L. D., Effects of geometrical aberrations on intensities in powder diffractometry, J. Appl. Cryst. 4 [1], 37-43 (1971).

## Discussion

Comment (Parrish): I don't believe your statement that the best resolution is obtained with a wide receiving slit is correct. Resolution refers to the width of profiles and ability to resolve them. You seem to have confused the meaning of the term in the context you used.

Response (Jennings): To the extent that resolution refers to the width of a scanned profile you are certainly correct. If we extend the definition to refer to the possibility of assigning received powder to a well defined portion of the diffraction cone, then a fixed wide receiving slit gives the best possible definition of the region, in addition to the primary advantage of a high count rate.

Comment (Parrish): I am not certain of the correctness of your statement that the best measure of the integrated intensity is with a receiving slit as wide as the full profile. In the past, the wider the r.s. the wider the profile and the lower the peak-to-background ratio the increased background may be considerable. It also implies the r.s. width would have to change with  $2\theta$  which may be impractical and introduce errors due to changing background levels. In the case of a diffracted beam monochromatic changing r.s.w. has little effect on the profile width.

Response (Jennings): Yes, there is no point to a wide receiving slit with a diffracted beam monochromator; this is one of the disadvantages of such a monochromator. Furthermore, in the course of an unknown sample or one with numerous peaks, the usual scanning strategy is best. Nevertheless, I assert that, in some cases where the problem is well defined and/or the peaks are widely separated and/or the integrated intensity is required with high accuracy in the minimum counting time, the use of a fixed wide receiving slit is the optimum strategy. In this case it is inappropriate to discuss the peak to background ratio (or the apparent width of a profile that might be obtained by scanning the wide slit. Instead one should focus on the required quantity: the difference between the power in some interesting region of the diffraction cone (the "peak area") and a nearby region (the "background"). Ideally, the fixed slit should be exactly as wide as the interesting region. We have found it helpful to use subsidiary slits (with known area relative to the standard slit) to help determine background in the case of closely spaced peaks. Thus, I agree that the optimum configuration would depend on  $2\theta$  (and other parameters) and a decision would therefore be required for each problem as to whether the much higher count rate obtained with the fixed slit warrants the overhead of getting organized.

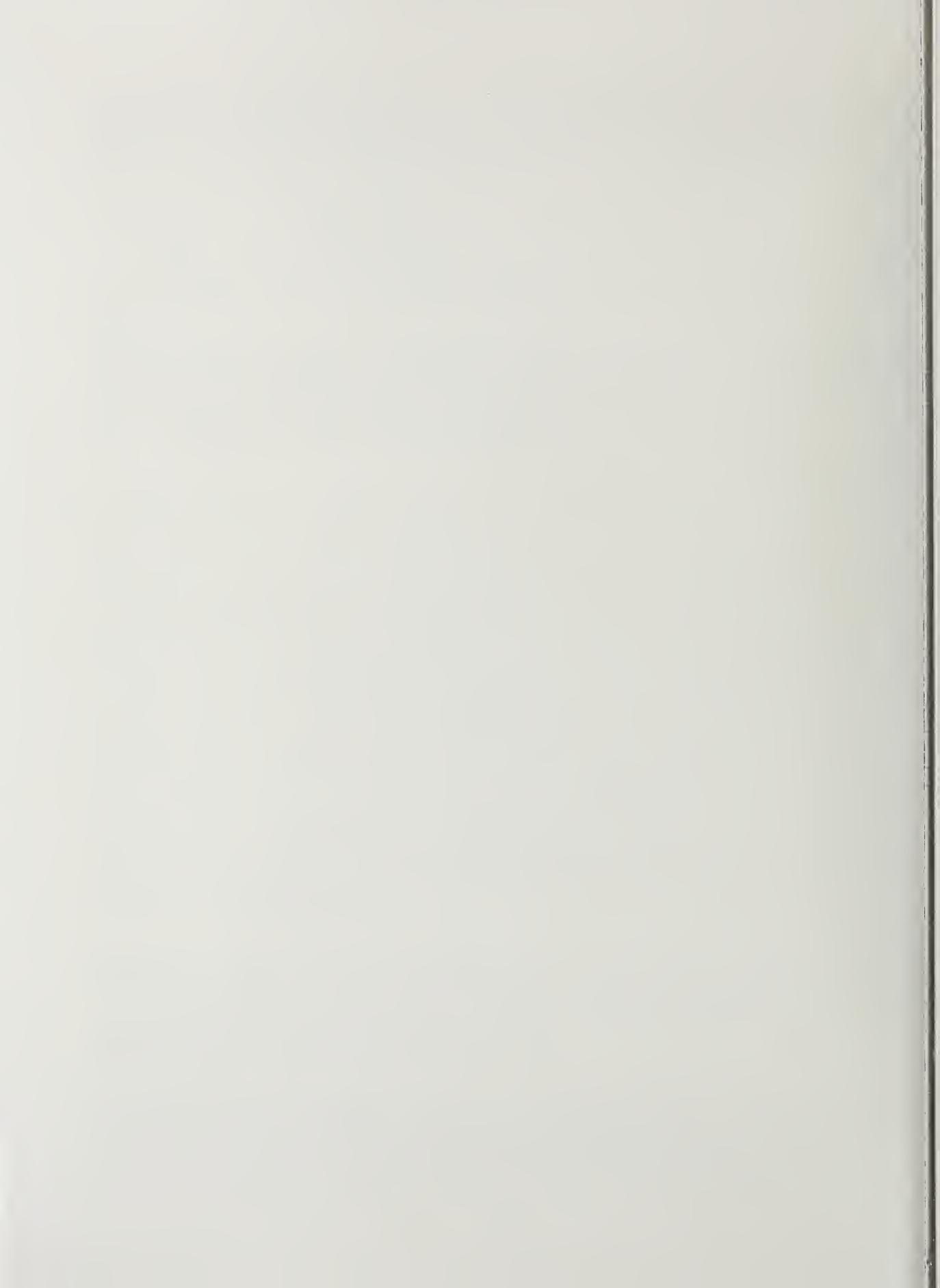
Question (Shirley): I'm not too happy about your use of the term "resolution" when referring to intensity measurement using a wide slit. Might this not be better described as aiming at the highest intensity signal/noise ratio (assuming the background level to be known) consistent with maintaining separation from other lines?

Comment (Jennings): Although a wide slit does give high count rates, there are other advantages which I wished to emphasize. In particular, the modest sized slit of figure 4b fails to resolve the peaks and thus a deconvolution would be required to get the individual integrated intensities. One might naively assume that a wider slit could only be worse.

However, a fixed wide slit spanning A to B and B to C in figure 4a completely "resolves" the two peaks. Thus, in this sense, the fixed wide slit has better "resolution" than the scanned slit of moderate width. The former cannot, of course, conveniently show the shapes of the peaks.

Comment (Ladell): The use of multiple foils for evaluating dead-time can be self-defeating if proper account is not made of the fluorescent x-rays generated by the foils, and also if selective absorption which modifies the transmitted spectral distribution is neglected.

Response (Jennings): These and other considerations (such as small angle scattering) must be taken into account of course, but they apply with equal force to both the master foil method and the multiple foil method. Beam hardening is considered in some detail in reference [3]. Using  $\beta$  filter material (e.g., Ni for  $\text{CuK}\alpha$ ) for the foils and crystal monochromated radiation, we found that the effects of fluorescence were negligible, but this should be checked in each case.



POSITION-SENSITIVE DETECTORS FOR  
POWDER DIFFRACTOMETRY<sup>1</sup>

R. W. Hendricks, M. K. Kopp, and A. H. Narten  
Oak Ridge National Laboratory  
Oak Ridge, TN 37830

We have applied both one- and two-dimensional position-sensitive detectors to powder diffractometry. The advantages of such detectors are (1) they are fast and have a wide dynamic range, (2) the acquired data are digital, and (3) in the case of neutrons they can also be used for time-of-flight (TOF) spectroscopy. The use of straight one-dimensional or flat two-dimensional detectors may introduce parallax errors if the detected angular range is too large. We will report on our experiences in neutron diffractometry with a 50 cm straight detector with 0.5° resolution and our evaluation of a prototype 130° two theta curved linear detector. We will also discuss a flat area x-ray detector (20x20 cm) which has been in use for several years with the 10 meter small-angle x-ray scattering camera. With this detector, powder patterns from structures with large d-spacings have been obtained. Finally, methods for improving the performance of such detectors both in spatial resolution and in count-rate capability will be outlined.

---

<sup>1</sup>Research sponsored by the Division of Materials Science, Department of Energy under contract W-7405-eng-26 with the Union Carbide Corporation



DETERMINATION OF THE SPECTRAL INTENSITY OF THE INCIDENT  
BEAM IN ENERGY DISPERSIVE X-RAY DIFFRACTION

R. Uno and J. Ishigaki  
Department of Physics  
College of Humanities and Sciences  
3-25-40 Sakurajosui, Setagaya-Ku,  
Tokyo, Japan

To determine the spectral intensity of the incident continuous x-ray in the energy dispersive x-ray diffraction, it was the best way to measure the integrated intensity of a well-defined Bragg reflection at several energies (J. Appl. Cryst. 8, 578 (1975)). The spectral intensity was obtained from the calculated structure factors of the reflection at relevant energies. However, this method requires measurements at several Bragg angles, so that one of the merits of the energy dispersive method is lost.

As a different method, the spectral intensity was directly measured by the SSD, when the x-ray tube current was reduced to several microampere. In this method we found two problems. The one was that the focus of tube current changed and sometimes another focus appeared, and the other was that the obtained spectral intensity depended on the intensity of the incident beam, when the spectrum was measured by the use of a usual multi channel analyzer. It seems better that the x-ray tube is new and the tube current is as low as possible if the x-ray due to the cold emission is very weak.

In the energy dispersive method, the structure factors are usually estimated under the assumption of unpolarized incident beam. The spectral intensity obtained from the diffraction measurement is modified by the polarization of the incident beam near the high energy limit, but this is preferable for the determination of the structure factors.

An irregular behavior of our apparent spectrum against x-ray intensity was found to be mainly due to the anomalous spotty x-ray source

which appeared at low tube-current. At higher tube-current the anomalous source became weaker than the regular one and negligible at the normal tube-current (see fig. 1). The pile-up effect of the amplifier was not so much when x-ray total intensity was less than 2000 cps.

### Change of X-ray Source by the Tube Current a New W-Tube at 40kV

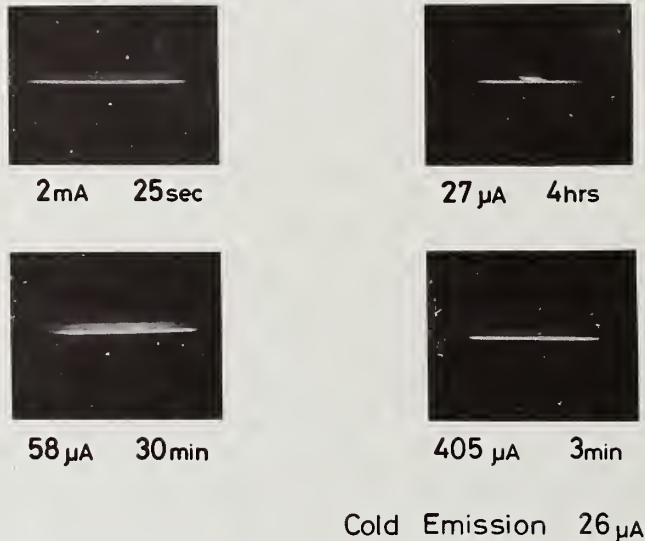


Figure 1.

#### Discussion

Question (Wilson): How accurately does Kramer's law describe the high-energy end of the spectrum?

Response (Uno and Ishigaki): Our results on the spectrum of the continuous x-rays from the tungsten tube was modified by the quantum efficiency of the Si(Li) solid state detector. Its quantum efficiency becomes lower and lower at energy higher than about 15 keV. As tube was operated at 40 kV, the high-energy end of the spectrum was modified very much. I did not mention it, because we could get the structure factor without any knowledge of the quantum efficiency of the detector since the integrated intensity of reflection was also measured with the same detector.

TIME-OF-FLIGHT NEUTRON POWDER DIFFRACTION AT PRESSURES TO 35 KILOBARS

J. D. Jorgensen  
Solid State Science Division  
Argonne National Laboratory  
Argonne, IL 60439

Neutron diffraction has proved to be particularly useful for obtaining structural information for samples under high pressure conditions because of the excellent penetrating power of neutrons. The time-of-flight technique offers the further advantages of being able to obtain complete diffraction data at a single scattering angle and markedly increasing the count rate by using large time-focussed detector arrays. The resolution function of such an instrument can be accurately characterized and remains constant over long periods of time since a typical instrument has no moving parts or variable physical parameters. Profile analysis techniques can be used to obtain atomic positions from the data. Moreover, the resolution function is sufficiently well known that peak broadening due to small symmetry distortions can be seen and analyzed.

The time-of-flight neutron powder diffractometer presently operating at Argonne's CP-5 reactor consists of a chopper 0.3 meters in front of the sample and a detector array 3.4 meters from the sample at  $2\theta = 90^\circ$ . The detector array contains 14  $^3\text{He}$  counters 2.5 cm diameter x 46 cm long. Samples are contained in a piston-cylinder pressure cell capable of reaching 35 kilobars. The powder sample along with a suitable hydrostatic liquid is contained in a sealed teflon capsule inserted into the bore of an  $\text{Al}_2\text{O}_3$  cylinder. The  $\text{Al}_2\text{O}_3$  is supported radially by a hardened steel binding ring which has slits at appropriate angles for the incident and scattered neutrons. The attenuation of neutrons in the  $\text{Al}_2\text{O}_3$  is small.

A recent study of the pressure-induced strain transition in  $\text{NiF}_2$  illustrates the utility of this technique for measuring small lattice distortions [1]<sup>1</sup>.  $\text{NiF}_2$  has a tetragonal structure at atmospheric pressure and undergoes an apparently continuous transition to a closely related orthorhombic structure at 18.3 kbar. The orthorhombic strain is sufficiently small (reaching about 1.3 percent at 32 kbar) that orthorhombic doublets are not actually resolved even at the highest pressure. However, the use of profile analysis, coupled with an accurate knowledge of the instrument's resolution function, allows the determination of the orthorhombic lattice parameters and the atomic displacements associated with the transition.

A study of compression mechanisms in the  $\alpha$ -quartz structures  $\text{SiO}_2$  and  $\text{GeO}_2$  further illustrates the ability of this method to measure small changes in atomic positions [2]. By determining bonds lengths and angles versus pressure it was possible to show that  $\text{SiO}_2$  compresses by a nearly rigid rotation of its corner-linked  $\text{SiO}_4$  tetrahedra while isostructural  $\text{GeO}_2$  compresses by distortion of bond angles within its  $\text{GeO}_4$  tetrahedra.

#### References

- [1] Jorgensen, J. D., Worlton, T. G., and Jamieson, J. C., *Phys. Rev. B* 17, 2212 (1978);  
Jorgensen, J. D., Worlton, T. G., and Jamieson, J. C., *High Pressure Science and Technology*, Vol. 1, 152; K. D. Timmerhaus and M. S. Barber, eds. (Plenum Publ. Corp., 1978).
- [2] Jorgensen, J. D., *J. Appl. Phys.* 49, 5473 (1978).

POWDER--A COMPUTING SYSTEM FOR X-RAY POWDER  
DIFFRACTION CALCULATIONS

B. C. Osgood and R. L. Snyder  
NYS College of Ceramics,  
Alfred University  
Alfred, NY 14802

A system has been designed and written to maintain all pertinent information and carry out the calculations associated with x-ray powder diffraction. The system has incorporated the following design features:

- (1) All computations may be carried out interactively.
- (2) All component programs may be executed independently, or as overlay segments of a large program, either interactively or in batch mode.
- (3) The system control program and all component programs are written almost exclusively in ANSI machine independent FORTRAN.
- (4) Language and notation used is designed to be understood by researchers and students outside the area of crystallography.
- (5) All program options default to reasonable values.
- (6) Incorporation of existing or newly developed programs is easily accomplished.

The system control program, called POWDER, creates, updates, and maintains a data file containing all of the needed information for a sample. Data may be input directly from automated diffractometer files or from films or strip charts. The most commonly used programs for phase identification, lattice parameter refinement, indexing and pattern calculation have been incorporated. The input sequence in the existing programs has not been altered, allowing for easy insertion of a new version of the code. This feature is accomplished by having the system control program read its data file and set up an input file for any of the application programs.

The purpose of the system is to allow the many powerful computational procedures developed in recent years to be routinely available to workers both in and outside the area of crystallography.



THRESHOLD LEVEL DETERMINATIONS FROM DIGITAL X-RAY POWDER  
DIFFRACTION PATTERNS

C. Mallory and R. L. Snyder  
NYS College of Ceramics  
Alfred University  
Alfred, NY 14802

A major difficulty in the reduction of digital x-ray powder diffraction data is the determination of an appropriate threshold level. Data above that threshold level may be considered as being due to a real diffraction peak. Traditional methods involve a mean value ( $\mu$ ) for the background and determine the threshold based upon the standard deviation ( $\sigma$ ), i.e. threshold =  $\mu + N\sigma$ . The value chosen for N introduces an undesirable degree of arbitrariness into the process. The result is an approximation of the threshold that often leaves a number of true background points present while, in other regions of the spectrum, small peaks may be rejected.

A procedure has been developed for determining a threshold level based directly on the maximum count rates found in the raw digital data. In this procedure the maximum intensity point in each  $2\theta$  segment, of a given width, in the pattern are analyzed for statistically significant increases from the previous maximum point. The test is based upon the standard deviation of the count rate of the individual maximum points. Data not passing this criterion are rejected as being part of a significant peak and a polynomial is fit to the remaining data. A spline fit is used to eliminate all points below the threshold. The threshold level is then defined as the intensity value of the polynomial evaluated at each  $2\theta$  step within each given  $2\theta$  segment.

This procedure produces a threshold line which passes through the maximum point in each  $2\theta$  interval determined to contain only background data and passes smoothly between these intervals under peaks. The subtraction of this threshold from the observed data, while giving all negative values, produces a series of clean peaks or peak clusters whose statistical significance is determined by the adjustable  $2\theta$  interval rejection criteria.



ACCURACY OF THE PROFILE FITTING METHOD FOR X-RAY POLYCRYSTALLINE DIFFRACTOMETRY

W. Parrish and T. C. Huang  
Research Laboratory  
International Business Machines Corporation  
San Jose, CA 95193

This paper presents the results of an experimental study of the accuracy of the profile fitting method in determining profile shapes, diffraction angles, peak and integrated intensities in x-ray powder diffractometry. The precision  $R$  in determining the standard profile shapes ( $W^*G$ ) of a number of powder profiles free of line broadening, is calculated from the differences between the fitted profile and the experimental points. Collecting about 30,000 counts on the peak of the profiles with a step size  $0.03^\circ$  gave an average better than  $R = 2$  percent for 35 profiles covering the range  $15^\circ$  to  $165^\circ$ ;  $RI$  (integrated intensity) = 0.3 percent for the same set of data. The precision of reflection angles and intensities of three profiles were each measured 10 times in  $0.01^\circ$  steps collecting 40,000 counts at the peaks and calculating up to  $0.05^\circ$  steps. Fifty-six percent of the 150 peak angle determinations agree to  $\pm 0.0001^\circ$  and 97 percent to  $\pm 0.0004^\circ$ . The precision of the peak and integrated intensities was 0.2 percent for steps  $0.01^\circ$  to  $0.05^\circ$  and 0.5 percent for steps  $0.06^\circ$  to  $0.09^\circ$ . Data for weak peaks and overlapped peaks resolved by profile fitting are described. The method applied to a typical powder pattern (garnet) routinely recorded at moderate- (25 min) and high-speed (3 min) gave  $R = 3.2$  percent and 6.6 percent, respectively, and average agreement exceeding  $\pm 0.01^\circ$  ( $2\theta$ ) and  $\pm 1$  percent intensities. This precision exceeds the curve fitting results of others, e.g., the Rietveld method as currently applied to x-ray powder diffraction. A method for handling systematic errors in lattice parameters using profile fitted angles is presented.

### 1. Introduction

The advantages of the profile fitting method are becoming more apparent and it is likely that it will soon be widely used in a variety of applications. In this paper, we evaluate the precision of our profile fitting method [1,2]<sup>1</sup> from measurements of powder patterns in brackets indicate the literature references at the end of this paper.

diffractometer profiles, reflection angles, and intensities. The emphasis will be on precision or reproducibility rather than accuracy because of uncertainties in absolute values available for comparison.

The precision achieved in the present state of development of the method already far exceeds most of the data in the standard Powder Diffraction File. The method also greatly reduces the time and labor in collecting and reducing powder data. It was recently shown that even a complicated pattern could be automatically recorded and a precise set of d's and I's obtained in a few minutes [3].

The use of computers is essential in applying the method making it possible to automatically control the diffractometer in collecting large sets of data and to do the involved calculations rapidly and accurately. Modern powerful minicomputers can now be used for this method [4].

Our method has greater precision and is quite different from the Rietveld method [5] applied to x-ray powder diffractometry. No prior crystallographic information on the material to be analyzed is required. It was not designed specifically for structure determination but rather for general diffractometer analysis. It determines integrated and peak intensities and diffraction angles of complete patterns or individual profiles with high precision. The experimental data are used without smoothing. Accurate fitting of the entire profile is achieved and we believe this to be essential to produce precise results. The ability to resolve overlapping peaks with a resolution far exceeding the original diffractometer recording makes it possible to derive good data from clusters of peaks and complex patterns. The method has been developed to the point that after the operator selects the experimental parameters, the entire run from data collection to reduction is automatic. It has also been used for qualitative analysis of mixtures [6] and variations of the method for energy dispersive spectral analysis [7].

## 2. Basis of the Profile Fitting Method

Our method is based on the well-known relation

$$P(\theta) = W * G * S + \text{background} \quad (1)$$

where  $P(\theta)$  = Profile measured with the diffractometer,

$W$  = Observed x-ray  $K\alpha$  spectral line profile,

$G$  = Convolution of all aberrations of the diffractometer  
and the diffraction process, and

$S$  = True diffraction effects of the specimen.

In our earlier papers, we showed that  $W$  must be the actual distribution observed in the apparatus being used rather than the double crystal profile, and that it was closely approximated by a high angle reflection virtually free of aberrations such as silicon (444) with  $\text{Cu}K\alpha$  radiation. In practice, there is no need to determine  $W$  separately. The convolution  $W*G$  is determined by accurate measurements of a series of profiles of a

per of carefully prepared "standard" powder specimens free of line broadening effects. This is equivalent to determining the instrument function in terms of the profile shapes at various reflection angles as described in Section 4.

When using  $\text{CuK}\alpha$  radiation the  $\text{K}\alpha_1$  and  $\text{K}\alpha_2$  peaks are each fitted with three Lorentzian profiles and the weak  $\text{K}\alpha_3$  satellite group with one. The number of Lorentzians required to obtain an accurate fit was determined empirically. Two Lorentzians gave good accuracy for the symmetrical higher angle reflections, but the more asymmetric lower angle reflections required three. Four did not significantly improve the accuracy but greatly increased the computing time.

Each Lorentzian is represented by three parameters,  $2\theta$ ,  $I$ , and  $w$ , defining the peak position, intensity, and width, respectively. The W\*G program adjusts the 21 parameters so that the sum of the seven Lorentzians makes the best fit to the experimental data points.

The W\*G profiles are normalized and interpolated between reflections to provide the true profile shapes at all  $2\theta$ 's. The data (i.e., the parameters) are stored in the computer for use in later computations of  $S$ .

Once W\*G is known, the true diffraction effect  $S$  of the specimen can be precisely determined. The diffraction profile  $s_i$  of a reflection without asymmetric broadening can be represented by a single Lorentzian with  $2\theta_i$ ,  $I_i$  and  $w_i$  as its parameters. If the specimen profiles are asymmetrically broadened, an asymmetric Lorentzian with different widths on each side of the peak is needed to obtain a good fit. The contribution  $S$  of the specimen to the profile is obtained by adjusting the parameters  $2\theta$ ,  $I$ , and  $w$  of the reflections recorded so that its convolution with W\*G, i.e.,  $(\text{W*G}) * S$  matches the experimental data points as closely as possible. The algorithm used to determine W\*G and  $S$  is essentially the nonlinear simplex method [8,9,10].

Irregular backgrounds such as those of a thin film on an amorphous or crystalline substrate can be handled routinely.

### 3. Instrumentation

The experiments were carried out with a Norelco vertical scanning-plane diffractometer, radius 185 mm and reflection specimen [11]. Various improvements that evolved over the years have been incorporated, although they are not essential for applying the profile fitting method. The principal changes were the addition of a diffracted beam, graphite monochromator and rebalanced worm gear, elimination of the parallel slit diffracted beam collimator, a vacuum path constructed in four sections and a rotating specimen device. The stepper motor is mounted at the rear and coupled directly to the drive. We used the Norelco long fine focus x-ray tube with  $12^\circ$  take-off angle, operated at 50 kV, 20 mA. The alignment and calibration was made with methods previously described [11].

The computer system is an on-line IBM System/7 for diffractometer control and data collection and an off-line host IBM System 370/168 for data reduction (reference [2], sections 1 and 2). We have recently developed the use of the IBM Series/1 minicomputer to

perform all the tasks of the large two computer system with reasonable turn-around time. This stand-alone computer has EDX and FORTRAN capabilities, and a description is being prepared [4].

#### 4. Determination of W\*G

A set of W\*G standard profiles covering the angular range to be used is required for each set of experimental conditions. Any change in instrument geometry or x-ray wavelengths that modifies the profile requires a separate set of standard profiles. Readjustment of the monochromator may modify W and the angular calibration, changing slit widths changes the profile widths and asymmetry, and different diffractometer geometries and x-ray tube targets will require a new set of standard profiles. The recording conditions such as the diffractometer step-angle  $\Delta 2\theta$ , and counting time do not change the shape. Remeasuring the W\*G dataset a few times a year is a good practice to assure that the profiles are accurately represented. It is essential that the adjustments, alignment and calibration be carefully done prior to starting the computer automation method.

The standard specimens were carefully prepared powders with average crystallite sizes 5 to 20  $\mu\text{m}$ , mounted with 1:10 collodion:amyl acetate on a flat 3/4 inch square single crystal silicon wafer cut parallel to (510). The silicon was mounted on an aluminum cylinder which was continuously rotated during data collection. We used all the reflections of silicon and tungsten in a silicon + tungsten mixture, and some of the reflection of quartz,  $\text{Gd}_3\text{Ga}_5\text{O}_{12}$  garnet,  $\text{Pb}(\text{NO}_3)_2$ , and a steroid for small  $2\theta$ 's. All reflections used had high intensity and P/B, no overlaps and showed no line broadening.

The goodness of fit between the observed and calculated profiles relating the individual step-scanned points  $I_i(\text{obs})$  to the same  $2\theta$ -angle points of the fitted profile  $I_i(\text{PF})$  is defined as

$$R(\%) = \left[ \frac{\sum_{i=1}^n [I_i(\text{obs}) - I_i(\text{PF})]^2}{\sum_{i=1}^n I_i(\text{obs})^2} \right]^{1/2} \times 100 \quad (2)$$

and the match of the integrated intensity of the entire profile is defined as

$$RI(\%) = \left[ \frac{\sum_{i=1}^n [I_i(\text{obs}) - I_i(\text{PF})]^2}{\sum_{i=1}^n I_i(\text{obs})} \right] \times 100 \quad (3)$$

We learned from many previous runs that the precision given in table 1 is typical and satisfactory for determining the W\*G profiles. The overall averages of the 23 profiles listed (35 were measured) were better than  $R = 2$  percent and  $RI = 0.5$  percent when accumulating about 30,000 counts at the  $K\alpha_1$  peaks and using the step-scan angles shown. Four of these profiles (fig. 1) were selected to illustrate typical cases of low R (a) and (c), and higher (though still good) R (b) and (d). The differences between the experimental and fitted points is shown below each profile. It should be noted that the fitted profiles (a) and (c) have a high accuracy as shown by the curve passing through all the

Table 1  
 Typical Precision of W\*G Profile Measurements

Angular Aperture 1°						Angular Aperture 4°					
Spec.	hkℓ	2θ Peak	R%	RI%	Counts at Peak (×10 <sup>3</sup> )	Spec.	hkℓ	2θ Peak	R%	RI%	Counts at Peak (×10 <sup>3</sup> )
G	211	17.54	1.2	0.1	20	Si	511/333	94.94	2.7	0.3	29
G	220	20.28	1.3	0.0	20	W	310	100.61	1.7	0.0	46
P	200	22.57	1.2	0.0	28	Si	440	106.70	1.4	0.5	25
P	210	25.28	0.9	0.1	20	W	222	114.92	1.9	0.1	32
Si	111	28.44	1.2	0.1	33	Si	620	127.54	1.0	0.1	30
G	420	32.32	1.0	0.2	49	W	321	131.15	1.6	0.1	42
G	422	35.50	1.3	0.3	29	Si	533	136.90	1.3	0.2	27
W	110	40.24	1.5	0.3	29	W	400	153.51	1.3	0.2	45
Si	220	47.30	1.7	0.6	35	Si	444	158.64	1.4	0.1	27
Si	311	56.12	3.1	0.1	44	Average 1.6 0.2 33.7					
Si	400	69.13	2.4	1.3	29	Specimens: G=Gd <sub>3</sub> Ga <sub>5</sub> O <sub>12</sub> , P=Pb(NO <sub>3</sub> ) <sub>2</sub> , Si=Silicon, W=Wungsten $\Delta 2\theta^\circ$ Range 2θ 0.01°      <60° 0.02°      60°-120° 0.03°      >120°					
Si	331	76.37	2.7	0.3	19						
W	220	87.01	2.5	1.1	27						
Si	511/333	94.96	2.7	0.6	20						
Average 1.8 0.4 28.7											

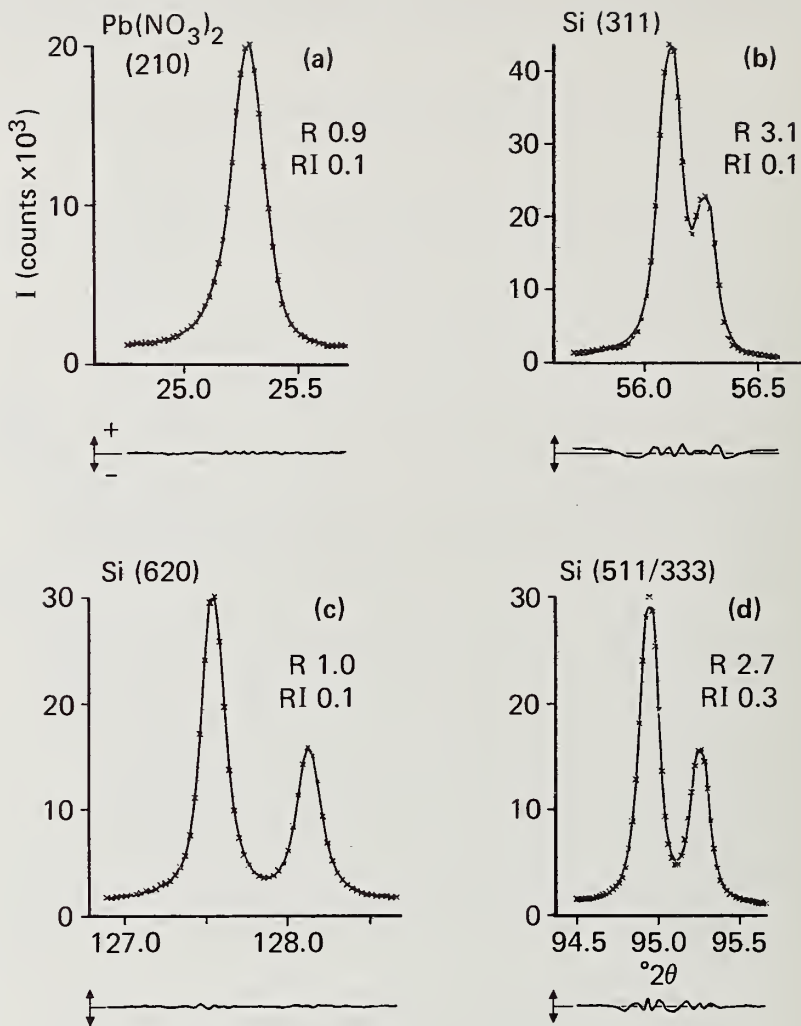


Figure 1. Four typical profiles used for W\*G determination. x = experimental measurements, solid line = fitted profile.  $\Delta 2\theta = 0.01^\circ$ , alternate x's omitted in (a) and (b). Angular aperture =  $1^\circ$  for (a) and (b) and  $4^\circ$  for (c) and (d). (a) and (c) have the lowest R, and (b) and (d) the highest R in table 1.

xperimental points including the tails that (b) and (d) have sufficient accuracy to represent the true profiles. Profile fitting of this accuracy is required to properly represent the experimental data and to achieve the precision in measuring reflection angles and intensities as described in the following sections.

## 5. Precision of Peak Angle Measurements

It was explained above that the calculations for determining the reflection angles and intensities require only one Lorentzian for each reflection. The computer program determines the angle corresponding to the peak of the reflection. Other measures such as the mid-point of chords at various heights, the centroid, etc., could be programmed if desired.

The following experiments were planned to determine the inherent precision of the profile fitting method by measuring individual reflections with good counting statistics. The time required to collect data for a single profile varied from 12 to 24 minutes depending on the scanning range required to record the entire profile and the background with  $0.01^\circ$  steps. It will be shown that the step sizes can be increased to  $0.05^\circ$  and counting time decreased without significant loss of precision, and hence, the experimental time can be greatly reduced.

Three reflections of a specimen containing a mixture of silicon and tungsten powder were used: silicon (111) to illustrate an unresolved doublet, silicon (311) for a partially resolved doublet, and tungsten (321) which is broader and has nearly complete resolution. Ten consecutive runs were made on each reflection with  $\Delta 2\theta = 0.01^\circ$  steps and counting times sufficient to collect about 40,000 counts at the  $K\alpha_1$  peaks. To determine the effect of the step size and to avoid rerunning with the different  $\Delta 2\theta$ 's, we used the same data for  $2\theta = 0.02^\circ$  by using alternate steps; this was repeated in the calculations up to  $2\theta = 0.05^\circ$  by using every fifth step.

The average peak angle was calculated from the five different  $\Delta 2\theta$  sets of each of the ten runs. The differences between these averages and the angles calculated from each  $2\theta$  in each run is used as a measure of the accuracy of the profile fitting program because systematic and drift errors are avoided. The average absolute difference is  $.0001^\circ$  or about 1/3 second of arc for tungsten (321) as shown in table 2. Figure 2 is a histogram of the 150 peak determinations of the three reflections; 56 percent lie between  $0.0001^\circ$  and 97 percent between  $\pm 0.0004^\circ$ . Although we have not included them, the calculations were continued to  $\Delta 2\theta = 0.09^\circ$  with virtually the same results obtained with the smaller  $\Delta 2\theta$ 's.

These data demonstrate the high precision that can be achieved by using the profile fitting method. However, there are well-known factors which may introduce systematic errors that are considerably larger than the inherent precision of the fitting procedure. These include the zero angle calibration of the diffractometer, specimen surface displacement, the geometrical aberrations such as flat specimen and transparency, the specimen temperature, slight shifts of the position of the x-ray tube focal line due to changes

Table 2. Precision of Peak Angle Determination Tungsten (321),  $\text{CuK}\alpha_1$

Run	Average						
	0.01° to 0.05°	$\Delta 2\theta =$	0.01°	0.02°	0.03°	0.04°	0.05°
1	131.1521	+0.0001		+1	-2	0	0
2	.1521		-2	0	-1	0	+2
3	.1515		-1	0	0	+2	0
4	.1511		-1	0	+1	0	0
5	.1508		0	0	+1	+2	-4
6	.1504		-1	0	-1	0	+4
7	.1498		0	-1	0	-1	+2
8	.1502		-1	+1	+1	+1	-4
9	.1498		-1	+1	0	-1	+1
10	.1497		+1	+1	+2	-4	+1
Average	131.1508		0.00009	05	09	11	18

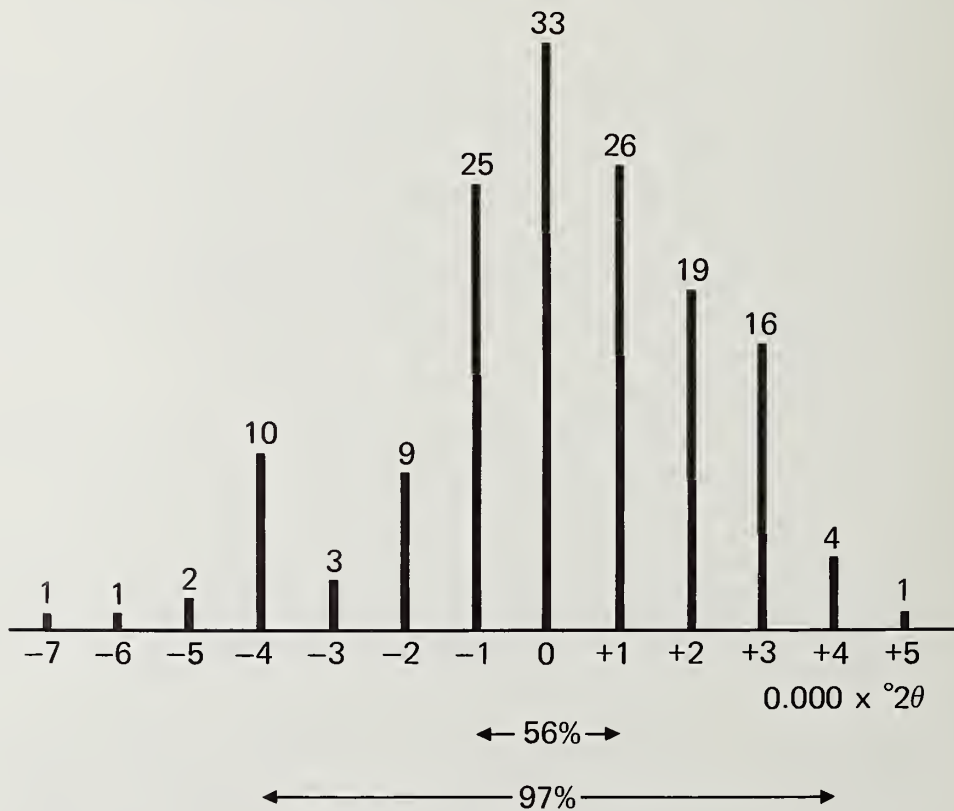


Figure 2. Precision peak angle determination by profile fitting. Fifty runs with  $\Delta 2\theta = 0.01^\circ$  to  $0.05^\circ$  for each of Si(111), Si(311) and W(321). Each horizontal unit =  $0.0001^\circ(2\theta)$ . Number of runs shown at top of bars.

the cooling water temperature, and others. The reduction of these sources of errors to the small errors achieved in profile fitting is a formidable task.

This problem is illustrated by the data in the second column of table 2 which shows gradual decrease in the average reflection angle in the ten consecutive runs. No temperature control of the specimen was used although the specimen was in a vacuum chamber and air conditioned room. The runs were made in a four-hour period following a one-hour warm-up of the x-ray generator (Philips PW 1310) at full power. The temperature was monitored at the edge of the rotating specimen device with an electronic thermocouple mounted through the specimen vacuum chamber. The temperature rose from 24.2 to 26.2 °C during these runs. This rise was caused by a slow increase in room temperature and heat generated by the synchronous motor and bevel gears of the rotating specimen device. The increase of 0.0024° corresponds to the thermal coefficient of expansion 0.0011°(2θ)/°C for the tungsten (321) reflection.

At a later time, the same specimen was remounted and another set of ten runs was made without specimen rotation. This time the temperature increase was 1 °C, the angle decreased 0.001°(2θ) which checks well with the previous runs. However, the average angle was 0.003° higher. This corresponds to a difference of specimen surface position of only 6 μm, which occurred when the specimen was remounted. It is probably impossible to avoid such small displacements of powder specimens.

## 6. Precision of Intensity Measurements

The profile fitting method provides precision measurements of the peak and integrated intensities even when overlapping occurs. The data listed in table 3 summarize the profile fitted intensity data of the same set of three profiles with the same experimental conditions used in table 2. The data were extended to  $2\theta = 0.09^\circ$  to show that accurate values can be obtained even when using large steps. No systematic drifts in the intensities was observed in these runs.

Each number in table 3 is the ratio (multiplied by 100) of the average of 10 runs for that  $\Delta 2\theta$  to the average of all 90 determinations (10 runs,  $\Delta 2\theta = 0.01^\circ$  to  $0.09^\circ$ ); which  $\Delta$  is the ratio of the average of the differences of each of the 10 runs of that  $\Delta 2\theta$  dataset. For example, the average peak intensity of 10 runs of silicon (111),  $\Delta 2\theta = 0.02^\circ$  is 37,543 counts, the overall average for the 90 runs was 37,506 and the ratio 1.00098 is listed as 100.1; the average of the differences regardless of sign was 58 and the ratio 0.0015 is listed as 0.2. The precision is thus about 0.2 percent for peak and integrated intensities with small  $\Delta 2\theta$  and increases to about 0.4 to 0.5 percent with large steps.

In Section 5, it was shown that errors from several sources may be larger than the precision with which the reflection angles can be measured with profile fitting. The same difficulty occurs in measuring intensities. Preferred orientation, crystallite size statistics and inhomogeneous specimen preparation may cause large errors. The use of transmission specimen or Seeman-Bohlin diffractometers to supplement the reflection specimen geometry data [12], rotating specimen device and careful specimen preparation will greatly reduce the errors.

Table 3. Precision of Intensity Measurements

$\Delta 2\theta^\circ$	Integrated			Peak		
	Si(111)	Si(311)	W(321)	Si(111)	Si(311)	W(321)
0.01	100.1 $\pm$ 0.2	100.3	99.7	100.1 $\pm$ 0.1	100.0	100.0
0.02	99.9 0.2	100.4	99.8	100.1 0.2	99.9	100.0
0.03	99.9 0.2	100.7	100.3	100.0 0.2	99.7	100.1
0.04	99.9 0.3	100.4	100.4	99.9 0.2	98.9	100.1
0.05	100.3 0.2	99.3	100.2	99.8 0.3	100.6	100.2
0.06	99.8 0.3	101.9	100.1	100.7 0.3	101.4	100.2
0.07	100.8 0.5	99.4	100.1	100.4 0.4	98.9	100.4
0.08	99.9 0.4	98.0	99.8	99.5 0.2	98.4	99.4
0.09	99.3 0.5	99.7	99.7	99.6 0.2	102.1	99.8
Average Peak Counts				37506	36320	42163

## 7. Weak and Overlapped Peaks

In this section, we will present some results obtained with low intensity, low P/B and overlapped peaks. For the case of an isolated peak, we used quartz (12.0) with P/B = 1.25. Ten runs were made with  $\Delta 2\theta = 0.01^\circ$  and  $t = 10$  seconds per step, and these were repeated with  $t = 1$  second. The profile fitting results are summarized in table 4, which includes data for  $\Delta 2\theta = 0.02^\circ$  to  $0.05^\circ$  obtained by skipping steps in the calculation as was done before. Although the large reduction of counts resulted in lower precision, the standard deviation was  $0.001^\circ$  with 1300 peak counts and  $0.008^\circ$  with 130 counts, and the average peak intensities were better than  $\pm 1\%$  for both.

A more difficult case is the measurement of a weak peak occurring on the tail of a strong peak such as quartz (00.3) on (11.2). The  $K\alpha_1$  peaks are separated  $0.48^\circ$ , the  $K\alpha$  doublet  $0.13^\circ$ , and the ratio of the intensities and P/B of (11.2) = 45. Using  $\Delta 2\theta = 0.01^\circ$ , collecting 741 counts on the (00.3)  $K\alpha_1$  peak,  $R = 2.4$ . The results of the profile fitting are shown as a plot in figure 3(a).

The ability to resolve overlapping reflections and to derive precise values of the  $2\theta$ 's, integrated and peak intensities of the resolved peaks is an important advantage of the method. When it is used in an automatic routine analysis, the ability to resolve overlaps depends on the separation of the peaks and the quality of the data. If the peaks are separated by at least the HWHM regardless of the  $K\alpha$  doublet separation, they can be resolved with

Table 4. Precision Determination of Weak Quartz Peak (12.0),  
P/B = 1.25, 10 Runs for Each Counting Time

Counting Time/Step	$\Delta 2\theta$	$2\theta$	Standard Deviation	Integrated I (Normalized)	Peak I (Counts)
10 sec.	0.01°	57.2075	0.0009	103	1292
	0.02	72	06	101	8
	0.03	75	23	99	0
	0.04	66	14	98	6
	0.05	87	19	99	0
	Average	57.2075	0.0014	100	1293
1 sec.	0.01	57.2088	0.0057	108	130
	0.02	83	72	101	129
	0.03	59	76	101	129
	0.04	83	65	94	129
	0.05	68	60	96	126
	Average	57.2076	0.0066	100	129

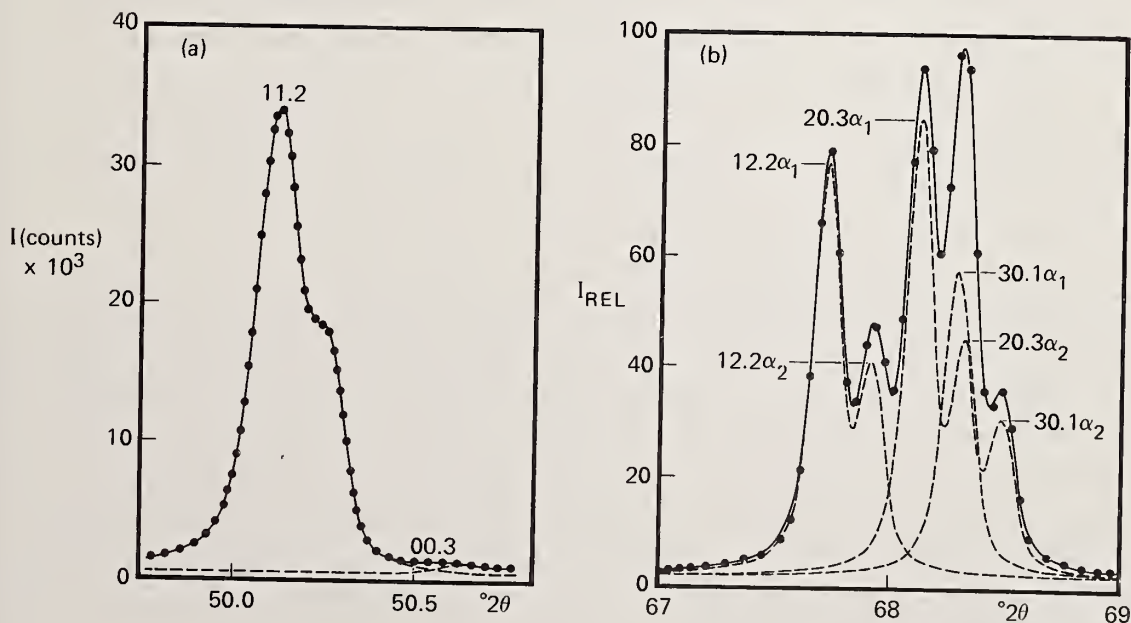


Figure 3. Profile fitting of quartz powder profiles. Dots = experimental measurements, solid line = fitted profile, dashed line = resolved profiles. (a) Resolution of (00.3) peak on tail (11.2); (b) Resolution of three overlapped  $CuK\alpha$  doublets.

good precision. If the indices and lattice parameter are known, peaks can be resolved with even smaller separations.

When several peaks are closely overlapped, it is difficult to determine the correct relative intensities and reflection angles with the usual recording methods. The often-used quartz cluster shown in figure 3(b) illustrates this. The  $\text{CuK}\alpha_1$  peaks of (12.2) and (20.3) are separated  $0.40^\circ$ , (20.3) and (30.1)  $0.17^\circ$ , and the doublets  $0.19^\circ$ . The intensity of the (30.1) peak read from a strip chart would be in error by about 40 percent. The correct relation of the three reflections is shown by the dashed curves obtained with profile fitting.

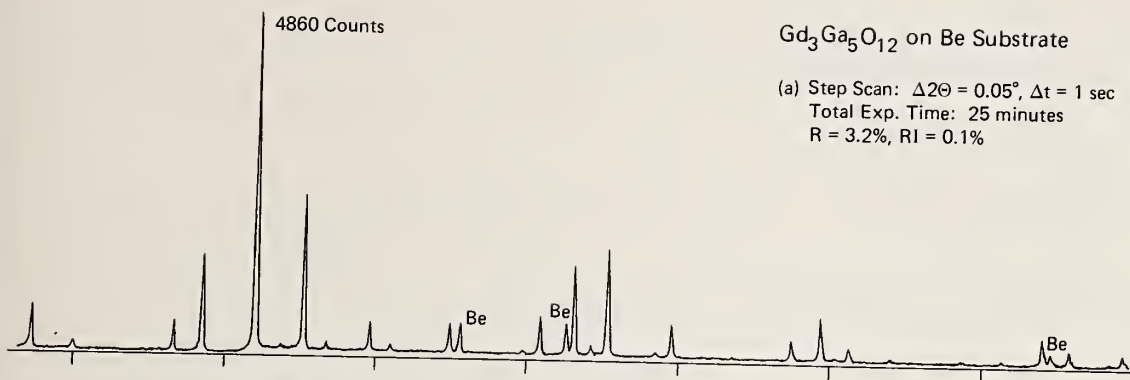
## 8. Profile Fitting Powder Patterns

An example of the profile fitting method applied to a typical powder pattern used for identification is shown in figure 4; these are Calcomp plots of the experimental data of a garnet collected at  $0.05^\circ$  steps. The powder was mounted on 0.125 mm thick Be foil and run with the transmission specimen diffractometer using a diffracted beam logarithmic spiral quartz monochromator [11,12,13]. The upper pattern has 29 reflections (plus 3 Be peaks), was recorded with 1 second counting time per step, and completed in 25 minutes. The profile fitted data were  $R = 3.2$  percent,  $RI = 0.1$  percent. The lower pattern was recorded with 0.1 second counting times and required only 3 minutes. To avoid computing difficulties arising from poor counting statistics on the weak peaks, the program used only peaks whose intensity exceeded  $3(B^{\frac{1}{2}})$  for the computer fitting. The 11 reflections dropped (marked x) were all less than 3 percent of the strongest peak. The results for the remaining 18 reflections were  $R = 6.6$  percent,  $RI = 0.6$  percent, average precision  $0.008^\circ(2\theta)$  and peak intensities 0.8 percent. These results are similar to those we recently reported on high-speed x-ray analysis of a more complicated powder pattern [3].

The accuracy reported here exceeds recently published results obtained with the Rietveld method for fitting x-ray powder patterns as shown by the following few examples. Malmros and Thomas [14] used a modified asymmetric Lorentz function to fit automatic microdensitometer recordings of Guinier-Hägg camera films of  $\alpha\text{Bi}_2\text{O}_3$ ; their diagrams show large discrepancies between observed points and the fitted profiles. Young, Mackie and von Dreele [15] reported that neither Gaussian nor Cauchy (Lorentz) functions have "adequate fittings" of powder diffractometer patterns and that better representations were needed to lower the R values in structure refinement. Khattak and Cox [16] used various functions to fit a rhombohedral powder diffractometer pattern containing 41 reflections in a  $76^\circ(2\theta)$  range. Even though over 63 hours were used to record the pattern using  $0.02^\circ$  steps, 60-second counting times and  $\text{CuK}\beta$  radiation (to avoid the  $\text{K}\alpha$  doublet "problem"), the matches between fitted and observed patterns were "distinctly inferior to that obtained in a typical neutron profile analysis" and their best value of  $R = 13.7$  percent was obtained using the Lorentz function.

### Gd<sub>3</sub>Ga<sub>5</sub>O<sub>12</sub> on Be Substrate

(a) Step Scan:  $\Delta 2\theta = 0.05^\circ$ ,  $\Delta t = 1$  sec  
Total Exp. Time: 25 minutes  
R = 3.2%, RI = 0.1%



(b) Step Scan:  $\Delta 2\theta = 0.05^\circ$ ,  $\Delta t = 0.1$  sec  
Total Exp. Time: 3 minutes  
R = 6.6%, RI = 0.6%

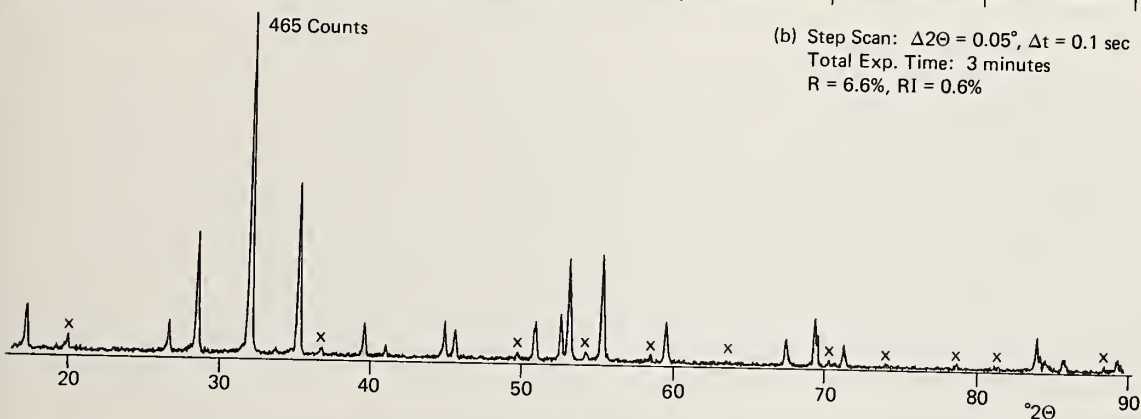


Figure 4. Transmission powder diffractometer patterns of garnet Gd<sub>3</sub>Ga<sub>5</sub>O<sub>12</sub> powder sample mounted on thin Be foil, CuK $\alpha$  radiation. Eleven reflections marked x in (b) had peak intensities less than  $3(B^{1/2})$  and were dropped from the profile fitting calculations; average of 18 peaks  $0.008^\circ(2\theta)$  and 0.8 peak intensities for 3 minute recording time.

### 9. Lattice Parameter Determination

It is well known that systematic errors limit the accuracy of lattice parameter determinations. It was shown in Section 4 that a good practical method of handling these errors is needed to take full advantage of the accuracy of the profile fitted values. A least-squares type of refinement of the profile fitted angle data may be useful for this purpose as shown in the following example.

A powder sample of a Czochralski-grown garnet boule, Gd<sub>3</sub>Ga<sub>5</sub>O<sub>12</sub>, was prepared on a silicon (510) substrate. Twenty-five patterns were run in the front-reflection region  $90^\circ$  to  $16^\circ$  which includes 27 reflections. The specimen was removed and replaced between runs to include specimen surface displacement errors. Each run was made with  $0.05^\circ$  steps and 1-second counting time.

The  $2\theta$ 's obtained by profile fitting were used to determine the lattice parameter by refinement of the coefficients defining the zero angle calibration, and the trigonometric

dependence of the specimen surface displacement and transparency corrections. The refinement was reached when the weighted sum of the absolute differences between the calculated  $2\theta$ 's obtained from these coefficients and the profile fitted  $2\theta$ 's of all reflections in a run was a minimum. The weighting factor of each reflection was made proportional to  $\tan\theta$  and the square root of the intensity.

Using Bearden's value for  $\text{Cu}\alpha_1 = 1.540562 \text{ \AA}$ , the average  $a = 12.3827 \text{ \AA}$  and the average  $\Delta a/a = 2.3 \times 10^{-5}$ . This accuracy of about 1:50,000 was obtained from 25 minute routine runs using only the front-reflection peaks. Because of the  $\tan\theta$  dependency of  $\Delta a$ , it is likely that the back-reflection region would have yielded a much higher accuracy.

## 10. Conclusions

A series of experimental tests of our profile fitting method applied to powder diffractometry shows it has high precision in determining full profile shapes, peak reflection angles, peak and integrated intensities.  $R$  is better than 2 percent on the average in fitting profiles when about 30 K counts are collected at the peak, peak angles can be determined to better than  $\pm 0.0004^\circ(2\theta)$ , and peak and integrated intensities to 0.5 percent. The precision for weak peaks (130 counts) is better than  $0.01^\circ$  and a few percent in peak intensities. Overlapped peaks can be resolved if their  $\text{K}\alpha_1$  peaks are separated by at least HWHM, thus avoiding gross errors in reading ratemeter strip charts. A possible method is introduced for handling the inherent systematic diffractometer/specimen errors with a least-squares type of refinement using the profile fitted angles for precision lattice parameter determination.

The method applied to a typical powder pattern routinely recorded at moderate- and high-speeds for identification purposes gave data better than  $0.01^\circ(2\theta)$  and 1 percent peak intensities. The Rietveld method as currently applied to x-ray powder diffractometer does not yet approach this precision.

## References

- [1] Huang, T. C. and Parrish, W., Accurate and rapid reduction of experimental x-ray data, *Appl. Phys. Letters*, 27, 123-124 (1975).
- [2] Parrish, W., Huang, T. C., and Ayers, G. L., Profile fitting: a powerful method of computer x-ray instrumentation and analysis, *Trans. Am. Cryst. Assoc.* 12, 55-74 (1976).
- [3] Ayers, G. L., Huang, T. C., and Parrish, W., High-speed x-ray analysis, *J. Appl. Cryst.* 11, 229-233 (1978).
- [4] Parrish, W., Ayers, G. L., and Huang, T. C., A minicomputer and methodology for x-ray analysis, 28th Denver Conf. on Applic. of X-ray Anal. (August 1-3, 1979).
- [5] Rietveld, H. M., A profile refinement method for nuclear and magnetic structures, *J. Appl. Cryst.* 2, 65-71 (1969).

- [6] Huang, T. C. and Parrish, W., Qualitative analysis of complicated mixtures by profile fitting x-ray diffractometer patterns, in Advances in X-Ray Analysis, Vol. 21 (Plenum Press, New York, 1978), pp. 275-288.
- [7] Huang, T. C., Rapid and precise method for analysis of energy dispersive x-ray spectra, IBM Jour. Res. & Dev. 29, 206-213 (1979).
- [8] Nelder, J. A. and Mead, R., A simplex method for function minimizations, Computer Jour. 7, 308-312 (1965).
- [9] Taupin, D., Automatic peak determinations in x-ray powder patterns, J. Appl. Cryst. 6, 266-273 (1973).
- [10] Robaux, O., Analysis de problems de "deconvolution," Rev. du Cathedec, NS74-2 (1974).
- [11] Parrish, W., X-ray Analysis Papers (Centrex Publ. Co., Eindhoven, 1965).
- [12] Parrish, W., Role of diffractometer geometry in the standardization of polycrystalline data, in Advances in X-Ray Analysis, Vol. 21 (Plenum Press, New York, 1974), 97-105.
- [13] Huang, T. C. and Parrish, W., The transmission-specimen powder diffractometry and the profile fitting method, Am. Cryst. Assoc. Meeting, Univ. of Hawaii (March 21, 1979).
- [14] Malmros, G. and Thomas, J. O., Least-squares refinement based on profile and analysis of powder film intensity data measured on an automatic densitometer, J. Appl. Cryst. 10, 7-11 (1977).
- [15] Young, R. A., Mackie, P. E. and Von Dreele, R. B., Applications of the pattern-fitting structure-refinement method to x-ray powder diffractometer patterns, J. Appl. Cryst. 10, 262-269 (1977).
- [16] Khattak, C. P. and Cox, D. E., Profile analysis of x-ray powder diffractometer data: structural refinement of  $\text{La}_{0.75}\text{Sr}_{0.25}\text{CrO}_3$ , J. Appl. Cryst. 10, 405-411 (1977).

#### Discussion

Comment (Edmonds): The R factor's are the same mathematically in form. However, a straight comparison is misleading since Malmorse and Thomas applied the neutron diffraction Rietveld structure refinement technique to digitized Guinier x-ray diffraction film data for which they had no accurate estimation of the true form and variation of the profile, whereas Dr. Parrish has accurately calibrated his instrument over a wide  $2\theta$  range. The profile shape for Guinier film data is much more complex than the single modified Lorentzian Malmorse and Thomas assumed, and the variation with  $2\theta$  is not the straightforward 3 parameter relationships used in the Rietveld technique.

Comment (Sabine): You state that your R factor is very much better than that given by the Rietveld method. You are measuring very different things. His Y calc is constrained by the structure. Yours is not; hence, it must be lower.

Response (Parrish): No direct comparisons were intended, but it is evident that the modified Lorentzian and other forms used by Malmorse and Thomas did not give as accurate a fitting as our model using the form of three Lorentzian for  $\text{CuK}\alpha$ , and the same for  $\text{CuK}\alpha$ .

Comment (Jorgensen): You have apparently developed a very accurate representation of the x-ray line shape. Your resolution function should now be used in a Rietveld-like analysis before you can give a meaningful comparison of which method is better, since previous x-ray Rietveld analysis programs have probably not used a resolution function as accurate as yours. At ANL, we have tried using direct deconvolution methods similar to yours on time-of-flight neutron data where the peak shape is well known. We found it difficult to find peaks whenever three or more peaks recurred in a cluster. Moreover, the Rietveld approach gives far superior structural information, in our case.

Response (Parrish): We do not use deconvolution; we synthesize profiles which very closely match the x-ray diffractometer profiles. As you saw in my slides, we were successful in resolving overlaps as for example the three quartz reflections at  $68^\circ$ .

Comment (Jorgensen): The R value you calculate is vastly different than the Rietveld R value and it is meaningless to compare them. The difference results because your Ycalc is simple a scale factor times the appropriate element of your compound Lorentzian resolution function while in the Rietveld program, Ycalc includes all of the structural parameters (i.e. Ycalc must obey the constraints of a structural model and is not free to independently scale to Yobs). The result of this is that your R value is only a measure of how well your resolution function fits the observed peak shapes while the Rietveld R is primarily dependent upon how well the structural model fits the data.

Response (Parrish): The R we use is given in the same mathematical form by Malmorse and Thomas who used a modified Lorentzian. I showed that we obtain accurate fitting of the entire profile at all  $2\theta$ 's and that we believe this is essential to obtaining accurate values of reflection angles and intensities. I stated at the beginning of my paper that our method was for general use in powder patterns; of course the precision integrated intensities obtained with the method could be used for structure determinations.

Comment (Prince): In the discussion of these papers, there seems to be a general misconception that there is a conflict between the profile fitting of Parrish and the total pattern analysis of Rietveld. The Rietveld technique takes a diffraction pattern and an assumed peak shape and determines crystallographic parameters. The Parrish work is a good representation of x-ray peak shape. What is needed now is the marriage of these techniques for x-ray refinement.

Response (Parrish): No comment made or necessary.

## PROFILE REFINEMENT OF NEUTRON POWDER DIFFRACTION PATTERNS

A. W. Hewat

Institut Max von Laue - Paul Langevin

156X Centre de Tri, 38042 Grenoble

France

The refinement of crystal structures directly from neutron powder diffraction patterns, without first extracting the structure factors, has become an important crystallographic technique in the ten years since Rietveld first introduced it. This profile refinement technique is related to, but different from, the line profile analysis techniques developed even earlier for x-ray powder diffraction. In this paper we first follow the contributions made by Rietveld and others by reviewing the applications of profile refinement to specific types of problems in solid state physics. Starting with magnetic structures, profile refinement was quickly adopted for studies of uranium halides, phase transitions, hydrogen bonding and disordered structures, especially ionic conductors. It has removed many of the limits imposed on classical crystallography by the availability of suitable crystals, extinction, twinning and different sample environments. In fact, it is equally easy to study the solid structure of materials which are normally gases or liquids. With this historical and applications background, we then examine the technique itself in more detail. The correct choice of weights, the use of molecular constraints and Fourier synthesis, the best description of thermal motion for individual atoms and rigid molecules, are all subjects still being debated, although a working consensus does exist. Improvements are also being worked out for the description of the line shape, the background contribution and the effect of absorption. We then turn to the existing experimental techniques, emphasizing the need for high resolution diffractometers, efficient multidetectors and focussing monochromators to give a wide choice of neutron wavelengths. The sample preparation and environment are seen to be simpler than for x-ray powder diffraction, large cryostats, furnaces, and pressure cells can be accommodated in a routine way and since the sample itself is much

larger, preferred orientation is a very much less serious problem. Finally, we mention some of the new experimental techniques being developed, especially the use of high efficiency multidetectors, and intense pulsed neutron sources for time-of-flight diffractometers. We do not believe that these new developments will produce the same kind of revolution that profile refinement did. Rather, we expect the continued improvement in resolution, intensity, and computing techniques to extend the application of neutron powder diffraction to even more fields in solid state chemistry and physics. Such work will be increasingly concentrated at a few large national or international centers open to a wide community of users.

### 1. Line Profile Analysis and Rietveld Refinement

Interest in powder diffraction profiles is not new. Long before neutron powder diffraction became important, x-ray line profiles were being studied in detail [1]<sup>1</sup>. Similar techniques of line profile analysis, though less widely known, have been described for single crystal data [2]. When computers became available, they were applied to x-ray line profile analysis, and this technique can now be used automatically for on-line experiments with a cycle time of the order of seconds [3]. Indeed, cycle times of the order of milliseconds may soon be expected for the study of the chemical kinetics of catalytic surfaces, the electrolysis of battery electrodes etc. [4].

What then is different about the Rietveld Type of profile refinement? With profile line analysis, the emphasis is still on treating single lines or groups of lines to extract the positions and intensities of their components. With the Rietveld technique, the crystal structure itself is refined to fit directly the complete diffraction pattern. There is no intermediate step of extracting intensities or structure factors. This does not mean that the standard crystallographic techniques, such as Fourier synthesis of the crystal structure, are not available [5]. However, it does mean that a starting model for the structure is necessary, and the Rietveld technique is of no use for direct methods of structure solution. An intermediate type of profile refinement is needed if such a starting model is not known.

To understand the differences between profile line analysis and Rietveld profile refinement, it is first necessary to understand some of the difficulties with the former. The Rietveld technique is an effort to circumvent these difficulties. Both techniques are of most value when the powder diffraction lines are not all completely resolved; otherwise integrated intensities can be used for the structure analysis, and profile refinement is really only useful for improving the precision of the measurements of peak positions and hence of the crystal cell dimensions.

<sup>1</sup>Figures in brackets indicate the literature references at the end of this paper.

With profile line analysis, one attempts to fit a group of overlapping lines with a function which is the sum of a number of individual lines. Obvious parameters are the positions and intensities of each of the individual lines, but one might also need additional parameters describing the background level and line shape as a function of the scattering angle. With x-ray powder diffractometers, the line shape in particular, may be a very complicated function (e.g., see [1]). Then, we need 2-4 parameters for each line in the diffraction pattern, which might contain up to  $10^3$  lines for the complete scan. If we are not to have an impossibly large number of parameters, we must identify distinct parts of the scan separated by regions where no lines contribute: these parts can then be treated independently, at least for a given cycle of refinement. The problem of finding such independent groups of lines is less serious for high resolution x-ray studies of inorganic compounds, but becomes virtually impossible for more complex organic structures, especially with relatively low resolution neutron diffractometers.

Apart from the number of parameters, and the need for regions where no lines contribute, the line profile analysis technique suffers from the problem of correlation between parameters. For example, for two closely spaced lines, there will be a strong correlation between the widths and positions (separation) of the lines: there are similar problems if one attempts to refine the background for a complex pattern containing only small regions where no lines contribute. For these reasons, the background levels are usually fixed at "reasonable" values, and an attempt is made to find a function which will also fix the shape of all the lines. This is not easy, because both background and line shape are both sample dependent, and cannot be measured once and for all for a given diffractometer. Even if this were possible, there would remain twice as many parameters as there are diffraction lines, and correlation would still exist between the different line positions and intensities.

The Rietveld technique drastically reduces the number of parameters, and new parameters are directly related to physical quantities. All of the line positions are determined by the unit cell dimensions (at most six parameters) and the line intensities are no longer independent, but are determined by the crystal structure itself. There is no longer any need to break the pattern into groups of lines and groups of parameters; indeed, the best results are obtained when all of the structural parameters are simultaneously refined to fit the complete diffraction pattern (profile). There are then only about  $10^2$  parameters for the  $10^3$  lines of the complete scan.

## 2. Applications of Neutron Powder Profile Refinement

### 2.1. Magnetic structures

Neutron profile refinement, in the Rietveld [6,7] sense, predated its application to x-rays by a decade. For some years, most other laboratories neglected the work at Petten, which was concerned largely with a rather special field of study, magnetic structures, which have little interest for x-ray crystallographers. Even neutron diffractionists

tended to discredit the use of powder diffraction for magnetic structures, since it was well known [8] that for high symmetry structures, as most commonly studied, some information about the nuclear spin orientation is irretrievably lost when the crystal is powdered. As well, powerful single crystal techniques for magnetic structures depend on applying magnetic fields in a specific crystallographic direction, and in using beams of polarized neutrons and measuring the difference in scattering for different relative orientations of polarization and crystal axes [9].

Such techniques lose much of their force with the random orientation of crystal axes in a powder. Powder diffraction, though most important in the early days of neutron crystallography, had come to be regarded as a poor man's alternative to these new single crystal techniques which had been made possible with the advent of high flux reactors.

However, much valuable work was accomplished in these early years at Petten on materials for which single crystal work was difficult for various reasons [7].

Similar early studies were taken up at Kjeller (Norway) with work by Andresen and van Laar [10] on the magnetic structure of  $\text{Fe}_3\text{Se}_4$ , and by Holseth, Kjekshus, and Andresen [11], on  $\text{FeSb}_2$  and the magnetic transition in  $\text{CrSb}_2$ . In the following years, Andresen and his colleagues remained an important group of users of the Rietveld technique for mainly magnetic structures.

## 2.2. Uranium halides

It was not, however, until 1973 that most other neutron diffraction laboratories took an interest in profile refinement. Taylor and Wilson [12,13] using their own profile refinement program, adapted from the ORFLS single crystal program, extended the work of Loopstra and Rietveld [14] on uranium oxides to halides such  $\text{UCl}_4$  and  $\text{UCl}_6$ . The interest in uranium compounds was of course mainly due to their importance in the nuclear research projects at Petten (The Netherlands) and Lucas Heights (Australia). Such halides are often volatile, corrosive, hygroscopic and unstable, and thus very difficult to study using normal crystallographic techniques. The early achievements of Zachariassen [15], who succeeded in obtaining the correct structure for  $\text{UCl}_6$  and many other such halides with milligram samples, must be regarded as an uncommon "tour de force." With powder profile refinement, Taylor and Wilson not only achieved more precise structures for many of these materials at low temperature, but demonstrated the transformation of some, such as  $\text{MoF}_6$  and  $\text{WF}_6$  to plastically crystalline phases, with rotations of the halide octahedra before the crystal actually melts.

## 2.3. Phase transitions in perovskites

Phase transitions were also being studied at Harwell at this time, using neutron profile refinement. Perovskite ferroelectrics, such as  $\text{KNbO}_3$  and  $\text{BaTiO}_3$  undergo a series of phase transitions to lower symmetry structures as the temperature is lowered. It is

ry difficult to obtain single crystals of such materials, since the crystal usually  
atters or becomes multiply twinned on passing into the lower symmetry phase. Even  
ough such transitions involve very small displacements of the atoms ( $\sim 0.05 \text{ \AA}$ ), the  
utron powder diffraction patterns look quite different for the different phases (fig. 1)  
d the structures can be readily obtained from profile refinement [16a]. In this case,  
ere were stringent checks on the correctness of the results. Not only could the higher  
mmetry phases be compared with careful single crystal measurements, but the low symmetry  
ructures could be used to calculate the spontaneous electrical polarization of these  
rroelectric materials; these calculations compared exceptionally well with macroscopic  
asurements. Many such ferroelectric and antiferroelectric phase transitions have been  
udied since [16b]. With the ILL high flux reactor, complete data sets can be obtained  
r many different temperatures in a short time. The temperature dependence of the order  
rameter in the antiferrodistortive material  $\text{KCaF}_3$  has thus been studied [17]. The  
ults are in excellent agreement with NMR measurements in the tetragonal phase, and a  
antitative relation has been found between the temperature dependence of the order  
rameter, the lattice dimensions and the anisotropic Debye-Waller factors.

#### 2.4. Phase transitions in inorganic materials

Structural phase transitions are really quite common in many "ordinary" materials.  
e "crystal structure" usually reported at standard temperature and pressure may not then  
present the true equilibrium structure, but only an approximation. The real crystal  
ructure must be determined near absolute zero temperature and although this presents  
fficulties for conventional techniques, there is no special problem with neutron powder  
ethods. Temperatures of millikelvins are even possible, but the boiling point of liquid  
lium is usually sufficiently low for most structural studies.

For example,  $\text{Pb}_3\text{O}_4$  undergoes a subtle phase transition at 170 K in which the  
plitting of the diffraction lines is only visible on a high resolution diffractometer.  
varri, Weigel and Hewat [18] have shown, by profile refinement of neutron powder data,  
at the transition occurs because of the opposition between  $\text{Pb}^{2+}$  ions, the  $\text{Pb}^{4+}$  and  $\text{O}^{2-}$   
ons playing no part. The structure simply contracts when the temperature is lowered, and  
170 K, the  $\text{Pb}^{2+}$  ions come into contact: there is then a shearing of the structure to  
oid a too close contact.

Such phase transitions represent very small changes of the structure: atomic  
splacements are a fraction of an angström unit. However, relatively large changes  
esult in the diffraction pattern, which is clearly very sensitive to any splitting of the  
nes. With a line resolution of  $\Delta d/d \sim 10^{-3}$ , even changes ten times smaller have a  
oticeable effect.

$\text{BiVO}_4$  is an example of a large group of so called "ferroelastic" materials, where the  
irection of polarization can be changed by some (often small) external stress.

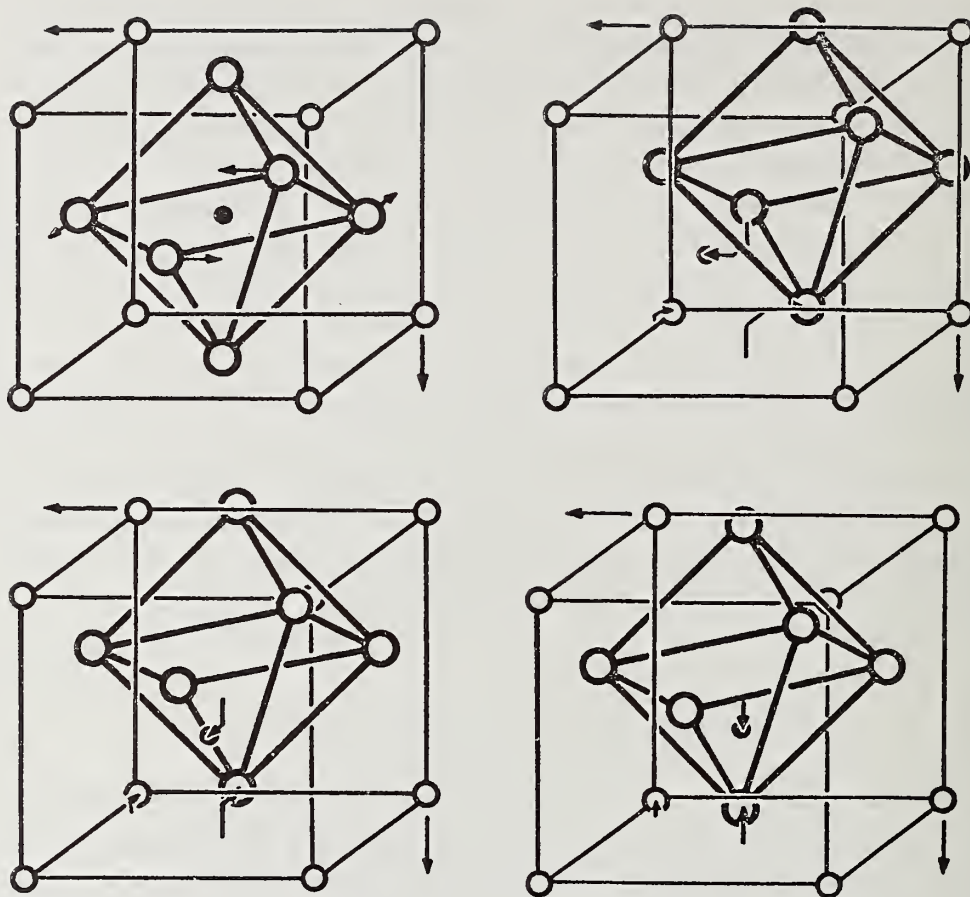


Figure 1. Successive phase transitions occur in most perovskite ferroelectrics. Neutron powder profile refinement has been used to study many such materials.

David, Glazer and Hewat [19] have shown how the bismuth atoms and the rigid  $\text{VO}_4$  tetrahedra move along the  $c$ -axis to produce this polarization; as the temperature is lowered, the crystal enters the ferroelastic phase at 255 °C. The data is sufficient to resolve even the position of the vanadium atom, which has an unusually weak scattering length for neutrons.

A number of other ferroelastic materials have been studied by Glazer, and also by Hidaka using profile refinement (e.g., see [20]).

### 2.5. Hydrogen bonds and phase transitions

Phase transitions in hydrogen bonded materials have also been studied for some time using neutron powder diffraction. For example, in  $\text{NH}_4\text{H}_2\text{PO}_4$  [21] single crystals are

destroyed on passing into the low temperature phase, which is antiferroelectric in contrast to the ferroelectric structure of the potassium isomorph  $\text{KH}_2\text{PO}_4$  [22]. This difference was shown to arise because the new hydrogen bonds between the  $\text{NH}_4$  and  $\text{PO}_4$  groups in  $\text{NH}_4\text{H}_2\text{PO}_4$  force the  $\text{H}_2$  atoms to take up an alternative hydrogen bonding arrangement, which is apparently less favorable in  $\text{KH}_2\text{PO}_4$ . More recent measurements on  $\text{NH}_4\text{H}_2\text{PO}_4$  [23] are sufficiently precise to allow a detailed interpretation of the anisotropic temperature factors obtained from profile refinement (fig. 2). We notice immediately that above the phase transition both the  $\text{NH}_4$  and  $\text{PO}_4$  groups are librating strongly. It is remarkable that the major axes of the thermal ellipsoids, although not constrained to lie in any particular direction, refine to be perpendicular to the bonds, as required for rigid body librations. The disordered O..D..O bonds appear to be significantly nonlinear, with the two half deuterium positions displaced from the line joining the oxygen atoms. This is not the correct interpretation; the two  $\text{PO}_4$  groups are no doubt librating  $180^\circ$  out of phase, synchronized with the motion of the D atom in its double well. The O-D..O or O..D-O bond can be linear at any given instant: the 1/2 D positions do lie on the line joining the opposite extremities of the O ellipsoids. The  $\text{D}_4$  ellipsoids show strong libration plus vibration along y, so as to make and break the O-D..O hydrogen bonds: this motion must also be synchronized with that of the  $\text{PO}_4$  and D groups. Then, instead of the simplified picture of hydrogen bonds tunneling between two minima of a double well potential, which is the classical picture of H-bonded ferroelectrics, we can see that the true "soft-mode" involves all of the atoms, coupled in a more complex collective oscillation. The transition mechanism can be more easily visualized by viewing the 5 K structure on top of that at 300 K.

This example illustrates the utility of using a complete description of the thermal motion, and indicates the potential of profile refinement for studying structures as a function of temperature.

## 2.6. Disordered structures

After 1973, an explosion of papers on neutron profile refinement occurred, as summarized by Cheetham and Taylor [24]. In one of the first, Cheetham and Norman [25] refined the structures of  $\text{YF}_3$  and  $\text{BiF}_3$  from data collected at Harwell. The group of Fender in Oxford applied the technique to many of the problems in chemical crystallography that they had already pioneered using classical neutron powder techniques [26,27,28].

In particular, the technique was applied to disorder configurations in non-stoichiometric oxides and hydrides. For example, Titcombe, Cheetham and Fender [29] repeated and extended their earlier conventional powder diffraction work on hydrogen ordering in  $\text{CeD}_2 + x$  [30].

Also at Oxford, Von Dreele and others applied profile refinement to large disordered structures made from simple blocks of titanium, niobium and germanium oxides [31]. These block structures are best known from the x-ray work of Wadsley [32] and especially the

# PHASE TRANSITION IN $\text{ND}_4\text{D}_2\text{PO}_4$

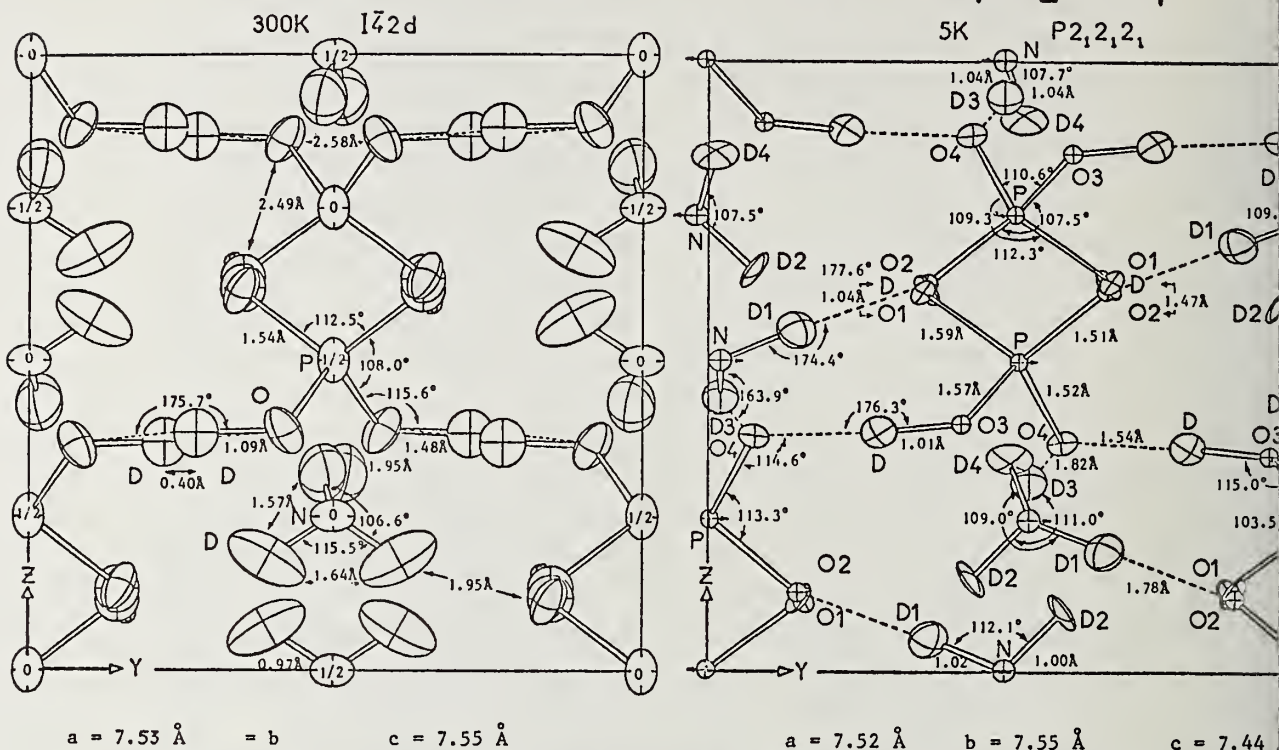


Figure 2. Ammonium dihydrogen phosphate is an example of a more complex type of phase transition studied by profile refinement.

electron diffraction lattice imaging technique developed by Allpress [33] and others (see Cowley and Iijima [34] for references). The characteristic feature of such structures is usually the regular array of defects joining large blocks of perfect order. Anderson, Bevan, Cheetham, Von Dreele, Hutchison, and Strähle [35] therefore had recourse to these latter techniques to interpret their profile refinement results for germanium niobium oxide.

In all of these non-stoichiometric problems, one attempts to refine the occupancy of the various sites, and the danger is the correlation to be expected with the Debye-Waller factor. One needs very good data, and even then a knowledge of the average occupation may be difficult to interpret in terms of the detailed crystal structure.

## 2.7. Fast ion conductors

Structures showing partial occupancy are, however, of increasing importance for the study of ionic conductors, and powder diffraction can make an important contribution here, provided the proper precautions are taken. Wright and Fender [36] studied the phase transition in which  $\text{AgI}$  becomes a conductor for  $\text{Ag}^+$  ions. England, Jacobsen and Tofield [37] showed that the hydrogen atoms in deuterated  $\beta$ -alumina, which are bonded to the oxygen atoms at 4.5 K, become available for ionic conduction at 823 K. A more detailed

unt, in which Fourier techniques are used to examine the hydrogen distribution at high eratures, is given by Tofield, Jacobsen, England, Clarke, and Thomas [5].

Bogacz, Bros, Gaune-Escard, Hewat, and Taylor [38] showed that in the ionic conductor  $\text{Br}_6$ , the sodium ions are freed at two successive phase transitions. Hewat [39] has ured the complete structure of  $\text{Bi}_2\text{O}_3$  at six temperatures from 300 K through the er-ionic" phase transition at 1000 K, where the oxygen ions become distributed over mpletely occupied holes. The intermediate phase previously reported on lowering the erature, was not found when the sample was prevented from taking up additional spheric oxygen.

## 2.8. Location of hydrogen atoms

Just as neutron diffraction is of value for studying heavy atom structures, such as e of uranium, it is invaluable for the location of very light atoms such as ogen. The scattering power for neutrons is of the same order for most elements, and roportional to the atomic number, as it is for x-rays. In addition to those quoted r earlier headings, the following example may be noted.

Some materials absorb so much hydrogen that they are known as "hydrogen sponges", and e this has possible applications for energy storage, work is currently under way to y the mechanism of such absorption using neutron powder diffraction. Earlier studies ydrogen in metals using neutron profile refinement include the work of Kuijpers and tra [40].

Sodium per carbonate ( $\text{Na}_2\text{CO}_3 - 1.5 \text{H}_2\text{O}_2$ ) is a well known industrial bleach, which is usually stable vehicle for hydrogen peroxide, or active oxygen. Adams, Pritchard, ewat [41] have determined the precise hydroxide configuration in this material, which rdered at room temperature but transforms to an ordered structure at low ratures. Other perhydrates, such as those of the oxalates of potassium and rubidium s, Ramdas and Hewat, [42] have also been studied in the same way. In such materials, much of the structure is already known from x-ray methods, the difference Fourier ique applied to neutron powder data immediately reveals the hydrogen atom ions.

## 2.9. Solid liquids and gases

The crystal structure of materials which are normally liquids or gases can most y be studied using powder diffraction. Sandor has studied the phase transitions in e molecular solids in this way, (e.g. see ref. [43]). Solid ammonia is another le which is ideal for studying the dynamics of such materials, and one may ask if the

ammonia molecules in the solid undergo hindered rotation as they do in many salts such as  $\text{NH}_4\text{NO}_3$  [44].

As an aid to the study of the molecular dynamics of ammonia, the solid was examined by neutron profile refinement as a function of temperature between 2 K and 180 K [45]. No phase transition was found, but even near absolute zero temperature, the ammonia molecule is librating strongly. The amplitude of libration does not increase with temperature as quickly as required for a purely harmonic model, and this suggests a possible quantum mechanical tunneling between the hydrogen sites.

Solid oxalic acid [46] and acetic acid [39] are being studied by profile refinement at low temperature to investigate the possibility of "resonance" structures in which the C-O and C=O bonds become equivalent above a certain transition temperature, with disordering of the hydrogen bonds.

### 3. Profile Refinement Theory

#### 3.1. Basic principals

All types of profile refinement can be justified by the following simple arguments [47]. Suppose that the count  $y_i(\text{obs})$  at the point  $i$  in the diffraction pattern is a sample of some model function  $y_i(\text{calc})$ . In the case of line profile analysis, this model function is the sum of the profiles of all of the individual lines; with the Rietveld method, these individual line profiles are calculated directly from the crystal structure model. Then the probability  $p_i$  that a given sample count  $y_i(\text{obs})$  will differ from  $y_i(\text{calc})$  is given by

$$p_i \propto \frac{1}{\sigma_i} \exp \left\{ - \frac{\frac{1}{2} [y_i(\text{obs}) - y_i(\text{calc})]^2}{\sigma_i^2} \right\}$$

since each sample count comes from a normal (exponential) distribution centered on  $y_i(\text{calc})$ , with standard deviation  $\sigma_i = \sqrt{y_i(\text{calc})}$ . The probability  $P$  that all of the counts are samples of the population  $y(\text{calc})$  is the product  $\prod_i p_i$  of the individual probabilities. Then

$$P = \prod_i p_i \propto \left\{ \exp - \frac{1}{2} \sum_i \frac{[y_i(\text{obs}) - y_i(\text{calc})]^2}{\sigma_i^2} \prod_i \left( \frac{1}{\sigma_i} \right) \right\}$$

since the product of exponentials  $p_i$  is the exponential of the sum of the separate exponents. The probability  $P$  is maximized if the exponent factor

$$\chi^2 = \sum_i \omega_i [y_i(\text{obs}) - y_i(\text{calc})]^2$$

minimized using the weighting scheme  $\omega_i = \frac{1}{\sigma_i^2} \approx \frac{1}{y_i(\text{calc})} \approx \frac{1}{y_i(\text{obs})}$ .

It should be noted that the statistical weight is of course calculated from the raw data before subtracting the background. Since the background is a smooth function obtained from the average of many points, the statistical error introduced by the background subtraction is usually neglected, as in single crystal measurements. However, systematic errors may occur; for example, an underestimation of the contribution of thermal diffuse scattering will lead to an underestimation of the overall temperature or for the crystal structure.

The "R-factor"  $\chi^2$  is well known in statistics. Indeed, the "chi-squared test" can be used to test the significance of the initial hypothesis that the  $y_i(\text{obs})$  are samples of  $y_i(\text{calc})$  i.e., that the observations are consistent with the model. Given  $\chi^2$ , the number of observations  $i$ , and the number of parameters used to minimize  $\chi^2$ , then one can consult a table to determine the probability that the model is correct. In practice, we calculate the  $\chi^2$  expected if the model were exact, and if the fluctuations in  $y_i(\text{obs})$  were purely statistical. The  $\chi^2$  obtained by refinement will always be larger than this, but will approach the ideal value as systematic errors in the data or the model are eliminated. The R-factor for integrated intensities is also calculated at the end of the refinement, after dividing each  $y_i(\text{obs})$  between the contributing lines according to the calculated intensities. This R-factor is twice the R-factor for structure factors usually used by crystallographers.

### 3.2. The weighting scheme

The weighting scheme used for profile refinement, derived purely from statistical arguments, is to be contrasted with the different weighting schemes devised for conventional single crystal structure analysis. In the latter case, an attempt is usually made to give lower weights to those observations most affected by systematic errors such as extinction. With neutron powder measurements, such systematic errors are usually much more important. However, if special care is taken to eliminate such systematic errors, a purely statistical scheme can also be used for single crystal measurements. Sakata and Sasaki [48] propose that the weight for an integrated Bragg reflection should then be inversely proportional to the integrated intensity, just as it is inversely proportional to the intensity for profile refinement. With this assumption, they then go on to show that the calculated standard errors are different for the same data treated by profile

refinement or by refinement on the integrated intensities. They conclude that the errors calculated by profile refinement must therefore be wrong. The details of this argument are correct, but the basic assumption and conclusion are not.

In fact, each count  $y_i(\text{obs})$  is an independent estimate of the integrated Bragg intensity; simply adding together these counts does not give the best possible estimate of the integrated intensity, but only an approximation which is not even very good for weak peaks on a high background. The idea of making the weight inversely proportional to this integrated intensity is again an approximation which takes no account of the fact that a number of independent, but not equally good, estimates (a step scan) was made of a function which we know to be a peak. Nor is it possible to argue that the observations are not independent estimates, because they all come from the same Bragg peak, nor to argue even that the Bragg peaks are not independent because they come from the same structure. Here we are concerned only with the notion of statistical independence.

Sakata and Cooper have then correctly demonstrated that, given these approximations, the calculated errors are not the same for the integrated intensity refinement as for profile refinement. They correctly attribute this to the different weighting scheme used especially for weak reflections. However, the correct conclusion should be that profile refinement must be used for single crystal data, as was shown long ago by Diamond [2].

### 3.3. Constrained profile refinement

The principals developed above apply to all types of profile refinement: only the parameters are different with different methods. With line profile analysis, we assume nothing at all about the structure; in fact this technique is especially useful for a preliminary analysis of unknown structures or even mixtures of unknown materials.

The positions and strengths of the strong lines can be obtained automatically and compared with a computer file to identify the components. However, if a model structure is already known, it is better to use the Rietveld technique to reduce the number of parameters to those few that are physically meaningful, thereby reducing the correlation between parameters and improving the result of the structure refinement. Intermediate types of refinement can also be envisaged. For example, the positions of the first few lines might be obtained by line profile analysis, these lines indexed using one of the computer programs now available [49], and then a new profile refinement attempted in which the parameters were just the lattice constants and the line intensities. This should have some of the advantages of the Rietveld technique in removing parameter correlation without the need to know the details of the structure, which could then be obtained from standard crystallographic techniques and perhaps even direct methods.

This intermediate profile refinement and the Rietveld refinement, can be regarded as constraining the basic line profile refinement to give results consistent with some additional knowledge--first of the unit cell, and then of the structure itself. We can go even further; if we assume that some components of the structure are rigid units, we need

only refine the positions and orientations of these units as a whole. A simple example, which is already possible with the Rietveld program, is the well known rigidity of the oxygen octahedra in most perovskite oxides [47]. These additional constraints can reduce the number of parameters and the correlations between them.

Pawley, Mackenzie and Dietrich [50] have written a new profile refinement program designed to exploit the full power of such constraints, which Pawley [51] has already developed for single crystal refinements. He has shown that in many molecular crystals, molecules, or at least parts of them, can be constrained to move as rigid units. This greatly simplifies the refinement, which can then give useful results for quite complex structures, using only the relatively small amount of information contained in a powder pattern. These developments will no doubt increase the upper limit on the size of the structure that can be treated with powder diffraction, now estimated to be a monoclinic cell of volume up to  $3500 \text{ \AA}^3$  [52].

Such constrained refinement techniques are also of value in studying the behavior of materials under different conditions of temperature and pressure. Often, it is only certain features of the structure which are changed; for example, one molecule sliding past another, or a rigid unit rotating to accommodate new crystal stresses. Once such features are identified, only the appropriate parameters need to be refined at each temperature or pressure.

### 3.4. Thermal motion and anisotropic Debye-Waller factors

Rietveld [7] worked with normally stable structures, often at low temperatures to avoid magnetic ordering. He used rather long wavelength neutrons ( $2.4 \text{ \AA}$ ) for reasons of resolution and intensity [53] and therefore obtained data of limited range in  $\sin\theta/\lambda$ . Under these conditions, isotropic Debye-Waller factors, or even an overall temperature factor, was sufficient. When the profile refinement technique was applied to other systems, especially those involving structural phase transitions, these approximations were no longer sufficient. A phase transition occurs because a structure is basically unstable, and precursor effects are seen as characteristically strong vibrations of groups of atoms. Such effects are described as "soft modes", and are far from isotropic. The Debye-Waller tensor may be four times larger in the soft direction than in the other directions and this makes a big difference to the intensities of high angle lines. To overcome this difficulty, powder diffraction may often be the only way of refining such structures where the crystal itself may be destroyed by the phase transition. Anisotropic Debye-Waller factors were therefore soon introduced into profile refinement [47]. Apart from permitting fits to the high angle data which could not be refined with the normal program, they offered physical insight into how soft modes produced phase transitions. At low resolution diffractometers of limited  $\sin\theta/\lambda$  range, the absolute values of the Debye-Waller factors may not be well determined because of systematic errors in the background measurement. However, even then, the relative values often showed the

characteristic librations or vibrations of groups of atoms. These effects are most convincing when the results of profile refinement are plotted with the ORTEP program, as in figure 2.

### 3.5. Cumulant expansion of thermal motion

However, even anisotropic Debye-Waller factors are not adequate for describing certain types of motion found in crystals, especially at high temperatures. These problems do not occur so often for single crystal measurements simply because such measurements are so often limited to standard temperatures and pressures. For example, in  $\text{MoF}_6$  at 263 K, the octahedra, which are very rigid units, begin to rotate [54]. Such dissociative phase transitions may be precursors to melting itself, or may for example be associated with the onset of superionic conductivity, as in  $\text{Na}_2\text{UBr}_6$  [38]. Levy et al. [54] have shown how the cumulant expansion developed by Seymour and Pryor [55] can be used to describe such structures with a few physically meaningful parameters suitable for profile refinement. The dissociation of the structure can then be followed as a function of temperature, since many complete data sets can be collected in a short period.

A similar solution to a related problem has been developed independently by Kurki-Suonio. In  $\text{NH}_4\text{NO}_3$  [44] this method has been used to find the preferred orientation of the  $\text{NH}_4^+$  and  $\text{NO}_3^-$  groups in the high temperature phase. These groups are rotating, but there is a definite correlation between their orientations. This type of hindered rotation must in fact be quite common, and many more examples will no doubt be discovered now that structures can be precisely measured at many different temperatures with profile refinement.

A related effect occurs in dynamically disordered materials. In  $\text{CsPbCl}_3$  [56] the anions occupy holes which are too large for them. At high temperature, they therefore move around these potential wells, but nevertheless, have preferred positions which can be found using the cumulant expansion technique. This effect can be called "anharmonic" thermal motion. At lower temperatures in  $\text{CsPbCl}_3$ , the ions no longer have the energy to move around, and become frozen in particular positions after a series of phase transitions. Profile refinement, using powerful on-line computers and interactive programs will be increasingly used to explore such effects, if only because life is not long enough to survey such structures as a function of temperature and chemical composition using traditional single crystal structural studies.

### 3.6. Fourier techniques

The Rietveld program refines the structure directly to fit the diffraction pattern, without first extracting the structure factors which are needed for Fourier synthesis. Fourier techniques cannot then be immediately applied. However, if a large part of the structure is already known, for example from x-ray work, it is possible to use this part

find the remainder from a difference Fourier synthesis. The refinement is set up in usual way, and just the scale factor and cell dimensions are refined using the partial structure. At the end of the refinement, even though the agreement between calculated and observed profiles will not be very good, the experimental structure factors are extracted dividing up intensities due to overlapping peaks according to the ratio of the calculated structure factors. The phases are also calculated from the model of the partial structure. A difference Fourier is then constructed and searched for features which might be identified with the unknown parts of the structure.

Some of the unknown atoms can then be placed, and the whole procedure repeated to find any remaining unknown atom positions. Such an approximate procedure does not of course produce precise atom coordinates, but only starting positions which can later be refined in the usual way. It works best when no more than about one quarter of the atom positions are unknown, and of course when the structure is centrosymmetric so that the phases are simply  $0^\circ$  or  $180^\circ$ .

Fourier syntheses have often been used to locate hydrogen atoms in structures where heavy atoms have already been found with x-rays (Sections 2.7 and 2.8). Such techniques should also be of value for disordered structures.

### 3.7. The line shape

The classical neutron powder diffractometer has an advantage over x-ray powder diffractometers for profile refinement: the line shape is much simpler. This is due to several reasons for a number of reasons.

- (i) A monochromated white source of neutrons does not of course contain sharp characteristic lines, such as the  $\alpha_1$  and  $\alpha_2$  components of x-rays.
- (ii) The resolution must usually be relaxed for neutrons, since the radiation source is much less bright. Then the effects of particle size and strain are not so important and the line shape is largely determined by the diffractometer, rather than the sample.
- (iii) The sample is much larger ( $\sim \text{cm}^3$ ) for neutrons, so that preferred orientation, surface texture effects etc. are not usually important.
- (iv) The geometry is simpler for neutron diffractometers. The sample is cylindrical and concentrated at the center of the counter bank. Söller collimators or position sensitive detectors are used to define the angular divergence: both have triangular acceptance functions, so that when several are convoluted together, an almost perfect Gaussian results.

Even for high resolution powder diffractometers ( $\Delta d/d \sim 10^{-3}$ ) the line shape is described very well by a simple Gaussian [57]. The only concession made by Rietveld [7] to the diffractometer geometry was to allow the line width to vary in a simple way

with scattering angle, and to correct the small asymmetry observed at low angles due to the finite vertical divergence. These approximations are the only ones used for almost all neutron powder work at present, but a number of authors have shown how they can be improved to describe more rigorously the experimental profiles.

Cooper and Sayer [58] and Thomas [59] have derived more complete corrections for the effect of vertical divergence. They have shown that in addition to a more complex form of asymmetry of the line shape, the centers of the lines are shifted slightly, and the integrated intensities must also be corrected. Of course, these effects are really only important for low (or high) angle lines on high resolution machines with rather large vertical divergences ( $\lambda \approx 5^\circ$ ). However, since new diffractometers do aim for fairly high resolution, with the vertical divergence increased to make up for the resulting intensity losses, these more precise corrections should be used more regularly.

Again, with higher resolution neutron diffractometers, the Gaussian line shape approximation which has up to now served so well, needs revision. Suorrti [60] has shown that with high resolution, tails can be seen on each side of the line; these tails cannot of course be described by the Gaussian approximation. He has introduced a Lorentz component to account for these tails and has shown that a very much better fit is obtained when the line shape is described by the convolution of a Gaussian and a Lorentzian, known as a Voigt function.

Since the effect of the tails becomes systematically more important at high scattering angles, the use of the usual Gaussian leads to an overestimation of the overall Debye-Waller factor, although the refined structural parameters are presumably not much affected.

Similar conclusions have been reached for x-ray line profiles. Langford [61] considers a Voigt function represented by the convolution of  $m$  Lorentzians and  $n$  Gaussian to represent the lattice strain, crystal imperfections and the shape and distribution of the crystallites in addition to the instrumental profile. Both Suorrti and Langford indicate how these more exact line shape functions might be incorporated into profile refinement programs.

### 3.8. Background subtraction

The existence of long tails on each line emphasizes a rather basic problem with profile refinement: what to do about the background. Profile refinement is needed to resolve overlapping lines for more complex structures, but in that case it becomes difficult to find regions where there are no lines and where the background can be measured. Sabine and Clarke [62] have proposed that just as the structure is refined to fit the peaks, other features such as defect distributions might be refined from the background. They see the background as a valuable source of additional information about the crystal, rather than a problem to be overcome. Windsor [63] has argued that the Debye-Waller factors should be refined to account for the angular dependence of the

ermal diffuse scattering as well as that of the Bragg peaks. Fender [64] has used modulations in the background, in addition to the Bragg peaks, to obtain the defect distribution. Boysen and Hewat [65] have shown that such background modulations in  $\text{SnCl}_6$  are due to a dynamic disorder at room temperature which tends to disappear as the crystal undergoes successive phase transitions at lower temperatures. In many such samples, the background can supply new information about the powdered crystal, but to set a model of the background for profile refinement, which contains only a few physically meaningful parameters, is not something that can yet be done routinely. Some physical insight into each special case is usually needed. At present, the background is measured at positions where no lines appear to contribute, and is thus not part of the profile refinement.

There are also experimental approaches to the background problem which will be discussed in Section 4.3.

### 3.9. Absorption corrections

Except for a few isotopes (for example, the most common isotopes of H, B, Cd, Gd, Eu and other transuranics), the effective absorption for neutrons is very much smaller than is for x-rays. Samples at least 1 cm thick are common. This means that a large cylindrical sample can be used, greatly simplifying the geometry, and providing a true bulk average of the crystal properties. However, even this small absorption ( $\mu R \sim 1$ ) can cause systematic errors in the temperature factors, which will then be underestimated. Rose et al. [66] and others have published tables of absorption corrections for such samples, but in fact the effect on the Debye-Waller factors can be calculated directly [68]. Such corrections are then best left to the end of the refinement.

In the few cases mentioned above where absorption is strong, a nonabsorbing isotope can be used in place of the natural element. Such isotopes are quite inexpensive for the lighter elements due to the advances made with isotope separation in the nuclear industry. For the transuranic elements, the absorption can in some cases be greatly reduced by using a shorter neutron wavelength, below the absorption edge (e.g., 0.5 Å neutrons for Gd).

## 4. Experimental Techniques

### 4.1. The classical neutron diffractometer

The classical neutron powder diffractometer, such as that used at Petten or Harwell in many of the early measurements using profile refinement, consists of three main parts (Fig. 3): a large monochromating crystal, a counter turning around the sample, and Söller collimators  $\alpha_1$ ,  $\alpha_2$  and  $\alpha_3$ . In some cases, such as at Lucas Heights and Brookhaven, an additional analyzing crystal is used in front of the counter to eliminate elastically scattered neutrons contributing to the background [69].

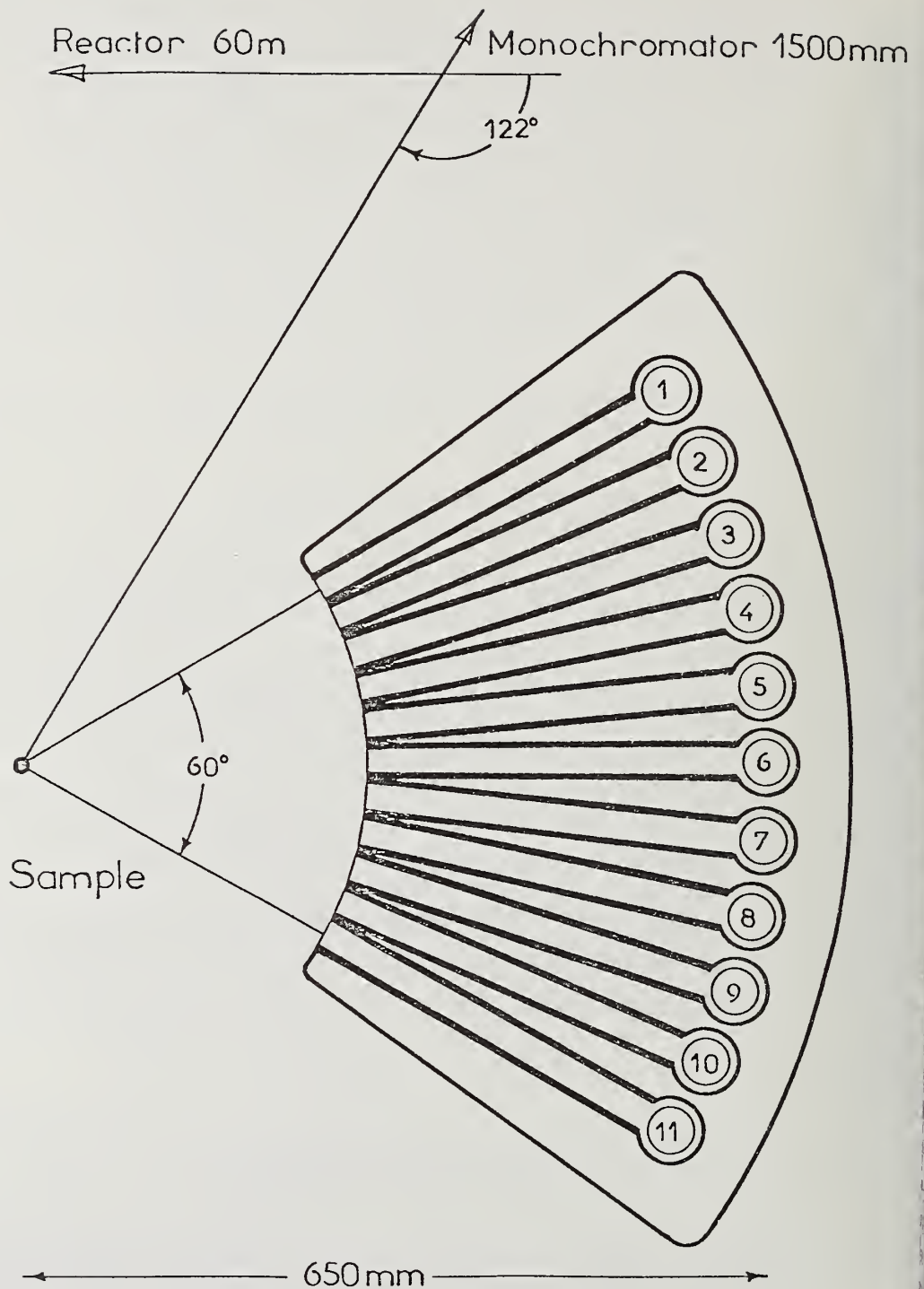


Figure 3. A conventional neutron powder diffractometer with a bank of Söller collimators and counters [57].

The transmission function for a Soller collimator is triangular, and the convolution of two such triangular functions is very nearly a Gaussian [70]. The mosaic spread of the monochromator ( $\beta$ ) is also a Gaussian if an average is taken over a volume large compared with the mosaic block size, as is true in this case. The intrinsic line shape from the particle size and strain in the sample does not enter for the typical medium resolution machine, where the instrument itself accounts for most of the line width  $A_{1/2}$  at half height (typically  $0.5^\circ$  in  $2\theta$ ). Caglioti et al. [71] have derived the dependence of  $A_{1/2}$  on scattering angle  $2\theta$  as

$$\left(A_{1/2}\right)^2 = U \tan^2\theta + V \tan\theta + W$$

where  $U$ ,  $V$ ,  $W$  are strictly functions of the divergence angles  $\alpha_1$ ,  $\alpha_2$ ,  $\alpha_3$  and  $\beta$ , but are usually treated as parameters in the refinement.

Together with an elementary correction for line asymmetry at small scattering angles, this simple description of the line shape continues to serve for almost all neutron profile refinements, and is in fact a very good approximation. It is only in the case of high resolution diffractometers that more sophisticated treatments become important (Section 3.7.).

#### 4.2. Requirements for high resolution

The line width can of course be reduced simply by reducing the divergences  $\alpha_1$ ,  $\alpha_2$ ,  $\alpha_3$  of the collimators. However, since the integrated line intensity is proportional to the product  $\alpha_1$ ,  $\alpha_2$ ,  $\alpha_3$ ,  $\beta$  [71] such a simplistic approach is not usually possible: the integrated intensity would be reduced by a factor of 16 for a reduction of a factor of 2 in each of  $\alpha_1$ ,  $\alpha_2$ ,  $\alpha_3$  and  $\beta$ . A one day experiment would then take two weeks. In practice, the situation is not quite so bad, since it is the peak intensity and not the integrated intensity that is important for profile refinement: the reduction in peak intensity would be "only" a factor of four. As well, we will see that because of focusing considerations, it is only necessary to reduce  $\alpha_1$  and  $\alpha_3$ : the peak intensity will then be simply proportional to the resolution.

Loopstra [53] has proposed another means of improving the resolution. If a longer wavelength is used, the low angle peaks are spread across the entire angular range, and are therefore better resolved. As well, the same total scattering power is now distributed over fewer reflections, so that the line intensity will actually increase for

longer wavelengths. This is offset somewhat because the peak intensity from the reactor comes at about 1 Å, but nevertheless, there is a net gain up to wavelengths of about 2.5 Å. The diffractometer of Petten is therefore designed to use such a relatively long wavelength, and a special graphite filter is used after the monochromator to remove shorter wavelength harmonics.

This solution is especially interesting for work on magnetic structures, where the magnetic form factors make it impossible in any case to collect data at large values of  $\sin\theta/\lambda$ . For crystal structures it is interesting to work with shorter wavelengths to better resolve the structure. For example, on the diffractometer D1A at the ILL, the usual wavelength is 1.9 Å, which gives data to  $\sin\theta/\lambda = 0.5$  Å, the usual copper limit for x-rays. However, wavelengths as long as 5.7 Å are used to index complex diffraction patterns, where the positions of the first few lines must be determined most precisely [72]. Longer wavelengths are also useful for very large molecular structures, where constrained molecular refinement can be used to limit the number of parameters, and hence reduce the amount of information needed from the diffraction pattern [50].

Fortunately, it is not necessary to have equally good resolution for all values of scattering angle. The density of lines reaches a maximum at  $2\theta \sim 90^\circ$ , and there are fewer lines at very low or very high angles. The best resolution is obtained when the scattering angle is about equal to the monochromator angle; the different wavelengths  $\Delta\lambda$  from the monochromator are then scattered back by the sample along the same direction as the incident beam. The line width is then essentially given by the convolution of  $\alpha_1$  and  $\alpha_3$ ; the collimator  $\alpha_2$  between the monochromator and sample, and the mosaic spread  $\beta$  may have any values. The monochromator angle should then be about  $90^\circ$  to coincide with the region of maximum line density. The objection to using such large monochromator angles  $\theta_M$  is that the reflectivity is then lower. This is partly due to the Debye-Waller factor for high order reflections from the monochromator, but mainly due to the reduced  $\Delta\lambda$  of wavelengths reflected

$$\frac{\Delta\lambda}{\lambda} = \mu \cot \theta_M .$$

The solution is to increase the monochromator mosaic spread  $\beta$ , which does not affect the focussing resolution, and eventually to cool the monochromator to reduce its Debye-Waller factor. With new hot pressing techniques for monochromators [73], the first solution is now easy, and the second is feasible but not usual. In practice, the monochromator angle is made even larger than  $90^\circ$  (on D1A it is  $122^\circ$ ), to compensate for the rapid increase in line width at high angles (with  $\sin^2\theta$ ). A more complete account of these considerations is given by Hewat [52].

### 4.3. Background

The experimental determination of the background level is difficult, and this sets limits on the precision with which site occupation numbers and temperature factors can be obtained. We need to have regions throughout the diffraction pattern where the Bragg peak contribution is negligible in order to measure the background level and interpolate to the other points. In particular, it is necessary to find such regions at high scattering angles. On a conventional diffractometer, this is still possible if the take-off angle is greater than  $90^\circ$ , because of the fall off in peak density again in this high angle region. On a time-of-flight machine this is more difficult, because the resolution is constant while the line density continually increases with  $\sin\theta/\lambda$ .

### 4.4. Multicounters

The simplest way of improving the statistics for a conventional diffractometer is to replace the single counter by a bank of counters and Söller collimators. However, until recently, it has been very difficult and expensive to make a bank of identical collimators. If the collimators are not identical, the profiles will not be identical either, and it will not be possible to simply add them together. Banks of counters have been used since at least 1966 for integrated intensity measurements (CURRAN at Harwell), but because of intercalibration difficulties the idea was dropped on later machines (PANDA at Harwell), and only taken up with recent advances in collimator design.

The best Söller collimators for neutrons are now made from stretched mylar foil, coated with neutron absorbing paint [74]. Such plastic collimators, first suggested by Foster et al. [70] have efficiencies of the order of 95 percent, but more importantly, collimators of 5' or 10' divergence can be made to be virtually identical at relatively low cost. Such collimators were first used routinely on the D1A diffractometer in Grenoble, where the results of a bank of ten collimators and counters are automatically added together to give a single composite profile for refinement. The computer program makes the remaining small corrections for relative efficiency and alignment, and each point in the profile is weighted according to the number of counters averaged to obtain it [7].

### 4.5. Position sensitive detectors

The D1B diffractometer at Grenoble also uses a multiple counter, but there are no collimators. Instead the counter consists of 400 independent elements, spaced at  $0.2^\circ$  (mm) to cover a total angle of  $80^\circ$  [75]. The angular resolution is determined by the size of the sample, the counting element, and the distance between them (1.5 m). This is then a medium resolution machine operating at rather long wavelengths (2.5 Å), which is of

particular interest for very high rates of data collection. For certain problems, useful diffraction patterns can be collected in times of the order of one second, so that for example, the crystalline products of chemical reactions can be monitored as a function of time. For such "kinetic" reaction experiments, even faster cycle times will be achieved on new instruments at the high flux reactor.

Collimators are still needed however, for high resolution diffractometers, since otherwise the sample would have to be very small.

#### 4.6. Focussing monochromators

Here we are talking about focussing a broad beam of radiation, up to 20 cm high, onto a small sample, 2 cm high for example. This is quite different to focussing a range of wavelengths into the same counter direction, which we have already discussed in Section 4.2. The monochromator is curved about a horizontal axis, so there is little effect on the wavelength composition of the beam.

Large gains in intensity are thus obtained for the usual small samples without much affecting the resolution. The reason is that the beam divergence in the vertical direction may be  $5^\circ$  or more for even a high resolution diffractometer, while the vertical divergence available from the reactor is usually  $1^\circ$  or less because of the extensive radiation shielding. Vertically focussing monochromators can therefore be used to increase this divergence at the expense of beam area, which is normally much larger than available samples. For the same reason, vertically extended counters are used to match the vertical divergences between counter/sample and sample/monochromator. The only disadvantage of divergences of  $5^\circ$  or more is an increased asymmetry of the low and high angle lines, but the corrections for these asymmetry effects [58,59] is a small price to pay for a large increase in intensity. The gains are of particular interest for diffractometers such as D1A and D1B on neutron guide tubes far from the reactor.

The 15 cm high focussing monochromator on D1A is composed of 30 strips of hot-pressed germanium, each 5 x 5 x 40 mm, glued onto a flexible aluminum plate. A relative alignment of the strips to within  $3'$  of arc is assured because they are cut from much larger strips of germanium already glued to a rigid alignment plate. The alignment of the original single crystal is thereby conserved throughout the cutting and transference to the aluminum focussing plate. The orientation of the parent crystal is chosen so that the mosaic spread is large in the horizontal plane, to ensure the selection of a large wavelength band  $\Delta\lambda$ , and small in the vertical plane to ensure the smallest focal spot size (15 mm). On D1A an order to magnitude is gained in the intensity using this focussing monochromator.

#### 4.7. Wavelengths between 1.1 Å and 5.7 Å

A supplementary advantage of using a large monochromator angle, is that a wide choice of wavelengths is then available simply by selecting different reflection planes. The D1A monochromator was designed to use the [117] plane in germanium to give 1.38 Å, but many other [hh1] planes can be obtained by simple rotation about the vertical axis. Thus focusing is still very good for [115] giving 1.9 Å and [119] giving 1.1 Å. Other useful wavelengths are 1.2 Å, 1.3 Å, 1.5 Å, 2.3 Å, 3.0 Å and 3.7 Å.

Longer wavelength harmonics are in all cases forbidden for such [odd, odd, odd] reflections, and of course  $\lambda/2$  is forbidden for the germanium structure.  $\lambda/3$  and higher harmonics are filtered out by the guide tube for  $\lambda < 2.6$  Å, but a graphite filter should be used for 3 Å, and a cooled beryllium filter for 5.7 Å.

The most common wavelengths used in practice are 1.9 Å for new work, 1.38 Å for refining well determined structures and 3 Å or 5.7 Å for indexing unknown structures. Any wavelength can be obtained within seconds, and under computer control if required.

#### 4.8. Cryostats, furnaces and pressure cells

Closed circuit refrigerators are available down to 10 K, but a helium cryostat is still preferred for most work. Such a cryostat works anywhere between 1.5 K and 310 K, and the ILL design has the advantage that the sample chamber is quite independent of the remainder of the cryostat, so that the sample may be changed within a few minutes.

The standard vacuum furnace works between 300 K and 1300 K with the sample usually sealed in a quartz glass tube. Special furnaces are available for the ranges of 20 °C to 1000 °C, 1000 °C to 1600 °C and 1000 °C to 2400 °C. Experiments at the highest temperatures must be completed in the shortest possible time because of possible crystal growth [76]; the sample may be sealed for example in an electron beam welded tungsten tube.

Various types of pressure cells for neutron scattering have been developed at the Grenoble CNRS laboratories under the direction of D. Block. The simplest type works with compressed helium gas, up to at least 7 kbar and in a cryostat at lower pressures, depending on the temperature. The sample size is of the order of 0.4 cm<sup>3</sup>. For pressures up to 10 kbar, 0.1 cm<sup>3</sup> samples are contained in a 5 mm hole in a single crystal of sapphire supported by an aluminum alloy cell. The pressure is applied by opposed tungsten carbide pistons acting on a special organic pressure transmitting liquid. Pressures of up to 30 kbar can be obtained by replacing the sapphire crystal by sintered alumina, but then additional lines due to the Al<sub>2</sub>O<sub>3</sub> powder are obtained in the diffraction pattern. Such a cell has been used, for example, to study the behavior of the hydrogen bonds in ferroelectric KH<sub>2</sub>PO<sub>4</sub> under pressures [77].

Pressures of up to 45 kbar can be obtained by using a special black alumina, which contains additives to improve its mechanical properties. Unfortunately, these additives

contribute yet more lines to the diffraction pattern, and this type of cell has so far only been used for studying compressibilities, and the behavior of isolated lines, not profile refinement.

#### 4.9. Sample preparation

Because such a large sample (1-5 cm<sup>3</sup>) is used, preparation is not so critical as for x-ray powder diffraction. The material is crushed very finely in a pestle and mortar. A dry glove bag is used if the sample is at all sensitive to moisture, because water scatters neutrons strongly, increasing the apparent absorption and background.

Even materials which are normally gases or liquids are best treated this way. In this case, the mortar is immersed in a bath of liquid nitrogen inside the glove bag. The boiling nitrogen readily excludes atmospheric moisture, which would otherwise condense. The pestle, sample can and spatula used to transfer the sample are likewise immersed in the nitrogen bath. The full sample can is left immersed in the liquid nitrogen until it is transferred to the cryostat (a few seconds exposure to the atmosphere), and then any liquid nitrogen which may have leaked into the sample is boiled off by briefly raising the temperature to 80 K. This procedure is surprisingly easy, and has been used even for poisonous gases such as ammonia after alternative methods, such as sublimation or shock freezing produced samples showing preferred orientation [45]. Even materials which have melting points above ambient temperature may be too soft to grind, and may benefit from such treatment.

The sample is pressed into the sample can, never shaken, and provided it has been thoroughly ground, preferred orientation cannot usually be detected. If it is, the preparation should be repeated more carefully. There are, however, three other techniques which may be needed occasionally. Firstly, since the sample is a cylinder, it can be rotated at say 1 revolution per second throughout the measurement: some workers routinely use this technique, which reduces the effect, but does little if the preferred axis is the axis of rotation. Riekel, Convert, Gobert and Lazaro [78], have used a spherical sample container, randomly spun on a jet of gas, so that a "powder pattern" may be obtained even from a single crystal.

The second technique is to dilute the sample with a large amount of some other powder which does not show preferred orientation. Materials with low absorption and simple diffraction patterns are needed, since their effect must later be subtracted. Powdered aluminium has been used, but there is a danger of reaction with finely divided metal powders, especially when used with oxidizing samples in furnaces. Carbon fibre or quartz wool has been used to prevent extensive crystal growth when a liquid is frozen, [50] and powdered quartz wool would seem to be the most generally useful material; it can be removed later by dissolving the sample.

Finally, if all else fails, a preferred orientation correction can be made during the refinement, as introduced by Rietveld [7]. Then something must be known a priori about

the nature of the preferred orientation. None of these three techniques, however, replaces a thorough grinding of the sample, at liquid nitrogen temperatures if necessary followed by annealing at high temperatures, and a careful filling of the sample can.

The can itself is normally a thin vanadium tube of between 5 and 15 mm diameter. Many such tubes have been manufactured at Harwell from electron beam welded vanadium sheet, with titanium ends made vacuum tight by indium wire seals. Because of the very small coherent scattering length of vanadium, no extra lines are introduced into the diffraction pattern. Such cans (without the indium) are also used in vacuum furnaces up to about 800 °C. For higher temperatures (up to 1100 °C) the sample is sealed under an appropriate atmosphere in a quartz glass tube, which has much lower absorption than ordinary borated glass. The diffuse scattering from the glass then adds to the background, but again there are no Bragg peaks. For still higher temperatures, or for reactive samples, other materials such as electron beam welded tungsten have been used. Neutron absorbing materials, such as cadmium in a cryostat, or boron nitride in a furnace, are used to shield parts which otherwise might scatter neutrons. With Söller collimators the furnace or cryostat dimensions can be chosen so that they are not seen by the counters. Normally then, there are no additional lines in the diffraction pattern, and it is not necessary to make a separate background scan with the sample removed.

#### 4.10. Data collection and treatment

Although the operation of a powder diffractometer is relatively simple, step scanning with one motor and storage of the results of the different counting elements, a small dedicated computer, such as the LSI-II based system used on DIA is of great value. Not only does it permit the storage of the results of a large bank of counters, and the automatic transmission of the data to the central computer, but it allows on-line examination and treatment of the data in the background mode even while controlling the diffractometer in the priority foreground mode (RT-II operating system). As well, with a multiple counter, rapid scans can be programmed at different temperatures and the results compared in a search for phase transitions. More detailed treatment of the data, and in particular, profile refinement, is best done by transmitting the results directly to a central computer, which can be used on-line in a time sharing mode. Eventually, such a system might lead to an automatic structure refinement "machine", which could be used to study the effect of external conditions, such as temperature and pressure, on a given crystal structure. Such a machine could reveal much more about a structure, its stability and the balance of interatomic force than do the present "static" crystallographic techniques.

## References

- [1] Wilson, A. J. C., Mathematical theory of x-ray powder diffraction, Eindhoven: Centrex (1963).
- [2] Diamond, R., Profile analysis in single crystal diffractometry, *Acta Cryst.* A25, 43-55 (1969).
- [3] Ayers, G. L., Huang, T. C., and Parrish, W., High speed x-ray analysis, *J. Appl. Cryst.* 11, 229-233 (1978).
- [4] Riekkel, C., Convert, P., Jacobé, J., and Klesse, K., Applications of high intensity neutron powder diffraction, ILL Internal Report (1979), in preparation.
- [5] Tofield, B. C., Jacobsen, A. J., England, W. A., Clarke, P. J. and Thomas, M. W., Deuterium beta alumina: atom location and structure refinement by powder neutron diffraction, *J. Solid State Chem.* (1979), in press.
- [6] Rietveld, H. M., Line profiles of neutron powder diffraction peaks for structure refinement, *Acta Cryst.* 22, 151-153 (1967).
- [7] Rietveld, H. M., A profile refinement method for nuclear and magnetic structures, *J. Appl. Cryst.* 2, 65-71 (1969).
- [8] Shirane, Gen, A note on the magnetic intensities of powder neutron diffraction, *Acta Cryst.* 12, 282-285 (1959).
- [9] Nathans, R., Alperin, H. A., Pickart, S. J., and Brown, P. J., Measurement of the covalent spin distribution in manganese fluoride using polarized neutrons, *J. Appl. Phys.* 34, 1182-1186 (1963).
- [10] Andresen, A. F. and van Laar, B., The magnetic structure of  $\text{Fe}_3\text{Se}_4$ , *Acta Chem. Scand.* 24, 2435-2439 (1970).
- [11] Holseth, A., Kjekshus, A., and Andresen, A., Neutron diffraction studies of  $\text{CrSb}_2$  and  $\text{FeSb}_2$ , *Acta Chem. Scand.* 24, 3309-3316 (1970).
- [12] Taylor, J. C. and Wilson, P. W., A neutron diffraction study of anhydrous  $\text{UCl}_4$ , *Acta Cryst.* B29, 1942-1944 (1973).
- [13] Taylor, J. C. and Wilson, P. W., Neutron and x-ray powder diffraction studies of the structure of uranium hexachloride, *Acta Cryst.* B30, 1481-1484 (1974).
- [14] Loopstra, B. O. and Rietveld, H. M., The structure of some alkaline earth metal uranates, *Acta Cryst.* B25, 787-791 (1969).
- [15] Zachariasen, W., Crystal chemical studies of the 5f series of elements V. uranium hexachloride, *Acta Cryst.* 1, 285-287 (1948).
- [16] (a) Hewat, A. W., Cubic-tetragonal-orthorhombic-rhombohedral ferroelectric transitions in perovskite potassium niobate, *J. Phys. C* 6, 2559-2572 (1973a).  
(b) Hewat, A. W., Neutron powder profile refinement of ferroelectric and antiferroelectric crystal structures: sodium niobate at 22 °C, *Ferroelectrics*, 7, 83-85 (1974).

- 17] Bulou, A., Etude du caractère ordre-désordre de la transition ferroélastique impropre de  $\text{RbCaF}_3$  à 198 J, Thèse de 3e cycle, Université Paris 6ème (1979).
- 18] Gavarrì, J. R., Weigel, D., and Hewat, A. W., Oxydes de plomb IV. Evolution structurale de l'oxyde  $\text{Pb}_3\text{O}_4$  entre 240 K et 5 K et mécanisme de la transition, J. Solid State Chem. 23, 327-339 (1978).
- 19] David, W. F., Glazer, A. M., and Hewat, A. W., The structure and ferroelastic phase transition in  $\text{BiVO}_4$ , Acta Cryst. (1979), in press.
- 20] Hidaka, M. and Hewat, A. W., Structural phase transitions in ferroelastic  $\text{CsVF}_4$ , Acta Cryst. (1979), to be published.
- 21] Hewat, A. W., Location of hydrogen atoms in ADP by neutron powder profile refinement, Nature 246, 90-91 (1973).
- 22] Bacon, G. E. and Pease, R. S., A neutron diffraction study of potassium hydrogen phosphate by Fourier synthesis, Proc. Roy. Soc. London A220, 397-421 (1953).
- 23] Hewat, A. W., Molecular structure transitions and neutron powder diffraction, Proc. 4th Europ. Cryst. Meet., Oxford, 387-389 (1977).
- 24] Cheetham, A. K. and Taylor, J. C., Profile analysis of neutron diffraction data: its scope, limitations and applications in solid state chemistry, J. Solid State Chem. 21, 253-275 (1977).
- 25] Cheetham, A. K. and Norman, N., The structure of yttrium and bismuth trifluorides by neutron diffraction, Acta Chem. Scand. A28, 55-60 (1974).
- 26] Armytage, D. and Fender, B. E. F., Anion ordering in  $\text{TaON}$ : A powder neutron diffraction investigation, Acta Cryst. B30, 809-812 (1974).
- 27] Jacobsen, A. J., Collins, B. M., and Fender, B. E. F., A powder neutron diffraction determination of the structure of  $\text{Ba}_5\text{W}_3\text{Li}_2\text{O}_{15}$ , Acta Cryst. B30, 816-819 (1974).
- 28] Collins, B. M., Jacobsen, A. J., and Fender, B. E. F., A powder neutron diffraction determination of the structure of  $\text{Ba}_4\text{Ta}_3\text{LiO}_{12}$ , J. Solid State Chem. 10, 29-35 (1974).
- 29] Titcombe, C. G., Cheetham, A. K., and Fender, B. E. F., A neutron diffraction study of the hydrides of the early lanthanide elements at room temperature, J. Phys. C 7, 2409-2416 (1974).
- 30] Cheetham, A. K. and Fender, B. E. F., Neutron diffraction study of non-stoichiometric cerium hydride, J. Phys. C 5, L35-40 (1972).
- 31] Von Dreele, R. B. and Cheetham, A. K., The structures of some titanium-niobium oxides b powder neutron diffraction, Proc. Roy. Soc. London A338, 311-326 (1974).
- 32] Wadlsey, A. D., Mixed oxides of titanium and niobium, Acta Cryst. 14, 660-664 and 664-570 (1961).
- 33] Allpress, J. G., Mixed oxides of titanium and niobium: intergrowth structures and defects, J. Solid State Chem. 1, 66-81 (1969).
- 34] Cowley, J. M. and Iijima, S., Electron microscopy of atoms in crystals, Physics Today, p. 33 (March 1977).

- [35] Anderson, J. S., Bevan, D. J. M., Cheetham, A. K., von Dreele, R. B., Hutchison, J. L., and Strähle, J., The structure of germanium niobium oxide, an inherently non-stoichiometric block structure, Proc. Roy. Soc. London A346, 139-156 (1975).
- [36] Wright, A. and Fender, B. E. F., The structure of superionic compounds by powder neutron diffraction I Cation distributions in  $\alpha$ -AgI, J. Phys. Chem. 10, 2261 (1977).
- [37] England, W. A., Jacobsen, A. J., and Tofield, B. C., Neutron diffraction determination of the structures of deuterium  $\beta$ -alumina at 4.5 K and 823 K, J. Chem. Soc., Chem. Coll., 895 (1976).
- [38] Bogacz, A., Bros, J., Gaune-Escard, M., Hewat, A. W., and Taylor, J. C., Constructing new fast ion conductors from uranium halides - the  $UCl_6/NaUCl_6$  structures, J. Phys. C. (1979), submitted.
- [39] Hewat, A. W. and Lehmann, M., The resonance structure of solid formic acid, ILL experimental proposal 5-22-137 (1979).
- [40] Kuijpers, F. A. and Loopstra, B. O., A neutron diffraction study of the structural relationships of  $RCO_5$  hydrides, J. Phys. Chem. Solids, 35, 301-306 (1974).
- [41] Adams, J. M., Pritchard, R. G., and Hewat, A. W., Neutron profile refinement and deuterium positions in  $Na_2CO_3 \cdot 1.5 D_2O_2$ , Acta Cryst. (1979), in press.
- [42] Adams, Ramdas, and Hewat, (1979).
- [43] Johnson, M. W., Sandor, E., and Arzi, E., The crystal structure of deuterium fluoride, Acta Cryst. B31, 1998-2003 (1975).
- [44] Ahtee, M., Kurki-Suonio, K., Lucas, B. W., and Hewat, A. W., Determination of molecular orientations in cubic  $ND_4NO_3$  by multipole analysis, Acta Cryst. (1979), in press.
- [45] Hewat, A. W. and Riekell, C., The structure of deuterio-ammonia between 2 K and 180 K by neutron powder profile refinement, Acta Cryst. A (1979), in press.
- [46] Lehmann, M. and Speakman, J. C., private communication (1979).
- [47] Hewat, A. W., The Rietveld computer program for the profile refinement of neutron diffraction powder patterns modified for anisotropic thermal vibrations, UKAERE Harwell, Report RRL 73/897 (1973).
- [48] Sakata, M. and Cooper, M. J., An analysis of the Rietveld profile refinement method, J. Appl. Cryst. (1979), in press.
- [49] Shirley, R., Data accuracy for powder indexing, this conference (1979).
- [50] Pawley, G. S., Mackenzie, G. A., and Dietrich, O. W., Neutron powder diffraction and constrained refinement, Acta Cryst. A33, 142-145 (1977).
- [51] Pawley, G. S., Constrained refinement in crystallography, in Advances in Structure Research by Diffraction Methods, W. Hoppe and R. Mason, eds., Vol. 4, 1-64 (Pergamon, Oxford, 1972).
- [52] Hewat, A. W., Design for a conventional high resolution neutron powder diffraction, Nucl. Inst. Methods 127, 361-370 (1975).

- [53] Loopstra, B. O., Neutron powder diffractometry using a wavelength of  $2.6 \text{ \AA}$ , Nucl. Inst. Methods 44, 181-187 (1966).
- [54] Levy, J. H., Sanger, P. L., Taylor, J. C., and Wilson, P. W., The structures of fluorides. XI cubic harmonic analysis of the neutron diffraction pattern of  $\text{MoF}_6$ , Acta Cryst. B31, 1065-1067 (1974).
- [55] Seymour, R. S. and Pryor, A. W., Neutron diffraction study of  $\text{NH}_4\text{Br}$  and  $\text{NH}_4\text{I}$ , Acta Cryst. B26, 1487-1491 (1970).
- [56] Ahtee, M., Kurki-Suonio, K., Valivaselk  and Hewat, A. W., Disordering in cubic  $\text{CsPbCl}_3$  by multipole analysis, Acta Cryst. (1979), to be published.
- [57] Hewat, A. W. and Bailey, I., DIA, a high resolution neutron powder diffractometer with a bank of mylar collimators, Nucl. Inst. Methods 137, 463-471 (1976).
- [58] Cooper, M. J. and Sayer, J. P., The asymmetry of neutron powder diffraction peaks, J. Appl. Cryst. 8, 615-619 (1975).
- [59] Thomas, M. W., Peakshifts and peak broadening in powder neutron diffraction patterns due to finite aperture counters, J. Appl. Cryst. 10, 12-13 (1977).
- [60] Suorrti, P., Components of total x-ray scattering, this conference (1979).
- [61] Langford, J. I., A rapid method for analysing the breadths of diffraction and spectral lines using the Voigt function, J. Appl. Cryst. 11, 10-14 (1978).
- [62] Sabine, T. M. and Clarke, P. J., Powder neutron diffraction - refinement of the total pattern, J. Appl. Cryst. 10, 277-280 (1977).
- [63] Windsor, C. J. and Sinclair, R. N., The Debye-Waller factor of nickel measured at high scattering vectors by pulsed neutron powder diffraction, Acta Cryst. A32, 395-409 (1976).
- [64] Fender, B. E. F., Diffuse scattering and the study of defect solids in Chemical Applications of Thermal Neutron Scattering, B. T. M. Willis, ed. (OUP London, 1973).
- [65] Boysen, H. and Hewat, A. W., A neutron powder investigation of the structural changes in  $\text{K}_2\text{SuCl}_6$ , Acta Cryst. B34, 1412-1418 (1978).
- [66] Rouse, K. D., Cooper, M. J., York, E. J., and Chakera, A., Absorption corrections for neutron diffraction, Acta Cryst. A26, 682-691 (1970).
- [67] Hewat, A. W., Absorption corrections for neutron diffraction, Acta Cryst. A35, 248 (1979).
- [68] Hewat, A. W., Temperature evolution of the structure and ionic conductivity in  $\text{Bi}_2\text{O}_3$ , J. Phys. Chem. (1979), to be published.
- [69] Caglioti, G., Conventional and three-axis neutron powder diffraction in Thermal Neutron Diffraction, B. T. M. Willis, ed., 14-33 (OUP, London, 1970).
- [70] Meister, H. and Weckermann, B., Neutron collimators with plates of self-contracting foils, Nucl. Inst. Methods 108, 107-111 (1973).
- [71] Paoletti, A., Caglioti, G., and Ricci, F. P., Choice of collimators for a crystal spectrometer for neutron diffraction, Nucl. Inst. Methods, 3 223-228 (1958).

- [72] Hewat, A. W., Shirley, R., and Pawley, G. S., Automatic indexing of neutron powder diffraction patterns, *J. Appl. Cryst.* (1979), to be published.
- [73] Freund, A., Proceedings of the conference on neutron scattering, R. M. Moon, ed. ORNC Report CONF-760601-02, pp. 1143-1150, Oak Ridge (1976); see also, Freund, A. and Forsyth, J. B., A treatise on materials and technology, H. Herman, ed., 15, chap. 10 (Academic Press, NY, 1979).
- [74] Carlile, C. J., Hey, P. D., and Mack, B., High efficiency Söller slit collimators for thermal neutrons, *J. Phys. E* 10, 543-546 (1977).
- [75] Allemant, R., Bourdel, J., Roudaut, E., Convert, P., Ibel, K. Jacobe, J., Cotton, J. P., and Farnoux, B., Position sensitive detectors for neutron diffraction, *Nucl. Inst. Methods* 126, 29-42 (1975).
- [76] Aldebert, P. and Traverse, J. P., Etude par diffraction neutronique des structures de haute température de  $\text{La}_2\text{O}_3$  and  $\text{Nd}_2\text{O}_3$ , *Mat. Res. Bull.* 14, 303-323 (1979).
- [77] Nelmes, R. J., Meyer, G. M., Baharie, E., Hutton, J., and Hewat, A. W., The pressure and temperature dependence of the structure of para-electric (tetragonal)  $\text{KH}_2\text{PO}_4$  and  $\text{KD}_2\text{PO}_4$ , XI Int. Conf. Cryst. Warsaw (August, 1978).
- [78] Riekel, C., Convert, P., Gobert, G., and Lazaro, C., A spherical sample container for neutron powder diffractometry, *Nucl. Inst. Methods* 151, 201-203 (1978).

#### Discussion

Comment (Ladell): The difference between Parrish et al. line profile analysis approach and the Rietveld method is that the former isolates the instrumental, spectral and aberrational line broadening factors from the crystal structure factors. By using the Rietveld approach, the least squares refinement may account for the instrumental effects at the expense of the crystallographic parameters since the minimization of errors to determine position and thermal parameters are clearly influenced by the approximation used to define the profile shape. If the models used on the Parrish procedure are correct, and his work seems to confirm that these models are correct at least for the x-ray case; the correct procedure should be to use these models to isolate the variables before using a Rietveld procedure.

Response (Hewat): There are only four "instrument parameters", U, V, W, and F used by Rietveld, and these are not at all strongly correlated with the crystal structure parameters. However, there are small errors in Rietveld's description of the line shape which should be corrected in the manner advocated by Parrish and others.

Comment (Edmonds): (Directed to question of difference between Parrish's profile fitting method and Rietveld analysis, and added after Ted Prince's (NBS) comment:)

Rietveld's technique applies crystal structure determining and data reduction parameters in a least squares fit to the raw data (entire pattern) while Parrish's suggestion would first apply data reduction techniques then least square crystal structure parameters to the derived data (discrete  $hkl$  and  $I$ ). If the same data reduction parameter were available to both formalisms, and the entirety of the powder pattern were used, there would be no differences in the results. However, using discrete data poses the problem of what to do with the weak or below threshold data when multiple  $hkl$ 's may be present, where the Rietveld technique will deal with the intensity sums on a dynamic basis. In any case, we are able to fit structural models only by comparing calculated data to observed data, be the latter derived or raw in nature. Forgetting this point will only magnify artificial or superficial differences between techniques and limitations.

Response (Hewat): The techniques would not be equivalent when applied to a complete diffraction pattern, because there would be many more parameters to determine with Parrish's technique. The Rietveld technique greatly reduces the correlation problems that one would have in this case. However, the Parrish technique is valuable for improving the description of single lines.

Comment (Prince): In the discussion of these papers, there seems to be a general misconception that there is a conflict between the profile fitting of Parrish and the total pattern analysis of Rietveld. The Rietveld technique takes a diffraction pattern and an assumed peak shape and determines crystallographic parameters. The Parrish work is a good representation of x-ray peak shape. What is needed now is the marriage of these techniques for x-ray refinement.

Response (Parrish): No comment made or necessary.

Question (Rush): I have several questions related to your high resolution diffraction procedures at Grenoble. How do you determine and subtract background? Do you change collimation or resolution conditions depending on the complexity of the structure? Do you have to worry about subtle changes in line shape when you vary the incident wavelength?

Response (Hewat): The background is measured in regions where no peaks are thought to contribute, using the cursor on a Tektronix screen. The wavelength is chosen according to the complexity expected for the pattern: usual choices are 1.91 Å and 1.38 Å, but wavelengths as long as 3 Å or 5.7 Å are used for indexing unknown patterns. No changes are possible in the collimation. The peak widths change with changes in the wavelength; three parameters are refined to describe the angular dependence of peak width.



STRUCTURAL ANALYSIS FROM X-RAY POWDER DIFFRACTION PATTERNS  
WITH THE RIETVELD METHOD

R. A. Young  
Georgia Institute of Technology  
Atlanta, GA 30332

The Rietveld method of whole-pattern fitting has now been successfully applied to x-ray data by several groups in Europe and the USA and others are known to be working with the method. Two types of angle-dispersive data (diffractometer and Guinier-Hägg camera) and energy-dispersive data (synchrotron source) have been used. Structures have been successfully refined for ~30 different materials in 15 space groups ranging from inorganic synthetics and an organic through several minerals to human tooth enamel. In the few cases wherein both x-ray and neutron data were analyzed, comparable results were obtained for the atom position coordinates. Standard deviations ( $\sigma$ ) tend to be an order of magnitude larger than with good single crystal refinements, partly because  $(\sin \theta)/\lambda$  is often more limited. The R values tend to be higher with angle dispersive x-ray data (e.g.  $R_p = 12-28$  percent with average near 20 percent) than with neutron data (e.g.  $R_p = 5-17$  percent with average near 10 percent). The extra size of the x-ray  $R_p$ 's is, probably, largely a consequence of the inadequacy of the reflection profile functions so far used (Gaussian, Lorentzian, two forms of modified Lorentzian). Voigt functions, the Pearson VII form, an Edgeworth series, and a polynomial form are now being tried by various groups.

The computer programs used with x-ray data have generally been adaptations of Rietveld's programs written for the neutron case, but recently at least three new programs for the angle dispersive case have been written. Added features include single pass operation, modular construction, multicomponent refinement capability, and generalized coordinates to deal with constraints.

Two general approaches have been followed by the various workers. In one, the lattice parameters are first determined in a separate step and then fixed while structure refinement is

carried out, often with the goal of obtaining "observed" Bragg intensities which are then used for the final structure analysis. In the second approach, lattice parameters are refined simultaneously with the structure parameters and the "best" structure results are taken to be those obtained directly from the Rietveld refinements. Position  $\sigma$ 's are comparable. Physically significant individual temperature parameters have so far received little attention.

Flat and false minima seem to be a particular problem, perhaps because the model is generally inadequate, at least in the reflection profile functions used. In initial refinements with many natural materials, there may be sufficient substitutions at unknown sites so that the structural model will be inadequate to the extent that false minima and the true minimum can not be distinguished by  $R_{wp}$  values, especially when  $R_{wp} > \sim 20$  percent.

M. J. Cooper (priv. comm.) has pointed out that the standards deviations are ordinarily calculated incorrectly, in principle. Comparison of results from different data sets on the same material suggest that the true  $\sigma$ 's may be 2 to 3 times those calculated.

The various difficulties of the method are receiving attention, however. Highly useful results are being obtained, the Rietveld method constitutes a major breakthrough for the usefulness of x-ray powder patterns, and activity in the field is growing rapidly.

## 1. Reported Results

### 1.1. Scope

The Rietveld [1,2]<sup>1</sup> method of crystal structural model refinement with powder diffraction data, widely used with neutron data for some years, has now been applied with x-ray data by several groups. In this method, the parameters in a structural model, plus necessary instrumental parameters, are adjusted in a computer calculation until the best fit, in a least squares sense, is obtained between the entire calculated and observed powder patterns. The diffraction data are obtained in digitized form through a step-scanning, or equivalent, procedure. Thus, the whole-pattern fitting is actually a fitting of calculated to observed intensity at each and every point, simultaneously, in the step scan. No a priori assumptions are made about how overlapped reflections should be resolved into separate Bragg reflections, and the absence of intensity also constitutes useful, and

---

<sup>1</sup>Figures in brackets indicate the literature references at the end of this paper.

used, information. Figure 1 gives, as an example, a visual comparison of observed and calculated x-ray diffraction patterns for fluorapatite after Rietveld structure refinement.

More than 30 different structures, with 15 different-space groups, have now been successfully refined from x-ray data with the Rietveld method. This number is small compared to that for neutrons (>200), but it is only two years since the first x-ray refinement was published [3]. The approximately thirty structures which have been Rietveld-refined from x-ray data, and for which we have been able to obtain information, are listed in table 1 along with some of the key information about each. Reference to this table is implied in the ensuing discussions of what the various research groups have done.

## 1.2. R factors

The various R factors listed are defined as follows, where  $I_B$  is the intensity assigned to a particular Bragg reflection and  $y_i$  is the intensity observed at the  $i$ th step in the step-scanned pattern.

$$R_F = \frac{\sum |\sqrt{I_B(\text{"obs"})} - \sqrt{I_B(\text{calc})}|}{\sum \sqrt{I_B(\text{"obs"})}}$$

$$R_B = \frac{\sum I_B(\text{"obs"}) - I(\text{calc})}{\sum I_B(\text{"obs"})}$$

$$R_p = \frac{\sum y_i(\text{obs}) - \frac{1}{c} y_i(\text{calc})}{\sum y_i(\text{obs})}$$

$$R_{wp} = \left[ \frac{\sum w_i (y_i(\text{obs}) - \frac{1}{c} y_i(\text{calc}))^2}{\sum w_i (y_i(\text{obs}))^2} \right]^{1/2}$$

In the foregoing,  $c$  is a scale factor and  $w_i$  is the weight.

In the definition of  $R_F$  and  $R_B$ , the "obs"--for observed--has been written in quotation marks because the Bragg intensities,  $I_B(\text{"obs"})$ , are not actually observed but are derived from a parceling out of the observed intensity, in a given  $2\theta$  range, in proportion to the calculated Bragg intensities,  $I_B(\text{calc})$ . Some workers appear to favor citing  $R_F$  or  $R_B$  because they most closely resemble the "conventional" R factors still widely used in single crystal structure analysis.  $R_p$  has the advantage that it is based on actual observations rather than partially calculated ones. The most significant R factor, however, is  $R_{wp}$  because the numerator of  $R_{wp}$  is the quantity that is actually minimized in the least

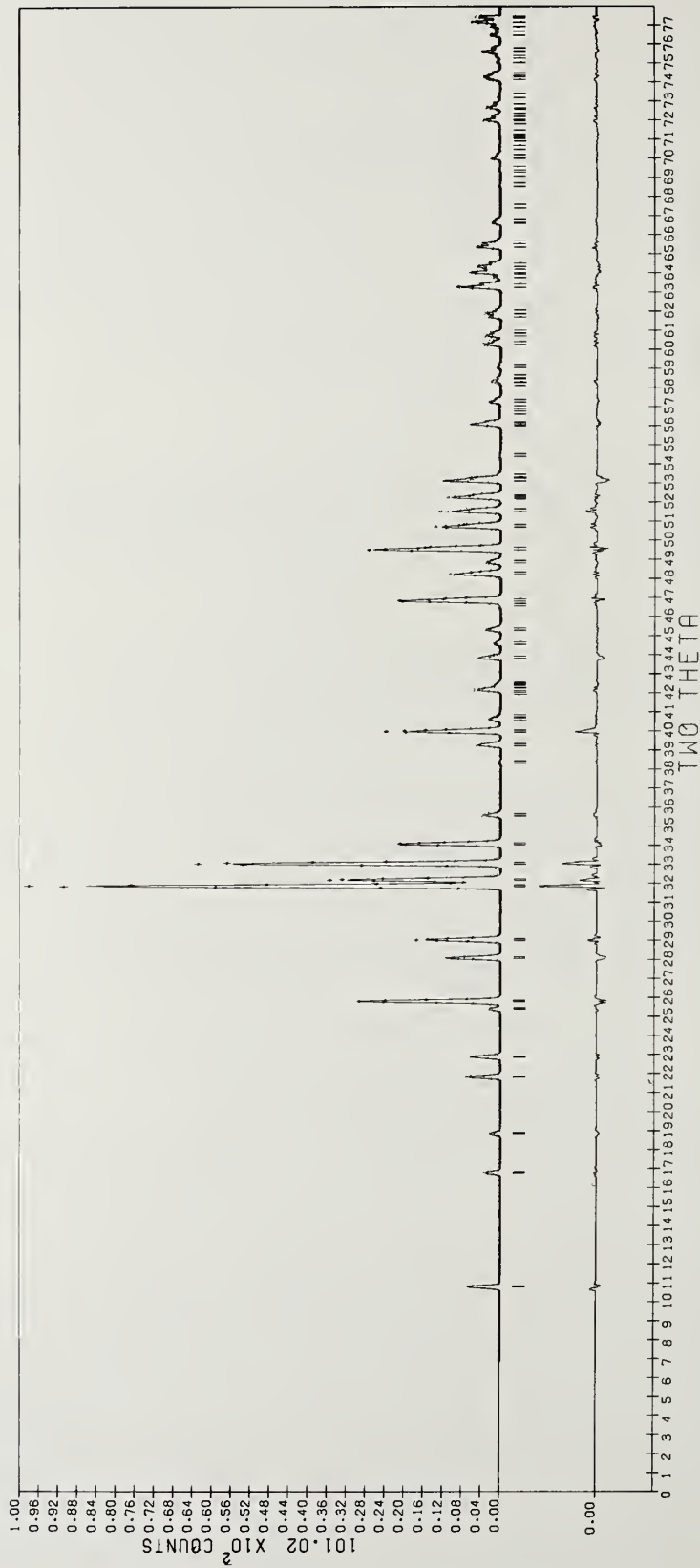


Figure 1. X-ray Rietveld refinement of fluorapatite. The observed pattern is shown by points with error bars, the calculated pattern is shown by the overlaying solid curves, and the difference is shown by the lower solid curves. Here  $R_{wp} = 15.5$  percent.

squares refinement procedure. To be objective, then, and to be able to tell whether one refinement model or result is better than another, one must cite  $R_{wp}$  even though it is, discomfortingly, the largest of the four. Unfortunately not all authors have listed  $R_{wp}$ , so we must look to other R's in table 1.

### 1.3. Different approaches

The approaches used by the various groups who have published data differ somewhat. The Stockholm/Upsala groups have used Guinier-Hägg film data digitized with a micro-densitometer [4]. The monochromating crystal was set to allow only the  $\alpha_1$  lines of the  $\alpha$  doublet to pass. Typically, though not always, they refine the lattice parameters in a separate operation and keep them fixed in the Rietveld refinements. This association of groups is responsible for the major portion of the x-ray Rietveld refinements published to date. These groups have frequently used the Rietveld refinement as a way to parcel out the observed intensity to individual Bragg reflections in order to use the resulting structure amplitudes ( $|F|$ ) in further refinements and in construction of electron density maps.

Khattak and Cox [5] used step-scanning diffractometer data and avoided the problem of having to handle the two wavelengths in the  $K\alpha$  doublet by using  $K\beta$  radiation. They also provided an interesting direct comparison of x-ray and neutron results by refining the same structure with both kinds of data. They included lattice parameters as a part of the Rietveld refinement.

Glazer, Hidaka and Bordas [6] took advantage of some of the newest instrumentation, primarily as a demonstration. They used a synchrotron source and an energy dispersive detector. In this case there was no  $\alpha$  doublet to deal with, only one wavelength at a time, but special computer programming was, of course, necessary to deal with this type of data. The  $R_p$  values reported are notably lower than those reported for other methods, probably because the instrumental profile is well fit by Gaussian in this case.

Both the Atlanta group and Immirzi have used step-scan diffractometer data collected with the use of crystal monochromatized  $K\alpha$  radiation in which both the  $\alpha_1$  and the  $\alpha_2$  components were present. Their refinement programs are able to handle the two wavelengths. Both also refine the lattice parameters as a part of the Rietveld refinement.

### 1.4. Generalizations

In addition to the lattice and crystal structural parameters, there are, usually, an overall scale factor, an overall "temperature" factor, a  $2\theta$ -zero correction, and two or three reflection-profile breadth parameters to be refined. The total number of refined parameters indicated by table 1 varies from 7 to 51.

Site occupancies have been refined with seeming validity, as judged from the fractional standard deviations shown for the Atlanta group in table 1, but never simultaneously with individual temperature factors. No one seems yet to have tried to refine anisotropic thermal parameters with x-ray data. Some individual isotropic temperature

Table 1. X-Ray Rietveld Refinements

Substance	Purity (%)	Space group	X-ray data type (see note 1)	No. data points	Max. (sm/Å)	Parameters (see table 2)		Profile function (see table 3)	R (%)			Thermal parameters refined (isotropic)		Line Number	Lattice Parameters				Appropriate's in structural parameters	Location	Comment	
						Structure	Total		R <sub>p</sub>	R <sub>w</sub>	R <sub>exp</sub>	Number	Comment		No. Bragg peaks	Number	c (Å)	a (parts in 10 <sup>4</sup> )				σ (deg.)
boehmite-H	90	Cmcm	Gh <sub>01</sub>	2000	0.38	27	6	R-NT ML	12.1					1	off					Budapest/Stockholm		
boehmite-S		Cmcm	Gh <sub>01</sub>	1588	0.44	25	6	R-NT ML	12.7					2	off					Budapest/Stockholm		
boehmite [Y=AlOH]	50	Cmcm	Gh <sub>01</sub>	1588	0.44	25	6	R-NT ML						3	off					Budapest/Stockholm		
Li <sub>2</sub> MO <sub>4</sub> (IV)		C2/c	Gh <sub>01</sub>	2636	0.45	51	67	R-NT ML	9.4			4	neg.	101	4	off				Waltersson, Werner & Wilhelm (1977a)		Initial structure from Patterson with resolved reflections, then Rietveld, then Fourier analysis with assigned F(obs).
Li <sub>2</sub> MO <sub>4</sub> (II)		no I <sub>4</sub> /and Gh <sub>01</sub>				18	18	R-NT ML	7.4			6	neg.	113	5	off				Stockholm		Initial structure solution from Patterson based on resolved reflections. Impurity lines removed.
Zn <sub>2</sub> Mg(OH) <sub>2</sub>		P2 <sub>1</sub> /n	Gh <sub>01</sub>	2000	0.38	27	22	R-NT ML	8.7 to 11.0			7	3 neg.	200	6	off				Stockholm		Four specimens were analyzed.
α-Bi <sub>2</sub> O <sub>3</sub>		P2 <sub>1</sub> /c		1588	0.44	20	25	R-NT G		12.8	23.9	28.8		7	off					Stockholm & Uppsala		
α-Bi <sub>2</sub> O <sub>3</sub>		P2 <sub>1</sub> /c		1588	0.44	20	25	R-NT L		11.0	22.1	26.1		8	off					Stockholm & Uppsala		
α-Bi <sub>2</sub> O <sub>3</sub>		P2 <sub>1</sub> /c		1588	0.44	20	25	R-NT ML		6.8	10.8	19.5	23.7	5	3 neg.					Stockholm & Uppsala		ML clearly best in tails but no profile function great.
organic		C2	Gh <sub>01</sub>	2636	0.45	51	3	R-NT ML	11			3		505	10	off				Stockholm		Convergence incomplete but main structural features det'd. Fourier methods were used. V=144Å <sup>3</sup> .
Li <sub>1-x</sub> Ta <sub>3-x</sub> O <sub>10-x</sub> F <sub>x</sub> (x=0.5)		Pnma	Gh <sub>01</sub>	~1900	0.45	26	31	R-NTW ML	10.7			27	same neg.	11	off					Stockholm		
Li <sub>1-x</sub> Ta <sub>3-x</sub> O <sub>10-x</sub> F <sub>x</sub> (x=0.25)		PMMA	Gh <sub>01</sub>	~1900	0.45	26	31	R-NTW ML	9.4			27	same neg.	12	off					Stockholm		

$L_{1,2,3}^2, 3, 8, 4, x(x=0)$	PMMA	GHe <sub>1</sub>	~1900	0.45	27	32	R-ITW	ML	8.8	25.5	2?	same neg.	13	off	0.5	0.5-8	1-11	Werner, Marinder & Magneli (1979)	Stockholm	V ≈ 2497 Å <sup>3</sup> (CrK <sub>α1</sub> )
Zr (in B-BZr B <sub>0</sub> 51)	RZm	GHe <sub>1</sub>	1602	0.30	11	18	R-MT	ML	6.3	8.4	12.4	16.8	1	92	14	4	0.1-5	Calner, Terenius & Thomas (1978)	Uppsala	Abstract only (Marsaw)
Cu <sub>0.92</sub> Co <sub>0.08</sub> Nb <sub>2.95</sub> S <sub>8</sub>	PZ <sub>1</sub> /a	GHe <sub>1</sub>			36	44	R-MT	ML	12.7				399	15				Werner, Mahlstrom & Marinder (1978)	Stockholm	V = 236 Å <sup>3</sup> , impurity lines removed
Mg <sub>3</sub> Nb <sub>6</sub> O <sub>11</sub>	not p <sub>1</sub> m	GHe <sub>1</sub>	2403	0.45	12	18	R-MT	ML	5.5	17.9	6	same neg.	399	16	off	0.3-3	20->100	Deinms & Werner (1978)	Stockholm/Bordeaux	V ≈ 1270 Å <sup>3</sup> , only abstract available (manuscript submitted)
K <sub>0.72</sub> (Li <sub>0.72</sub> Sb <sub>0.28</sub> ) <sub>2</sub>	PFm2	GHe <sub>1</sub>		0.44	6		R-ITW		12.8		1	neg.	32	17	off	1-2	3-6	Willestrom, Carlsson & Rundqvist (1979)	Uppsala	Multicomponent (2) refinement, testing program to do it. Worked well.
Hf <sub>3</sub> As	CZ/c												18					Werner, Salami, Malmros & Thomas (1979)	Stockholm/Uppsala	
CaF <sub>2</sub> ·5H <sub>2</sub> O													19					Kajjar (1976)	Krakow	
Rhombohedral Graphite													20					Glazer, Hikada & Bords (1978)	Oxford & Daresbury	Min (S1nb)/Λ ≈ 0.3
Si	FD3m	S, red	1024?	0.60	0	7	GHB	G	3.4	3.7	7.2	0	21	off				Bords, Glazer, Hikada & Bords (1978)	Oxford & Daresbury	Min (S1nb)/Λ ≈ 0.3
8aTiO <sub>3</sub>	P4/mmm	S, red	1024?	0.62	7	12	GHB	G	2.4	4.8	8.1	4	22	off		5-22	4->100	Buras, et al. (1979)	Oxford & Daresbury	
Urea	P4 <sub>2</sub> /n	S, red			5	10	GHB	G	6.3	5.4	10	2	23	off		1-2	10	Buras, et al. (1979)	Oxford, Copenhagen, Lyngby & Risø	
Naphthalene	P2 <sub>1</sub> /a	S, red			4	9	GHB	G	6.3	6.1	14.2	1	24	off				Buras, et al. (1979)	Oxford, Copenhagen, Lyngby & Risø	Molecular Euler angles refined
La <sub>0.75</sub> Sr <sub>0.25</sub> CrO <sub>3</sub>	R3c	D, β	3800	0.56	4	107	R-KC	G	9.0	22.3	27.3	3	25	2	0.4	0.002	4	Khatata & Cox (1977)	Brookhaven	Zhk change better than 3hk
La <sub>0.75</sub> Co <sub>0.25</sub> CrO <sub>3</sub>	R3c	D, β	3800	0.56	4	107	R-KC	L	3.1	13.7	17.1	3	26	2	0.2	0.001	3	Khatata & Cox (1977)	Brookhaven	No profile function fits as well as does G in the neutron case.
La <sub>0.75</sub> Co <sub>0.25</sub> CrO <sub>3</sub>	R3c	D, β	3800	0.56	4	107	R-KC	ML	4.2	15.7	19.0	3	27	2	0.2	0.001	3	Khatata & Cox (1977)	Brookhaven	
La <sub>0.75</sub> Co <sub>0.25</sub> CrO <sub>3</sub>	R3c	D, β	3800	0.56	4	107	R-KC	IL	3.3	14.4	17.3	3	28	2	0.2	0.001	3	Khatata & Cox (1977)	Brookhaven	
La <sub>0.75</sub> Co <sub>0.25</sub> CrO <sub>3</sub>	R3c	Neutron	3800	0.56	4	107	R	G	2.5	7.8	8.9	3	29	2	1.5	0.004	0.4	Khatata & Cox (1977)	Brookhaven	
Fluorapatite	P6 <sub>3</sub> /m	D, α, α <sub>2</sub>	1900	0.4	20	28	R-HW	G	9.4	12.1	13.9	1	116	30	2	0.3	1	Young, Mackie & Von Orreele (1977)	Atlanta & Tempe	G to L, get negative correlation between $\theta_g$ and $\theta_p$
Fluorapatite	P6 <sub>3</sub> /m	D, α <sub>1</sub> , α <sub>2</sub>	1900	0.4	20	28	R-HW	L	8.2	21.4	23.9	1	116	31	2	0.4	1-2	Young, Mackie & Von Orreele (1977)	Atlanta & Tempe	

Quartz "sharp"	$P_{3,2}$	$0.4\alpha_2$	800	0.4	7	14	R-HW/G	11.7	14.2	16.3	1	34	32	2	0.7	1-2	-2	Young, Mackie & Von Dreele (1977)	Atlanta & Tempe	
Quartz "sharp"	$P_{3,2}$	$0.4\alpha_2$	1200	0.4	7	14	R-HW/L	9.8	26.6	31.2	1	34	33	2	0.6	1-2	3	Young, Mackie & Von Dreele (1977)	Atlanta & Tempe	
Quartz "broad"	$P_{3,2}$	$0.4\alpha_2$	800	0.4	7	14	R-HW/G	12.5	18.4	20.7	1	34	34	2	1.5	1-2	3	Young, Mackie & Von Dreele (1977)	Atlanta & Tempe	
Quartz "broad"	$P_{3,2}$	$0.4\alpha_2$	850	0.4	7	14	R-HW/L	7.4	19.4	21.2	1	34	35	2	0.7	1-2	3	Young, Mackie & Von Dreele (1977)	Atlanta & Tempe	
$LaPO_4$ -I	no	$P_{2,1}^n$	1390	18	26	26	R-HW/G	12.8	18.6	21.4	1	260	36	4	6	0.04	1-10	2	Young, Mackie & Von Dreele (1977)	Atlanta & Tempe
$LaPO_4$ -II	no	$P_{2,1}^n$	1390	0.4	18	26	R-HW/G	17.6	21.0	23.0	1	260	37	4	6	0.04	1-10	2	Young, Mackie & Von Dreele (1977)	Atlanta & Tempe
$CO_3$ -apatite $-Ca_{10}(PO_4)_6(CO_3)_2O_1-x$	$P_3$	$0.4\alpha_2$	1280	0.36	17	27	R-HW/G	23	42	1	75	38	2	0.4	2-5	2-5	1-2	Young, Mackie & Wiles (Unpublished)	Atlanta	
$CO_3$ -apatite	$P_{6,3}^m$	$0.4\alpha_2$	1040	0.40	20	28	OBW/G	20	25	2	107	39	2	0.4	1	1-2	1-2	Young, Mackie & Wiles (Unpublished)	Atlanta	
Tooth Enamel, Human	$P_{6,3}^m$	$0.4\alpha_2$	1070	0.41	20	28	OBW/G	23	26	3	140	40	2	0.4	1	1-2	1-2	Young & Mackie (to be published)	Atlanta	
Pyrene + TCQOH	$P_{2,1}^a$	$0.4\alpha_2$			3	A1	P	<30?				41	4					Imrizi (1978)	Milano	

Note 1: Symbols for data type: G/W, + Guinier-Hagg film data and strictly monochromatic radiation; S, ed + Synchrotron source and energy dispersive detector used; O, B + data collected with a standard  $\theta$ - $2\theta$  diffractometer and the single x-ray wavelength  
 K8:  $0.4\alpha_2$  = data collected with a standard  $\theta$ - $2\theta$  diffractometer and both x-ray wavelengths in the  $\alpha$  doublet; Neutron + neutron data, included for comparison.

factors were refined satisfactorily in the Khattak and Cox [5] work and in the synchrotron experiment [6]. However, in most of the refinements based on Guinier-Hägg film data these temperature factors tended to become negative. The Stockholm/Upsala authors have often mentioned this in their papers and suggest it is due to uncorrected absorption.

Standard deviations in the coordinate parameters for the various atoms in the refinements listed in table 1 range from  $10^{-4}$  to  $10^{-2}$  of the unit cell dimension with  $10^{-3}$  being average. For single crystal x-ray work, one would probably expect an average of about one-tenth of this, i.e. a standard deviation of about 0.0001 of the cell dimension.

Except for the unusual case of the synchrotron experiment, the  $R_p$  values run from about 12 percent to 27 percent with an average around 20 percent. There is little or no correlation between  $R_p$  values and the number of parameters adjusted. This average  $R_p$  value is about twice that for the neutron cases, which range from 5 percent to 17 percent with an average near 10 percent for the 170 structures reviewed by Cheetham and Taylor [7].

## 2. Computer Programs for Rietveld Analysis of X-ray Data

Most of the results indicated in table 1 have been obtained with one or another modification of Rietveld's [2] program written for the neutron case. This fact is indicated in table 1 by the letter R as the first symbol in the "Program" column. By arranging experimentally to have only one wavelength present, both Malmros and Thomas [3] and Khattak and Cox [5] avoided the need to make the program handle two wavelengths. The "RHVM" [8], on the other hand, does handle explicitly the two wavelengths of the  $\alpha$  doublet. The ratio of intensities of the two wavelengths (via scale factors) is one of the parameters refined. Hewatt modified Rietveld's program to handle anisotropic thermal parameters and von Dreele and Mackie then modified that program to handle the x-ray case, hence the designation RHVM.) Both the RMT and the RHVM programs have been distributed to more than a dozen groups in many countries.

Recently, several programs have been written specifically for the angle-dispersive x-ray case, quite independently of the Rietveld program. Table 2 gives some comparison of features for those programs about which we have enough information to say anything. In the table, a blank at an intersection means that we have no information about that feature for that program. A dash means that the implication from information we do have is that a "No" belongs there, but our information is not explicit. A question mark means that the implied answer is "Yes" but, again, we do not have explicit information.

Although a multiphase capability is roundly desired and many workers intend to implement one, the RWSMT program [9] modified from the original Rietveld one, seems to be the only reported success to date.

The DBW(II) program (D.B. Wiles, version II, see Wiles & Young [10]) has been designed for user convenience and for easy use by groups having access to any of the standard large computers. It is written to ANSI code standards for portability, is of

Table 2. Some Computer Programs for Rietveld Analysis of Angle Dispersive X-ray Data

FEATURE	PROGRAM						
	RMT	RHVM	RKC	RWSMT	AI	DBW(II)	BH
All space groups "as is"	-	No	No	-	?	Yes	
Single pass operation	-	No	No	-	?	Yes	-
Modular	-	No	No	?		Yes	
ANSI	-	No	No	-	?	Yes	
$\alpha$ doublet	No	Yes	No	No	Yes	Yes	No
Multiphase capability	No	No	No	Yes	No	No	-
Constraint functions		Yes			Yes	Yes	Ye
Generalized coordinates	No	No	No	No	Yes	No	No
Profile functions	ML	G,L	G,ML,L,IL	ML	PVII	G,L	Po
Refines preferred orientation parameter		Yes			Yes	Yes	Ye
Refines asymmetry parameter		Yes			Yes	Yes	Ye
Refines lattice parameters	-	Yes	Yes	-	Yes	Yes	Ye
R-factors in various shells		No	No		Yes	No	No
Set up list for another run		No(?)				Yes	
Plotter output		Yes				Yes	
Data type	GH	$\theta-2\theta$	$\theta-2\theta$	GH	$\theta-2\theta$	$\theta-2\theta$	$\theta$
Used by other groups	Yes			Yes		No	
Anomalous dispersion		Yes			No	Yes	

modular construction to facilitate changes, and handles all space groups without additional programming. (Only a space group code is required in the input.) It incorporates a large data base of atomic scattering factors and anomalous dispersion correction.

The AI (A. Immirzi [11,12]) program has been written particularly with complex structures in mind, e.g. molecular crystals, polymers, fibrous structures, in which a great deal of information may already be available about multiple-atom structural units. In such cases, the total number of parameters can be greatly reduced if the a priori information is entered into the programs as constraints. Thus, Immirzi has designed his program to allow treatment of any kind of constraint with the writing of "only a very small ad hoc routine." In an application to a molecular complex of pyrene and tetracyanoquinodimethane he used  $D_{2h}$  molecular models and refined three rotation angles per model. He reports a convergence neighborhood of  $\sim$ at least  $15^\circ$  and good agreement with single crystal results.

Another unusual feature of the AI program is the use of the Pearson VII profile function, to which we return later in this paper.

The BH (Bärlocher and Hepp [13]) program is designed to make use of weighted constraints, both holonomic and non-holonomic, and the basic reflection profile to be used is programmatically determined by least-squares fitting of a resolved reflection by a particular polynomial expression (see the following section).

Four of the seven programs in table 2, including all of the three which are independent of the Rietveld program, have been completed within the last year. One hears of others being written. Clearly, the field of x-ray Rietveld analysis will not long be wanting for a selection of good programs.

### 3. Profile Functions

While Gaussian functions fit neutron powder diffraction profiles well, such is not the case for x-ray powder diffraction profiles (Bragg reflections). As was cited in section 1 on the basis of table 1 plus the Cheetham and Taylor [7] review,  $R_p$  values typically run nearly twice as large for the x-ray cases as for the neutron cases. The reason is primarily the inadequacy of the profile functions used. The actual reflection profiles are neither Gaussian (G) nor Lorentzian (L). In fact, as can be seen from the Atlanta group's quartz work cited in table 1, how these two compare for poorness of fit depends on the broadening of the diffraction profiles. Further, the different R factors increase and decrease together in the Khattak and Cox [5] work and the Malmros and Thomas [3] work in table 1, but this is not true for the Young, Mackie and von Dreele work [8] on quartz, in which two specimens were studied in which differing degrees of crystallite size and strain broadening were present. By the criterion that  $R_{wp}$  is the really significant R factor, the ML (modified Lorentzian) function is better in the Malmros and Thomas [3] work but not as good as either the IL (intermediate Lorentzian) or L function in the Khattak and Cox [5] work. X-ray emission spectra are Lorentzians but in the angle-dispersive x-ray methods, the actual instrumental resolution functions and intrinsic diffraction broadening functions are not. It is easily realized that, until better profile functions can be implemented for x-ray Rietveld analysis, much of the structural detail, that which makes only small differences in  $R_{wp}$ , will stay out of actual reach of the method; an important part of the method's potential will not be realized.

Several pragmatic suggestions which have been made for replacement of the Gaussian and Lorentz functions are listed in table 3. Malmros and Thomas [3] and followers have used the modified Lorentzian (ML), while Khattak and Cox [5] found the intermediate Lorentzian (IL) to be preferable in their work. Immirzi [11,12] has suggested the "Pearson VII" function and has incorporated it in his computer program (table 2) because, with appropriate choices of  $m$ , it varies from Lorentzian ( $m = 1$ ) to Gaussian ( $m = \infty$ ). In principle, one could refine the parameter  $m$  as a part of the Rietveld refinement. In fact, Immirzi's program provides for this. But he notes (priv. comm.) that, even in a test case with simulated error-free data,  $m$  underwent very large oscillations in the process of convergence. With actual data, then, convergence might be denied. Clearly, this is an interesting function to explore, both by refining  $m$  and by fixing it at different values, and we will no doubt be seeing more of it in future work.

Table 3. Profile Functions

Symbol	Name	Function: I(X) =	Reference
G	Gaussian	$A e^{(-x^2/k^2)}$	
L	Lorentzian	$A (1+k^2x^2)^{-1}$	
ML	Modified Lorentzian	$A (1+k^2x^2)^{-2}$	Malmros & Thomas [3]
IL	Intermediate Lorentzian	$A(1+k^2x^2)^{-1.5}$	Khattak & Cox [5]
P	Pearson VII	$\frac{2\sqrt{(m)}\sqrt{2\left(\frac{1}{m}\right)-1}}{\sqrt{\pi}} \frac{\sqrt{\left(\frac{1}{m}\right)-1}}{\Gamma(m-\frac{1}{2})} \frac{1}{k} \left[ 1+4\frac{x^2}{k^2} \left(2\left(\frac{1}{m}\right)-1\right) \right]^{-m}$	Immirzi [11][Hall et al, 1977, J. Appl. Cryst. <u>10</u> , 66.]
V	Voigt	$A \int_{-\infty}^{\infty} L(x') G(x-x') dx'$	Langford [14]; Suortti, Ahtee and Unonius [15]
Poly	Polynomial	$\frac{A}{P} \left(1-\frac{x}{Q}\right)$ P and Q are polynomials with even exponents, only.	Bärlocher and Hepp [13]

NOTE: In the above expressions:

- x is distance from Bragg peak position, e.g.  $2\theta_i - 2\theta_B$
- A is the required normalization factor
- k is a constant related to profile breadth

Another function that has been suggested [14] because it is intermediate to Gaussian and Lorentzian functions is the Voigt function. Langford [14] has carried out the individual convolution, via Fourier transforms, to obtain the two parameters (essentially the individual breadths of the component Gaussian and Lorentzian function) to be adjusted in the refinement process. Suortti, Ahtee, and Unonius [15] have tested the function by applying it to both x-ray and neutron data on Ni powders. They found it was a substantial improvement over Gaussian function for the neutron case but not so satisfactory for the x-ray case. It is better than either Gaussian or Lorentzian, but still did not satisfactorily lead to determination of the average crystallite size and strain values, as had been hoped. Nonetheless, it apparently would lead to lower  $R_{wp}$  values in other cases, and therefore better detail in structure refinement, and hence should be explored by other workers.

The most recent suggestion for a new profile function is that by Bärlocher and Hepp [13], the polynomial expression in table 3. They do a least squares fitting of this function to a resolved profile, then store the result and modify it as needed to take account of the dependence of breadth on  $2\theta$ . They report good results but no quantitative details were available at this writing.

Another potentially interesting profile function, not yet tried in Rietveld analyses, combination of Lorentzians such as has been successfully used in pattern decomposition.

Taupin [16] represented the x-ray reflection profile as a series of Lorentzians, usually 3 or 4, in a markedly successful automatic method for peak determination and integration. Huang [19], Parrish [17], Parrish, Huang and Ayers [18], and Parrish have used a composite of seven Lorentzians (three for  $\alpha_1$ , three for  $\alpha_2$ , and one for  $\alpha_3$ ) in decomposing patterns into component (overlapping) reflection peaks. Probably the three-Lorentzian representation could accommodate diffraction broadening better than a single Lorentzian, ML, or IL function if the breadths, relative heights, and separations of the three Lorentzians were made adjustable variables for each new pattern.

A function with a better theoretical basis, but one which has not yet been tried experimentally, has been suggested by Wilson [20]. Noting the variety of contributions to diffraction profile broadening, and drawing on the central limit theorem, he suggested that some complex of Gaussian functions with skewness and kurtosis might be physically reasonable and appropriate. He has, therefore, suggested the Edgeworth series, in which the coefficients have the added advantage of being related directly to the moments,  $m$ , of the profile. The Edgeworth series may be written as

$$I(x) = \phi(x) - \frac{1}{3!} \gamma_1 \phi^{iii}(x) + \frac{1}{4!} \gamma_2 \phi^{iv}(x) + \frac{10}{6!} \gamma_1^2 \phi^{vi}(x) + \dots$$

$$\phi(x) = \frac{1}{\sqrt{2\pi}} e^{-x^2/2}$$

$$\gamma_1 = k_3 \sigma^{-3} = \text{coefficient of skewness}$$

$$\gamma_2 = k_4 \sigma^{-4} = \text{coefficient of excess (kurtosis)}$$

$$k_1 = m_1 = m$$

$$k_2 = m_2 - m_1^2 = \sigma^2$$

$$k_3 = m_3 - 3m_1 m_2 + 2m_1^3$$

$$k_4 = m_4 - 3m_2^2 - 4m_1 m_3 + 12m_1^2 m_2 - 6m_1^4$$

$x$  is expressed in units of  $\sigma$ , the square root of the variance.

Any profile whose moments are all finite can be represented by such an Edgeworth series.

In using it with Rietveld analyses, one would hope that very few terms would be needed.

In conclusion to this section, one may say that while it is true that better profile functions are needed, especially more fundamentally based ones, several already exist which have not been thoroughly evaluated.

## 4. Characteristics of the Refinements

### 4.1. Convergence range

More than a hundred Rietveld refinements have now been carried out in our laboratory with x-ray data. Our general experience has been that, compared to single crystal analysis, the starting model has to be more nearly correct or the Rietveld refinement will not "go". Other workers have also remarked orally to us upon this characteristic. One normally proceeds in steps, first refining only one or two parameters (e.g. overall scale factor) and then gradually letting more and more of the parameters be varied in the successive least-squares refinement cycles. That is to say, the range of convergence is not as great with Rietveld refinements as it is with single crystal structure refinements done with, for example, the widely used Busing, Johnson, Ellison, Thiesen and Levy [22] program. This is, of course, related to the prevalence of false minima discussed in the next section. Rather than being surprised at the limitation on the convergence range, perhaps one ought to be surprised that the refinements converge to meaningful results at all--the  $F(hkl)$  data are badly superimposed by multiplicity, reflection overlap produces more superimposition and partial reduction of the effective  $(\sin \theta/\lambda)$  range (Young, Mackie and Wiles [23]) the general signal-to-noise level is poor compared to that for most single crystal data, and background intensities cannot be well determined independently of the refinement (except in such simple cases that Rietveld refinement is not needed anyway). The use of two wavelengths at once (e.g., the  $\alpha$  doublet) may make matters worse by superimposing two complete patterns--although the additional data should improve the statistics and the simultaneous fitting of the calculated patterns to two sets of observed data (one with each wavelength) can also be regarded as a valuable internal consistency requirement.

### 4.2. "Flat" and false minima

"Flatness" of the minima in Rietveld refinements is another characteristic about which many users comment privately. "Flatness" is indicated by relative insensitivity of  $R_{wp}$  (for example) to parameter shifts greater, or much greater, than the standard deviations in them. Such insensitivity is often noted. Since the  $R_{wp}$  is held rather high (compared to good neutron cases) because of model inadequacies such as in the profile functions, because of the background assessment problems, and because multiplicity and reflection overlap cause the number of effectively independently determinable Bragg reflection intensities  $|F_{hkl}|^2$  to be much smaller than it is for the single crystal case, "flatness" of the minima must be expected. Further, even when better profile functions are used, some "flatness" must be still accepted as an intrinsic characteristic of structure refinement with powder diffraction patterns.

False minima also seem to be more prevalent with Rietveld refinements than with single crystal refinements. Table 4 gives an example with fluorapatite ( $Ca_5(PO_4)_3F$ ). Refinements A and B were carried out with the same data and program; the only difference

Table 4. Fluorapatite (P<sub>63</sub>/M)  
(All Parameters x 10<sup>3</sup>)

	Ca(1)		Ca(2)		P		O(1)		O(2)		O(3)	
	Z	X	Y	X	Y	X	Y	X	Y	X	Y	Z
t A	014	246	992	402	356	416	524	640	484	363	276	032
t B	001	246	992	399	369	328	485	587	465	344	258	070
A	012 <sub>1</sub>	245 <sub>0</sub>	991 <sub>0</sub>	403 <sub>0</sub>	363 <sub>0</sub>	398 <sub>1</sub>	513 <sub>1</sub>	652 <sub>1</sub>	490 <sub>1</sub>	342 <sub>1</sub>	262 <sub>0</sub>	041 <sub>1</sub>
B	002 <sub>0</sub>	243 <sub>0</sub>	992 <sub>0</sub>	398 <sub>0</sub>	367 <sub>0</sub>	326 <sub>0</sub>	488 <sub>0</sub>	589 <sub>1</sub>	467 <sub>0</sub>	341 <sub>0</sub>	260 <sub>0</sub>	066 <sub>0</sub>

Site-Occupancy Parameters

	Ca(1)	Ca(2)	P	O(1)	O(2)	O(3)	F	a(Å)	C(Å)	Rwp(%)
t A	263	500	483	440	294	940	250	9.3653	6.8826	
t B	270	477	492	280	580	940	255	9.3653	6.8826	
A	353 <sub>2</sub>	594 <sub>3</sub>	457 <sub>3</sub>	504 <sub>6</sub>	461 <sub>4</sub>	940-	159 <sub>2</sub>	9.3664	6.8816	23.0
B	299 <sub>1</sub>	454 <sub>1</sub>	429 <sub>2</sub>	418 <sub>2</sub>	425 <sub>2</sub>	940-	147 <sub>1</sub>	9.3667	6.8821	15.5

and B used same data and program.

cycles; all final  $\Delta < \sigma$ .

in the starting parameters used. The initial A and B locations for O(1) differ by 0.72 Å and the refined positions by 0.59 Å. For O(2) the differences are 0.43 Å initially and 0.2 Å finally. Thus, choices of atom starting positions that differ by less than 1 Å have, led to refined ("minima") positions differing by about one-half angstrom, which is more than 50 times the calculated standard deviations for the atom positions.

In this fluorapatite case, the false minima could be distinguished from the true minimum on the basis of  $R_{wp}$  (23 percent vs 15.5 percent), but that is not always possible. Fluorapatite is a very nearly stoichiometric, well crystallized material and its structure is known in great detail. [The final position parameters for refinement B in table 4 do agree with the single crystal results [24] within 3  $\sigma$  and mostly within 2  $\sigma$  except for Ca(1)), for which the A result happens to be the single crystal result.] Most materials for which one would wish to use the Rietveld method will not be stoichiometric ones with structures well known in detail. The structural model will, at first at least, have significant deficiencies and as a consequence the R factors will tend to be higher than they were in the B refinement of fluorapatite. Table 5 gives an example of a false minimum in the

Rietveld refinement of human tooth enamel [25]. The final positions for 0(1) and 0(2) differ by 0.51 Å and 0.43 Å, respectively, in the two cases (A and B). In this case, it is not possible to tell from the  $R_{wp}$  values which, if either, of the minima is the true one. Because both  $R_{wp}$  values are as high as that for the false minimum with fluorapatite, one might try to assume that both A and B refinements represent false minima. But that is not permissible, either. At this stage, the TE structure refinement is still preliminary and some moieties known to be present, e.g. a few wt% of  $CO_3$  and  $H_2O$ , are not included in the model because their locations are not known. One would like to know which of the refinements A or B, is the better one to take as a starting point for adding in these moieties in their locations in the structural model to be refined. The difference in  $R_{wp}$  between case A and B is not obviously large enough to permit such a judgment and the familiar Hamilton [26] R-test is not applicable because the observations are not directly of independent Bragg intensities. Thus, one can only conclude that, at least when the  $R_{wp}$  values are still as high as

Table 5. Human Tooth Enamel on Hydroxyapatite Model ( $P6_3/M$ )  
(All Parameters  $\times 10^3$ )

	Ca(1)	Ca(2)		P		0(1)		0(2)		0(3)		Z
	Z	X	Y	X	Y	X	Y	X	Y	X	Y	Z
Start A	014	249	989	402	356	416	524	640	484	363	276	03
Start B	009	250	985	406	362	323	487	613	476	357	282	05
End A	009 <sub>0</sub>	247 <sub>0</sub>	988 <sub>1</sub>	400 <sub>1</sub>	357 <sub>1</sub>	406 <sub>1</sub>	517 <sub>1</sub>	642 <sub>2</sub>	472 <sub>2</sub>	366 <sub>1</sub>	278 <sub>1</sub>	04
End B	003 <sub>1</sub>	250 <sub>0</sub>	994 <sub>1</sub>	402 <sub>1</sub>	359 <sub>1</sub>	332 <sub>1</sub>	484 <sub>2</sub>	589 <sub>1</sub>	460 <sub>1</sub>	364 <sub>1</sub>	277 <sub>0</sub>	05
End C	002 <sub>1</sub>	249 <sub>1</sub>	993 <sub>1</sub>	403 <sub>1</sub>	358 <sub>1</sub>	326 <sub>1</sub>	483 <sub>1</sub>	593 <sub>1</sub>	451 <sub>1</sub>	353 <sub>1</sub>	264 <sub>1</sub>	06

Site-Occupancy Parameters

	Ca(1)	Ca(2)	0(1)	0(2)	0(3)	X-ION at Z =			a(Å)	c(Å)	Rwp(%)
						0.05	0.15	0.25			
Start A	263	500-	483	440	294	976	169	423	012	9.4415	6.8964
Start B	280	365	404	307	416	1000-	125	125	125	9.4415	6.8964
End A	302 <sub>2</sub>	500-	494 <sub>4</sub>	592 <sub>8</sub>	281 <sub>8</sub>	1200 <sub>2</sub>	199 <sub>6</sub>	400 <sub>13</sub>	048 <sub>8</sub>	9.4406	6.8761
End B	239 <sub>2</sub>	389 <sub>2</sub>	412 <sub>3</sub>	257 <sub>5</sub>	469 <sub>5</sub>	1000-	162 <sub>4</sub>	345 <sub>10</sub>	034 <sub>6</sub>	9.4417	6.8770
End C	298 <sub>3</sub>	419 <sub>3</sub>	413 <sub>4</sub>	364 <sub>7</sub>	433 <sub>7</sub>	1000-	091 <sub>6</sub>	186 <sub>14</sub>	066 <sub>9</sub>	9.4451	6.8813

A and B: same data.

C: Separate data, same material, same initial parameters as B.

Eight cycles, all  $\Delta < \sigma$ .

25 percent, false minima can occur relatively nearby true ones and cannot be effectively recognized on the basis of R values.

It may be that, if the second order derivative term in the shifts were implemented in the computer program, which it is not<sup>2</sup> in those we have used, the convergence neighborhood might be significantly increased and false minima would be less prevalent. This seems to be a possibility that should be explored in order that the effectiveness of the Rietveld method can be maximized.

#### 4.3. Standard deviations

The calculated standard deviations seem to be physically reasonable in some cases, but in others they are too small.

Two examples of reasonableness are these:

(1) Rietveld results and single crystal results frequently agree within  $3\sigma$  or less, e.g. for fluorapatite (cf. table 4 with Sudarsanan, Mackie, and Young [24]) and for quartz (Young, Mackie and von Dreele [8]).

(2) Rietveld refinements were carried out with 29 sets of data collected at different temperatures (25-500 °C) on the same TE specimen. With few exceptions, all 29 values of each positional parameter were the same within  $2\sigma$  [23]. (Experimentally, this was something of a disappointment because we were hoping to see some dramatic changes produced by heating.)

In the fluorapatite example, the refinements were done with the DBW program (table 2) and the others were done with the RHVM program. Because of an internal difference the RHVM program calculates larger standard deviations. (Factors of 1 to 3 have been observed.)

There are also cases in which the calculated standard deviations seem to be too small. Refinements B and C in table 5 illustrate one. The data came from specimens taken from the same large and presumably homogenized supply of dense-fraction human tooth enamel. The same starting parameters and program (DBW) were used for both refinements. But the refined positional parameters differ by more than  $3\sigma$  in 5 instances and nearly 10 in one. Clearly, if the calculated  $\sigma$ 's were 2 or 3 times as large, we would probably conclude that the positional parameters did not differ significantly between the two refinements.

Dr. Martyn Cooper [27,28] has pointed out that the calculations of standard deviations done in most or all current Rietveld refinement programs are wrong in principle. A central part of this point is easily grasped. The usual way to calculate standard deviations is as

the calculated parameter-shift term formally given by

$$-\sum_i 2w_i \left[ \left( y_{0i} - \frac{1}{c} y_{Ci} \right) \frac{\partial^2 y_{Ci}}{\partial x_j \partial x_k} - \left( \frac{\partial y_{Ci}}{\partial x_j} \right) \left( \frac{\partial y_{Ci}}{\partial x_k} \right) \right]$$

where  $x_j, x_k$  are the  $j$ th and  $k$ th parameters being varied, is approximated by dropping the second order derivative terms.

$$\sigma_j^2 = A_{jj}^{-1} \frac{\sum w_i (y_i(\text{obs}) - \frac{1}{c} y_i(\text{calc}))^2}{N-P}$$

where  $y_i$  is the intensity observed at the  $i$ th step in the scan,  $A_{jj}^{-1}$  is the (diagonal) element of the inverse normal equations matrix,  $P$  is the number of parameters adjusted, and  $N$  is the number of independent observations. Most of the parameters are crystallographic and depend on  $F(hkl)$  but not on the reflection profile shape or position. The value used for  $N$  is usually the number of steps in the scan, which far exceeds the number of independent  $F(hkl)$ 's. Thus, the denominator is made too large, and  $\sigma$  too small, by this usual procedure. Is there any reasonably practical way to treat separately the two kinds of parameters and observations, Bragg intensity and profile shape and position in order to calculate  $\sigma$ 's correctly in principle? Perhaps the work of Dr. Cooper or others will tell us. If not, we will have to rely on the accumulating experience of many workers to learn some kind of recipe for the factor by which the calculated  $\sigma$ 's are too small under what conditions.

## 5. Conclusions

Application of Rietveld analyses with x-ray data lagged by several years the application with neutron data. Probably because the x-ray reflection profiles are less well represented by simple functions, x-ray results to date for  $R_p$  are typically about twice those for neutron results although standard deviations on positional parameters are comparable. Several all-new computer programs with various special virtues have recently been written for x-ray Rietveld analysis. The problem of appropriate representation of the reflection profiles is receiving attention. Flat and false minima problems do limit the straightforward application of the method somewhat, but there is reason to hope that these problems can be reduced with the use of improved profile functions and algorithms. The calculated standard deviations are often too small, perhaps by a factor of 2 or 3. This problem is receiving attention.

Nonetheless, x-ray Rietveld analyses have already produced highly useful structural results for a number of materials which are simply not available, or for other reasons cannot be studied, in single crystal form. Human tooth enamel is one of them. The pace of activity in x-ray Rietveld analysis is picking up rapidly now and, because x-ray beams are much more widely available than neutron beams, one can anticipate that the x-ray activity will soon exceed the very substantial neutron activity.

---

It is a pleasure to thank Dr. J. O. Thomas for keeping me informed of the work of the Stockholm/Upsala group at the manuscript stage, Dr. A. M. Glazer for keeping me similarly informed about the work of the Oxford and associated groups, Dr. A. Immirzi

for supplying extensive information on his still unpublished program and test work with  
t, Dr. Martyn Cooper for alerting me to the in-principle problem with standard devia-  
ions via a draft manuscript and "discussions" of unpublished work, Professor A. J. C.  
ilson and many other colleagues here and abroad for discussions and correspondence,  
r. Bärlocher for an advance copy of his abstract for this conference, my colleagues  
r. P. E. Mackie and D. B. Wiles for assistance and permission to quote unpublished  
ork, and the USPHS for financial support through NIH-NIDR Grant DE-01912.

#### References

- [1] Rietveld, H. M., Line profiles of neutron powder-diffraction peaks for structure refinement, *Acta Cryst.* 22, 151 (1967).
- [2] Rietveld, H. M., A profile refinement method for nuclear and magnetic structures, *J. Appl. Cryst.* 2, 65-71 (1969).
- [3] Malmros, G. and Thomas, J. O., Least-squares structure refinement based on profile analysis of powder film intensity data measured on an automatic micro-densitometer, *J. Appl. Cryst.* 10, 7-11 (1977).
- [4] Malmros, G. and Werner, P. E., Automatic densitometer measurements of powder diffraction photographs, *Acta Chemica Scandinavica*, 27, 493-502 (1973).
- [5] Khattak, C. P. and Cox, D. E., Profile analysis of x-ray powder diffractometer data: Structural refinement of  $\text{La}_{0.75}\text{Sr}_{0.25}\text{CrO}_3$ , *J. Appl. Cryst.* 10, 404-411 (1977).
- [6] Glazer, A. M., Hidaka, M., and Bordas, J., Energy-dispersive powder profile refinement using synchrotron radiation, *J. Appl. Cryst.* 11, 165-172 (1978).
- [7] Cheetham, A. K. and Taylor, J. C., Profile analysis of neutron diffraction data: Its scope, limitations, and applications in solid state chemistry, *J. Solid State Chem.* 21, 253-275 (1977).
- [8] Young, Mackie and von Dreele (1977).
- [9] Werner, P. E., Salmoné, S., Malmros, G., and Thomas, J. O., Quantitative analysis of multicomponent powders by full-profile refinement of Guinier-Hägg x-ray film data, *J. Appl. Cryst.*, in press (1979).
- [10] Wiles, D. B. and Young, R. A., Improved computer programs for Rietveld analysis of x-ray powder diffraction patterns, *American Crystallographic Association Program and Abstracts*, 6, 56 (1979).
- [11] Immirzi, A., Profile fitting refinements using generalized coordinates, *Acta Cryst.* A34, S348-S349 (1978).
- [12] Immirzi, A., (unpublished work, 1979).
- [13] Bärlocher, Ch. and Hepp, A., A new pattern fitting structure refinement program for x-ray powder data (1979). This conference.
- [14] Langford, J. I., A rapid method for analyzing the breadths of diffraction and spectral lines using the Voigt function, *J. Appl. Cryst.* 11, 10-14 (1978).

- [15] Suortti, P., Ahtee, M. and Unonius, L., Voigt function fit of x-ray and neutron powder diffraction profiles, Report series in Physics HU-P-163, University of Helsinki, 16 pp. (1978).
- [16] Taupin, D., Automatic peak determination in x-ray powder patterns, J. Appl. Cryst. 6, 266-273 (1973)
- [17] Huang, T. C. and Parrish, W., Accurate and rapid reduction of experimental x-ray data, Appl. Phys. Lett. 27, 123-125 (1975).
- [18] Parrish, W., Huang, T. C., and Ayers, G. L., Profile fitting: A powerful method of computer x-ray instrumentation and analysis, Trans Am. Cryst. Assoc., 12, 55-75 (1976).
- [19] Parrish, W. and Huang, T. C., Accuracy of the Profile Fitting Method for X-Ray Polycrystalline Diffractometry, this volume.
- [20] Wilson, A. J. C., Note on the aberrations of a fixed-angle energy-dispersive powder diffractometer, J. Appl. Cryst. 6, 230-237 (1973).
- [21] Cramer, H., Mathematical Methods of Statistics (Almqvist and Wiksells, Uppsala, 1945), pp. 228-229.
- [22] Busing, W. R., Johnson, C. K., Ellison, R. D., Thiesen, W. E., and Levy, H. A., World list of crystallographic computer programs, ORXFLS3, Accession No. 84, J. Appl. Cryst. 6, 309-346 (1973).
- [23] Young, R. A., Mackie, P. E., and Wiles, D. B., Rietveld pattern-fitting structure-refinement ('Profile Refinement') with x-ray powder diffraction data, Acta Physica Polonica, in press (1979).
- [24] Sudarsanan, K., Mackie, P. E., and Young, R. A., Comparison of synthetic and mineral fluorapatite,  $\text{Ca}_5(\text{PO}_4)_3\text{F}$ , in crystallographic detail, Mat. Res. Bull. 7, 1331-1338 (1972).
- [25] Young, R. A. and Mackie, P. E., Crystallographic studies of human tooth enamel: Initial structure refinement, submitted for publication (1979).
- [26] Hamilton, W. C., Significance tests on the crystallographic R factor, Acta Cryst. 18, 502-510 (1965).
- [27] Cooper, M. (private communication).
- [28] Sakata, M. and Cooper, M., An analysis of the profile refinement method, Report MPD/NBS Bibliography/95, AERE, Harwell (1978).

#### Bibliography

- Kajzar, F., A profile refinement method for determination of the contribution of rhombohedral structure in graphite, Rap. - Inst. Fiz. Tech. Jad. AGH, Issue INT 112/PS, 32 pp. (1976) (Abstract in CA).
- Buras, B., Gerward, L., Glazer, A. M., Hidaka, M., and Staun Olsen, J., Quantitative structural studies by means of the energy dispersive method with x-rays from a storage ring, to be published (1979).

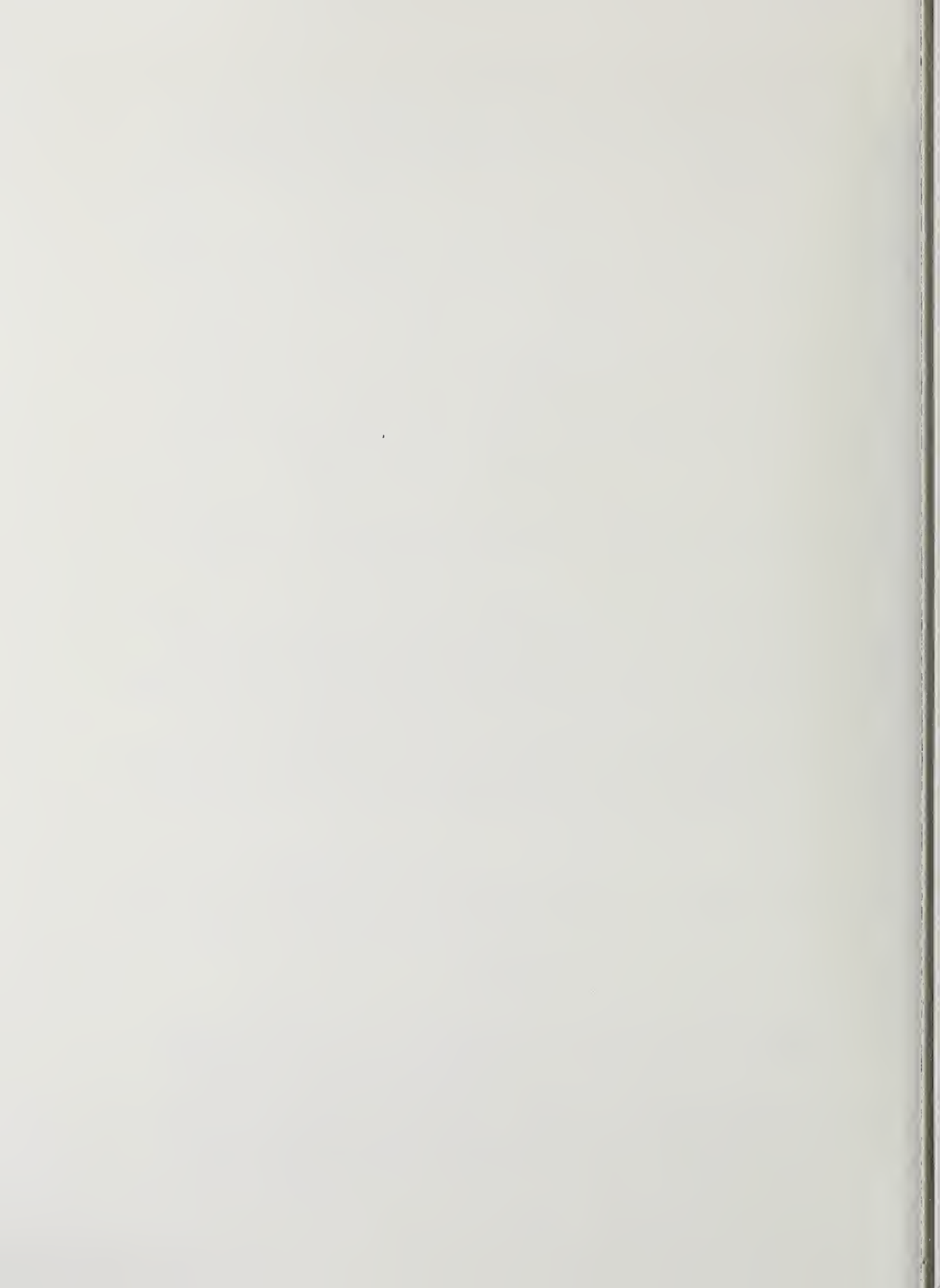
## Discussion

Comment (Sabine): I think that you should not state that the Rietveld method underestimates standard deviation. All that is known is that the two methods give different measurements in some cases.

Response (Young): The full text of this presentation cites examples in which the e.s.d.'s appear to be physically reasonably larger as well as examples in which they are smaller than the actual observed lack of reproducibility. However, the RHVM program has an internal feature which causes it to produce e.s.d.'s larger by a factor of  $\sqrt{2}$  than does the DBW II program. Unfortunately, the RHVM was used for the examples in which the e.s.d.'s were realistically large and the DBW II program was used in the examples in which the e.s.d.'s could be seen to be "too small." Thus, I am afraid, we do not yet have unambiguous examples of the e.s.d.'s being as large as intercomparisons suggest they should be.

Question (Snyder): Given the high degree of precision obtainable from this method, what is your estimate of the degree of accuracy of the lattice parameter and how are the any systematic errors allowed for?

Response (Young): We have made no effort to assess accuracy, only precision. However, the lattice parameter results we have obtained in Rietveld analysis of fluoroapatite, for example, compare well (within  $3\sigma$ ) with those obtained with single crystals and with other powder methods. The only systematic error currently allowed for is a  $2\theta$  zero error. It should not be difficult to incorporate a specimen displacement error correction also, but the small estimated standard deviation we are getting suggests that such correction, if incorporated, would usually be small for the rather strongly absorbing materials we have been studying.



A NEW PATTERN FITTING STRUCTURE REFINEMENT  
PROGRAM FOR X-RAY POWDER DATA

Ch. Baerlocher and A. Hepp  
Institut für Kristallographie und Petrographie  
ETH Zürich, Switzerland

An entirely new program package has been written for the profile fitting method, designed specifically for x-ray powder data. It uses a novel function for the peak shape which gives excellent agreement between observed and calculated profiles. Additional information such as known interatomic distances and angles can be readily included as weighted constraints and/or their expected ranges imposed as boundary conditions. This improves greatly the convergence and it becomes also possible to refine structures with up to 100 or more positional parameters. To achieve the necessary resolution, diffractometer data are used with strictly monochromatic  $\alpha_1$  radiation.

In a first step the true background is determined and  $2\theta$  and  $L_p$  corrections are applied. All possible reflections (excluding extinctions) are generated from the lattice parameters and assigned to the measured profile steps. Next, the function which approximates best the form of a single, non-overlapping peak is determined with a special least squares procedure. This function has essentially the form

$$F = \frac{\text{const.}}{P} \cdot \left[ 1 - \frac{\Delta 2\theta}{Q} \right] ,$$

where  $P$  and  $Q$  are polynomials having only even exponents. All starting parameters are estimated by the program. The final function is normalized, its values stored and then used as a standard in the subsequent profile fitting structure refinement program. This employs a variable metric algorithm, which efficiently handles the above mentioned constraints and boundary conditions by a projection method. The algorithm is also very stable towards high correlation. Apart from structural parameters, the program refines lattice constants, linear  $2\theta$  correction, half width as a function of  $2\theta$  and  $hkl$  (if necessary), preferred orientation, and profile asymmetry. The input for the programs is kept to a minimum and is mostly in free format. Examples will be shown.



THE DETERMINATION OF STRUCTURAL PARAMETERS AND THEIR  
STANDARD DEVIATIONS FROM POWDER DIFFRACTION PATTERNS

M. J. Cooper, M. Sakata<sup>1</sup> and K. D. Rouse  
Materials Physics Division  
AERE Harwell, OX11 0RA, England

An analysis of the Rietveld Profile Refinement Method has shown that statistical correlation, which must occur for points on the same Bragg peak, introduces bias into the estimates of the structural parameters and also results in the standard deviations being determined incorrectly. Because of this correlation it is not valid to derive the standard deviations for the profile and structural parameters in the same way, since the structural parameters depend only on the intensity of the Bragg peaks and not their shape. This has been confirmed by the analysis of a number of simple neutron diffraction patterns using both Profile Refinement and integrated intensity methods, and in some cases the standard deviations were found to be underestimated by the Profile Refinement Method by a factor of at least 2, compared to those given by an integrated intensity method, although overestimation is also possible.

Our analysis indicates that all standard deviation values which have been derived by the Rietveld Profile Refinement Method are wrong and no simple modification of the method is possible to overcome this problem. An alternative approach has therefore been formulated in order to provide reliable estimates of the structural parameters and their standard deviations, and results of its use are presented.

### 1. Introduction

The Rietveld Profile Refinement Method [1]<sup>2</sup> is now extensively used for the analysis of powder diffraction data. The method was first developed some ten years ago but, until recently, no adequate theoretical understanding existed of the results which it gives. It is the purpose of this paper to outline the results of a recent analysis [2] aimed at providing such

---

<sup>1</sup> on leave from Nagoya University, Nagoya, Japan.

Figures in brackets indicate the literature references at the end of this paper.

a theoretical understanding, at least for simple cases, and to indicate how the analysis of powder diffraction data might be developed in order to provide more reliable results.

## 2. Structural Parameter Values

The Rietveld method involves the minimization of the function:

$$M_p = \sum_i w_i (y_i - \sum_k y'_{i,k})^2 \quad (1)$$

where  $y_i$  is the observed background-corrected intensity at a single point on the diffraction profile and  $w_i$  is the statistical weight associated with that observation.  $y'_{i,k}$  is the contribution from a single Bragg reflection to the theoretical intensity at that point and is given by:

$$y'_{i,k} = K I_k(k, p_c) G_{i,k}(i, k, p_p) \quad (2)$$

where  $K$  is a scale factor,  $I_k$  is the calculated Bragg intensity and  $G_{i,k}$  is a normalized peak shape function, which for neutron diffraction is usually taken to be a Gaussian. The refinable parameters can be divided into structural and profile parameters and it is usually assumed that  $I_k$  is a function of the structural parameters ( $p_c$ ) only and  $G_{i,k}$  is a function of the profile parameters ( $p_p$ ) only, as indicated in equation [2]. As we shall see, the separation of the two types of parameters in this way has an extremely important consequence for the results given by the method.

The easiest way to visualize the significance of the results given by the method is to compare them with those which would be obtained from a conventional least-squares analysis of the integrated Bragg intensities. For a diffraction pattern with overlapping peaks the minimization function  $M_p$  becomes:

$$M_p = \sum_i w_i (y_i - K \sum_k I_k G_{i,k})^2 \quad (3)$$

whereas that for an integrated intensity analysis would be:

$$M_I = \sum_k w_k (\sum_i y_{i,k} - K I_k)^2 \quad (4)$$

The values of  $\frac{\partial M_p}{\partial x}$  and  $\frac{\partial M_I}{\partial x}$ , where  $x$  is a structural parameter, are thus:

$$\frac{\partial M_p}{\partial x} = -2K \sum_i w_i \sum_k G_{i,k} (y_i - K \sum_k I_k G_{i,k}) \frac{\partial I_k}{\partial x} \quad (5)$$

$$\frac{\partial M_I}{\partial x} = -2K \sum_k w_k \left( \sum_i y_{i,k} - KI_k \right) \frac{\partial I_k}{\partial x} \quad (6)$$

In general, therefore, the two methods will not give identical values for the structural parameters, although it is not clear how they will differ.

In order to clarify the situation we have therefore considered the more simple case when the peaks are resolved. In this case the minimization functions can be written as:

$$M_P = \sum_k \sum_j w_{j,k} (y_{j,k} - K I_k G_{j,k})^2 \quad (7)$$

$$M_I = \sum_k w_k \left( \sum_j y_{j,k} - K I_k \right)^2 \quad (8)$$

where  $j$  represents a point on a single Bragg's peak and the summation over  $j$  can be carried out before the summation over  $k$ .

The values for  $\frac{\partial M_P}{\partial x}$  and  $\frac{\partial M_I}{\partial x}$  are then:

$$\frac{\partial M_P}{\partial x} = -2K \sum_k \sum_j w_{j,k} G_{j,k} (y_{j,k} - K I_k G_{j,k}) \frac{\partial I_k}{\partial x} \quad (9)$$

$$\frac{\partial M_I}{\partial x} = -2K \sum_k w_k \left( \sum_j y_{j,k} - K I_k \right) \frac{\partial I_k}{\partial x} \quad (10)$$

These again show that the values of the structural parameters will not, in general, be identical. However, it is now possible to derive fairly simple relations between the weighting schemes which would result in the derivatives being equal and thus give identical values for the structural parameters. Two particularly simple cases are:

$$w_{j,k} = w_k / G_{j,k} \quad (11)$$

$$w_{j,k} = 1/y_{j,k} \text{ and } w_k = 1/\sum_j y_{j,k} \quad (12)$$

The latter is that appropriate to a case and zero background ( $B_i=0$ ) which is, of course, rather unrealistic. That given by equation [11] shows that the weights would have to be increased for points on the tails of the Bragg peaks. This is indicative of the different statistical bias introduced in the two methods, but does infer that the values given by the profile refinement method may possibly be more appropriate estimates of the structural parameters, although they may well not differ significantly from those given by an integrated intensity analysis.

### 3. Standard Deviations

We must also consider the standard deviation values given by the profile refinement method. These are derived from the minimization function through the standard equation:

$$\sigma_i^2 = A_{ii}^{-1} \frac{M}{N-P} \quad (13)$$

where  $A_{ii}^{-1}$  is the appropriate diagonal element of the inverse normal matrix and  $N-P$  is the number of degrees of freedom ( $N$  is the number of statistically independent observations and  $P$  is the number of independently varied parameters).

Again, comparing the results with those for a conventional integrated intensity analysis we see that the elements of the normal matrix, which are given by:

$$(A_{pq})_P = \sum_k \sum_j w_{j,k} G_{j,k}^2 \frac{\partial(K I_k)}{\partial x_p} \frac{\partial(K I_k)}{\partial x_q} \quad (14)$$

$$(A_{pq})_I = \sum_k w_k \frac{\partial(K I_k)}{\partial x_p} \frac{\partial(K I_k)}{\partial x_q} \quad (15)$$

and hence the values of  $A_{ii}^{-1}$ , will not usually be the same.

We can define an agreement factor, given by

$$A = \left( \frac{M}{N-P} \right)^{\frac{1}{2}} \quad (16)$$

the values of which are:

$$A_P^2 = \left\{ \sum_k \sum_j w_{j,k} \Delta_{j,k}^2 \right\} / (N_P - P_P - P_C) \quad (17)$$

$$A_B^2 = \left\{ \sum_k w_k \Delta_k^2 \right\} / (N_B - P_C) \quad (18)$$

where  $\Delta_{j,k} = y_{j,k} - y'_{j,k}$ ,  $\Delta_k = \sum_j \Delta_{j,k}$ ,  $N_P$  is the number of points in the profile,  $N_B$  is the number of Bragg reflections and  $P_P$  and  $P_C$  are the number of profile and structural parameters respectively. Again, these will be different and it is not clear how the values of the estimated standard deviations will differ.

However, it is at this point that we must consider the significance of the fact that we can separate the observed intensity into two factors, each of which depends on one type of parameter only. In particular  $I_k$  has an identical value for each point on the same Bragg peak, so that the values of  $\Delta_{j,k}$  are in fact correlated over each peak. This is illustrated in figure 1 for a peak for which  $\Delta_k$  is positive, giving a positive mean value for the

individual  $\Delta_{j,k}$  values. This correlation between a sequence of  $\Delta_{j,k}$  values in fact invalidates the use of the agreement factor  $A_p$  in the derivation of the standard deviations.

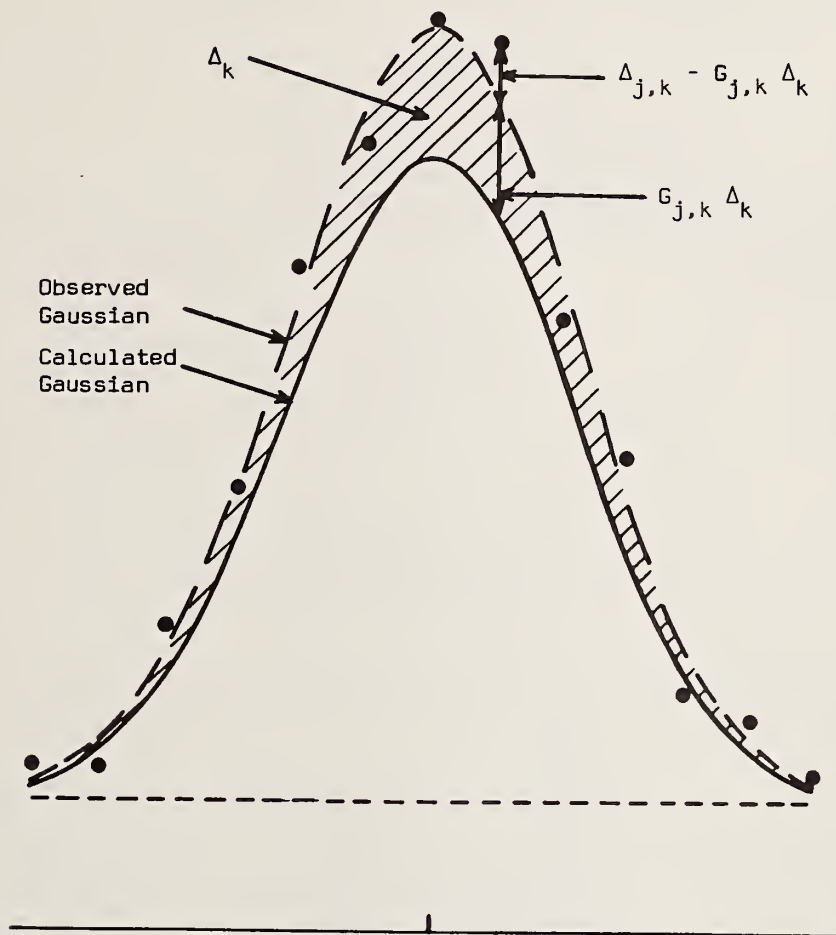


Figure 1. Illustration of the correlation between  $\Delta_{j,k}$  values for the same Bragg peak. The observed points are distributed randomly about the observed Gaussian rather than the calculated Gaussian, so that the differences which must be considered statistically are  $\Delta_k$  and  $\Delta_{j,k} - G_{j,k} \Delta_k$  rather than  $\Delta_{j,k}$ .

The observed points are distributed about an observed Gaussian curve rather than the calculated curve, so that the differences which must be considered statistically are  $\Delta_k$  and  $\Delta_{j,k} - G_{j,k} \Delta_k$ , rather than  $\Delta_{j,k}$ .

This correlation is illustrated for some experimental data in figure 2(a). This shows the differences observed for a number of peaks for a  $UO_2$  sample. The solid lines represent the mean difference values for each peak, with the shaded areas corresponding to  $\Delta_k$ . This is also illustrated in figure 2(b) in which the solid curve represents the difference between the observed and calculated Gaussians ( $G_{j,k} \Delta_k$ ).

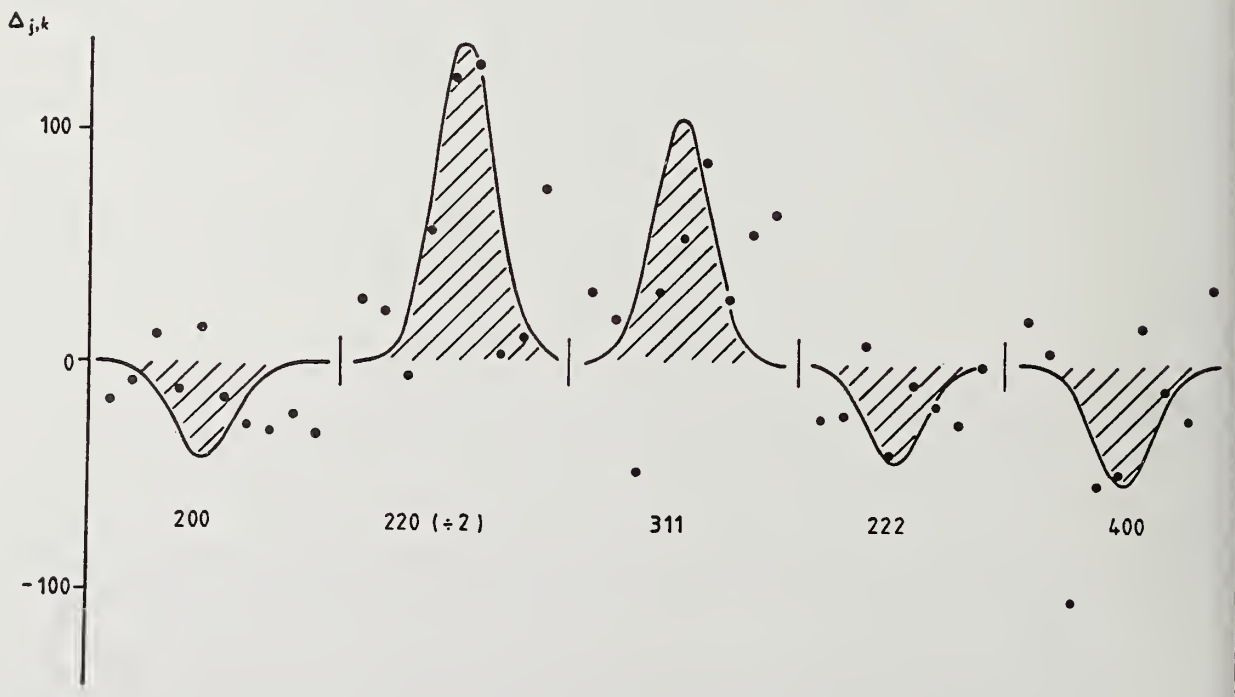
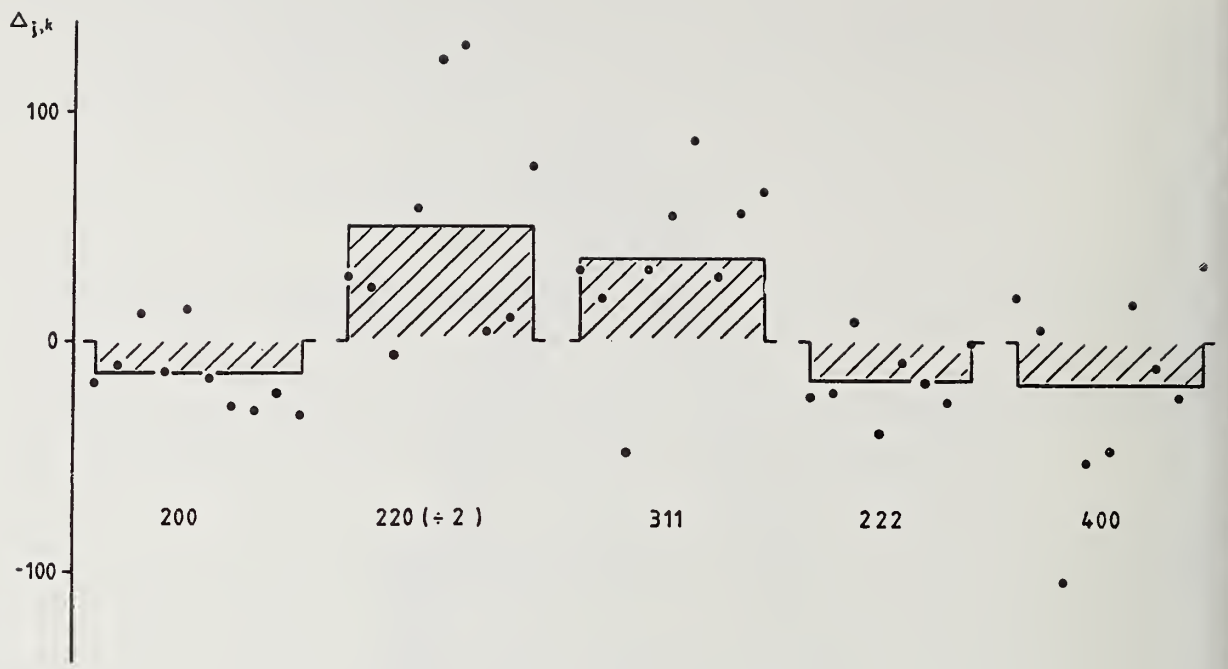


Figure 2.

We must therefore consider two agreement factors relating to the fitting of the peak shapes and the peak intensities respectively, given by:

$$A_S^2 = \left\{ \sum_k \sum_j w_{j,k} (\Delta_{j,k} - G_{j,k} \Delta_k)^2 \right\} / (N_p - P_p) \quad (19)$$

$$A_B^2 = \left\{ \sum_k w_k \Delta_k^2 \right\} / (N_B - P_C) \quad (20)$$

The ratio of the estimated standard deviation given by the two methods is then given by:

$$\frac{(\sigma_i^2)_P}{(\sigma_i^2)_I} = \frac{(A_{ii}^{-1})_P}{(A_{ii}^{-1})_I} \frac{A_P^2}{A_B^2} \approx \frac{1}{\epsilon'} \frac{A_P^2}{A_B^2} \quad (21)$$

which can also be written in the form:

$$\frac{(\sigma_i^2)_P}{(\sigma_i^2)_I} = \frac{(A_{ii}^{-1})_P}{(A_{ii}^{-1})_I} \left\{ \frac{A_S^2}{A_B^2} + \epsilon \frac{N_B - P_C}{N_p - (P_C + P_p)} \right\} \quad (22)$$

$\epsilon$  and  $\epsilon'$  are both functions of the weighting scheme, having values in the range 1 to 2, given by:

$$\epsilon \sum_k w_k \Delta_k^2 = \sum_k \sum_j w_{j,k} G_{j,k}^2 \Delta_k^2 \quad (23)$$

$$\epsilon' \sum_k w_k = \sum_k \sum_j w_{j,k} G_{j,k}^2 \quad (24)$$

Equation [21] enables us to predict the ratio from the agreement factors given by the two methods, whilst equation [22] shows how the ratio is related to the agreement factors appropriate to the shape and intensity fitting. Since the number of degrees of freedom is normally much larger for the profile data than for the integrated intensity data, the second term will be small and the standard deviation ratio will usually be determined by the ratio of these agreement factors, rather than the different number of degrees of freedom.

#### 4. Experimental Results

We have analyzed a number of experimental data sets using both methods in order to provide a quantitative illustration of these results. Table 1 summarizes the results obtained for the  $UO_2$  data which include those shown in figure 2. The values of the structural parameters are not significantly different, but the agreement factors are, and consequently

the standard deviation ratio is less than 0.5, i.e. the profile refinement method underestimates these standard deviations by more than 2. The magnitude of this factor is well predicted by our analysis.

Table 2 shows some similar results for data from  $\alpha$ -AgI, which was studied by Wright and Fender [3] using the Rietveld method. We have therefore reanalyzed their data using an integrated intensity analysis and compared the two sets of results for two different structural models. Again, the most significant differences are in the values of the standard deviations, the profile refinement method underestimating them by a factor which varies between 2 and 5, thus giving values which are particularly misleading. For example, the difference between the values given for the positioned parameter  $x_{Ag}$  appears to be  $4\frac{1}{2}$  times its standard deviation instead of just over 1.

Table 1. Results of Profile and Integrated Intensity Refinements of  $UO_2$  Data

	<u>Profile</u>	<u>Intensity</u>
$n_o$ (rel.occ.)	1.005 (14)	0.977 (32)
$B_u$ ( $\text{\AA}^2$ )	0.254 (32)	0.246 (75)
$B_o$ ( $\text{\AA}^2$ )	0.541 (38)	0.522 (82)
$R(F^2)$ (%)	4.03	-
$R(I)$ (%)	-	3.92
A	1.60	-
$A_B$	-	2.92
Scale (rel)	1.0000	1.0139

Table 2. Results of Profile and Integrated Intensity Refinements for  $\alpha$  - AgI

	Model 1		Model 2	
	<u>Profile</u>	<u>Intensity</u>	<u>Profile</u>	<u>Intensity</u>
Ag site	12 (d)	12 (d)	24 (g)	24 (g)
$x_{Ag}$	-	-	0.308 (2)	0.299 (7)
$B_{Ag}$ ( $\text{\AA}^2$ )	11.7 (4)	12.4 (2.1)	9.7 (8)	11.5 (1.4)
$B_I$ ( $\text{\AA}^2$ )	7.5 (3)	7.8 (9)	7.1 (3)	7.8 (5)
$R(I)$ (%)	8.5	8.3	4.5	4.7

We have recently analyzed several further sets of data from  $UO_2$ , at five different temperatures [4]. Table 3 summarizes some of the relevant results. This gives the values of  $\epsilon'$  and the agreement factors for the two methods of analysis. From these we can predict a value for the mean standard deviation ratio, which can then be compared with the observed value. It can be seen that, although the ratio varies between 0.6 and 1.7, we can in all cases predict its value to within 10 percent. These results also show that the profile refinement method can overestimate, as well as underestimate, the standard deviations. However, the agreement factor  $A_p$  is somewhat larger for these data than is usual and it is our opinion that, at least for neutron data when the peak shape is usually quite well predicted, it is more likely that the standard deviations will be underestimated.

Table 3. Standard Deviation Ratios for  $UO_2$

Temp (°C)	$\epsilon'$	$A_p$	$A_I$	$\bar{\sigma}_p/\bar{\sigma}_I$		Calc Obs
				Calc	Obs	
20	1.37	3.07	4.23	0.62	0.60	1.03
800	1.46	2.47	2.01	1.02	0.99	1.03
1100	1.51	2.51	1.10	1.86	1.71	1.09
1400	1.40	2.85	3.24	0.74	0.68	1.09
1460	1.39	2.48	1.94	1.08	1.00	1.08
—	—	—	—	—	—	—
Mean	1.43	2.68	2.50	1.06	1.00	1.06

### 5. An Alternative Approach

The situation is clearly more complicated when appreciable peak overlap occurs and the results given by the Rietveld method may well become more unreliable. Moreover there is no simple way in which the method can be modified to give reliable standard deviation estimates. We have therefore formulated an alternative approach, which is illustrated in figure 3. This is a prototype system using existing programs as far as possible.

Firstly KDRREF generates a list of reflections so that any unseparable peaks, i.e. peaks separated by less than the step size, can be identified. Profile data are generated as before by the Rietveld PREPROF program and initial values for the Bragg intensities are generated from the structural model by the TAILS program. The SCRAP program then refines the profile parameters and the values of the Bragg intensities, which are then analyzed by the TAILS program to give the structural parameters. This method thus allows any uncertainty associated with the magnitude of the Bragg intensities to be reflected in the standard deviations estimated for the structural parameters.

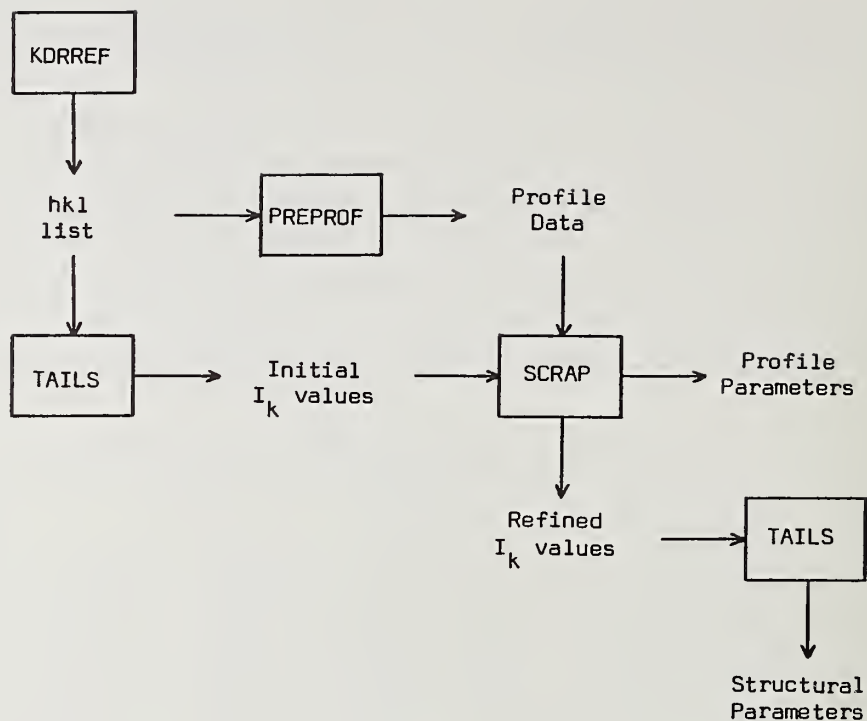


Figure 3. Analysis of powder data.

We have now used this program to analyze a number of sets of data. The results for the room temperature  $UO_2$  data, referred to earlier, are illustrated in table 4 and figure 4. Table 4 gives the final values for the refined parameters and Bragg intensities, with their estimated standard deviations. The standard deviations of the intensities are larger than those calculated by the Rietveld program from the specified weights by about 50 percent. Figure 4 shows the fitting of a number of the peaks, which can be seen to be quite good. The fitted values for the Bragg intensities were then analyzed by the TAILS program, giving the values for the structural parameters given in the last column of table 5.

The SCRAP analysis leads to values of the agreement factor and the R-factor which are lower than those for the other two methods indicating that, for these data, the SCRAP program provides the most reasonable estimates of the Bragg intensities and their standard deviations. The standard deviation values are also appreciably less than those given by the integrated intensity analysis. This is therefore an example in which the peak shape is quite well approximated by a Gaussian, as illustrated by the data shown in figure 4, so that the use of a profile fitting technique has advantages over a simple summation of the Bragg intensity.

Table 4

I	V(I)	S.D. OF V(I)
V	-0.58010977E+04	0.81595856E+02
W	0.18237734E+04	0.31276672E+02
LAMBDA	0.10033150E+01	0.40039566E-04
OFFSET	-0.32192368E+02	0.20681435E+00

## INT NO.

1	7218.2	153.5
2	478.7	72.6
3	23350.0	254.6
4	6200.8	140.7
5	115.4	59.8
6	5357.7	133.2
7	3434.9	112.8
8	337.2	66.3
9	14280.8	204.0
10	3182.1	113.2
11	5254.8	137.3
12	3824.3	123.4
13	197.6	72.8
14	8323.3	166.9
15	1546.1	99.4
16	149.3	77.8
17	2432.4	112.6
18	2859.9	120.1
19	172.2	84.7
20	12146.5	202.0
21	3725.8	136.9
22	1295.3	112.7
23	1293.5	116.6
24	89.3	103.2
25	7962.2	181.8

RESIDUAL SUM OF SQUARES = 0.75901294E+03  
 DEGREES OF FREEDOM = 301  
 VARIANCE RATIO = 0.25216370E+01  
 PROBABILITY = 0.0

The same is not true, however, when the peak shape is not well approximated, as illustrated in the following example. This is the  $UO_2$  data set obtained at 1100 °C [4], which we have also analyzed using the SCRAP program. The results are compared with those for the Rietveld and integrated intensity methods in table 6. In this case the estimated standard deviation values given by the Rietveld method are nearly twice those obtained from the integrated intensity method, with the latter giving agreement factor and R-factor values less than half those given by the Rietveld method. In contrast to the previous example the SCRAP program leads to values of the standard deviations and the R-factor which are larger than those given by the integrated intensity analysis, and the agreement factor is also further from 1. These results are therefore consistent with an inadequacy of the peak shape fitting, which is illustrated in figure 5 and arise from deviations from a Gaussian shape function which are present at all temperatures. In these circumstances profile fitting therefore leads to poorer estimates of the Bragg intensities and their standard deviations.

X	OBS Y	FITTED Y	DIFF	RANGE	IS	+ OR -	200	MAX DIFF.	=	190	RATIO =
1815	81	12	69	I				I			I
1825	188	92	96	I				I	*		I
1835	567	417	150	I				I	*		I
1845	1334	1144	190	I				I		*	I
1855	1999	1902	97	I				I			*I
1865	1908	1920	-12	I				I		*	I
1875	988	1177	-189	I*				I*			I
1885	285	438	-153	I	*			I			I
1895	65	99	-34	I		*		I			I
1905	14	14	0	I			*	I*			I

2105	-16	2	-18	I				I	*		I
2115	1	11	-10	I				I	*		I
2125	58	43	15	I				I	*		I
2135	96	101	-5	I				I	*		I
2145	164	139	25	I				I	*		I
2155	105	112	-7	I				I	*		I
2165	29	53	-24	I				I	*		I
2175	-14	15	-29	I				I	*		I
2185	-20	2	-22	I				I	*		I
2195	-29	0	-29	I				I	*		I

3005	233	192	41	I				I	*		I
3015	1149	1196	-47	I				I	*		I
3025	3973	3971	2	I			*	I	*		I
3035	7064	7022	42	I				I	*		I
3045	6668	6613	55	I				I	*		I
3055	3215	3317	-102	I	*			I	*		I
3065	875	886	-11	I				I	*		I
3075	272	126	146	I				I	*		I
3085	135	10	125	I				I	*		I

3535	44	14	30	I				I	*		I
3545	145	129	16	I				I	*		I
3555	558	623	-65	I		*		I	*		I
3565	1540	1553	-13	I			*	I	*		I

Figure 4.

3575	1997	2001	-4	I	*		I
3585	1378	1332	46	I	I	*	I
3595	472	458	14	I	I	*	I
3605	135	81	54	I	I	*	I
3615	73	7	66	I	I	*	I

3705	-22	1	-23	I	*		I
3715	-9	8	-17	I	I	*	I
3725	48	23	25	I	I	*	I
3735	23	37	-14	I	I	*	I
3745	43	30	13	I	I	*	I
3755	4	13	-9	I	I	*	I
3765	-21	3	-24	I	I	*	I
3775	0	0	0	I	I	*	I

4295	26	7	19	I	I	*	I
4305	80	72	8	I	I	*	I
4315	305	392	-87	I	I	*	I
4325	1118	1129	-11	I	I	*	I
4335	1718	1705	13	I	I	*	I
4345	1416	1352	64	I	I	*	I
4355	573	563	10	I	I	*	I
4365	104	123	-19	I	I	*	I
4375	48	14	34	I	I	*	I

4705	24	9	15	I	I	*	I
4715	70	72	-2	I	I	*	I
4725	350	325	25	I	I	*	I
4735	770	798	-28	I	I	*	I
4745	1020	1067	-47	I	I	*	I
4755	779	778	1	I	I	*	I
4765	394	309	85	I	I	*	I
4775	105	67	38	I	I	*	I
4785	32	8	24	I	I	*	I

4835	16	1	15	I	I	*	I
------	----	---	----	---	---	---	---

Figure 4 Concluded

X OBS Y FITTED Y DIF F RANGE IS + OR 200 MAX DIF. 190 RATIO =

X	OBS Y	FITTED Y	DIFF	RANGE	IS	+ OR -	800	MAX DIFF.	=	705	RATIO =
2740	109	8	101	I				I	*		I
2750	233	67	166	I				I	*		I
2760	635	376	259	I				I	*	*	I
2770	1575	1310	265	I				I	*	*	I
2780	3240	2841	399	I				I	*	*	I
2790	4111	3844	267	I				I	*	*	I
2800	3057	3242	-185	I				I	*	*	I
2810	1197	1705	-508	I		*		I	*	*	I
2820	365	559	-174	I			*	I	*	*	I
2830	117	114	3	I				I	*	*	I
2840	28	15	13	I				I	*	*	I
-----											
3130	39	4	35	I				I	*	*	I
3140	41	23	18	I				I	*	*	I
3150	101	87	14	I				I	*	*	I
3160	203	198	5	I				I	*	*	I
3170	288	270	18	I				I	*	*	I
3180	184	220	-36	I				I	*	*	I
3190	112	108	4	I				I	*	*	I
3200	35	32	3	I				I	*	*	I
3210	51	6	45	I				I	*	*	I
3220	10	1	9	I				I	*	*	I
-----											
4330	406	167	239	I				I	*	*	I
4340	1303	1268	35	I				I	*	*	I
4350	4409	5114	-705	I		*		I	*	*	I
4360	10673	10947	-274	I			*	I	*	*	I
4370	12787	12438	349	I				I	*	*	I
4380	7998	7501	497	I				I	*	*	I
4390	2576	2401	175	I				I	*	*	I
4400	463	408	55	I				I	*	*	I
4410	181	37	144	I				I	*	*	I
-----											
5280	1	0	1	I				I	*	*	I

Figure 5.

5290	-61	1	-62	1	I	I	I
5300	1	4	-3	I	I	I	I
5310	9	8	1	I	I	I	I
5320	29	8	21	I	I	I	I
5330	-14	4	-18	I	I	I	I
5340	-8	1	-9	I	I	I	I
5350	-41	0	-41	I	I	I	I

6110	32	44	-12	I	I	I	I
6120	299	353	-64	I	I	I	I
6130	1271	1391	-120	I	I	I	I
6140	2534	2686	-152	I	I	I	I
6150	2725	2546	179	I	I	I	I
6160	1366	1185	181	I	I	I	I
6170	255	271	-16	I	I	I	I
6180	51	30	21	I	I	I	I

6680	49	14	35	I	I	I	I
6690	129	131	-2	I	I	I	I
6700	625	611	14	I	I	I	I
6710	1444	1452	-8	I	I	I	I
6720	1788	1755	33	I	I	I	I
6730	1088	1079	9	I	I	I	I
6740	262	338	-76	I	I	I	I
6750	48	54	-6	I	I	I	I
6760	-10	4	-14	I	I	I	I

6860	-1	0	-1	I	I	I	I
6870	-31	2	-33	I	I	I	I
6880	39	15	24	I	I	I	I
6890	30	47	-17	I	I	I	I
6900	85	76	9	I	I	I	I
6910	67	64	3	I	I	I	I
6920	23	28	-5	I	I	I	I
6930	-17	6	-23	I	I	I	I
6940	-30	1	-31	I	I	I	I

7570	134	13	121	I	I	I	I
------	-----	----	-----	---	---	---	---

Figure 5. Concluded.

Table 5. Results of Different Refinements of UO<sub>2</sub> Data at R.T.

	<u>Profile</u>	<u>Intensity</u>	<u>SCRAP</u>
n <sub>o</sub> (rel. occ.)	1.005 (14)	0.977 (32)	1.001 (21)
B <sub>u</sub> (Å <sup>2</sup> )	0.254 (32)	0.246 (75)	0.262 (46)
B <sub>o</sub> (Å <sup>2</sup> )	0.541 (38)	0.522 (82)	0.520 (50)
R(F <sup>2</sup> ) (%)	4.03	-	-
R(I) (%)	-	3.92	3.33
A <sub>p</sub>	1.60	-	-
A <sub>B</sub>	-	2.92	1.36
Scale (rel)	1.0000	1.0139	0.9977

Table 6. Results of Different Refinements for UO<sub>2</sub> data at 1100 °C

	<u>Profile</u>	<u>Intensity</u>	<u>SCRAP</u>
B <sub>u</sub> (Å <sup>2</sup> )	1.31 (9)	1.40 (5)	1.30 (7)
B <sub>o</sub> (Å <sup>2</sup> )	2.19 (11)	2.20 (6)	2.22 (10)
R(F <sup>2</sup> ) (%)	2.57	1.13	
R(I) (%)	-	-	1.76
A <sub>p</sub>	2.51	-	-
A <sub>B</sub>	-	0.95	0.89

Finally, we have also analyzed a set of data from Al<sub>2</sub>O<sub>3</sub>, for which a certain amount of peak overlap occurs, as illustrated in figure 6. (Beyond 2θ = 92° peak overlap becomes more severe and so further background points are observed.) The results given by the SCRAP program are shown in table 7. In this case a few pairs of reflections occur within 0.1 or 0.2 of each other and the intensities of these cannot therefore be estimated accurately, as shown by the large standard deviation values and correlation factors. Examples of the latter are shown in the section of the correlation matrix is given in table 8. Results from the least squares analysis of these intensities are compared with those given by Rietveld and integrated intensity analyses in table 9. Because of overlap 40 Bragg reflections were included in the integrated intensity, but as only 18 separate observations, 7 of which are multiple leaks containing up to 8 Bragg reflections. In this case the integrated intensity and SCRAP analyses gave similar results, but as would be expected the standard deviations are appreciably larger for the integrated intensity analysis. We have not been able to obtain a stable refinement using the Rietveld method, even with the starting values for the parameters set very close to

those given by the other methods. This is illustrated by the results given in table 7 following one cycle of refinement only. Although the standard deviation values are already comparable to those given by the SCRAP analysis the value of  $B_0$  is negative and differs significantly from the values given by the other methods. What is perhaps more significant is the fact that when we keep the temperature factors fixed at their starting values the Rietveld method still gives a solution with identical R factor values. This is indicative of an extremely flat minimum of the type commented on by Young [5]. In contrast, the SCRAP program is well behaved and converges quickly to a good solution.

Table 7. Results of Different Refinements of  $Al_2O_3$  Data

	<u>PROFILE</u>	<u>INTENSITY</u>	<u>SCRAP</u>
$N_I$	43	18 (40)	43
$x_{Al}$	0.3524 (4)	0.3528 (5)	0.3529 (3)
$x_O$	0.5571 (4)	0.5559 (7)	0.5559 (4)
$B_{Al}$ ( $\text{\AA}^2$ )	0.38 (9)	0.23 (15)	0.12 (8)
$B_0$ ( $\text{\AA}^2$ )	-0.13 (5)	0.27 (7)	0.22 (5)
R(I) (%)	8.89	2.16	5.34
$A_p$	3.82	-	-
$A_B$	-	4.32	1.38

## 6. Conclusions

Our analysis indicates that all standard deviation values which have been derived by the Rietveld Profile Refinement Method are wrong and that no simple modification of the method is possible to overcome this problem. If the peak shape is well determined it is possible that the standard deviations are underestimated, particularly if appreciable peak overlap occurs.

The SCRAP method, outlined in this paper, provides reliable estimates of the structural parameters and their standard deviations, which are superior to those given by an integrated intensity method if the peak shape is well determined. Comparison with the Rietveld method indicates that the profile fitting is both faster and more stable with the SCRAP method.

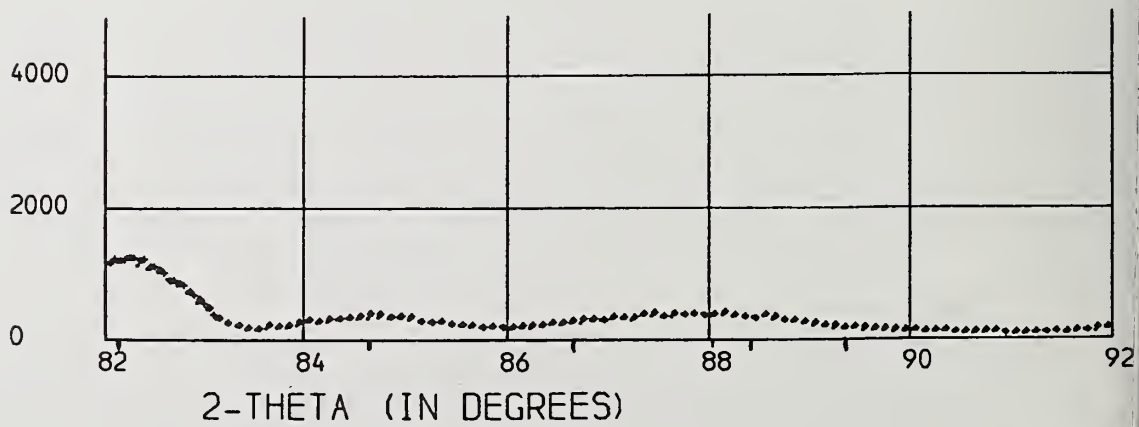
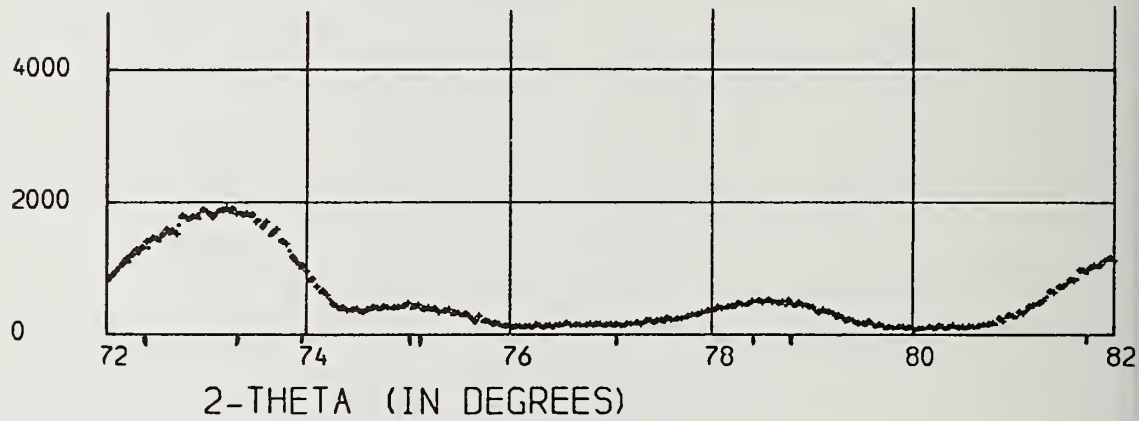
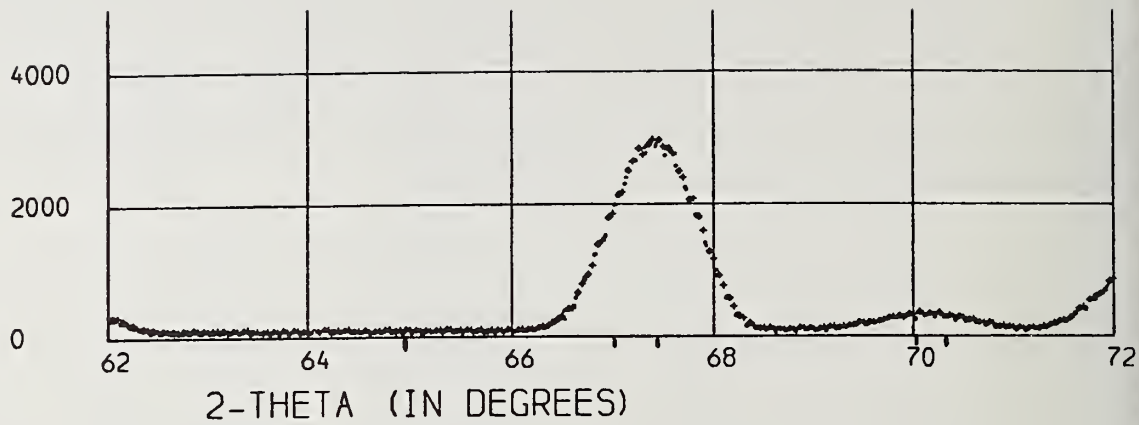


Figure 6.

Table 8

U	0.52210477E+05	0.17139536E+04
V	-0.32285629E+05	0.15905103E+04
W	0.65861289E+04	0.35240942E+03
OFFSET	-0.17595169E+02	0.96862018E-01

INT NO.

1	544.2	65.6
2	7653.5	168.9
3	69147.7	482.1
4	135.8	53.6
5	8919.1	182.0
6	34440.0	344.4
7	3775.6	127.8
8	0.0	234.6
9	1975.0	247.4
10	8428.5	182.1
11	38477.1	366.0
12	2918.0	121.0
13	42.0	69.7
14	4298.2	446.5
15	24755.3	514.7
16	2453.6	279.6
17	199.8	270.3
18	12473.2	268.2
19	19045.7	417.5
20	1281.9	345.9
21	2067.4	1082.6
22	1732.6	1011.5
23	733.6	108.6
24	5382.0	292.6
25	246.4	259.9
26	1633.4	500.9
27	15267.3	545.2
28	4198.8	156.8
29	2550.8	173.6
30	4379.2	536.8
31	417.5	562.3
32	676.1	189.5
33	3750.1	2584.3
34	4.7	3950.9
35	0.0	8655.4
36	4990.5	7372.4
37	13566.7	446.1
38	9498.8	2242.4
39	851.9	2554.3
40	0.0	801.9
41	2755.1	605.6
42	22670.9	922.4
43	4101.4	2073.8

RESIDUAL SUM OF SQUARES = 0.16787471E+04  
DEGREES OF FREEDOM = 509  
VARIANCE RATIO = 0.32981272E+01  
PROBABILITY = 0.0

Table 9

	31	32	33	34	35	36	37	38	39	40
31	-1.000	-0.025	-0.008	0.009	-0.002	-0.006	0.000	-0.005	0.024	-0.000
32	-0.025	1.000	-0.082	0.039	-0.032	0.015	-0.000	-0.001	0.006	-0.000
33	-0.008	-0.082	1.000	-0.473	0.390	-0.210	0.002	-0.000	-0.008	0.000
34	0.009	0.039	-0.473	1.000	-0.933	0.578	-0.006	0.004	0.006	-0.000
35	-0.002	-0.032	0.390	-0.933	1.000	-0.707	0.007	-0.006	0.002	-0.000
36	-0.006	0.015	-0.210	0.578	-0.707	1.000	-0.011	0.012	-0.015	0.000
37	0.000	-0.000	0.002	-0.006	0.007	-0.011	1.000	-0.989	0.846	-0.000
38	-0.005	-0.001	-0.000	0.004	-0.006	0.012	-0.989	1.000	-0.905	0.000
39	0.024	0.006	-0.008	0.006	0.002	-0.015	0.846	-0.905	1.000	-0.000
40	-0.027	-0.007	0.009	-0.007	-0.001	0.015	-0.817	0.880	-0.998	1.000
41	0.021	0.006	-0.009	0.008	-0.002	-0.009	0.299	-0.339	0.470	-0.000
42	-0.003	-0.001	0.001	-0.001	-0.000	0.003	-0.172	0.194	-0.268	0.000
43	0.006	0.002	-0.002	0.002	-0.000	-0.003	0.154	-0.175	0.244	-0.000
44	-0.011	-0.003	0.005	-0.005	0.002	0.004	-0.112	0.128	-0.185	0.000
45	-0.040	-0.010	0.016	-0.017	0.007	0.009	0.057	-0.057	0.049	-0.000
46	0.051	0.014	-0.022	0.023	-0.010	-0.013	-0.034	0.028	-0.000	-0.000
47	-0.019	-0.005	0.009	-0.009	0.004	0.005	0.025	-0.024	0.018	-0.000

We are grateful to Mr. G. G. Proudfoot, Dr. M. W. Thomas and Dr. B. T. M. Willis providing us with unpublished experimental data.

#### References

- [1] Rietveld, H. M., *Acta Cryst.* 22, 151-152 (1967); and *J. Appl. Cryst.* 2, 65-71 (1969).
- [2] Sakata, M. and Cooper, M. J., *J. Appl. Cryst.* (1979), in the press.
- [3] Wright, A. F. and Fender, B. E. F., *J. Phys. C.* 10, 2261-2267 (1977).
- [4] Albinati, A., Cooper, M. J., Rouse, K. D., Thomas, M. W. and Willis, B. T. M. *Submitted to Acta Cryst.* (1979).

#### Discussion

Comment (Sabine): I do not think that you can state that the Rietveld method underestimates e.s.d.'s. All you can say is that the two methods give different results in some cases.

Response (Cooper, Sakata, and Rouse): I can state that the Rietveld method provides reliable estimates for the standard deviations of the structural parameters. These may be underestimates or overestimates of the best values, depending on the relative goodness of fit of the peak shape function and the Bragg intensities and also on the degree of peak overlap. It is probable that these factors will lead to underestimation of the standard deviations for most neutron diffraction data.

ment (Prince): The individual data points within the same Bragg peak are not statistically correlated. The Rietveld procedure is in fact mathematically basically correct. A procedure which refines integrated intensities, particularly if profile and crystallographic parameters are treated separately, neglects various cross correlations between the intensities of overlapping peaks and between profile and structural parameters. If these are correctly included, the procedure becomes substantially equivalent to the Rietveld procedure.

sponse (Cooper et al.): Individual observed data are of course not correlated, but in this case the residuals obtained from their comparison with calculated data are. This means that the Rietveld method is in fact not statistically correct. Since the expression for calculated intensity is separable into two terms, each of which depends on one type of parameter only, correlation between the two types of parameter and between different Bragg peaks can and is, taken into account correctly in the SCRAP method. It is in fact the Rietveld method which fails to do this, which is why no one has been able to give a valid justification of the method.



STRUCTURAL REFINEMENT OF NEUTRON AND X-RAY DATA BY THE RIETVELD METHOD:  
APPLICATION TO  $Al_2O_3$  AND  $BiVO_4$

D. E. Cox and A. R. Moodenbaugh  
Brookhaven National Laboratory<sup>1</sup>  
Upton, New York 11973

A. W. Sleight and H.-Y. Chen  
E. I. du Pont de Nemours and Company  
Wilmington, Delaware 19198

The application of the Rietveld refinement technique to neutron and x-ray powder data from standard samples of  $Al_2O_3$  is described. The results are compared with those obtained by conventional refinements of the corresponding integrated intensities, and also with x-ray single crystal data. The Rietveld technique has also been used to analyze neutron and x-ray powder data in a structural study of  $BiVO_4$ . Since V has a very small neutron scattering amplitude, the x-ray data allow a more accurate determination of the V position to be made.

The use of the Rietveld technique for refinement of powder diffraction data has been reviewed in these proceedings by Hewat [1]<sup>2</sup> and Young [2] for the case of neutrons and x-rays, respectively. The neutron technique is now firmly established and has been used in hundreds of structural investigations, but the x-ray technique is still in its infancy, and a number of fundamental problems remain. Chief among these are the lack of a suitable function to describe the peak shape, and where to truncate the peak tails. It may also be necessary to make allowance for preferred orientation.

The possibility of combining the powerful Rietveld technique with the better resolution of x-ray diffractometers provides a powerful stimulus for overcoming these limitations. In addition, the availability of monochromated radiation from synchrotron sources in the next few years offers the prospect of obtaining very high resolution powder data with peak profiles which are much closer to Gaussian.

<sup>1</sup>This work is supported in part by the Department of Energy under contract number EY-76-C-02-0016.

<sup>2</sup>Figures in brackets indicate the literature references at the end of this paper.

One approach to the analysis of x-ray powder data is described in these proceedings by Parrish and Huang [3]. In this, integrated intensities can be obtained by deconvolution of powder data with the aid of measured values of the full profiles of a number of standard specimens. As far as is known, this technique has not yet been applied in structural refinement. A more common current approach, as described by Young [2], is to modify the Rietveld program for neutron refinement. In the present work, this has been done as simply as possible. A comparison is made between the results obtained in refinements of neutron and x-ray data for  $\text{Al}_2\text{O}_3$ , which is a commonly used standard, and  $\text{BiVO}_4$ , which undergoes an interesting ferroelastic phase transition at 255 °C [4].

The neutron data from  $\text{Al}_2\text{O}_3$  were collected for an intercomparison project of the Neutron Diffraction Commission of the International Union of Crystallography [5]. The sample was a sintered pellet made from Linde A grade  $\text{Al}_2\text{O}_3$  [6] about 1.4 cm in diameter and 1.8 cm in length weighing 10.5 g. Pyrolytic graphite was used as monochromator in the (002) reflection setting to give neutrons of wavelength 1.424 Å, and as an analyzer in the (004) setting. Higher order components of wavelength were removed with a graphite filter. Collimation was 20' in-pile, 40' monochromator-to-sample, 40' sample-to-analyzer, and 10' analyzer-to-counter. Data were collected at 0.05° steps over a 2θ range of 22.0 - 124.4° with a counting time of 38 seconds per step. Refinement was carried out with a modified version [7] of the Rietveld program [8] with individual isotropic temperature factors. Scattering amplitudes were taken as 0.345 and  $0.580 \times 10^{-12}$  cm for Al and O, respectively. The results are summarized in table 1, and the fitted profile is shown in figure 1. Agreement is very good, as seen by comparison of  $R_{\text{WP}}$ , the weighted profile R factor, with  $R_{\text{E}}$ , the expected, or statistical, value (for definitions, see reference 7).

The x-ray data were collected on a General Electric XRD-5 diffractometer with a fine-focus Cu target (take-off angle 6°) and a bent graphite monochromator of normal mosaic spread 0.4° in the diffracted beam tuned for Cu Kβ radiation. The sample consisted of a pressed pellet of NBS 0.3 μm  $\text{Al}_2\text{O}_3$  powder which had been sintered overnight at 1000 °C. Collimation consisted of a standard 1° horizontal divergence collimator with medium resolution Soller slits in the incident beam, and medium resolution Soller slits and an 0.05° receiving slit in the diffracted beam. Data were collected at 0.02° steps over selected ranges of 2θ between 22° and 136° with counting times ranging between 20 and 80 seconds according to the intensity of the peak.

A scan of the (116) peak is shown in figure 2a, and for comparison, the corresponding neutron scan in figure 2b. A Gaussian peak gives a good fit to the latter as shown by the solid line, with  $R_{\text{WP}} = 0.038$  ( $R_{\text{E}} = 0.031$ ). The x-ray data in figure 2a were fitted to three Lorentzian functions of the type  $A/[1+C(\Delta 2\theta)^2]^n$ ; a simple Lorentzian  $L(n = 1)$ , an intermediate  $IL(n = 1.5)$ , and a modified  $ML(n = 2)$ . The results are summarized in table 2, and it can be seen that the quality of the fit is not as good as in the neutron case. The intermediate function gives the best fit over this range of data, which is about five full-widths at half-maximum (FWHM), and is shown as a solid line in figure 2a.

Table 1. Results of structure refinements for  $Al_2O_3$ .  $N(hkl)$  is the number of reflections used in the refinement. Other quantities are defined in text or ref. [7].  $R_I$  and  $R_{WP}$  are based on point-by-point or integrated intensities as appropriate. A value of  $0.04 \text{ \AA}^2$  has been added to the neutron B's to allow for the effects of absorption as described by Hewat [9].

Parameter	Neutron (1.424 Å)		X-ray (1.392 Å)		X-ray Crystal [12]
	Profile	Integrated	Profile	Integrated	
Al:z	0.35221(8)	0.3521(2)	0.35200(7)	0.3522(2)	0.35219(1)
Al:B(Å <sup>2</sup> )	0.22(2)	0.26(5)	0.40(1)	0.24(6)	----
O:x	0.30636(9)	0.3060(2)	0.3064(3)	0.3066(8)	0.30633(5)
O:B(Å <sup>2</sup> )	0.23(1)	0.25(3)	0.51(2)	0.15(8)	----
G(rad <sup>-2</sup> )	----	----	0.195(9)	0.19(3)	----
a(Å)	4.7640(1)	----	4.75855(2)	----	----
c(Å)	13.0091(3)	----	12.9906(1)	----	----
U(deg <sup>2</sup> )	1.42(11)	----	0.0084(12)	----	----
V(deg <sup>2</sup> )	-1.62(14)	----	0.0117(19)	----	----
W(deg <sup>2</sup> )	0.55(4)	----	0.0073(6)	----	----
$R_I$	0.018	0.019	0.038	0.053	----
$R_{WP}$	0.071	0.024	0.149	0.082	----
$R_E$	0.060	----	0.111	----	----
N(hkl)	60	60	69	71	----

Table 2. Results of least-squares fits to the data in figure 2. Background was determined well away from the peak, and was not a variable in the refinement. NO is the number of observations.

	X-ray (1.392 Å)			Neutron (1.424 Å)
	L	IL	ML	G
Peak amplitude	2224(76)	2054(53)	1958(70)	4359(40)
Peak position (deg)	51.494(2)	51.494(2)	51.493(2)	52.77(1)
FWHM (deg)	0.100(3)	0.121(3)	0.132(4)	0.312(2)
Background	←————— 21.3 —————→			35.3
$R_{WP}$	0.106	0.086	0.124	0.038
$R_e$	←————— 0.041 —————→			0.031
NO	←————— 31 —————→			32

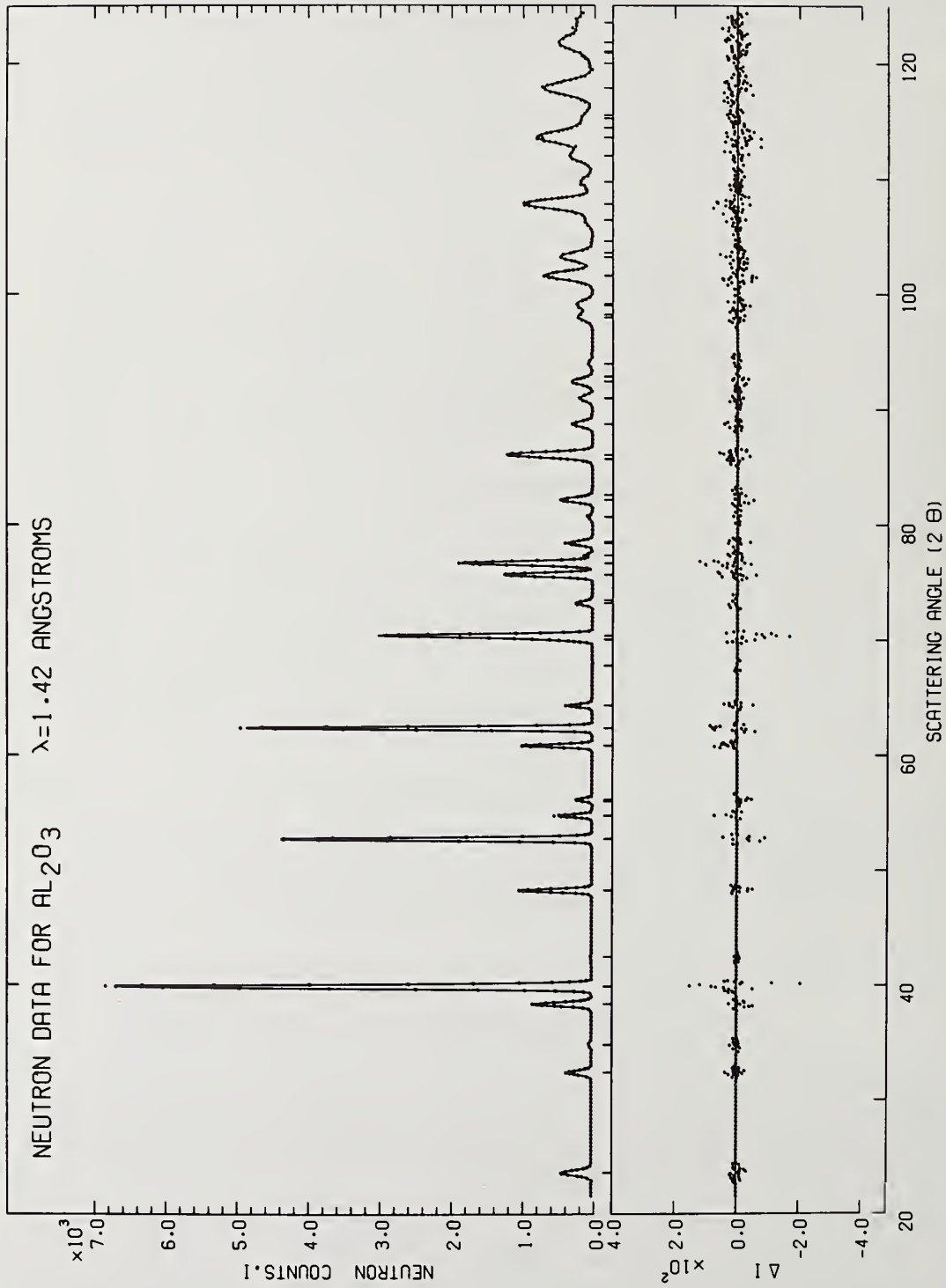


Figure 1. Neutron profile fit and difference pattern for  $\text{Al}_2\text{O}_3$

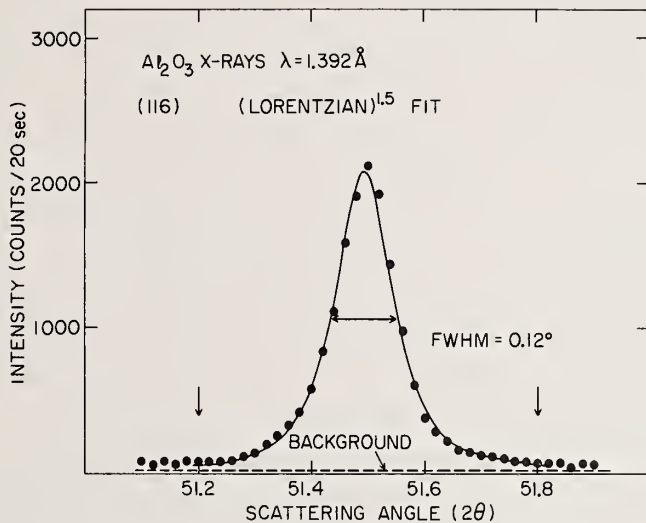


Figure 2a. Diffraction data for the [116] reflection of  $\text{Al}_2\text{O}_3$ : x-rays Cu K $\beta$ . Solid lines are fitted curves as described in text.

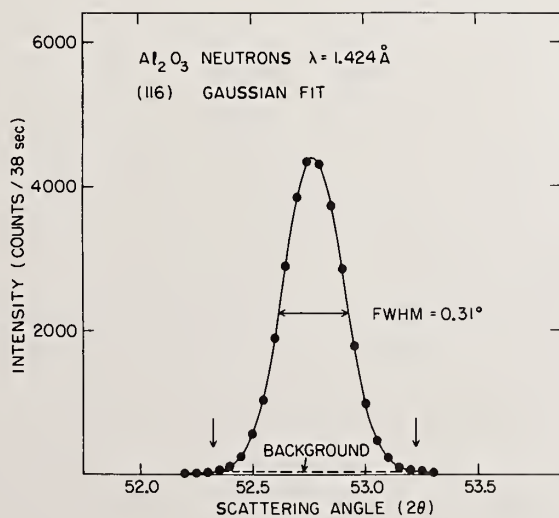


Figure 2b. Diffraction data for the [116] reflection of  $\text{Al}_2\text{O}_3$ : Neutrons. Solid lines are fitted as described in text.

A modified version of the Rietveld program described previously [10] was used to refine the x-ray data, which were fitted to the intermediate Lorentz function over a range of two FWHM's on each side. Scattering factors for  $Al^{3+}$  [11] and  $O^{2-}$  [12] corrected for the real dispersion term were used. At present the program has not been modified to incorporate the imaginary dispersion term. The initial fit was quite encouraging ( $R_{WP} = 0.165$ ,  $R_E = 0.066$ ), but the intensities showed unmistakable evidence of (001) preferred orientation. In Rietveld's original program [8], provision is made for a correction of the type  $I_{corr} = I_{obs} \exp(-G\phi^2)$  where  $\phi$  is the acute angle between the scattering vector and the normal to the crystallites.  $G$  is the preferred orientation parameter and is a measure of the half-width of the assumed Gaussian distribution of the normals about the preferred orientation direction, which is along the axis of the cylindrical samples usually used in powder neutron diffraction. This expression is not appropriate for flat-plate x-ray samples, but inspection of the observed and calculated intensities showed as exponential-type dependence which could be approximated by a slightly modified expression of the type  $I_{corr} = I_{obs} \exp[-G(\pi/2 - \phi)^2]$ . With this correction, most of the systematic discrepancies disappeared and  $R_{WP}$  showed a significant decrease to 0.149. This is illustrated in figure 3, which shows the ratio of the observed and calculated intensities for several of the stronger peaks with and without the correction.

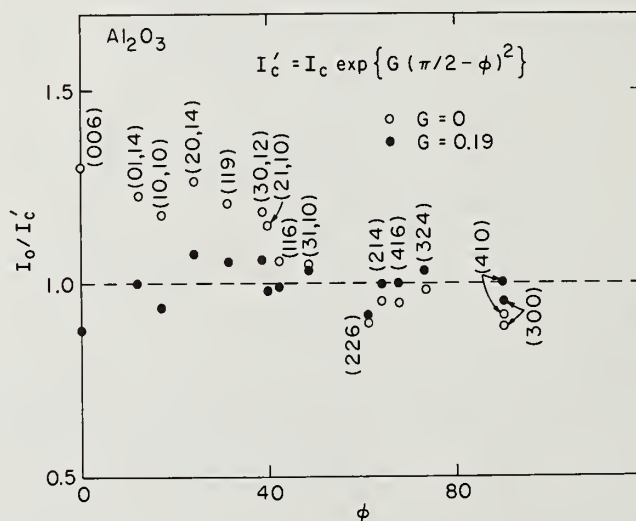


Figure 3. Ratio of observed and calculated integrated x-ray intensities for for  $Al_2O_3$  as a function of  $\phi$ , the angle between the normal to the plane  $hkl$  and the  $[001]$  axis. Open circles--no correction. Closed circles--preferred orientation correction applied.

The results of the refinement are summarized in table 1, and the profile fit is shown in figure 4, with all intensities normalized to a counting time of 40 seconds.

Integrated neutron and x-ray intensities were determined and refined with a program which allows overlapping peaks to be included. The final results are also summarized in table 1, together with some recent x-ray single crystal results [13].

There is agreement among the various sets of positional parameters to within 1-2 esd's. However, the esd's derived from the integrated intensities are a factor of 2-3 higher than those from the profile refinements. This subject is discussed in more detail by Cooper et al. [14] elsewhere in the proceedings.

The x-ray profile temperature factors are clearly systematically high by a factor of two or so. Since the integrated values are in reasonable agreement with the neutron values, it is likely that the problem lies in the peak shape function rather than in other possible sources of error such as surface roughness, choice of scattering factors of the Lorentz-polarization correction.

The difference between the neutron and x-ray lattice parameters determined in the profile refinements can be largely accounted for by a small error in the neutron wavelength of about 0.13 percent. The apparent precision of the x-ray values is rather unexpected, since no attempt was made to allow for systematic deviations in peak positions as a function of  $2\theta$  or aberrations in peak shape. This precision could be quite valuable in investigations of phase transitions or thermal expansion behavior.

The observed and fitted values of peak FWHM's are shown as a function of  $2\theta$  in figure 5 for the neutron and x-ray profile refinements. The usual expression  $(FWHM)^2 = U \tan^2 \theta + V \tan \theta + W$  has been employed in both cases.

The x-ray Rietveld technique has been used in conjunction with the neutron technique in a structural study of  $\text{BiVO}_4$  [15]. This has monoclinic symmetry at room temperature and undergoes a ferroelastic structural transition at 255 °C to a tetragonal scheelite-type structure. The neutron scattering amplitude of V is small, about  $-0.05 \times 10^{-12}$  cm, and the V shifts from the ideal scheelite positions are rather poorly determined ( $\sim 0.06$  Å,  $\sigma = 0.03_5$  Å) in the neutron refinement. An x-ray refinement was accordingly undertaken in order to obtain a more accurate value. A comparison of the neutron and x-ray results is given in table 3, and the fitted profiles are shown in figures 6 and 7. Once again, in the initial stages of the x-ray refinement systematic discrepancies were observed which indicate (001) preferred orientation. Inclusion of a correction of the form described earlier gave a much-improved fit, with  $R_{wp}$  decreasing from 0.223 to 0.178.

From table 3 it can be seen that the Bi positional parameters are equally well determined in the two refinements, while those of vanadium and oxygen are a factor of about five better determined in the x-ray and neutron refinements, respectively, as is to be expected from the relative scattering amplitudes. Agreement is generally within 2-3 esd's. Although these may be underestimated as discussed by Cooper et al. [14], it seems likely that part of the disagreement lies in systematic errors in the x-ray analysis. This certainly appears to be the case for the temperature factors, where agreement is very poor. It is to be noted that the neutron results, including temperature factors, are in better agreement (1-2 esd's) with those of an independent neutron study by David et al. [16].

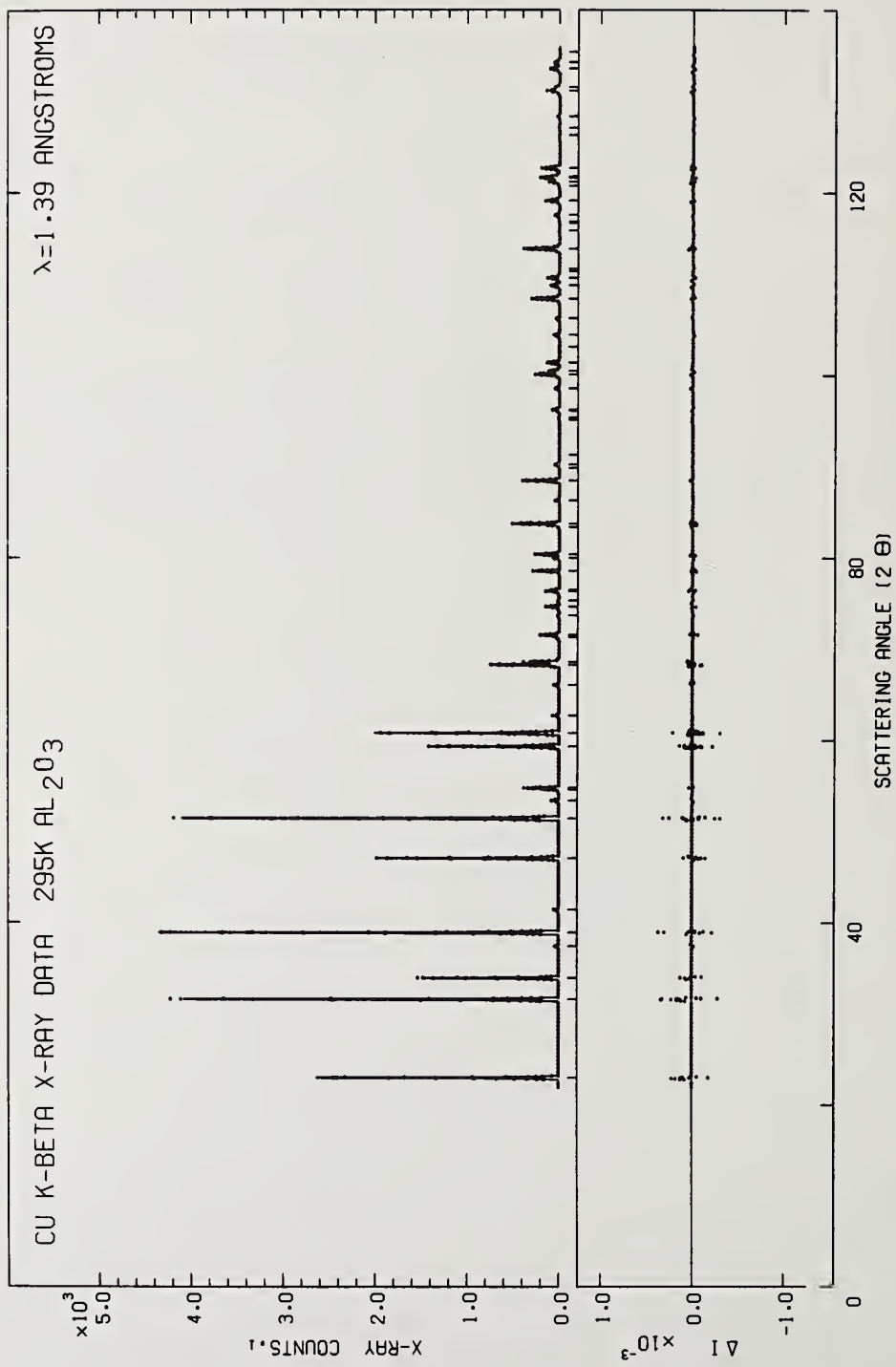


Figure 4. X-ray profile fit and difference pattern for Al<sub>2</sub>O<sub>3</sub>.

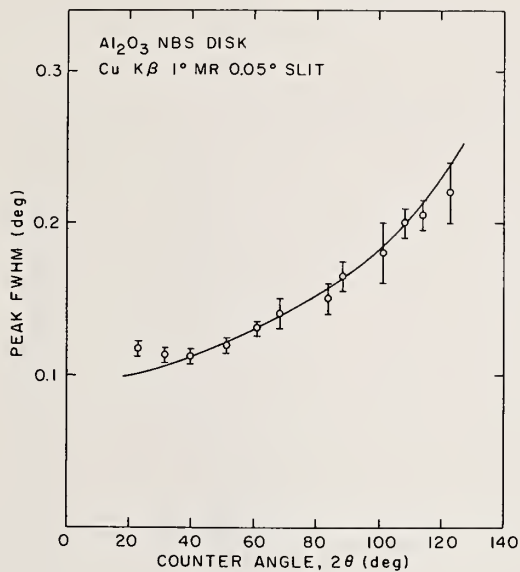


Figure 5a. Variation of FWHM of Al<sub>2</sub>O<sub>3</sub> diffraction peaks as a function of scattering angle 2θ for the experimental conditions listed: x-rays, Cu Kβ.

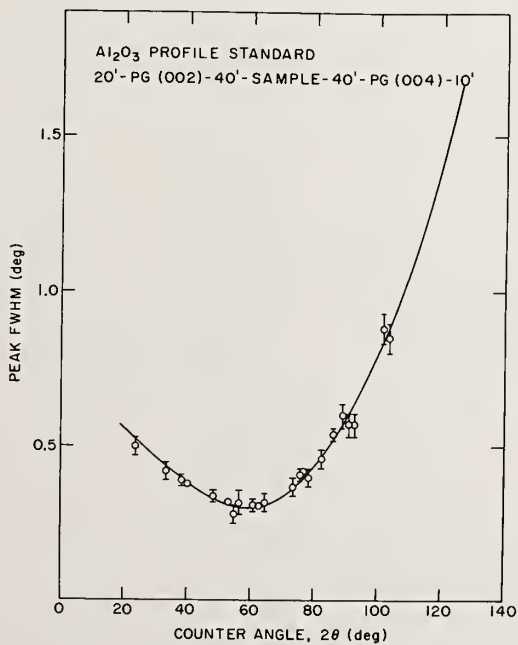


Figure 5b. Variation of FWHM of Al<sub>2</sub>O<sub>3</sub> diffraction peaks as a function of scattering angle 2θ for the experimental conditions listed: neutrons, λ = 1.424 Å.

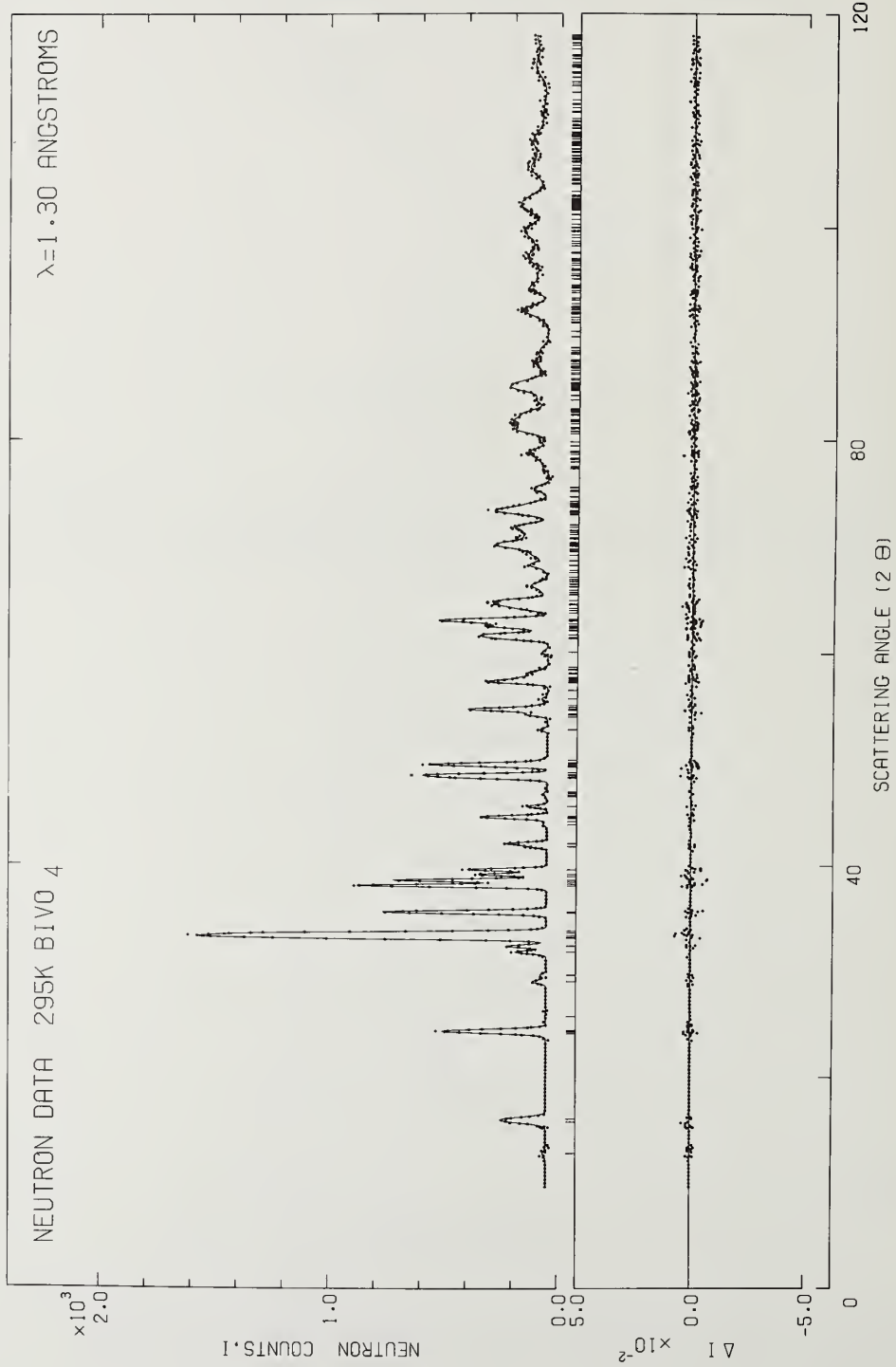


Figure 6. Neutron profile fit and difference pattern for  $\text{BiVO}_4$  at 295 K. Scattering amplitudes taken as 0.852, -0.052 and  $0.580 \times 10^{-12}$  cm for Bi V and O, respectively.

amplitudes taken as 0.852, -0.052 and 0.580 x 10

cm 101 51

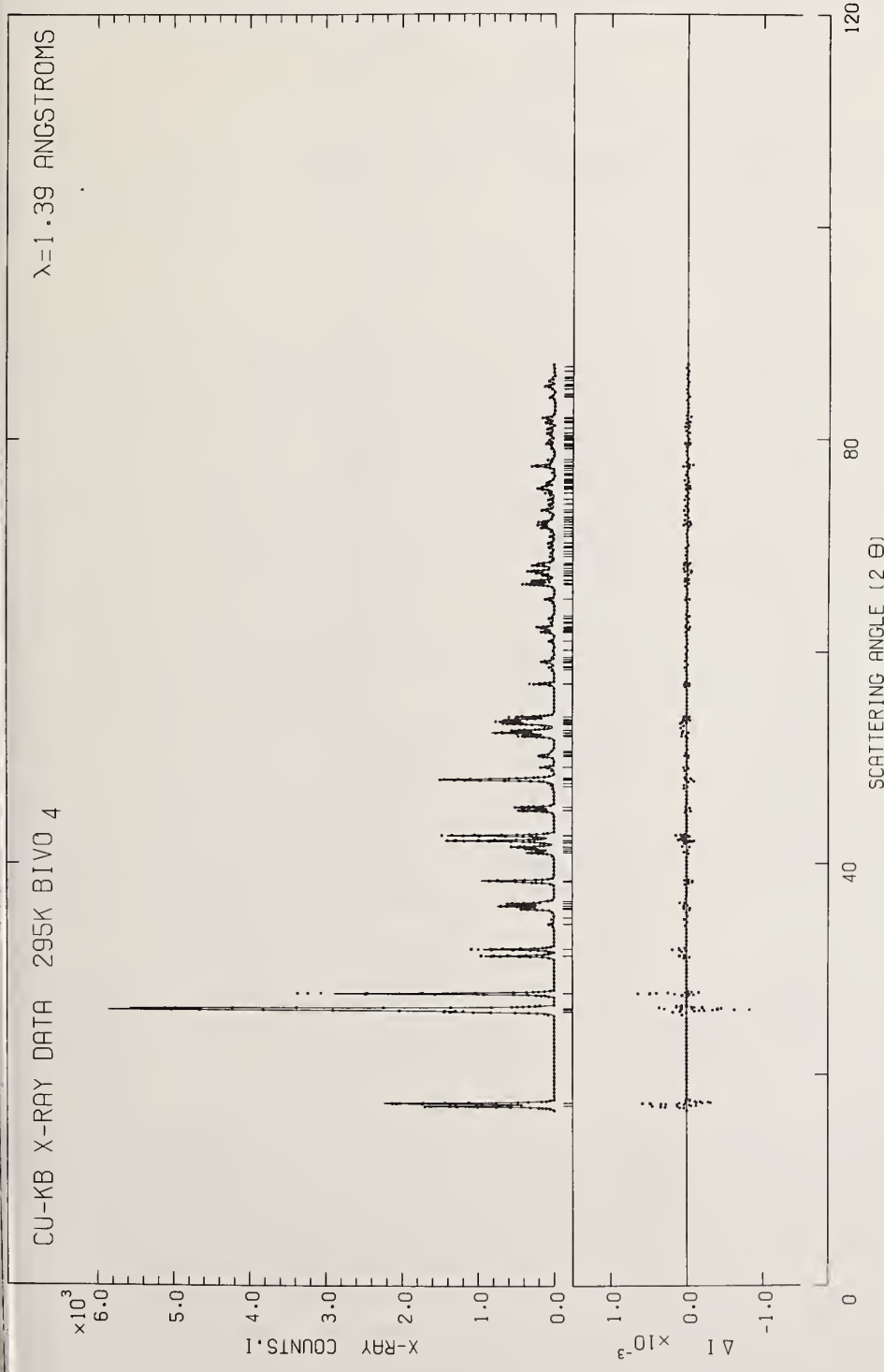


Figure 7. X-ray profile fit and difference pattern for  $\text{BiVO}_4$  at 295 K. Scattering factors for  $\text{Bi}^{3+}$  and  $\text{V}^{5+}$  taken from reference 11, and for  $\text{O}^{2-}$  from reference [12]. Peaks have been fitted over a range of 2.5 FWHM's.

Table 3. Structural parameters for  $\text{BiVO}_4$  at 295 K from Rietveld refinement of neutron and x-ray powder data.  $N(hkl)$  is the number of reflections used in the refinement.

	Neutron (1.302 Å)	X-ray (1.392 Å)
Bi:z	0.6335(2)	0.6341(2)
Bi:B(Å <sup>2</sup> )	0.80(3)	0.36(2)
V:z	0.130(3)	0.1315(6)
V:B(Å <sup>2</sup> )	-0.3(4)	0.13(6)
0(1):x	0.1465(4)	0.143(3)
0(1):y	0.5077(4)	0.512(3)
0(1):z	0.2082(2)	0.211(1)
0(1):B(Å <sup>2</sup> )	0.85(4)	1.9(2)
0(2):x	0.2606(5)	0.252(3)
0(2):y	0.3810(4)	0.362(4)
0(2):z	0.4493(2)	0.446(1)
0(2):B(Å <sup>2</sup> )	0.85(4)	2.0(2)
G(rad <sup>-2</sup> )	----	0.30(1)
a(Å)	5.1935(3)	5.1956(1)
b(Å)	5.0898(3)	5.0935(1)
c(Å)	11.6972(8)	11.7044(2)
γ(deg)	90.387(4)	90.383(1)
U(deg <sup>2</sup> )	2.53(6)	0.049(7)
V(deg <sup>2</sup> )	-2.03(6)	-0.020(6)
W(deg <sup>2</sup> )	0.495(13)	0.0165(11)
R <sub>I</sub>	0.028	0.077
R <sub>WP</sub>	0.123	0.178
R <sub>E</sub>	0.117	0.097
N(hkl)	391	154

There is once again a small systematic difference between the neutron and x-ray lattice parameters which reflects an 0.05 percent error in the neutron wavelength. The two values of the monoclinic angle  $\gamma$ , which is independent of wavelength, are in excellent agreement. The precision of the x-ray values is again quite striking.

From the above comparisons, one can conclude that the refinement of x-ray data by the Rietveld technique can give useful results for the positional parameters in spite of the problems of peak shape, truncation, and aberrations. However, further work in this area is obviously necessary. One useful approach is suggested by the work of Wertheim

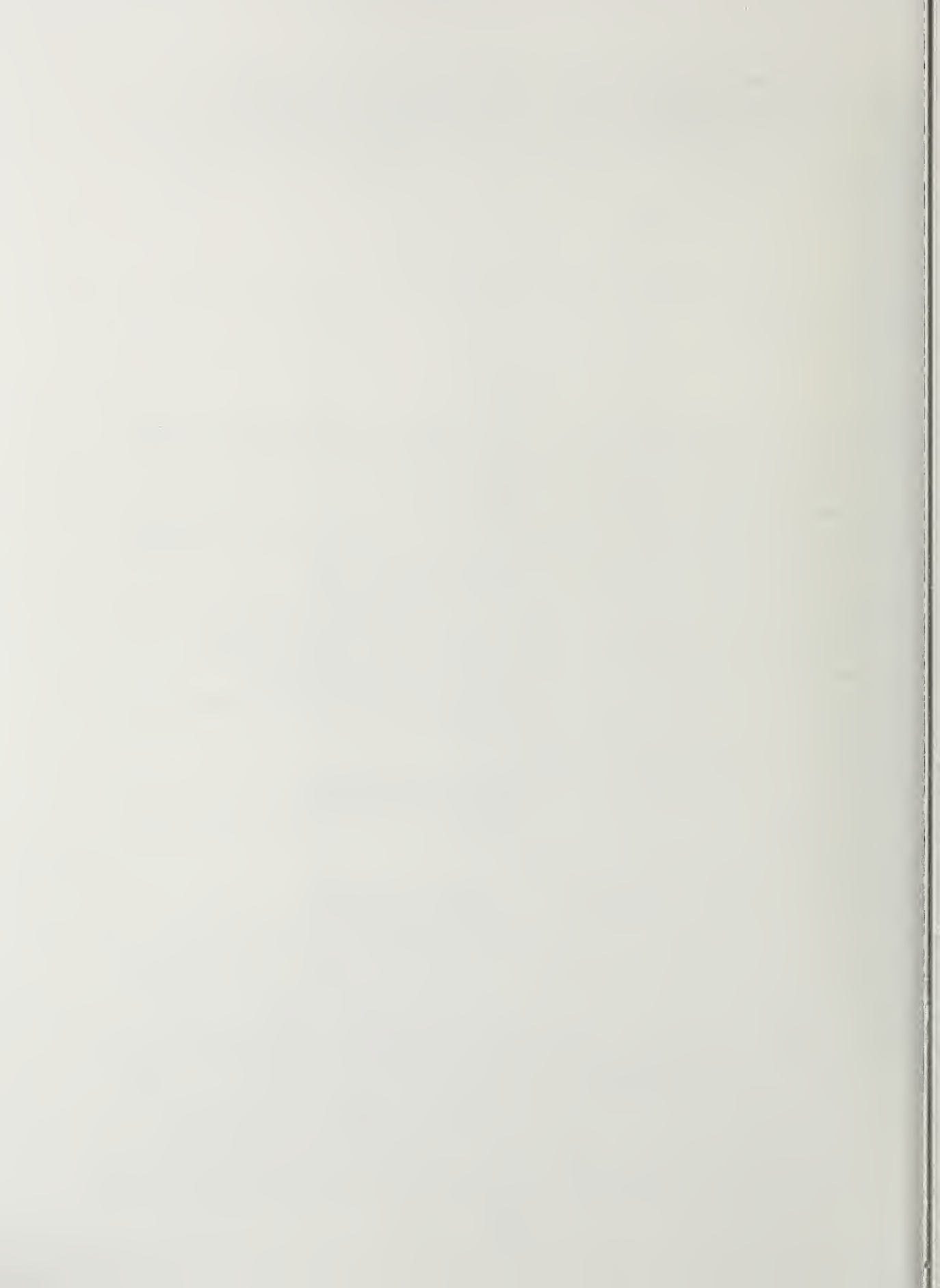
et al. [17], in which a Voigt line shape is approximated by a linear combination of Gaussian and Lorentzian components. Such an approximation gives a significantly better fit to the data in figure 2a,  $R_{WP}$  decreasing to 0.070. It is also necessary to obtain more rigorous expressions for the angular dependence of the FWHM, and for preferred orientation.

---

We would like to thank L. D. Calvert for sending us single crystal data on  $Al_2O_3$  prior to publication.

#### References

- [1] Hewat, A. W., Symposium on Accuracy in Powder Diffraction, National Bureau of Standards, Gaithersburg, Maryland, June 11-15, 1979.
- [2] Young, R. A., Symposium on Accuracy in Powder Diffraction, National Bureau of Standards, Gaithersburg, Maryland, June 11-15, 1979.
- [3] Parrish, W. and Huang, T. C., Symposium on Accuracy in Powder Diffraction, National Bureau of Standards, Gaithersburg, Maryland, June 11-15, 1979.
- [4] Bierlein, J. D. and Sleight, A. W., Solid State Commun. 16, 69-70 (1975).
- [5] Andresen, A. F., Hewat, A. W., and Sabine, T. M., Conference on Diffraction Profile analysis, Cracow, Poland August 1978. J. Appl. Cryst. (to be published).
- [6] Andresen, A. F. and Sabine, T. M., J. Appl. Cryst. 10, 497-501 (1977).
- [7] Hewat, A. W., U.K. Atomic Energy Authority Research Group Report RRL 73/897 (1973).
- [8] Rietveld, H. M., J. Appl. Cryst. 2, 65-71 (1969).
- [9] Hewat, A. W., Acta Cryst A35, 248 (1979)
- [10] Khattak, C. P. and Cox, D. E., J. Appl. Cryst 10, 405-411 (1977).
- [11] International Tables for X-ray Crystallography, Vol. Iv (The Kynoch Press, Birmingham, 1974).
- [12] Tokonami, M., Acta Cryst. 19, 486 (1965).
- [13] LePage, Y., Gabe, E. J., and Calvert, L. D. (to be published).
- [14] Cooper, M. J., Sakata, M., and Rouse, K. D., Symposium on Accuracy in Powder Diffraction, National Bureau of Standards, Gaithersburg, Maryland, June 11-15, 1979.
- [15] Sleight, A. W., Chen, H.-Y., Ferretti, A., and Cox, D. E., Mater. Res. Bull. (to be published).
- [16] David, W. I. F., Glazer, A. M., and Hewat, A. W., J. Phys. C. (to be published).
- [17] Wertheim, G. K., Butler, M. A., West, K. W., and Buchanan, D. N. E., Rev. Sci. Instrum. 45, 1369-1371 (1974).



TEMPERATURE DEPENDENCE OF THE ATOMIC THERMAL  
DISPLACEMENTS IN  $UO_2$ : A TEST CASE FOR THE  
RIETVELD PROFILE REFINEMENT METHOD

A. Albinati  
Institute of Chemistry  
The Polytechnic  
Milan, Italy

M. J. Cooper, K. D. Rouse, M. W. Thomas, and B. T. M. Willis  
Materials Physics Division  
Atomic Energy Research Establishment  
Harwell, OX11 0RA, England

The neutron diffraction powder pattern of  $UO_2$  has been measured at five temperatures between 20 °C and 1460 °C, and the data have been analyzed by two methods: the Rietveld profile refinement method and the more conventional procedure based on integrated intensities. The thermal displacements of the uranium and oxygen atoms, as derived by the two methods, are in agreement within one standard deviation at each temperature. The standard deviations from the Rietveld analysis are lower at some temperatures than those from the conventional analysis, but at 1100 °C the e.s.d.'s from the Rietveld method exceed those from the conventional procedure. These differences are readily explained in terms of the different ways of calculating the e.s.d.'s in the two methods. The observed displacements are a little higher than those calculated by lattice dynamics, but the discrepancies are probably caused by the neglect of anharmonic effects in the calculations.

We shall also discuss the system, hexamethylene tetramine, which has been analyzed in a similar way at a number of temperatures. Here, both positional and thermal parameters are obtained from the powder data.

## 1. Introduction

For the past ten years, the profile refinement method of Rietveld [1,2]<sup>1</sup> has been widely used for the interpretation of neutron diffraction powder patterns; more recently, the procedure has been extended to the analysis of x-ray diffraction powder data too (see references [3] and [4]). Intensity points at small intervals in the diffraction pattern are treated as individual observations which may arise from contributions from a number of Bragg reflections, so that the profile refinement method can be used even when there is a large number of overlapping peaks. On the other hand, in the more conventional refinement procedure the integrated intensities are derived by assuming that the Bragg reflections are separated from one another; this approach cannot be used where there is severe overlapping of adjacent peaks.

Sakata and Cooper [5] have carried out a statistical analysis of the Rietveld method and have raised a number of questions regarding its validity. In particular, they show that the crystallographic parameters derived by the two types of refinement are not necessarily the same, and that the estimated standard deviations of the parameters are different.

In the present paper we test these theoretical predictions by applying both refinement procedures to the same experimental measurements. The system we have chosen is polycrystalline uranium dioxide, examined by neutron diffraction over a wide range of temperature from 20 °C to 1460 °C. By using a sufficiently long neutron wavelength and a high take-off angle at the monochromator, most of the Bragg peaks were well separated in the diffraction pattern. The scattering data could be analyzed satisfactorily, therefore, by both methods.

## 2. Conventional Refinement

The neutron powder diffraction pattern of  $UO_2$  was recorded with the PANDA diffractometer installed at the PLUTO reactor, Harwell. The polycrystalline sample, of composition close to  $UO_{2.00}$ , was enclosed in a cylindrical can of tantalum. With a wavelength of 1.334 Å and a range of scattering angles of  $18^\circ \leq 2\theta \leq 114^\circ$ , all reflections up to 533 were observed.

Relative values of the observed structure factors  $F(\text{obs})$  were obtained at the five temperatures 20, 800, 1100, 1400 and 1460 °C. A least-squares refinement was then carried out for each temperature, where the quantity

$$\sum_{hkl} w_{hkl} \left| (F(\text{obs}))^2 - s(F(hkl))^2 \right|^2 \quad (1)$$

was minimized to yield the scale factor  $s$  and the thermal parameters  $B_U$  and  $B_O$ .  $F(hkl)$  is the calculated structure factor and is of the form

<sup>1</sup>Figures in brackets refer to the literature references at the end of this paper.

$$\begin{aligned}
 F(hkl) &= 4b_U \exp(-B_U \sin^2\theta/\lambda^2) + 8b_O \exp(-B_O \sin^2\theta/\lambda^2) \\
 &\dots h+k+l = 4n \\
 &= 4b_U \exp(-B_U \sin^2\theta/\lambda^2) \dots h+k+l = 4n\pm 1 \quad (2) \\
 &= 4b_U \exp(-B_U \sin^2\theta/\lambda^2) - 8b_O \exp(-B_O \sin^2\theta/\lambda^2) \\
 &\dots h+k+l = 4n+2
 \end{aligned}$$

with  $b_U$  and  $b_O$  representing the neutron scattering amplitudes of uranium and oxygen respectively.  $w_{hkl}$  in eq. (1) is the weight of  $(F(\text{obs}))^2$  and was calculated from

$$w_{hkl} = \frac{1}{\sigma_{hkl}^2}, \quad \sigma_{hkl} = (F(\text{obs}))^2 \frac{(I+B)^{\frac{1}{2}}}{(I-B)} \quad (3)$$

where  $B$  is the background count and  $I$  is the integrated intensity count plus the background count. The computer program used for the refinement was ORXFLS 3 [6].

Table 1 lists the thermal parameters of the two atoms, together with their estimated standard deviations. We also give the agreement factor  $A_B$ , defined by

$$A_B^2 = \sum w \left| (F(\text{obs}))^2 - s(F(hkl))^2 \right|^2 \div (N_I - P_S) \quad (4)$$

where  $N_I$  is the number of independent integrated intensities and  $P_S (=3)$  is the number of structural parameters.

Table 1. Results given by Conventional Refinement Method  
(using Integrated Intensities)

Temp. (°C)	$B_U$ (Å <sup>2</sup> )	$B_O$ (Å <sup>2</sup> )	$N_I$	$A_B$
20	0.18 (10)	0.66 (12)	9	4.23
800	0.91 (7)	1.68 (9)	9	2.01
1100	1.40 (5)	2.20 (6)	9	1.10
1400	1.68 (17)	2.79 (21)	8	3.24
1460	1.73 (10)	3.03 (14)	8	1.94

### 3. Profile Refinement

The same set of observations was then analyzed by the Rietveld method. Each observation  $y_i$  of the background-corrected intensity at the scattering angle  $2\theta_i$  was assigned a weight

$$w_i = \frac{1}{Y_i + B_i} \quad (5)$$

where  $B_i$  is the background and  $Y_i (= y_i + B_i)$  is the total intensity.  $B_i$  was estimated by interpolation between regions with no Bragg intensity. The number of observations  $y_i$  was restricted to cover the same range of  $\theta_i$ 's as was used in the conventional refinement (Section 2). The computer program used for the profile refinement has been described by Hewat [7], and has minor improvements made later by one of the present authors (M.W.T.).

The refinement yielded the three structural parameters ( $s, B_U, B_0$ ), four instrumental parameters and the lattice parameter  $a_0$ . The four instrumental parameters are  $U, V, W$ , governing the  $\theta$ -dependence of the half-width of the reflections (see ref. [2]), and the zero- $2\theta$  position of the diffractometer. Table 2 lists the thermal parameters and the lattice parameters, together with their e.s.d's. Also given are: the number of experimental points  $N_p$ , separated by  $0.1^\circ$  in  $2\theta$ , at which the profile was sampled; and the agreement factor  $A_p$  defined by

$$A_p^2 = \frac{\sum_i w_i (y_i(\text{obs}) - s y_i(\text{calc}))^2}{N_p - P_p - P_s} \quad (6)$$

where  $P_p (=5)$  is the number of profile parameters (i.e.  $U, V, W$ , zero- $2\theta$  and  $a_0$ ), and  $P_s$  is the number of structural parameters.

Table 2. Results given by Profile Refinement Method

Temp. (°C)	$B_U$ (Å <sup>2</sup> )	$B_0$ (Å <sup>2</sup> )	$N_p$	$A_p$	$a_0$ (Å)
20	0.12 (6)	0.51 (7)	99	3.07	5.4710 (2)
800	0.84 (7)	1.70 (9)	105	2.47	5.5135 (3)
1100	1.31 (9)	2.19 (11)	107	2.51	5.5333 (3)
1400	1.59 (11)	2.70 (15)	93	2.85	5.5538 (4)
1460	1.67 (10)	2.92 (14)	89	2.48	5.5580 (1)

The B values from tables 1 and 2 are in close agreement, at each temperature, for the two methods of analysis. In principle, the structural parameters given by the two treatments are not identical [5], but in the present case they do not differ significantly.

The ratio of  $(\sigma_i)_P$ , the e.s.d. of the  $i^{\text{th}}$  parameter as determined by the Rietveld method, to  $(\sigma_i)_I$ , the corresponding quantity for the conventional treatment, is given by:

$$\frac{(\sigma_i^2)_P}{(\sigma_i^2)_I} = \frac{(A_{ii}^{-1})_P A_P^2}{(A_{ii}^{-1})_I A_B^2} \quad (7)$$

where  $A_{ii}^{-1}$  is the diagonal element of the inverse normal matrix corresponding to the  $i^{\text{th}}$  parameter. Sakata and Cooper have shown that the value of  $(A_{ii}^{-1})_P / (A_{ii}^{-1})_I$  can be estimated from the approximate expression:

$$\frac{(A_{ii}^{-1})_P}{(A_{ii}^{-1})_I} \cong \frac{1}{\epsilon'}$$

where the factor  $\epsilon'$  is determined by the weights given to the observations in the two methods of refinement. The equation defining  $\epsilon'$  is:

$$\epsilon' \sum_k w_k = \sum_k \sum_j w_{j,k} G_{j,k}^2$$

the summation on the left-hand side is over the  $k$  reflections, each with weight  $w_k$ , and the summation on the right-hand side over  $j$  refers to the profile points for an individual reflection with each point weighted by  $w_{j,k}$ .  $G_{j,k}$  represents a normalized Gaussian centered at  $2\theta_k$ , with variance  $2\sqrt{\ln 2}/H_k$  where  $H_k$  is the F.W.H.H. of the reflection. Equation (7) can be replaced, therefore, by

$$\frac{(\sigma_i)_P}{(\sigma_i)_I} = \frac{1}{\sqrt{\epsilon'}} \frac{A_P}{A_B} \quad (8)$$

The standard deviation ratios predicted by equation (8) are compared with those observed, in table 3. Columns 2 to 5 in the table list the e.s.d. values given by the two analyses and the ratios of these are given in columns 7 and 8. Column 6 gives the standard deviation ratio derived from equation (8), using  $\epsilon' = 1.5$  and the agreement factors listed in tables 1 and 2. (None of the individual values of  $\epsilon'$  differ from 1.5 by more than 10 percent.) The ratios in column 6 are in reasonable agreement with the observed ratios in the last two columns. We conclude that equation (8), derived by Sakata and Cooper, accounts satisfactorily for the differences in the estimated standard deviations of the structural parameters obtained by the two methods of analysis.

Table 3. Estimated Standard Deviation Ratios  
for Profile and Conventional Refinements

Temp. (°C)	$(\sigma_i)_P$ :		$(\sigma_i)_I$ :		$\frac{1}{\sqrt{\epsilon^T}} \frac{A_P}{A_B}$	$(\sigma_i)_P \div (\sigma_i)_I$	
	profile		conventional			$B_U$	$B_O$
	$i = B_U$ (Å <sup>2</sup> )	$i = B_O$ (Å <sup>2</sup> )	$i = B_U$ (Å <sup>2</sup> )	$i = B_O$ (Å <sup>2</sup> )			
20	0.062	0.072	0.102	0.120	0.59	0.61	0.60
800	0.071	0.091	0.074	0.120	1.01	0.96	1.01
1100	0.086	0.107	0.052	0.061	1.87	1.65	1.75
1400	0.113	0.145	0.166	0.211	0.71	0.68	0.69
1460	0.104	0.137	0.104	0.138	1.04	1.00	0.99

#### 4. Hexamethylenetetramine (HMT)

We have also examined fully deuterated hexamethylenetetramine,  $C_6N_4D_{12}$ , by powder neutron diffraction, using the Rietveld method to analyse the data. DHMT is especially suitable for study, as it crystallizes in a body-centered cubic lattice, so that the peaks are well separated from one another in the powder pattern and are uniformly spaced. Here, we shall present some preliminary results only.

Choosing the origin of the unit cell at the center of the molecule, the atomic coordinates are

$$\begin{array}{ll}
 u & 0 & 0 & \text{for carbon} \\
 v & v & v & \text{for nitrogen} \\
 \text{and} & x & x & z & \text{for hydrogen (deuterium).}
 \end{array}$$

Thus, there are four positional coordinates:  $u$ ,  $v$ ,  $x$  and  $z$ .

A powder diffraction pattern at liquid-helium temperature was analyzed by the Rietveld procedure to give

$$\begin{array}{ll}
 u = 0.238 (1), & v = 0.126 (1), \\
 x = 0.084 (1), & z = -0.332 (1).
 \end{array}$$

These estimates can be compared with

$$\begin{aligned}u &= 0.2391 (8), & v &= 0.1243 (4), \\x &= 0.0918 (8), & z &= -0.3278 (12)\end{aligned}$$

which were derived by Duckworth, Willis and Pawley [8] in a room-temperature neutron-diffraction study of a single crystal of HMT. The atomic coordinates of the carbon and nitrogen atoms for the powder and the single crystal are within one or two standard deviations of one another. The agreement is less satisfactory for the hydrogen atom, but this may be due to the replacement of H by D in the polycrystalline sample.

## 5. Conclusions

Sakata and Cooper [5] have analyzed several sets of powder diffraction data obtained with neutrons, and have found that for most of these the standard deviations were underestimated by the Rietveld procedure by a factor of at least two. The inference that this factor could be as large as this for most neutron diffraction data is not supported by the present results. Indeed, in two of the five data sets (800 °C and 1460 °C) for  $UO_2$  the standard deviations given by the conventional and Rietveld refinements are about the same, and in one data set (1100 °C) the Rietveld method leads to standard deviations which exceed those from the conventional refinement by a factor of nearly two.

However, the differences between the e.s.d.'s obtained at each of the five temperatures for the two types of refinement can be accounted for satisfactorily by the analysis of Sakata and Cooper. The agreement factor  $A_B$  (see eq. (4)) in the conventional refinement reflects the degree of matching between the observed and calculated integrated intensities, whereas the agreement factor  $A_p$  (see eq. (6)) for the Rietveld refinement reflects not only the degree of matching between integrated intensities but also that between the shape functions describing the profile of the individual reflections. The structural parameters are determined by the integrated intensities and the profile parameters by the shape functions: it is not surprising that the e.s.d.'s from the Rietveld refinement are different from those from the conventional refinement. Equation (8) with  $\varepsilon' = 1.5$  accounts satisfactorily for the e.s.d. ratios in  $UO_2$ . The larger values obtained for  $(\sigma_i)_p/(\sigma_i)_I$  are due to the unusually small agreement factors  $A_B$  for these data sets.

The numerical estimates of the thermal parameters of  $UO_2$ , derived from either the profile or the integrated intensity method, are in fairly close agreement with one another over the temperature range 20-1460 °C. There is similar agreement in the estimates of the positional parameters of all the atoms (except hydrogen) in hexamethylenetetramine. In the latter case the comparison was made between a single-crystal, room-temperature analysis of HMT and a powder, liquid-helium profile analysis of DHMT.

## References

- [1] Rietveld, H. M., Line profiles of neutron powder-diffraction peaks for structure refinement, *Acta Cryst.* 22, 151-152 (1967).
- [2] Rietveld, H. M., A profile refinement method for nuclear and magnetic structures, *J. Appl. Cryst.* 2, 65-71 (1969).
- [3] Young, R. A., Mackie, P. E., and Von Dreele, R. B., Application of the pattern-fitting structure-refinement method to x-ray powder diffractometer patterns, *J. Appl. Cryst.* 10, 262-269 (1977).
- [4] Malmros, G. and Thomas, J. O., Least-squares refinement based on profile analysis of powder film intensity data measured on an automatic microdensitometer, *J. Appl. Cryst.* 10, 7-11 (1977).
- [5] Sakata, M. and Cooper, M. J., An analysis of the Rietveld profile refinement method, *J. Appl. Cryst.* (1979), in the press.
- [6] Busing, W. R., Martin, K. O., Levy, H. A., Ellison, R. D., Hamilton, W. C., Ibers, J. A., Johnson, C. K., and Thiessen, W. E., ORXFLS3, Oak Ridge National Laboratory Report ORNL-59-4-37 (1972).
- [7] Hewat, A. W., The Rietveld computer program for the profile refinement of neutron diffraction powder patterns modified for anisotropic thermal vibrations, Report No. RRL 73/239, Atomic Energy Research Establishment, Harwell, England (1973).
- [8] Duckworth, J. A. K., Willis, B. T. M., and Pawley, G. S., Neutron diffraction study of the atomic and molecular motion in hexamethylenetetramine, *Act Cryst.* A26, 263-271 (1970).

## Discussion

Comment (Cooper): The existence of very large residuals for these data is illustrated in figure 5 of the paper by Cooper, Sakata, and Rouse. These large residuals occur systematically at all temperatures and lead to unusually large values of the Agreement Factor  $A_p$ . Since the Gaussian function is not a good approximation to the observed peak shapes, these results cannot be considered to be typical neutron diffraction results, but are nevertheless entirely consistent with the conclusions of Cooper, Sakata, and Rouse.

STUDIES OF THERMAL MOTION USING CONSTRAINED PROFILE ANALYSIS

E. Prince

National Measurement Laboratory  
National Bureau of Standards  
Washington, DC 20234

C. S. Choi and S. F. Trevino  
Energetic Materials Division  
LCWSL, ARRADCOM  
Dover, NJ 07801

A constrained refinement procedure which treats atomic groups as rigid bodies and uses the elements of the  $\underline{I}$ ,  $\underline{L}$ , and  $\underline{S}$  tensors as the independent variables has been successfully applied to single crystal diffraction data. In order to determine if similar procedures can be applied to powder data, in spite of the loss of information due to overlapping peaks and the difficulty of determining background, we have modified the Rietveld-Hewat profile analysis program to incorporate rigid-body constraints. Subroutines have been added which evaluate anisotropic temperature factor coefficients, and also third cumulant coefficients, and their derivatives in terms of the  $\underline{I}$   $\underline{L}$   $\underline{S}$  tensor elements, and the treatment of constraints has been changed so that relationships are applied directly so as to reduce the size of the Hessian matrix. The program has been applied to an analysis of data taken from potassium azide, with results that are generally consistent with single crystal results, although they are considerably less precise. Constrained refinement has also been applied to powder data from nitromethane and a high temperature phase of ammonium nitrate, with reasonably satisfactory results. It appears that, although profile analysis is much less powerful than corresponding single crystal techniques, it can in favorable circumstances yield meaningful thermal motion information.

## Discussion

Comment (Edmonds): One normally considers the low angle three dimensional x-ray diffraction data as determining the positional parameters and the high angle data defining the thermal motion parameters. Since the Rietveld method uses the collapsed one dimensional data, there is a significant loss of information necessary to define thermal anisotropy. One must be very careful in choosing a constrained model which may neglect information which is present in order to allow access to information which may be only marginally present. At this point I would still feel quite cautious on this matter for the x-ray case.

Response (Prince): I agree that the loss of information due to collapsing the three dimensions of reciprocal space to one dimension is particularly detrimental to the determination of thermal parameters. This makes it especially important to constrain the model to conform to the laws of physics. For x-rays, the problem of line shape, among others, will have to be solved before thermal parameters can be considered meaningful.

ACCURACY OF CRYSTALLITE SIZE AND STRAIN VALUES FROM X-RAY DIFFRACTION  
LINE PROFILES USING FOURIER SERIES

R. Delhez, Th.H. deKeijser and E. J. Mittemeijer  
Laboratory of Metallurgy  
Delft University of Technology  
Rotterdamseweg 137, 2628 AL Delft  
The Netherlands

The accuracy of size-strain analysis using Fourier series is determined by: (i) the methods and experimental procedures used in obtaining the Fourier coefficients of the pure, only structurally broadened, line profile; (ii) the model used to describe the arrangement of the atoms in the specimen and the approximations used in relating Fourier coefficients to the structural parameters of the model; and (iii) the availability of corrections for systematic errors.

Attention is paid to procedures for deconvolution,  $\alpha_2$  elimination, correction for the angle dependence of Lorentz and polarization factors, assignment of origins and the choice of background level. The errors in the Fourier coefficients of the measured profiles and of the pure, only structurally broadened profile are considered.

Methods for the separation of the order-dependent and order-independent parts of the broadening in the Warren-Averbach theory are examined (including single-line techniques). The best way of separating these parts depends on a priori knowledge about the imperfections (e.g., distribution functions), but in general a plot of the cosine Fourier coefficient versus the square of the order of the reflection is most appropriate.

Correction methods for the errors accumulated in values for size and strain are discussed for the case of a non-ideal standard line profile. Especially the mean square strain values are affected heavily by application of a standard specimen with a spacing only a few percent different from that of the ideal one. Nevertheless, without these corrections, relative determinations of size and strain can be made accurately.

The determination of the crystallite size distribution is considered separately in view of the high sensitivity to error propagation.

## 1. Introduction

Properties of crystalline materials are determined by the imperfectness of their structure. The x-ray powder diffraction method is a non-destructive technique and it averages over a reasonable volume. From the analysis of x-ray diffraction line profiles measures for deviations from the perfect crystal structure can be obtained. Principal imperfections are crystallite size and lattice distortions.

For the analysis of the peak shape several methods have been proposed. Much work has been done using the integral breadth and full width at half maximum. This technique has gotten an impulse recently [1,2,3]<sup>1</sup>. For a more detailed analysis a variance method [4] and a Fourier series method [5] are available.

In this paper, we will confine our attention to size-strain analysis using Fourier series representations of the line profiles measured. From a minimum of assumptions very detailed information can be obtained.

The accuracy of size-strain analysis using Fourier series is determined by:

- (i) the methods and experimental procedures used in obtaining the Fourier coefficients of the pure, only structurally broadened, line profile;
- (ii) the model used to describe the arrangement of the atoms in the specimen and the approximations used in relating the measured Fourier coefficients to the structural parameters of the model; and
- (iii) the availability of corrections for systematic errors.

## 2. Errors in Line Profiles

In this paper, it is assumed that all line profiles are recorded by a step-scanning technique. Most aspects of the choice of step size, angular range sampled, radiation and monochromatization, slit widths, counting time and dead time of the counter can be found in handbooks (e.g. reference [6]). Specimen preparation should be carefully dealt with: effects of surface roughness, specimen transparency, inhomogeneous density and grain size may be overlooked easily.

### 2.1. Elimination of background

Estimation of the background level is still more an art than a science, although methods have been developed to find a justified estimate [7,8,9]. Usually it is assumed that the background is linear, which is often not true, because of the presence of e.g. thermal

---

<sup>1</sup>Figures in brackets indicate the literature references at the end of this paper.

diffuse scattering<sup>2</sup> or the white spectrum (including a K-edge of the  $K_{\beta}$  filter). Since one becomes accustomed to the use of computers in powder diffraction work the experimentalist should calculate these effects before estimating a remaining linear background with one of the methods referred to.

Because all physical quantities are calculated from profiles minus background and because the background has to be taken as a smooth curve all statistical fluctuation in the total profiles are found in the net profile. Therefore, it is advantageous to keep the background as low as possible. This can be done by using (i) a vacuum chamber on the diffractometer to reduce air scatter, (ii) an x-ray wavelength such that fluorescence is minimal, and (iii) a monochromator (which also avoids the step in the background due to the K-edge of the  $K_{\beta}$  filter).

## 2.2. Elimination of the broadening due to instrumental aberrations and the x-ray spectrum used

A line profile  $h$  measured on a specimen containing structural imperfections is determined by:

- (i) The structural imperfections to be investigated which cause line broadening effects contained in the structurally broadened profile  $f$ .
- (ii) The non-ideal geometry of the diffractometer and the specimen.
- (iii) The wavelength distribution.
- (iv) Angle dependent factors (Section 2.4.).

Usually (ii) and (iii) are taken together into one function  $g$  called the standard line profile, which can be observed with good approximation on a suitable standard specimen (cf. Section 5.1.). In most experiments (ii) and (iii) constitute the major part of the profile at low Bragg angles (ii) is predominant and at high angles it becomes negligible, while (iii) the reverse holds [11].

The line profile  $h$  can be described by a convolution

$$h(x) = \frac{1}{A} \int_{-\infty}^{+\infty} f(y) g(x-y) dy \quad (2.1)$$

where  $A = \int_{-\infty}^{+\infty} g(z) dz$ . It is advantageous to take  $x$ ,  $y$ , and  $z$  on a  $\sin\theta$ -scale [12].

An example of a significant contribution of thermal diffuse scattering to the background was found during the evaluation of the concentration-penetration curve from line profiles of diffused copper-nickel "single crystals" [10]: the analysis would have been impossible if a linear background had been chosen.

This equation implies that the shape of  $g$  should be constant within the range of the profile. If this condition is not met satisfactorily,  $f$  can only be evaluated using a set of linear equations analogous to the convolution integral (cf. e.g. reference [13]).

### 2.2.1. Deconvolution

Many investigators in many disciplines have noticed difficulties in the deconvolution (i) arbitrarily small variations of  $h$  may correspond arbitrarily to great changes in the deconvolute (unstable solution), and (ii) eq. (2.1) does not have a solution for every  $h$ .

For a short discussion on seven methods used in x-ray powder diffraction see reference [13]. Here we will restrict ourselves to the solution using Fourier series, firstly applied to powder diffraction by Stokes [14]. Since convolution of functions is equivalent to multiplication of the complex Fourier coefficients of these functions, deconvolution can be accomplished using

$$F(n) = H(n)/G(n) \quad , \quad (2.2)$$

where  $F(n)$ ,  $G(n)$ , and  $H(n)$  are the Fourier coefficients of the profiles  $f$ ,  $g$  and  $h$  respectively, normalized such that  $F(0) = G(0) = H(0) = 1$  and  $n$  is the harmonic number<sup>3</sup>.

Other procedures for deconvolution used in powder diffraction may be regarded as simple deconvolution by use of eq. (2.2) after smoothing of the profiles [16]. Therefore most conclusions given here will also hold for these other methods.

Croche and Gatineau [13] state the thumbrule that deconvolution should be applied only if the ratio of the widths of the profiles  $h$  and  $g$  is between 2 and 6: below 2 any existing deconvolution procedure becomes too inaccurate<sup>4</sup> and above six deconvolution seems to have no effect but enlarging the statistical fluctuations. Further, they propose a procedure to choose optimal experimental conditions such that the ratio mentioned is as close as possible to 6 with yet acceptable counting accuracy.

In some cases, the  $f$  profile cannot be recovered from the  $h$  profile with the  $g$  profile belonging to it, namely if the Fourier coefficients of the  $f$  profile are not vanishing but those of the  $g$  profile. An example is a line profile of a diffused copper-nickel single crystal already referred to in Section 2.1.: the  $f$  profile contains two "discontinuities" at the Bragg positions of the pure metals: between these positions a continuously varying intensity is present, outside there is no intensity. For such a case see Section 2.2.2.

<sup>3</sup>A good, and also pictorial, description of the convolution equation and the use of Fourier series in connection with this is given by Brigham [15].

<sup>4</sup>Schwartz and Cohen [17, p. 391] state that  $h$  should be at least 20 percent broader than  $g$  which implies an upper limit of about 100 nm for the determination of effective crystal size.

Every deconvolution procedure leaves some "residual smearing" in the resulting profile. This can be regarded as a residual instrumental function [18], which is obtained, when the instrumental profile  $g$  is deconvoluted with itself using the same number and values of parameters as in the deconvolution of  $h$  with  $g$ . In the case of the Fourier method discussed in this paper, the  $f$  profile is synthesized from a limited number of its Fourier coefficients: the Fourier transform of the  $f$  profile is truncated. Since the Fourier transform of a regular truncation function is of the form  $(\sin ax)/x$ , this is also the shape of the residual instrumental function for the Stokes method. It is this function that leaves the "Fourier ripple," as it is sometimes referred to, in the synthesized  $f$  profile<sup>5</sup>. It is obvious, that details corresponding to Fourier coefficients above the cut-off value will not be found in the  $f$  profile, although they are present in the  $h$  profile.

### 2.2.2. Elimination of the $\alpha_2$ component<sup>6</sup>

Deconvolution is impossible in cases as mentioned in Section 2.2.1. or if no appropriate standard specimen is available. In these cases an  $\alpha_2$  elimination should be performed at small  $2\theta$  angles, since the doublet causes the greater part of the broadening especially at not too large Bragg angles. The spectral part of the resulting  $\alpha_1$  profile may be removed to a large extent by using a Cauchy or Voigt profile having a width in agreement with known data (see also note Section 5.2.1.). Further an  $\alpha_2$  elimination is helpful to separate partially overlapping peaks.

The assumptions on which  $\alpha_2$  elimination is based, are: (i) the  $\alpha_2$  component has the same shape as the  $\alpha_1$  component, (ii) the intensity ratio  $R [= I_{a_2}(\max)/I_{a_1}(\max)]$  is known, (iii) the doublet separation  $\delta$  is known. In practice the first assumption is much more fulfilled on a  $\lambda$ -scale (equivalent to a  $\sin\theta$ -scale) than on a  $2\theta$ -scale [12]. The doublet separation  $\delta$  can be calculated from literature data of wavelength values and the intensity ratio  $R$  is about 0.5 in most cases, but can be significantly different if a monochromator is used.  $R$  can then be found by optimization [11].

If  $I_t$ ,  $I_1$ , and  $I_2$  denote the total, the  $\alpha_1$  and  $\alpha_2$  profiles respectively, then the  $\alpha_2$  elimination can be written using the basic assumption mentioned:

$$I_1(x) = I_t(x) - RI_1(x-\delta) \quad (2.3)$$

the expression for  $I_1(x-\delta)$  obtained by replacing  $x$  by  $x-\delta$  in eq. (2.3) is substituted into eq. (2.3) and the substitution is made repeatedly eq. (2.3) becomes

the  $f$  profile would have been obtained too, if the  $h$  profile prior to deconvolution had first been convolved (smoothed) using the appropriate function  $(\sin ax)/x$ . The main field of application of the  $\alpha_2$  elimination is its use in line profile analysis methods on the basis of line widths.

$$I_1(x) = \sum_{m=0}^M (-R)^m \cdot I_t(x-m\delta) \quad (2.4)$$

If  $H_t(n)$  is the Fourier coefficient of  $I_t$ , normalized such that  $H_t(0) = 1$ , then using eq. (2.4) the normalized Fourier coefficient  $H_1(n)$  of  $I_1$  is obtained as (cf. reference [19])

$$H_1(n) = H_t(n)(1+R/\{1+R\exp 2\pi i n \delta/a\}) = H_t(n)/P(n) \quad (2.5)$$

where  $a$  is the period on a  $\sin\theta$  scale.

### 2.3. Counting statistics

When a line profile is sampled, e.g. using the fixed time counting method, each observed number of counts is subject to a statistical error; the variance is equal to the number of counts of the observation concerned. The observations are statistically independent. Statistical errors can be handled in three ways:

- (i) By smoothing. As stated in Section 2.2. a number of deconvolution procedures contain an implicit smoothing process [16]. The experimentalist should always be aware of the fact that smoothing may introduce periodicities which were not present initially (cf. the residual instrumental function in Section 2.2.) or that it may eliminate meaningful periodicities.
- (ii) By curve fitting. Then the mathematical form of the line profile has to be known to a good approximation. Additional advantages are that uncertain regions (peak overlap) may be ignored and that the tails of a profile may be estimated more accurately.
- (iii) By regarding these errors as an intrinsic part of the profile. This implies that the statistical fluctuations are deconvolved along with the exact  $h$  profile resulting in much larger fluctuations in the resulting profile and its Fourier transform (see also footnote to eq. (5.12)).

The approach (iii) will be followed in this paper. For most deconvolution procedures the sensitivity to these errors obliges to measure the profiles with less than 1 percent statistical error [13]. This emphasizes once more the importance of a low background level (cf. Section 2.1.).

### 2.4. Corrections for the angle dependence of Lorentz, polarization and atomic scattering factors

In the interpretation of the broadening of x-ray diffraction line profiles it should be recognized that the Lorentz (L), polarization (P) and atomic scattering factors are

is dependent within a given profile. If accurate line profile analysis is demanded this dependence should be accounted for. With respect to values for crystallite size, in experimental line profiles it was shown that errors of 10 percent may occur when this dependence is ignored [20].

Rules are given which, in our opinion, should be followed when correcting for the dependence of L, P and atomic scattering factors.

#### 2.4.1. Formulae for the Lorentz-polarization factor

In textbooks normally the LP factor is given for the integrated intensity of a reflection. However, in structurally broadened line profiles the LP factor relevant to the distribution of the intensity over  $2\theta$  has to be considered. Warren and Averbach [21] have calculated this LP factor for a powder specimen. Following the same procedure one can calculate the corresponding LP factor for a single crystal.

It can be useful to perform line profile analysis on a  $\sin\theta$ -scale [12]. Then the LP factors for the integrated intensity and for the distribution of the intensity over  $\sin\theta$  are the same. This LP factor (omitting constant factors) for a single crystal is

$$\frac{1 + B\cos^2 2\theta}{\sin 2\theta} \quad (2.6)$$

for a powder specimen

$$\frac{1 + B\cos^2 2\theta}{\sin^2 \theta \cos \theta} \quad (2.7)$$

for an unpolarized incident beam and without monochromator  $B = 1$ , whereas with an ideally perfect monochromator crystal  $B = \cos^2 2\theta_m$ , where  $\theta_m$  is the Bragg angle for the reflecting planes in the monochromator. For a particular monochromator crystal  $B$  can be easily measured [22].

In case one has to deal with (even strongly) texturized specimens it can be shown that it is allowed to use the LP factor for a powder specimen [23].

#### 2.4.2. Correction for the angle dependence of the Lorentz-polarization factor

Here only line profiles on a  $\sin\theta$ -scale are considered. The analogous correction of line profiles on a  $2\theta$ -scale is described elsewhere [24]. Two cases have to be considered in practice.

- (i) The broadening due to instrumental aberrations is dominant in the g profile. This occurs at the smaller  $2\theta$  values. If we assume that the wavelength distribution is a delta function, each  $f$  value is diffracted at a sharply defined diffraction angle; however, the intensity is recorded over a range of measured  $2\theta$  values for which the L and P factors are

determined by that one sharply defined diffraction angle. Therefore, both the g and h profile should not be corrected for the angle dependence of the L and P factors. After the deconvolution procedure the f profile should be corrected for the angle dependence of the L and P factors.

- (ii) The spectral broadening dominates in the g profile. This occurs at the larger  $2\theta$  values. With only spectral broadening present, each f value is diffracted by the whole wavelength distribution, leading to recorded intensities over a range of measured  $2\theta$  values. The recorded intensity at each  $2\theta$  value is dependent upon the L and P factors for that  $2\theta$  value. Therefore, both the g and the h profile should be corrected for the angle dependence of the L and P factors before performing a deconvolution procedure.

#### 2.4.3. Correction for the angle dependence of the atomic scattering factor

Within the g profile taken from an ideal standard specimen (no structural broadening) the atomic scattering factor is not angle dependent at all. It is clear that a correction for the angle dependence of the atomic scattering factor should be performed after the deconvolution procedure.

### 3. Errors in Fourier Coefficients of Line Profiles

#### 3.1. Sampling and truncation

In practice no continuous line profile is recorded. Instead, the profile is sampled at certain equidistant locations on the s-axis. This can be considered as a multiplication of the profile  $f(s)$  with the sampling function  $\Delta(s)$ , where  $\Delta(s)$  denotes an infinite series of equidistant impulses separated by the sample interval T. Then, according to the convolution theorem, in Fourier space ( $\nu$  domain) the effect of sampling implies a convolution of the continuous Fourier transform  $F(\nu)$  of  $f(s)$  with the Fourier transform  $\Delta(\nu)$  of  $\Delta(s)$ , where  $\Delta(\nu)$  denotes an infinite series of equidistant impulses separated by  $1/T$ . As a result, the Fourier transform of the sampled profile has become periodic with period  $1/T$  (the first period is confined to  $-1/2T < \nu \leq 1/2T$ ). It will be clear that in case the true Fourier transform has no vanishing values at  $|\nu_c| = 1/2T$ , sampling will result in overlapping: "aliasing." Aliasing can be reduced by enlarging the period  $1/T$  of  $\Delta(\nu)$ , i.e. reducing the sample interval T on the s-axis. It is concluded that there is no loss of information if sampling occurs such that  $F(\nu) = 0$  for  $|\nu| \geq |\nu_c|$  where  $|\nu_c| \leq |\nu_d|$ . This can physically be interpreted as that no significant changes occur in the line profile within the sampling distance T.

Further, it has to be recognized that the Fourier transform cannot be computed as a continuous function; only sample values can be determined. As sampling of the profile leads to periodicity in Fourier space (see above), the reverse is also true. Hence the discrete Fourier transform pair amenable to machine computation (by for example using a Fast Fourier Transform technique [15]) requires that both the line profile and its transform are modified such that they become periodic functions.

A second, normally more serious, distortion of the true Fourier transform arises from the limitation that intensity measurements have to be restricted to a certain range in  $s$ -space. This inevitable truncation can be considered as a multiplication of the profile  $F(s)$  with the function  $r(s)$ , where

$$r(s) = 1 \text{ if } -a/2 < s \leq a/2 \text{ and elsewhere } r(s) = 0 \quad (3.1)$$

Then, in Fourier space the affected transform  $F'(v)$  is obtained from the convolution

$$F'(v) = \int F(\rho) \frac{\sin \pi a(v-\rho)}{\pi(v-\rho)} d\rho \quad (3.2)$$

An important effect of truncation may be its contribution to the so-called "hook" effect: The curvature of  $F'(v)$  near  $v = 0$  will be smaller than the corresponding one of  $F(v)$ . In the field of x-ray diffraction this effect has been recognized first by Bertaut [25]. Model calculations by Young, Gerdes, and Wilson [26] showed that a truncation of the line profile at positions corresponding to intensity values of the order of 1 percent of the peak maximum may introduce a detectable "hook" already (see also Section 4.4.4.).

Further, the Fourier transform becomes broader (smeared) and a ripple may appear on it due to the oscillatory nature of the Fourier transform of the rectangular truncation function.

Without intervention the rectangular truncation function is implied by experiment. The ripple on  $F'(v)$  thus introduced, can be suppressed by multiplying the profile by a non-rectangular artificial truncation function with a corresponding Fourier transform which possesses oscillations of smaller magnitude (see for example the Hanning function [15, p. 141]). The effect of such a truncation function is to reduce the effects of the discontinuities of the rectangular truncation function. However, the more the ripple is reduced in this way, the broader the  $F'(v)$  curve will become. Although never applied in the analysis of x-ray diffraction line profiles such a procedure may be of some value in calculating size distributions (cf. Section 6.), since this calculation is highly sensitive to fluctuations on the  $F'(v)$  curve.

Finally, it can be remarked that the transform of the  $g$  profile is usually much broader than the one of the  $h$  profile and thus the error in the Fourier transform of the  $f$  profile induced by truncation originates from the  $h$  profile [26].

### 3.2. Background errors

In practice the background level is more readily over- than underestimated, owing to overlapping tails of neighboring reflections. Then, a zero level is assigned unjustly to the line profile at its extremities. Such a line profile can be considered as truncated at

positions where the intensity apparently falls to zero. Suppose that these positions are found at  $-b/2$  and  $b/2$  ( $b/2 < a/2$ , where  $a$  is the period in  $s$ -space; cf. Section 3.1.) and that the background is overestimated with an amount  $\phi$ . It follows for the background affected Fourier transform  $F'(v)$  [26]:

$$F'(v) = F(v) - \phi \frac{\sin \pi b v}{\pi v} \quad (3.3)$$

The discrete Fourier transform is sampled at  $v = n/a$  ( $n = 0, 1, 2, \dots$ ; cf. Section 3.1.) Normally,  $[F(0) - F(1/a)]/F(0) < [\phi b - \phi(\sin \pi b/a)(\pi/a^{-1})]/\phi b$  and as a consequence a "hook" effect will be introduced. For this case the effects on size-strain values as obtained from the Warren-Averbach analysis (cf. Section 4.) have been assessed by model calculation from simulated line profiles [27]. Although the Fourier coefficients of a single line profile may be affected appreciably, it was shown that compensation for the errors in the size-strain values, arising from analogous errors on the first and second order reflections can occur. This effect may be more pronounced for the mean square strain values than for the average crystallite size values (see also reference [28]).

If the background is constant it may be advantageous to underestimate the background with an amount  $\phi$  as has been proposed by Young, Gerdes and Wilson [26]. Then it follows:

$$F'(v) = F(v) + \phi \frac{\sin \pi a v}{\pi v} \quad (3.4)$$

Now  $F'(v) = F(v)$  for  $v = n/a$  ( $n = 1, 2, \dots$ ), which are exactly those values of  $v$  where the Fourier transform is sampled except for  $n = 0$ , (cf. Section 3.1.). This implies that an underestimated constant background need not be corrected, except for  $F'(0)$ . Then, in the Warren-Averbach analysis (cf. Section 4.2.) no errors are introduced when the size and strain values are obtained from the other coefficients.

### 3.3. Statistical variance

The errors due to counting statistics in Fourier coefficients will be estimated by calculating the statistical variances. Only line profiles recorded using the fixed time counting method will be considered. Calculations for the fixed count timing method are analogous, but of less interest because the variances are generally larger than for fixed time counting. The minimum variance counting method will not be considered here [9].

Variances  $\sigma^2$  due to counting statistics can be estimated using the formulae (cf. [29]

$$\sigma^2(W) = \sum_{ij} \frac{\partial W}{\partial x_i} \frac{\partial W}{\partial x_j} \text{cov}(x_i, x_j) \quad i, j = 1, 2, 3, \dots \quad (3.5)$$

$$\text{cov}(x_j, x_j) = \sigma^2(x_j)$$

$$\text{cov}(U, V) = \sum_j \frac{\partial U}{\partial y_j} \frac{\partial V}{\partial y_j} \sigma^2(y_j) \quad (3.6)$$

where  $W$  is a linear function of the variables  $x_1, x_2, x_3, \dots$  and  $U$  and  $V$  are linear functions of the variables  $y_1, y_2, y_3, \dots$  and where  $\text{cov}(z_i, z_j)$  means covariance of the functions of the independent variables  $z_i$  and  $z_j$  and  $\text{cov}(z_i, z_j) = 0$ , if  $z_i$  and  $z_j$  are statistically independent and  $\text{cov}(z_i, z_i) = \sigma^2(z_i)$ , the variance of  $z_i$ . If  $W$  is a non-linear function of  $x_1, x_2, x_3, \dots$  then eq. (3.5) may yield a good approximation if the variance of each  $x_j$  is small.

On the basis of eqs. (3.5) and 3.6) Wilson [29] calculated the variances of quantities useful in x-ray powder diffraction. His formulae (slightly rearranged) concerning the normalized cosine (A) and sine (B) Fourier coefficients of a measured profile are adopted here:<sup>7</sup>

$$\sigma^2[A(n)] = a\{L_i + L_b + L_i A(2n) + 2(L_b - L_i)A^2(n)\}/2L_i^2 t \quad (3.7)$$

$$\sigma^2[B(n)] = a\{L_i + L_b - L_i A(2n) + 2(L_b - L_i)B^2(n) + 2(-1)^n a(G_R - G_L)B(n)/\pi n\}/2L_i^2 t \quad (3.8)$$

$$\text{cov}[A(n), B(n)] = a\{L_i B(2n) + 2(L_b - L_i)A(n)B(n) + a(G_R - G_L)[(-1)^n A(n) - 1/4]/\pi n\}/2L_i^2 t \quad (3.9)$$

here:

$$A(n) = L_i^{-1} \sum_j (I_j - G_j \cos(2\pi n j/a)); \quad B(n) = L_i^{-1} \sum_j (I_j - G_j) \sin(2\pi n j/a);$$

$$L_i = \sum_j (I_j - G_j) \quad ; \quad L_b = (G_R + G_L)a/2$$

In these formulae the period  $a$  is taken here as the (odd) number of observations;  $t$  is the total measuring time;  $I_j$  and  $G_j$  are the observed intensity and the interpolated background intensity at the  $j$ -th position;  $G_L$  and  $G_R$  are the background intensities measured just outside (left and right) the range  $a$  of the profile (to make the background statistically independent of the profile) and  $n$  is the harmonic number.

Only normalized Fourier coefficients are of interest in size-strain analysis (Section 4.). For not-normalized Fourier coefficients eq. (3.5) holds strictly. In the evaluation of eqs. (3.8) and (3.9) slight approximations were made.

As can be seen from the limiting forms of eqs. (3.7) and (3.8) as given in table 1 the general trend for the variance of the cosine Fourier coefficient is an increase with  $n$  if  $L_i > 2L_b$  and a decrease with  $n$  if  $L_i < 2L_b$ , while the general trend for the variance of the sine Fourier coefficient is an increase with  $n$ . All variances will be the smaller the lower the background.

### 3.3.1. Deconvolution

On the basis of eqs. (3.5) and (3.6) cumbersome expressions are obtained for the variances of the cosine ( $A_f$ ) and sine ( $B_f$ ) Fourier coefficients of the pure line profile  $f$ , which expressions are approximations because  $A_f$  and  $B_f$  are not linearly dependent on the cosine ( $A_h$  and  $A_g$ ) and the sine ( $B_h$  and  $B_g$ ) Fourier coefficients of the  $h$  and  $g$  profiles (cf. eq. (2.2)). Three limiting cases are considered: (i)  $n$  very close to zero, (ii) vanishing values of  $B_h$  and  $B_g$ ; this is usually the case for small values of  $n$  if origins are chosen on centroids in the Fourier series evaluation, and (iii) vanishing values of  $A_h$  and  $B_h$  (and nonvanishing values of  $A_g$  and  $B_g$ ); this is the case for large values of  $n$ . In these cases the covariances are neglected. The resulting expressions are listed in table 1. The expression for the mean square value of the modulus of the error as calculated, for all  $n$ , by Stokes [14] is analogous to the result for  $n$  small given here.

During deconvolution there is the problem of choosing the cut-off harmonic number. This choice may be based on the formulae in table 1 for large  $n$ . Evidently, only the statistical errors in the  $h$  profile determine such a criterion.

### 3.3.2. $\alpha_2$ elimination

On the basis of eq. (3.5) expressions are obtained for the variances of the cosine ( $A_1$ ) and the sine ( $B_1$ ) Fourier coefficients of the  $\alpha_1$  line profile. Since  $A_1$  and  $B_1$  are linearly dependent on the cosine ( $A_t$ ) and sine ( $B_t$ ) Fourier coefficients of the total line profile the calculation of variances from eq. (2.5) holds exactly. Results are given in table 1. It is seen that the variances are periodic with  $n$  (cf. reference [19], where also the effect of errors in  $R$  and  $\delta$  is considered).

## 4. Separation of Size and Strain Broadening

### 4.1. Elements of the Warren-Averbach theory

Both small crystallite sizes and lattice distortions in (poly)crystalline materials are known to bring along x-ray diffraction line broadening. Other causes of line broadening may be the presence of deformation and twin faults (cf. reference [5]) and concentration variations [30].

Table 1. Formulae for the variances of the cosine (A) and sine (B) Fourier coefficients of the profile as measured, after deconvolution and after  $\alpha_2$  elimination. The subscripts f, g and h refer to the deconvoluted, standard and measured profiles respectively [cf. eq. (2.1)], while the subscripts t and 1 refer to the total and  $\alpha$  eliminated profiles respectively.  $A_p(n)$  and  $B_p(n)$  denote the real and imaginary part of  $P(n)$  in eq. (2.5). Further, a and t are the period and total measuring time respectively;  $L_i$  and  $L_b$  denote the integrated intensities of the net and background profile respectively [eqs. (3.7) and 3.8)]. In the calculations the covariances of the corresponding cosine and sine Fourier coefficients [eqs. (3.9) and 3.8)]. In the calculations the covariances of the corresponding cosine and sine Fourier coefficients [eq. (3.9)] have been neglected since these are very small normally.

		n close to zero $A(n) \approx 1; B(n) \approx 0$ $B_h(n) \approx 0; B_g(n) \approx 0$	n small $B(n) \approx 0$ $B_h(n) \approx 0; B_g(n) \approx 0$	n large $A(n) \approx 0; B(n) \approx 0$ $A_h(n) \approx 0; B_h(n) \approx 0$
measured profile	$\sigma^2[A(n)]$	$3aL_b/2L_i^2t$	$a\{L_i+L_b+A(2n)+2(L_b-L_i)A^2(n)\}/L_i^2t$	$a\{L_i+L_b\}/2L_i^2t$
	$\sigma^2[B(n)]$	$aL_b/2L_i^2t$	$a\{L_i[-1-A(2n)]+L_b\}/2L_i^2t$	$a\{L_i+L_b\}/2L_i^2t$
deconvoluted profile	$\sigma^2[A_f(n)]$	$A_f^2(n)\{\sigma^2[A_h(n)]/A_h^2(n)+\sigma^2[A_g(n)]/A_g^2(n)\}$	$A_f^2(n)\{\sigma^2[A_h(n)]/A_h^2(n)+\sigma^2[A_g(n)]/A_g^2(n)\}$	$\sigma^2[A_h(n)]/\{A_g^2(n)+B_g^2(n)\}$
	$\sigma^2[B_f(n)]$	$A_f^2(n)\{\sigma^2[B_h(n)]/A_h^2(n)+\sigma^2[B_g(n)]/A_g^2(n)\}$	$A_f^2(n)\{\sigma^2[B_h(n)]/A_h^2(n)+\sigma^2[B_g(n)]/A_g^2(n)\}$	$\sigma^2[A_h(n)]/\{A_g^2(n)+B_g^2(n)\}$
$\alpha_2$ eliminated profile	$\sigma^2[A_1(n)]$	$aL_b\{3A_p^2(n)+B_p^2(n)\}/\{A_p^2(n)+B_p^2(n)\}^2L_i^2t$	$a\{A_p^2(n)[L_i+L_b+L_iA_t(2n)+2(L_b-L_i)A_t^2(n)]+B_p^2(n)[L_i(1-A_t(2n))+L_b]\}/\{A_p^2(n)+B_p^2(n)\}^2L_i^2t$	$a\{L_i+L_b\}/\{A_p^2(n)+B_p^2(n)\}2L_i^2t$
	$\sigma^2[B_1(n)]$	$aL_b\{A_p^2(n)+3B_p^2(n)\}/\{A_p^2(n)+B_p^2(n)\}^2L_i^2t$	$a\{B_p^2(n)[L_i+L_b+L_iA_t(2n)+2(L_b-L_i)A_t^2(n)]+A_p^2(n)[L_i(1-A_t(2n))+L_b]\}/\{A_p^2(n)+B_p^2(n)\}^2L_i^2t$	$a\{L_i+L_b\}/\{A_p^2(n)+B_p^2(n)\}2L_i^2t$

The presently most widely applied theory to describe size-strain broadening was developed by Warren and Averbach [21]<sup>8</sup>. In this theory, regions in the sample which scatter the x-rays coherently are designated as domains. The different domains are thought to diffract essentially incoherently.

According to the kinematical diffraction theory the diffracted intensity of a domain corresponds to

$$I \div \sum_m \sum_{m'} \exp 2\pi i \underline{H} \cdot (\underline{R}_{m'} - \underline{R}_m) \quad (4.1)$$

where  $\underline{H}$  and  $\underline{R}_m$  are the reciprocal lattice vector and the position vector of the  $m$ -th unit cell respectively according to

$$\underline{H} = h_1 \underline{b}_1 + h_2 \underline{b}_2 + h_3 \underline{b}_3$$

$$\underline{R}_m = (m_1 + X_m) \underline{a}_1 + (m_2 + Y_m) \underline{a}_2 + (m_3 + Z_m) \underline{a}_3$$

where  $\underline{a}_1, \underline{a}_2, \underline{a}_3$  and  $\underline{b}_1, \underline{b}_2, \underline{b}_3$  are the unit vectors in real and reciprocal space respectively and  $X_m, Y_m, Z_m$  are the displacements with respect to the reference lattice in units  $\underline{a}_1, \underline{a}_2, \underline{a}_3$ . Each (hkl) reflection from a crystal of any symmetry can be considered as a (00 $\ell$ ) reflection from a crystal having orthorhombic axes [33,34]. Thus, the length of the diffraction vector can be approximated by  $h_3 |\underline{b}_3|$ .

Further, the domain is thought to consist of columns of unit cells, perpendicular to the (00 $\ell$ ) planes. Then it can be shown (cf. reference [5]) that the diffracted powder per unit length of the intersection of the diffraction cone with the receiving surface can be expressed as the Fourier series

$$P(h_3) \div \sum_{n=-\infty}^{+\infty} F(n) \exp 2\pi i n h_3 \quad (4.2)$$

with

$$F(n) = A^S(n) F^D(n, \ell) \quad (4.3)$$

The size Fourier coefficient  $A^S(n)$  is real and independent of the order  $\ell$  of the reflection in contrast with the distortion Fourier coefficient  $F^D(n, \ell)$ :

<sup>8</sup>Other theories are given by Krivoglaz [31] and Ergun [32].

$$A^S(n) = \frac{N(n)}{N_3} = \frac{1}{N_3} \int_n^\infty (i - n)p(i)di \quad (4.4)$$

$$F^D(n, \ell) = A^D(n, \ell) + iB^D(n, \ell) = \langle \exp 2\pi i \ell Z(n) \rangle \quad (4.5)$$

By averaging over all columns in the sample,  $N(n)$  is the average number per column of domains of unit cells a distance of  $n$  cells apart,  $N_3$  is the average domain size in unit cells perpendicular to the reflecting planes,  $p(i)di$  is the fraction of columns of lengths between  $i$  and  $i+di$  cells and  $Z(n)$  is the difference between the displacements (in units  $a_3$ ) of two domains  $n$  cells apart in a column. Usually  $Z(n)$  is replaced by the strain  $e(n) = Z(n)/n$ . From eq. (4.4) it is obtained

$$\left. \frac{dA^S(n)}{dn} \right|_{n \rightarrow 0} = -\frac{1}{N_3} \quad (4.6)$$

Now the problem arises of what a domain represents actually. The theory was developed originally for cold-worked materials. According to Warren [35,5] cold work can produce dislocation arrays, such as small angle boundaries, which subdivide the material into the domains as mentioned above. Then the theory implies that the change in orientation over a boundary is abrupt enough to cause the domains to scatter incoherently. With respect to the latter point some doubts have been raised [38,28]: A small angle boundary does not interrupt coherence for very small  $n$ -values (corresponding to an averaging distance for the  $e$  factor (eq. (4.5)) of a magnitude equal to the range of the strain field of the dislocation array), since the orientation changes gradually and not abruptly over the boundary. Also, according to Ergun [32], if the lattice is highly defective, the domain concept may fail and then the notion of defect broadening can be introduced, which gives rise to Cauchy-shaped profiles. It was demonstrated that the experimental size Fourier coefficients for cold-worked tungsten and aluminum might be described by such Cauchy functions. Thus, for the case of cold-worked materials care should be taken in identifying the  $n$  with a physical entity.<sup>9</sup>

In the case of deformation and twin faults are present, the initial slope of the size Fourier coefficient curve (cf. eq. (4.6)) does not correspond to the true column size  $N_3$ , but its value is denoted as an "effective" size. Therefore, the methods to be presented in the following sections, which provide sizes on the basis of eq. (4.6), are equally well applicable to obtain effective sizes in case deformation and twin faults are present. Procedures exist to evaluate the true column size from the effective size (cf. [5]).

On the other hand, for many specimens the interpretation is less ambiguous: In case the powder specimen to be investigated consists of a system of loosely bound particles (e.g. catalysts, colloids) each particle may be monocrystalline and hence can be identified as a domain. Also, the domain concept is very useful in case abrupt changes in orientation occur, as is, for example, the case with high angle boundaries.

#### 4.2. Classical method

The original analysis for separating the effects of size and strain is due to Warren and Averbach [37]. Normally, in the Fourier analysis of line profiles the origins are confined to the respective centroids and consequently the imaginary parts of the Fourier coefficients are small. Then the analysis is restricted to the real part of the Fourier coefficients:

$$A(n, \ell) = \langle \cos 2\pi \ell n e(n) \rangle N(n)/N_3 \quad (4.7)$$

Since  $A^D(n, \ell)$  is dependent on  $\ell$  and  $A^S(n)$  is not, size and strain effects can be separated by taking the logarithm of eq. (4.7):

$$\ln A(n, \ell) = \ln[N(n)/N_3] + \ln \langle \cos 2\pi \ell n e(n) \rangle \quad (4.8)$$

Two power series expansions are applied:

$$\begin{aligned} \langle \cos 2\pi \ell n e(n) \rangle &= 1 - \frac{[2\pi \ell n e(n)]^2}{2!} + R_4^{\cos} \\ &\approx 1 - 2\pi^2 \ell^2 n^2 \langle e^2(n) \rangle \end{aligned} \quad (4.9)$$

$$\begin{aligned} \ln[1 - 2\pi^2 \ell^2 n^2 \langle e^2(n) \rangle] &= -2\pi^2 \ell^2 n^2 \langle e^2(n) \rangle + R_4^{\ln} \\ &\approx -2\pi^2 \ell^2 n^2 \langle e^2(n) \rangle \end{aligned} \quad (4.10)$$

where  $R_4^{\cos}$  and  $R_4^{\ln}$  are the remainders of the two series expansions. From eqs. (4.8), (4.9), and (4.10), it follows that

$$\ln A(n, \ell) \approx \ln[N(n)/N_3] - 2\pi^2 \ell^2 n^2 \langle e^2(n) \rangle \quad (4.11)$$

If at least two orders of a reflection are available then values for  $N(n)/N_3$  and  $\langle e^2(n) \rangle$  can be obtained from the slope and intercept of a plot of  $\ln A(n, \ell)$  versus  $\ell^2$ .

Now the errors arising from both series expansions will be investigated. If  $\langle e^2(n) \rangle^2$  is approximated by  $\langle e^4(n) \rangle$ , a maximal estimate for the remainder  $|R_4^{\cos}|$  and a minimal estimate for  $|R_4^{\ln}|$  yields (cf. reference [38]):

$$\left| R_4^{\ln} \right|_{\min} = 3 \left| R_4^{\cos} \right|_{\max} \quad (4.12)$$

Since the cosine is underestimated with  $|R_4^{\cos}|$  and the logarithm is over-estimated with  $|R_4^{\ln}|$  it follows from eq. (4.12) that the logarithm series expansion introduces an error in the final result at least twice that of the cosine series expansion.

Let us also consider the ratio R of the relative errors caused by truncation of the series after the terms with  $\ell^2$ . Defining  $q = 2\pi^2 \ell^2 n^2 \langle e^2(n) \rangle$ , it follows from eqs. (4.9) and (4.10) with the additional assumption  $e(n) = \langle e^2(n) \rangle^{1/2}$  that:

$$R = \frac{R_4^{\ln} / \ln(1-q)}{R_4^{\cos} / \cos\sqrt{2q}} = \frac{[\ln(1-q) - (-q)] / \ln(1-q)}{[\cos\sqrt{2q} - (1-q)] / \cos\sqrt{2q}} \quad (4.13)$$

The relative errors in the cosine and logarithm series expansions and their ratio R, as defined by eq. (4.13), are plotted in figure 1. It is clear that at small values of q the neglect of higher-order terms in the logarithm series is much more important than in the cosine series; at larger values of q the difference becomes less pronounced.

#### 4.3. Modified method

The errors introduced by the series expansion for the logarithm (eq. (4.10)) can be avoided [39]. The direct substitution of the power series expansion for  $\langle \cos 2\pi \ell n e(n) \rangle$  according to eq. (4.9) into eq. (4.7) yields:

$$A(n, \ell) \simeq \frac{N(n)}{N_3} - \frac{N(n)}{N_3} 2\pi^2 \ell^2 n^2 \langle e^2(n) \rangle \quad (4.14)$$

Now the influence of size and strain are not separated as in eq. (4.11). However, if two orders of a reflection are available the values of  $N(n)/N_3$  and  $\langle e^2(n) \rangle$  are readily obtained from a plot of  $A(n, \ell)$  versus  $\ell^2$ .

The results derived from both methods of separation will be compared. As can be shown [39] values of  $A^S(n)$  and  $\langle e^2(n) \rangle$  obtained with the modified method (eq. (4.14)) are always smaller than the values deduced with the classical method (eq. (4.11)) and these differences increase with increasing values of n. This also implies that the average crystallite size as determined from eq. (4.6) is smaller for the modified method. This is illustrated for some practical examples in table 2.

In practice the second order of a reflection is usually measured less accurately than the first order. Therefore, spurious variations may be present on the Fourier coefficients

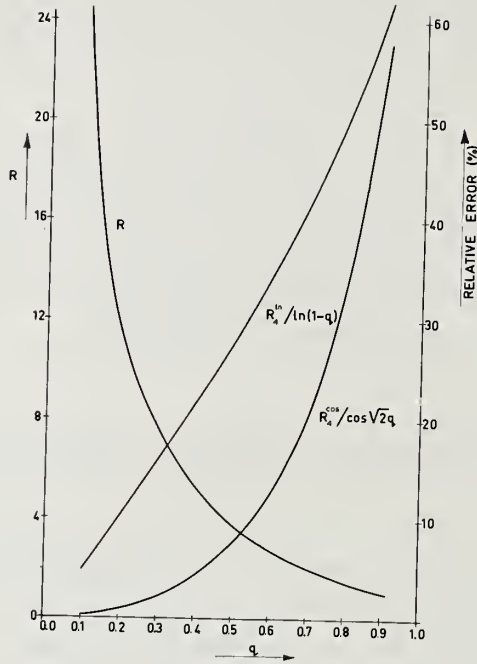


Figure 1. The relative error in the series expansion for the cosine:  $R_4^{\cos}/\sqrt{2q}$ ; the relative error in the series expansion for the logarithm:  $R_4^{\ln}/\ln(1-q)$  and their ratio  $R$  as a function of  $q = 2\pi^2 \ell^2 n^2 \langle e^2(n) \rangle$ .

of the second order mainly. This will produce spurious ripples on the  $A^S(n)$  curve. These ripples will be enhanced in the  $A^S(n)$ -curve obtained from eq. (4.11) as compared to the  $A^S(n)$ -curve obtained from eq. (4.14). Also  $\langle e^2(n) \rangle$  obtained from eq. (4.11) is more sensitive to spurious variations in the Fourier coefficients of the second order as compared to  $\langle e^2(n) \rangle$  obtained from eq. (4.14) [39].

Seldom more than two orders of a reflection are available. But for such a case one more term in the series for  $\langle \cos 2\pi \ell n e(n) \rangle$  can be considered: If terms in  $\ell^6$  and higher orders are neglected, the Fourier coefficient of the total line profile can be expressed as:

$$A(n, \ell) = a - b\ell^2 + c\ell^4 \quad (4.15)$$

where  $a = N(n)/N_3$ ;  $b = a2\pi^2 n^2 \langle e^2(n) \rangle$  and  $c = a2\pi^4 n^4 \langle e^4(n) \rangle/3$ . As in eq. (4.14), again the influences of size and strain are not separated, but the three coefficients  $a$ ,  $b$ , and  $c$  are readily obtained if three orders of a reflection are available. After substitution of  $a [=N(n)/N_3]$  in  $b$  and  $c$ , values for  $\langle e^2(n) \rangle$  and  $\langle e^4(n) \rangle$  are found.

Table 2. Effective [see footnote to eq. (4.6)] crystallite sizes ( $D_e$ ) and root mean square strains ( $\langle e^2(L) \rangle^{1/2}$ ) in some cold-worked metals and alloys, as obtained by the classical method [eq. (4.11)] and the modified method [eq. (4.14)] (data from Misra and Ghosh [47]).

Metal/Alloy	(hkl) Type		Classical Method	Modified Method
Ti	001	$D_e$ (nm)	38.0	37.3
		$\langle e^2(10 \text{ nm}) \rangle^{1/2} \times 10^3$	1.58	1.55
Zr	001	$D_e$ (nm)	28.0	21.0
		$\langle e^2(10 \text{ nm}) \rangle^{1/2} \times 10^3$	2.10	1.66
Ag-15%In	111	$D_e$ (nm)	8.0	7.5
		$\langle e^2(D_e) \rangle^{1/2} \times 10^3$	3.50	2.60
	100	$D_e$ (nm)	4.5	4.0
		$\langle e^2(D_e) \rangle^{1/2} \times 10^3$	5.50	3.90
Cu-12.46%Ge	001	$D_e$ (nm)	9.2	8.8
		$\langle e^2(5 \text{ nm}) \rangle^{1/2} \times 10^3$	3.30	3.00
Cu-17.72%Ge	001	$D_e$ (nm)	17.6	17.0
		$\langle e^2(5 \text{ nm}) \rangle^{1/2} \times 10^3$	2.65	2.42

#### 4.4. Evaluation of results

##### 4.4.1. Mean square strain values

The x-ray diffraction technique is one of the few experimental tools which provide quantitative information about non-uniform microstrains averaged over moderately large volumes. Therefore, a discussion will be dedicated to the mean square strain values found.

Normally, the  $\langle e^2(n) \rangle$  values found will increase as  $n$  decrease<sup>10</sup>, and the largest value might be found at a distance close to the interplanar spacing ( $n = 1$ ), or, as an approximation, zero averaging distance. There, the true strain component is found. This extrapolation is difficult to perform in practice (due to experimental uncertainties such as the "hook" effect (Section 4.4.4.)). An extrapolation of the logarithm of the strain value versus  $n$  to  $n = 0$  might be carried out easier [40]. If an extrapolation is omitted, one often tabulates the (root) mean square strain values at a fixed distance  $L = n \left| a_3 \right|$ , such as 5 or 10 nm, or  $L = \alpha N_3 \left| a_3 \right|$ , where  $\alpha$  can be 1/2 or 1, for example, (see table 2).

Rothman and Cohen [41,42] suggested that, if dislocations are the principal cause of microstrains a reasonable approximation for  $\langle e^2(n) \rangle$  may be

$$\langle e^2(n) \rangle = c_1/n \quad (4.16)$$

where  $c_1$  is a constant for the reflection considered. From eq. (4.16) with eqs. (4.5) and (4.9) it is found:

$$A^D(n, \ell) \approx 1 - 2\pi^2 \ell^2 n c_1 \approx \exp \{-2\pi^2 \ell^2 c_1 n\} \quad .$$

Eastabrook and Wilson [43] showed, on another basis, that for larger values of  $n$  the following approximation holds

$$A^D(n, \ell) = \exp \{-c_2 n\} \quad . \quad (4.17)$$

The above suggests that the approximation (4.16) is especially useful for larger values of  $n$ . Also, Gangulee [44] concluded that eq. (4.16) will generally not hold for small values of  $n$ . Hence, a method [45] for the separation of size and strain effects by use of the initial slope ( $n \rightarrow 0$ ) of the  $A(n, \ell)$ -curve, based on eq. (4.16), may be less reliable<sup>11</sup>.

For arbitrary dislocation configurations the mean square strain curves may be calculated numerically. Comparison of experimental and simulated  $\langle e^2(n) \rangle$  curves may give some insight into the imperfect structure. Such a computer program has been developed for elastically isotropic materials by Turunen [46].

In general for different (hkl) types of reflections, different  $\langle e^2(n) \rangle$  values will be found. This may, for example, be due to oriented defects (such as precipitate particles growing preferentially on specific (hkl) planes) and/or the elastic anisotropy of the material. One might rationalize (e.g. for the case of cold-work deformation) the (hkl) dependence of the microstrain in the same way as can be done for the macrostrain: For macrostrain it

<sup>10</sup>Instead of  $n$ , the variable  $L = n \left| a_3 \right|$ , a real distance perpendicular to the reflecting planes, is often used.

<sup>11</sup>In case the approximation (eq. (4.16)) is used, nevertheless, a single-line method (with  $n > 0$ ) should be preferred (cf. Section 4.5.).

has been found that the Voigt-Reuss-mean (also designated as Voigt-Reuss-Hill) model affords a sufficient description [48,41]. Models with a better theoretical basis [49] do not give essentially different results [50,51]. If  $e_h$  and  $e_p$  are the strain in the specimen surface and in a direction perpendicular to the surface respectively,  $\sigma$  denotes the stress parallel to the surface and  $s_{ij}$  are the elastic coefficients in Voigt notation, it follows for cubic crystals

$$e_h^{hkl} = (1/2) \left\{ s_{11} - s_{12} s \cdot S + \frac{4s(s_{11}+2s_{12})+5s_{44}(s_{11}+s_{12})}{6s+5s_{44}} \right\} \sigma$$

$$e_p^{hkl} = \left\{ s_{12} + s \cdot S + \frac{2s(2s_{11}+2s_{12})+5s_{12}s_{44}}{6s+5s_{44}} \right\} \sigma \quad (4.18)$$

where

$$S = \frac{h^2 k^2 + h^2 \ell^2 + k^2 \ell^2}{(h^2 + k^2 + \ell^2)^2}$$

and

$$s = \frac{s_{11} - s_{12} s_{44}}{2}$$

These formulae can be derived on the basis of the reference [52] and are valid only if no texture in the specimen exists. If  $\langle e^2(n) \rangle^{1/2}$  is identified with  $e_p$ ,  $e_h$  and  $\sigma$  can be calculated while the  $(hkl)$  dependence is provided by  $S$ .

#### 4.4.2. Strain distribution

Introducing a strain distribution  $g[e(n)]$  such that  $\int_{-\infty}^{\infty} g[e(n)] de(n) = 1$ , it follows

$$A^D(n, \ell) = \langle \cos 2\pi \ell n e(n) \rangle = \int_{-\infty}^{\infty} g[e(n)] \cos \{2\pi \ell n e(n)\} de(n) \quad (4.19)$$

For a Gaussian distribution  $g[e(n)] = a/\sqrt{\pi} \exp\{-a^2 e^2(n)\}$  with  $\langle e^2(n) \rangle = (2a^2)^{-1}$  it is obtained:

$$A^D(n, \ell) = \exp \{-\pi^2 \ell^2 n^2 / a^2\} = \exp \{-2\pi^2 \ell^2 n^2 \langle e^2(n) \rangle\} \quad (4.20)$$

Hence, for this special case the classical method of separating size and strain (eq. 4.11) yields the exact results. However, other distribution functions may be nearer to practice (for example, a Cauchy function with cut off tails as suggested by Williamson and Smallman [53]; see also reference [35]). Also, there is no a priori need that the shape of the distribution function is independent of  $n$ . Therefore, in general, the modified method (eq. (4.14)) is expected to give more correct results.

A consequence of eq. (4.19) is that the strain distribution function can be determined if sufficient orders of a reflection are available, since by Fourier transformation

$$g[e(n)] = 2n \int_0^{\infty} A^D(n, \ell) \cos \{2\pi \ell n e(n)\} d\ell \quad (4.21)$$

In general, however, not enough data will be available to determine the dependence of the distortion Fourier coefficient on  $\ell$ . Only for cold-worked elastically isotropic materials, where all peaks available can be combined (cf. reference [5]), it is possible to determine strain distributions for not too small values of  $n$  [54].

#### 4.4.3. Determination of the average crystallite size

Usually, the average crystallite size is determined from the initial slope of the size Fourier coefficient curve (eq. (4.6)). In principle, it is possible to obtain the average crystallite size before size and strain are separated. If it is considered that  $d[\langle e^2(n) \rangle]/dn (n \rightarrow 0) = \text{finite}$ , it immediately follows from eq. (4.14)

$$\left. \frac{dA(n, \ell)}{dn} \right|_{n \rightarrow 0} = \left. \frac{dA^S(n)}{dn} \right|_{n \rightarrow 0} = -\frac{1}{N_3} \quad (4.22)$$

In case  $\langle e^2(n) \rangle$  is described by eq. (4.16) an additional term will be introduced at the right-hand side of eq. (4.22) (cf. reference [45]). However, since finite values of  $\langle e^2(n) \rangle$  for  $n \rightarrow 0$  are more realistic (cf. references [54, 40, 36]) eq. (4.16) is not suitable for  $n \rightarrow 0$ . In practice the determination of the initial slope may be problematic because of the "hook" effect (see next section).

#### 4.4.4. "Hook" effect

In the experimental  $A(n, \ell)$  and  $A^S(n)$  curves often a negative curvature near  $n = 0$  is observed, whereas the Warren-Averbach theory prescribes a positive curvature (eq. (6.1)). Two experimental errors have been indicated for this effect: truncation of the line profile (Section 3.1.) and a background estimated too high (Section 3.2.).

The usual method of correction for the "hook" effect consists of extrapolating the straight portion of the Fourier coefficient curve at small values of  $n$  to  $n = 0$ .

However, it was shown [28, 36] that there may be also a theoretical background to a "hook" effect in the  $A^S(n)$  curve. For wide strain distributions the truncation of the series expansion in eq. (4.9) (and in eq. (4.10)) if the classical method of size-strain separation is used) after the term with  $\langle e^2(n) \rangle$  may introduce errors such that a plot of  $A(n, \ell)$  versus  $\ell^2$  (classical:  $\ln A(n, \ell)$  versus  $\ell^2$ ) is no longer linear in fact. Linear

extrapolation, if performed, may introduce a "hook" in the  $A^S(n)$  curve. In such a case, an average crystallite size determination according to eq. (4.22) may be advised before size and strain effects are separated.

#### 4.5. Single-line methods

There are many practical cases where crystallite size and strain are anisotropic and where higher orders of a reflection cannot be measured reliably or only one reflection is available (e.g. for supported catalysts, oriented thin films, multiphase composites and heavily deformed materials). Hence, one is interested in obtaining size-strain parameters from a single line profile. Then additional assumptions are required.

All single-line methods proposed approximately the size Fourier coefficient (eq. (4.4)) by

$$A^S(n) = 1 - n/N_3 \quad . \quad (4.23)$$

This implies that all columns in the range of  $n$ -values considered are assumed to be of equal length. If  $e(n)$  is approximated with its mean  $\langle e \rangle$ , it follows

$$A(n, \ell) = (1 - n/N_3) \cos 2\pi \ell n \langle e \rangle \quad . \quad (4.24)$$

Then the parameters  $N_3$  and  $\langle e \rangle$  can be solved from eq. (4.24) for any two Fourier coefficients  $A(n_1, \ell)$  and  $A(n_2, \ell)$ . In general, different (if plausible) values will be obtained from different  $(n_1, n_2)$  pairs. Then some kind of curve fitting will provide more realistic estimates [55]. In case it is assumed in addition that the strain distribution is Gaussian and independent of  $n$  [56], it is obtained

$$\ln A(n, \ell) = \ln(1 - n/N_3) - 2\pi^2 \ell^2 n^2 \langle e^2 \rangle \quad (4.25)$$

which can also be considered as obtained by series expansion from eq. (4.24) with  $\langle e \rangle^2 \approx \langle e^2 \rangle$ . The average crystallite size can be determined according to eq. (4.22) and according to eq. (4.25),  $\langle e^2 \rangle$  can be obtained from the slope of the straight line in the plot of  $\ln\{A(n, \ell)/(1 - n/N_3)\}$  versus  $n^2$ .

The methods discussed above characterize the microstrains present in the crystallites by a single parameter. In our opinion these single-line Fourier methods are less practicable than a recently proposed rapid single-line integral breadth method [3]. In this method, it was assumed that the crystallite size effect gave rise to a Cauchy profile (corresponding to  $A^S(n) = \exp\{-n/N_3\}$ ) and that the microstrain effect gave rise to a Gaussian profile (corresponding to  $A^D(n, \ell) = \exp\{-2\pi^2 \ell^2 n^2 \langle e^2 \rangle\}$ ).

On the other hand single-line Fourier methods may provide additional information if a certain dependence of  $\langle e^2(n) \rangle$  on  $n$ , say  $f(n)$ , is assumed. It follows

$$A(n, \ell) = (1 - n/N_3) [1 - 2\pi^2 \ell^2 n^2 f(n)] \quad . \quad (4.26)$$

For example,  $f_1(n) = c_1/n$  ( $c_1 > 0$ ) (cf. eq. 4.16) or  $f_2(n) = \exp\{c_3 n + c_4\}$  ( $c_3, c_4 < 0$ ) may be applied. With  $f_1(n)$  from eq. (4.26)  $N_3$  and  $c_1$  can be solved for any two Fourier coefficients  $A(n_1, \ell)$  and  $A(n_2, \ell)$  and with  $f_2(n)$  from eq. (4.26)  $N_3$ ,  $c_3$  and  $c_4$  can be solved for three Fourier coefficients  $A(n_1, \ell)$ ,  $A(n_2, \ell)$  and  $A(n_3, \ell)$ .

Applying  $f_1(n)$  Gangulee [44] found valid and invalid solutions (e.g. negative size and strain values). Especially for very small values of  $(n_1, n_2)$  invalid solutions were obtained which may be attributed to the invalidity of the approximation  $f_1(n)$  for very small values of  $n$  (see the discussion below eq. (4.17)) and experimental errors (e.g. the "hook" effect). For this case, Mignot and Rondot [57] tried to overcome these difficulties by fitting a polynomial of second degree (cf. eq. (4.26) after substitution of  $f_1(n)$ ) to the experimental Fourier coefficient curve using a least squares method for different ranges of  $n$ -values and selecting the most appropriate solution.

No experience exists with  $f_2(n)$ . It may give better results for small values of  $n$ .  $f_2(n)$  was applied in reference [40] to determine  $\langle e^2(0) \rangle$  by extrapolation from the values of  $\langle e^2(n) \rangle$  obtained by a multiple line method.

## 5. Line Profile Analysis Using a Non-Ideal Standard Specimen

Because of unavoidable alignment errors [6] the standard line profile  $g$  cannot be calculated, but has to be determined experimentally. However, the ideal standard specimen is seldom available. In many cases a standard line profile is recorded from a standard specimen different in composition [58] or even made of another material (e.g. reference [59]). Furthermore, the standard specimen may contain some structural defects (e.g. reference [60]). This leads to non-ideal, approximate standard line profiles at an incorrect  $\sin\theta$  range with an incorrect broadening. Large errors may result from such defects (cf. reference [61,62]).

It is the purpose of this section to present some rules for the assignment of origins to the profiles in the deconvolution procedure and to propose correction factors for the elimination of errors due to incorrect broadening of the standard line profile.

### 5.1. The ideal standard line profile

The ideal standard line profile  $g$  comprises exactly the broadening by the instrumental conditions and the wavelength distribution present in the  $h$  profile. The ideal standard line profile can be described by the convolution  $g^i * g^s$ , where  $g^i$  and  $g^s$  represent the broadening by the instrumental conditions and the wavelength distribution respectively. The origins for  $g^i$  and  $g$  are taken at the same value of  $\sin\theta$  and the centroid of  $g^s$  is at the origin.

The ideal standard line profile is not really constant over the  $\sin\theta$  range of the  $f$  profile. In practice, applying Stokes' method (eq. (2.2)) some position in the  $\sin\theta$  range of the  $h$  profile should be chosen as a reference for the ideal standard line profile. For that purpose the centroid of the  $h$  profile is used in this paper. Thus, the ideal standard line profile should be recorded from an ideal standard specimen with an interplanar spacing

such that the centroids of the h and g profiles coincide ( $d_c$  is determined after correction for the centroid shift due to instrumental aberrations). By choosing the origins of the g and h profiles at the same value of  $\sin\theta$  the centroid of the resulting f profile will be at the origin (since  $\langle h \rangle = \langle g \rangle + \langle f \rangle$  and  $\langle h \rangle = \langle g \rangle$ ; the brackets denote the centroids of the profiles on the  $\sin\theta$  scale).

For the subsequent interpretation of the structural broadening the centroid of the profile has to be identified with  $\sin\theta = \langle \lambda_c \rangle / 2d_c$ , where  $\langle \lambda_c \rangle$  is the centroid wavelength of the x-ray spectrum used. The strain values  $e(n)$  obtained from the Warren-Averbach analysis are then related to the reference spacing  $d_c$ . A macrostrain follows from the difference  $d_c - d_0$ , where  $d_0$  is the spacing of the material under investigation when the material is ideally crystallized.

It is remarked that an ideally crystallized specimen does not necessarily produce an ideal standard line profile because its centroid is not necessarily at the same  $\sin\theta$  value as the centroid of the h profile (cf. references [5,62]).

## 5.2. The non-ideal standard line profile and its relation to the ideal standard line profile

In the non-ideal standard line profile the following types of deviations are distinguished:

- (i) the standard profile is measured at a position on the  $\sin\theta$  scale different from that of the desired exact standard profile g;
- (ii) the standard profile is measured from a standard with a specimen transparency effect different from that of the specimen to be investigated; and,
- (iii) the physical profile  $f_0$  of the standard specimen is not a delta function, but it is (slightly) broadened by strain and finite crystallite size.

In general, the measured non-ideal standard line profile  $g_m$  can be described by the convolution  $g_m^i * g_m^s * f_0$ . It may be displaced at the  $\sin\theta$  scale relative to the ideal standard line profile and contain an erroneous broadening. With  $G_m(n)$  being the Fourier coefficient of the measured line profile  $g_m$  and  $F_0(n)$  the Fourier coefficient of the profile  $f_0$  such that  $F_0(0) = G(0) = G_m(0) = 1$ , we introduce a correction factor

$$C(n) = \frac{F(n)}{F_m(n)} = \frac{G_m(n)}{G(n)} = \frac{G_m^i(n)G_m^s(n)F_0(n)}{G^i(n)G^s(n)} \quad (5.1)$$

where  $F_m(n) = H(n)/G_m(n)$  is the approximate, "measured" Fourier coefficient of the pure profile and the superscripts refer to the corresponding profiles.

In general, the correction factor  $C(n)$  (eq. (5.1)) is the product of the correction factors for displacement and incorrect broadening. Provided the origins for the h and  $g_m$  profiles are chosen at the same value of  $\sin\theta$ , the correction for the displacement

can be accomplished by

$$C(n) = \exp \frac{2\pi i n \Delta}{a} , \quad (5.2)$$

where  $\Delta = \langle g_m \rangle - \langle g \rangle = \langle g_m \rangle - \langle h \rangle$ . It is not necessary to calculate the centroids, since  $\Delta$  can be found from the initial slope of the sine Fourier coefficients  $B_m(n)$  of the  $f_m$  profile obtained by using the  $g_m$  profile in the deconvolution. It follows that

$$\frac{1}{F_m(0)} \left. \frac{dB_m(n)}{dn} \right|_{n \rightarrow 0} = - \frac{2\pi \Delta}{a} \quad (5.3)$$

Alternatively, in case the centroids are determined the correction implied by eq. (5.2) may be performed by choosing the origins at the centroids of the  $h$  and  $g_m$  profiles.

Correction factors for the errors due to the incorrect broadening of  $g_m$ , after choosing the origins at the centroids of the profiles, will be discussed below.

#### 5.2.1. A standard specimen with an improper spacing

Assuming the same effects due to the instrumental aberrations in the  $g$  and  $g_m$  profiles (see also below eq. (5.5)) the displacement  $\Delta$  (eq. (5.2)) takes the form

$$\Delta_1 = \frac{\langle \lambda_c \rangle}{2} \left( \frac{1}{d_m} - \frac{1}{d_c} \right) \quad (5.4)$$

According to Bragg's law, a non-ideal standard specimen with a spacing  $d_m \neq d_c$  "projects" the wavelength distribution on the  $\sin\theta$  scale at a different position and with a different broadening as compared to the ideal standard line profile.

A solution to this problem may be obtained by applying the profile fitting method [63]. In this method, an instrumental line profile is approximated by a small number of Cauchy-functions. Several instrumental line profiles taken over a large range of  $\theta$  values are measured. The parameters for the Cauchy-functions are obtained by fitting. Normally, an instrumental line profile is needed at an unmatched  $\theta$  value. The parameters necessary for the evaluation in terms of Cauchy-functions of that profile are obtained by interpolation. However, in case of size-strain analysis on the basis of the method developed by Warren and Averbach, the Fourier coefficients of the pure profile are required. Therefore, a direct description in terms of Fourier coefficients is preferable. For the determination of Fourier coefficients of instrumental profiles at unmatched  $\theta$ -values an analogous interpolation procedure can be followed as for the determination of the parameters of the Cauchy-functions.

Although the above mentioned interpolation procedures are possible methods for size-strain analysis, it should be recognized that these procedures are laborious and still do not give exact results. Moreover, any change in the experimental conditions (e.g. slit

width, x-ray spectrum<sup>12</sup>, absorption in the specimen) obliges to measure again the instrumental profiles.

An alternative, analytical and quick method is possible to correct for standard profiles measured at incorrect  $\theta$  values [61,62]. The method is based on an analytical description of the  $K\alpha$  doublet [11]: The standard line profile  $g(x)$ , with  $x$  defined on a  $\sin\theta$  scale, is taken as the sum of the  $\alpha_1$  and  $\alpha_2$  components. The shape and position of the components is related to a standard profile  $g_c(x)$  intermediate between that of the  $\alpha_1$  and  $\alpha_2$  components.  $g_c(x)$  is considered as the convolution of the spectral profile  $g_c^s(x)$  of the intermediate wavelength distribution and the profile  $g_c^i(x)$  due to the broadening caused by the instrumental conditions. For  $g_c^s(x)$  the generally accepted Cauchy wavelength distribution is adopted [6,64]. This model has been experimentally verified [62,65].

Applying eq. (5.1) and using the model for the  $K\alpha$  doublet the correction for the incorrect broadening of  $g_m$  can be accomplished by

$$C_1(n) = \frac{G_{c,m}^i(n)}{G_c^i(n)} \frac{(1+R)}{(1+R_m)} \frac{\exp\{-inR_m\alpha_m\} + R_m \exp\{in\alpha_m\}}{\exp\{-inR\alpha\} + R \exp\{in\alpha\}} \times \\ \times \exp\left\{-\frac{\pi n w}{2a} \left(\frac{1}{d_m} - \frac{1}{d_c}\right)\right\} \quad (5.5)$$

where  $G^i(n)$  is the Fourier coefficient of  $g^i$ ;  $R = g_{\alpha_2}(\max)/g_{\alpha_1}(\max)$ ;  $\alpha = \pi (\langle\lambda_2\rangle - \langle\lambda_1\rangle/d(1+R)a)$ , where  $\langle\lambda_1\rangle$  and  $\langle\lambda_2\rangle$  are the centroids of the  $\alpha_1$  and  $\alpha_2$  wavelength distributions respectively [ $\langle\lambda_c\rangle = (\langle\lambda_1\rangle + R\langle\lambda_2\rangle)/(1+R)$ ] and  $w$  is the weighted average (cf.  $\langle\lambda_c\rangle$ ) of the widths at half height of the spectral  $\alpha_1$  and  $\alpha_2$  components. From experimental results on the determination of the broadening by the instrumental aberrations [11] it was concluded that for practical cases  $G_{c,m}^i(n)/G_c^i(n) = 1$ , especially for the small values of  $n$ , which are of interest in size-strain analysis. Then the correction factor  $C_1(n)$  can be calculated since all other factors are known<sup>13</sup>.  $R$  should be taken from the  $h$  profile since  $R_m$  is not necessarily equal to  $R$  [66]. A method to determine  $R$ -values is given in reference [11].

<sup>12</sup>Assuming that a high angle reflection of a standard specimen is broadened only by the x-ray spectrum used [63] a high angle reflection has to be measured again with change of x-ray spectrum.

<sup>13</sup>In addition it is noted that if a deconvolution procedure cannot be applied [10,30] the Fourier coefficient of the pure  $f$  profile can be approximated by dividing the Fourier coefficients of the  $h$  profile by  $(1+R)^{-1} [\exp\{-inR\alpha\} + R \exp\{in\alpha\}] \exp\{-\pi n w/2da\}$ . This is a better correction than a single  $\alpha_2$  elimination, since not only the  $\alpha_2$  component is removed from the line profile, but also the broadening by the spectral component (see also Section 2.2.2.).

### 5.2.2. Standard specimen with an improper transparency

Specimen transparency causes an asymmetric line broadening: an extension of the line profile to lower  $\sin\theta$  values. As compared to a specimen with no transparency at all, it can be shown that for a specimen with an effective linear adsorption coefficient  $\mu$  the centroid of the line profile is shifted on the  $\sin\theta$  scale by  $\delta_t = -\sin\theta_c \cos^2\theta_c / 2\mu r$ , where  $r$  is the radius of the goniometer and  $\theta_c$  corresponds to the centroid on a  $\sin\theta$  scale (cf. [67]).

A standard specimen with a linear absorption coefficient  $\mu_m$  different from the linear absorption coefficient  $\mu$  of the specimen to be investigated diffracts in a different  $\sin\theta$  range with a different broadening as compared to the ideal standard specimen.

The displacement  $\Delta$  (eq. (5.2)) of  $g_m$  with respect to  $g$  is

$$\Delta_2 = - \frac{\sin\theta_c \cos^2\theta_c}{2r} \left( \frac{1}{\mu_m} - \frac{1}{\mu} \right) \quad (5.6)$$

Using eq. (5.1) and a model of Keating and Warren [68] for the broadening due to specimen transparency it follows that the correction for the incorrect broadening of  $g_m$ , in case "infinitely thick" specimens are considered, is performed by

$$C_2(n) = \frac{(1-2\pi i n \delta_t/a) \exp\{2\pi i n \delta_t/a\}}{(1-2\pi i n \delta_{t,m}/a) \exp\{2\pi i n \delta_{t,m}/a\}} \quad (5.7)$$

It is remarked that the model of Keating and Warren is less accurate when the angular aperture of the diverging slit is not smaller than that of the receiving slit and the absorption coefficient is very low [69].

### 5.2.3. Standard specimen containing structural defects

Many standard specimens give rise to a slight structural broadening (cf. reference [60]). Applying the Warren-Averbach method (see Section 4) from eq. (5.1) the following correction factor for the incorrect broadening of  $g_m$  can be obtained:

$$C_3(n) = F_o(n) = A_o^S(n) A_o^D(n, \ell) = 1 - n/N_{3,0} (1 - 2\pi^2 \ell^2 n^2 \langle e_o^2(n) \rangle) \quad (5.8)$$

where the subscripts "o" refer to the non-ideal standard specimen. The distortion sine coefficients of the non-ideal standard specimen were assumed to be zero, which is exact for symmetrical distortion broadening. The crystallite size distribution in the non-ideal standard specimen was neglected, which is justified for a correction factor.

#### 5.2.4. Combined effects

In case the effects of different spacing, different specimen transparency and structural broadening in the standard specimen are superimposed it follows that

$$\Delta = \Delta_1 + \Delta_2 \text{ and } C(n) = C_1(n)C_2(n)C_3(n) \quad (5.9)$$

### 5.3. Effect of an approximate standard profile in size-strain analysis

#### 5.3.1. Consequences of the displacement $\Delta$ of the standard line profile

Clearly, values calculated for the strain will be heavily affected because the fractional displacement  $\Delta/a$  can easily be of the same order of magnitude as the strain  $e(n)$ .

Since the average crystallite size follows from  $dA^S(n)/dn$  for  $(n \rightarrow 0)$  (eq. (4.22)) it can be shown from eqs. (5.1) and 5.2) that in principle the crystallite size is not affected by a displacement. However, because of the "hook" effect (Section 4.4.4.), the first cosine Fourier coefficients are normally determined too small. The usual method of correction for the "hook" effect consists of extrapolating the straight portion of the cosine Fourier coefficient curve at small values of  $n$  to  $n = 0$ . Therefore, in practice the crystallite size determined will be affected by the displacement too.

Errors due to the displacement are avoided when the origins for the Fourier series evaluation of the profiles are chosen at their centroids (see discussion to eqs. (5.2) and (5.3)).

#### 5.3.2. Consequences of the incorrect broadening of the standard line profile

By power series expansion of the exponentials in eqs. (5.5) and (5.7) the product  $C_1(n)C_2(n)$  can be approximated by

$$C_1(n)C_2(n) = \frac{1-n^2 R_m \alpha_m^2 / 2}{1-n^2 R \alpha^2 / 2} \exp \left\{ -\frac{\pi n w}{2a} \left( \frac{1}{d_m} - \frac{1}{d_c} \right) \right\} \times \frac{1+2\pi^2 n^2 \delta_t^2 / a^2}{1+2\pi^2 n^2 \delta_{t,m}^2 / a^2} \quad (5.10)$$

Thus, within the approximations used, this factor is real. Since all quantities in eq. (5.10) are known a corrected cosine Fourier coefficient can be defined (cf. eqs. (5.1) and (5.8)):

$$A_m^{\text{corr}}(n, \ell) = A_m(n, \ell) C_1(n)C_2(n) = \frac{A^S(n)}{A_0^S(n)} \frac{A^D(n, \ell)}{A_0^D(n, \ell)} \quad (5.11)$$

With respect to the separation of size and strain effects, a plot of  $\ln A_m^{\text{corr}}(n, \ell)$  versus  $\ell^2$  and a plot of  $A_m^{\text{corr}}(n, \ell)$  versus  $\ell^2$  (classical and modified methods; Sections 4.2 and 4.3) both yield

$$A_m^S(n) = A^S(n)/A_0^S(n) \quad (5.12)^{14}$$

and

$$\langle e_m^2(n) \rangle = \langle e^2(n) \rangle - \langle e_0^2(n) \rangle \quad (5.13)$$

The relation between the measured crystallite size  $N_{3,m}$ , the true crystallite size  $N_3$  and the crystallite size  $N_{3,0}$  of the standard specimen follows from eqs. (5.12) and (4.6)

$$(N_{3,m})^{-1} = (N_3)^{-1} - (N_{3,0})^{-1} \quad (5.14)$$

Note that this relation also holds when  $B_0^D(n, \ell) \neq 0$  (see Section 5.2.3.). In an x-ray diffraction study of deformation in Ag-Si alloys [70] formulae related to eqs. (5.13) and (5.14) were used. These equations were applied for relative determinations. From the treatment given here it may be concluded that accurate relative determinations using these equations are possible even in the case that the line profile under investigation and the line profile of the reference specimen are at different  $\sin\theta$  values, provided the correction implied by eq. (5.11) has been performed. Furthermore, from these relations the accuracy of size-strain analysis can be estimated.

From eqs. (5.1), (5.5), and (5.7), it follows directly that

$$\left. \frac{dA_m(n, \ell)}{dn} \right|_{n \rightarrow 0} = \frac{-1}{N_{3,m}} + \frac{\pi w}{2a} \left( \frac{1}{d_m} - \frac{1}{d_c} \right) \quad (5.15)$$

which means that  $N_{3,m}$  can be determined directly from the  $A_m(n, \ell)$  values. Omission of the spectral term in eq. (5.15) produces errors of a few percent in the value calculated for the crystallite size.

Finally, because determinations of crystallite size and strain can be performed independently of distortion (eq. (5.14)) and strain (eq. (5.13)) in the standard specimen, it might be suggested that, for example, with a view to extinction problems, for the determination of crystallite size a slightly deformed standard specimen should be used and for the determination of distortion colloids as a standard specimen should be used.

<sup>14</sup>For an ideal standard specimen  $A_0^S(n) = 1$  (infinite particle size) for all  $n$ . In practice, the standard specimen has a large, however finite, particle size  $N_{3,0}$ . Hence  $A_0^S(n)$  tends to zero at large  $n$ . Combined with the effect of counting statistics this may be responsible (cf. eq. (5.12)) for the large spurious ripples in the Fourier coefficients of a deconvoluted line profile at large  $n$  ( $n > N_{3,0}$ ) (see also Section 3.3.1.).

## 6. Determination of Column Length Distribution

In many areas of applied science knowledge of the particle size distribution is desired. For example, in the field of catalysis size distributions influence the activity and selectivity of the catalyst.

It has been first shown by Bertaut [71,72] that the column length distribution can be obtained from the second derivative of the size Fourier coefficient  $A^S(n)$  (cf. [5,73]:

$$\frac{d^2 A^S(n)}{dn^2} = \frac{p_s(n)}{\langle N_{3,s} \rangle} = \frac{p_v(n)}{n} \quad (6.1)$$

where  $p_s(n)$  and  $p_v(n)$  denote the area weighted and volume-weighted distributions respectively. Obviously, the distribution functions can also be obtained directly from a purely size-broadened line profile  $f^S(x)$  according to

$$\frac{d^2 A^S(n)}{dn^2} = - \frac{4\pi^2}{a^3} \int_{-a/2}^{+a/2} x^2 f^S(x) \exp\left\{\frac{2\pi i n x}{a}\right\} dx \quad (6.2)$$

The mean values of the  $p_s$  and  $p_v$  distributions are the area-weighted and volume-weighted average crystallite sizes (mean column lengths)  $\langle N_{3,s} \rangle^{15}$  and  $\langle N_{3,v} \rangle$  respectively, measured in unit cells along the (00 $l$ ) direction. The following relation holds

$$\langle N_{3,v} \rangle = \langle N_{3,s}^2 \rangle / \langle N_{3,s} \rangle \quad (6.3)$$

$\langle N_{3,v} \rangle$  can be obtained from the integral breadth of the line profile (by application of the Scherrer-equation  $\langle N_{3,v} \rangle = \lambda/\beta \cos\theta$ , where  $\beta$  is the integral breadth on a  $2\theta$ -scale,  $\beta$  can be obtained from the sum of the real parts of all Fourier coefficients), whereas  $\langle N_{3,s} \rangle$  follows from the initial slope of the Fourier coefficient curve (Section 4.4.3.). Since  $\langle N_{3,s}^2 \rangle \geq \langle N_{3,s} \rangle^2$ , as obtained from the Schwarz's inequality, it follows

$$\langle N_{3,v} \rangle \geq \langle N_{3,s} \rangle \quad (6.4)$$

Thus, for a monodisperse system of spheres with diameter  $N_d$ , it is obtained  $\langle N_{3,s} \rangle = \frac{2}{3} N_d$  and  $\langle N_{3,v} \rangle = \frac{3}{4} N_d$ . The differences between  $\langle N_{3,s} \rangle$  and  $\langle N_{3,v} \rangle$  will be the larger the broader the distribution, as the small crystallites have a relatively large contribution in the area-weighted average.

When the relation with the surface area available in the specimen is desired (e.g., as with catalysts), only the area-weighted size and distribution are of interest. For

<sup>15</sup>It should be recognized that the symbol  $N_3$  as used elsewhere in this paper, actually denotes  $\langle N_{3,s} \rangle$ .

example for a polydisperse system of spheres the surface area  $S$  is given by the same relation as for a monodisperse system [74]:

$$S = 4M/\rho \langle N_{3,s} \rangle \quad (6.5)$$

where  $M$  and  $\rho$  are mass and density of a sphere, respectively. It is concluded that for the relation between x-ray diffraction line broadening and surface area the Fourier methods discussed in this paper should be preferred over integral breadth methods.

Since for the calculation of the column length distribution a twofold differentiation of the Fourier coefficient curve is required, the resulting distribution function is highly sensitive to error propagation. Erroneous oscillations on the distribution may be obtained, which can easily be of the same order of magnitude as the actual  $p$  values<sup>16</sup>. However, it is interesting to note that experiment shows that from the error affected volume-weighted distribution functions mean crystallite sizes are obtained which are close to the values derived from integral breadth measurements [75,76].

The spurious features may be caused, for example, by low accuracy in the tails of the line profile and truncation effects. The consequence of the "hook" effect (Section 4.4.4.) should be noted: negative  $p$  values for very small  $n$ .

Furthermore, in case size and strain broadening occur simultaneously, both influences have to be separated, which in practice can be done only reliably for small values of  $n$  (cf. Sections 4.2. and 4.3.). Therefore, in our opinion, a trustworthy column length distribution can only be obtained if the line profile to be investigated is purely size-broadened<sup>17</sup>. With this restriction in mind, some of the methods to remove or to avoid the spurious features on the size distribution functions will be discussed shortly.

### 6.1. Elimination of the effect of truncation on the size distribution function

Using Bertaut's result [25] truncation of the profile (cf. Section 3.1) leads to

$$\begin{aligned} \frac{d^2 A_m^S(n)}{dn^2} &= \frac{1}{\langle N_{3,s} \rangle} \left[ -\frac{\sin \pi n}{\pi n} + \int p_s(n') \frac{\sin \pi(n-n')}{\pi(n-n')} dn' \right] \\ &= \frac{1}{\langle N_{3,s} \rangle} \left[ -\frac{\sin \pi n}{\pi n} + p_s'(n) \right] = \frac{p_{s,m}^{(n)}}{\langle N_{3,s} \rangle} \end{aligned} \quad (6.6)$$

<sup>16</sup>This situation resembles the problems to be dealt with in calculating the radial distribution function from diffraction data of amorphous materials.

<sup>17</sup>In case both size and strain broadening occur, size distribution functions may, for example, be obtained by small-angle x-ray scattering (e.g. [77]).

where  $A_m^S$  is the size Fourier coefficient obtained from the truncated profile and  $p_{s,m}$  is the apparent distribution function. From the first term within the brackets it is seen that  $p_{s,m}$  is negative for  $n = 0$ , while for the other  $n$  values  $p_s' = p_{s,m}$ .

The true distribution  $p_s$  should be obtained from  $p_s'$  by deconvolution. Dealing with the form  $(\sin \pi n)/\pi n$ , standard deconvolution procedures are impossible. This problem has been tackled by Popescu and Benes [78]. A modified version of the successive convolution unfolding method [79] was proposed: the convolution product should only be calculated over the range where the distribution function has no vanishing values. Outside this range the convolution has no physical bearing. This "finite-range" successive folding method gave reasonable results for a theoretical experiment. It was shown that a qualitatively correct distribution function might be obtained from a line profile taken over a range of two or three times the line width, instead of the normal range of five to six times the line width.

## 6.2. Smoothing and iterative methods

The fluctuations due to counting statistics in the tails of the line profile may lead to serious errors in the distribution function. Smoothing of the tails of the profile may lead to improvement. For example, the tails may be approximated with  $a/x^2 + b$  [80] or  $a \exp\{-bx\}$  [81] where  $a$  and  $b$  are found by curve fitting.

Very often negative values are observed in the distribution function obtained. These are physically unrealistic. Then the following iterative method may be applied to eliminate the spurious features on the distribution function [81]:

- (i) Cut off all negative regions in the distribution function.
- (ii) Recalculate  $f^S(x)$  by Fourier transformation (cf. eq. (6.2)) from this "corrected" distribution function.
- (iii) Replace, except for its tails, this  $f^S(x)$  by the experimental function.
- (iv) Calculate the new distribution function from this modified line profile.
- (v) Repeat steps (i) - (iv) until a sufficient convergence is obtained.

The Fourier method can be avoided. In case of pure size broadening the line profile equals

$$f^S(x) = \frac{1}{\langle N_{3,s} \rangle} \sum_{n=1}^{\infty} p_s(n) \frac{\sin^2 \pi n x}{\sin \pi x} \quad (6.7)$$

This result can be considered as a set of linear equations which may be solved by least-squares methods. It can be shown that the resulting  $p_s(n)$  has no essential differences with the result obtained from the second derivative of the Fourier coefficient (eq. (6.1)) [76]. The same spurious features are present. Hence, as compared to the Fourier method, no specific advantages are expected from methods based on eq. (6.7). Nevertheless, in case one desires to apply eq. (6.7), of course, methods can be developed to suppress the oscillations [75,76], as for the Fourier method.

### 6.3. The true particle size distribution

From x-ray diffraction line broadening only the mean column length and the column length distribution can be obtained, whereas one wishes to know the average particle size and the particle size distribution.

A first limitation arises from the recognition that each particle need not be monocrystalline. In that case, the centroid of the distribution function as determined by a technique as small-angle x-ray scattering will be larger than the one obtained from the x-ray diffraction line broadening method (for an example see reference [75]).

A second limitation is introduced by the notion of column length (cf. Section 4.1.)). Particle size and particle size distribution are intuitively expressed in terms of a parameter  $\Lambda$  such as the diameter of a sphere or the edge of a cube. In general, these measures are not compatible with the mean column length and the column length distribution. Thus for a system of spheres with diameter  $N_d$  it follows  $\langle N_{3,s} \rangle = \frac{2}{3} N_d$  and although the system is monodisperse a column length distribution does exist. If the particle size distribution in terms of the parameter  $\Lambda$  is denoted by  $p(\Lambda)$ , then for the total number of columns with lengths between  $n$  and  $n + dn$  it follows

$$p_s(n) dn = \int_{\Lambda_0(n)}^{\infty} g(n,\Lambda) p(\Lambda) d\Lambda dn \quad (6.8)$$

where  $g(n,\Lambda)dn$  corresponds to the number of columns with lengths between  $n$  and  $n + dn$  present in a crystallite of length  $\Lambda$  and  $\Lambda_0(n)$  is the minimum value of  $\Lambda$  for a certain  $n$  (for a sphere as well as for a cube, viewed along the edge,  $\Lambda_0(n) = n$ ). Now the question is to derive  $p(\Lambda)$  from the  $p_s(n)$  data. Smith [82] has considered this problem for some simple shapes and orders of reflection for crystals of the cubic system. One of the interesting results is that irrespective of the nature of the true particle size distribution a maximum in the column length distribution will always occur from any reflection from a system of spheres and will never occur from any reflection from a system of tetrahedra, while a system of cubes takes an intermediate position (hoo reflection maximum; hho and hhh reflections: no maximum).

In general, it can be said that information on the true particle size distribution can only be obtained with difficulty from the column length distribution (a third or higher differentiation of the original Fourier coefficients may be necessary; cf. eq. (6.8)).

---

We are indebted to Professor B. Okkerse for his guidance and to Dr. F. W. Schapink for his interest, with respect to our research in this field during the last years.

## References

- [1] Langford, J. I., A rapid method for analysing the breadths of diffraction and spectral lines using the Voigt function, *J. Appl. Cryst.* 11, 10-14 (1978).
- [2] Langford, J. I., this conference.
- [3] Keijser, Th.H. de, Mittemeijer, E. J., and Vogels, A. B. P., Experiences with the Voigt function for a single-line technique in the analysis of x-ray diffraction line broadening, to be published.
- [4] Wilson, A. J. C., *Elements of x-ray crystallography* (Addison Wesley, Reading, MA, 1970).
- [5] Warren, B. E., *X-ray diffraction* (Addison Wesley, Reading, MA, 1969).
- [6] Klug, H. P. and Alexander, L. E., *X-ray diffraction procedures* (John Wiley and Sons, New York, 1974).
- [7] Langford, J. I. and Wilson, A. J. C., On variance as a measure of line broadening in diffractometry: some preliminary measurements on annealed aluminum and nickel and on cold-worked nickel, *Crystallography and Crystal Perfection*, G. N. Ramachandran, ed., pp. 207-222 (Academic Press, London 1963).
- [8] Mitra, G. B., X-ray diffraction profiles from deformed metals, *Brit. J. Appl. Phys.* 16, 77-84 (1965).
- [9] Azároff, L. V., Kaplow, R., Kato, N., Wilson, A. J. C., and Young, R. A., *X-ray diffraction* (McGraw-Hill, Inc., New York, 1974).
- [10] Delhez, R. and Mittemeijer, E. J., On the analysis of x-ray diffraction line profiles from small epitaxial binary diffusion couples: determination of concentration profile and influence of TDS, *J. Appl. Phys.* 49, 4770-4775 (1978).
- [11] Delhez, R., Keijser, Th.H. de, and Mittemeijer, E. J., The x-ray diffraction line broadening due to the diffractometer condition as a function of  $2\theta$ , *J. Phys. E: Sci. Instrum.* 11, 649-652 (1978).
- [12] Delhez, R. and Mittemeijer, E. J., An improved  $\alpha_2$  elimination, *J. Appl. Cryst.* 8, 609-611 (1975).
- [13] Croche, R. and Gatineau, L., Correction des aberrations instrumentales: critères expérimentaux pour l'utilisation des méthodes de déconvolution, *J. Appl. Cryst.* 10, 479-485 (1977).
- [14] Stokes, A. R., A numerical Fourier-analysis method for the correction of widths and shapes of lines on x-ray powder photographs, *Proc. Phys. Soc. London*, 61, 382-391 (1948).
- [15] Brigham, E. O., *The fast Fourier transform* (Prentice-Hall, Inc., Englewood Cliffs, NJ, 1974).
- [16] Cheng, R., Williams, B., and Cooper, M., The treatment of errors in the deconvolution of line profile measurements, *Phil. Mag.* 23, 115-133 (1971).
- [17] Schwarz, L. H. and Cohen, J. B., *Diffraction from materials* (Academic Press, New York, 1977).

- [18] Paatero, P., Manninen, S., and Paakkari, T., Deconvolution in Compton profile measurements, *Phil. Mag.* 30, 1281-1293 (1974).
- [19] Delhez, R. and Mittemeijer, E. J., An analysis of errors in the Fourier coefficients of the  $\alpha_1$  line profile, *J. Appl. Cryst.* 8, 612-614 (1975).
- [20] Moraweck, B. and Imelik, B., Elargissement des raies de diffraction. Influences de facteurs angulaires. Comparaison des différentes méthodes de correction des profils expérimentaux, *C. R. Acad. Sc. Paris*, B 268, 1754-1756 (1969).
- [21] Warren, B. E. and Averbach, B. L., The effect of cold-work distortion on x-ray patterns, *J. Appl. Phys.* 21, 595-599 (1950).
- [22] Page, Y., le Gabe, E. J., and Calvert, L. D., X-ray beam polarization measurement, *J. Appl. Cryst.* 12, 25-26 (1979).
- [23] Keijser, Th.H. de, On structures developed by spinodal decomposition. The interpretation of the x-ray diffraction and the role of excess vacancies in the coarsening, Thesis, Delft (1977).
- [24] Delhez, R., Mittemeijer, E. J., Keijser, Th.H. de, and Rozendaal, H. C. F., Corrections for the angle dependence of Lorentz, polarization and structure factors in x-ray diffraction line profiles, *J. Phys. E: Sci. Instrum.* 10, 784-785 (1977).
- [25] Bertaut, E. F., Sur la correction de la transformée de Fourier d'une raie de Debye-Scherrer dans la mesure de dimensions cristallines, *Acta Cryst.* 5, 117-121 (1952).
- [26] Young, R. A., Gerdes, R. J., and Wilson, A. J. C., Propagation of some systematic errors in x-ray line profile analysis, *Acta Cryst.* 22, 155-162 (1967).
- [27] Gilli, G. and Borea, P. A., Effects of symmetrical background error in the Warren-Averbach analysis, *J. Appl. Cryst.* 3, 205-211 (1970).
- [28] Wilkens, M. and Hartmann, R. J., Zur Interpretation der Ergebnisse der Warren-Averbach Analyse von Debye-Scherrer-Linien, *Z. Metallkunde*, 54, 676-682 (1963).
- [29] Wilson, A. J. C., Statistical variance of line-profile parameters. Measures of intensity, location, and dispersion, *Acta Cryst.* A23, 888-898 (1967); *Acta Cryst.* A24, 478 (1968); *Acta Cryst.* A25, 584 (1969).
- [30] Mittemeijer, E. J. and Delhez, R., Determination of compositional variations by x-ray diffraction line profile analysis, this conference.
- [31] Krivoglaz, M. A., Theory of x-ray and thermal-neutron scattering by real crystals (Plenum Press, New York, 1969).
- [32] Ergun, S., X-ray scattering by very defective lattices, *Phys. Rev. B*, 1, 3371-3380 (1970).
- [33] Stokes, A. R. and Wilson, A. J. C., A method of calculation the breadth of Debye-Scherrer lines: generalization to non-cubic crystals, *Proc. Camb. Phil. Soc.* 40, 197-198 (1944).
- [34] Warren, B. E., A generalized treatment of cold work in powder patterns, *Acta Cryst.* 8, 483-486 (1955).

- 35] Warren, B. E., X-ray studies of deformed metals, in Progress in Metal Physics, B. Chalmers and R. King, eds., Vol. 8, pp. 147-202 (Pergamon Press, London, 1959).
- 36] Wilkens, M., X-ray diffraction line broadening of crystals containing small-angle boundaries, J. Appl. Cryst. 12, 119-125 (1979).
- 37] Warren, B. E. and Averbach, B. L., The separation of cold-work distortion and particle size broadening in x-ray patterns, J. Appl. Phys. 23, 497 (1952).
- 38] Jeffreys, H. and Swirles, B., Methods of Mathematical Physics, p. 51 (University Press, Cambridge, 1962).
- 39] Delhez, R. and Mittemeijer, E. J., The elimination of an approximation in the Warren-Averbach analysis, J. Appl. Cryst. 9, 233-234 (1976).
- 40] Opinsky, A. J., Orehotsky, J. L., and Hoffman, C. W. W., X-ray diffraction analysis of crystallite size and lattice strain in tungsten wire, J. Appl. Phys. 33, 708-712, (1962).
- 41] Rothman, R. L. and Cohen, J. B., A new method for Fourier analysis of shapes of x-ray peaks and its application to line broadening and integrated intensity measurements, in Adv. X-ray Analysis, C. S. Barrett, J. B. Newkirk, and G. R. Mallett, eds. 12, 208-235 (1969).
- 42] Rothman, R. L. and Cohen, J. B., X-ray study of faulting in bcc metals and alloys, J. Appl. Phys. 24, 971-979 (1971).
- 43] Eastabrook, J. N. and Wilson, A. J. C., The diffraction of x-rays by distorted-crystal aggregates III: remarks on the interpretation of the Fourier coefficients, Proc. Phys. Soc. London, B65, 67-75 (1952).
- 44] Gangulee, A., Separation of the particle size and microstrain components in the Fourier coefficients of a single diffraction profile, J. Appl. Cryst. 7, 434-439 (1974).
- 45] Misra, N. K. and Ghosh, T. B., Determination of lattice defects from the initial slopes of the Fourier coefficient against order-curves for x-ray diffraction profiles, Indian J. Pure Appl. Phys. 14, 928-930 (1976).
- 46] Turunen, M. J., A method for computing dislocation stress fields and its application to x-ray diffraction analysis, Computer simulation for materials applications, R. J. Arsenault, J. R. Beeler, Jr., and J. A. Simmons, eds., Nuclear Metallurgy, 20, part 2, 850-857 (1976).
- 47] Misra, N. K. and Ghosh, T. B., Determination of particle size and strain by Fourier analysis of x-ray diffraction profiles, Indian J. Pure Appl. Phys. 16, 620-622 (1978).
- 48] Hill, R., The elastic behaviour of a crystalline aggregate, Proc. Phys. Soc. A65, 349-354 (1952).
- 49] Kröner, E., Berechnung der elastischen Konstanten des Vielkristalls aus den Konstanten des Einkristalls, Z. F. Phys. 151, 504-518 (1958).
- 50] Chung, D. H. and Buessem, W. R., The Voigt-Reuss-Hill approximation and elastic moduli of polycrystalline MgO, CaF<sub>2</sub>,  $\beta$ -ZnS, ZnSe, and CdFe, J. Appl. Phys. 38, 2535-2540 (1967).

- [51] Warlimont, H. and Hausch, G., Elastische Anisotropie von Metallen und Legierungen, *Mechanische Anisotropie*, H. P. Stüwe, ed., pp. 35-62 (Springer Verlag, Wien, 1974).
- [52] Möller, H. and Martin, G., Elastische Anisotropie und röntgenographische Spannungsmessung, *Mitt. K.-Wilh.-Inst. Eisenforsch.* 21, 261-269 (1939).
- [53] Williamson, G. K. and Smallman, R. E., The use of Fourier analysis in the interpretation of x-ray line broadening from cold-worked iron and molybdenum, *Acta Cryst.* 7, 574-581 (1954).
- [54] McKeehan, M. and Warren, B. E., X-ray study of cold-work in thoriated tungsten, *J. Appl. Phys.* 24, 52-56 (1953).
- [55] Smith, R. S., Measurement of crystallite size and strain of electroplated films, *IBM J. Res. Develop.* 4, 205-207 (1960).
- [56] Mitra, G. B. and Misra, N. K., Line shape analysis of cold-worked magnesium, *Acta Cryst.* 22, 454-456 (1967).
- [57] Mignot, J. and Rondot, D., Méthode de separation des dimensions de domaines et des microdéformations a partir des coefficients de Fourier d'un seul profil de raie de diffraction X, *Acta Met.* 23, 1321-1324 (1975).
- [58] O'Holleran, T. P., McKinstry, H. A., and Stubican, V. S., Microstrain in some oxide crystalline solutions, *Phil. Mag.* 35, 485-492 (1977).
- [59] Halder, N. C. and Johnston, E. E., X-ray diffraction study of HCP metals II. Line broadening in polycrystalline Zn and Mg powder, *Z. Naturforsch.* 30a, 825-830 (1975).
- [60] Urban, J. P., X-ray measurements of strain and mosaic particle size in annealed tungsten powder, *J. Appl. Cryst.* 8, 459-464 (1975).
- [61] Keijser, Th.H. de and Mittemeijer, E. J., Correction for errors in microstrain values from x-ray diffraction line profiles, *Phil. Mag.* 36, 1261-1264 (1977).
- [62] Keijser, Th.H. de and Mittemeijer, E. J., Analysis of x-ray diffraction line broadening using a non-ideal standard specimen, *Z. Naturforsch.*, 33a 316-320 (1978).
- [63] Huang, T. C. and Parrish, W., Qualitative analysis of complicated mixtures by profile fitting x-ray diffractometer patterns, *Adv. X-ray Analysis*, C. S. Barrett, D. E. J. B. Newkirk, and C. O. Ruud, eds., 21, 275-288 (1978).
- [64] Compton, A. H. and Allison, S. K., *X-rays in theory and experiment* (McMillan, London, 1935).
- [65] Delhez, R., Keijser, Th.H. de, Mittemeijer, E. J., and Pers, N. M., van der, An experimental determination of the x-ray diffraction line broadening due to the non-ideal geometry of the diffractometer; consequences for size-strain analysis, *Proceedings Conference on Applied Crystallography*, Kozubnik, Poland, August 1978, in press.
- [66] Kidron, A. and Cohen, J. B., Some comments on line broadening analysis, *J. Appl. Cryst.* 6, 8-11 (1973).
- [67] Wilson, A. J. C., Geiger-counter x-ray spectrometer. Influence of size and absorption coefficient of specimen on position and shape of powder diffraction maxima, *J. Sci. Instrum.* 27, 321-325 (1950).

- Keating, D. T. and Warren, B. E., The effect of a low absorption coefficient on x-ray spectrometer measurements, *Rev. Sci. Instrum.* 23, 519-522 (1952).
- Dineen, C., On the correction of the shapes of x-ray diffraction line profiles for absorption broadening, *J. Appl. Cryst.* 6, 474-477 (1973).
- Zemitis, M. A., Kidron, A., and Cohen, J. B., A study by x-ray diffraction of the deformation of Ag-Si alloys, *Scripta Met.* 6, 875-882 (1972).
- Bertaut, E. F., Etude aux rayons X de la repartition des dimensions des cristallites dans une poudre cristalline, *C. R. Acad. Sci. Paris*, 228, 492-494 (1949).
- Bertaut, E. F., Raies de Debye-Scherrer et répartition des dimensions des domaines de Bragg dans les poudres polycristallines, *Acta Cryst.* 3, 14-18 (1950).
- Guinier, A., X-ray diffraction (W. H. Freeman and Company, San Francisco, 1963).
- Smith, W. L., Crystallite sizes and surface areas of catalysts, *J. Appl. Cryst.* 5, 127-130 (1972).
- Moraweck, B., Montgolfier, Ph. de, and Renouprez, A. J., X-ray line-profile analysis. II. Determination of the crystallite-diameter distribution functions, *J. Appl. Cryst.* 10, 191-196 (1977).
- Le Bail, A. and Louër, D., Smoothing and validity of crystallite-size distributions from x-ray line-profile analysis, *J. Appl. Cryst.* 11, 50-55 (1978).
- Vonk, C. G., On two methods for determination of particle size distribution functions by means of small-angle x-ray scattering, *J. Appl. Cryst.* 9, 433-440 (1976).
- Popescu, Fl. and Benes, L., Elimination of the finite-range effect on the block-size distribution from the Fourier transform, *Acta Cryst.* A33, 323-326 (1977).
- Ergun, S., Direct method for unfolding convolution products. Its application to x-ray scattering intensities, *J. Appl. Cryst.* 1, 19-23 (1968).
- Bley, F., Calvayrac, Y., and Fayard, M., Distribution en epaisseur des domaines antiphase dans un alliage ordonné, *J. Appl. Cryst.* 7, 493-497 (1974).
- Pausescu, P., Manaila, R., Popescu, M., and Jijovici, E., Crystallite size distribution in supported catalysts, *J. Appl. Cryst.* 7, 281-286 (1974).
- Smith, W. L., Crystallite shape and the Fourier analysis of diffraction line profiles, *J. Appl. Cryst.* 9, 187-189 (1976).

#### Discussion

Question (Edmonds): Have you based the determination of the unknown line broadening on an unusual sample (e.g.  $\text{Cu}^{85}\text{Ge}^{15}$ ) only upon a standard which is very close in transparency to the sample (e.g. Cu), or have you tried using standards which are very different in transparency, for instance  $\alpha\text{Al}_2\text{O}_3$ ?

Response (Delhez, Keijser, and Mittemeijer): In case one is obliged to use a non-ideal standard specimen, correction for an improper spacing (e.g. (5.5) in this paper) and an improper transparency (e.g. (5.7) in this paper) are possible (see also e.g. (5.10)). The correction factors are based on models that are approximations. Therefore, the differences

in spacing and transparency between the standard specimen used and the ideal standard specimen should be kept as small as possible. We have not investigated the effect of the corrections in case of large differences.

Question (Cohen): (1) Can you tell us, for example, if the standard peak is  $1^\circ$  or  $2^\circ$  or  $3^\circ$  from the peak to be analyzed, by what percent are the cosine Fourier coefficients affected, in your opinion? It would be useful to have such information, as to when a correction is really needed. (2) Can you make any comments on the recent work by M. Wilkens, where he shows that a hook effect can arise due to strains from dislocations? He also has questioned the usual two order analysis,  $\ln A_L$  vs  $h^2 + k^2 + l^2$ .

Response (Delhez, Keijser, and Mittemeijer): (1) Especially strain values are affected when standard specimens with an improper spacing and transparency are used. When the centroids of the standard peak and the peak to be analyzed are just a few degrees apart ( $x = 0$  is confined to the centroid in the Fourier series evaluation) already errors of more than 10 percent occur in the mean square strain values for small harmonic number (see refs. [61-62] in this paper); the error in the crystallite size is a few percent. (2) We have not yet studied Wilkens paper (ref. [36] in this paper) in detail, however, a few comments are made in this paper. It seems that the domain concept (see Section 4.1. of this paper) may introduce difficulties. The two-order analysis of the Fourier coefficients is indeed not always allowed because of the truncation of the series expansions (see Section 4.4.4. of this paper).

Question (Laddell): In deconvolutioning by means of Stokes method, what do you do when the denominator Fourier coefficient is zero or close to zero? This could happen for real profiles which are not strictly monotonic decreasing in both sides.

Response (Delhez, Keijser, and Mittemeijer) (See comments made by J. Cohen.) In addition to the comment of Professor Cohen on this question, it is remarked that the profile  $h$  to be investigated (with the coefficients  $H$ ) is the convolution of the structurally broadened profile  $f$  (with coefficients  $F$ ) and the instrumental profile  $g$  (with coefficients  $G$ ). Therefore,  $H = F \times G$ . When  $G$  is zero,  $H$  should be zero too, and, in principle, there are no problems in the deconvolution. However, because of experimental errors, difficulties can arise when  $H$  and  $G$  are near to each other for the same harmonic number. As pointed out by Cheng, Williams, and Cooper (ref. [16] in this paper, see also Section 2.2.1.) other procedures for deconvolution may be regarded as a Stokes deconvolution with additional smoothing (see Section 2.3. of this paper). The best way out for obtaining reliable results is to improve the quality of the measurement.

Comment (Cohen): Dr. Laddell has asked what happens when the Stoke's correction diverges, because a Fourier coefficient of the standard becomes zero. Actually, in doing this analysis, because of the various approximations, useful information is obtained only from the Fourier coefficients of low order. This divergence does not occur in this region.

Also, to obtain some idea of the accuracy of these techniques, they have been compared to particle sizes determined by hydrogen chemisorption, in a paper by S. Sashital, *J. Catalysis*, 51, S. of Catalysis, 1978.

Let me add a comment to my reply to Dr. Laddell's question concerning the possible divergence of  $\Delta n$ . For particles sizes 1000 Å - 2000 Å or less there is generally no problem, as I mentioned above. However, when there is a broadening less than about 20 percent greater than the standard, i.e. for larger sizes, then such a problem can arise. It would be interesting to follow up on Dr. Laddell's suggestion that in such a case another more recent method than the Stoke's correction could prove interesting.



ACCURACY OF CRYSTALLITE SIZE AND STRAIN DETERMINED  
FROM THE INTEGRAL BREADTH OF POWDER DIFFRACTION LINES

J. I. Langford  
Department of Physics  
University of Birmingham  
Birmingham B15 2TT  
England

Although the integral breadth has been used extensively as a measure of diffraction broadening for the past fifty years, there have been few serious attempts to assess its accuracy or estimate the uncertainty in any crystallite size or strain derived from it. Some errors, such as the effect of counting statistics, for example, are calculable, but others, including the correction for instrumental aberrations, cannot readily be treated analytically. Statistical methods can be used to estimate the uncertainty in the apparent size, but the reliability of any estimate of the true size is influenced by the shape of the crystallites and the distribution of size. Similarly, analysis of the strain will depend on the validity of any assumed stress or strain distribution.

The application of the integral breadth requires careful collection and systematic interpretation of the data, due consideration being given to counting statistics. The broadening of standard data used to correct for instrumental effects should be inappreciable and any assumed functions used in the analysis must approximate closely to experimental profiles. If these precautions are observed, the integral breadth provides a method for determining crystallite size and strain which is both reliable and, in general, easy to apply; any remaining uncertainties should then be mainly attributable to the properties of the specimen under investigation.

## 1. Introduction

The integral breadth was introduced as a measure of diffraction broadening in 1926 by Laue [1]<sup>1</sup> and it has since been used extensively in the study of imperfections in powder samples. A comprehensive account of the method and its applications has been given by Klug and Alexander

---

<sup>1</sup>Figures in brackets indicate the literature references at the end of this paper.

[2] and only the main features will be reviewed here. Recent developments are, however, considered in greater detail, since these should result in an improvement in the accuracy of strain and crystallite-size measurements.

The integral breadth is defined as the width of a rectangle having the same area and height as the diffraction line after subtraction of the background<sup>2</sup>, or

$$\beta = \frac{S}{I_0 - B_0}. \quad (1)$$

It is thus relatively easy to obtain, compared with the calculation of the variance of a diffraction line [3] or deconvolution procedures, such as the Stokes correction [4] or the LWL method [5]. Furthermore, the integral breadth is less prone to subjective errors than the full width at half maximum intensity (FWHM), particularly if a least-squares parabola is fitted to the peak in order to find  $I_0$  [6]. In any detailed study of imperfection broadening where reliability and accuracy are of importance, it is usually desirable and often necessary, to use two or more measures of breadth, as is shown below. However, the purpose of this review is to discuss the accuracy of the integral-breadth method and the reliability of other measures of line broadening are not considered.

The principal disadvantage of the integral-breadth method, as with the FWHM, is that the instrumental, broadened and diffraction profiles are assumed to approximate to analytical functions, usually Cauchy (Lorentzian) or Gaussian. In the Cauchy case the integral breadth (or FWHM's) of the constituent profiles are additive, or

$$\beta_h = \beta_f + \beta_g, \quad (2)$$

and for the Gaussian the squares of the breadths are additive, or

$$\beta_h^2 = \beta_f^2 + \beta_g^2. \quad (3)$$

There is evidence that the Gaussian is a better approximation in many cases, particularly strain broadening is dominant for example [7-9], and hitherto this function has been widely used in practice. Equally, it has been shown that the profile generated by a distribution of crystallite sizes is nearer Cauchy in form [10,11], as is the instrumental function with  $K\alpha$  radiation [12]. It is clear, therefore, that in general the observed line will be of intermediate form, as will be the majority of diffraction profiles. Although equations (2) and (3) greatly facilitate the separation of the constituent breadths, they impose a considerable limitation on the reliability of any derived parameters and should only be used where order-of-magnitude calculations are acceptable. A better approximation is the Voigt function, or convolution of Cauchy and Gaussian curves [12-16] and its use will be assumed in the following discussion. (See also reference [17].)

<sup>2</sup>Principal symbols are listed in the appendix.

The integral breadth of a diffraction profile is also proportional to the inverse sum of the Fourier cosine coefficients [4]:

$$\beta_f = \Delta(2\theta) / \sum_n \underline{A}_n \quad (4)$$

Thus, if the  $h$ -profile is corrected for instrumental effects by means of the Stokes method, the resulting estimate of  $\beta_f$  does not depend on ascribing a closed function to the constituent profiles. However, the problem of separating the contributions from various imperfections remains. The accuracy of  $\beta_f$  can be evaluated from the expressions given by Wilson [18-20] for the standard deviation in  $\underline{A}_n$ . (See also Delhez, de Keijser and Mittemeijer: this symposium.)

## 2. Crystallite-size and Strain Determination

The importance of careful and systematic collection and interpretation of data in any line-broadening application cannot be overemphasized. Indeed, failure to observe certain basic requirements can lead to serious and often unpredictable inaccuracies in derived parameters. The recommended procedure in the integral-breadth method, assuming that the data are collected by step-scanning each profile, is as follows. The technique is essentially the same for continuous scanning, but the analysis of errors will differ somewhat.

### 2.1. Data collection

Whenever practicable, data should be recorded for as many reflections as possible, both for the sample under investigation and for the "standard." The method can be applied to a single line [21,22], but only at the expense of accuracy and the amount of information which can be obtained about any imperfections present. The step length should not be too large and, though the optimum value varies from sample to sample, as a rule the step length should not be greater than about 5 percent of the FWHM for accurate work. A counting strategy should be chosen to reduce random errors to an acceptable level, as is indicated below. (See also reference [18].) It is customary to increase the counting time (or to time a larger count) in the tails of a profile to reduce uncertainties in the estimated background and it is sometimes advantageous to reduce the standard error of the peak count in the same way. The usual precautions must be taken to ensure that intrinsic broadening of the standard data is negligible and that instrumental broadening is the same as that of the specimen under investigation.

### 2.2. Correction for $\underline{K}\alpha_1 - \underline{K}\alpha_2$ doublet

Ideally the data should be obtained with monochromatic radiation, though this is less important if the integral breadth is derived from the Fourier coefficients. Otherwise, if  $\underline{K}\alpha$  x-rays are used, a correction for the  $\alpha_1 - \alpha_2$  doublet must be applied in the majority of applications. Of the various methods available, that of Rachinger [23] has been widely

used in the past, though the correction curves of Klug and Alexander [2] are easier to apply. A more systematic approach to the problem of removing the  $\alpha_2$  component is that devised by Delhez and Mittemeijer [24], or the least-squares method of Narayan [25].

### 2.3. Correction for instrumental broadening

In common with most other measures of line broadening, the integral breadth of the  $h$ -function must be corrected for instrumental effects and the normal procedure is to obtain  $g$ -profile from a "standard" sample. In the present method the correction requires the peak height, total intensity, integral breadth and FWHM of each profile. Particular care should be taken in estimating the background level, but the slope is less important, provided it is not too large. The variance method automatically gives an estimate of the true background level, but the slope is less important, provided it is not too large. The variance method automatically gives an estimate of the true background [26], as does the Fourier method in principle, though this is less sensitive to small changes in the background level [27]. Perhaps the most appropriate method of obtaining the background is that described by Lundy and Eanes [28]. This approach is based on the same assumption as is inherent in the variance procedure, namely, that there is an approximate inverse-square variation of intensity in the tails of a profile, and it avoids the use of more elaborate methods. A useful technique for obtaining the integrated intensity, particularly when the peak-to-background ratio is small, has been devised by Rigault [29].

The next step is to see if the  $g$ - and  $h$ -profiles are approximately Cauchy or Gaussian or whether the Voigt is a better approximation, when the Cauchy and Gaussian components may be obtained. Langford [12 (22)] has derived the following explicit equation for a Voigt function in terms of the parameters defining the constituent curves:

$$\underline{I}(x) = \text{Re} \left\{ \beta_{\underline{C}} \underline{I}_{\underline{O}\underline{C}} \underline{I}_{\underline{O}\underline{G}} w[\pi^{1/2} x / \beta_{\underline{G}} + i \underline{k}] \right\}, \quad (5)$$

where  $w[\underline{u} + i \underline{v}]$  is the complex error function<sup>3</sup> and

$$\underline{k} = \beta_{\underline{C}} / \pi^{1/2} \beta_{\underline{G}}, \quad (6)$$

and has shown that the curve may be characterised by the ratio  $2\underline{w}/\beta$ . This ratio has limiting values of  $2/\pi = 0.63662$  (Cauchy) and  $2(\log_e 2)^{1/2}/\pi^{1/2} = 0.93949$  (Gaussian). Examination of this ratio for the experimental data thus gives an indication of the nature of the  $g$ - and  $h$ -functions. If  $2\underline{w}/\beta$  lies outside this range, and the precautions given above have been observed, then the Voigt function is not a good approximation to the profile. The FWHM and integral breadth are related by the equations (see ref. [12 (27)])

$$\text{Re} \left\{ w[\pi^{1/2}(2\underline{w})/2\beta_{\underline{G}} + i \underline{k}] \right\} = \frac{1}{2} w[i \underline{k}] = \beta_{\underline{G}}/2\beta, \quad (7)$$

<sup>3</sup>An algorithm for evaluating the complex error function has been devised by Gautschi [30]

which can be solved to give  $\beta_{\underline{C}}$  and  $\beta_{\underline{G}}$ . Thus, provided that the lines are reasonably symmetrical,  $\beta_{\underline{gC}}$ ,  $\beta_{\underline{gG}}$  and  $\beta_{\underline{hC}}$ ,  $\beta_{\underline{hG}}$  can be found from equation (7) and  $\beta_{\underline{fC}}$ ,  $\beta_{\underline{fG}}$  are then obtained from equations (2) and (3). The method has recently been extended by de Keijser, Bittermeijer and Vogels [22] to take into account an asymmetry of the g-function.

The solution of eq. (7) can be carried out by graphical methods or by interpolation from tabulated data, but de Keijser, et al. have also devised the following approximate equations which are more amenable to calculation:

$$\beta_{\underline{C}}/\beta = \underline{a}_0 + \underline{a}_1\phi + \underline{a}_2\phi^2 \quad (8)$$

$$\beta_{\underline{G}}/\beta = \underline{b}_0 + \underline{b}_{1/2}(\phi - 2/\pi)^{1/2} + \underline{b}_1\phi + \underline{b}_2\phi^2, \quad (9)$$

where  $\phi = 2w/\beta$ ,  $\underline{a}_0 = 2.0207$ ,  $\underline{a}_1 = -0.4803$ ,  $\underline{a}_2 = -1.7756$ ,  $\underline{b}_0 = 0.6420$ ,  $\underline{b}_{1/2} = 1.4187$ ,  $\underline{b}_1 = -2.2043$  and  $\underline{b}_2 = 1.8706$ . (10)

The errors arising from the use of eqs. (8) and (9) do not exceed 1 percent.

#### 2.4. Determination of strain and crystallite size

$\beta_{\underline{fC}}$  and  $\beta_{\underline{fG}}$  are then separated into the contributions from size effects ( $\beta_{\underline{CC}}$ ,  $\beta_{\underline{GC}}$ ) and strain ( $\beta_{\underline{CS}}$ ,  $\beta_{\underline{GS}}$ ), if these are the dominant source of broadening. From the Scherrer equation, the apparent crystallite size is

$$\varepsilon = \underline{p}/\underline{K}_{\beta} = \lambda/\beta_{\underline{C}} \cos\theta, \quad (11)$$

where  $\beta_{\underline{C}}$  is the size component of  $\beta_{\underline{f}}$  in units of  $2\theta$ , and Stokes and Wilson [31] defined an apparent strain as

$$\eta = \beta_{\underline{S}} \cot\theta \quad 5.0 < \langle e^2 \rangle^{1/2}, \quad (12)$$

where  $\beta_{\underline{S}}$  is the strain component of  $\beta_{\underline{f}}$  and  $\langle e^2 \rangle$  is the mean-square strain. Thus, for the Cauchy components

$$\beta_{\underline{fC}} \cos\theta = \beta_{\underline{CC}} + \beta_{\underline{CS}} \sin\theta \quad (13)$$

and, for the Gaussian part,

$$\beta_{\underline{fG}}^2 \cos^2\theta = \beta_{\underline{GC}}^2 + \beta_{\underline{GS}}^2 \sin^2\theta. \quad (14)$$

$\beta_{\underline{c}c}$ ,  $\beta_{\underline{c}s}$  are then the slope and intercept of equation (13),  $\beta_{\underline{f}c} \cos\theta$  being plotted as a function of  $\sin\theta$  for several reflections, and  $\beta_{\underline{g}c}$ ,  $\beta_{\underline{g}s}$  are obtained from the slope and intercept of equation (14). If the intercept of (14) is zero, then there is no Gaussian size component and the apparent size is given by the substitution of  $\beta_{\underline{c}c}$  for  $\beta_{\underline{c}}$  in (11). Similarly,  $\beta_{\underline{g}s}$  is substituted for  $\beta_{\underline{s}}$  in (12) if the slope of (13) is zero. However, in general  $\beta_{\underline{c}c}$ ,  $\beta_{\underline{g}c}$  and  $\beta_{\underline{g}s}$  are then recombined by the method given by Langford [12] to give  $\beta_{\underline{c}}$  and  $\beta_{\underline{s}}$ , or alternatively the following approximate equation of de Keijser, et al. can be used:

$$\beta_{\underline{x}} = \beta_{\underline{g}x} / [ -\frac{1}{2}k\underline{\pi}^{\frac{1}{2}} + \frac{1}{2}(\pi k^2 + 4)^{\frac{1}{2}} - 0.234k \exp(-2.176 k) ], \quad (15)$$

where  $\underline{x} = \underline{c}$  or  $\underline{s}$ .

If the data are for two or more orders of a reflection, the crystallite size and strain relate to one particular crystallographic direction. Otherwise, the values obtained are averaged for all reflections.

### 2.5. Analysis of crystallite size and strain

Equations (11) and (12) yield the average apparent size and strain. Furthermore, the deviation of  $\beta_{\underline{f}c} \cos\theta$  and  $\beta_{\underline{f}g}^2 \cos^2\theta$  in (13) and (14) contains three components: a random contribution arising from counting statistics, which is calculable, and systematic contributions due to the variation of the apparent size with  $hkl$  and to anisotropy of strain. If crystallite size is the dominant source of broadening, a comparison of the apparent sizes for several reflections often yields information about the shape and true size of the crystallites [32]. If, on the other hand, size effects are negligible or can be separated, the variation of the apparent strain can be interpreted in terms of elastic anisotropy and possibly stress variations within the crystallites [31,33]. The extent to which intermediate cases can be analysed depends on numerous factors, such as the number of orders of reflection which can be recorded, or the relative magnitudes of the Cauchy and Gaussian components of strain and size breadths. In this instance it is usually better to compare parameters derived from several measures of breadth, combined with information obtained from peak displacement

### 3. Sources of Error

For many years diffractionists have been conscious of the limitations of the integral-breadth method and various procedures for reducing uncertainties in the derived parameters have been summarised by Klug and Alexander [2]. However, there do not appear to have been any serious attempts to estimate the magnitude of the errors in crystallite-size or strain measurements, though Wilson [18-20] evaluated the standard deviation in the integral breadth due to counting statistics.

Inaccuracies arise from systematic errors in the collection and analysis of data, which in general cannot be treated analytically, and from random errors due to counting statistics

which are calculable. A major potential source of error is the use of standard data for which diffraction broadening is not negligible. This can be avoided if a check is made to ensure that the breadths of the  $g$ -profiles are not appreciably greater than that of the wavelength distribution, perhaps by measuring the  $\alpha_1$ - $\alpha_2$  separation, if the doublet is present. The breadths should also increase monotonically with angle, aside from the scatter due to counting statistics.

A second source of systematic error can arise from the removal of the  $\alpha_2$  line. This should be inappreciable if the correct procedure is adopted (see Section 2.2.) and is eliminated if the  $\alpha_2$  component is removed by means of a monochromator.

An incorrect choice of background level can also introduce serious inaccuracies. For example, if an incorrect background results in the integrated intensity being underestimated by 5 percent, then the component breadths of an assumed Voigt function are overestimated by about 15 percent. Again, background errors are not easy to quantify and if possible the level should be obtained by one of the methods given in Section 2.3. In any event background data should be collected at points well away from the profile tails if they are not overlapped by neighbouring lines. The background under the peak is usually assumed to vary linearly with angle. This is a possible source of error, since it makes no allowance for the increase in thermal diffuse scattering under the Bragg peak and similar effects.

A further cause of appreciable uncertainty could arise from the assumption that the  $g$ -,  $h$ - and  $f$ -profiles all approximate to Cauchy or Gaussian functions. The resulting error could perhaps be evaluated, but in many cases it is reduced substantially if the Voigt method is used to correct for instrumental effects and to analyse the breadths of the diffraction profile. The errors arising from counting statistics with this technique are derived in Section 4. The standard deviation in the observed and derived parameters can be calculated and, if desired, the procedure can be used in reverse to design an experiment which will yield results having a predetermined accuracy.

If the foregoing points are observed, it should be possible to evaluate the error in the apparent size and strain for a particular crystallographic direction. Uncertainties in the estimated "true" size and strain are, in general, difficult to quantify, since they depend on the shapes of the crystallites, the distribution of size, any assumed models of stress or strain distribution, and so on. It may, however, be possible to separate these effects from uncertainties due to data collection and analysis and to represent them as "apparent errors."

#### 4. Errors Due to Counting Statistics

##### 4.1. Integral breadth and FWHM

The statistical variances of the integral breadth and FWHM, together with other line-profile parameters, have been evaluated by Wilson [18-20] for various counting strategies, but only fixed-time counting will be considered here, since this is the method commonly used in practice. For fixed-count timing and other strategies, the original paper should be consulted.

Wilson assumed that observations are made at an odd number of equally spaced points with the range adjusted until the mid point is within a step of the peak or centroid, that the effect of variations in the step length is negligible, and that the background varies linearly under the peak. He showed that the variance of the integral breadth is (Wilson's equation 64)

$$\sigma^2(\beta) \cong \frac{\underline{s}^2}{\underline{q}\underline{I}_0^3} \left( 1 - \frac{\underline{q}\underline{I}_0}{\underline{s}} \right) + \frac{\underline{B}_0[\underline{R}\underline{P} - (\underline{R} - \beta)^2]}{\underline{p}\underline{I}_0^2}, \quad (16)$$

provided the peak-to-background ratio is not too small. (For weak lines, Wilson's equation 63 should be used.)

The points of inflection of a line profile occur at roughly half the maximum height, so the variation in intensity is approximately linear in the region where the profile is intersected by a chord drawn at this height and parallel to the background. If the peak is reasonably symmetrical and the linear region on one side has an intercept  $\underline{a}$  and slope  $\underline{b}$ , the FWHM is

$$2\underline{w} \cong \frac{1}{\underline{b}}(\underline{I}_0 + \underline{B}_0 - 2\underline{a}), \quad (17)$$

and its variance (Wilson's equation 58) is

$$\sigma^2(2\underline{w}) \cong \frac{1}{\underline{b}^2} \left( \frac{\underline{I}_0}{\underline{q}} + \frac{\underline{B}_0}{\underline{p}} + \frac{2\underline{a}}{\underline{s}} \right), \quad (18)$$

where the linear region on each side of the peak is averaged over  $\underline{s}$  points.

#### 4.2. Form factor ( $\phi = 2\underline{w}/\beta$ )

The FWHM and integral breadth are statistically dependent, since both are functions of  $\underline{I}_0$  and  $\underline{B}_0$ <sup>4</sup>. The variance of  $\phi$  is therefore given by

$$\sigma^2(\phi) = \left( \frac{\partial \phi}{\partial (2\underline{w})} \right)^2 \sigma^2(2\underline{w}) + \left( \frac{\partial \phi}{\partial \beta} \right)^2 \sigma^2(\beta) + \left( \frac{\partial \phi}{\partial (2\underline{w})} \frac{\partial \phi}{\partial \beta} \right) \text{cov}(2\underline{w}, \beta), \quad (19)$$

where

$$\text{cov}(2\underline{w}, \beta) = \left( \frac{\partial (2\underline{w})}{\partial \underline{I}_0} \frac{\partial \beta}{\partial \underline{I}_0} \right) \sigma^2(\underline{I}_0) + \left( \frac{\partial (2\underline{w})}{\partial \underline{B}_0} \frac{\partial \beta}{\partial \underline{B}_0} \right) \sigma^2(\underline{B}_0). \quad (20)$$

<sup>4</sup>Strictly, they are also functions of  $\underline{I}_i$  ( $i \neq 0$ ), since a few intensities on each side of the peak are used to obtain  $\underline{a}$  and  $\underline{b}$ . The resulting correlations are neglected in the above analysis.

From eqs. (1) and (17)

$$\frac{\partial(2w)}{\partial I_0} = \frac{\partial(2w)}{\partial B_0} = \frac{1}{b} \quad \text{and} \quad \frac{\partial\beta}{\partial I_0} = -\frac{\partial\beta}{\partial B_0} = -\frac{s}{L_0} \quad (21)$$

and

$$\text{cov}(2w, \beta) = -\frac{\beta}{b} \quad (22)$$

Hence

$$\sigma^2(\phi) = \phi^2 \left[ \frac{\sigma^2(2w)}{(2w)^2} + \frac{\sigma^2(\beta)}{\beta^2} + \frac{1}{b(2w)} \right] \quad (23)$$

#### 4.3. Cauchy and Gaussian components of the integral breadth

The approximations to the components of the Voigt-function breadth given by eqs. (8) and (9) can be used to estimate the variances of  $\beta_C$  and  $\beta_G$ . That of  $\beta_C$  is

$$\sigma^2(\beta_C) = \left( \frac{\partial\beta_C}{\partial\beta} \right)^2 \sigma^2(\beta) + \left( \frac{\partial\beta_C}{\partial\phi} \right)^2 \sigma^2(\phi) + \left( \frac{\partial\beta_C}{\partial\beta} \frac{\partial\beta_C}{\partial\phi} \right) \text{cov}(\beta, \phi) \quad (24)$$

where

$$\text{cov}(\beta, \phi) = \left( \frac{\partial\beta}{\partial I_0} \frac{\partial\phi}{\partial I_0} \right) \sigma^2(I_0) + \left( \frac{\partial\beta}{\partial B_0} \frac{\partial\phi}{\partial B_0} \right) \sigma^2(B_0) + \left( \frac{\partial\beta}{\partial s} \frac{\partial\phi}{\partial s} \right) \sigma^2(s) \quad (25)$$

with a similar expression for  $\sigma^2(\beta_G)$ . From eqs. (1) and (17),

$$\phi = \frac{1}{bS} (I_0 + B_0 - 2a)(I_0 - B_0) \quad (26)$$

Hence,

$$\frac{\partial\phi}{\partial I_0} = 2(I_0 - a)/bS, \quad \frac{\partial\phi}{\partial B_0} = 2(a - B_0)/bS, \quad \frac{\partial\phi}{\partial s} = -\phi/S \quad \text{and} \quad \frac{\partial\beta}{\partial s} = 1/L_0 \quad (27)$$

From Wilson ([18] eqs. (23) and (145)), provided that the background slope is small,

$$\sigma^2(s) = s + \frac{RB_0}{p} (1 + R/p) \quad (28)$$

Hence,

$$\sigma^2(\beta_C) = \frac{\beta_C^2}{b^2} \sigma^2(\beta) + \beta_C^2 (a_1 + 2a_2\phi)^2 \sigma^2(\phi) + \beta_C (a_1 + 2a_2\phi) \text{cov}(\beta, \phi) \quad (29)$$

where

$$\text{cov}(\beta, \phi) = \frac{1}{L_0} \left\{ \frac{2}{b} (\underline{a} - \underline{I}_0) \underline{I}_0 + \frac{2}{b} (\underline{a} - \underline{B}_0) \underline{B}_0 - \frac{\phi}{\beta} [\beta \underline{L}_0 + \underline{R} \underline{B}_0 (1 + \underline{R}/\underline{P})] \right\} \quad (30)$$

Similarly,

$$\begin{aligned} \sigma^2(\beta_{\underline{G}}) &= \frac{\beta_{\underline{G}}^2}{\beta^2} \sigma^2(\beta) + \beta^2 \left[ \frac{b_{1/2}}{2} (\phi - d/\pi)^{-1/2} + \underline{b}_1 + 2\underline{b}_2 \phi \right]^2 \sigma^2(\phi) \\ &+ \beta_{\underline{G}} \left[ \frac{b_{1/2}}{2} (\phi - 2/\pi)^{-1/2} + \underline{b}_1 + 2\underline{b}_2 \phi \right] \text{cov}(\beta, \phi) \quad (31) \end{aligned}$$

#### 4.4. Integral breadth of the size or strain function

After the size and strain components of the constituent functions have been separated by the method described in Section 2.4,  $\beta_{\underline{C}\underline{C}}$ ,  $\beta_{\underline{G}\underline{C}}$ , or  $\beta_{\underline{C}\underline{S}}$ ,  $\beta_{\underline{G}\underline{S}}$  in general are recombined to give the breadths  $\beta_{\underline{C}}$ ,  $\beta_{\underline{S}}$  of the size or strain profiles. The variance of these parameters is

$$\sigma^2(\beta_{\underline{X}}) = \left( \frac{\partial \beta_{\underline{X}}}{\partial \beta_{\underline{C}\underline{X}}} \right)^2 \sigma^2(\beta_{\underline{C}\underline{X}}) + \left( \frac{\partial \beta_{\underline{X}}}{\partial \beta_{\underline{G}\underline{X}}} \right)^2 \sigma^2(\beta_{\underline{G}\underline{X}}) + \left( \frac{\partial \beta_{\underline{X}}}{\partial \beta_{\underline{C}\underline{X}}} \frac{\partial \beta_{\underline{X}}}{\partial \beta_{\underline{G}\underline{X}}} \right) \text{cov}(\beta_{\underline{C}\underline{X}}, \beta_{\underline{G}\underline{X}}) \quad (32)$$

where  $\underline{X} = \underline{C}$  or  $\underline{S}$  and, from the approximation of de Keijser, et al. given by eq. (15),

$$\begin{aligned} \frac{\partial \beta_{\underline{X}}}{\partial \beta_{\underline{C}\underline{X}}} &= - \frac{\beta_{\underline{X}}^2}{2\beta_{\underline{G}\underline{X}}^2} \left[ \beta_{\underline{C}\underline{X}} (\beta_{\underline{C}\underline{X}}^2 + 4\beta_{\underline{G}\underline{X}}^2)^{-1/2} - 1 - 0.264(1 - 1.228\beta_{\underline{C}\underline{X}}/\beta_{\underline{G}\underline{X}}) \right. \\ &\quad \left. \exp(-1.228\beta_{\underline{C}\underline{X}}/\beta_{\underline{G}\underline{X}}) \right] - 2\beta_{\underline{G}\underline{X}} (\beta_{\underline{C}\underline{X}}^2 + 4\beta_{\underline{G}\underline{X}}^2)^{-1/2} \end{aligned}$$

and

$$\frac{\partial \beta_{\underline{X}}}{\partial \beta_{\underline{G}\underline{X}}} = \frac{\beta_{\underline{X}}^2}{\beta_{\underline{C}\underline{X}}^2} \left[ \frac{2\beta_{\underline{G}\underline{X}}}{\beta_{\underline{X}}} + 0.162 \frac{\beta_{\underline{C}\underline{X}}^2}{\beta_{\underline{G}\underline{X}}^2} \exp(-1.228\beta_{\underline{C}\underline{X}}/\beta_{\underline{G}\underline{X}}) - 2\beta_{\underline{G}\underline{X}} (\beta_{\underline{C}\underline{X}}^2 + 4\beta_{\underline{G}\underline{X}}^2)^{-1/2} \right] \quad (33)$$

and  $\sigma^2(\beta_{\underline{c}_x})$ ,  $\sigma^2(\beta_{\underline{g}_x})$  and  $\text{cov}(\beta_{\underline{c}_x}, \beta_{\underline{g}_x})$  are obtained in the usual way from the variances of the constituent parameters. For example, the variance of  $\beta_{\underline{c}}$  when the contribution from size broadening is entirely Cauchy is

$$\sigma^2(\beta_{\underline{c}}) = \sigma^2(\beta_{\underline{f}_c}) = \sigma^2(\beta_{\underline{g}_c}) + \sigma^2(\beta_{\underline{h}_c}) \quad , \quad (34)$$

where  $\sigma^2(\beta_{\underline{g}_c})$ ,  $\sigma^2(\beta_{\underline{h}_c})$  are given by eq. (29). Similarly, the variance of  $\beta_{\underline{s}}$  when strain broadening is entirely Gaussian is

$$\sigma^2(\beta_{\underline{s}}) = \sigma^2(\beta_{\underline{f}_g}) = \frac{1}{\beta_{\underline{f}_g}^2} [\beta_{\underline{g}_g}^2 \sigma^2(\beta_{\underline{g}_g}) + \beta_{\underline{h}_g}^2 \sigma^2(\beta_{\underline{h}_g})] \quad , \quad (35)$$

where  $\sigma^2(\beta_{\underline{g}_g})$ ,  $\sigma^2(\beta_{\underline{h}_g})$  are obtained from eq. (31).

From eqs. (11) and (12), the standard deviation in the apparent crystallite size and strain, arising from random fluctuations in the count rate, are then

$$\sigma(\varepsilon) = \frac{\varepsilon}{\beta_{\underline{c}}} \sigma(\beta_{\underline{c}}) \quad (36)$$

and

$$\sigma(\eta) = \frac{\eta}{\beta_{\underline{s}}} \sigma(\beta_{\underline{s}}) \quad (37)$$

## 5. Summary

The accuracy of the crystallite size and strain obtained from the integral breadths of powder diffraction lines can be affected by numerous factors. Sources of systematic error include the use of standard data to correct for instrumental effects, the removal of the  $K\alpha_2$  line, background corrections and the choice of analytic function to describe the line profiles. Additionally, there are calculable random errors arising from statistical fluctuations in the count rate.

In general, systematic errors cannot readily be calculated, but can be minimised by means of careful experimental procedure (Section 2) and by applying various tests to ensure that their effect is inappreciable (Section 3). The Voigt function is considered to be an adequate approximation to line profiles in the majority of applications (Sections 2.3. and 2.4.), and this is used to estimate the error in the apparent crystallite size and strain due to counting statistics.

It is thus possible to estimate the accuracy of the apparent size and strain. There will, however, be additional uncertainties in the "true" values which cannot readily be calculated, since they depend on the shapes of the crystallites, the distribution of size and strain and other factors.

Appendix  
List of Principal Symbols

$\underline{A}_n$	Fourier cosine coefficient of order n
$\underline{a}, \underline{b}$	Intercept and slope of approximate linear region of peak
$\underline{B}_0$	Mean background level
$\underline{C}$	(Suffix): Cauchy function
$\underline{c}$	(Suffix): Crystallite-size function
$\langle e^2 \rangle^{\frac{1}{2}}$	r.m.s. strain
$\underline{f}$	(Suffix): Pure diffraction profile, including contributions due to crystallite and strain
$\underline{g}$	(Suffix): Instrumental profile, including wavelength distribution and contribution from physical factors
$\underline{G}$	(Suffix): Gaussian function
$\underline{h}$	(Suffix): Experimental (broadened) profile
$\underline{I}_i$	Observed intensity at $i$ th step
$\underline{I}_0$	Observed peak intensity
$\underline{K}_\beta$	Integral-breadth Scherrer constant
$\underline{k}$	$= \beta_C / \pi^{\frac{1}{2}} \beta_G$
$\underline{L}_0$	Peak intensity of line-less-background
$\underline{p}$	True crystallite size; factor by which counting time is increased to determine background
$\underline{q}$	Factor by which counting time is increased to determine peak
$\underline{R}$	Total number of steps
$\underline{S}$	Integrated intensity of line-less-background
$\underline{s}$	Number of intensities on each side of peak used to estimate FWHM; (Suffix): Strain
$\underline{2w}$	Full width at half maximum intensity (FWHM)
$\beta$	Integral breadth
$\Delta(2\theta)$	Angular range of profile for which Fourier coefficients are calculated
$\varepsilon$	Apparent crystallite size
$\eta$	Apparent strain
$\theta$	Bragg angle
$\lambda$	Wavelength
$\phi$	Form factor ( $= \underline{2w}/\beta$ )

## References

- [1] Laue, M. von, Lorentz-faktor und Intensitätsverteilung in Debye-Scherrer-Ringen, *Z. Krist.* 64, 115-142 (1926).
- [2] Klug, H. P. and Alexander, L. E., X-ray Diffraction Procedures for Polycrystalline and Amorphous Materials, 2nd edition (Wiley, New York, 1974).
- [3] Wilson, A. J. C., Mathematical Theory of X-ray Diffractometry (Centrex, Eindhoven, 1963).
- [4] Stokes, A. R., A numerical Fourier-analysis method for the correction of widths and shapes of lines on x-ray powder photographs, *Proc. Phys. Soc. Lond.* 61, 382-391 (1948).
- [5] Louër, D., Weigel, D., and Louboutin, R., Méthode directe de correction des profils de raies de diffraction des rayons X. I. Méthode numérique de déconvolution, *Acta Cryst.* A25, 335-338 (1969).
- [6] Wilson, A. J. C., The location of peaks, *Brit. J. Appl. Phys.* 16, 665-674 (1965).
- [7] Murdock, C. C., The form of the x-ray diffraction bands for regular crystals of colloidal size, *Phys. Rev.* 35, 8-23 (1930).
- [8] Warren, B. E., X-ray studies of deformed metals, in Prog. in Met. Phys. 8, 147-202 (Pergamon Press, London, 1959).
- [9] Wagner, C. N. J. and Aqua, E. N., Analysis of powder pattern peaks from cold-worked face-centred cubic metals, in Adv. in X-ray Anal. 7, 46-65 (Plenum Press, New York, 1964).
- [10] Jones, F. W., The measurement of particle size by the x-ray method, *Proc. Phys. Soc. Lond.* A166, 16-43 (1938).
- [11] Alexander, L. E., Geometrical factors affecting the contours of x-ray spectrometer maxima. I. Factors causing asymmetry, *J. Appl. Phys.* 19, 1068-1071 (1948).
- [12] Langford, J. I., A rapid method for analysing the breadths of diffraction and spectral lines using the Voigt function, *J. Appl. Cryst.* 11, 10-14 (1978).
- [13] Ruland, W., The integral width of the convolution of a Gaussian and a Cauchy function, *Acta Cryst.* 18, 581 (1965).
- [14] Ruland, W., The separation of line-broadening effects by means of line-width relations, *J. Appl. Cryst.* 1, 90-101 (1968).
- [15] Schoening, F. R. L., Strain and particle size values from x-ray line breadths. *Acta Cryst.* 18, 975-976 (1965).
- [16] Halder, N. C. and Wagner, C. N. J., Separation of particle size and lattice strain in integral breadth measurements, *Acta Cryst.* 20, 312-313 (1966).
- [17] Hulst, H. C. van de and Reesinck, J. J. M., Line breadths and Voigt profiles, *Astrophys J.* 106, 121-127 (1947).
- [18] Wilson, A. J. C., Statistical variance of line-profile parameters, Measures of intensity, location and dispersion, *Acta Cryst.* 23, 888-898 (1967).
- [19] Wilson, A. J. C., Statistical variance of line-profile parameters, Measures of intensity, location and dispersion: Corrigenda, *Acta Cryst.* A24, 478 (1968).

- [20] Wilson, A. J. C., Statistical variance of line-profile parameters: Addendum, *Acta Cryst.* A25, 584 (1969).
- [21] Gupta, R. K. and Anantharaman, T. R., Shape analysis of x-ray diffraction broadening from deformed tungsten, *Z. Metallk.* 62, 732-735 (1971).
- [22] De Keijser, Th. H., Mittemeijer, E. J., and Vogels, A. B. P., Experiences with the Voigt function for a single-line technique in the analysis of x-ray diffraction line broadening, submitted for publication (1979).
- [23] Rachinger, W. A., A correction for the  $\alpha_1\alpha_2$  doublet in the measurement of widths of x-ray diffraction lines, *J. Sci. Instrum.* 25, 254-255 (1948).
- [24] Delhez, R. and Mittemeijer, E. J., An improved  $\alpha_2$  elimination, *J. Appl. Cryst.* 8, 609-611 (1975).
- [25] Narayan, R., The separation of  $K\alpha_1$  and  $K\alpha_2$  components in x-ray line profile analysis, *J. Appl. Cryst.* 10, 351-352 (1977).
- [26] Langford, J. I. and Wilson, A. J. C., On variance as a measure of line broadening in diffractometry: some preliminary measurements on annealed aluminum and nickel and on cold-worked nickel, in *Crystallography and Crystal Perfection*, G. N. Ramachandran, ed. (Academic Press, London, 1963), pp. 207-222.
- [27] Langford, J. I., The variance and other measures of line broadening in powder diffractometry. I. Practical considerations, *J. Appl. Cryst.* 1, 48-59 (1968).
- [28] Lundy, D. R. and Eanes, E. D., A computer program for the separation of linearly sloping backgrounds in x-ray line broadening analysis, *J. Appl. Cryst.* 5, 380-381 (1972).
- [29] Rigault, J., Détermination de l'intensité intégrée en step-scanning, *J. Appl. Cryst.* 12, 116-118 (1979).
- [30] Gautschi, W., Algorithm 63: complex error function, *Commun. A.C.M.* 12, 635 (1969).
- [31] Stokes, A. R. and Wilson, A. J. C., The diffraction of x-rays by distorted crystal aggregates. I. *Proc. Phys. Soc. Lond.* 56, 174-181 (1944).
- [32] Langford, J. I. and Wilson, A. J. C., Scherrer after sixty years: a survey and some new results in the determination of crystallite size, *J. Appl. Cryst.* 11, 102-113 (1978).
- [33] Langford, J. I., X-ray powder diffraction studies of Vitromet samples, *J. Appl. Cryst.* 4, 164-168 (1971).

#### Discussion

Question (Jennings): If an experimental peak can be fitted within experimental accuracy by a 3 (or 4 or 5) parameter function, clearly these parameters (or quantities derived from them) represent the most that can be said. How many parameters are required in a typical case? Do you agree with me that the coefficient of the  $1/x^2$  behavior of the wings is one of the important parameters (where  $x$  is the deviation of  $\sin \theta/\lambda$  from the Bragg condition)?

Response (Langford): Four parameters are required if an experimental peak is assumed to be Voigtian--the peak height, integrated intensity, FWHM and mean background. These parameters

are sufficient to give the lattice strain and the apparent crystallite size,  $E_{11}$  based on a volume average. A fifth parameter could be included to represent skewness if the profile is asymmetric. Provision for background slope could also be included, but this is not important in the method described.

The coefficient of the  $1/x^2$  behavior in the profile tails is an important parameter, since it provides a size estimate,  $E_2$  based on an average. If this is also obtained, a comparison of  $E_1$  and  $E_2$  may well give an indication of the "average" shape of the crystallites.

Question (Suortti): When subtracting the background, the non-linear behavior of the TDS was not taken into account. What effect would this have?

Response (Langford): The integral-breadth method does not produce results of high accuracy and it is doubtful if the omission of a TDS correction leads to a measurable increase in the overall error. However, an appropriate correction could be made if the Voigt function is used in structure determination from powder data.



DETERMINATION OF COMPOSITIONAL VARIATIONS  
BY X-RAY DIFFRACTION LINE PROFILE ANALYSIS

E. J. Mittemeijer and R. Delhez  
Laboratory of Metallurgy  
Delft University of Technology  
Rotterdamseweg 137, 2628 Al Delft  
The Netherlands

In the analysis of the x-ray diffraction line broadening due to concentration variations three types of specimens are distinguished: (a) powder samples where the "same" concentration variation occurs within each individual crystallite; (b) powder blends with concentration variations across the contact places of the particles (each particle consists of a number of crystallites or domains); (c) monocrystals where the concentration variation extends over many coherently diffracting domains.

For the first type of specimens the concentration profile can be obtained from the sine Fourier coefficients of a single line profile. This analysis appears to be especially suited for the investigation of concentration inhomogeneities occurring within the crystallites of alloy catalysts.

For the description of diffusional homogenization of compacted powder blends--the second type of specimens--a method for the calculation of concentration-effective penetration curves was proposed by Rudman. A fast and simple method is possible utilizing the position of the maximum of an intensity band. Applying such methods best results are obtained by modeling the powder blend as a conglomerate of concentric spheres.

For the third type of specimens Houska and co-workers calculated the concentration profile by: (i) an iterative method using two or more orders of the reflection and (ii) computer simulation of a single profile. Further, using a single profile, a direct method without iterations or simulations is possible. The background is dominated by thermal diffuse scattering (TDS) and thus a linear background profile is a poor approximation to the real background. The TDS background can be calculated iteratively.

## 1. Introduction

From a technological point of view the study of concentration variations is very important, in particular in those cases where the concentration variations occur over small (about 1  $\mu\text{m}$ ) and very small (about 1 nm) distances. This is illustrated by the following examples which are closely related to this paper: (a) The numerous applications of micro-electronic devices and metal coatings stimulate the interest in the diffusion-induced concentration variations in thin metal films [1]<sup>1</sup>. (b) The increasing importance of alloy catalysts necessitates the study of local concentration inhomogeneities occurring in the small catalyst particles [2]. (c) Several technologically important binary metal alloys are produced by diffusional homogenization of a compacted powder blend of the constituting metal components [3].

Lattice parameter variations broaden x-ray diffraction line profiles. Therefore the analysis of x-ray diffraction line broadening may afford a powerful nondestructive quantitative method to study compositional variations (cf. fig. 1).

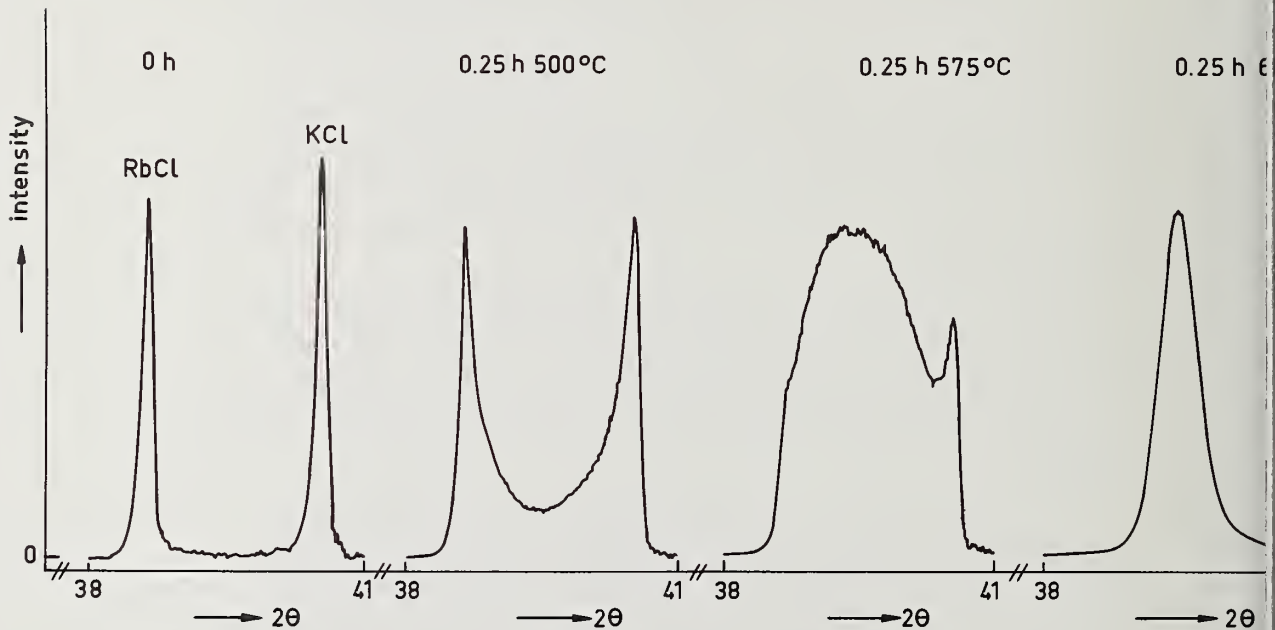


Figure 1.  $220 \alpha_1$  line profiles recorded with  $\text{CuK}\alpha$  radiation from an  $\text{RbCl/KCl}$  powder specimen interdiffused at various temperatures.

Until now there has been a very limited interest in the application of x-ray diffraction methods to study concentration variations (for a review of the older literature see reference [4]). In this paper recent methods for the analysis of x-ray diffraction line broadening du

<sup>1</sup>Figures in brackets indicate the literature references at the end of this paper.

to concentration variations are presented for three types of specimens: (i) powder samples where the concentration variation occurs within coherently diffracting crystallites or domains; (ii) powder blends where the concentration variations occur across the contact places of the particles (each particle consists of a number of crystallites or domains); (iii) monocrystals where the concentration variation extends over many coherently diffracting domains. Results obtained and difficulties encountered in practice are discussed.

This survey is preceded by a development of the theory of x-ray diffraction line broadening of a domain containing a gradient of spacing.

## 2. Theory of Diffraction of a Domain Containing a Gradient of Spacing

For a coherently diffracting domain the diffracted intensity can be expressed as the Fourier series [5,6],

$$P(h_3) = C \sum_{n=-(N_3-1)}^{N_3-1} F(n) \exp 2\pi i n h_3, \quad (2.1)$$

where

$$F(n) = \sum_{m_3=0}^{N_3-1-|n|} \exp 2\pi i \ell S_c(m_3, n) \quad (2.2)$$

with

$$\begin{aligned} S_c(m_3, n) &= \Delta_{m_3+|n|} - \Delta_{m_3} \quad \text{for } n \geq 0 \\ &= \Delta_{m_3} - \Delta_{m_3+|n|} \quad \text{for } n \leq 0. \end{aligned}$$

where  $\Delta_{m_3} \langle a_3 \rangle$  is the displacement of the  $m_3$ -th lattice plane from its reference position  $m_3 \langle a_3 \rangle$ . In the following, only positive values of the harmonic number  $n$  will be considered. Orthorhombic axes have been used, which transform reflections of  $(hkl)$  type into  $(00\ell)$  type [7,8]. The reciprocal lattice vector is defined by  $h_3 b_3$ , where  $|b_3| = 1/\langle a_3 \rangle$ . The number of diffracting lattice planes is  $N_3$ . The quantity  $C$  comprises the usual angle-dependent factors [5]. If  $a_3$  denotes the first interplanar spacing, the  $m_3$ -th lattice plane is found at

$$R_{m_3} = m_3 \underline{a}_3 + \left\{ \sum_{k=1}^{m_3} \Delta'_k \right\} \underline{a}_3$$

or in terms of the reference spacing  $\langle \underline{a}_3 \rangle$

$$\underline{R}_{m_3} = m_3 \langle \underline{a}_3 \rangle + \Delta_{m_3} \langle \underline{a}_3 \rangle \quad (2.3)$$

where

$$\Delta_{m_3} = \left\{ \sum_{k=1}^{m_3} \Delta'_k - \frac{m_3}{N_3-1} \sum_{k=1}^{N_3-1} \Delta'_k \right\} \frac{|\underline{a}_3|}{|\langle \underline{a}_3 \rangle|} \quad (2.4)$$

If it is assumed for our model calculations that the spacing varies linearly such that

$$\Delta'_k = (k-1)\delta \quad (2.5)$$

then substituting eq. (2.5) into eq. (2.4), using the approximation  $|\underline{a}_3|/|\langle \underline{a}_3 \rangle| \cong 1$ , and summing the arithmetic series it is obtained

$$\Delta_{m_3} = \frac{1}{2} \delta m_3 (m_3 - N_3 + 1) \quad (2.6)$$

Substitution of eq. (2.6) into eq. (2.2) yields

$$F(n) = \sum_{m_3=0}^{N_3-1-n} \exp 2\pi i \ell [\delta m_3 n + \frac{1}{2} \delta n (n - N_3 + 1)]$$

$$= \frac{\sin \pi \delta n \ell (N_3 - n)}{\sin \pi \delta n \ell} \quad (2.7)$$

after summing the geometric series. In this case "long-range" displacements exist, unlike in the case of Warren's strain broadening. This Fourier coefficient is analogous to expressions obtained by Borie [9] and Houska [10].

In practice the replacement of the sine in the denominator of  $F(n)$  by its argument and the replacement of the summation in eq. (2.1) by an integration is justified. Hence it follows for the diffracted intensity ( $N_3-1 \cong N_3$ ):

$$P(h_3) = C \int_{-N_3}^{N_3} \frac{\sin \pi \delta n \ell (N_3 - n)}{\pi \delta n \ell} \exp(2\pi i n h_3) dn \quad (2.8)$$

After definition of the factor  $S = \delta \ell N_3^2$  and replacement of variable  $n$  by  $x = n/N_3$  eq. (2.8) can be rewritten

$$P(h_3) = CN_3^2 \int_{-1}^1 \frac{\sin \pi S x (1-x)}{\pi S x} \exp[2\pi i x (N_3 h_3)] dx \quad (2.9)$$

We now introduce the notion of comparable graphs for the shape of the intensity function of a particle with lattice spacing variations [11]. As is well known, the intensity function of a particle without lattice spacing variation is given by  $C \sin^2 \pi N_3 h_3 / \sin^2 \pi h_3$  having an absolute maximum proportional to  $N_3^2$  and a width proportional to  $N_3^{-1}$ . Let us define a function which characterizes--independent of the total amount of diffracting material--the shape of the intensity function of a particle without lattice spacing variation. This can be realized by dividing the intensity values by  $C N_3^2$  and multiplying the variable  $h_3$  by  $N_3$ . In a similar way the intensity function of a particle with lattice spacing variations is normalized. Then it is obtained

$$P^n(h_3^n) = \int_{-1}^1 \frac{\sin \pi S x (1-x)}{\pi S x} \exp(2\pi i x h_3^n) dx \quad (2.10)$$

where

$$P^n(h_3^n) = P(h_3) / CN_3^2 \text{ with } h_3^n = h_3 N_3$$

It is concluded that the shape of the diffraction profile is adequately described by the combination of  $\delta$ ,  $\ell$  and  $N_3$  in the factor  $S = \delta \ell N_3^2$ .

Characteristic diffraction profiles are presented in figure 2. For small  $S$ -values the profile resembles the profile due to pure size broadening, while for large  $S$ -values the profile has a rectangular shape (see also ref. [10]). This can be understood as follows: For small  $S$

$$\frac{\sin \pi S x (1-x)}{\pi S x} \rightarrow 1-x = 1-n/N_3$$

which is exactly the Fourier transform for crystallite size broadening.

For large values of  $S$ , for no vanishing values of the Fourier transform  $x \ll 1$ , and

$$\frac{\sin \pi S x (1-x)}{\pi S x} \rightarrow \frac{\sin \pi S x}{\pi S x}$$

which is the well-known (e.g. ref. [12]) Fourier transform of a rectangular function in real space.

The changes in the diffraction profile can be illustrated clearly by plotting  $T = 1 - P^N(h_3^N = \ell N_3)$ , which represents the decrease in top intensity, as a function of  $S$  (fig. 3). For small values of  $S$  ( $S < 1.5$ ),  $T$  is a parabolic function of  $S$  [a series expansion of eq. (2.10) results in  $T \approx \pi^2 S^2 / 180$ ].  $T$  is small in this region of  $S$  and the shape of the profile is approximately the ideal one. For larger values of  $S$  the subsidiary maxima rise at the cost of the originally absolute maximum at  $h_3 = \ell$  (cf. fig. 2). If  $S > 6$  the profile has approximately a rectangular shape and the following formulation can be given:

Defining  $\underline{a}_3$  and  $\underline{a}_3^\ell$  as the two outermost interplanar spacings present, it follows for the difference  $\Delta \underline{a}_3 = \underline{a}_3^\ell - \underline{a}_3$  that

$$\Delta \underline{a}_3 = (N_3 - 2) \delta \underline{a}_3 \approx N_3 \delta \underline{a}_3 \quad (2.11)$$

The distance  $|\underline{\Delta H}| = \Delta h_3 | \underline{b}_3 |$  along the reciprocal lattice vector, where in the case of a  $(00\ell)$  reflection intensity can be found, conforms to

$$|\underline{\Delta H}| = \Delta h_3 | \underline{b}_3 | = \ell (1/| \underline{a}_3 | - 1/| \underline{a}_3^\ell |). \quad (2.12)$$

Using eqs. (2.11) and (2.12) it is found for the shape factor  $S = \delta \ell N_3^2$  that

$$S = \Delta h_3 N_3 | \underline{a}_3^\ell | / | \underline{a}_3 | \quad (2.13)$$

Because the diffraction profile is of rectangular shape and the integrated intensity equals the constant  $C N_3$ , it follows for the top intensity of the normalized diffraction profile that

$$P^N(h_3^N = \ell N_3) = C N_3 / \Delta h_3 C N_3^2 = 1 / \Delta h_3 N_3 \quad (2.14)$$

Applying eqs. (2.13) and (2.14) it is finally found that

$$T = 1 - P^N(h_3^N = \ell N_3) = 1 - | \underline{a}_3^\ell | / | \underline{a}_3 | S \approx 1 - 1/S \quad (2.15)$$

For those cases where the concentration profile extends over many coherently diffracting domains, the methods used in sections 4 and 5 divide the concentration profile into segments involving that on the  $2\theta$ -axis the diffracted intensity from a specific segment is restricted to a narrow range around the  $2\theta$ -value corresponding to the average composition of that segment according to Bragg's law. Each segment may consist of one or more domains. Then, in this segmenting procedure it is always assumed that the effect of domain size broadening is

small, which will normally be the case. It is implied also that the additional broadening due to the change of spacing should be small. Otherwise in the integrated intensity ascribed to a segment intensity of its own will be missed and intensity from neighboring segments will be present; in general these effects will not compensate each other.

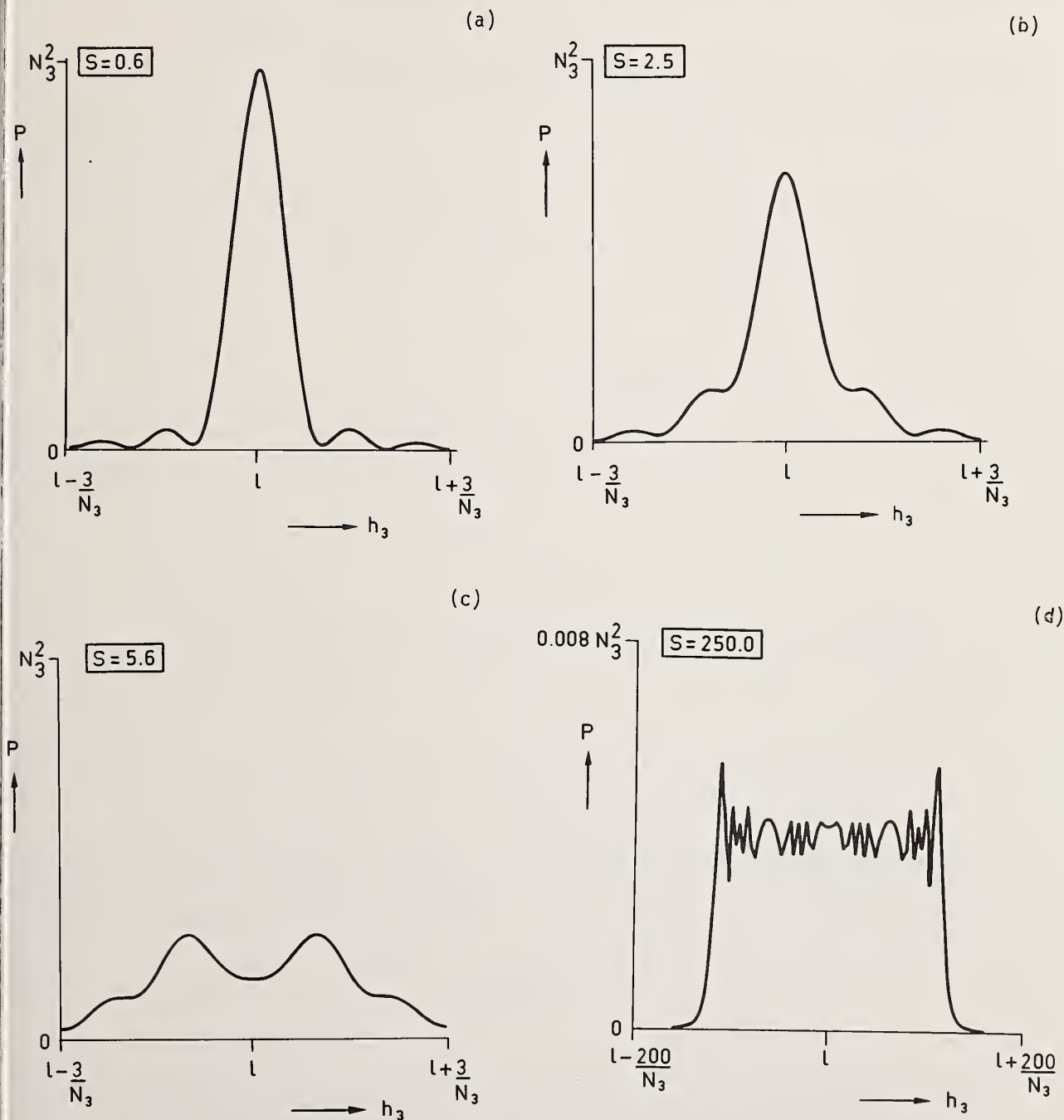


Figure 2. Diffraction profiles for some values of the shape factor  $S$ . Figures 2a-c have been normalized [see eq. (2.10)]. In figure 2d no normalization has been carried out to demonstrate the rectangular shape for large values of  $S$ .

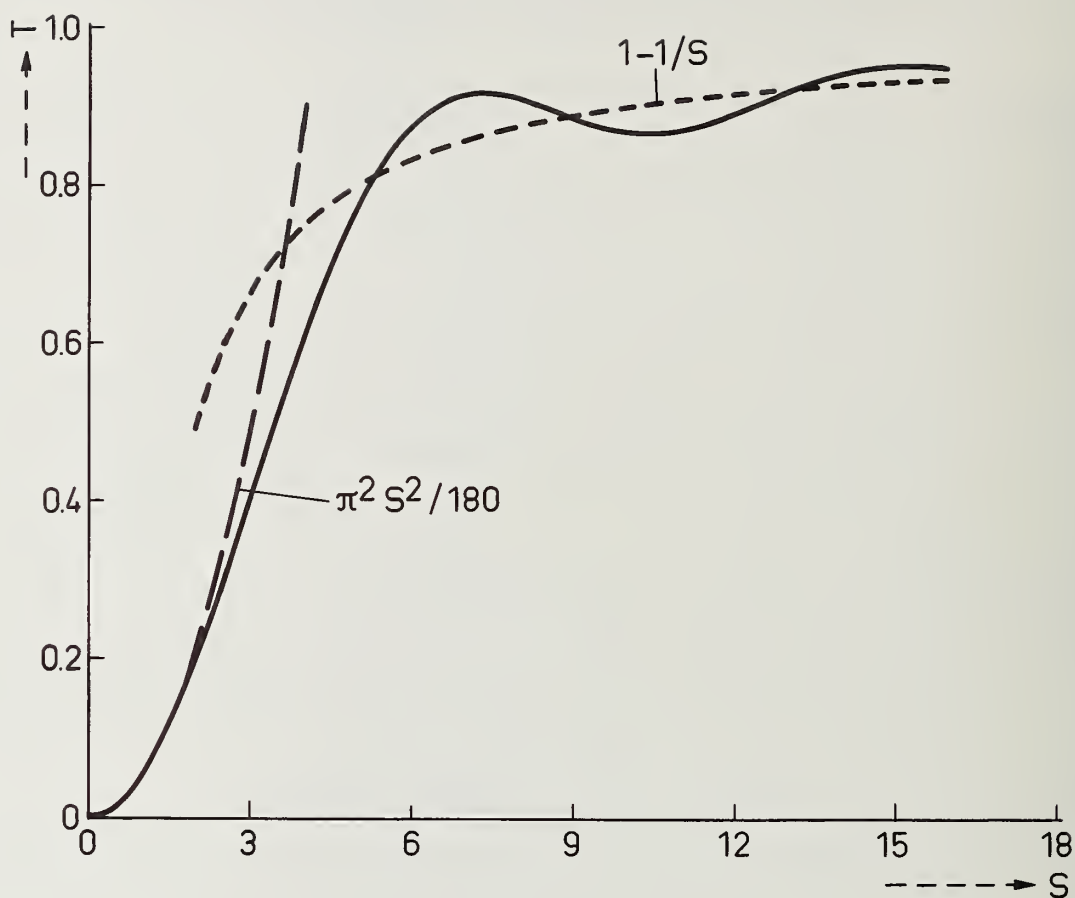


Figure 3. The decrease in top intensity  $T$  versus the shape factor  $S$ .

Approximating the change of spacing in the domain as linear, the above discussion leads to the requirement that  $S$  should be small, say  $S \leq 1.5$  (dominant size broadening; see above). From the definition of  $S$  [below eq. (2.8)] it then follows for the domain size  $L_D (= N_3 \langle a_3 \rangle)$

$$L_D \leq \frac{1.5 \delta}{|\Delta a|/|a|} \quad (2.16)$$

where  $\delta$  has been substituted according to eq. (2.11) with  $|\Delta a|/|a| = |\Delta a_3|/|a_3|$  corresponding to the fractional change of lattice parameter in the segment and  $d = |a_3|/\ell$  is the lattice spacing of the diffracting  $(00\ell)$  planes.

For the Cu/Ni and RbCl/KCl systems investigated in Sections 4 and 5 total fractional changes of spacing  $(|\Delta a|/|a|)_t$  of 2.5 percent and 4.5 percent, respectively, occur over diffusion zones  $Z$  of the order of  $5 \mu\text{m}$ . Then the criterion (2.16) for the domain size can

rewritten as (see also ref. [13])

$$L_D \leq \left\{ \frac{1.5 Z d}{(|\Delta a|/|a|)_t} \right\}^{1/2} \quad (2.17)$$

which leads to  $L_D^{\text{Cu/Ni}}(\text{nm}) \leq 173 \{d(\text{nm})\}^{1/2}$  and  $L_D^{\text{RbCl/KCl}}(\text{nm}) \leq 129\{d(\text{nm})\}^{1/2}$ . From measurements [14] an upper estimate for the domain size in the Cu/Ni system may be taken as 100 nm.<sup>2</sup> It is concluded that in general the criterion (2.17) will be fulfilled for practical cases where the concentration profile extends over several micrometers.

However, if the entire concentration profile is restricted to a very small range in the specimen (e.g. in the early stages of interdiffusion), a 1 percent change in spacing may be taken as a maximum before coherence is disrupted anyhow. Then from the inequality (2.16)

$$L_D \leq 150 d \quad (2.18)$$

For these cases this criterion may lead to a critical domain size which can be smaller than the domains diffracting actually coherently; i.e. the actual domain size corresponding to a 1 percent change in spacing may be larger than the critical domain size prescribed by (2.18).

### 3. Concentration Variations Within Small Crystallites

In this section we deal with the x-ray diffraction investigation of concentration variations occurring within the individual crystallites (coherently diffracting domains). Up to the present the x-ray diffraction method was applied to non-systematical deviations in lattice parameter only (e.g. resulting from cold-work) by using the Warren-Averbach analysis [5,6] based on the cosine Fourier coefficients of the pure line profile. Here, an x-ray diffraction method will be presented for the investigation of long-range displacements (cf. Section 2) by employing the sine Fourier coefficients of the pure line profile.

This method may be especially useful in the field of alloy catalysis [18]. Alloy catalysts are developed to obtain a higher selectivity, a higher activity and a higher stability (i.e. resistance against poisoning).

It is well known that deviations from the average composition can occur in alloy catalysts. The concentration inhomogeneity is localized within the crystallites because significant variations of composition on a macroscale are improbable usually [2].

The line broadening phenomena to be analysed are illustrated in fig. 4, where the 400  $\alpha_1$  line profiles are shown of a Au standard powder sample, a sintered AuPt catalyst (9 at% Pt) and an unsintered AuPt catalyst (14 at% Pt). It is seen that both AuPt specimens give rise to considerable line broadening. In the sintered specimen, no large concentration variations within the crystallites are expected. The line profile should then be mainly symmetrically

<sup>2</sup>The domain boundaries may be grain boundaries which developed during interdiffusion: "diffusion-induced substructure" (cf. refs. [14-17]).

broadened due to small particle size, and, accordingly, the peak position should practically correspond with the average composition, as is observed. The line profile of the unsintered specimen is substantially asymmetrically broadened which is indicative (see Section 3.2) of considerable concentration variations. For this case, the peak position, in general, will correspond with the average composition, as is observed.

### 3.1. Method of profile analysis [19]

Crystallite size, cold work, and concentration variations contribute to the x-ray diffraction line broadening. Here, only spacing changes due to concentration variations are considered. The presence of strain from another origin is not considered, which is justified for alloy catalysts. Further, the composition dependence of the atomic scattering factor is not taken into account. This is not a serious limitation, since in many cases the scattering factors are approximately equal and/or the concentration variation usually covers only a part of the possible composition range.

In Section 2 the kinematical theory of x-ray diffraction from a crystallite with a linear concentration profile has been developed. Nonlinear concentration profiles will be dealt with below.

Analogous to the Warren-Averbach treatment [5,6], the diffracted intensity of a system of unequally sized binary A/B crystallites in which a lattice spacing variation due to a concentration profile is present, can be expressed as the Fourier series (see also Section

$$P(h_3) = C \sum_{n=-\infty}^{+\infty} F(n) \exp 2\pi i n h_3 \quad (3.1)$$

As before, the quantity C comprises the usual angle-dependent factors and orthorhombic axes have been used which transform reflections of (hkl) type into (00l) type. Here, the reciprocal lattice vector is defined by  $h_3 b_B$  where  $\frac{1}{a_B} \cdot \frac{1}{b_B} = \frac{1}{a_A}$  and  $\frac{1}{a_B}$  are the 00l spacings of the pure components A and B, respectively).

The Fourier coefficient  $F(n) = A(n) + iB(n)$  can be written as the product

$$F(n) = A^S(n) F^C(n, \ell), \quad (3.2)$$

where

$$A^S(n) = N_n / N_3 \quad (3.3)$$

and

$$F^C(n, \ell) = \langle \exp 2\pi i \ell S_C(m_3, n) \rangle \quad (3.4)$$

$A^S(n)$ , the "size" Fourier coefficient, is real and independent of the order  $\ell$  of the reflection in contrast to the "concentration" Fourier coefficient  $F^C(n, \ell) = A^C(n, \ell) + iB^C(n, \ell)$ .  $N_n$  denotes the average number per column of pairs of unit cells a distance  $n$  cells apart.

The average in eq. (3.4) is the average over such pairs] and  $N_3$  is the average crystallite (domain) size in unit cells perpendicular to the reflecting (00 $l$ ) planes. The displacement of lattice plane  $m_3$  from its reference position  $m_{3a_B}$  is  $\Delta m_{3a_B}$  and thus ( $n > 0$ ) [cf. eq. (2.2)]

$$S_c(m_3, n) = \Delta_{m_3+n} - \Delta_{m_3} \quad (3.5)$$

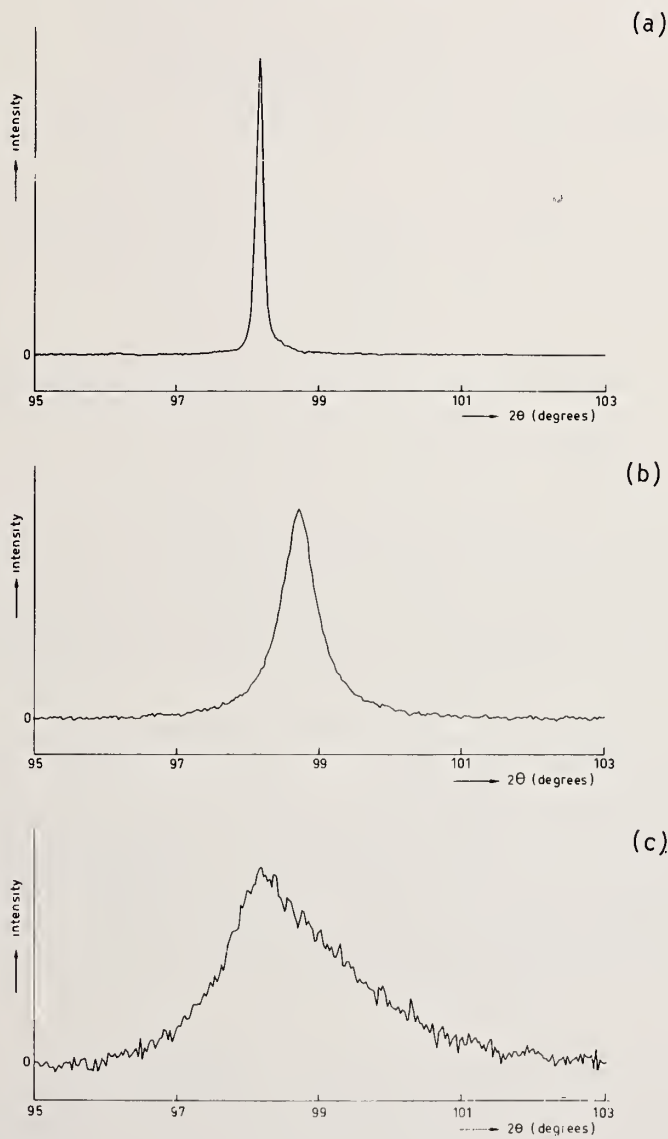


Figure 4. 400  $\alpha_1$  line profiles of the Au standard powder sample (a), the sintered AuPt (9 at% Pt) powder specimen (b), and the unsintered AuPt (14 at% Pt) powder specimen (c).

denoting  $c_{A,k}$  as the atomic fraction of component A in the  $k$ -th lattice plane and using Vegard's law which is valid for most binary systems<sup>3</sup>, it follows that

More complicated composition--lattice parameter dependencies can be dealt with analogously.

$$S_c(m_3, n) = \delta_a \sum_{k=m_3+1}^{m_3+n} c_{A,k} \quad (3.6)$$

where

$$\delta_a = (|a_A| - |a_B|) / |a_B| .$$

$F^C(n, \ell)$  is approximated for small values of  $n$  [cf. eq. (3.6)] by

$$F^C(n, \ell) = 1 + 2\pi i \ell \langle S_c(m_3, n) \rangle - 2\pi^2 \ell^2 \langle S_c(m_3, n)^2 \rangle \quad (3.7)$$

and thus

$$A(n, \ell) = A^S(n) - A^S(n) 2\pi^2 \ell^2 \langle S_c(m_3, n)^2 \rangle \quad (3.8)$$

and

$$B(n, \ell) = A^S(n) 2\pi \ell \langle S_c(m_3, n) \rangle \quad (3.9)$$

Equation (3.9) makes evident that the presence of concentration variations within crystallites gives rise to non-zero sine Fourier coefficients indicating asymmetrical line broadening.

Obviously investigation of  $\langle S_c(m_3, n) \rangle$  is more easily done than of  $\langle S_c(m_3, n)^2 \rangle$ . Therefore, in the following, it is attempted to obtain information on the concentration profile from the sine Fourier coefficients  $B(n, \ell)$  of the line profile.

Use of eq. (3.9) necessitates knowledge of the "crystallite-size" Fourier coefficient  $A^S(n)$ : If two orders,  $\ell_1$  and  $\ell_2$ , of a reflection are available, values of  $A^S(n)$  [and  $\langle S_c(m_3, n)^2 \rangle$ ] are obtained by plotting  $A(n, \ell)$  versus  $\ell^2$  [cf. eq. (3.8) and see also ref. [2]. The particle size  $N_3$  follows from  $\{-[dA^S(n)/dn]\}_{n \downarrow 0}^{-1}$ .  $\langle S_c(m_3, n) \rangle$  can be rewritten

$$\begin{aligned} \langle S_c(m_3, n) \rangle &= [1/(N_3 - n)] \sum_{m_3=0}^{N_3-1-n} (\Delta_{m_3+n} - \Delta_{m_3}) \\ &= [1/(N_3 - n)] \sum_{m_3=0}^{n-1} (\Delta_{N_3-1-m_3} - \Delta_{m_3}) \quad (3.10) \end{aligned}$$

We shall restrict ourselves to symmetrical concentration profiles, which is a condition usually met in practice. Then,

$$\Delta_{N_3-1-m_3} = \delta_a N_3 \bar{c} - \Delta_{m_3-1} \quad (3.11)$$

where  $\bar{c}$  is the known average composition of the crystallite. Substitution of eq. (3.11) into eq. (3.10) leads to

$$\langle S_c(m_3, n) \rangle = [1/(N_3-n)] [n\delta_a N_3 \bar{c} - f(n)], \quad (3.12)$$

where

$$f(n) = \Delta_{n-1} + 2 \sum_{k=0}^{n-2} \Delta_k \quad (3.13)$$

Combination of eqs. (3.9) and (3.12) finally results in

$$f(n) = n\delta_a N_3 \bar{c} - [B(n, \ell)/A^S(n)] [(N_3-n)/2\pi\ell]. \quad (3.14)$$

All factors at the right-hand side of eq. (3.14) are known. Hence,  $f(n)$  can be calculated for successive values of  $n$  ( $n=1, 2, \dots$ ). Then, as follows from eq. (3.13), the  $\Delta_n$  values ( $n=0, 1, 2, \dots$ ) can be calculated from the  $f(n)$  values by applying the recursive equation

$$\Delta_n = f(n+1) - f(n) - \Delta_{n-1}. \quad (3.15)$$

Because  $\Delta_n = \delta_a \sum_{k=0}^n c_{A,k}$  [cf. eq. (3.6)],  $\sum_{k=0}^n c_{A,k}$  can also be calculated, implying the determination of the concentration profile. In the above derivation no assumption is made on the shape of the particles, but it only holds for not too large values of  $n$  [cf. eq. (3.7)].

### 3.2. Results from AuPt alloy catalysts

According to eq. (3.8) the crystallite size Fourier coefficients  $A^S(n)$  can be determined from two orders of a reflection<sup>4</sup>. After substitution of the  $A^S(n)$  coefficients into eq. (3.14), the  $f(n)$  values are obtained. On these  $f(n)$  values a correction for the "hook" effect can be performed [19]. The resulting concentration profiles as calculated from the 200 line profiles of a sintered AuPt catalyst (9 at% Pt) and of an unsintered AuPt catalyst (14 at% Pt) are shown in figures 5a and b, respectively.

The result for the sintered specimen (fig. 5a) shows that in the interior of the crystallite the concentration maintains a constant value of 9 at% Pt which agrees very well

In case only a single line profile is available  $A^S(n)$  can be approximated with  $1-n/N_3$ , where  $N_3$  can be determined from the initial slope of the  $A(n)$ -curve [21].

with the average composition. In the surface region, enrichment by gold is observed. This is in agreement with Auger electron spectroscopical [22] and hydrogen adsorption [23] data. The enrichment of the surface region by the component with the lower heat of sublimation (i.e. gold) was also theoretically predicted [24,25].

From figure 5a it is seen that after the surface region where enrichment of gold is observed, an inversion region occurs with platinum enrichment, as compared to the average composition. Until now this effect has not been explained theoretically by thermodynamic models for endothermic systems as AuPt (cf. ref. [25]). After submission of the above results for publication [19], comparable results for CuNi alloys were published [26]; applying ultraviolet photoemission spectroscopy, it was shown that the surface region was enriched with Cu and that the composition as a function of depth below the surface did not approach the bulk value monotonically, but at least one oscillation occurred. For both endothermic systems, AuPt and CuNi, neither the quasichemical approach nor the regular solution model explain such behaviour. These theories explain surface enrichment on the basis of a driving force due to a difference in the pure metal surface energies. A more general theory [27] also includes the influence due to a difference in atomic size and the contribution of the heat of solution. But for the systems considered the latter effects are expected to be negligible. It is suggested that spinodal decomposition in the surface region may be responsible for the oscillation observed.

The result for the unsintered specimen (fig. 5b) shows that the concentration variations are much larger than in the sintered specimen. For those concentration variations, neither other experimental data, nor theoretical predictions, exist. Since the specimens are prepared by chemical reduction it may be expected that the nucleus of the crystallite should be platinum-rich, surrounded by a gold-rich shell. This corresponds with the experimental observation. The platinum enrichment of the surface, as compared to the average composition, is not understood at present.

Surface compositions of alloy catalysts are determined usually by Auger electron spectroscopy and selective chemisorption [18]. The validity of the latter technique has been questioned [28] since the method itself may influence the surface composition. With Auger electron spectroscopy it is possible to obtain an impression of the concentration variations below the surface using low- and high-energy transitions, which allow to distinguish between the compositions of the first and deeper atomic layers [29]. Analogously qualitative results can be obtained by ultraviolet photoemission spectroscopy, referred to above [26]. For these methods it is difficult to assign a certain concentration to a specific location below the surface. Further, the destructive sputter depth profiling techniques are difficult to quantify [30], for example preferential sputtering of one of the components might occur [2]. Therefore, in the field of alloy catalysts, the non-destructive x-ray diffraction method presented above can be useful, the more since, in contrast with the other methods mentioned, it enables to investigate the supported alloy catalysts as used in practice.

The method of profile analysis presented in this section may also be used profitably to investigate spinodal decomposition, clustering phenomena and mechanical deformation and interdiffusion in very thin solid films which are transparent for x-rays.

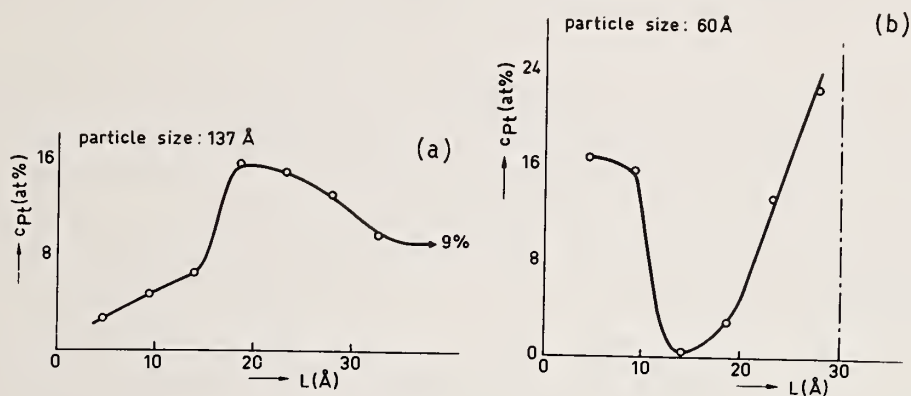


Figure 5. Atomic fraction of platinum  $c_{Pt}$  versus the distance  $L$  perpendicular to the reflecting planes for the sintered AuPt catalyst (9 at% Pt) (a), and the unsintered AuPt catalyst (14 at% Pt) (b).

#### 4. Diffusional Homogenization in Powder Blends

The fabrication of alloys by diffusional homogenization of compacted powder blends is technologically important [3]. To control such processes characterization of the interdiffusion occurring in the powder blend is necessary. On diffusion-annealing numerous diffusion couples operate simultaneously in a powder blend. One wishes to characterize the progress of homogenization in terms of average parameters simplifying the powder blend as a conglomerate of model systems.

X-ray diffractometry yields a description of the imperfect structure as an average over a moderately large diffracting volume. Therefore x-ray diffraction line profile analysis appears to be a powerful quantitative nondestructive method for the study of diffusional homogenization in powder blends (Note the prominent changes in the line profiles on diffusion-annealing in fig. 1.)

##### 4.1. A model of interdiffusion: the concentric sphere model

Metallographic evidence [31-33] indicated that the geometry in binary powder specimens may be described by the concentric sphere geometry. A perfect distribution of the minor component A in the matrix of the major component B is assumed, or in case there are equal portions of both components it is generally assumed that the material with the lower melting point envelopes the particles of the material with the higher melting point at the start of homogenization. Then, a concentric sphere with A and B constituting the sphere and the shell, respectively, may be a reasonable approximation of reality.

A general solution to Fick's second law with a concentration independent diffusion coefficient for diffusion in a sphere with impermeable surface was given by Crank (eq. (6.47)

in ref. [34]). In our case the concentration distribution  $f(r)$  at  $t=0$  is given by

$$0 < r < a \quad f(r) = 1 \quad \text{and} \quad a < r < b \quad f(r) = 0 \quad (\text{case 1})$$

where  $a$  and  $b$  are the radii of the nucleus and the concentric sphere respectively.

It can be shown experimentally (cf. Section 4.3.2) that at the start of interdiffusion (very fast) surface diffusion occurs at the original interfaces of both components. The more realistic description of homogenization may be obtained if a pre-alloyed shell at the A/B interface is thought to be present at  $t=0$ . Then, for the initial concentration distribution  $f(r)$  it follows

$$0 < r < a - \Delta_1 \quad f(r) = 1; \quad a - \Delta_1 < r < a + \Delta_2 \quad f(r) = c_L$$

and

$$a + \Delta_2 < r < b \quad f(r) = 0, \quad (\text{case 2})$$

where  $\Delta_1 + \Delta_2$  is the radial dimension of the pre-alloyed shell and  $c_L = \{a^3 - (a - \Delta_1)^3\} / \{(a + \Delta_2)^3 - (a - \Delta_1)^3\}$ . Evaluation of the integrals in Crank's formula yields

$$c(r) = \frac{a^3}{b^3} + \frac{2b}{r} \sum_{n=1}^{\infty} \exp\{-Dt \alpha_n^2\} \frac{\sin \alpha_n r}{\sin^2 \alpha_n b} E_n \quad (4.1)$$

with 
$$E_n = \frac{-a}{\alpha_n b^2} \cos \alpha_n a + \frac{1}{\alpha_n^2 b^2} \sin \alpha_n a \quad \text{for case 1}$$

$$E_n = \left\{ \frac{-(a - \Delta_1)}{\alpha_n b^2} \cos \alpha_n (a - \Delta_1) + \frac{1}{\alpha_n^2 b^2} \sin \alpha_n (a - \Delta_1) \right\} (1 - c_L) + \left\{ \frac{-(a + \Delta_2)}{\alpha_n b^2} \cos \alpha_n (a + \Delta_2) + \frac{1}{\alpha_n^2 b^2} \sin \alpha_n (a + \Delta_2) \right\} c_L \quad \text{for case 2}$$

where  $c(r)$  is the volume fraction of material A and  $\alpha_n$  is the  $n$ -th positive root of the transcendental equation  $b \alpha_n \cot b \alpha_n = 1$ .

<sup>5</sup>For the concentration profile as obtained from the x-ray diffraction experiment, the concentration is expressed normally in terms of the mole fraction of one of the components. Before the results can be related with eqs. (4.1), (4.2) and (4.3), mole fractions should be converted into volume fractions.

The quantity of material  $m_t$  which has crossed the interface after a given diffusion time and the quantity of material  $m_\infty$  which will cross in infinite time follow from

$$m_t = 4\pi \int_0^{a/b} (1-c)\left(\frac{r}{b}\right)^2 d\left(\frac{r}{b}\right) + 4\pi \int_{a/b}^1 c\left(\frac{r}{b}\right)^2 d\left(\frac{r}{b}\right)$$

$$m_\infty = \frac{8\pi a^3}{3b^3} \left(1 - \frac{a^3}{b^3}\right)$$

The degree of interdiffusion  $F$  as defined by the ratio  $m_t/m_\infty$  (cf. Section 4.3.1) can be calculated from ( $0 \leq F \leq 1$ )

$$F = 1 - \frac{6}{\frac{a}{b^3} \left(1 - \frac{a}{b^3}\right)} \sum_{n=1}^{\infty} \exp\{-Dt\alpha_n^2\} \frac{1}{\alpha_n b \sin^2 \alpha_n b} \cdot \left(-\frac{a}{b} \cos \alpha_n a + \frac{1}{a_n b} \sin \alpha_n a\right) E_n \quad (4.2)$$

If it is assumed that the position of the maximum of the line profile observed corresponds to the concentration of which the maximum amount is present, then this position--expressed as the "relative peak position"  $p_r$  [cf. Section 4.2.2. and eq. (4.9)]--can also be calculated from eq. (4.1). It follows that this position usually corresponds to the position at  $r=b$ . Taking the peak position as the reciprocal of the lattice spacing of the reflecting planes it is obtained for cubic substances ( $0 \leq p_r \leq 1$ )

$$p_r = \left[ \frac{b^3}{a^3} - 1 + \frac{a_B^2}{a_A^2} \right] \left[ \left( \frac{a^3}{b^3} + 2 \sum_{n=1}^{\infty} \exp\{-Dt\alpha_n^2\} \frac{E_n}{\sin \alpha_n b} \right)^{-1} - 1 + \frac{a_B^2}{a_A^2} \right]^{-1} \quad (4.3)$$

where  $a_A$  and  $a_B$  correspond to the lattice parameters of nucleus and shell material respectively.

## 4.2. Methods of profile analysis

### 4.2.1. Rudman's method [35]

The concentration profile is divided into a number of segments. Each segment may consist of one or more coherently diffracting domains. It is implicitly assumed that the grain size is smaller than the critical domain size as prescribed by eqs. (2.16)-(2.18).

The present version of this method differs from the previous ones [35,36], where the concentration profile was described as a continuous function, although a stepped function was implicitly assumed by the diffraction equations used. According to the kinematical diffraction theory the integrated intensity  $P_m$  of a segment corresponds to

$$P_m = \frac{P_0}{16\pi R} C(LP)_m F_m^2 (1/v_m^2) A_m p_m \quad (4)$$

where  $P_0$  is the power in the primary beam,  $R$  is the radius of the goniometer and  $C = r_e^2/\lambda^3$  with  $r_e$  and  $\lambda$  being the classical radius of the electron and the x-ray wavelength respectively;  $LP_m$  comprises the Lorentz and polarization factors,  $F_m^2$  is the squared modulus of the structure factor (including the Debye-Waller factor) and  $v_m$  is the unit cell volume;  $A_m$  is the absorption factor which is approximately constant:  $A_m \cong 1/2 \mu_{\text{eff}}$ , where  $\mu_{\text{eff}}$  is the effective linear absorption coefficient in the sample;  $p_m$  denotes the volume fraction of compositions contained within the segment.

Previous investigators [3,31,32,35] did not consider the concentration dependence of the unit cell volume. [This implies that 9 percent and 15 percent intensity lapses in the profiles of Cu/Ni and RbCl/KCl powder blends (cf. Section 4.3) are not taken into account.]

Applying eq. (4.4) the volume fraction  $p_m$  can be obtained from experimentally determined intensity bands (cf. fig. 1). Subsequently an effective penetration depth of segment  $m$  can be calculated according to

$$y(x_m) = \sum_{i=1}^m p_i \quad 0 \leq y \leq 1 \quad (4)$$

where  $x_m$  is the average composition of segment  $m$  and then a plot of  $x$  versus  $y$  is analogous to normal concentration--penetration curves.

Rudman [35] proposed the degree of interdiffusion  $F$  as a parameter to characterize the stage of homogenization.  $F$  is defined by the ratio of the quantity of material which has crossed the Matano interface after a given diffusion time to the quantity of material which will cross in infinite time:

$$F = \frac{\int_{x=0}^{x(y=y_M)} (y_M - y) dx + \int_{x(y=y_M)}^{x=1} (y - y_M) dx}{\bar{x}y_M + (1-y_M)(1-\bar{x})} = \frac{2 \int_{x=0}^{x(y=y_M)} (y_M - y) dx}{2\bar{x}y_M} \quad (5)$$

where  $y_M$  represents the Matano interface and  $\bar{x}$  the average composition of the sample. In the concentric sphere model the ratio  $F$  is calculated analytically in Section 4.1. The dependence of  $F$  on  $Dt/a^2$ , where  $D$  is the interdiffusion coefficient,  $a$  is the radius of the nucleus of the concentric sphere and  $t$  is the annealing time, is shown in figure 6. [In the previous paper [36] a numerical error was made for the curve based on the modified concentric sphere model. The correct one is presented here.]

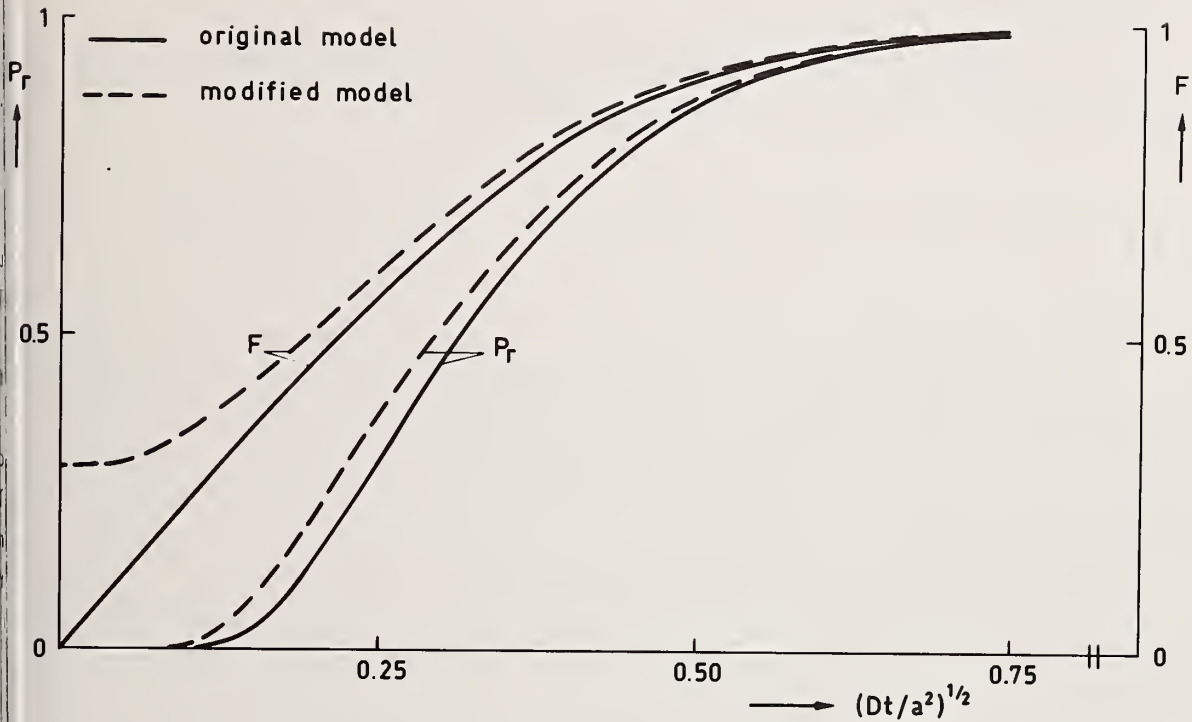


Figure 6. The dependence of the degree of interdiffusion  $F$  and the relative peak position  $p_r$  on  $Dt$ , where  $D$  is the diffusion coefficient and  $t$  the annealing time, according to the original concentric sphere model and the modified one (cf. Section 4.2), for a 30A/70B powder blend.

#### 4.2.2. Line profile simulation method [36]

Consider the segmented concentration profile. Each segment  $m$  will diffract at a certain  $s (=2\sin\theta/\lambda)$  value, say  $s_m$ . We assume that all the segments give rise to a diffracted profile of the same shape. This implies that the structural broadening of a segment owing to its concentration variation is neglected as compared to the spectral and instrumental broadening. The intensity of the profile of segment  $m$  will be proportional to the amount of material of segment  $m$ . Then, according to the concentric sphere geometry the profile  $i_m(s)$  of segment  $m$  can be written as

$$i_m(s) = C \frac{1}{\sqrt{2}} \frac{4}{3} \pi \left\{ (R_s - r_{m-1})^3 - (R_s - r_m)^3 \right\} f(S - S_m) \quad (4.7)$$

where  $C$  is a constant (including the absorption factor which is approximately constant),  $v_m$  is the average unit cell volume of segment  $m$ ,  $R_s$  is the radius of the concentric sphere, radii  $r_{m-1}$  and  $r_m$  enclose segment  $m$  ( $m=1,2,\dots$  and  $r_0=R_s$ ) and  $f$  describes the shape of the diffracted profile such that  $f(0)=1$ .

The total line profile of the powder specimen will be the sum of the profiles of all segments. Dividing the intensities by the peak intensity  $I_0$  of the major component before interdiffusion, the total line profile is given by

$$\frac{I(s)}{I_0} = \frac{v_B^2}{\{R_s^3 - (R_s - r_B)^3\}} \sum_m \frac{1}{v_m^2} \{(R_s - r_{m-1})^3 - (R_s - r_m)^3\} f(s - s_m) \quad (4.7)$$

Mostly the spectral broadening dominates over the broadening due to the instrumental conditions [37]. It is generally accepted that the spectral component can be described by a Cauchy-function [38]. Therefore, this function was used as a reasonable approximation for the shape function  $f$ . The full width at half maximum of this function should be determined experimentally from the  $\alpha_1$  component of the line profile recorded from a standard specimen (cf. refs. [36,39]).

Results of simulations of the 220 line profile of an interdiffused Cu/Ni powder specimen on the basis of eq. (4.8) are shown in figure 7 for various stages of interdiffusion (the corresponding concentration profiles were calculated according to the concentric sphere model).

It is proposed to characterize homogenization by the relative peak position  $p_r$  defined as

$$p_r = (p - p_0) / (p_\infty - p_0) \quad (4.8)$$

where  $p$  is the actual peak position and  $p_0$  and  $p_\infty$  correspond to the peak positions at the start and at the end of homogenization respectively.  $p_\infty$  can be calculated from the mean composition. In figure 7 the behaviour of the copper-side peak maximum on annealing is indicated (dashed curve). On the basis of the line profile simulations according to the concentric sphere model the relative peak position is plotted as a function of  $Dt/a^2$  in figure 6. This plot plays the same role for the relative peak position as the corresponding one for the degree of interdiffusion; once the value of  $p_r$  is established the value of  $Dt/a^2$  is obtained according to the concentric sphere model. It is clear that the relative peak position is much easier as well as much faster to determine than the degree of interdiffusion.

### 4.3. Practice

#### 4.3.1. Determination of concentration profiles and degrees of interdiffusion; deconvolution versus $\alpha_2$ elimination

Deconvolution potentially is the best method for purification of experimentally determined line profiles, but often only  $\alpha_2$  elimination is or can be employed. If considerable amounts of pure component material are still present after annealing, deconvolution is inappropriate because the Fourier series of the deconvolved line profile diverges due to the presence of  $\delta$ -functions. The  $\alpha_2$  elimination does not remove all instrumental and spectral broadening. Therefore, the behaviour of the corresponding concentration profile in the neighbourhood of  $y=0$  and  $y=1$  is not physically significant: the range of compositions seems to be wider than in reality. Examples of concentration-effective penetration curves as calculated according to Section 4.2.1. from the  $\alpha_1$  line profiles of Cu/Ni powder blends (0.3 atomic fraction nickel, [36]) are shown in figure 8.

For experiments with equiatomic RbCl/KCl powder blends at 500, 575 and 650 °C [39] the concentration-effective penetration curves could be obtained from the deconvolved line profiles, except for the experiment of 0.25 h at 500 °C where the concentration profile was obtained from the  $\alpha_2$  eliminated line profile. The corresponding degrees of interdiffusion  $F$ , obtained from the concentration-effective penetration curves according to eq. (4.6), are gathered in table 1. The incomplete removal of instrumental and spectral broadening by  $\alpha_2$  elimination leads to an apparent enhancement of interdiffusion at short diffusion times and an apparent retardation at long times. If  $F_{\alpha_2}$  and  $F_d$  denote the degrees of interdiffusion obtained after  $\alpha_2$  elimination and after deconvolution respectively, we expect  $F_{\alpha_2} > F_d$  for small  $F$  and  $F_{\alpha_2} < F_d$  for large  $F$ . This corresponds with the experimental finding (table 1).

#### 4.3.2. Surface diffusion

From the degrees of interdiffusion or the relative peak positions  $Dt$ -values can be obtained (cf. fig. 6). A typical result is given in figure 9. If the concentric sphere model could be ideally suited to describe the interdiffusion occurring, straight lines of  $Dt$  versus  $\ln$  should have been obtained, with slopes corresponding to the respective diffusion coefficients. Clearly, this is not the case.

Experiments with powder blends at relatively low temperatures show that (very fast) surface diffusion contributes significantly to the homogenization observed at the start of homogenization [36,39]. This process is demonstrated by the 220  $\alpha_1$  line profile of the Cu/Ni powder specimen annealed at 634 °C for 15 min (fig. 10). Two maxima between the nickel and copper peak can be observed, which show that homogenization occurred locally not affecting the bulk of the copper and nickel particles.

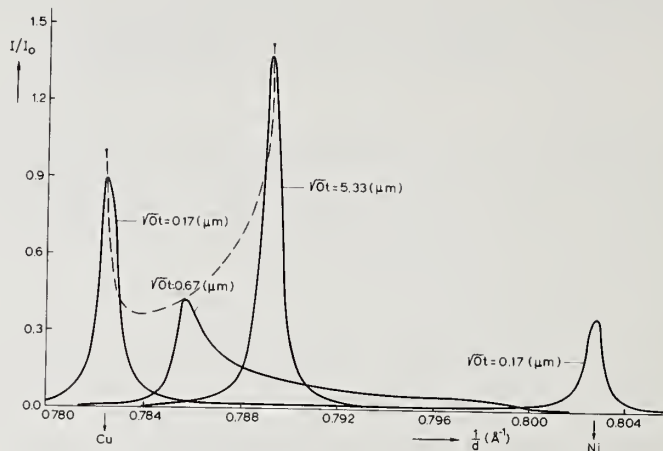


Figure 7. Computer simulations of  $220 \alpha_1$  line profiles of 70 Cu/30 Ni powder specimens for various stages of interdiffusion according to the concentric sphere model. The behaviour of the copper-side peak maximum on annealing is indicated by the dashed curve. The full width at half maximum of the shape function was taken as  $0.8 \times 10^{-3} \text{ \AA}^{-1}$ .

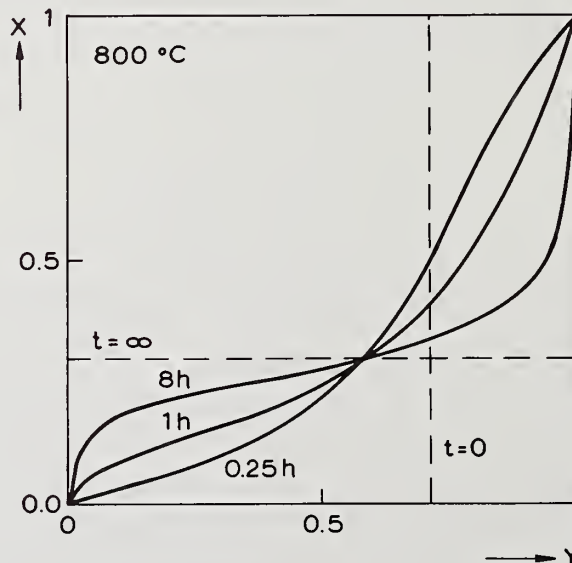


Figure 8. Concentration-effective penetration curves from Cu/Ni powder specimens (0.3 atomic fraction nickel) as calculated according to the method outlined in Section 4.3.1.  $x$  is the atomic fraction nickel and  $y$  is the effective penetration distance [eq. (4.4)].

Table 1. Degrees of interdiffusion as calculated from  $\alpha_2$ -eliminated line profiles ( $F_{\alpha_2}$ ) and deconvoluted line profiles ( $F_d$ ) and the relative peak position  $p_r$ . T is the annealing temperature and t is the annealing time.

T	500 °C			575 °C			650 °C		
t(h)	$F_{\alpha_2}$	$F_d$	$p_r$	$F_{\alpha_2}$	$F_d$	$p_r$	$F_{\alpha_2}$	$F_d$	$p_r$
0.25	0.32	0.29 <sup>a</sup>	0.03	0.55	0.54	0.75	0.78	0.79	0.93
1.0	0.45	0.44	0.19	0.71	0.72	0.91	0.86	0.88	0.96
2.0	0.53	0.52	0.40	0.78	0.79	0.93	0.89	0.91	0.97
4.0	0.60	0.60	0.78	0.83	0.84	0.94	0.89	0.92	0.97

<sup>a</sup>unreliable value (see text).

#### 4.3.3. Activation energy and diffusion mechanism

It is possible to determine the activation energy of the diffusion process without knowing the actual diffusion geometry in the powder specimens employed. Assuming one diffusion mechanism to be dominant, it is recognized that equal values of the relative peak position or the degree of interdiffusion at different temperatures imply identical stages of homogenization in the powder specimen. Hence the ratios of the diffusion coefficients at these temperatures are given by the ratios of the corresponding annealing times.

From Arrhenius plots the activation energies for Cu/Ni and RbCl/KCl powder blends are obtained

$$Q_{\text{Cu/Ni}} = 7.6 \text{ kJ/mol}$$

$$Q_{\text{RbCl/KCl}} = 10 \text{ kJ/mol}$$

As compared with data on volume diffusion [40,41] these activation energies indicate a dominant grain boundary diffusion for Cu/Ni (cf. ref. [42]) and a dominant volume diffusion for RbCl/KCl. This difference between Cu/Ni and RbCl/KCl may be understood since it has been experimentally shown [43] that grain boundaries do not enhance the cation diffusivities of the salts.

Figure 9 shows that the apparent diffusion coefficients become small at large annealing times. This can be attributed to deviations in the powder specimen from the diffusion geometry adopted: larger diffusion distances (e.g. contiguous Ni and KCl particles, respectively, for the powder blends considered) become dominant at longer diffusion times causing a progressive decrease of the rate of homogenization. This problem can be dealt with using two theses: (i) at one temperature the diffusion coefficient D should be constant and (ii) equal values of  $p_r$  or F at different temperatures indicate equal stages of homogenization. From (i) follows that the apparent change found in D can be ascribed to a change in radius a of the nucleus of the concentric sphere since for a concentration independent D, Fick's second law can be solved for concentric sphere geometries in terms of

$Dt/a^2$ . The change of  $a$  with annealing time is described by a change in the effective particle size  $a_e = a/a_r$ , where  $a_r$  is a reference particle size (cf. ref. [32]). From (ii) follows that equal  $p_r$  or  $F$  values observed at different temperatures imply that the effective particle sizes are the same. In this way effective particle sizes at different temperatures can be brought into accordance (see fig. 11). It is seen that all effective particle sizes observed lie approximately on a single curve. This illustrates that one single diffusion mechanism is dominant in the temperature range applied, as was assumed for the determination of the activation energy.

#### 4.3.4. Deficiencies of the concentric sphere model

To investigate the validity of the concentric sphere model results obtained from the relative peak position and the degree of interdiffusion can be interrelated. The values  $p_r$  and  $F$  calculated for the concentric sphere model are plotted in figure 12 together with experimental data: theory does not agree very well with experiment. Recalling the fast surface diffusion process at the start of homogenization (cf. Section 4.3.2.) a better description of the diffusion behaviour may be obtained if a prealloyed layer at the interface of both components is assumed to be present at  $t=0$ . Although a better fit of theory with experiment is obtained at the first stages of homogenization no improvement is observed at the later stages [39]. Other models proposed [44,45] are less general than the concentric sphere model and do not afford a better correspondence of theory with experiment.

For an overall description of homogenization the concentric sphere geometry remains attractive because it is applicable to powder blends of any average composition and the experimentally determinable particle size of one of the components enters into the equations.

#### 4.3.5. Comparison of both methods of profile analysis

With the Rudman method (Section 4.2.1.) a  $Dt$ -value can be obtained after the degree of interdiffusion had been determined from the concentration profile calculated from the line profile. With the line profile simulation method (Section 4.2.2.) a  $Dt$ -value can be obtained after the relative peak position has been determined from the line profile. It has been shown that applying both methods the same conclusions are obtained from the experiments [36,39]. However the relative peak position is much more rapidly obtained, and therefore this parameter may be applied more efficiently in practice to characterize the stage of homogenization in a powder blend.

### 5. Concentration Profiles in Small Epitaxial Binary Diffusion Couples

The accessibility of small diffusion zones is of great technological importance in view of the many applications of microelectronic devices. X-ray diffraction may afford a powerful tool for the investigation of interdiffusion in thin films where the concentration variation occurs over distances of one to several micrometers.

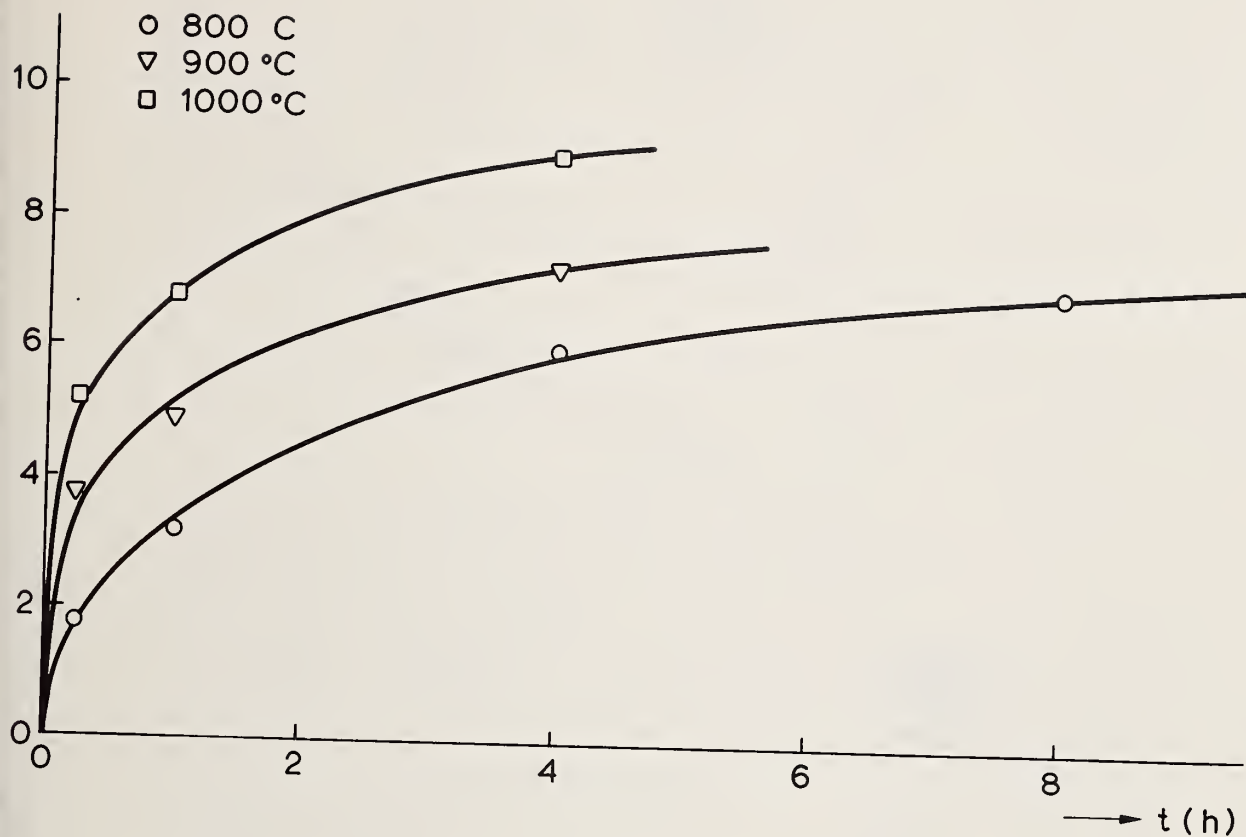


Figure 9. Graphs of  $Dt$  versus  $t$  for Cu/Ni powder blends (0.3 atomic fraction nickel);  $Dt$  values are calculated according to the concentric sphere model.

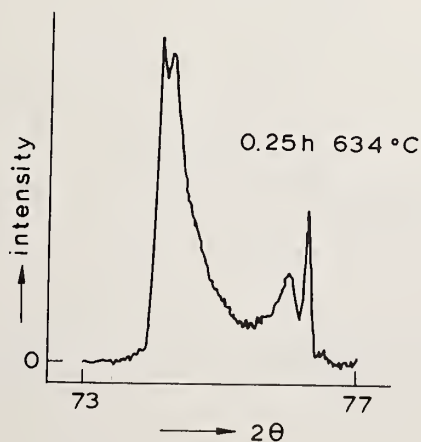


Figure 10.  $220 \alpha_1$  line profile recorded with  $\text{CuK}\alpha$  radiation from a Cu/Ni powder specimen annealed at 634 °C for 15 min.

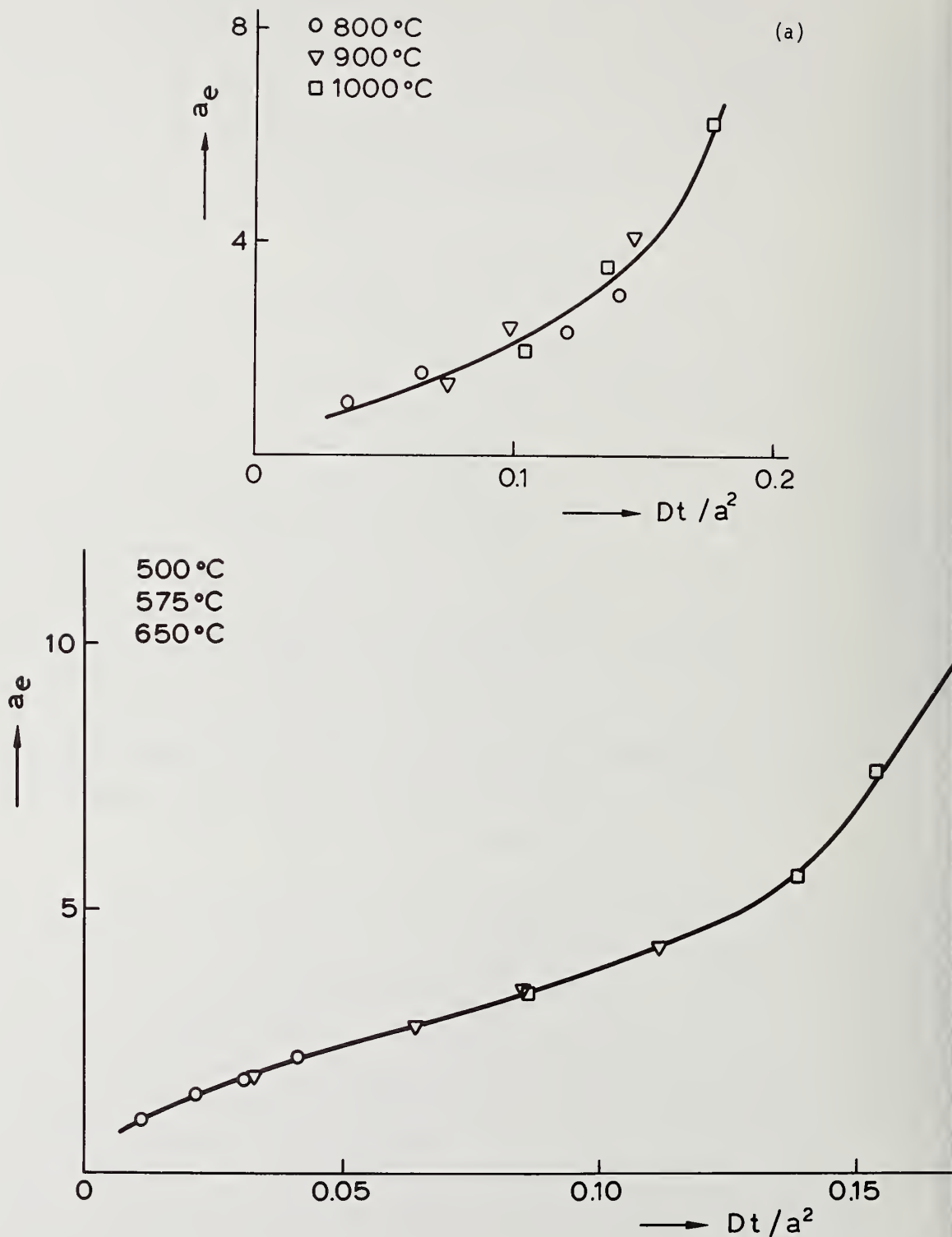


Figure 11. The effective particle sizes  $a_e$  as a function of  $Dt/a^2$ , where  $a$  is the radius of the nucleus, for Cu/Ni (a) and RbCl/KCl (b) powder blends. The effective particle size was arbitrarily set equal to 1 for the experiment at 800 °C with 15 min. annealing time for Cu/Ni and for the experiment at 500 °C with 15 min. annealing time for RbCl/KCl.

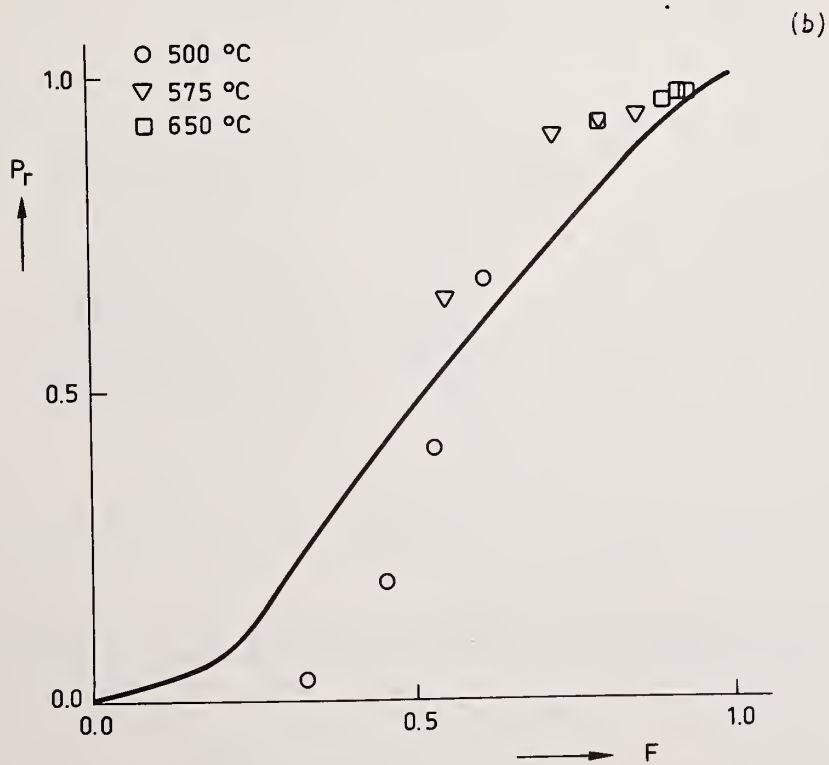
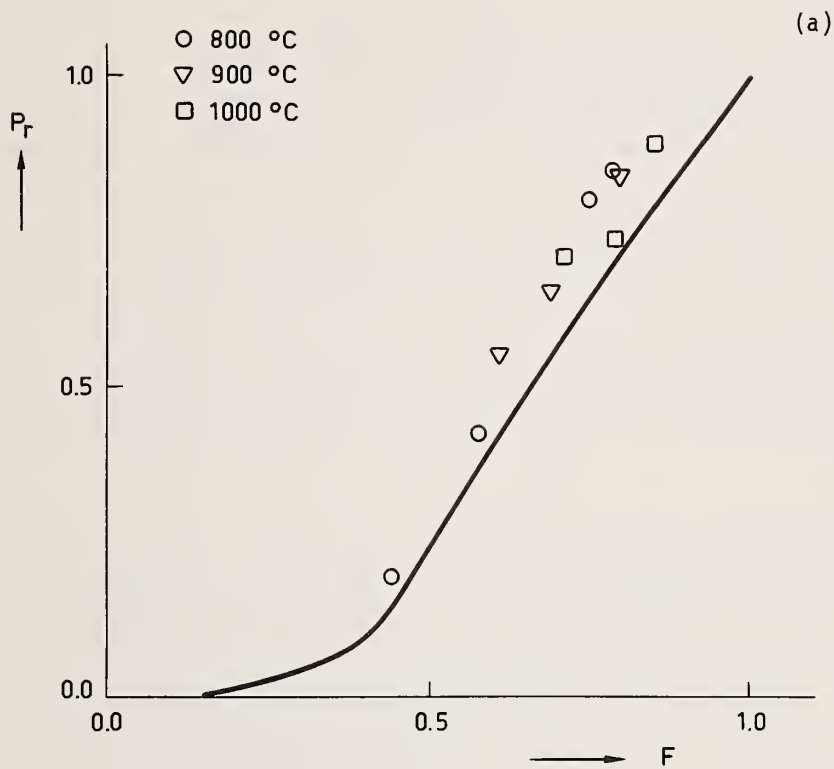


Figure 12. The relative peak position  $p_r$  as a function of the degree of interdiffusion  $F$  according to the concentric sphere model for Cu/Ni (a) and RbCl/KCl (b) powder blends. The experimental data points are also shown.

In the following three methods for the analysis of x-ray diffraction line profiles from small epitaxial binary diffusion couples will be discussed.

A few notes should be made in advance: (i) The penetration of x-rays is restricted to depths of several times  $\sin\theta/\mu$  where  $\mu$  is the linear absorption coefficient of the material. This is at the same time the limitation and the power of x-ray diffraction analysis. (ii) With respect to the determination of the concentration profile, the spatial resolution obtainable is directly proportional to the difference  $[\Delta(2\sin\theta/\lambda)]$  between the reciprocal spacings  $1/d_A$  and  $1/d_B$  of the reflecting planes of both components. (iii) The x-ray diffraction method is non-destructive and may be performed in situ. (iv) The methods to be discussed in this section assume that the concentration varies monotonically with the distance below the surface (in contrast with the method discussed in Section 3).

### 5.1. Basis

Consider the geometry of figure 13: the specimen may be thought to consist of a series of segments parallel to the free surface by adopting some fixed change in concentration; the composition of each segment may be considered constant. In this way the gradual change in composition is approximated by a series of steps. Each segment may consist of one or more coherently diffracting domains. It is implicitly assumed that the domain size is smaller than the critical domain size as prescribed by eqs. (2.16)-(2.18).

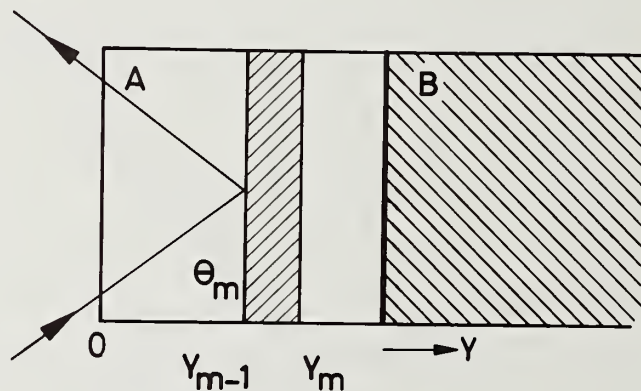


Figure 13. Schematic representation of specimen and diffraction geometry.

Applying the kinematical diffraction theory [6], the following expression is obtained for the integrated intensity  $P_m$  of segment  $m$  extending from the penetration distance  $y_{m-1}$  to  $y_m$  [46]

$$P_m = P_0 C(LP)_m F_m^2 (1/v_m^2) A_m V_m, \quad (5.1)$$

where  $P_0$  is the power in the primary beam and  $C = r_e^2 \lambda^3$ , with  $r_e$  and  $\lambda$  being the classical radius of the electron and the x-ray wavelength respectively;  $LP_m$  comprises the Lorentz and polarization factors.

polarization factors;  $F_m^2$  is the squared modulus of the structure factor (including the Debye-Waller factor), and  $v_m$  is the unit-cell volume. The incident beam is absorbed partially in reaching segment  $m$ , and the intensity diffracted by segment  $m$  is absorbed partially on leaving ( $m > 1$ ). The absorption by the nondiffracting segments 1 to  $m-1$  is described by

$$A_m = \exp\{-2 \sum_{j=1}^{m-1} \mu_j \Delta y_j / \sin \theta\}, \quad m=2,3,\dots, \quad (5.2)$$

and for  $m=1$ ,  $A_1=1$ . The absorption in the diffracting segment  $m$  is included in

$$V_m = g_m [1 - \exp(-2\mu_m \Delta y_m / \sin \theta_m)] (2\mu_m)^{-1}, \quad (5.3)$$

where  $\theta_m$  is the angle of incidence,  $\mu_m$  is the linear absorption coefficient, and  $\Delta y_m = y_m - y_{m-1}$ . The orientation factor  $g_m$  ( $0 \leq g_m \leq 1$ ) is introduced, since in the specimens employed in practice, often only a fraction of the material is in epitaxial position [47-49].

## 5.2. Methods of profile analysis

### 5.2.1. Multiple-line method

Houska and collaborators [47,50] approximated the product  $A_m V_m$  with

$$A_m V_m \cong \frac{g_m \Delta y_m}{\sin \theta_m} \exp \left\{ \frac{-2}{\sin \theta_m} \int_0^{y'_m} \mu(y) dy \right\} \quad (5.4)$$

where  $y'_m = \frac{1}{2}(y_{m-1} + y_m)$ . Then after substitution of eq. (5.4) into eq. (5.1) and by taking the logarithm at both sides of the latter equation it follows

$$\ln P_m = \ln \alpha - \frac{2}{\sin \theta_m} \int_0^{y'_m} \mu(y) dy \quad (5.5)$$

where

$$\alpha = P_0 C(LP)_m F_m^2 \frac{1}{v_m} \frac{g_m \Delta y_m}{\sin \theta_m}$$

For each segment  $m$ ,  $\int_0^{y'_m} \mu(y) dy$  can be determined from measurements of  $P_m$  from at least two orders of a reflection. Then the concentration profile can be obtained from the  $\int_0^{y'_m} \mu(y) dy$  data using an iterative procedure starting with [47]

$$\int_0^{y'_m} \mu(y) dy \cong \frac{1}{2} [\mu(0) + \mu(y'_m)] y'_m$$

It should be noted that approximation (5.4) is only valid for small values of the thickness  $\Delta y_m$  of the segment. In case a segment extends over several microns as can be the case for the end regions of the concentration profile, a procedure based on eq. (5.4) cannot be used. Further the need for at least two orders of a reflection and the iterative nature of the procedure may be considered as disadvantages of this method.

### 5.2.2. Line profile simulation method<sup>6</sup>

When a concentration profile is assumed and segmented subsequently the integrated intensity of each segment can be calculated by application of eq. (5.1). Then a certain distribution function for this integrated intensity around  $\theta_m$  has to be assumed. A Cauchy-shaped profile and a Gaussian-shaped profile may provide suitable descriptions at first and final stages of interdiffusion respectively [51]. After summing the intensity values for all segments, a simulated intensity band is obtained. This method was applied successfully [14,48,49,51,52] although the approximation (5.4) was used again. It is suggested that a higher accuracy may be obtained by using the more exact eqs. (5.2) and (5.3). Further, the concentration profile assumed has to be adopted by trial and error, until satisfactory agreement exists between simulation and experiment.

### 5.2.3. Direct single-line method

A direct method can be applied for the determination of the concentration profile [46]

$$y_m = y_{m-1} + \Delta y_m \quad (m = 1, 2, \dots), \quad (5.6a)$$

where according to eqs. (5.1)-(5.3)

<sup>6</sup>Note the parallel with the line profile simulation method for the characterization of diffusional homogenization in powder blends (Section 4.2.2.).

$$\Delta y_m = \frac{-\sin\theta_m}{2\mu_m} \ln \left\{ 1 - \frac{P_m v_m^2 2\mu_m}{P_o C(LP_m) F_m^2 A_m g_m} \right\} \quad (5.6b)$$

this way the concentration profile can be calculated recursively, starting from the free face with  $y_0=0$  and  $A_1=1$  [cf. eq. (5.2)].

The price for this single-line method is that  $P_o$  should be known:  $P_o$  can be obtained either by direct measurement [53,54] or by indirect calculation [For example,  $P_o$  (as well as plating thickness) may be obtained from integrated intensity measurements before interdiffusion.]

The direct method has the advantages that neither iterative nor trial and error procedures are required and that only a single order of a reflection is required. The latter effect may be of great practical importance; since the penetration depth depends on the Bragg angle, the reflection to be measured can be chosen in relation to the plating thickness applied to provide optimal information (thin plating: low order; thick plating: high order).

### 5.3. Elimination of the background from an intensity band

Commonly the intensity bands measured are corrected for background radiation by applying linear interpolation between both extremities of the intensity bands [47]. The background regions of a Cu/Ni bicrystal before diffusion annealing are shown in figure 14. Note that the signs of the slopes of the background profile at both sides of each Bragg reflection are opposite, and that no constant background level is reached. Therefore, a linear background is a poor approximation to the actual background profile.<sup>7</sup> The type of background observed in fig. 14) is characteristic for thermal diffuse scattering (TDS).

TDS contributes significantly to the integrated intensities measured, as is shown by the ratio  $\alpha$  (=integrated TDS intensity/integrated kinematical intensity) for copper and nickel in the 222 to 555 MoK $\alpha$  line profiles at room temperature (see table 2). These calculations are based on the approximate analytical expression for first-order TDS derived by Nilsson for cubic single crystals [55-58].

In the following calculation [46] of the background of an intensity band from a diffusion zone, it is assumed that the background consists dominantly of TDS. Since the TDS profile from each segment extends over the whole  $2\theta$  range investigated, overlap should be taken into account. The background for segment  $i$  is determined by the total TDS contribution from all  $M$  segments, so we have

$$b_i = \sum_{j=1}^{M-1} \alpha_{ij} P_j \quad (5.7)$$

Especially at the early stages of interdiffusion a linear background tends to overestimate the real one at  $\theta_m$  positions between those of the pure components. This may result in apparently negative intensity values, although noticeable interdiffusion has occurred.

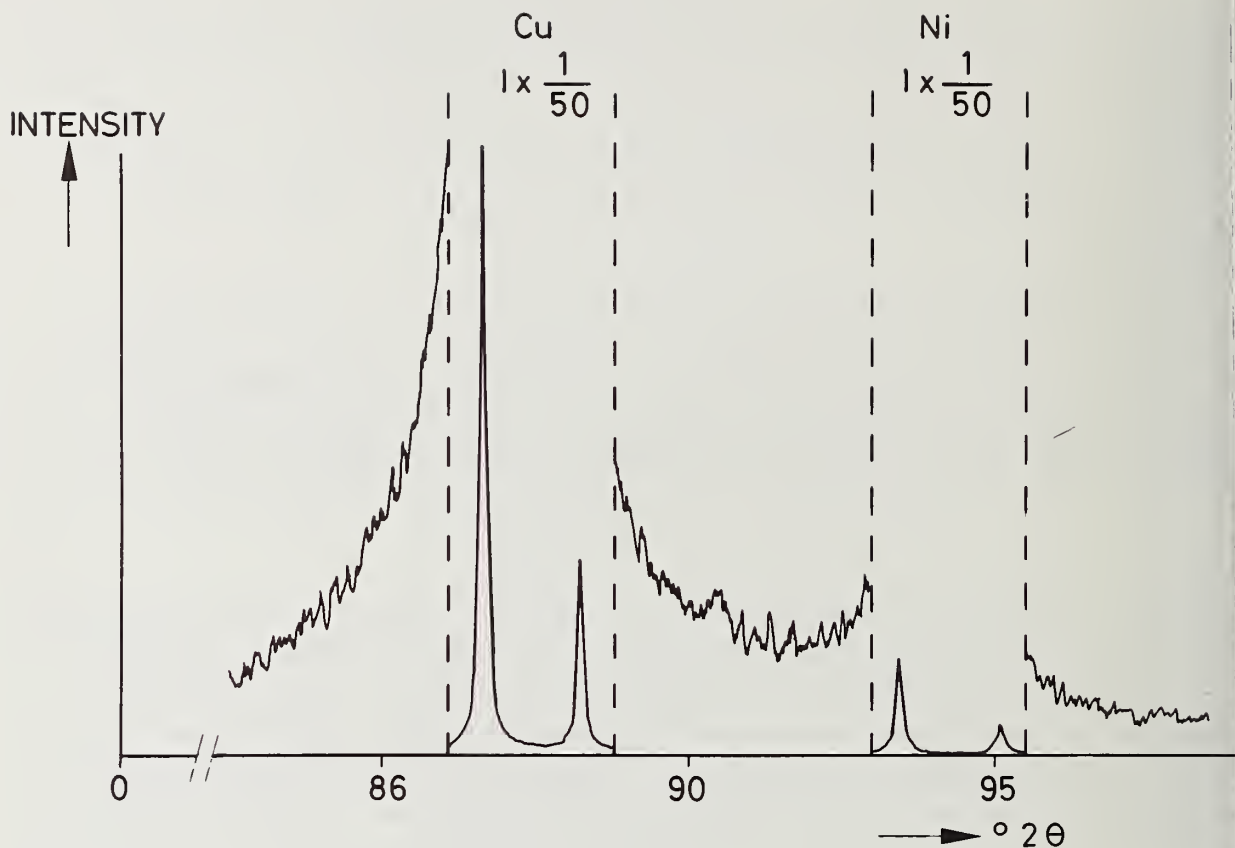


Figure 14. The  $444 \text{ MoK}\alpha$  intensity band recorded from a Cu/Ni bicrystal before diffusion annealing. The intensity scale for the background regions is 50x larger than for the Bragg reflections. The TDS character of the background is less pronounced for Ni, since the integrated kinematical Bragg intensity and  $\alpha$  are smaller (cf. table 2).

where  $\alpha_{ij}$  denotes the ratio of the integrated TDS intensity of segment  $j$  at the  $2\theta$  range of segment  $i$  to the integrated intensity  $P_j$  (without background  $b_j$ ) of segment  $j$ . The  $\alpha_{ij}$  values can be calculated from the Nilsson formula [55]. Because the  $P_j$  values are unknown the  $b_j$  values cannot be determined directly.

Table 2. The ratio  $\alpha$  (= integrated TDS/integrated kinematical intensity) for Cu and Ni at room temperature in the 222, 333, 444, and 555 MoK $\alpha$  line profiles according to Nilsson's formula (see ref. [55]). The elastic constants needed are taken from ref. [63]. The  $2\theta$  integration ranges given are 1/2 and 1/4, respectively, of the separation of the Cu and Ni Bragg positions. The  $\omega$  integration range is  $10^\circ$ .

	Integra- tion range $2\theta$	$\alpha_{\text{Cu}}$ (%)	$\alpha_{\text{Ni}}$ (%)	Integra- tion range $2\theta$	$\alpha_{\text{Cu}}$ (%)	$\alpha_{\text{Ni}}$ (%)
222	$1.08^\circ$	9.4	5.9	$0.54^\circ$	5.6	3.5
333	$1.77^\circ$	21.0	13.1	$0.885^\circ$	12.6	7.8
444	$2.79^\circ$	37.6	23.2	$1.395^\circ$	22.5	13.9
555	$4.97^\circ$	59.5	35.4	$2.485^\circ$	35.6	21.1

By assuming that the main contribution to TDS in segment  $j$  originates from segment  $j$ , a first estimate of background is obtained from

$$b_i^1 = \sum_{j=1}^M \frac{\alpha_{ij}}{1+\alpha_{jj}} P_j^t, \quad (5.8)$$

where  $P_j^t$  is the observed intensity (including background  $b_j$ ) of segment  $j$ . Since the TDS profiles of the different segments overlap  $b_j^1$  is an overestimate. Then, the following iterative method can be applied to determine the integrated intensities:

$$P_i^k = P_i^t - b_i^k \quad (5.9a)$$

$$b_i^{k+1} = \sum_{j=1}^M \alpha_{ij} P_j^k \quad (5.9b)$$

The correct values of  $b_i$  and  $P_i$  are approached alternately by underestimates and overestimates ( $k=1,2,\dots$ ). Calculations should be continued until all segments give rise to  $P_i$  or  $b_i$  values which differ less than an arbitrarily fixed fraction from the previous set obtained in the iterative procedure. It was found that normally 3-10 iterations (depending on the reflection considered) suffice if for any segment a 5 percent difference between the last two iterations is allowed.

The calculation of the background in the manner proposed above gives a physically more sound base for the calculation of concentration profiles from x-ray diffraction line profiles than a linear interpolation procedure.

#### 5.4. Practice

In the diffractometer recording of the intensity bands care should be taken to collect all diffracted intensity. Because of the mosaic structure of the samples at each value of  $\theta$ , intensity measurements should be performed over a range of angles  $\omega$  and  $\chi$ , the  $\omega$  axis being perpendicular to the diffractometer plane and the  $\chi$  axis being in the plane of diffraction perpendicular to the  $\omega$  axis. Integration over  $\chi$  can be established by removing the Soller slits, thus allowing for  $\pm 4^\circ$  axial divergence. Integration over  $\omega$  is performed by rocking the crystal.

Purification of the measured profiles by deconvolution will be impossible usually since the presence of pure components (pure component B will normally be visible in the line profile, cf. fig. 13) should lead to Dirac-functions. Therefore, the  $\alpha_2$  component should be eliminated experimentally by using a high resolution monochromator or by computation [59]. For the latter technique the ratio  $R = [I_{\alpha_2}(\text{max})/I_{\alpha_1}(\text{max})]$  can be determined according to ref. [37]. Corrections for the angle dependence of Lorentz and polarization factors should be applied [21], while the angle dependence of the scattering factor can usually be taken as  $f = xf_B + (1-x)f_A$ , where  $x$  is the atomic fraction B.

In figure 15 the concentration profile is shown of a Cu/Ni bicrystal diffusion-annealed for 1 h at 925 °C. The bicrystal was prepared by electrodeposition of 14  $\mu\text{m}$  Cu onto a Ni monocrystal with a 111 surface. From the integrated intensities measured before interdiffusion, it was found that for this specimen the orientation factor  $g=1$ , indicates perfect epitaxy. The concentration profiles were calculated according to the direct single-line method from the 222, 333, 444, and 555 intensity bands after elimination of the respective TDS background profiles [46]. For this relatively thick specimen it should be noted that the lower the order of the reflection, the smaller the part of the concentration profile which can be obtained reliably, due to decreasing penetration depths of the x-rays (this stresses the need for a method where the concentration profile is obtained from a single order of the reflection). It is seen from figure 15 that the results of the intensity bands coincide very well as far as penetration depths of the x-rays allow comparison.

In figure 16 the concentration profile is shown of a Cu/Ni bicrystal diffusion-annealed for 16 h at 550 °C [46]. The bicrystal was prepared by vapour deposition of 2  $\mu\text{m}$  Cu onto a Ni monocrystal with a 111 surface. From the integrated intensities measured before interdiffusion, it was found that the orientation factor  $g=0.70$  for the vapour-deposited copper layer. For the calculation of the concentration profile, it was assumed that  $g_m$  in eq. (5.6b) was constant (0.70) for the segments in the region originally occupied by the pure

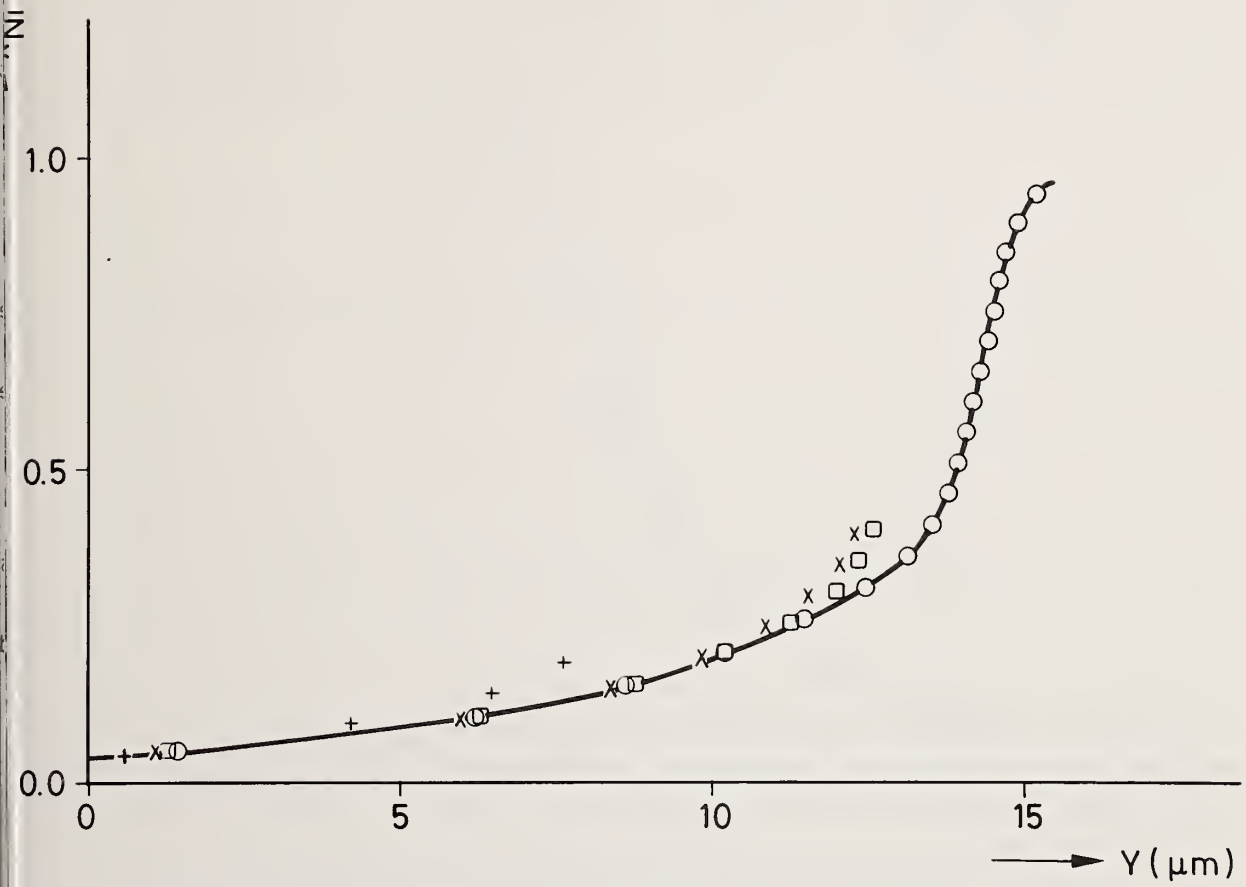


Figure 15. The concentration profiles as calculated from the 222 (+), 333 (x), 444 (□) and 555 (o) MoK $\alpha_1$  intensity bands for the "thick" Cu/Ni bicrystal diffusion annealed for 1 h at 925 °C. It is remarked that the lower the order of the reflection, the smaller the part of the concentration profile which can be obtained reliably, due to decreasing penetration depths of the x-rays.

copper layer (in the nickel region  $g=1$ ), because previous experiments with the Cu/Ni system did not show a concentration dependence of  $g$  [60]. This need not be true for other cases (cf. ref. [48]). The concentration profiles were calculated according to the direct single-line method from the 222 and 333 intensity bands after elimination of the respective

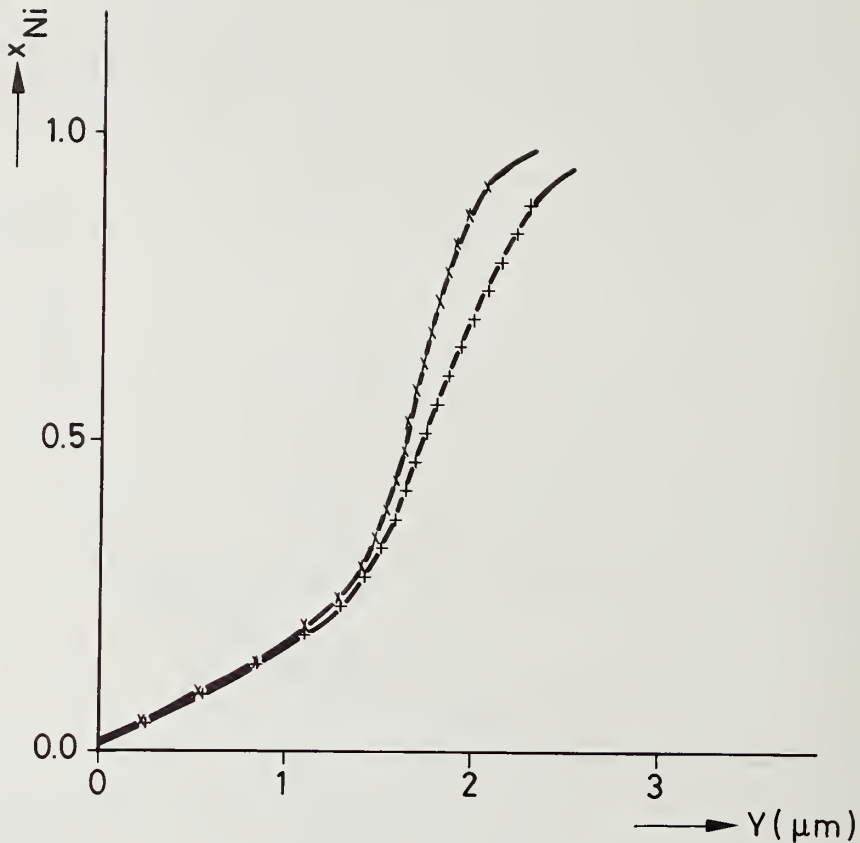


Figure 16. The concentration profiles as calculated from the 222 (+) and 333 (x)  $\text{MoK}\alpha_1$  intensity bands for the "thin" Cu/Ni bicrystal diffusion annealed for 16 h at 550 °C.

TDS background profiles. The results for both orders coincide satisfactorily especially in the surface region; at relatively large penetration depths some disagreement is observed. The result from the 222 intensity band, however, is considered to be the most reliable, since the TDS calculations revealed that in the  $2\theta$  region corresponding to the larger penetration depths about 60 percent of the diffracted intensity in the 333 intensity band is TDS, whereas it is 25 percent for the 222 intensity band. With respect to the TDS background, the 111 intensity band would be even more useful, but the effects of instrumental broadening are too large. The 222 intensity band is the best compromise.

It is concluded that a single order of the reflection may be selected which can be used most profitably for the calculation of the concentration profile [thick plating: high order (cf. fig. 15); thin plating: low order (cf. fig. 16)]. Hence, in practice the direct single line method may be advised provided  $P_0$  can be determined (cf. Section 5.2.3.). Otherwise the simulation method may be used.

The methods of profile analysis discussed in this section open perspectives not only to investigations of interdiffusion (or evaporation or depletion of a component from an alloy) but also to the investigation of mechanical deformation (e.g. by rolling, or H<sub>2</sub> enclosure accompanying the electrocrystallization of metals) as a function of the distance to the surface.

---

We are indebted to Prof. B. Okkerse for his guidance and to Dr. F. W. Schapink for his interest, with respect to our research in this field during the last years.

### Appendix

#### Suggestion for a Rapid Method for the Characterization of the Stage of Interdiffusion.

In case one desires to estimate very quickly the stage of interdiffusion in a binary system accessible to x-ray diffraction, the more accurate methods discussed in this paper may be less appropriate.

Here a rapid method is suggested which may be useful for the characterization of the stage of interdiffusion directly from the measured line profiles. The method requires only the determination of the peak position in a line profile and can be used for specimens where the concentration variation extends over many coherently diffracting domains: types (ii) and (iii) mentioned in Section 1 and dealt with in Sections 4 and 5. The method is based on a simple model applied successfully in electron diffraction investigations on diffusion-annealing [61,62,16].

#### A.1. A model

Before diffusion occurs the specimen is described by a binary system consisting of crystal A ( $N_A$  moles) with spacing  $d_A$  and of crystal B ( $N_B$  moles) with spacing  $d_B$ . After a certain time of diffusion the average spacings  $\langle d_A \rangle$  and  $\langle d_B \rangle$  in crystals A and B, respectively, may be given by

$$\langle d_A \rangle = (1-x_{B,A})d_A + x_{B,A}d_B \quad (\text{A.1a})$$

$$\langle d_B \rangle = (1-x_{A,B})d_B + x_{A,B}d_A \quad (\text{A.1b})$$

where  $x_{B,A}$  is the mole fraction of component B present in crystal A after a certain time of annealing, and  $x_{A,B}$  is defined analogously. From eqs. (A.1a, and b) it follows

$$1 - \frac{\langle d_A \rangle - \langle d_B \rangle}{d_A - d_B} = x_{A,B} + x_{B,A} \quad (\text{A.2})$$

It is assumed that the diffusion coefficient is constant and hence the quantity of material that has crossed the original interface is the same in both directions. The degree of interdiffusion  $F$  is defined as the ratio of the quantity of material  $m_t$  which has crossed the interface in both directions at time  $t$  to the quantity of material  $m_\infty$  which will cross in infinite time [cf. eq. (4.6)]. It follows

$$m_t = 2x_{B,A} N_A = 2x_{A,B} N_B \quad (\text{A.3a})$$

and since  $x_{A,B}(\text{at } t=\infty) = N_A / (N_A + N_B)$

$$m_\infty = 2 \frac{N_A N_B}{N_A + N_B} \quad (\text{A.3b})$$

From eqs. (A.3a and b) it is obtained

$$x_{A,B} + x_{B,A} = \frac{m_t}{m_\infty} \equiv F \quad (\text{A.4})$$

and thus [eqs. (A.2) and (A.4)]

$$1 - \frac{\langle d_A \rangle - \langle d_B \rangle}{d_A - d_B} = F \quad (\text{A.5})$$

If the peak positions after a time of annealing  $t$  are identified with  $\langle d_A \rangle$  and  $\langle d_B \rangle$ , respectively, the approximate degree of interdiffusion ( $0 \leq F \leq 1$ ) can be calculated using eq. (A.5). This implies that this method can be used only as long as the peaks of the two components are observed separately. It should be remarked too that this procedure does not take into account the effects of specimen absorption on the incident and diffracted x-rays. This is justified for powder blends (Section 4). For specimens with a plane geometry (cf. fig. 13; Section 5) absorption has major effects on the line shape, but the effects on the peak position are much less. Further, substrate B (cf. fig. 13) may often be considered as semi-infinite medium and the x-rays will "see" so much of pure component B that peak "B" hardly moves at all on diffusion-annealing. Then only peak "A", corresponding to diffraction from the surface layers, moves significantly and thus dominates for the changes in the left hand side of eq. (A.5).

It may be valuable to continue this analysis one step further: A specific expression for the dependence of  $F$  on  $Dt$ , where  $D$  is the diffusion coefficient, can be obtained if the appropriate diffusion geometry is considered. For the concentric sphere geometry  $F$  is calculated in Section 4.1 [eq. (4.2)]. For the plane geometry (cf. fig. 13) the derivation is given below.

If  $z_A$  and  $z_B$  denote the thicknesses of layers A and B, respectively, it follows for the concentration profile in the specimen as a function of the depth  $z$  below the surface [34]

$$c_A(z) = \frac{z_A}{z_A + z_B} + \frac{2}{\pi} \sum_{n=1}^{\infty} \frac{1}{n} \sin \frac{\pi n z_A}{(z_A + z_B)} \exp \left\{ - \frac{\pi^2 n^2 D t}{(z_A + z_B)^2} \cos \frac{\pi n z}{(z_A + z_B)} \right\} \quad (\text{A.6})$$

where  $0 \leq c_A \leq 1$ . Since  $(dm_t/dt) = -2D(\partial c/\partial z)$  (at  $z=z_A$ ) it is obtained from eq. (A.6) for the degree of interdiffusion  $F = m_t/m_{\infty}$

$$F = \frac{2}{\pi^2} \frac{(z_A + z_B)^2}{z_A z_B} \sum_{n=1}^{\infty} \frac{1}{n^2} \sin^2 \frac{\pi n z_A}{(z_A + z_B)} \left[ 1 - \exp \left\{ \frac{-\pi^2 n^2 D t}{(z_A + z_B)^2} \right\} \right] \quad (\text{A.7})$$

In case no late stages of homogenization are considered, then in solving Fick's second law reflection at the surfaces need no be considered (double-infinite case) and eq. (A.7) is replaced by

$$F = \left( \frac{1}{z_A} + \frac{1}{z_B} \right) \left( \frac{D t}{\pi} \right)^{\frac{1}{2}} \quad (\text{A.8})$$

From the expressions for  $F$  [eqs. (4.2), (A.7) and (A.8)]<sup>8</sup> the dependence of  $F$  on  $Dt$  can be calculated. Once  $F$  is determined according to eq. (A.5) a value of  $Dt$  is found from the curve  $F(Dt)$ .

This simple model with the resulting eqs. (A.7) and (A.8) for the plane geometry was applied successfully in an electron diffraction investigation of interdiffusion in Cu/Ni foils [61,62,16]. In that case  $(\langle d_A \rangle - \langle d_B \rangle) / (d_A - d_B)$  [cf. eq. (A.5)] corresponds to the ratio  $M_0/M$  where  $M_0$  and  $M$  are the moiré spacings observed at the start of interdiffusion and after a given annealing time respectively.

<sup>8</sup>In fact these equations for  $F$  only hold if the concentration is expressed in terms of volume fractions, while  $F$  in eq. (A.4) is based on mole fractions. Conversions of mole into volume fractions and vice versa can be performed easily, but, in view of the simplicity of the model used here, these will not be necessary normally.

## References

- [1] Thin Solid Films, 25 (1975) containing papers presented at the International Conference on Low Temperature Diffusion and Applications to Thin Films; Yorktown Heights; NY, USA August 12-14, 1974.
- [2] Moss, R. L., Pope, D. and Gibbens, H. R., Ethylene hydrogenation over nickel-palladium alloy films, J. Catal. 46, 204-213 (1977).
- [3] Heckel, R. W., Diffusional homogenization of compacted blends of powders, Powder metallurgy processing, H. A. Kuhn and A. Lawley, eds., pp. 51-97 (Academic Press, New York, 1978).
- [4] Carpenter, J. A. and Tenney, D. R., A review of x-ray diffraction methods for diffusion studies, Adv. in X-ray Analysis, C. L. Grant, C. S. Barrett, J. B. Newkirk, and C. O. Ruud, eds., Vol. 17, 395-415 (1974).
- [5] Warren, B. E. and Averbach, B. L., The effect of cold-work distortion on x-ray patterns, J. Appl. Phys. 21, 595-599 (1950).
- [6] Warren, B. E., X-ray Diffraction (Addison-Wesley, Reading, MA, 1969).
- [7] Stokes, A. R. and Wilson, A. J. C., A method of calculating the breadths of Debye-Scherrer lines: Generalization to non-cubic crystals, Proc. Camb. Phil. Soc. 40, 197-198 (1944).
- [8] Warren, B. E., A generalized treatment of cold work in powder patterns, Acta Cryst. 8, 483-486 (1955).
- [9] Borie, B., A diffraction measurement of the structure of  $\text{Cu}_2\text{O}$  films grown on copper, Acta Cryst. 13, 542-545 (1960).
- [10] Houska, C. R., X-ray diffraction from a binary diffusion zone, J. Appl. Phys. 41, 69-75 (1970).
- [11] Mittemeijer, E. J. and Delhez, R., A note on the kinematical theory of x-ray diffraction from concentration profiles, J. Appl. Phys. 47, 1702-1703 (1976).
- [12] Brigham, E. O., The fast Fourier transform, p. 24 (Prentice-Hall Inc., Englewood Cliffs, New Jersey, 1974).
- [13] Houska, C. R., Broadening of x-ray diffraction lines from small subgrains containing gradients of spacing, J. Appl. Phys. 49, 2991-2993 (1978).
- [14] Houska, C. R., Dietrich, F. and Subbaraman, G., Time-dependent diffusion coefficients obtained from diffused films: the Cu-Ni system, Thin Solid Films, 44, 217-231 (1977).
- [15] Beers, A. M. and Mittemeijer, E. J., Dislocation wall formation during interdiffusion in thin bimetallic films, Thin Solid Films, 48, 367-376 (1978).
- [16] Beers, A. M., Mittemeijer, E. J. and Delhez, R., Effects of interdiffusion on the misfit dislocation configuration and the moiré patterns of thin bimetallic films, Inst. Phys. Conf. Ser. 41 (Proceedings of the International Conference on the Occasion of the 50th Anniversary of the Discovery of Electron Diffraction, London, September 19-21, 1977), 363-369 (1978).
- [17] Beers, A. M. and Mittemeijer, E. J., Modification of interfaces in thin epitaxial bimetallic films during interdiffusion, Thin Solid Films, 50, 33-37 (1978).
- [18] Ponec, V., Surface composition and catalysis on alloys, Surf. Sci. 80, 352-366 (1979).

- [19] Mittemeijer, E. J. and Delhez, R., Concentration variations within small crystallites studied by x-ray diffraction line profile analysis, *J. Appl. Phys.* 49, 3875-3878 (1978).
- [20] Delhez, R. and Mittemeijer, E. J., The elimination of an approximation in the Warren-Averbach analysis, *J. Appl. Cryst.* 9, 233-234 (1976).
- [21] Delhez, R., Keijser, Th.H. de and Mittemeijer, E. J., Accuracy of crystallite size and strain values from x-ray diffraction line profiles using Fourier series, this conference.
- [22] Kuijers, F. J., private communication.
- [23] Kuijers, F. J., Dessing, R. P. and Sachtler, W. M. H., Hydrogen-Deuterium exchange on evaporated films of platinum and platinum-gold, *J. Catal.* 33, 316-321 (1974).
- [24] Meijering, J. L., Concentrations at interfaces in binary alloys, *Acta Met.* 14, 251-258 (1966).
- [25] Williams, F. L. and Nason, D., Binary alloy surface compositions from bulk alloy thermodynamic data, *Surf. Sci.* 45, 377-408 (1974).
- [26] Ling, D. T., Miller, J. N., Lindau, I., Spicer, W. E. and Stefan, P. M., Oscillations in the compositional depth profile of CuNi alloys: a study by UPS, *Surf. Sci.* 74, 612-620 (1978).
- [27] Miedema, A. R., Surface segregation in alloys of transition metals, *Z. Metallkde.* 69, 455-461 (1978).
- [28] Brongersma, H. H., Sparnaay, M. J. and Buck, T. M., Surface segregation in Cu-Ni and Cu-Pt alloys; a comparison of low-energy ion-scattering results with theory, *Surf. Sci.* 71, 657-678 (1978).
- [29] Losch, W., and Kirschner, J., Surface composition of polycrystalline Au-Cu alloys as a function of temperature, *J. Vac. Sci. Technol.* 15, 1591-1598 (1978).
- [30] Lee, W. Y., Lee, M. H., and Eldridge, J. M., Alloy compositional profiles by AES, ESCA, and ion sputtering: air-exposed  $Fe_{1-x}Pd_x$  films, *J. Vac. Sci. Technol.* 15, 1549-1553 (1978).
- [31] Fisher, B. and Rudman, P. S., X-ray diffraction study of interdiffusion in Cu-Ni powder compacts, *J. Appl. Phys.* 32, 1604-1611 (1961).
- [32] Heckel, R. W., An analysis of homogenization in powder compacts using the concentric-sphere diffusion model, *Trans. ASM*, 57, 443-463 (1964).
- [33] Holloway, P. H. and Mohanty, G. O., A diffraction study of diffusion in the Mo-Cr system, *J. Phys. Chem. Solids*, 32, 2656-2659 (1973).
- [34] Crank, J., *The Mathematics of Diffusion* (At the Clarendon Press, Oxford, 1956).
- [35] Rudman, P. S., An x-ray diffraction method for the determination of composition distribution in inhomogeneous binary solid solutions, *Acta Cryst.* 13, 905-909 (1960).
- [36] Delhez, R., Mittemeijer, E. J., and Bergen, E. A. van den, X-ray diffraction line profile analysis of diffusional homogenization in powder blends, *J. Mater. Sci.* 13, 1671-1679 (1978).
- [37] Delhez, R., Keijser, Th.H. de and Mittemeijer, E. J., The x-ray diffraction line broadening to the diffractometer condition as a function of  $2\theta$ , *J. Phys. E: Sci. Instrum.* 11, 649-652 (1978).

- [38] Klug, H. P. and Alexander, L. E., X-ray Diffraction Procedures for Polycrystalline and Amorphous Materials, 2nd edition, p. 297 (John Wiley, New York, 1974).
- [39] Bergen, E. A. van den, Delhez, R., and Mittemeijer, E. J., An x-ray diffraction study of diffusional homogenization in RbCl/KCl powder blends, *Phys. Stat. Sol. (a)*, 44, 517-5 (1977).
- [40] Butrymowicz, D. B., Manning, J. R., and Read, M. E., Diffusion in copper and copper alloys, part IV. Diffusion in systems involving elements of group VIII, *J. Phys. Chem. Ref. Data*, 5, 103-200 (1976).
- [41] Kantola, M. and Lindström, R., Chemical diffusion coefficient to the KCl-RbCl couple, *Ann. Acad. Sci. Fenn.*, AVI 222, 1-11 (1967).
- [42] Askill, J., Tracer Diffusion Data for Metals, Alloys and Simple Oxides, p. 11 (Plenum Press, New York, 1970).
- [43] Benard, J. and Cabane, J., Diffusion in the alkali halides, Sintering and Related Phenomena, G. C. Kuczynski, N. A. Hooton and C. F. Gibbon, eds., *Proc. Intern. Conf. on Sintering and Related Phenomena*, June 1965, pp. 1-28 (Gordon and Breach, New York, 1967).
- [44] Duwez, P. and Jordon, C. B., Application of the theory of diffusion to the formation of alloys in powder metallurgy, *Trans. ASM*, 41, 194-212 (1949).
- [45] Weinbaum, S., Alloying of metal powders by diffusion, *J. Appl. Phys.* 19, 897-900 (1948).
- [46] Delhez, R. and Mittemeijer, E. J., On the analysis of x-ray diffraction line profiles from small epitaxial binary diffusion couples: Determination of concentration profiles and influence of TDS, *J. Appl. Phys.* 49, 4770-4775 (1978).
- [47] Tenney, D. R., Carpenter, J. A., and Houska, C. R., X-ray diffraction technique for the investigation of small diffusion zones, *J. Appl. Phys.* 41, 4485-4492 (1970).
- [48] Murakami, M., Fontaine, D. de and Fodor, J., X-ray diffraction study of interdiffusion in bimetallic Au/Pd thin films, *J. Appl. Phys.* 47, 2850-2856 (1976).
- [49] Murakami, M. and Fontaine, D. de, X-ray diffraction study of interdiffusion in bimetallic Ag/Cu thin films, *J. Appl. Phys.* 47, 2857-2861 (1976).
- [50] Carpenter, J. A., Tenney, D. R., and Houska, C. R., Method for determining compositional profiles and diffusion-generated substructure in small diffusion zones, *J. Appl. Phys.* 42, 4305-4312 (1971).
- [51] Unnam, J. and Houska, C. R., An X-ray study of diffusion in the Cu-Ag system, *J. Appl. Phys.* 47, 4336-4342 (1976).
- [52] Unnam, J., Carpenter, J. A., and Houska, C. R., X-ray diffraction approach to grain boundary and volume diffusion, *J. Appl. Phys.* 44, 1957-1967 (1973).
- [53] Chipman, D. R., Conversion of relative intensities to an absolute scale, *Acta Cryst.* A25, 209-214 (1969).
- [54] Inkinen, O., Assessment of accuracy in powder intensity measurement, *Acta Cryst.* A25, 214-217 (1969).
- [55] Nilsson, N., On the corrections of the measured integrated Bragg reflections due to thermal diffuse scattering, *Ark. Fys.* 12, 247-257 (1957).

- [56] Cooper, M. J. and Rouse, K. D., The correction of measured integrated Bragg intensities for first order thermal diffuse scattering, Acta Cryst. A24, 405-410 (1968).
- [57] Willis, B. T. M., Lattice vibrations and the accurate determination of structure factors for the elastic scattering of x-rays and neutrons, Acta Cryst., A25, 277-300 (1969).
- [58] Renninger, M., Experimental determination of the integrated contribution of temperature diffuse scattering in x-ray reflections, Adv. X-ray Analysis, J. B. Newkirk and G. R. Mallet, eds., 10, 42-45 (1967).
- [59] Delhez R. and Mittemeijer, E. J., An improved  $\alpha_2$  elimination, J. Appl. Cryst. 8, 609-611 (1975).
- [60] Houska, C. R., personal communication.
- [61] Dijk, T. van and Mittemeijer, E. J., The effect of interdiffusion on moiré patterns of thin bimetallic films, Thin Solid Films, 41, 173-178 (1977).
- [62] Mittemeijer, E. J. and Beers, A. M., Recrystallization and interdiffusion in thin bimetallic films, to be published.
- [63] K. H. Hellwege (ed.), Landolt-Börnstein Numerical Data and Functional Relationships in Science and Technology, New Series, Group III, Vol. 1, 6-7 (Springer Verlag, Berlin, 1966) and Vol. 2, 2-6 (Springer Verlag, Berlin, 1969).

#### Discussion

Question (Snyder): It seems to me that producing a quantitative concentration profile is considerably more difficult than you have shown. In general, the problems arising from the differences in the mass absorption coefficients of the various crystallites present, and the differences in the diffracting abilities of the end members, are very serious and certainly cannot be neglected. Has any effort been put into allowing for these problems?

Response (Delhez and Mittemeijer): I presume your question deals with the powder blends. From the powder blends a concentration-effective penetration curve is obtained (cf. Section 4.3.1. of this paper). This "average" concentration profile represents in a useful way the highly complicated processes occurring on diffusion-annealing in powder blends. Differences in the intensity profiles of the different segments are not important; only the integrated intensities are used. Problems associated with differences in mass absorption coefficients between the components are small, because the incident and diffracted beams pass through a number of grains in which material of all possible compositions is present. Thus, for the recorded intensity of a specific segment, an effective absorption coefficient can be introduced which is constant for all segments. Allowance is made for the differences in scattering factor (cf. refs. [36, 3g]). (Corresponding remarks for the other types of specimens are made in this paper).

Question (Suoritti): Referring to your concentric sphere model for interdiffusion in powder blends, have you studied the actual shape of the powder grains by scanning electron microscopy?

Response (Delhez and Mittemeijer): Yes, we did. Also, optical microscopy and microprobe analysis were applied. It was found that after the start of homogenization the geometry in the powder blend can be approximated indeed by the concentric sphere geometry (cf. Sections 4.1 and 4.3.2. of this paper and see also the optical micrographs published in refs. [31-33]).

Comment (Parrish): It is advisable in practice to consider the use of other analytical methods which may be more appropriate than x-ray powder analysis. For example, in material characterization in solid state electronics, wavelength-and/or energy-dispersive methods with the electron microprobe and scanning electron microscope gives far better spatial resolution and chemical composition for segregated and nonhomogeneous specimens than the broad area analysis of x-ray powder diffractometry. Changing electron beam voltage and/or using Auger electron spectroscopy permits measuring the variations in composition with respect to depth which we use in thin films such as permalloy. Direct SEM observation provides size and morphology of small particles, even if only a few occur as is often the case. Single- and double- crystal methods are necessary for measuring the precise lattice parameter and  $\Delta a/a$  epitaxial films. We cannot become parochial in selecting analytical methods to obtain the best possible results.

Comment (Ladell): In the case of the epitaxial single crystal example, how do you account for the change in diffraction profile due to entering first a perfect crystal then proceeding, through a region which is imperfect and then coming again to a perfect region? Near the surface, the diffraction is dynamic, in the immediate interior kinematic. This means shifted peaks and enhanced intensity which influence the assessment of diffusion concentration.

Response (Delhez and Mittemeijer): As a result of specimen preparation (e.g., vapour deposition or electrocrystallization) the order layer (cf. fig. 13) is not a perfect single crystal. Further, on diffusion-annealing a diffusion-induced substructure develops (dc. ref. [14-17]). Then, the kinematical diffraction equations can be applied to the diffraction from the material covered by the concentration variation.

STRUCTURES FROM POWDER DATA: DATA SAMPLING, REFINEMENT AND ACCURACY

W. J. Mortier

Katholieke Universiteit Leuven  
Centrum voor Oppervlaktescheikunde en Colloïdale Scheikunde  
De Croylaan 42  
B-3030 Heverlee, Belgium

Some important features of the procedure followed to obtain accurate intensity data for powder samples and for the determination of crystal structures from these data are presented. One extension of an earlier described method for the deconvolution of overlapping peaks using an experimental profile is described, with the refinement of a width function and the  $\alpha_2/\alpha_1$  ratio. Topics of the least-squares refinement for powders and the statistical evaluation of the parameter sets for two isotopic structures are discussed. A general program package for the determination of structures from powder samples is presented.

### 1. Introduction

There are several reasons why one has to rely on crystal structures determined from powder samples for the research of some materials. The most obvious reason is that single crystals might not be available. Studying the physicochemical properties of materials such as zeolites, severe pretreatment conditions are required, resulting more often than not in the destruction of single crystals.

Moreover, parameters of critical importance such as temperature, dehydration and adsorption of gases are more easy to control for powders. The influence of a single parameter can be evaluated from the gradual changes in a series of structures with this parameter as a variable. Finite conclusions could rarely be derived from a single study based on powder data.

This type of study requires a highly accurate data sampling with a minimum number of variables, a most careful refinement of the structural parameters, (some of which are highly correlated), a refinement which is based on independent observations such as the intensities of combined peaks and the statistical comparison of isotopic structures for the evaluation of the significance of differences between such isotopic structures.

During several years we have been able to develop the data sampling, refinement procedure and the statistical evaluation for powder samples. The recent availability of automated

powder diffractometers has substantially increased the accuracy and has considerably extended the possibilities. A package of programs, allowing a flexible data collection, crystallographic computations and statistical evaluations is presented here. All of these have proved to be useful for the determination of structures from "poorly" crystalline zeolite powders.

## 2. Data Sampling

### 2.1. Experimental

The recordings reported here were made with an automated SEIFERT-SCINTAG PAD II powder diffractometer using Ni-filtered Cu radiation and a proportional counter. Technical specifications of the diffractometer slit system are given in figure 1. A high resolution was ensured by the use of a large goniometer measuring circle ( $R = 220$  mm), a low take-off angle ( $3.5^\circ$ ), a fine focus ( $0.4 \times 8$  mm) Phillips x-ray tube, the use of a supplementary scatter slit (S) in connection with the divergence slit (D) (width of the scatter slit S being twice the width of the divergence slit (D)), and the use of long parallel slits (P) (50 mm long, 1 mm between the foils) in both the incident and diffracted beam. A receiving slit R of 0.2 mm was used for all samples. An angular divergence  $\phi$  of the incident beam of  $0.4^\circ$  was used for the recording of the Si powder standard and for the lower  $2\theta$  angles of the zeolite powders reported. For higher angles of the zeolite powder diffraction profile, an aperture of  $0.8^\circ$  was used. Fixed counting times per step of  $0.01^\circ$  varied between 10 s (Si) and 18 or 36 s (zeolite). A supplementary Ni filter was placed in the diffracted beam for all samples

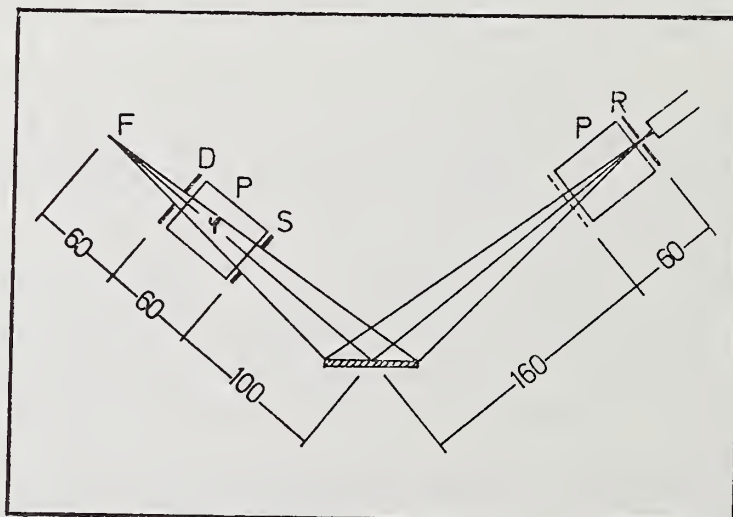


Figure 1. PAD II diffractometer slit system. F: x-ray linefocus; D: divergence slit; S: scatter slit (aperture  $S = 2 \times$  aperture D); R: receiving slit;  $\phi$  divergence angle; P: parallel slit assembly. All dimensions are given in mm.

## 2.2. Deconvolution of overlapping peaks

In an earlier study [1]<sup>1</sup> a method has been presented for the deconvolution of overlapping peaks in x-ray powder patterns with the use of an experimental profile. This profile is the  $\alpha_1$  profile as it can be derived from the Fourier coefficients of a combined  $\alpha_1\alpha_2$  diffracted peak as described by Gangulee [2]. The Fourier series being unique for a particular peak, a transformation of the abscissa accounts for the angular dependence of the actual profile and the height is adjusted by a constant. The intensity function for a combined profile was given as [1]

$$I(x) = \sum_{i=1}^s \left[ H_i \left\{ A'_0 (1+R) / 2 \right. \right. \\ \left. \left. + \sum_{n=1}^{\infty} (A'_n p_{n,i} - B'_n q_{n,i}) \cos n(x - a_i + b) \right. \right. \\ \left. \left. + \sum_{n=1}^{\infty} (B'_n p_{n,i} + A'_n q_{n,i}) \sin n(x - a_i + b) \right\} \right]$$

where  $s$  = number of  $\alpha_1\alpha_2$  combined peaks

$$p_{n,i} = 1 + R \cos n \Delta_i$$

$$q_{n,i} = R \sin n \Delta_i$$

$\Delta_i$  = the separation of the  $\text{CuK}\alpha_1$  and  $\text{CuK}\alpha_2$  components

$R$  = intensity ratio  $\alpha_2/\alpha_1$

$a_i$  = abscissa values of the maximum of the  $\alpha$  components

$b$  = abscissa value of the maximum of the standard profile.

$H_i$  = the height of the peak

$A'$  and  $B'$  = the Fourier coefficients of the  $\alpha_1$  standard profile.

The arguments of the sine and the cosine function must be within the range  $[0, 2\pi]$  and all abscissa values are expressed in the same units. It was reported before [1] that the width parameter, adjusting the abscissa increments such that at each diffracted angle the same half width as the standard profile was obtained, could be derived from the width of the  $\alpha_1$  component of three separate peaks in the range of the data collection. It was also

<sup>1</sup>Figures in brackets indicate the literature references at the end of this paper.

mentioned that a linear variation of the width with  $2\theta$  was observed in the same range. However, this was found to cause problems in that it was sometimes difficult to find intense well resolved peaks at higher  $2\theta$  angles. The method was therefore extended to refine on a width parameter. A supplementary parameter ( $w$ ) can be introduced on the abscissa values modifying the arguments of the sine and cosine functions as  $n(x - a_1) w + b$ . Accordingly,  $\Delta_i$  must also be multiplied by  $w$ . Furthermore,  $R$  can also be taken as a variable and refined. A combined profile can therefore be fitted using a very limited number of parameters, i.e.  $H$  one single parameter  $b$  since the relative position of the peaks can be calculated from the lattice parameters, one width parameter  $w$  for the entire profile and one parameter  $R$ . A width function can however be established by fitting a number of intense profiles refining on  $H_i$ ,  $b$  and  $w$ .  $R$  can be kept constant once determined. Therefore, usually only  $s + 1$  parameters are fitted for a profile of  $s$  peaks and at most  $s + 3$  parameters. During our data sampling all diffracted peaks were fitted giving the advantage of a more reliable intensity estimation for small peaks.

### 2.3. The standard profile

An analysis of the diffraction profiles of Si powder was made using two different standards: the  $\alpha_1$  profile of the  $N (=h^2 + k^2 + l^2) = 8$  peak ( $2\theta \approx 47^\circ$  for  $\text{CuK}\alpha$  radiation) and  $N = 35$  ( $2\theta \approx 114^\circ$ ). It was observed that there was a difference in line shape between the lower order and higher order diffractions. Therefore, two standard profiles had to be used, i.e.  $N = 8$  up to  $2\theta = 80^\circ$  and  $N = 35$  for higher  $2\theta$  values in order to obtain a sufficiently good agreement between the observed and calculated profiles (i.e. 1 à 2 percent difference in observed and calculated intensity). The difference in profile is illustrated for the lowest diffracted peak, i.e.  $N = 3$  ( $2\theta = 28.47^\circ$ ) in figure 2.

A good fit was obtained using the  $N = 8$  standard profile (full line, 1). When using the  $N = 35$  standard, deviations in the profile are important in the tails and the top (dotted line, 3). The two different fits with the  $N = 35$  profile were refinements including the  $\alpha_2/\alpha_1$  ratio and with fixed  $R$  ratio. It is important to emphasise that when refining with an incorrect standard profile, the calculated  $\alpha_2/\alpha_1$  ratio was considerably in error. Indeed, the better fit (intermittent line, 2) on the  $\alpha_2$  component for the  $N = 35$  standard was obtained with an  $\alpha_2/\alpha_1$  ratio of  $0.353 \pm 0.025$ . Using the  $N = 8$  profile, the  $\alpha_2/\alpha_1$  ratio was  $0.513 \pm 0.024$ . There is no such important deviation however when the  $\alpha_1$  and  $\alpha_2$  components are better resolved as for the higher order diffractions.

### 2.4. Intensities

In the study of powder samples such as zeolites, peaks above a diffraction angle of  $80^\circ$  ( $2\theta$ ) are almost not present or they do not contain sufficient information (too many coinciding reflections). The same standard  $\alpha_1$  profile for  $N = 8$  of Si powder can be used throughout to separate overlapping peaks as it is shown in figure 3 for peaks diffracted at  $2\theta \approx 16^\circ$  and  $70^\circ$  of a dehydrated  $\text{CaAgA}$  zeolite and in figure 4 for a series of peaks at a diffraction

gle of  $\approx 68^\circ$  for a dehydrated Ru exchanged  $\text{NH}_4\text{Y}$  zeolite. The highest peak of figure 4 is only three times the background. The relative peak heights and widths together with the standard deviation and correlation matrix are given in the caption of this figure. Convergence is usually obtained after three cycles. If only the peak heights and the positional parameter is refined, two cycles are sufficient.

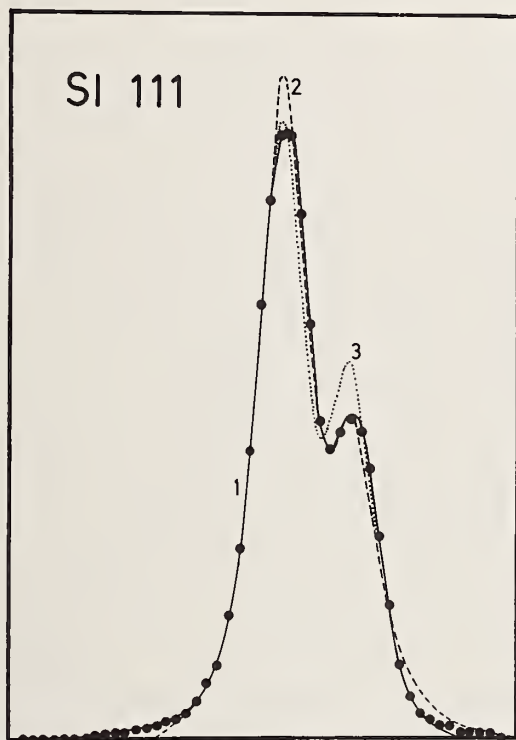


Figure 2. Si-powder 111 peak ( $2\theta \approx 28.5^\circ$ ) in steps of  $0.01^\circ$  ( $\bullet$ ), counting time 10 s, fitted with (1) standard  $\alpha_1$  profile derived from the silicon 220 peak ( $2\theta \approx 47^\circ$ ) (full line), and (2), (3) fitted with the  $\alpha_1$  standard derived from the silicon 531 peak ( $2\theta \approx 114^\circ$ ). Intermittent line 2 is profile fitted when refining on the  $\alpha_2/\alpha_1$  intensity ratio. The dotted line 3 is fitted with constant  $\alpha_2/\alpha_1$  ratio of 0.5.

Errors in the intensity of the individual peaks include counting errors and deconvolution errors. The number of counts per step and per minute being given by  $c_i$  {= accumulated counts / measurement time (t)}, and  $\sigma_{c_i} = \sqrt{c_i/t}$ . The total number of counts in a profile is obtained  $C = \sum c_i$  and  $\sigma_C = (\sum \sigma_{c_i}^2)^{1/2}$ . Since the intensity  $I_i$  of a single peak in the profile is proportional to the height  $H_i$  ( $I_i = \frac{H_i}{\sum H_i} \cdot C$ ),

$$\sigma_{I_i} = \frac{1}{\sum_i H_i} \left[ (\sigma_{H_i} \cdot C)^2 + (\sigma_C \cdot H_i)^2 \right]^{1/2},$$

$\sigma_{H_i}$  being obtained by the least squares fit and  $\sum H_i$  being treated as a constant.

### 3. The Least-Squares Refinement

Unlike single crystal studies, powder samples do not always allow the determination of structure factors from diffracted peaks because of coinciding reflections. An example is a cubic system where all reflections with the same  $N = h^2 + k^2 + l^2$  are coinciding. To determine the structure factors, one can only rely on the ratio of the calculated intensities to the observed intensities of systematically coinciding reflections. In this way, the model is already included in the observed intensities which results in a biased parameter estimation. It is possible, however, by minimizing  $\sum w_N (I_N^O - I_N^C)^2$  in the least-squares refinement. Divergence and oscillations can easily be avoided by the use of damping factors.

It is also difficult to estimate the scale factor. This is more so if partial occupancies are to be refined as it is the case for zeolite-type structures. This is solved by the use of a modified Wilson-type plot [3]. Since

$$k I_{\text{obs}} = I_{\text{calc}} \cdot \exp \left( - 2B \frac{\sin^2 \theta}{\lambda^2} \right),$$

where  $k$  = scale factor and  $B$  = overall temperature factor, we have

$$\ln (I_{\text{obs}}/I_{\text{calc}}) = \ln(1/k) - 2B \left( \frac{\sin^2 \theta}{\lambda^2} \right).$$

A plot of  $\ln(I_{\text{obs}}/I_{\text{calc}})$  vs  $(\sin^2 \theta / \lambda^2)$  for every 10 reflections, e.g. allows to determine the scale factor and temperature factor corrections.

### 4. Accuracy

For zeolites, the structural studies parallel the research of the physicochemical and catalytic properties. The influence on the structure of some parameters can be followed by a structure analysis varying a single parameter. Considering the reduced amount of information and the statistical significance of the differences observed in the structural parameters should be determined. A statistical comparison might however be limited because of the correlation problems (scale factor, occupancy factors and temperature factors) which do not allow the determination of the entire variance-covariance matrix. If no full matrix is available, statistical tests of significance of the parameters can only be based on the conditional distribution

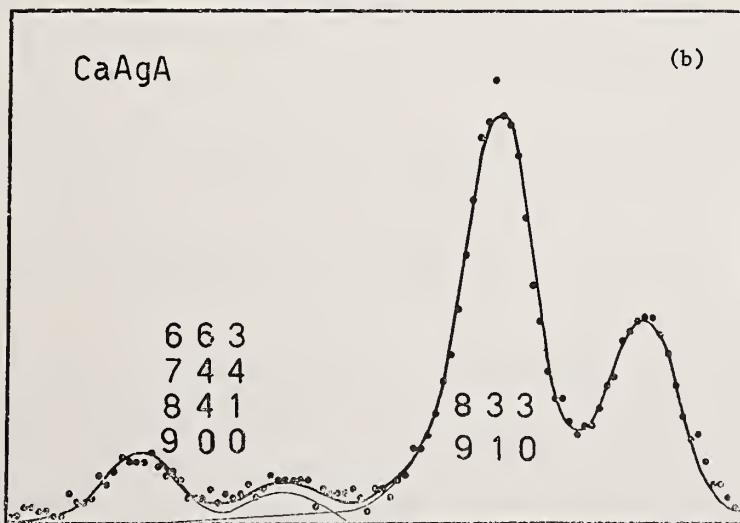
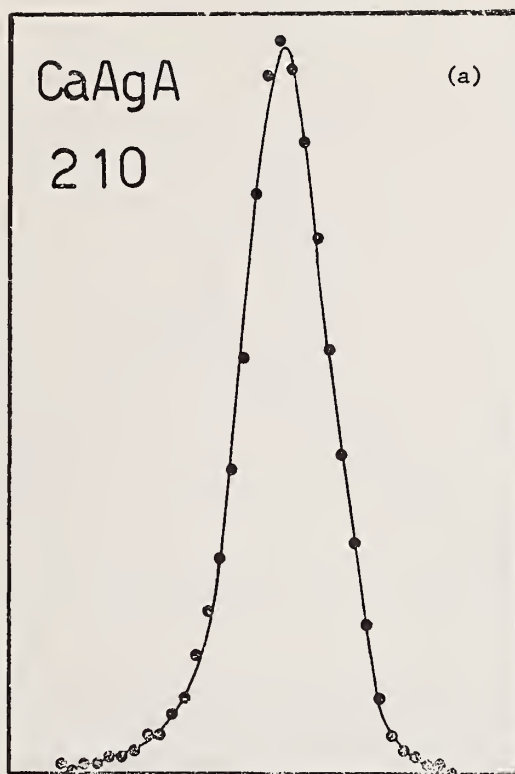


Figure 3. Selected peaks of a dehydrated CaAgA zeolite powder ( $Pm3m$ ,  $\alpha_0 = 12.34 \text{ \AA}$ ) fitted with the silicon  $\alpha_1$  standard derived from the Silicon 220 peak: (a) 210 peak ( $2\theta \approx 16^\circ$ ), counting time per step: 18 s, (b) 663, 744, 841, 900 and 833, 910 diffracted peaks, counting time per step: 18 s,  $2\theta \approx 68.5^\circ$ .

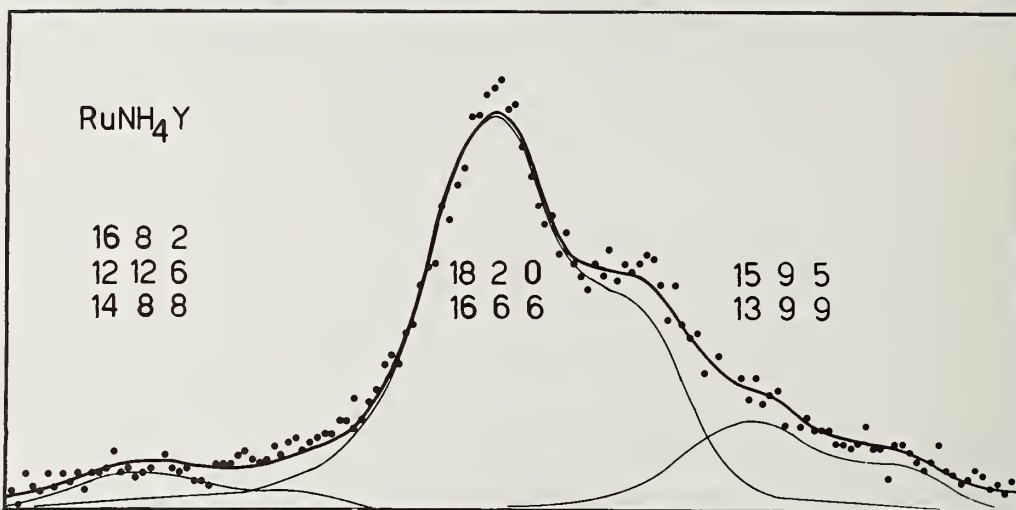


Figure 4. Part of profile fitted with the silicon  $\alpha_1$  standard (220 reflection) for a dehydrated  $\text{RuNH}_4\text{Y}$  type zeolite (Fd3m,  $a_0 = 24.78$ ) at  $2\theta \approx 68.5^\circ$ , counting time per step: 36 s. Peak heights ( $H_i$ , arbitrary units): 0.0075(5), 0.0770(12), 0.0175(11); width parameter  $w$ : 0.380(6); Correlation between  $H_i$  and  $H_j$  1, 2: 0.098; 2, 3: 0.094; 1, 3: 0.030; Correlation between width and  $H_i$  of peaks 1, 2 and 3: 0.191, 0.786 and 0.327, respectively.

the parameter set. It has been shown [4] that the evaluation of  $Q$

$$Q = \frac{(\hat{\beta}_1 - \hat{\beta}_0)' S_1^{-1} (\hat{\beta}_1 - \hat{\beta}_0)}{2 q s^2} = F_{q, n-p}(\alpha)$$

can be used to test the significance of the parameter differences  $(\hat{\beta}_1 - \hat{\beta}_0)$ . [ $n$  = number of observations,  $p$  = number of parameters;  $q$  = number of parameters compared,  $S_1$  is the matrix of the coefficient of the normal equations for the  $q$  compared parameters; and  $s^2 = \sum w (\Delta F)^2 / (n-p)$ ]. This  $F$  test is then based on the conditional density function of the subset of  $q$  parameters. If the entire matrix of normal equations ( $S$ ) is available the test can also be performed on a subset using the marginal distribution if the rows and columns are crossed from  $(S^{-1})$  giving  $S_1^{-1}$  before evaluating  $Q$ . Notice that  $t_{n-p}^2 = F_{1, n-p}$  and that the expression can be used for the comparison of two single parameters ( $\hat{u}_1$ ) by  $(\hat{u}_1^2 - \hat{u}_1^1) / s(2S_{11}^{-1})^{1/2} = t_{n-p}$  where  $S_{11}^{-1}$  is the diagonal element of the matrix inverse of  $S$ .

## 5. The Programs

The programs for the above calculations are available from the authors. ALPHA1 calculates the Fourier coefficients of a standard  $\alpha_1$  profile starting from a combined  $\alpha_1\alpha_2$  profile. AKFIT performs the deconvolution of the peaks on the basis of this experimental profile. The program POWLS is a general least-squares program for centric spacegroups (a largely modified version of Hamilton's [5] program) and allows the refinement based on structure factors, on individual intensities  $I_{hkl}$  or on coinciding or quasi-coinciding reflections. Other programs are the same as for single crystal studies such as JIMDAP for the calculation of the electron densities, using an intermediate file written by POWLS; ORFFE [6] for the calculation of interatomic distances and bond angles and LIST for the listing of observed and calculated structure factors for publication. The statistical F-test can be performed by a program VMATVP, using the matrix of normal equations punched by POWLS as an input file. All programs are written in FORTRAN IV.

---

The author wishes to acknowledge the "Belgisch Nationaal Fonds voor Wetenschappelijk Onderzoek" for a research grant as "aangesteld navorser" and the Belgian Government (Dienst voor programmatie van het wetenschapsbeleid) for financial aid.

### References

- [1] Mortier, W. J. and Costenoble, M. L., J. Appl. Cryst. 6, 448 (1973).
- [2] Gangulee, A., J. Appl. Cryst. 3, 272 (1970).
- [3] Lipson, H. and Cochran, W., The Determination of Crystal Structures, (G. Bell & Sons Ltd, London, 1968), p. 72.
- [4] Mortier, W. J., Acta Crystallogr. A29, 473 (1973).
- [5] Hamilton, W. C., POWOW, Brookhaven National Laboratory, Brookhaven, New York (1962).
- [6] Busing, W. R., Martin, K. O., and Levy, M. A., ORFFE, Report ORNL-TM-306, Oak Ridge National Laboratory, Oak Ridge, Tenn.

### Discussion

Comment (Edmonds): I would like to clarify the use of the term "deconvolution". Deconvolution should be reserved to describe the separation of physical phenomena that interact multiplicatively to give the observed profile. Peak resolution, or another appropriate term, should be used to describe the separation of individual peak shapes that add to yield the final observed profile.

Question (unidentifiable source): Did you determine the accuracy of your fitting method by calculating an R-Factor?

Response (Mortier): We calculate the sum of the squared errors of fit as a means of following the convergence, although we could as well have used a reliability index. The latter, however, would not teach us much more for low intensity data with a large scatter in the measured points. Therefore, a visual inspection is our criterion for correction of the background or the standard profile.

## ACCURACY IN METHODS OF LATTICE-PARAMETER MEASUREMENT

A. J. C. Wilson  
Department of Physics  
University of Birmingham  
Birmingham B15 2TT, England

The geometrical and physical aberrations relevant in powder diffractometry are discussed, particularly in connection with the determination of lattice parameters by means of a Bragg-Brentano (Parrish) parafocusing powder diffractometer. Other diffractometers and photographic methods are mentioned more briefly. The displacements of the centroid of the line profile that depend only on the specimen can be eliminated simply by extrapolation methods. Some of those, depending on the radiation and the apparatus, can be eliminated in the same way, but others require more detailed treatment. Attention is given also to peak methods, to profile-fitting methods, to energy-dispersive diffractometers, and to statistical assessment of the parameters obtained.

An extensive, but not exhaustive, bibliography contains some papers not explicitly cited in the main text.

### 1. Historical Background

Since about 1930, it has been claimed that the lattice parameters of cubic and other high-symmetry substances could be measured within one part in about 50,000 by powder methods (see, for example, reference [1]<sup>1</sup>). It is unquestionable that measurements on the same material by the same investigators were reproducible within this limit, even when different cameras, different radiations, and different film mountings were used (see, for example, reference [2]). However, different investigators often did not achieve this degree of agreement with one another, and in April 1956 the Commission on Crystallographic Apparatus of the International Union of Crystallography decided to arrange an inter-laboratory comparison of measurements of the lattice parameters of three cubic substances (diamond, silicon, and tungsten) with widely different linear absorption coefficients. Powders of the three substances, of the highest purity readily available, were homogenized and samples distributed by sixteen laboratories in nine countries,

---

<sup>1</sup>Figures in brackets indicate the literature references at the end of this paper.

though not all laboratories reported on all three. The results [3] were illuminating, though perhaps disappointing. For each substance there was one maverick determination, differing from the mean of the rest by one or two parts in 10,000. The remaining determinations agreed reasonably well with one another, the standard deviation from the mean being about one part in 30,000--twice the expected amount. No correlation could be found between the deviation from the mean and the method, wavelength, or type of apparatus used. There were, however, few diffractometer measurements, and it would be interesting to repeat the comparison now, as diffractometers are generally believed to be less subject than cameras to systematic error.

## 2. Ideal and Real Diffractometers

An ideal angle-dispersive diffractometer would consist of a point source emitting strictly monochromatic x-rays of wavelength  $\lambda$ , a specimen of negligible physical dimensions and without strain or other intrinsic defects, and a point detector. An ideal energy-dispersive diffractometer would be similar, except that the source would emit a wide range of wavelengths (photon energies) and the detector would have perfect wavelength (energy) discrimination. In either case, the lattice spacing  $d$  of the diffracting planes would then be related to the wavelength  $\lambda$  and the diffraction angle  $2\theta$  by Bragg's law

$$\lambda = 2d \sin\theta, \quad (1)$$

the only deviations from it being random errors in the measurement of the angle (wavelength, energy). If measurements of several different interplanar spacings were made the lattice parameters could be obtained from the known relations between interplanar spacing, Miller indices, and lattice parameters (International Tables, Vol. II, 1959, pp. 106-158) and the values obtained from different sets of spacings would agree within limits of the random errors in measuring the  $\theta$ 's ( $\lambda$ 's).

In practice, in order to obtain sufficient intensity for any measurements to be made, the source, specimen, and detector must all be of finite size and a finite range of wavelengths must be used. The parameters now show a systematic drift with angle--there are systematic as well as random errors affecting them. The systematic errors are usually called aberrations, and can be divided into two main classes: (i) geometrical aberrations, and (ii) physical aberrations. The geometrical aberrations are those that depend on the dimensions of the source, specimen and detector (or of the slits that limit their effective dimensions), the physical aberrations are those that depend on the intensity distribution in the range of wavelengths used (in the angle-dispersive case; or the response characteristics of the detector and associated circuits in the energy-dispersive case).

There are two errors that in ordinary circumstances would not reveal themselves through inconsistencies or systematic variations in the values obtained for the lattice parameters. The first is that the wavelength to be inserted in eq. (1) is not known with

gh accuracy. The wavelengths given by spectroscopists (the exact feature to which they refer is not known, but it is probably nearer to the peak than to the centroid) are subject to uncertainties of one part in 50,000 (see, for example, reference [4], especially, p. 157), though this uncertainty is reduced by a factor approaching ten for more recent measurements known to refer to the peak defined by, say, the extrapolated mid-point of chords [5]. Energy-dispersive systems are usually calibrated by reference to such x-ray wavelengths, so the absolute energy scale is uncertain to at least the same extent.

The wavelength distributions in the emission spectra of the elements ordinarily used in x-ray crystallography are not noticeably affected by the methods used for preparing the targets, though Lipson and Rogers [6] have reported some variation for manganese. There will be a slight dependence, at about the limit of detectability, on operating voltage, take-off angle, and degree of filtration [7-11]. Effective monochromators will produce large variations [12]. However, eq. (1) depends only on the ratio of  $d$  to  $\lambda$ , so that relative spacings can be determined without regard to the accuracy of  $\lambda$ , provided that nothing is done that alters the wavelength distribution between measurements, and that the same identifiable feature of the distribution is used throughout.

The other error of this type is that arising from refraction. X-rays, unless incident normally, are refracted away from the normal on entering matter, and while inside matter have a longer wavelength than in vacuo. Both effects are small, but the former leads to a measurable geometrical aberration for solid specimens (that is, without voids or binder) with flat surfaces (single crystals or polished metal blocks). For the usual powder compacts, it leads to a broadening rather than a displacement Wilson, [13,14]; but compare Wilkens, [15]. The greater wavelength within the crystal leads to a pseudo-aberration; the actual wavelength ought to be used in eq. (1), and if the in-vacuo wavelength is used the lattice spacing obtained will be too small by a fraction equal to the amount by which the refractive index differs from unity.

### 3. Centroid and Peak Displacements, Line Profiles

The diffractometer aberrations shift and distort the diffraction maxima. The study of their effects can be divided into four stages, corresponding to four levels of mathematical difficulty, and the stage to which it is necessary to carry the calculation depends on the purpose in view and the 'identifiable feature' of the wavelength distribution that it is intended to adopt as a measure of the position of the line profile. The three usual features are: (i) the centroid (centre of gravity, mean, average) of the wavelength distribution; (ii) the peak (mode, maximum); and (iii) the best overall fit between the observed and the synthesized line profile. The first of these, the centroid, requires only the first stage of calculation for the geometrical aberrations and the first and second stages for the physical. The third, best overall fit, requires all four stages; the second, the peak, logically requires all four, but approximations can be obtained at the second stage.

The first stage of the calculation is the determination of the effect of the aberration on the centroid of the diffraction maximum, and ordinarily this presents

little, or at least no insurmountable, difficulty, and is all that is required for the correction of centroid positions of line profiles for geometrical aberrations [16-23].

The additivity of centroid displacements should be exact for geometrical aberrations and other functions with finite variance, but is subject to some limitations for functions like the wavelength distribution and the diffraction profile, and depends to some extent on the truncation procedures [24]. This limitation of the use of centroids has been discussed by Wilson [25]; it depends on the initial slopes and curvatures of the Fourier components of the profiles that are folded together. The initial slopes vanish for the geometrical aberrations, so that non-additivity should not affect the determination of the lattice parameter of well-crystallized materials.

The second stage is the calculation of the mean-square broadening (variance). This is not necessary for parameter determination from centroid measurements, but it can be used to obtain a reasonable approximation to the correction to peak positions over a wide range of Bragg angles [26-28]. To this approximation, the position of the observed peak is given by

$$(2\theta)_{\text{obs}} = (2\theta)_{\text{true}} + \langle \Delta(2\theta) \rangle + \frac{W I''}{2I'},$$

where  $\langle \Delta(2\theta) \rangle$  is the centroid and  $W$  is the variance of the geometrical aberration and  $I''$  and  $I'$  are the second and third derivatives of the observed line profile evaluated at its maximum. The physical aberrations of the centroid depend on the variance of the part of the wavelength distribution used in determining the centroid [7,11,29]. Those of the centroid depend on the ratio of the peak intensity  $I$  to its second derivative  $I''$  [11,26,30].

The third stage is the calculation of the line profile corresponding to each geometrical aberration. These aberration profiles can be combined by convolution (folding), either directly or by Fourier methods, and, in the fourth stage, the combined aberration profile can be convoluted with the profile of the wavelength distribution of the emission profile of the x-ray source (or of the emission profile as trimmed by a monochromator, pulse-height filter, etc.) and with the diffraction profile corresponding to the state of strain, crystallite size, etc. of the specimen. This calculation of the composite line profile is a necessary preliminary to an exact use of peak positions or overall profile-fitting in lattice-parameter determination. Such calculations were proposed many years ago, for example, by Alexander [31-34], and have been used by Beu and his collaborators (for references, see Section 6), and Boom [35]; Boom and Smits, [36]).

Until recently the use of exact-peak or overall-fitting methods of lattice-parameter determination could only be regarded as an occasional tour-de-force. With the development and greater availability of computers, they are now within striking distance of becoming routine. The most common approach, based on the proposal of Rietveld [37,38], is empirical rather than the fundamental one outlined above. In outline, a function resembling the diffraction profile and containing several functions of angle with adjustable parameters is chosen, and an adjustable multiple of it is placed near the expected position of each diffraction peak. The adjustable parameters (multiple, centroid shift, breadth, skewness, excess, etc.) are then varied until the best least-squares fit between the total observed pattern and the

calculated pattern is obtained [37-44]; (reference [44] contains references to many other papers). In much of this work the emphasis has been on either the closeness of the fit between the observed and calculated patterns of individual lines, or on obtaining structural parameters by making the 'multiple' depend explicitly on them, so that deducing lattice parameters from the centroid shifts has received little attention, and it is not clear to what extent the results are dependent on the choice of the approximation function.

#### 4. Aberrations

The symmetrical Bragg-Brentano (Parrish) and the Seemann-Bohlin angle-dispersive diffractometers are so well known that no description is needed here. The centroid displacements and the variance of the aberrations of the Parrish type have been collected by Wilson [11,30] and displayed in tabular form ([45], pp. 34-35, 143). A similar table for the peak displacements has been given by Wilson [26]. For the Seemann-Bohlin type they are collected in table 1, mainly from Wilson [46] and the references cited there. The aberrations are expressed in inverse powers of the source-specimen distance  $\underline{S}$  and the specimen-detector distance  $\underline{R}$ , and tend to be larger for the Seemann-Bohlin than for the symmetrical arrangement. For the latter,  $\underline{S}$  and  $\underline{R}$  are constant and equal to the radius, say  $\underline{R}_0$ , of the diffractometer, whereas for the former

$$\underline{S} = 2\underline{R}_0 \sin\psi \quad (3)$$

$$\underline{R} = 2\underline{R}_0 \sin(2\phi - \psi), \quad (4)$$

where  $\psi$  is the constant angle that the incident x-rays make with the specimen surface. In the Seemann-Bohlin case  $\underline{S}$  will be constant at a value depending on the choice of the angle  $\psi$ , but probably less than  $\underline{R}_0$ , and  $\underline{R}$  will vary with  $2\phi$ , approaching zero as  $\phi$  approaches  $\frac{1}{2}\psi$ . There will thus be a range of  $2\phi$  for which the Seemann-Bohlin aberrations containing  $\underline{R}$  become very large. Mack and Parrish [47] have confirmed experimentally the expected differences in favour of the Bragg-Brentano arrangement for general use, even though the effective equatorial divergence ('flat-specimen error') can be greatly reduced by appropriately curving the specimen. The aberrations in table 1 reduce to those for the symmetrical case for  $\underline{R} = \underline{S} = \underline{R}_0$ ,  $\psi = \phi$ .

An energy-dispersive diffractometer can be made from an angle-dispersive one simply by (i) replacing the usual counter by a solid-state detector, (ii) replacing the usual electronic circuits by a multi-channel pulse-height analyser, and (iii) keeping the specimen and detector stationary while the counts are accumulated. When so used, the geometrical aberrations are essentially the same as those of an angle-dispersive diffractometer, though the greater penetration of the higher-energy x-rays means that greater attention must be paid to the irradiated volume and the specimen transparency [41,48-51]. As Sparks and Gedcke [52] emphasize, spacing measurements made with such a diffractometer are subject to large specimen-surface displacement and transparency aberrations, and the corrections required to allow for them are difficult

Table 1. Centroid displacement  $\langle \Delta(2\theta) \rangle$  and variance  $W$  for certain aberrations of the angle-dispersive diffractometer; for references see Wilson [11,30,46] and Gillham [55]. For the Seemann-Bohlin arrangement  $\underline{S} = 2R_0 \sin\psi$  and  $\underline{R} = 2R_0 \sin(2\phi - \psi)$ , where  $R_0$  is the diffractometer radius,  $2\phi$  is the diffractometer setting, and  $\psi$  is the angle at which the X-rays are incident on the specimen. For the symmetrical Bragg-Brentano arrangement  $\underline{R} = \underline{S} = R_0$  and  $\psi = \phi$ ; the tables in Wilson [45] will be more convenient in this case. Other notation is explained at the end of the table.

Aberration	$\langle \Delta(2\theta) \rangle$	$W$
Zero-angle calibration	Constant	Zero
Specimen displacement	$-\underline{S}\{R^{-1}\cos(2\phi - \psi) + \underline{S}^{-1}\cos\psi\}$	Zero
Specimen transparency		
Thick specimen	$-\sin 2\phi / \mu(R + \underline{S})$	$\sin^2 2\phi / \mu^2 (R + \underline{S})^2$
Thin specimen	see Wilson [46], p. 547	
2:1 mis-setting	Zero if centroid of illuminated area of specimen centred on axis of rotation	$\frac{1}{3}\beta^2 A^2 \{R^{-1}\cos(2\phi - \psi) + \underline{S}^{-1}\cos\psi\}^2$
Inclination of plane of specimen to axis of rotation	Zero if centroid of illuminated area on equator of specimen	$\frac{1}{3}\gamma^2 h^2 \{R^{-1}\cos(2\phi - \psi) + \underline{S}^{-1}\cos\psi\}^2$ for uniform illumination
Flat specimen	$\frac{-A^2 \sin 2\phi}{3RS}$	$\frac{4A^4 \sin^2 2\phi}{45R^2 \underline{S}^2}$
Focal-line width	Small	$\sim \underline{f}_1^2 / 12\underline{S}^2$ , but depends on intensity variation across focal line
Receiving-slit width	Small	$\underline{r}_1^2 / 12\underline{R}^2$
Cross term between equatorial extensions of focal line and specimen	Small if adjustment reasonable	$\sim \frac{f_2^2 A^2 \sin^2 \psi}{36\underline{S}^4}$ , but depends on intensity variation across focal line

Table 1. (continued)

<p>Cross term between equatorial extension of specimen and non-equality of source-specimen and specimen-receiving-slit distances</p>	<p>Proportional to <math>r_2</math> and distance between axis of rotation and centroid of illuminated area, and thus vanishes if the latter is centered.</p>	$\frac{r_2^2 \Delta^2 \sin^2(2\phi - \psi)}{3R^4}$
<p>Axial divergence</p>		
<p>A. No Soller slits, source, specimen and receiver equal</p>	$-\frac{1}{3}h^2[(S^{-2} + R^{-2})\cot 2\phi + (RS)^{-1}\csc 2\phi]$	$\frac{h^4}{45}[(7S^{-4} + 2S^{-2}R^{-2} + 7R^{-4})\cot^2 2\phi + 14(RS)^{-1}(S^{-2} + R^{-2})\cot 2\phi \csc 2\phi + 19S^{-2}R^{-2}\csc^2 2\phi]$
<p>B. One set of Soller slits (i) Narrow slits in incident beam (ii) Narrow slits in diffracted beam (iii) Wide slits</p>	$-\left[\frac{\Delta^2}{12} + \frac{h^2}{3R^2}\right]\cot 2\phi$ <p>Replace <math>R</math> to <math>S</math> in case B(i) See references in C(ii)</p>	$\left[\frac{7\Delta^4}{720} + \frac{7h^4}{45R^2}\right]\cot^2 2\phi + \frac{\Delta^2 h^2}{9R^2}\csc^2 2\phi$
<p>C. Two sets of Soller slits (i) Narrow slits (ii) Wide slits</p>	$-\frac{1}{6}\Delta^2 \cot 2\theta$ <p>Complex. See Pike [56], Langford [48], Wilson [11,46] and Gillham [55].</p>	$\frac{1}{360}\Delta^4(10 + 17\cot^2 2\theta)$

Table 1. (continued)

Refraction  $\sim -2\delta \tan\theta$   $\sim \frac{\delta^2}{4\mu p} [-6.1 \log_e(\delta/2) + 25]$

Physical aberrations See Wilson [11,30,45,46] and Gillham and King [57]

Notation:  $2A$  = illuminated length of specimen;  $\beta$  = angle of equatorial mis-setting of specimen;  $\gamma$  = angle of inclination of plane of specimen to axis of rotation;  $\Delta$  = angular aperture of Soller slits;  $\mu$  = linear absorption coefficient;  $r_1$  = width of receiving slit (varies with  $\phi$  in some designs of diffractometer);  $r_2$  = distance of receiving slit from focusing circle;  $s$  = specimen-surface displacement;  $f_1$  = projected width of focal line;  $f_2$  = width of focal line;  $h$  = half height of focal line, specimen receiving slit, taken as equal;  $1-\delta$  = index of refraction;  $p$  = effective particle size.

to make. [There seems to be either a typographical or a mathematical muddle in their equation (5), which carries over into equations derived from it.] Fukamachi, Hosoya, and Terasaki [53]; and Nakajima, Fukamachi, Terasaki and Hosoya [54] show that this difficulty can be avoided if the Soller slits are rotated about the beam directions by 90°, so that they limit the equatorial divergence instead of the axial; this was, of course, the orientation used by Soller himself [58]. Any effect of specimen-surface displacement and transparency is then negligible if the ordinary care in adjustment is used, and the specimen may be placed in either the reflection, the symmetrical transmission, or the unsymmetrical transmission position [59]. The aberrations of an energy-dispersive diffractometer are collected in table 1, mostly from the paper of Wilson [59] just cited. The geometrical aberrations apply to the original Soller orientation of the Soller slits; as already mentioned, the usual expressions apply for the other orientation. Except where otherwise stated, the physical aberrations are the same for both orientations. The most difficult one is probably the correction for the energy distribution in the incident x-ray beam; aspects of this have been discussed by Bourdillon, Glazer, Hidaka and Bordas [60]; Buras, Staun Olsen, Gerward, Will, and Hinze [61]; Fukamachi, Hosoya and Terasaki [53]; Laguitton and Parrish [62]; and Wilson [59]; only the last is directly relevant to the lattice-spacing problem. The best results so far reported seem to be those of Fukamachi, Hosoya and Terasaki (0.01 percent in the lattice parameter).

Okazaki and Kawaminami [63] have suggested the use of a stationary specimen followed by analysis of the diffracted x-rays with a single-crystal spectrometer. This would give some of the advantages of energy-dispersive diffractometry (easy control of temperature, etc., because only small windows would be needed), but there would be no reduction in the time required for recording a pattern.

Statistical fluctuations in the numbers of counts recorded are not exactly aberrations, but influence the precision with which angles of diffraction, and hence lattice parameters, can be determined. Space does not permit a detailed discussion, and a paper on statistical aspects is scheduled elsewhere in this Symposium. Among the many papers relevant to the problem are Mack and Spielberg [64], Pike and Wilson [23], Thomsen and Yap [65,66], Wilson [30,67-72], Wilson, Thomsen and Yap [73], and Zevin, Umanskij, Khejker and Pancenko [74]. The formulae are complicated, and depend on the measure of location that is adopted for the diffraction profile. In general, however, the standard deviation of the angle is inversely proportional to the square root of the number of counts accumulated.

## 5. Extrapolation Methods

From eq. (1) it follows immediately that in angle-dispersive diffractometry the fractional error in a lattice spacing is related to the error in the measurement of the Bragg angle by

$$\frac{\Delta d}{d} = -\cot\theta\Delta\theta. \quad (5)$$

Table 2. Centroid displacement  $\langle \Delta E/E \rangle$  and variance  $\bar{W} = \langle \Delta E/E \rangle^2$  for certain aberrations of an energy-dispersive diffractometer, mainly from Wilson [59], where more detailed results are given for some aberrations. The Soller slits are taken to be in the Soller (1926) orientation.

Aberration	$\langle \Delta E/E \rangle$	$\bar{W}$
Specimen displacement*	$\sim 0$	Included in equatorial divergence
Specimen transparency*	$\sim 0$	
	[*In the non-Soller orientation Table 1 applies.]	
Equatorial divergence	$\sim 0$	$\frac{1}{24} \cot^2 \theta (\underline{A}^2 + \underline{B}^2)$ for narrow Soller slits
Axial divergence	$-\frac{1}{24} \underline{R}^{-2} \csc^2 \theta [\underline{X}^2 \cos 2\theta + 4\underline{Y}^2 \cos^2 \theta + \underline{Z}^2 \cos 2\theta + 5\underline{X}^2 \underline{Z}^2 + 5\underline{Y}^2 (\underline{X}^2 + \underline{Z}^2)(1 + \cos 2\theta)^2]$	
Refraction	Probably negligible at present stage of technique	
Response variations:		
Centroid	$\frac{Vf'}{Ef'} + \frac{f''}{Ef}$	$\left[ \frac{1}{2} \underline{H}_3 - \frac{V^2 f'}{f} \right]$ ?
Peak	$-\frac{f'I}{EfI''}$	-

Table 2. (continued)

Interaction of Lorentz etc.  
factors and geometrical  
aberrations

$$\begin{aligned}
 & \frac{1}{2} \langle (\Delta\theta)^2 \rangle & - \cot\theta \langle \Delta\theta \rangle + \frac{g'}{g} \langle (\Delta\theta)^2 \rangle & - \cot\theta \langle (\Delta\theta)^3 \rangle - \langle \Delta\theta \rangle \langle (\Delta\theta)^2 \rangle \\
 & - \cot\theta \langle \Delta\theta \rangle + \frac{g'}{g} \langle (\Delta\theta)^2 \rangle & + \cot^2\theta \left[ \langle (\Delta\theta)^2 \rangle - \langle \Delta\theta \rangle^2 \right] & + \cot^2\theta \left[ \langle (\Delta\theta)^3 \rangle - \langle \Delta\theta \rangle \langle (\Delta\theta)^2 \rangle \right] \\
 & + \cot^2\theta \frac{EI'}{I} \langle (\Delta\theta)^2 \rangle & & + \dots \\
 & + \dots & & + \dots
 \end{aligned}$$

Notation:  $\underline{A}$  and  $\underline{B}$  are the angular apertures (possibly equal) of the two sets of Soller slits;  $E$  is the energy of the detected photon,  $f(E)$  is the variation of a response (energy of the continuous radiation, absorption in the specimen etc.) with  $E$ ;  $g(\theta)$  is an angle-dependent response (Lorentz factor etc.);  $I(E-E_1)dE$  is the counting rate recorded at  $E$  when the energy of the incident photons is actually  $E_1$ ;  $\underline{R}$  is the diffractometer radius;  $\underline{V}$  is the variance and  $\mu_3$  the third central moment of the energy-resolution function  $I$ ;  $2X$ ,  $2Y$  and  $2Z$  are the effective axial dimensions (possibly equal) of the source, specimen and detector; the primes indicate differentiation; the averages  $\langle (\Delta\theta)^2 \rangle$  etc. are over the range of Bragg angles permitted by the dimensions of the slits etc.

The effect of random errors in measuring  $\theta$ , therefore, becomes very small as the Bragg angle approaches  $90^\circ$ . The same is true for all aberrations that remain finite in the back-reflection region. Reference to table 1 (or more conveniently, tables 3-3 and 3-4 of Wilson, [25,45] shows that this includes all the geometrical aberrations except part of the axial divergence not dependent on the specimen size (Wilson, [11], p. 39). If the lattice parameter is plotted against  $\theta$ , therefore, and a smooth curve through the experimental points is extrapolated to  $\theta = 90^\circ$ , the extrapolated value should be free of most geometrical aberrations. Refraction and the part of the axial aberration dependent on the source and the detector (Wilson, [11], p. 39), extrapolate to a constant fractional error in the spacing, for which a correction can be applied when it is large enough to be significant.

A plot of lattice parameter against  $\theta$  is usually strongly curved, so that considerable time and ingenuity have been expended in attempts to find a function of  $\theta$  such that a plot against it would give a straight-line extrapolation. Perhaps the best simple function for diffractometry is  $\cos\theta\cot\theta$ , the correct form for the specimen-surface-displacement and the specimen-transparency aberrations. These are ordinarily the largest aberrations in the low-and moderate-angle range, though axial divergence may take over in the back-reflection region. Functions for camera use have been discussed by Bradley and Jay [1], Nelson and Riley [75], Taylor and Sinclair [76], and others. The function  $\frac{1}{2}\cos^2\theta(\csc\theta + \theta^{-1})$  is often very satisfactory;  $\theta$  must, of course, be expressed in radians.

The preceding paragraph has been written with the implicit assumption that the extrapolation is done graphically. This procedure is quick and easy for cubic substances with only one lattice parameter to be determined, and is possible for hexagonal, rhombohedral and tetragonal [2,77], but it is not elegant, and becomes practically impossible for less symmetric substances. Graphical methods, even in the one-parameter case, are somewhat subjective, and Cohen [78] proposed that an extrapolation line (in the cubic case) should be fitted by least-squares methods. Such analytical extrapolation is readily extended to crystals of low symmetry; in the triclinic case there are six lattice parameters ( $a$ ,  $b$ ,  $c$ ,  $\alpha$ ,  $\beta$ ,  $\gamma$ ), plus one coefficient of the extrapolation function, to be found. The least-squares method is thus used to fit a hyper-plane, and was very tedious before computers came into common use. The program described by Mueller, Heaton and Miller [79] allows up to three trigonometric extrapolation functions to be used simultaneously, so that, for example, specimen-surface displacement, axial divergence, and a physical aberration could be allowed for simultaneously; other programs have been described by Vogel and Kempter [80] and later workers. The number of well-resolved and accurately measured lines required for the reliable estimation of lattice parameters goes up with the number of parameters and coefficients of extrapolation functions that have to be estimated from the data. Weighting schemes have been discussed by Hess [81]; Langford and Wilson [82]; Langford [83]; Warczowski and de Wolff [84]; Warczowski [85], and others. Fitting the full pattern (see Section 3) can be regarded as an advanced method of analytical extrapolation.

The effect of geometrical aberrations either vanishes on extrapolation or, at worst, leads to a small fractional error in the lattice spacings that does not interfere with the extrapolation process. Some physical aberrations for the centroid, on the other hand, become

very large at high angles, varying approximately as  $\tan^3\theta$ , and thus producing a curvature when the usual extrapolation functions are used. Gillham and King [57] have confirmed this theoretical prediction experimentally, using a series of alloys that shifted the lines progressively to higher angles. The net effect on the peaks is considerably smaller, increasing only as  $\tan\theta$ , and thus producing a fractional error in the derived parameters that does not interfere with the extrapolation process--they are approximately equivalent to a wavelength error (see Section 2) for peak measurements (Wilson, [11], pp. 79-81; [30], pp. 87-90). Analytical extrapolation procedures, as mentioned in the preceding paragraph, could, in principle, cope with this behaviour, even for the centroid case, but progress has been made with correcting the measurement of each diffraction maximum for all known aberrations before the lattice spacing is calculated, and thus obtaining lattice parameters that do not show a systematic variation with angle. A few examples are given in Section 6.

## 6. Elimination of Aberrations

In the absence of aberrations, all lines in the pattern of a cubic material would give the same value of the lattice parameter  $a$ . Similarly, for a non-cubic material, any selection of lines would give the same values of the two, three, four or six lattice parameters required to characterize its unit cell. Aberrations lead to a dependence of the derived lattice parameter(s) on the particular choice of line(s). Graphical or analytical extrapolation methods are an attempt to remove the effect of aberrations, making use of an approximate knowledge of their functional dependence on Bragg angle, but without making any attempt to assess their magnitude a priori. Obviously, it would be more satisfactory if it were possible to assess the actual magnitude of each aberration for each line, and correct each measured Bragg angle for all aberrations, thus obtaining estimates of the lattice parameter(s) that show no drift with angle. Straumanis and Ievičs [86] attempted this for the geometrical aberrations by reducing the dimensions of the collimating apertures of their camera and the diameter of the specimen to the point where the aberrations became negligible, but more recent work (for example, Delf, [87]; Boom and Smits, [36]; and Boom, [35]) has relied on careful measurement of the diffractometer dimensions and of the properties of the specimen, so that each aberration of the type listed in table 1 can be individually calculated and applied to the measured Bragg angle. Delf used the centroid (see Section 3) as the measure of line position, and his measurements have been used for illustration by, for example, Beu [88] and Wilson [25,45], pp. 46-47). Boom and Smits used the best overall fit between observed and synthesized line profiles (see Section 3), and Bond [89] used peak positions (extrapolated mid-points of chords) in a study of a silicon single crystal. All achieved remarkable constancy of the lattice parameter (of cubic substances) derived from lines at a number of Bragg angles. The question arises: is the observed variation more than would reasonably be expected on statistical grounds?

Karl Beu and his collaborators have published an extensive series of papers on accuracy and precision in the determination of lattice parameters [88,90-94]. They had photographic methods chiefly in mind, and the full program was frustrated by Beu's death; but the papers by Beu, Musil and Whitney [90,91] and Beu [88] go a long way toward answering the question at

the end of the preceding paragraph. They proposed a particular method of estimating the lattice parameters, the maximum-likelihood method, and a test for deciding whether the remanent differences between observed and calculated Bragg angles were too great to be reasonably attributed to statistical fluctuations, and thus indicative of uncorrected systematic error.

The modern use of maximum-likelihood estimates seems to go back to Fisher ([95], where the name is not used explicitly; [96,97]). Their merits relative to other estimation methods have been the subject of some debate (see, for example, Edwards, [98], who cites an historical example from 1760). They are not, however, very familiar to the average crystallographer, though Beu et al. have been followed in their use by Boom and Smits [36], Boom [35], and Ki and Caulfield [99]. More recently, Price [100] has proposed a maximum-likelihood method of estimating structural parameters, assuming a Poisson distribution of counting fluctuations. Maximum-likelihood estimates depend fundamentally on a knowledge of, or on an assumption about, the exact form of the distribution function of the statistical fluctuations, and are thus more model-dependent than the method of least squares, which requires little more than that the variance of the fluctuations be finite. Both maximum-likelihood and least-squares estimates may be biased when based on a small number of observations. Beu, Musil and Whitn [90] assumed that the random errors in the measured Bragg angles were normally distributed with known variance, possibly without realizing, and certainly without emphasizing, that under these assumptions the maximum-likelihood and the least-squares estimate are equivalent (see, for example, Hamilton, [101], pp. 37-42, or Bard, [102], p. 63). Since determination of parameters by least squares is much more familiar, and avoids detailed assumptions about distribution functions, it seems worthwhile to rewrite the argument of Beu et al. in the more familiar form.

In the present application, the quantity to be minimized is the sum of the squares of the differences between the observed Bragg angles and those calculated from the lattice parameter (in the cubic case: lattice parameters in systems of lower symmetry) with appropriate weights; in other words the residual to be minimized is

$$\underline{R} \equiv \sum_{\underline{i}} \underline{w}_{\underline{i}} (\phi_{\underline{i}} - \theta_{\underline{i}})^2 \quad (6)$$

where  $\phi_{\underline{i}}$  is the observed Bragg angle and  $\theta_{\underline{i}}$  is the Bragg angle calculated from

$$\lambda = 2\underline{d}_{\underline{i}} \sin \theta_{\underline{i}} ; \quad (7)$$

$\theta_{\underline{i}}$  is thus a function of the lattice parameters entering into  $\underline{d}_{\underline{i}}$ , the  $\underline{i}$ th interplanar spacing. In the cubic case

$$\underline{d}_{\underline{i}} = \underline{a} (\underline{h}_{\underline{i}}^2 + \underline{k}_{\underline{i}}^2 + \underline{l}_{\underline{i}}^2)^{-1/2} , \quad (8)$$

formulae for the less symmetrical crystal systems are to be found in most elementary texts. The residual  $\underline{R}$  is thus a function of the single parameter  $\underline{a}$  for cubic crystals and up to six parameters ( $\underline{a}$ ,  $\underline{b}$ ,  $\underline{c}$ ,  $\alpha$ ,  $\beta$ ,  $\gamma$ ) for crystals of lower symmetry. Provided that the number,

say  $\underline{n}$ , of lines measured is greater than the number, say  $\underline{m}$ , of parameters to be determined, the residual can be minimized by standard methods and least-squares estimates of the parameters found.

Under the hypothesis that the observed angles  $\phi_{\underline{i}}$  have been corrected for all systematic errors, so that the differences between the  $\phi_{\underline{i}}$ 's and the  $\theta_{\underline{i}}$ 's are due only to the random errors of measurement, and with the weight  $w_{\underline{i}}$  chosen as the reciprocal of the variance of the corresponding  $\phi_{\underline{i}}$ , say  $\sigma_{\underline{i}}^2$ , eq. (6) for the residual becomes

$$\underline{R} = \sum_{\underline{i}=1}^{\underline{n}} (\phi_{\underline{i}} - \theta_{\underline{i}})^2 / \sigma_{\underline{i}}^2, \quad (9)$$

the sum of  $\underline{n}$  variables each having the mean value unity. In theory, of course, the sum could have any value between zero and infinity, but very large values are unlikely. The expected value is

$$\langle \underline{R} \rangle = \sum_{\underline{i}=1}^{\underline{n}} 1 = \underline{n}, \quad (10)$$

--or it would be if the  $\underline{n}$  terms entering into  $\underline{R}$  were entirely independent. In fact, when the lattice parameters are chosen so as to minimize  $\underline{R}$ , they are slightly influenced by the actual errors in determining the  $\phi_{\underline{i}}$ , in such a direction as to make the expected value of each term somewhat less than unity, and a little calculation shows that the reduction is 1 for each parameter determined. The expected value of  $\underline{R}_{\min}$  is thus  $\underline{n} - 1$  for cubic crystals,  $\underline{n} - 2$  for tetragonal or hexagonal (including rhombohedral),  $\underline{n} - 3$  for orthorhombic,  $\underline{n} - 4$  for monoclinic, and  $\underline{n} - 6$  for triclinic, say  $\underline{n} - \underline{m}$  in general. The variance of  $\underline{R}_{\min}$  depends on the exact distribution of the errors of measurement, but for a normal distribution (as assumed by Beu, Musil and Whitney), it is easily found to be

$$\sigma_{\underline{R}}^2 = 2(\underline{n} - \underline{m}). \quad (11)$$

Other reasonable distributions would change the numerical coefficients of  $\underline{n}$  and  $\underline{m}$ . The probability of getting a random deviation of  $2\sigma_{\underline{R}}$  or more from the expected value is a few percent for any reasonable distribution, so that values of  $\underline{R}_{\min}$  up to

$$\begin{aligned} (\underline{R}_{\min})_{\text{critical}} &= \langle \underline{R} \rangle + 2\sigma_{\underline{R}} \\ &= \underline{n} - \underline{m} + 2[2(\underline{n} - \underline{m})]^{1/2} \end{aligned} \quad (12)$$

are not unlikely to arise by chance, but larger values are progressively less likely, and if large values are found they indicate that some systematic error has not been accounted

for--if the remanent systematic error in  $\phi_i$  is  $\delta_i$ , there will be additional component of about

$$\sum_i \delta_i^2 / \sigma_i^2 \quad (13)$$

in  $R_{\min}$ . The contribution of the systematic errors to  $R_{\min}$  is positive, whatever the sign of the actual error  $\delta_i$ .

Some critical values of  $R_{\min}$  calculated from eq. (12) for various values of  $(\underline{n} - \underline{m})$  are given in the second column of table 3; the meaning of the third column is given in below. Beu, Musil and Whitney argue that values of  $R_{\min}$  as large as those given in table 3 can happen quite frequently through random error, so that (though we may harbour our private suspicions) if  $R_{\min}$  is less than that given in the appropriate line of the table, we cannot reject the hypothesis that the corrections for systematic error have, in fact, been done correctly. On the other hand, values very much larger are more and more improbable, so that if  $R_{\min}$  much exceeds the appropriate value we can be practically certain that systematic errors are still present.

Table 3. Some values of  $R$  corresponding to a deviation of  $2\sigma_R$  greater than chance expectation; for the third column, see  $R_{\min}$  below.

$\underline{n} - \underline{m}$	$\underline{n} - \underline{m} + 2[2(\underline{n} - \underline{m})]^{1/2}$	5% critical value of chi-squared
1	3.85	3.84
2	6.00	5.99
3	7.90	7.82
4	9.66	9.49
5	11.32	11.07
6	12.93	12.59
7	14.48	14.07
8	16.00	15.51
9	17.49	16.92
10	18.94	18.31

Beu applied the likelihood-ratio method to Bond's [89,103] measurements on silicon [90] and to Delf's [87] measurements on tungsten [88]. In the latter case, it was found that the six corrections applied by Delf were necessary and sufficient ( $R_{\min} = 2.5$ ; critical value for  $\underline{n} - \underline{m} = 3$  is 7.9). In the former case, in contrast, it was found that only one (refraction at the crystal surface) was necessary; those for axial divergence and Lorentz-polarization factor were not, and, in fact, caused a small increase in  $R_{\min}$  (from 0.3 to 0.6 either value is small compared with the critical value of 6.0 for  $\underline{n} - \underline{m} = 2$ ). Possibly the correct inference would have been that the corrections were incorrect or incomplete rather than unnecessary. There are at least six papers dealing with specimen- and beam-tilt errors in Bond's method (Burke and Tomkeieff, [104,105]; Gruber and Black, [106]; Halliwell, [107]; Hubbard and Mauer, [108]; Walder and Burke, [109]). All seem to be incomplete in the sense

that they assume a parallel beam at a fixed angle of incidence, whereas in reality the angle of incidence varies over a range determined by the size of the x-ray source and the slit system. Bond [89] himself attempted to deal with this aberration, but his treatment is presumably in need of the same type of improvement. Some preliminary results have appeared [110,111]. Bond applied no correction for dispersion, stating that none is necessary if the tabulated wavelength values refer to peak positions. The physical aberrations resulting from dispersion and Lorentz and polarization factors are closely connected, and their combined effect on peak positions has been discussed by Pike and Wilson [26,30,112]; the treatment in Wilson [11] is less complete).

There is some evidence [3,113,114] that the lattice parameter of powdered silicon is a few parts in  $10^5$  smaller than that of single-crystal silicon, even when both specimens are taken from the same boule. It is not known whether this phenomenon is specific to silicon (resulting, according to one suggestion, from stress generated by formation of a layer of amorphous  $\text{SiO}_2$  on the surface of the powder grains), or is a function of the surface/volume ratio and would be shown by other substances if investigated with the same care, or whether there is an as-yet undetected systematic error in powder diffractometry. Variations in the lattice parameters of metals after cold-working are, of course, well-known (see, for example, [115,116]). There are many explanations of this behaviour, and differences generally become imperceptible after suitable annealing.

The method of Beu, Musil and Whitney, as set out by them, is complex in notation and somewhat difficult to follow. It is hoped that the above description is easier to grasp and that it does not differ in any essential. The function actually minimized by them is

$$\underline{W} = \sum_{\underline{i}=1}^{\underline{n}} \underline{n}_{\underline{i}} \log_e [1 + (\phi_{\underline{i}} - \theta_{\underline{i}})^2 / \underline{s}_{\underline{i}}^2] , \quad (14)$$

where  $\underline{n}_{\underline{i}}$  (not to be confused with  $\underline{n}$ ) is the number of measurements made of the position of the  $\underline{i}$ th line and  $\underline{s}_{\underline{i}}$  is the estimated standard deviation of a single measurement (not to be confused with  $\sigma_{\underline{i}}$ ; roughly  $\underline{n}_{\underline{i}} \sigma_{\underline{i}}^2 = \underline{s}_{\underline{i}}^2$ , but  $\sigma_{\underline{i}}$  is the standard deviation of the 'population' of all possible measurements of  $\phi_{\underline{i}}$ , and is never known exactly, being estimated from the scatter of the actual observations). The function  $\underline{W}$  has approximately the same distribution as the chi-squared function (see, for example, Cramér, [117], p. 233) critical values of which are given in the third column of table 3. It will be seen that, at the 5 percent level used by Beu *et al.*, they do not differ appreciably from those given by the  $2\sigma_R$  criterion. The second term within the square brackets in eq. (14) is of the order of  $\underline{n}_{\underline{i}}^{-1}$ , so that  $\underline{W}$  reduces to  $\underline{R}$  if  $\underline{n}_{\underline{i}}$  is great enough to allow the approximation  $\log_e(1 + x) = x$ .

There is a procedural difficulty if  $\underline{n}_{\underline{i}}$  is not large: the variances  $\underline{s}_{\underline{i}}$  as well as the lattice parameters are estimated from the angle observations, so that the value of  $\underline{m}$  to be used in testing for remanent systematic error becomes indefinite without a more detailed statistical study of the whole process.

It must be pointed out that certain systematic errors would not be detected by the likelihood-ratio test proposed by Beu, Musil and Whitney or the practically equivalent procedure outlined above. As mentioned in Section 2, errors in the assumed wavelength do not reveal themselves through any inconsistency between values of lattice parameters determined at different Bragg angles. Consideration of eq. (5) indicates that the same would be true of any aberration producing a systematic error in  $\theta$  proportional to  $\tan\theta$  or approximately so. For the symmetrical diffractometer, the summaries given by Wilson [11,45,46] suggest that this undetectable category would include part of the axial divergence; absorption in the specimen, filters, etc.; variation of quantum-counting efficiency; refraction; and, for peaks but not for centroids, dispersion-plus-Lorentz-factor.

## 7. Summary

Analysis of the systematic errors affecting angle-dispersive powder diffractometry and the agreement between measurements made with different techniques within the same laboratory indicate that the accuracy of lattice-parameter measurement by powder methods ought to approach one part in 100,000.

A comparison made twenty years ago showed that the accuracy actually achieved in inter-laboratory comparisons was considerably lower, being hardly better than one part in 10,000. The development of diffractometry in the intervening years makes it probable that better accuracy could be achieved now, but there has been no recent comparison on the same scale.

Lattice-parameter measurement by energy-dispersive diffractometry has not been investigated as thoroughly; the best accuracy so far claimed is one part in 10,000.

There may be a systematic discrepancy between lattice parameters determined by single crystal and by powder methods (see Section 6), but, on the whole, the difference seems to be more probably related to imperfections introduced in the process of powdering.

Statistical tests exist for the effectiveness of the correction of certain systematic errors (see Section 6).

---

I am indebted to Professor B. Buras, Professor Michael Hart, Dr. L. D. Jennings, Dr. John Mandel, Dr. William Parrish and Professor R. A. Young for correspondence and offprints. Travel assistance from the International Centre for Diffraction Data is gratefully acknowledged.

## References

- [1] Bradley, A. J. and Jay, A. H., A method for deducing accurate values of the lattice spacing from x-ray powder photographs taken by the Debye-Scherrer method, Proc. Phys. Soc. 44, 563-579 (1932).

- [2] Wilson, A. J. C. and Lipson, H., The calibration of Debye-Scherrer x-ray powder cameras, Proc. Phys. Soc. Lond. 53, 245-250 (1941).
- [3] Parrish, W., Results of the I.U.Cr. precision lattice-parameter project, Acta Crystallographica, 13, 838-850 (1960).
- [4] Sandström, A. E., Experimental methods of x-ray spectroscopy: ordinary wavelengths, in Handbuch der Physik, Vol. 30 (Springer, Berlin, 1957), pp. 78-245, especially p. 157.
- [5] Thomsen, J. S., High-precision x-ray spectroscopy, in X-ray Spectroscopy, Chapter 2, L. V. Azaroff, ed. (McGraw-Hill, New York, 1974), pp. 26-132.
- [6] Lipson, H. and Rogers, E. R., The measurement of x-ray wavelengths by the powder method, Philosophical Magazine, 35, 544-549 (1944).
- [7] Wilson, A. J. C., Effect of absorption on mean wavelength of x-ray emission lines, Proc. Phys. Soc. Lond. 72, 924-925 (1958).
- [8] Delf, B. W., The effect of absorption in the  $\beta$  filter on the mean wavelength of x-ray emission lines, Proc. Phys. Soc. Lond., 78, 305-306 (1961a).
- [9] Delf, B. W., Response of an x-ray opposite window monitor system to changes in tube conditions, J. Sci. Instrum. 38, 359-360 (1961b).
- [10] Delf, B. W., Method of determining the specimen-surface displacement of an x-ray diffractometer, Brit. J. Appl. Phys. 12, 421-423 (1961c).
- [11] Wilson, A. J. C., Mathematical Theory of X-ray Powder Diffractometry (Centrex, Eindhoven, 1963), pp. x + 128.
- [12] Barth, H., Möglichkeit der Präzisionsgitterkonstantenmessungen mit hochmonochromatischer Röntgen-Strahlung, Acta Crystallographica 13, 830-832 (1960).
- [13] Wilson, A. J. C., On the correction of lattice spacings for refraction, Proc. Camb. Phil. Soc. 36, 485-489 (1940).
- [14] Wilson, A. J. C., Refraction broadening in powder diffractometry, Proc. Phys. Soc. Lond. 80, 303-305 (1962a).
- [15] Wilkens, M., Zur Brechungskorrektur bei Gitterkonstantenmessungen an Pulverpräparaten, Acta Crystallographica, 13, 826-828 (1960).
- [16] Spencer, R. C., Additional theory of the double x-ray spectrometer, Phys. Rev. 38, 618-629 (1931).
- [17] Spencer, R. C., The effect of the spectrometer on the width of spectral lines, Phys. Rev. 48, 473 (1935).
- [18] Spencer, R. C., A theorem on the effect of vertical divergence, Phys. Rev., 52, 761 (1937).
- [19] Spencer, R. C., The correction of experimental curves for the resolving power of the apparatus, Phys. Rev. 55, 239 (1939).
- [20] Spencer, R. C., Optimum design of physical apparatus, Phys. Rev. 60, 172 (1941).
- [21] Spencer, R. C., Discussion of "Geometrical factors affecting x-ray spectrometer maxima," J. Appl. Phys. 20, 413-414 (1949).
- [22] Wilson, A. J. C., Geiger-counter x-ray spectrometer - influence of size and absorption coefficient of specimen on position and shape of powder diffraction maxima, J. Sci. Instrum. 27, 321-325 (1950).

- [23] Pike, E. R. and Wilson, A. J. C., Counter diffractometer - the theory of the use of centroids of diffraction profiles for high accuracy in the measurement of diffraction angles, *Brit. J. Appl. Phys.* 10, 57-68 (1959).
- [24] Edwards, H. J. and Toman, K., The additivity of variances in powder diffraction profile analysis, *J. Appl. Cryst.* 3, 165-171 (1970).
- [25] Wilson, A. J. C., Limitations on the additivity of moments in line-profile analysis, *J. Appl. Cryst.* 3, 71-73 (1970b).
- [26] Wilson, A. J. C., A note on peak displacements in x-ray diffractometry, *Proc. Phys. Soc. Lond.* 78, 249-255 (1961).
- [27] Gale, B., The positions of Debye diffraction line peaks, *Brit. J. Appl. Phys.* 14, 357-364 (1963).
- [28] Gale, B., The aberrations of a focusing x-ray diffraction instrument: second-order theory, *Brit. J. Appl. Phys. (J. Phys. D)*, 1, 393-408 (1968).
- [29] Wilson, A. J. C. and Delf, B. W., Effect of variations in the quantum counting efficiency of detectors on the mean wavelength of x-ray emission lines, *Proc. Phys. Soc. Lond.* 78, 1256-1258 (1961).
- [30] Wilson, A. J. C., Röntgenstrahlpulverdiffraktometrie. Mathematische Theorie (Centrex, Eindhoven, 1965c), pp. ix + 139.
- [31] Alexander, L., Geometrical factors affecting the contours of x-ray spectrometer maxima. I. Factors causing asymmetry, *J. Appl. Phys.* 19, 1068-1071 (1948).
- [32] Alexander, L., Geometrical factors affecting the contours of x-ray spectrometer maxima. II. Factors causing broadening, *J. Appl. Phys.* 21, 126-136 (1950).
- [33] Alexander, L., The effect of vertical divergence on x-ray powder diffraction lines, *Brit. J. Appl. Physics*, 4, 92-93 (1953).
- [34] Alexander, L., The synthesis of x-ray spectrometer line profiles with application to crystallite size measurements, *J. Appl. Phys.* 25, 155-161 (1954).
- [35] Boom, G., Accurate Lattice Parameters and the LPC Method (Groningen: van Denderen, 1966), pp. x + 212.
- [36] Boom, G. and Smits, D. W., Calculation of Debye-Scherrer diffraction line profiles and their applications in precision determination of lattice parameters, *Proc. K. Ned. Akad. Wetensch., Amsterdam*, B68, 46-52 (1965).
- [37] Rietveld, H. M., Line profiles of neutron powder-diffraction peaks for structure refinement, *Acta Crystallographica*, 22, 151-152 (1967).
- [38] Rietveld, H. M., A profile refinement method for nuclear and magnetic structures, *J. Appl. Cryst.* 2, 65-71 (1969).
- [39] Glazer, A. M., Hidaka, M., and Bordas, J., Energy-dispersive powder profile refinement using synchrotron radiation, *J. Appl. Cryst.* 11, 165-172 (1978).
- [40] Huang, T. C. and Parrish, W., Accurate and rapid reduction of experimental x-ray data, *Applied Physics Letters*, 27, 123-124 (1975).
- [41] Mantler, M. and Parrish, W., Energy dispersive x-ray diffractometry, *Advances in X-ray Analysis*, 20, 171-186 (1977).
- [42] Parrish, W., Huang, T. C., and Ayers, G. L., Profile fitting: a powerful method of computer x-ray instrumentation and analysis, *Trans. ACA* 12, 55-73 (1976).

- [43] Young, R. A., Mackie, P. E., and Von Dreele, R. B., Application of pattern-fitting structure-refinement method to x-ray diffractometer patterns, *J. Appl. Cryst.* 10, 262-269 (1977).
- [44] Young, R. A., Mackie, P. E., and Wiles, D. B., Rietveld pattern-fitting-structure-refinement ('profile refinement'), private communication. (To be published, 1979.)
- [45] Wilson, A. J. C., Elements of X-ray Crystallography (Addison-Wesley, Reading, Massachusetts, 1970a), pp. 256.
- [46] Wilson, A. J. C., Powder diffractometry, in X-ray Diffraction, Chapter 6, L. V. Azaroff, R. Kaplow, N. Kato, R. J. Weiss, A. J. C. Wilson, and R. A. Young (McGraw-Hill, New York, 1974), pp. 438-499 and 637-643.
- [47] Mack, M. and Parrish, W., Seemann-Bohlin x-ray diffractometry. II. Comparison of aberrations and intensity with conventional diffractometer, *Acta Crystallographica*, 23, 693-700 (1967).
- [48] Langford, J. I. and Wilson, A. J. C., Counter diffractometer: the effect of specimen transparency on the intensity, position and breadth of x-ray powder diffraction lines, *J. Sci. Instrum.* 39, 581-585 (1962).
- [49] Milberg, M. E., Transparency factor for weakly absorbing samples in x-ray diffractometry, *J. Appl. Phys.* 29, 64-65 (1958).
- [50] Vonk (1961).
- [51] Wilson, A. J. C., Counter diffractometer: The effect of specimen position on the intensity, position, and breadth of x-ray powder diffraction lines, *Soviet Physics-Crystallography*, 16, 991-993 (1972).
- [52] Sparks, C. J. and Gedcke, D. A., Rapid recording of powder diffraction patterns with Si(Li) x-ray energy analysis system: W and Cu targets and error analysis, *Advances in X-ray Analysis*, 15, 240-253 (1972).
- [53] Fukamachi, T., Hosoya, S., and Terasaki, O., The precision of interplanar distances measured by an energy-dispersive diffractometer, *J. Appl. Cryst.* 6, 117-122 (1973).
- [54] Nakajima, T., Fukamachi, T., Terasaki, O., and Hosoya, S., The detection of small differences in lattice constant at low temperature by an energy-dispersive x-ray diffractometer, *J. Appl. Cryst.* 9, 286-290 (1976).
- [55] Gillham, C. J., Centroid shifts due to axial divergence and other geometrical factors in Seemann-Bohlin diffractometry, *J. Appl. Cryst.* 4, 498-506 (1971).
- [56] Pike, E. R., Counter diffractometer - the effect of vertical divergence on the displacement and breadth of powder diffraction lines, *J. Sci. Instrum.* 34, 355-361 (1957).
- [57] Gillham, C. J. and King, H. W., Measurement of centroid and peak shifts due to dispersion and the Lorentz factor at very high Bragg angles, *J. Appl. Cryst.* 5, 23-27 (1972).
- [58] Soller, W., A new precision x-ray spectrometer, *Phys. Rev.* 24, 158-167 (1924).
- [59] Wilson, A. J. C., Note on the aberrations of a fixed-angle energy-dispersive diffractometer, *J. Appl. Cryst.* 6, 230-237 (1973).

- [60] Bourdillon, A. J., Glazer, A. M., Hidaka, M., and Bordas, J., High-resolution energy-dispersive diffraction using synchrotron radiation, *J. Appl. Cryst.* 11, 684-687 (1978).
- [61] Buras, B., Staun Olsen, J., Gerward, L., Will, G., and Hinze, E., X-ray energy-dispersive diffractometry using synchrotron radiation, *J. Appl. Cryst.* 10, 431-438 (1977).
- [62] Laguitton, D. and Parrish, W., Experimental spectral distribution versus Kramers' Law for quantitative x-ray fluorescence by the fundamental parameters method, *X-ray Spectrometry*, 6, 201-203 (1977).
- [63] Okazaki, A. and Kawaminami, M., Accurate measurement of lattice constant in a wide range of temperature: use of white x-rays and double-crystal diffractometry, *Jap. J. Appl. Phys.* 12, 783-789 (1973).
- [64] Mack, M. and Spielberg, N., Statistical factors in x-ray intensity measurements, *Spectrochim. Acta*, 12, 169-178 (1958).
- [65] Thomsen, J. S. and Yap, F. Y., Effect of statistical counting errors on wavelength criteria for x-ray spectra, *J. Res. Nat. Bur. Standards*, 72A, 187-205 (1968a).
- [66] Thomsen, J. S. and Yap, F. Y., Simplified method of computing centroids of x-ray profiles, *Acta Crystallographica*, A24, 702-703 (1968b).
- [67] Wilson, A. J. C., On variance as a measure of line broadening in diffractometry. IV. The effect of physical aberrations. *Proc. Phys. Soc. Lond.* 85, 171-176 (1965a).
- [68] Wilson, A. J. C., The location of peaks, *Brit. J. Appl. Phys.* 16, 665-674 (1965b).
- [69] Wilson, A. J. C., Statistical variance of line-profile parameters. Measures of intensity, location and dispersion, *Acta Crystallographica* 23, 888-898 (1967).
- [70] Wilson, A. J. C., Statistical variance of line-profile parameters. Measures of intensity, location and dispersion: Corrigenda, *Acta Crystallographica*, A24, 478 (1968).
- [71] Wilson, A. J. C., Statistical variance of line-profile parameters: Addendum, *Acta Crystallographica*, A25, 584-585 (1969).
- [72] Wilson, A. J. C., Some statistical considerations in the location of Mössbauer lines, *Nuclear Instruments and Methods*, 94, 225-227 (1971).
- [73] Wilson, Thomsen, and Yap (1965).
- [74] Zevin, L. S., Umanskij, M. M., Khejker, D. M., and Pančenko, J. M., The question of diffractometer methods of precision measurement of unit-cell parameters, *Soviet Physics-Crystallography*, 6, 277-283 (1961).
- [75] Nelson, J. B. and Riley, D. P., An experimental investigation of extrapolation methods in the derivation of accurate unit-cell dimensions of crystals, *Proc. Phys. Soc.* 57, 160-177 (1945).
- [76] Taylor, A. and Sinclair, H. B., The influence of absorption on the shapes and positions of lines in Debye-Scherrer powder photographs, *Proc. Phys. Soc.* 57, 108-135 (1945).
- [78] Cohen, M. U., Precision lattice constants from x-ray powder photographs, *Rev. Sci. Instrum.* 6, 68-74 (1935).

- [79] Mueller, M. H., Heaton, L., and Miller, K. T., Determination of lattice parameters with the aid of a computer, *Acta Crystallographica*, 13, 828-829 (1960).
- [80] Vogel, R. E. and Kempter, C. P., A mathematical technique for the precision determination of lattice parameters, *Acta Crystallographica*, 14, 1130-1134 (1961).
- [81] Hess, J. B., A modification of the Cohen procedure for computing precision lattice constants from powder data, *Acta Crystallographica*, 4, 209-215 (1951).
- [82] Langford, J. I. and Wilson, A. J. C., Geometrical and statistical aspects of the accuracy of camera powder data, *J. Appl. Cryst.* 6, 197-202 (1973).
- [83] Langford, J. I., The accuracy of cell dimensions determined by Cohen's method of least-squares and the systematic indexing of powder data, *J. Appl. Cryst.* 6, 190-196 (1973).
- [84] Warczewski, J. and de Wolff, P. M., Standard deviations of lattice parameters obtained from powder data measurements, *J. Appl. Cryst.* 7, 585-587 (1974).
- [85] Warczewski, J., An Improved Computer Program for the Determination of Standard Deviations of Lattice Parameters Obtained from the Powder Patterns. Full Description (Instytut Fizyki i Techniki Jadrowej AGH, Kraków, 1977), pp. 40.
- [86] Straumanis, M. and Ievičs, A., Präzisionsaufnahmen nach der Verfahren von Debye and Scherrer. II, *Z. Physik*, 98, 461-475 (1936).
- [87] Delf, B. W., The practical determination of lattice parameters using the centroid method, *Brit. J. Appl. Phys.* 14, 345-350 (1963).
- [88] Beu, K. E., The evaluation of centroid lattice parameter data for tungsten by the likelihood ratio method, *Acta Crystallographica*, 17, 1149-1154 (1964).
- [89] Bond, W. L., Precision lattice constant determination, *Acta Crystallographica*, 13, 814-818 (1960).
- [90] Beu, K. E., Musil, F. J., and Whitney, D. R., Precise and accurate lattice parameters by film powder methods. I. The likelihood ratio method, *Acta Crystallographica*, 15, 1291-1301 (1962).
- [91] Beu, K. E., Musil, F. J., and Whitney, D. R., The likelihood ratio method for the precise and accurate determination of lattice parameters for tetragonal and hexagonal crystals, *Acta Crystallographica*, 16, 1241-1242 (1963).
- [92] Beu, K. E. and Scott, D. L., Precise and accurate lattice parameters by film powder methods. II. An exact eccentricity correction for cylindrical film cameras, *Acta Crystallographica*, 15, 1301-1304 (1962).
- [93] Beu, K. E., Landstrom, D. K., Whitney, D. R., and Pike, E. R., Precise and accurate lattice parameters by film powder methods. III. An exact graphical method for axial (vertical) divergence profiles for cylindrical diffraction cameras, *Acta Crystallographica*, 17, 639-645 (1964).
- [94] Langford, J. I., Pike, E. R., and Beu, K. E., Precise and accurate lattice parameters by film powder methods. IV. Theoretical calculations of axial (vertical) divergence profiles, centroid shifts, and variances for cylindrical powder diffraction cameras, *Acta Crystallographica*, 17, 645-651 (1964).
- [95] Fisher, R. A., On an absolute criterion for fitting frequency curves, *Messenger of Mathematics*, 41, 155-160 (1912).

- [96] Fisher, R. A., On the 'probable error' of a coefficient of correlation deduced from a small sample, *Metron*, 1, part 4, 3-32 (1921).
- [97] Fisher, R. A., On the mathematical foundations of theoretical statistics, *Phil. Trans. Roy. Soc.* A222, 309-368 (1922).
- [98] Edwards, A. W. F., *Likelihood* (University Press, Cambridge, 1972), pp. xv + 235.
- [99] Kirk, D. and Caulfield, P. B., Location of diffractometer profiles in x-ray stress analysis, *Advances in X-ray Analysis*, 20, 283-289 (1977).
- [100] Price, P. F., A comparison of least-squares and maximum-likelihood estimators for counts of radiation quanta which follow a Poisson distribution, *Acta Crystallographica* A35, 57-60 (1979).
- [101] Hamilton, W. C., *Statistics in Physical Science* (The Ronald Press, New York, 1964), pp. xi + 230.
- [102] Bard, Y., *Nonlinear Parameter Estimation* (Academic Press, New York, 1974), pp. x +
- [103] Bond, W. L., Precision lattice constant determination. Erratum, *Acta Crystallographica*, A31, 698 only (1975).
- [104] Burke, J. and Tomkeieff, M. V., Specimen and beam tilt errors in Bond's method of lattice parameter determination, *Acta Crystallographica*, A24, 683-685 (1968).
- [105] Burke, J. and Tomkeieff, M. V., Errors in the Bond method of lattice parameter determination - Further considerations, *J. Appl. Cryst.* 2, 247-248 (1969).
- [106] Gruber, E. E. and Black, R. E., Analysis of the axial misalignment error in precision lattice parameter measurement by the Bond technique, *J. Appl. Cryst.* 3, 354-357 (1970).
- [107] Halliwell, M. A. G., Measurement of specimen tilt and beam tilt in the Bond method, *J. Appl. Cryst.* 3, 418-419 (1970).
- [108] Hubbard, C. R. and Mauer, F. A., Precision and accuracy of the Bond method as applied to small spherical crystals, *J. Appl. Cryst.* 9, 1-8 (1976).
- [109] Walder, V. and Burke, J., The elimination of specimen and beam tilt errors in the Bond method of precision lattice parameter determinations, *J. Appl. Cryst.* 4, 337-339 (1971).
- [110] Łukaszewicz, K., Pietraszko, A., Kucharczyk, D., Malinowski, M., Stępiń-Damm, J., and Urbanowicz, E., *Precyzyjne pomiary stałych sieciowych kryształów metoda Bond'a* (Wrocław: Instytut Niskich Temperatur i Badań Strukturalnych PAN, 1976), pp. 100.
- [111] Urbanowicz, E., The application of the convolution relations to the x-ray diffraction profile analysis in Bond's method, *Acta Crystallographica*, A34, S35 only (1978).
- [112] Pike, E. R. and Wilson, A. J. C., Effect of Lorentz factor and dispersion on measurement of lattice parameters with powder cameras, *Proc. Phys. Soc. Lond.* 72, 908-910 (1958).
- [113] Hubbard, C. R., Swanson, H. E., and Mauer, F. A., A silicon powder diffraction standard reference material, *J. Appl. Cryst.* 8, 45-48 (1975).
- [114] Ando, M., Bailey, D., and Hart M., A simple Bragg-spacing comparator, *Acta Crystallographica*, A34, 484-489 (1978).
- [115] Wilson, A. J. C., The thermal expansion of aluminium from 0° to 650°C, *Proc. Phys. Soc. Lond.* 53, 235-244 (1941).

- [116] Wilson, A. J. C., The thermal expansion of aluminium: further experiments, Proc. Phys. Soc. Lond. 54, 487-491 (1942).
- [117] Cramér, H., Mathematical Methods of Statistics (Almqvist and Wiksells, Uppsala, 1945), pp. xvi + 575.

#### Bibliography

- Ayers, G. L., Huang, T. C., and Parrish, W., High-speed x-ray analysis, J. Appl. Cryst. 11, 229-233 (1978).
- Buras, B., Niimura, N., and Staun Olsen, J., Optimum resolution in x-ray energy-dispersive diffractometry, J. Appl. Cryst. 11, 137-140 (1978).
- Delf, B. W., A comment on centroid truncation procedures, Acta Crystallographica, 17, 770-771 (1964).
- Fukamachi, T., Nakano, Y., Hosoya, S., and Shimomura, O., Applications of a two-circle SSD diffractometer in the angle-dispersive mode, J. Appl. Cryst. 11, 688-692 (1978).
- Kunze, G., Korrekturen höherer Ordnung für die mit Bragg-Brentano- und Seemann-Bohlin-Systemen gewonnenen Messgrößen (unter Berücksichtigung der Primärstrahl-divergenz), Zeitschrift für angewandte Physik, 17, 412-421 (1964a).
- Kunze, G., Intensitäts-, Absorptions- und Verschiebungsfaktoren von Interferenzlinien bei Bragg-Brentano- und Seemann-Bohlin-Diffraktometern. I. Zeitschrift für angewandte Physik, 17, 522-534 (1964b).
- Kunze, G., Intensitäts-, Absorptions- und Verschiebungsfaktoren von Interferenzlinien bei Bragg-Brentano- und Seemann-Bohlin-Diffraktometern. II. Zeitschrift für angewandte Physik, 18, 28-37 (1964c).
- Ladell, J., Mack, M., Parrish, W., and Taylor, J., Dispersion, Lorentz and polarization effects in the centroid method of precision lattice parameter determination, Acta Crystallographica 12, 567-570 (1959).
- Ladell, J., Parrish, W., and Taylor, J., Center-of-gravity method of precision lattice parameter determination, Acta Crystallographica, 12, 253-254 (1959a).
- Ladell, J., Parrish, W., and Taylor, J., Interpretation of diffractometer line profiles, Acta Crystallographica, 12, 561-567 (1959b).
- Lang, A. R., Effect of dispersion and geometric intensity factors on x-ray back-reflection line profiles, J. Appl. Phys. 27, 485-488 (1956).
- Lipson, H. and Wilson, A. J. C., The derivation of lattice spacings from Debye-Scherrer photographs, J. Sci. Instrum. 18, 144-148 (1941).
- Mitchell, C. M. and de Wolff, P. M., Elimination of the dispersion effect in the analysis of diffraction line profiles, Acta Crystallographica, 22, 325-328 (1967).
- Parrish, W., X-ray intensity measurements, Geiger, proportional and scintillation counters, in International Tables for Crystallography, Vol. III (The Kynoch Press, Birmingham, 1962), pp. 144-156.
- Parrish, W. and Mack, M., Seemann-Bohlin x-ray diffractometry. I. Instrumentation, Acta Crystallographica, 23, 687-692 (1967).

- Parrish, W. and Wilson, A. J. C., Precision measurement of lattice parameters of polycrystalline specimens, International Tables for X-ray Crystallography, Vol. II (The Kynoch Press, Birmingham, 1959), pp. 216-234.
- Parrish, W. and Wilson, A. J. C., Precision measurement of lattice parameters of polycrystalline specimens: Erratum in the International Tables for X-ray Crystallography, Acta Crystallographica, 14, 439 (1961).
- Pike, E. R., Lattice parameter determination from broad diffraction lines, J. Sci. Instrum. 35, 34-35 (1958).
- Pike, E. R., Counter diffractometer - the effect of vertical divergence on the displacement and breadth of powder diffraction lines. Errata, J. Sci. Instrum. 36, 52-53 (1959a).
- Pike, E. R., Counter diffractometer - the effect of dispersion, Lorentz and polarisation factors on the positions of x-ray powder diffraction lines, Acta Crystallographica, 12, 87-92 (1959b).
- Pike, E. R. and Ladell, J., The Lorentz factor in powder diffraction, Acta Crystallographica, 14, 53-54 (1961).
- Taylor, J., Mack, M., and Parrish, W., A method for the determination of the centroid of an x-ray distribution, Acta Crystallographica, 16, 1179-1180 (1963).
- Tempest, P. A., The influence of specimen absorption and beam divergence on the accurate determination of lattice parameters by the Debye-Scherrer method, J. Appl. Cryst. 10, 238-246 (1977).
- Wassermann, G. and Wiewiorowsky, J., Über ein Geiger-Zählrohr-Goniometer nach dem Seemann-Bohlin-Prinzip, Z. Metallkunde, 44, 567-570 (1953).
- Weyerer, H., Verfeinerung der Auswerteverfahren für die Präzisionsbestimmung von Gitterkonstanten kubischer Kristalle nach der Pulvermethode, Z. Kristallogr. 109, 338-353 (1957a).
- Weyerer, H., Extrapolationsmethoden für Pulveraufnahmen von nichtkubischen Kristallen, Z. Kristallogr. 109, 354-366 (1957b).
- Willis, K. E., An explicit expression for the lattice parameters of cubic crystals for the ratio method, Acta Crystallographica, 14, 1090-1091 (1961).
- Wilson, A. J. C., Straumanis' method of film-shrinkage correction modified for use without high-angle lines, Rev. Sci. Instrum. 20, 831-832 (1949).
- Wilson, A. J. C., X-ray emission spectra and lattice-parameter determination, Bulletin of the National Institute of Sciences of India, No. 14, pp. 91-93 (1959a).
- Wilson, A. J. C. Some problems in the definition of wavelengths in x-ray crystallography, Z. Kristallogr. 111, 471-476 (1959b).
- Wilson, A. J. C., On variance as a measure of line broadening in diffractometry. I. General theory and small particle size, Proc. Phys. Soc. Lond. 80, 286-294 (1962b).
- Wilson, A. J. C., Aberrations and line broadening in x-ray powder diffractometry, in Advanced Methods of Crystallography, G. N. Ramachandran, ed. (Academic Press, London, 1964), pp. 221-250.

de Wolff, P. M., Reliability of unit cells derived from powder diffraction patterns, *Acta Crystallographica*, 14, 579-582 (1961).

Young, R. A., Gerdes, R. J., and Wilson, A. J. C., Propagation of some systematic errors in x-ray line-profile analysis, *Acta Crystallographica*, 22, 155-162 (1967).

Zevin, L. S., Umanskij, M. M., and Khejker, D. M., Geometric aberrations and optimum conditions for diffractometric measurements of polycrystals, *Soviet Physics-Crystallography*, 8, 663-673 (1963).

#### Discussion

Question (Calvert): Do you have any comments on reports of accuracy of  $1:10^7$  by Baker and co-workers at Harwell with a diffractometer (Publ. in Nature)?

Response (Wilson): The reference is T. W. Baker, J. D. George, B. A. Ballamy and Causer, *Nature*, 210, 720-721 (1966). The method is essentially that of Bond, though the accuracy of angle measurement, temperature control etc. is unusually high. The precision of 1 in  $10^7$  is thus credible.



## SOME STATISTICAL ASPECTS OF LATTICE PARAMETER EVALUATION

John Mandel  
National Measurement Laboratory  
National Bureau of Standards  
Washington, DC 20234

### 1. Introduction

Translated into statistical terminology the problem of estimating lattice parameters may be regarded as that of estimating the unknown parameters of a distribution function, given a statistical model and a set of experimental data. In this formulation, the nature of the distribution function of the observed data is assumed to be known. In practice, a Gaussian distribution is generally assumed to hold. On the other hand, the method of least squares does not require that such a specific assumption be made, unless it is desired to make tests of significance.

In Chapter 10, Kaelble's Handbook of X-Rays [1]<sup>1</sup>, entitled "The Precise and Accurate Determination of Lattice Parameters", by Karl E. Beu, a special statistical technique, known as the Likelihood Ratio Method (LRM), is proposed for the statistical treatment of lattice parameter measurements. The objective of this paper is to discuss this technique and to compare it with the more commonly used least squares estimation procedure.

### 2. The Likelihood Ratio Method

As an illustration, we will use the data discussed by Beu in his chapter: Delf's centroid data on tungsten. The data are summarized in table 1. The objective is to determine the parameter  $a_0$  in the equation

$$a_0 \sin \theta_i = K_i \quad (1)$$

where  $K_i$  is a known function of wavelength for each diffraction line. The statistical model underlying the Likelihood Ratio Method is best understood by rewriting the model as shown in table 2. It is assumed that a set of (systematic) "corrections" have been applied to the observed Bragg angles, yielding the corrected values  $\psi_{ij}$ , where the index  $j$  refers to the  $j$ th replicate measurement made for the diffraction line  $i$ . A random measurement error,  $\delta_{ij}$ , with standard deviation  $\sigma_i$ , affects the corrected value. Furthermore, the possibility is considered that the systematic corrections that were made may be inadequate, leaving an

<sup>1</sup>Figures in brackets indicate the literature references at the end of this paper.

Table 1. Delf's Centroid Data on Tungsten

$i = (hkl)$	$n_i$	$\bar{\psi}_i$ degrees	$S_i$ degrees
(110)	7	19.75061	$8.42 \times 10^{-4}$
(211)	7	36.23581	5.91 "
(310)	9	49.96961	9.23 "
(321)	8	65.30461	26.23 "

Table 2. Statistical Model

$$a_0 \sin \theta_i = K_i$$

$$i = (hkl)$$

$$a_0 \sin[(\psi_j + \delta_j)_i + e_i] = K_i$$

$\psi_j$  = corrected measurement of Bragg angle

$\delta_j$  = random error

$e_i$  = remaining systematic error

unknown residual systematic error  $e_i$  that affects all measurements made for the diffracted line  $i$ . This yields the equation

$$a_0 \sin[(\psi_j + \delta_j)_i + e_i] = K_i \quad (2)$$

For the Delf data,  $i$  goes from 1 to 4. Therefore the number of parameters is 9: one for  $a_0$ , four for the  $\sigma_i$  and four for the  $e_i$ . We can visualize the values of these parameters as a point in a nine-dimensional space, and the objective of the statistical analysis proposed by Beu is to find the "best" point in this space, and to estimate its adequacy. For this effect, a two-step analysis is made.

The first step, which uses the Likelihood Ratio, is essentially a statistical test whether the point in question lies in a specified subspace  $\underline{w}$ , (see fig. 1) given that it lies in the larger subspace  $\underline{Q}$ . This requires that both subspaces  $\underline{w}$  and  $\underline{Q}$  be completely specified. Beu specifies them through the statements shown in figure 2. Thus, the question to be answered by the Likelihood Ratio Test is whether it is reasonable to conclude

## Likelihood Ratio Method, I

### Parameters

$$\left. \begin{array}{l} a_0 \\ \sigma_i ; i = 1 \text{ to } 4 \\ e_i ; i = 1 \text{ to } 4 \end{array} \right\} 9 \text{ parameters}$$

### Nine-Dimensional Parameter Space

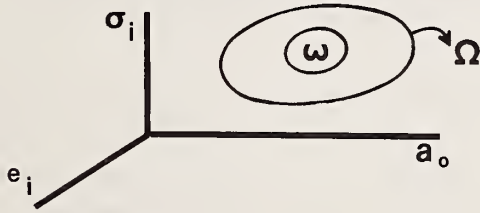
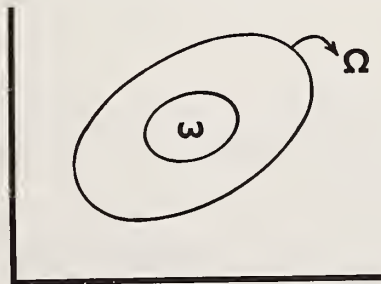


Figure 1.

## Likelihood Ratio Method, II



$$\Omega \text{ defined by } \sum_i e_i = 0$$

$$\omega \text{ defined by } e_i = 0 \text{ for all } i$$

Figure 2.

that no systematic errors  $e_i$  remain, given that the algebraic sum of the four systematic errors  $e_i$  is zero. The Likelihood Ratio Test consists in first finding the point in  $\underline{\Omega}$  for which the probability of the observed data is maximum, and calculating this probability, denoted by  $P_{\text{Max}}(\underline{\Omega})$ . Next the same procedure is followed for  $\underline{w}$ , yielding the probability  $P_{\text{Max}}(\underline{w})$ . Finally, the "likelihood ratio"  $\lambda$  is calculated by the equation (see fig. 3):

$$\lambda = \frac{P_{\text{Max}}(\underline{w})}{P_{\text{Max}}(\underline{\Omega})} \quad (3)$$

A large value of  $\lambda$  indicates, roughly stated, that the probability that the true parameter point is in  $\underline{w}$  is almost as large as the probability that it is in  $\underline{\Omega}$ , thus giving credibility to the hypothesis that the point is in  $\underline{w}$ . The statistical procedure for test  $\lambda$  is through the use of the chi-square distribution [2].

If the outcome of the Likelihood Ratio Test points to the acceptability of  $\underline{w}$ , then the second step of the analysis is carried out. This consists in adopting the point in  $\underline{w}$  for which the maximum probability was realized, as the best estimate point of the unknown parameters, and to calculate the standard errors of these parameter estimates.

The results of Beu's analysis are shown in table 3, for six different sets of corrections (see Beu's chapter for a description of these corrections). For purposes of comparison, the table also shows the results of the weighted least squares analysis.

For our problem, the least squares analysis reduces to a simple weighted straight line regression [3,4], by writing eq. (1) in the form:

$$\sin \theta_i = \frac{1}{a_0} K_i + \text{error} \quad (4)$$

The  $\theta_i$  are estimated by the corresponding  $\psi_i$  (see table 1). Equation (4) shows that  $\frac{1}{a_0}$  is the slope of a straight line going through the origin. The error term can be specified by calculating the standard error of  $\sin \theta_i$ , for each  $i$ , using the estimates of the standard deviations  $s_i$  of table 1, and the law of propagation of errors [4], to convert an error of an angle to the corresponding error of its sine. The calculations are those of a weighted straight line regression through the origin. The quantity denoted as "Weighted Root Mean Square Residual" is discussed below.

### 3. Discussion

The Likelihood Ratio method, as used by Beu, raises a number of important points.

1. The specification for the  $\underline{\Omega}$  region is highly artificial. There appears to exist no logical basis for defining  $\underline{\Omega}$  by the constraint that the algebraic sum of the remaining systematic errors must be zero. Against this it may be argued that the test is probably not too much affected by the exact nature of the constraint used to define  $\underline{\Omega}$ . Be that as it may, the logic of the procedure appears to be less than satisfactory.

## Likelihood Ratio Method, III

1. In  $\Omega$ , find point for which the probability of the observed data is maximum:

$$P_{\text{Max}} (\Omega)$$

2. In  $\omega$ , find point for which the probability of the observed data is maximum:

$$P_{\text{Max}} (\omega)$$

3. Test criterion for  $\omega$ :

$$\lambda = \frac{P_{\text{Max}} (\omega)}{P_{\text{Max}} (\Omega)}$$

Figure 3

Table 3. Results for Delf's Data

Corrections	Maximum Likelihood			Weighted Least Squares		
	$\hat{a}_0$	$s_{\hat{a}_0}$	$\chi^2$ Test	$\hat{a}_0$	$s_{\hat{a}_0}$	s
none	3.183657	$14 \times 10^{-6}$	significant	3.187413	$6000 \times 10^{-6}$	61.67
+ 3	3.165020	$14 \times 10^{-6}$	significant	3.165175	$207 \times 10^{-6}$	21.68
+ 2 + 3	3.164937	$14 \times 10^{-6}$	significant	3.165061	$163 \times 10^{-6}$	17.04
+ 2 + 3 + 4	3.164934	$12 \times 10^{-6}$	significant	3.164966	$48 \times 10^{-6}$	4.99
+ 2 + 3 + 4 + 6	3.164934	$10 \times 10^{-6}$	significant	3.164930	$18 \times 10^{-6}$	1.89
1 6	3.164942	$10 \times 10^{-6}$	not significant	3.164942	$9 \times 10^{-6}$	.90

2. Beu uses nine parameters to describe the parameter space. Four of these are the standard deviations  $\sigma_i$ . But our interest is predominantly in  $a_0$  and the adequacy of the corrections (i.e. the equality of all  $e_i$  to zero). To include the  $\sigma_i$  in the estimation process appears to be undesirable. By contrast, the least squares procedure uses the estimates of the  $\sigma_i$  only as weighting factors. It is well known that the results of a least squares analysis are not greatly affected by moderate changes in the weights. If attention is at all directed to the  $\sigma_i$ , through examination of their estimates  $s_i$ , it should be in terms of detecting possible outliers in the data, by comparing the  $s_i$  with corresponding values obtained in previous experiments.

3. The Likelihood Ratio Method requires the assumption of a specific underlying error distribution for the measurements. It is here assumed that the random errors in measuring Bragg angles are Gaussian. To give credibility to this assumption, it should be subjected to experimental verification. The method of least squares, on the other hand, can be justified without recourse to assumptions of normality and is indeed less vulnerable than the Likelihood Method to departures from Gaussian behavior.

4. The use of the chi-square distribution to test the likelihood ratio  $\lambda$  is valid asymptotically when the number of degrees of freedom is large [2]. In the present case, it is used for 3 degrees of freedom, raising questions of validity of the test.

5. Finally, there appears to be an advantage in the use of the Likelihood Ratio Method, over the least squares procedure in that the former provides a statistical test of the adequacy of the corrections. But it has already pointed out that the validity of this test is questionable for small numbers of degrees of freedom. Furthermore, the weighted least squares method too provides means to judge the adequacy of the corrections. Indeed an examination of the weighted residuals, and their mean-square, can throw considerable light on the adequacy of the data. This may be illustrated by comparing, for example, the third and the sixth sets in table 3.

Let us first define the "weighted residuals." If  $w_i$  is the weight (reciprocal of the error variance) for the  $i^{\text{th}}$  point in the equation

$$y_i = \beta x_i + \varepsilon_i$$

then the  $i^{\text{th}}$  weighted residual is defined by

$$d_i = (y_i - \hat{\beta} x_i) \sqrt{w_i}$$

where  $\hat{\beta}$  is the least squares estimate of  $\beta$ . In our case,  $x_i = K_i$  and  $y_i = \sin \psi_i$ . It can be shown that if the  $w_i$  are the correct weights (or reasonably close to the correct weights) and if the straight line assumption is valid, then the sum of the squares of the  $d_i$ , divided by one less than the number of points, has an expected value of unity. Furthermore, these residuals should be randomly distributed above and below the fitted line.

The weighted residuals for the two sets in question are shown in table 4, together with the weighted root mean square residuals. It is clear that the correction set (1+2+3) does not yield a satisfactory fit, whereas the correction set (1+2+3+4+5+6) is entirely satisfactory.

Table 4. Weighted Residuals

<u>Corrections (1 + 2 + 3)</u>	<u>Corrections (1 + 2 + 3 + 4 + 5 + 6)</u>
-21.66	-1.38
-12.25	.52
8.65	-.28
13.31	.40
WRMSR <sup>a</sup> 17.04	.90

(a) weighted root mean square residual

#### 4. Conclusion

The Likelihood Ratio method presents an interesting approach to the problem of lattice parameter estimation. It lends itself to the simultaneous estimation of any number of parameters, provided sufficient data are available. However, this method suffers from a number of drawbacks not shared by the least squares estimation procedure. There seems to be no convincing reasons for adopting this technique without further study and refinements.

#### References

- Kaelble, E. F., Handbook of X-Rays (McGraw-Hill Book Company, N.Y., 1967).  
 Larson, H. J., Introduction to Probability Theory and Statistical Inference (John Wiley & Sons, N.Y., 1974).  
 Draper, N. R. and Smith, H., Applied Regression Analysis (John Wiley & Sons, N.Y., 1966).  
 Mandel, J., The Statistical Analysis of Experimental Data (John Wiley & Sons, N.Y., 1964).

## Discussion

Comments (Wilson): Since submitting my typescript I have looked into the problem of estimating the standard deviation,  $\sigma_R$ , of  $R_{\min}$  when the distribution of the random error measured angles  $\phi_i$  is not normal. The expected value of  $R_{\min}$  remains  $\underline{n-m}$ , but equation is replaced by

$$\sigma_R^2 = (2+\gamma_2)\underline{n} - 2(1+\gamma_2)\underline{m} \quad , \quad (15)$$

plus a further complicated term depending on the fourth-order products of the derivative of  $\theta_i$  with respect to the parameters to be estimated;  $\gamma_2$  is a measure, called the excess or the kurtosis, of the extent to which the error distribution is taller and slimmer than the normal (shorter and fatter for negative  $\gamma_2$ ). Examination of the raw data used by Langford (1973) indicated that for actual film measurements some observers had appreciable non-normal error distributions, with values of  $\gamma_2$  lying in the range -1 to +1. For diffractometer measurements a theoretical value of  $\gamma_2$  could be obtained by an extension of the methods used for the variance (Wilson, 1968), but I have not yet tried to do so.

In the simple case of  $\underline{m} = 1$  the additional complicated term reduces to

$$\frac{\gamma_2 \sum_i \left( \frac{1}{\sigma_i} \frac{\partial \theta_i}{\partial \underline{a}} \right)^4}{\left[ \sum_i \left( \frac{1}{\sigma_i} \frac{\partial \theta_i}{\partial \underline{a}} \right)^2 \right]^2} \quad , \quad (16)$$

vanishing, as it should, for  $\gamma_2 = 0$ , and being in any case of the order of  $\gamma_2/\underline{n}$ .

## DATA ACCURACY FOR POWDER INDEXING

Robin Shirley

Chemical Physics Department, University of Surrey  
Guildford, Surrey GU2 5XH, England

Powder indexing involves taking the one-dimensional spacing information present in a powder diffraction pattern, and hence reconstructing the previously unknown three-dimensional lattice that produced it. We need to be able to do this economically and reliably for any single solid phase, irrespective of symmetry. For most materials of orthorhombic symmetry or lower, this is only practicable by computer methods, and care taken over the resolution and accuracy of the diffraction measurements will be amply rewarded in terms of reliable cells and short computing times.

The crucial requirement is resolution, which must be to at least  $0.25^\circ$  in  $2\theta$  ( $\text{CuK}\alpha$ ), so that use of a diffractometer or focussing camera is essential. Effective resolution can be improved more than tenfold by use of a profile analysis and peak-stripping program on carefully measured profiles.

Only the first 20-30 lines are needed, but must be measured with great care. In this low-angle range, the systematic errors can for the most part be combined into a single  $2\theta$  zero-error term, which must be corrected to better than  $0.02^\circ$  in  $2\theta$ , preferably by calibration against an internal standard. It is shown here that self-calibration using second-order diffraction lines is often also possible. The problem of spurious lines is discussed, and the need emphasised for these to be identified as such and removed before indexing commences.

Data supplied for indexing purposes as a list of d-spacings ought not to be rounded to less than four decimal places, and it is urged that measured  $2\theta$ 's should always be reported in literature patterns.

An outline of the nature of indexing solution space is given. A powder pattern does not usually lead to a single obvious indexing solution, which can be verified as correct by visual inspection alone. Apart from alternative settings within the same lattice, there may be geometrical ambiguities, and there will usually be a number of multiple solutions which have quite distinct Niggli reduced cells, especially when a dominant

zone is present. These solutions can be assessed by figures of merit, and it is shown that  $M_{20}$  is more suitable for this purpose than  $F_N$ , which is however a good measure of data quality. Some further criteria for recognising a correct solution are given.

Available indexing programs are classified both according to their search methods and their sensitivity to data quality, and a guide provided to their typical success rates and run times. A list of data problems with advice concerning their remedies is provided, and an attempt made to estimate what effects these will have on computing time, both singly and in combination.

## 1. Importance of Accurate Data

There can be few fields of endeavour in which careful data preparation is as dramatically rewarded as in computer-based powder indexing. A properly measured and calibrated pattern is usually solved almost immediately, while mediocre data can run forever!

By powder indexing, I mean taking the one-dimensional spacing information present in a powder-diffraction pattern, and reconstructing the previously unknown three-dimensional lattice that produced it, and doing this reliably and economically for any single solid phase of any symmetry.

Some of you already have a wide experience of indexing, and will be familiar with much of what I shall say, but I assume that there are also many who have very little acquaintance with modern indexing practice and probably regard the subject with some scepticism, because manual powder indexing used to have a deservedly poor reputation. In order to clarify what these methods can offer the practical powder diffraction scientist we shall start by outlining some basic features of the subject.

However, the emphasis will be on accuracy of data, because that is the subject of this symposium, and most appropriately so, for this is a field in which a few minutes extra care from the experimenter can save literally hours of computing. Lack of that care can turn a rapid interactive computation into a long trail of abortive and expensive batch runs that may never reach a satisfactory conclusion. Until, that is, the experimenter does what he should have done in the first place, and goes back to remeasure the pattern (with a little more feeling this time).

Powder indexing is not like structure analysis, which works well on good data, and usually get by on poor data given a little more time and attention. Powder indexing works beautifully on good data, but with poor data it usually will not work at all.

## 2. Introduction to Powder Indexing

### 2.1. Powder constants and zones

If a lattice is described by its six direct cell constants, the general d-spacing equation needs implicitly to include transformations between direct and reciprocal space

It becomes complex and unwieldy. For indexing purposes, it is much simpler to convert spacing data to  $Q = 1/d^2$ , and the reciprocal cell to its quadratic form, giving the six powder constants:

$$\begin{aligned} Q_A &= a^2 & Q_D &= 2b^*c^*\cos\alpha^* \\ Q_B &= b^2 & Q_E &= 2c^*a^*\cos\beta^* \\ Q_C &= c^2 & Q_F &= 2a^*b^*\cos\gamma^* \end{aligned}$$

The various calculated  $Q_{hkl}$  are then given by the equation:

$$Q_{hkl} = h^2Q_A + k^2Q_B + l^2Q_C + klQ_D + lhQ_E + hkQ_F$$

Reciprocal lattice points lying in a plane through the origin constitute a central zone in reciprocal space, and the corresponding powder lines are said to belong to the same powder zone. Assuming a provisional assignment of axes, any such zone may be described as  $hkl=0$ , and needs only three powder constants:

$$Q_{hk0} = h^2Q_A + k^2Q_B + hkQ_F$$

Q-values tend to be small fractions, and to give more convenient numbers, it has become customary to multiply them by  $10^4$ . Throughout this paper we shall adopt these Q-units of  $10^4 \times 10^{-4} = 10^{16} \text{ m}^{-2}$  (abbreviated to QU).

## 2.2. Figures of merit

Experience has often shown that a list giving apparently good agreement between observed and calculated d-values is an untrustworthy guide to the correctness of a proposed cell. This is because d-spacings are so non-linear with respect to the measurement accuracy of  $2\theta$ , and because an increase in the volume of the proposed cell can "improve" such a comparison to any arbitrary degree.

To correct these deficiencies, we need to relate the discrepancies between observed and calculated lines to the maximum value they could have had, and to do so using the linear Q-values in place of d's. The discrepancy  $\delta_i$  for the i-th observed line is defined as its absolute difference in QU from the nearest calculated line. This difference must not exceed a target  $\epsilon_j$  which is half the separation in QU between the two calculated lines which bracket the observed one. The ratio  $\langle \epsilon \rangle : \langle \delta \rangle$  between mean target and mean discrepancy resists spurious "improvement" with increasing volume, and forms the basis of a well-behaved family of figures of merit [1]<sup>1</sup>.

Figures in brackets indicate the literature references at the end of this paper.

The most useful of these for comparison purposes is the simplest, M1:

$$M1 = \frac{\langle \varepsilon \rangle}{\langle \delta \rangle} = \frac{Q_{\text{calcmax}}}{2 N_{\text{calc}} \langle \delta \rangle} .$$

$N_{\text{calc}}$  is the number of distinct and potentially observable calculated lines up to the last observed line used ( $N_{\text{obs}}$ ), and should not include additional symmetry-equivalent lines, nor space group absences, as far as they are known. It is thus effectively the same as  $N_{\text{poss}}$  of Smith and Snyder [2] and  $N_{20}$  of de Wolff [3,4] when  $N_{\text{obs}} = 20$ .

If  $N_{\text{obs}} = 20$ , and all 20 observed lines are counted as indexed, we arrive broadly at the original de Wolff [3] figure of merit,  $M_{20}$ , which has become the generally adopted indicator of the reliability of proposed powder cells. Using the nomenclature of this paper, it is defined as:

$$M_{20} = \frac{Q_{\text{obsmax}}}{2 N_{\text{calc}} \langle \delta \rangle} .$$

The question of impurities and the treatment of unindexed lines is one that we shall be returning to later. Note that the formula above will also work correctly for values of  $N$  (i.e.,  $N_{\text{obs}}$ ) other than 20, to give a figure of merit  $M_N$ , as used, for example, by Marriner, Langford and Tarney [5]. A different form  $M_N^1$  has been used by Snyder, et al. [6] and Smith and Snyder [2], but this is not really a generalisation of  $M_{20}$  because it has acquired an extra factor of  $N_{\text{obs}}$  in the numerator, and so is strongly dependent on line number.

Smith and Snyder [2] have also proposed a quite different figure of merit  $F_N$  based on 20 differences, and claimed that it should replace  $M_{20}$ . We shall be returning to this point later, where it will be argued that while  $F_N$  is more suitable for assessing measurement accuracy,  $M_{20}$  is still superior for evaluating indexing solutions. Using the nomenclature of this paper,  $F_N$  is defined as:

$$F_N = \frac{1}{\langle \delta_{20} \rangle} \cdot \frac{N_{\text{obs}}}{N_{\text{calc}}} .$$

In practice it is hard to give an exact and definitive value of  $M_{20}$  (or  $F_N$ ) for a particular indexing solution, because of sensitivity to slight cell parameter changes, etc which cause disproportionate changes to the residuals in the denominator of the figure of merit formula. Slightly different refinement conditions may well yield figures of merit differing by more than 10 percent for the same solution, and only differences between solutions that are clearly larger than this should be considered significant. Further work in this area leading to a firmer consensus would be useful. Heavy-handed rounding of the d-spacings has particularly disastrous effects here, a point that we shall be coming back later.

### 2.3. Recognising a correct solution

It will be shown later that, because of zone dominance, it is ultimately only the relative value of  $M_{20}$  compared with other possible solutions that matters, and so we cannot lay down any absolute value of  $M_{20}$  (or any other figure of merit) that guarantees correctness. Nevertheless, one can still give some very helpful guidelines:

(1) False solutions generally have  $M_{20} < 10$ , and resist attempts to improve them by full refinement or adjusting the calibration constants, because the information simply is not there.

(2) A solution that indexes all the first 20-30 lines and has  $M_{20} > 20$  is nearly always correct, especially if this is twice that of the next best solution and the list of 20 differences contains no unexplained excursions greater than three times the expected  $\sigma(2\theta)$ .

(3) The correct solution also gives itself away in less quantitative ways to the discerning eye. It tends to recur with different indexing methods and from different starting points. It is also readily improved by fine adjustments to the calibration constants, because its internal consistency takes over as a stronger indicator of the correct settings than the original calibration method.

(4) Finally, because it contains genuine information, the correct solution will usually start to make crystallographic and structural sense. A level-by-level listing of the pattern will usually suggest systematic absences that will lead to a few possible space groups. The formula weight and a density estimate will lead to a clear indication of the number of formula units per cell that will be consistent with the possible space groups and molecular symmetry. Finally, the cell geometry will often indicate relationships with other materials and perhaps suggest a packing scheme and structure, or do so after transformation to a more suitable setting. (However, one should not be too insistent on this, as one of the attractions of research is that the truth is sometimes unexpected.)

### 3. Nature of Indexing Solution Space

The attention we have been giving to figures of merit and choosing the correct solution, implies that there may be a number of solutions to choose between, and this is indeed the case, as we shall see.

#### 3.1. Alternative settings

A lattice can be described by an infinite number of choices of unit cell within it, and a very high-symmetry lattice yields numerous, less convenient cells in lower crystal systems. However, these alternative settings are easily recognised as the same solution, because they all lead to the same reduced (Niggli) cell [7]. If sub- or superlattices are obtained, for example by halving or centering the true cell, again the reduced cells will indicate that these are not independent solutions. In all such cases, the cell volumes will be either

equal or in a simple ratio; this is a useful guide, but not as conclusive as reduced cell comparisons.

### 3.2. Geometrical ambiguities

Mighe11 and Santoro [8] have shown that certain distinct lattices, with different, though related reduced cells, can give geometrically identical powder patterns. This geometrical ambiguity is only found when special relationships exist between the parameters of the two lattices, and cannot occur between general cells of orthorhombic or lower symmetry. However, it always occurs when the metrical symmetry of one of the lattices is higher than orthorhombic. For example, if one examines the numerous lower-symmetry cells that can account for a hexagonal pattern, it will be found that some of them are true geometrical ambiguities.

In practice this is easily detected, because as far as is known, the volumes of such cells will always be in a simple relationship (though not necessarily an integer one -- factors of  $\sqrt{2}$  can occur, for example). The higher symmetry solution is usually the correct one, although one cannot be sure of this without studying the line multiplicities or intensities, and exceptions have occurred. For example  $\alpha$ -Li<sub>4</sub>B<sub>2</sub>O<sub>5</sub> [3] can be indexed exact as hexagonal, but has been shown by single crystal work actually to be orthorhombic.

### 3.3. Multiple solutions

If we look at the figure of merit surface for a particular powder pattern, possible solutions will appear as peaks. Figure 1 shows the sharpened figure of merit (WM3<sup>3</sup>) surface for hexamethylbenzene, in the plane through the correct solution with only Q<sub>D</sub> and Q<sub>E</sub> varied (generated by the grid-search method using the POWDER 49 program). This is equivalent to varying only the reciprocal angles  $\alpha^*$  and  $\beta^*$  while keeping the remaining cell constants fixed. It can be seen that there is only a single prominent peak, and so in this case a unique solution. We are usually not so fortunate.

A quite different situation is shown in figure 2, the M1 surface for the blue pigment  $\alpha$ -Cu phthalocyanine. In this case there are numerous peaks, and hence many plausible false solutions (pseudo-solutions) in addition to the correct one. The material is actually triclinic, though pseudo-monoclinic with angles of 90.8° and 90.3°, and was sufficiently colloidal to exhibit appreciable line-broadening. The best five solutions index all the first 20 lines with figures of merit of 12.7, 9.7, 9.6, 8.6, and 8.5 respectively, so this was not an easy case to solve.

Fortunately the first solution (M1<sub>20</sub> = 12.7) is indeed the correct one (indicated by an arrow on the diagram), but all the first 20 solutions look acceptable in the form of the traditional d<sub>obs</sub>-d<sub>calc</sub> list, although in fact they are quite distinct, with different volumes and densities.  $\alpha$ -Cu phthalocyanine was one of the first instances of multiple solutions to be studied in detail, but many more striking examples have since been discovered.

The first three solutions for monoammonium urate have  $M_{20} = 21, 15,$  and  $13$  while for monosodium urate monohydrate (the crystals which cause gout) the best five cells give  $30, 21, 20, 19,$  and  $18,$  and no less than  $31$  cells index all the first  $20$  lines with a figure of merit better than  $10.$  There are, in fact, some  $200$  tolerably plausible solutions for this pattern, although only the best  $36$  have been examined in detail. More extreme examples are not uncommon: using the LOSH and LZON programs, the search for solutions that index the first  $20$  lines within their  $2\theta$  error limits is often terminated at  $500$  cells, the present storage maximum. These cases generally arise through the mechanism of zone dominance.

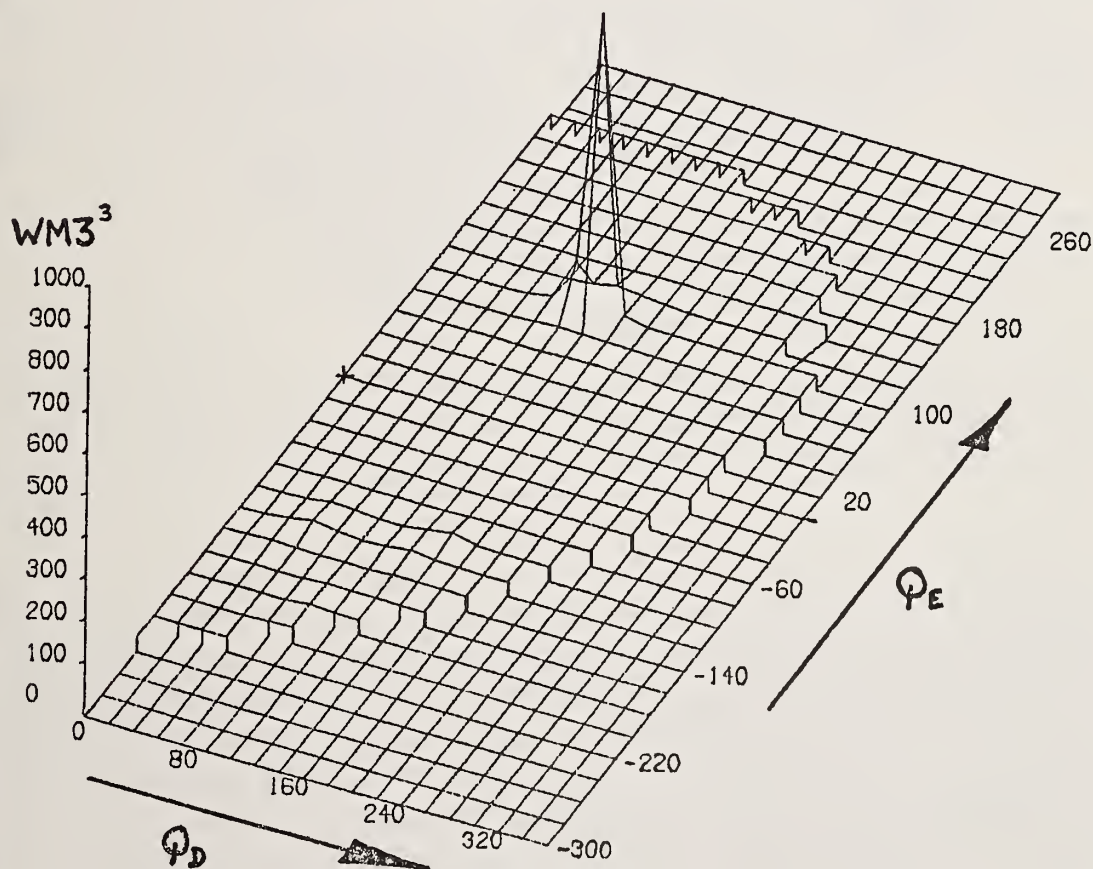


Figure 1. Hexamethylbenzene \*\*  $WM3^3$ .

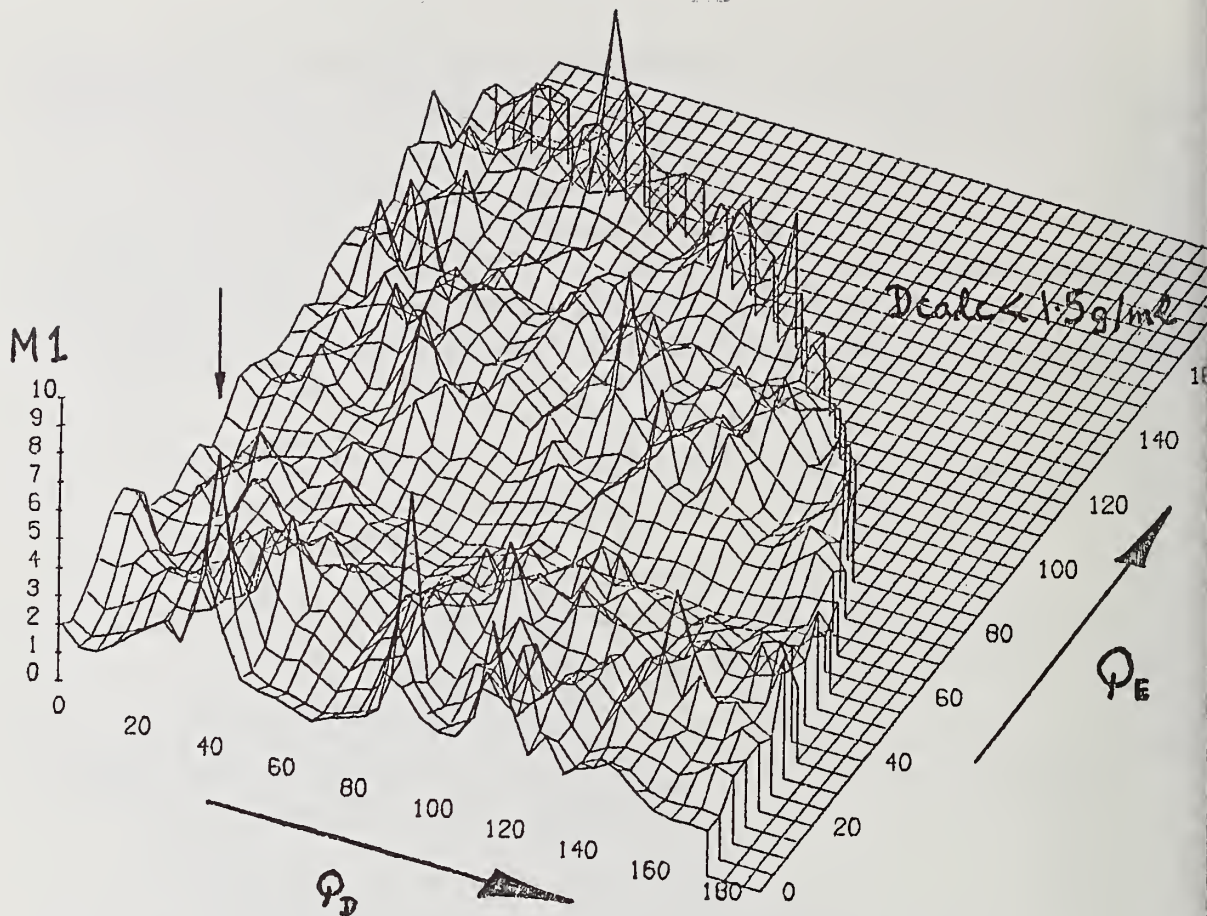


Figure 2. LPHA CU-Phthalocyanine HK1 > VVW W/O 001 Theta < 17.5 \*\* M1.

### 3.4. Dominant zones

The powder zone with the largest direct space constants, and hence whose reciprocal net cell has smallest area  $S$ , will generate most of the calculated lines near the origin, and, unless it is also a glide plane, will index most of the low angle observed lines.

When  $S$  approaches half the geometrical mean value  $(v^*)^{2/3}$ , this dominant zone will probably index about 10 out of the first 20 lines, leaving the remaining three powder constants to explain only about 10 upper-level lines. This is not very difficult to do by chance, at least approximately, so such materials will tend to give many plausible, multiple solutions as occurs with the three examples above. In each case the solution with highest figure of merit is correct, but can only be identified by comparison with the entire set.

Dominant zones can in principle occur in any crystal system, but their effects are most noticeable among triclinics. In such cases no level of figure of merit can, by itself, guarantee correctness, since false solutions can occur with arbitrarily high values. It is better to work with more than 20 lines so as to include a higher proportion of upper-level ones, and to use the fact that, for sufficiently accurate data, the correct solution will always fit appreciably better than any pseudo-solution.

Given good data, materials with dominant zones no longer present any serious difficulty, since this is the type of problem that grid-search programs (such as LOSH, LZON and POWDER 49) like best.

### 3.5. Problem of immensity

It would be reassuring to be able to locate all the multiple solutions for each pattern by an exhaustive search, but as we go to lower symmetry and so have more variable dimensions, the combinatorial explosion takes over. Assuming reasonable search limits and working on a 5 QU grid, it turns out that more than  $10^{14}$  different lattices are possible. At the rate of one per 3 ms (just about achievable on a CDC7600), they would take 12000 years to search by direct exhaustive trial, and at least 10 years by the optimal algorithm in parameter space (successive dichotomy, a form of binary search). It is thus not likely that an exhaustive search will ever be feasible in the general case.

It is, however, a reasonable method for high-symmetry systems down to orthorhombic, if a suitable algorithm is used (programs LOUV and POWDER = TAUP). In lower symmetry systems, semi-exhaustive methods predominate, in which the search is restricted to two or three dimensions by carefully chosen simplifying assumptions.

Similar conclusions can be drawn if one approaches the problem by assigning Miller indices to each of N observed lines, where N need not exceed the number of unknown parameters so that solutions are located in a 3N-dimensional index-space in which only integer coordinates are possible.

The obvious moral is that we cannot hope to tackle more than one unknown phase at a time in lower symmetry systems (up to six more parameters per impurity), and are likely to have great difficulty with inadequately calibrated patterns (at least one or two more parameters).

## 4. Data Requirements

For indexing work it is not necessary, nor even desirable, to measure the entire diffraction pattern. Information about the correctness of the unit cell is concentrated at the low angle end, where the lines are relatively well separated and are resistant to displacement by small cell parameter changes. It is generally sufficient to measure the positions of the first 20-30 lines, provided that this is done thoroughly and accurately.

If powder measurements are progressively degraded by errors, indexing becomes difficult and more time-consuming, and eventually impossible, even in principle. In general, it is a waste of time to attempt to index poor data, unless the solution is trivially simple.

If data errors were negligibly small, the correct solution would have an enormous figure of merit compared with the much smaller ones of the pseudo-solutions. Data errors degrade the true solution, but have relatively little effect on the field of pseudo-solutions produced by accidental superimpositions. For every peak that declines, another is as likely to improve, so that the general character of the group of false

solutions is resistant to change. In the limit, the true solution (the signal) is no longer distinguishable from the pseudo-solutions (the background noise), and the data become unsolvable.

#### 4.1. Resolution

Probably the most exacting requirement for successful indexing is the need to observe most of the first 20-30 lines (that are not too weak) as distinct individuals, rather than merged groups. Typically, this means the need to distinguish adjacent lines separated by no more than  $0.25^\circ$  of  $2\theta$  at  $\text{CuK}\alpha$  wavelengths, which effectively rules out Debye-Scherrer data. Resolution in this sense can be taken as being numerically equivalent to the line width, expressed as full-width at half maximum height (f.w.h.m.). Inadequate resolution nearly always makes the data impossible to index.

The paramount importance of resolution for indexing work explains the high success rate for focussing camera data, especially from Guinier-Hägg instruments, whose resolution can only be described as superb. It is rather less common (and considerably more expensive) to obtain as good resolution with diffractometer data.

The effective resolution of any instrument can be increased without theoretical limit (other than signal/noise ratio considerations) if the full profile is measured and a profile analysis and peak stripping program used.

Resolution can also generally be improved by increasing the wavelength, which is especially relevant for neutron work. Some very recent experiments on the D1A neutron diffractometer at the I.L.L., Grenoble, demonstrated that its effective resolution, which was insufficient for most indexing work at 1.9 Å, became quite reasonable at 3 Å and very satisfactory by 5.7 Å.

We can say in general that different kinds of work have different minimum resolution requirements. For phase identification and quantitative analysis, it is often sufficient to work at quite low  $2\theta$  resolution (about  $1^\circ$ , for example), if this matches that of the standards used. For indexing, adjacent lines must be resolved, so a higher resolution ( $<0.25^\circ$ ) is required. This is also more than sufficient for many structure refinements using the Rietveld profile-fitting method, for which  $<0.5^\circ$  will often suffice. It is, however, not nearly enough for ab initio structure solution, for here we need to observe not only a large number of lines but also the gaps between them, to identify accidental absences and establish background levels in order to build up the 50-200 terms needed for Pattersons and  $\Delta F$  syntheses. Hence, the highest available resolution ( $\lesssim 0.1^\circ$ ) is desirable.

#### 4.2. Accuracy

Measurement accuracy comprises precision (random errors) and correction (systematic errors), and powder indexing responds very differently to these two contributions.

Indexing is surprisingly tolerant of imprecision. Random variation with  $\sigma(2\theta)$  up to  $0.03^\circ$  (absolute error limits of  $\pm 0.08^\circ$ ) will increase the computation time, but probably not prevent the solution from being found. This is easily met, since  $\sigma(2\theta) < 0.02^\circ$  is common in routine measurements.

Systematic error is much more serious. In the low angle region that is of interest to powder indexing, the important effects can be summarized as a zero error in  $2\theta$ . Quite small increases will cause computing time to increase rapidly and depress the figure of merit of the correct solution so much that it becomes hard to recognize with any confidence.

Zero error particularly affects powder diffractometers with the usual parafocussing geometry, because of sensitivity to errors of less than 0.1 mm in the effective sample position, varying from sample to sample with absorption and surface roughness. The only completely satisfactory answer is to do a calibration run using an internal standard to obtain unbiased  $2\theta$ 's for the major peaks, from which a run using the pure sample may be corrected.

Line profiles in the low  $2\theta$  range of interest are often erratic and sharply skew near the intensity maximum, and so appreciable error can result if peak position is taken as the criterion of line  $2\theta$ . An equally rapid and much stabler procedure is to use the center of the chord at about 80 percent of maximum height.

#### 4.3. Self-calibration

In principle, calibration knowledge for a pattern is present in the measured powder lines themselves, but cannot be accessed until the pattern has been indexed (or at least individual zones). However, one special case exists for which indices are not required -- that of any observed line  $2\theta_1$ , and its second order  $2\theta_2$  (other higher orders are seldom available).

The required zero correction  $Z_{2\theta}$  can be obtained from the iterative formula:

$$Z'_{2\theta} = Z_{2\theta} + 2 \left\{ 2 \arcsin \left[ \frac{1}{2} \sin(\theta_2 \text{corr}) \right] - 2\theta_1 \text{corr} \right\}$$

where  $2\theta_{\text{corr}} = 2\theta_{\text{raw}} + Z_{2\theta}$ . From an initial estimate of zero, this expression converges rapidly in about five cycles, and is easily implemented on a programmable pocket calculator.

A quick search through the line listing will usually reveal three or four possible second order relations, of which the one yielding smallest  $Z_{2\theta}$  would be first choice for self-calibration. If two such relations produce the same  $Z_{2\theta}$ , it may be accepted with considerable confidence. For high-precision data, this simple procedure can produce reliable zero calibrations to better than  $0.01^\circ$ , and I have found it invaluable both for refining an existing calibration and for salvaging precise but poorly calibrated data from other sources.

$Z_{2\theta}$  determination from internal consistency of the data offers further interesting possibilities. If  $Z_{2\theta}$  were included in zone indexing programs as a variable parameter during the refinement of trial zones, correct zones would tend to reveal themselves by

all giving the same  $Z_{2\theta}$  value. Thus, we might be able to overcome one of the major obstacles to routine fast indexing--the lack of a reliable criterion for identifying correct zones.

#### 4.4. Spurious lines

It is very desirable to eliminate spurious lines which do not belong to the phase under investigation, because, as we have seen, they introduce additional unknown parameters, as well as serious methodological difficulties.

If we permit observed lines to be discarded as "not indexed", we are then changing our data to fit the proposed model--a dubious scientific practice in itself, and very hazardous when multiple solutions are to be expected. The only safe course is to remove all doubtful lines on a priori grounds.

For a start, an impurity level of <1 percent should be sought, and preferably verified in a density gradient column. Known impurities need not cause serious trouble because their lines can simply be omitted, although they may obscure some of the unknown pattern. Differences in line widths, or variations in intensity ratios in different samples, may offer some useful clues here, but direct examination by microscopy or electron probe microanalysis is the surest test. Finally, it is nearly always best to omit all very weak lines at this stage, and only return to them after the cell has been found. They will rarely be precisely measured, and should be suspected as possible contaminants until their indexings have been confirmed.

Spurious lines are particularly damaging to exhaustive search procedures. Although some programs permit a specified number (NSPURI) of poor indexings to be omitted, this is liable to cause an exponential increase in run times, and so should not be used without good cause.

#### 4.5. Number of digits specified

A surprisingly common source of data degradation is simply heavy-handed rounding of d-values when a measured pattern is reported.

Werner [9] has shown that rounding errors alone will place a ceiling on the figure of merit for a particular cell volume V, according to:

$$M_{20}^{\max} \approx \frac{3md_{20}}{8\pi V \langle \delta \rangle}$$

where  $d_{20}$  is the d-spacing of the 20th observed line, m is the multiplicity factor and  $\langle \delta \rangle$  is the estimation precision in  $1/d^2$ , in this case arising from rounding. A simple estimator for V is given by Smith [10].

It can be shown that two decimal places are virtually never enough, three are often insufficient, and even four may not be overgenerous. This point is also made by Smith and Snyder [2], who join the overwhelming majority of those engaged in indexing work in

urging that the list of observed  $2\theta$ 's should be published, as is done for National Bureau of Standards data. It is to be hoped that this will soon become the accepted convention, as has been recommended by the A.C.A. subcommittee on this subject, whose report we shall be hearing later in the symposium (Calvert, et al. [11]).

## 5. Indexing Programs

Details of the methods used by particular indexing programs are discussed in a recent [1], and we shall confine ourselves here to a classification and overview of the various programs, with particular reference to their sensitivity to data quality.

### 5.1. General classification

Powder indexing requires either that the correct values of the cell constants (or powder constants, etc.) are found in a continuous parameter-space of up to six dimensions, or that the appropriate values of the Miller indices for each line are located in a  $3N$ -dimensional integer-valued index-space, where  $N$  is the number of observed lines to be indexed. These two objectives are equivalent, and are both fulfilled when the correct solution is found.

Index- and parameter-space methods are considerably different in approach, and can act as useful complements (or checks) for each other. In general, parameter-space methods lend themselves more to the inclusion of cell information and constraints, while index-space programs are the stronger in the presence of unhelpful accidental or systematic absences.

Programs may also be classified according to whether they adopt a mainly deductive or exhaustive approach. Broadly, deductive methods try to infer the values of lattice parameters from coincidences and relations between the observed lines, to achieve speed at the cost of rigour. By contrast, exhaustive methods systematically search the relevant solution space, gaining rigour at the expense of speed. Deductive methods try to work out quickly what the solution ought to be, but may fail with poor data or a tricky problem. Exhaustive methods eliminate everywhere that the solution cannot be a procedure which must succeed but is slow in low-symmetry cases.

The classification is not rigid, because programs often incorporate some aspect of both approaches. For example, deductive programs usually try some kind of systematic combination of the deduced possibilities, while most of the new programs are semi-exhaustive, making judicious deductions to limit the solution field to be searched, in order to gain speed.

	<u>Parameter-space</u>	<u>Index-space</u>
Deductive:	Visser (ITO=FZON)	Smith & Kahara (QTEST)
Semi-exhaustive:	Shirley (POWDER49) Louër & Shirley (LOSH) Shirley, Louër & Visser (LZON)	Werner (TREOR=TRER) Kohlbeck (TMO=KOHL)
Exhaustive:	Louër (LOUV, LOUM, DICVOL)	Taupin (POWDER=TAUP)

Modern indexing programs tend to be large and complex, especially the semi-exhaustive ones, because they are effectively experiments in artificial intelligence. They apply carefully evolved heuristics to try to quickly locate solutions that are wholly out of reach by the best exhaustive algorithms.

A summary of the characteristics of the major programs is shown in table 1. More details are given in Shirley [1]. This library is available from me, on receipt of a magnetic tape and information about preferred tape formats.

In general, exhaustive methods are excellent down to orthorhombic, but run away from us somewhere between three and five unknown parameters. For monoclinic, and certainly for triclinic, we should first try deductive programs (although these are less tolerant of data errors), and then semi-exhaustive ones.

## 5.2. Tolerance of data errors

The table which follows should be regarded as an approximate guide only:

		<u>Tolerance of spurious lines</u>		
		<u>Sensitive</u>	<u>Insensitive</u>	
<u>Tolerance of</u>	}	<u>Sensitive</u>	LZON,TAUP	FZON,TRER,(QTEST)
<u>Inaccuracy</u>		<u>Insensitive</u>	LOUV,LOUM DICVOL,LOSH	KOHL

## 5.3. Standardization of data formats

It is obviously desirable that all indexing programs should accept data in the same format, so as to eliminate the labour and introduction of errors involved in reformatting and retyping for each program tried, and to simplify the exchange of data sets between

Table 1. Summary of characteristics of major powder indexing programs.

Program	Version (FORTRAN Deck)	Authors	Crystal Systems	Fully Automatic	Exhaustive	Success Rate (approx)	Execution sec (CDC 7600)
ITO	FZON	Visser	Any	Yes	No	75%	1-5
LOUV	LOUV	Louër	Orthorhombic+	Yes	Yes	(100%)	1-5
LOUM	LOUM	Louër	Monoclinic	Yes	Yes	(80%+)	30-1200
LOSH	LOSH	Louër & Shirley	Any	No	Semi	80%+	10-300
LZON	LZON	Shirley, Louër & Visser	Any	Yes	Semi	?High	30-1200
POWDER 49	(Algol)	Shirley	Any	(Yes)	Semi	80%	(20-300)
POWDER	TAUP	Taupin	Any (triclinic impractical)	Yes	Yes	50%+	50-1200+
TMO	KOHL	Kohlbeck	Any	Yes	Semi	80%+	2-200
TREOR	TREOR	Werner	Monoclinic+	Yes	Semi	(75%)	2-100
QTEST	---	Smith & Kahara	Monoclinic	Yes	No	(60%)	(30)

Notes: 1) Crystal system followed by + means "and all higher systems".

2) Success rate in brackets means "within its crystal system limits".

3) Other bracketed quantities indicate an estimate, or some other qualification.

4) Execution times show the typical range for that program, but not absolute maxima.

laboratories. A Standard Powder Data Interchange Format (SPDIF - see fig. 3) has been designed for this purpose, in consultation with most of the program authors and other interested parties [12]. In due course, all the major indexing programs, as well as those for many related calculations, will be able to accept SPDIF as an alternative to their own input formats. In the interim I have written two short programs, PDAT and QDAT, which accept data in an easily typed form, and then generate suitably formatted data decks for any or all of the major indexing programs, as well as an SPDIF deck.

---

```

SPDIF      5
TITLE RUBIDIUM CARBONATE, RB2CO3.H2O, AFTER J.W.VISSER
REMARK TEST DATA FOR ZONE-INDEXING PROGRAMS (40 LINES)
REMARK MONOCLINIC I-CENTERED CELL, GIVING M20=54.2
DEFPAR 71      0.03      1.54050
LINE      139.0
      .
      .
      .
LINE      1868.9
END
TITLE ALPHA CU-PHTHALOCYANINE: ALL DATA>VWV, R.SHIRLEY
REMARK DATA MEASURED BY R. SHIRLEY FROM PHOTOGRAPH SUPPLIED BY C.J.BROWN
REMARK TRICLINIC, PSEUDO-MONOCLINIC. FIRST 8 LINES IN DOMINANT HKO ZONE
DEFPAR 11
REMARK NONIUS GUINIER-DE WOLFF CAMERA: XMM GIVES 4THETA IN DEGREES
REMARK CALIBRATED AGAINST BETA CU-PHTHALOCYANINE TRACK ON SAME FILM
XCALIB      0.06      0.5
CELMAX      1000.    576.084    1.6
LINE      31.5      VVS      6      1
      .
      .
      .
LINE      85.25      M      24
END
FINISH

```

Figure 3. Example of SPDIF Deck, Containing Two Data Sets

## 6. Comparison of Figures of Merit

Figures of merit for powder data are needed in two rather different circumstances, and to some extent the requirements are conflicting.

For phase identification, we need to know the quality of measurement of the reference patterns in the literature. For this purpose, the published unit cells can be assumed to be correct, because if not, the real figure of merit will be higher, and we shall merely

have erred on the side of caution. Thus only the accuracy and completeness of the line listings are relevant, and any dependence on cell volume, symmetry, etc., will only be a disadvantage.

Clearly  $F_N$  meets these criteria better than  $M_{20}$ , and would do so more if its wavelength dependence could be eliminated, as we shall see.

In powder indexing the situation is quite different--it is not the quality of the data but the reliability of proposed unit cells that we wish primarily to assess.

In this case the fall in  $M_{20}$  with lower crystal system and with increasing cell volume becomes an advantage, because it demands a higher standard of agreement for proposed large, low-symmetry cells (those with more degrees of freedom, and hence overdetermined by a smaller margin), and this is supported by both theory and practical experience.

Hence, to give an example, we might find  $M_{20} = 50$  given both by an excellent set of data for a large monoclinic or triclinic cell, and by a relatively poor cubic pattern. In both cases the reliabilities of their cells would be about the same (i.e. very good), although the data qualities of the two are very different. By Occam's razor, we require stricter evidence to support the more complicated model.

If we compare  $M_{20}$  and  $F_N$  for  $N_{\text{obs}} = 20$ :

$$\begin{aligned} \frac{F_{20}}{M_{20}} &= \frac{40}{Q_{\text{obsmax}}} \cdot \frac{\sum \delta Q}{\sum \delta 2\theta} \\ &= \frac{4\pi}{9\lambda^2 Q_{\text{obsmax}}} \cdot \frac{\sum (\sin 2\theta \cdot \delta 2\theta)}{\sum \delta 2\theta} \end{aligned}$$

The first term is constant for a particular data set, while the second term indicates the slightly different weighting of the residuals for the two measures and approximates to  $\langle \sin 2\theta \rangle$ , depending on the particular  $2\theta$ 's present. Comparing data at different wavelengths for the same sample, we see the strong  $1/\lambda^2$  dependence of  $F_N$ , as at present defined. Comparing different materials at the same wavelength, a variation of  $M_{20}$  with  $V^{-2/3}$  occurs via the term in  $Q_{\text{obsmax}}$ . A more subtle effect of this term is to introduce the greater symmetry dependence of  $M_{20}$ , because of its relative increase with increasing symmetry as more reciprocal lattice points are needed on average to produce a new observed line. The  $\langle \sin 2\theta \cdot \delta 2\theta \rangle$  term introduces a further approximate dependence on  $V^{1/3}$ , so that the overall volume dependence of  $M_{20}$  is roughly as  $V^{-1/3}$ . It is argued here that these features of  $M_{20}$  are beneficial to its purpose, but that the  $\lambda^{-2}$  dependence of  $F_N$  is not.

As presently defined,  $F_N$  measures the quality of the experimenter--how well he or she measured the actual  $2\theta$ 's at the wavelength used. But it would be more useful to remove the wavelength dependence and know how good the data are. This could be done by converting the

observed differences in  $2\theta$  to differences in  $d$ , then back to differences in  $2\theta$  at a standard wavelength, say  $\text{CuK}\alpha_1$ . The standardized  $F_N$  would then reflect the improvement in accuracy that can be obtained by measuring the expanded pattern at a longer wavelength.

An instance of this arose last month while collecting neutron powder data at the I.L.L., Grenoble, where it was possible to more than double the accuracy in  $d$  by changing to a longer wavelength, but this was not reflected in  $F_N$ , which was in fact halved because of a drop in the uncorrected  $2\theta$  resolution with increasing wavelength!

Ideally, three assessment measures should be given, because there are three distinct needs to be satisfied. These are: (1)  $\sigma(2\theta)$ , the estimated standard deviation in the original  $2\theta$  measurements, so that we may judge the accuracy of experimental measurement, assuming the cell to be correct; (2) the standardized figure of merit  $F_N$ , with  $2\theta$ 's referred to a standard wavelength ( $\text{CuK}\alpha_1$ ), so that we may gauge the quality of the resulting data set, again assuming the cell to be correct; (3) the properly calculated de Wolff figure of merit  $M_{20}$  or  $M_N$ , so that we may assess the reliability of the proposed unit cell, or, if this is not in question, to add to the accumulated experience through which we make this judgement in other cases.

## 7. Summary of Data Problems for Indexing Work

The two intolerable problems for indexing work are insufficient resolution or not enough digits reported for the data. The presence of either of these will ensure that a study is abortive. However, there are a number of other problems, which may be tolerable in isolation, though probably not in combination:

- (1) imprecision (lengthens computing time);
- (2) poor calibration, particularly zero error (self-calibration is often possible);
- (3) impurity contamination (exponential rise in computing time if using NSPURI facility);
- (4) awkward accidental absences, such as from a strong subcell (index space methods preferable here);
- (5) awkward cell shape, producing a dominant zone and numerous multiple solutions (grid-search programs needed);
- (6) high cell volume (requires correspondingly high accuracy).

Low symmetry is not a problem in itself, but will make the other problems much worse, since there may be a need to use exhaustive methods, which are much slower in low symmetry.

As a rough guide, we may relate the number of problems to probable computing time needed (CDC 7600) as follows:

<u>Number of problems</u>	<u>7600 time</u>
0	under 1 minute
1	5-30 minutes
2	1-3 hours
3	get better data

## 8. Conclusion

Modern computer-based powder indexing is sufficiently easy and well-proven for it to be worth the while of serious powder diffraction workers to include it in their repertoire of techniques.

We now have available a number of powerful and mature programs, all of which usually succeed in at least 50 percent of cases, and many achieve better than 80 percent. Because they use quite distinct and complementary methods, their limitations tend to affect different problems, so that with several of them available one will seldom be unable to index a properly measured pattern. By knowing the right order to apply them, which broadly means trying the speedy deductive methods first, then working down from high symmetry with the more powerful exhaustive and semi-exhaustive methods, computing cost should not be a problem.

But that takes us back to where we started--the quality of the data. Although there remain many fascinating ideas to be followed up in the field of indexing programs, we now understand that aspect of the problem reasonably well, and the ball is back in the court of the experimentalists.

The equipment required to record patterns with excellent resolution and accuracy is quite inexpensive (under \$8000 for a Guinier-Hägg camera), and in any case, as the JCPDS Associateship at NBS have shown, if you keep in mind the important requirements, it is very likely that existing equipment can be persuaded to produce data of sufficient quality.

Until a pattern is indexed, it is difficult to demonstrate its quality, or to show that it does not contain spurious lines. Without indexing, it is impossible to proceed to the powerful and elegant structural investigations that we have been hearing about.

## References

- [1] Shirley, R., Indexing powder diagrams, Crystallographic Computing, H. Schenk, ed. (Delft University Press, 1978).
- [2] Smith, G. S. and Snyder, R. L.,  $F_N$ : A criterion for rating powder diffraction patterns and evaluating the reliability of powder-pattern indexing, J. Appl. Cryst. 12, 60-65 (1979).
- [3] de Wolff, P. M., A simplified criterion for the reliability of a powder pattern indexing, J. Appl. Cryst. 1, 108-113 (1968).
- [4] de Wolff, P. M., The definition of the indexing figure of merit  $M_{20}$ , J. Appl. Cryst. 5, 243 (1972).
- [5] Marriner, Langford and Tarney, J. Appl. Cryst. (1979).
- [6] Snyder, R. L., Johnson, A.C., Kahara, E., Smith, G. S., and Nichols, M. C., An analysis of the powder diffraction file, Report UCRL-52505 (Lawrence Livermore Lab., University of California, 1978).
- [7] Mighell, A. D., The reduced cell: Its use in the identification of crystalline materials, J. Appl. Cryst. 9, 491-498 (1976).

- [8] Mighell, A. D. and Santoro, A., Geometrical ambiguities in the indexing of powder patterns, *J. Appl. Cryst.* 8, 372-374 (1975).
- [9] Werner, P.-E., On the determination of unit cell dimensions from inaccurate powder data, *J. Appl. Cryst.* 9, 216-219 (1976).
- [10] Smith, G. S., Estimating the unit-cell volume from oneline in a powder diffraction pattern: the triclinic case, *J. Appl. Cryst.* 10, 252-255 (1977).
- [11] Calvert, L. D., Flippen-Anderson, J. L., Hubbard, C. R., Johnson, Q. C., Lenhart, P. G., Nichols, M. C., Parrish, W., Smith, D. K., Smith, G. S. Snyder, R. L., and Young, R. A., The standard data form for powder diffraction data, *Proceedings of Symposium on Accuracy in Powder Diffraction*, Washington, D.C., June 1979.
- [12] Shirley, R., SPDIF - A standard interchange format for powder diffraction data, *Proceedings of Applied Crystallography Conference*, Kozubnik, Poland, 1978 - in press (1979).

#### Bibliography

- Commission on Crystallographic Data, Powder data, *J. Appl. Cryst.* 4, 81-86 (1971).
- Ishida, T. and Watanabe, Y., Probability computer method of determining the lattice parameters from powder diffraction data, *J. Phys. Soc. Japan*, 23, 556-565 (1967).
- Ishida, T. and Watanabe, Y., Analysis of powder diffraction patterns of monoclinic and triclinic crystals, *J. Appl. Cryst.* 4, 311-316 (1971).
- Ito, T., A general powder x-ray photography, *Nature*, 164, 755-756 (1949).
- Ito, T., *X-ray Studies on Polymorphism*, 187-228 (Maruzen, Tokyo, 1950).
- Kohlbeck, F. and Hörl, E. M., Indexing program for powder patterns especially suitable for triclinic, monoclinic and orthorhombic lattices, *J. Appl. Cryst.* 9, 28-33 (1976)
- Kohlbeck, F. and Hörl, E. M., Trial and error indexing program for powder patterns of monoclinic substances, *J. Appl. Cryst.* 11, 60-61 (1978).
- Lipson, H., Indexing powder photographs of orthorhombic crystals, *Acta Cryst.* 2, 43-45 (1949).
- Louër, D. and Louër, M., Méthode d'Essais et Erreurs pour l'Indexation Automatique des Diagrammes des Poudre, *J. Appl. Cryst.* 5, 271-275 (1972).
- Marriner, G. F., Langford, J. I. and Tarney, J., Crystal data for  $\text{CaF}_2 \cdot \text{SiO}_2$ , *J. Appl. Cryst.* 12, 131-132 (1979).
- Rouse, J. E., M.Sc. Dissertation, University of Surrey, England (1973).
- Runge, C., Analysis of Crystal Structure by x-rays, *Z. Zeits.* 18, 509-515 (1917).
- Shirley, R., Recent advances in determining unknown unit cells from powder diffraction data, *Acta Cryst.* A31, S197 (abstract) (1975).

- Shirley, R. and Louër, D., New powder indexing programs for any symmetry which combine grid-search with successive dichotomy, Acta Cryst. A34, S382 (abstract) (1978).
- Smith, G. S. and Kahara, E., Automated computer indexing of powder patterns: the monoclinic case, J. Appl. Cryst. 8, 681-683 (1975).
- Smith, G. S., Estimating unit cell volumes from powder diffraction data: the triclinic case, J. Appl. Cryst. 9, 424-428 (1976).
- Taupin, D., Une methode generale pour l'indexation des diagrammes des poudres, J. Appl. Cryst. 1, 178-181 (1968).
- Taupin, D., A powder-diagram automatic-indexing routine, J. Appl. Cryst. 6, 380-385 (1973).
- Visser, J. W., A fully automatic program for finding the unit cell from powder data, J. Appl. Cryst. 2, 89-95 (1969).
- Werner, P.-E., Trial and error computer methods for the indexing of unknown powder patterns, Z. Kristallogr. 120, 375-387 (1964).
- de Wolff, P. M., On the determination of unit-cell dimensions from powder diffraction patterns, Acta Cryst. 10, 590-595 (1957).
- de Wolff, P. M., Detection of simultaneous zone relations among powder diffraction lines, Acta Cryst. 11, 664-665 (1958).
- Wolff, P. M. de, Indexing of powder diffraction patterns, Adv. X-Ray Anal. 6, 1-17 (1963).

#### Discussion

Question (Snyder): Assuming a constant measuring error  $\Delta 2\theta$  it is clear that  $\Delta Q$  will increase with line number and, in turn,  $Q$  and  $M_N$  will be functions of line number.  $M_N$  will also show functional dependence on cell volume and symmetry.  $F_N$ , however, is more nearly independent of cell volume symmetry and line number. Thus,  $F_N$  will have a constant set of boundaries determining the corrections or incorrections of indexing. Why do you prefer  $M_N$  which requires a different set of criteria for each crystal class?

Response (Shirley): It does not seem to be in dispute that large volume and/or lower symmetry make it harder to establish the correctness of a proposed cell. Therefore, a reliability measure for indexings ought to vary with volume and with symmetry to the appropriate degree so as to correct for these influences.  $M_{20}$  does this to approximately the right extent, because it was intended for this purpose, but  $F_N$  was specifically designed to be independent of volume and crystal system, so as to be a more suitable measure of data quality.  $F_N$  tests the quality of the data,  $M_{20}$  the reliability of the model.  $M_{20}$  requires approximately the same set of criteria for each crystal class, because it has already taken into account the different level of agreement (from random

scatter) that each class requires to achieve a particular level of confidence. The increase of  $\Delta Q$  with line number contributes a factor of  $V^{1/3}$  which is included in the overall volume dependence of  $V^{1/3}$  exhibited by  $M_{20}$ , which is appropriate for its function of evaluating proposed indexings.

Comment (Girgis): (1) When indexing powder patterns, if I get a primitive cell, I take care and I am a little bit suspicious. If I get extinctions and can find a space group, then I feel at ease. (2) The percentage of the indexed lines to the calculated lines: the higher percentage gives an indication of the right solution.

Response (Shirley): (1) If you can see systematic absences that come together to make a valid space group, or short list of possible space groups, then this is a good confirmation that the indexing is correct. I would not be worried by a primitive unit cell, because most materials do indeed have primitive lattices, as long as the figure of merit  $M_{20}$  was over 20 and this did not conceal particular lines with unacceptable  $\Delta 2\theta$ 's. With triclinic cells, of course, I should not expect to see any systematic absences, and would feel that more investigation was needed if any seemed to be present.

(2) I agree that good coverage of the calculated pattern by observed lines is a comforting situation, although I would only pay attention to the region near the origin of the reciprocal lattice, because the general picture is already taken care of by the Nobs/Ncalc term contained in all the continually used figures of merit. Low angle unobserved lines that are not accounted for by systematic absences should not be present in quantity, although nearly every pattern seems to have two or three. Absent reflections like 200, 020, 002 are definitely disquieting and deserve further investigation, but correctly indexed patterns sometimes exhibit such absences, so it is best to keep a reasonably open mind.

Comment (Girgis): We found it very helpful for indexing using besides the indexing programs, other physical measurements: e.g., (1) optical measurements to find out if the crystal is uniaxial, (2) electron diffraction, and (3) density measurements.

Response (Shirley): I fully agree--this kind of supplementary information is very valuable, especially electron diffraction which can give definite confirmation of the corrections and symmetry of a number of zones. Polarizing microscopy is useful, especially to confirm a high symmetry cell, but does usually require that the material is transparent, and can be seriously impeded by twinning. Density measurements can be extremely helpful, as Dr. Louër's talk will show, but one must be careful that the chemical formula of the material is correct and that it is stoichiometric.

## SUCCESSIVE DICHOTOMY METHOD FOR INDEXING POWDER PATTERNS

D. Louër

Université de Rennes  
Laboratoire de Cristallographie  
Campus de Beaulieu  
35042 Rennes-Cédex - France

The successive dichotomy method [1] is an efficient procedure for indexing accurate powder patterns. Such a procedure was used in computer programs for indexing orthorhombic or higher symmetry systems or, more recently, by incorporating it in a grid search program [2] for lower symmetry systems.

The successive dichotomy method is a form of binary search with an exhaustive strategy in parameter-space. Each variable parameter is divided into sections. Combination of these sections forms domains. Using rigorous inequalities based on the experimental error of the observed lines, each domain is tested. When a possible solution is contained in a domain, a dichotomy process is used for reducing the domain boundaries.

The introduction of a partition of volume-space, or domains of volumes defined from density and error on density, decreases the cpu time, and allows an extension of the dichotomy method to monoclinic system. With this strategy two previous experimental versions of programs (LOUV and LOUM) [3] were realized, and described in a paper by Shirley [4]. They have been incorporated in DICVOL, which allows a search for systems down to monoclinic. The realization of a definitive program based on the successive dichotomy method is in progress.

### References:

- [1] Louër, D. and Louër, M., J. Appl. Cryst. 5I 271-275 (1972).
- [2] Shirley, R. and Louër, D., Acta Cryst. A34, S 382 (1978).
- [3] Louër, D., unpublished work.
- [4] Shirley, R., Crystallographic Computing (Delft University Press Oosthoek, 1978).



THE DETERMINATION OF THE PRECISE LATTICE PARAMETER  
OF A DIFFUSE MINOR PHASE IN A DILUTE BINARY URANIUM ALLOY

D. A. Carpenter and C. M. Davenport  
Oak Ridge Y-12 Plant<sup>1</sup>  
Oak Ridge, TN 37830

When a uranium-5.9 atomic percent niobium rod is extruded in the alpha-phase region, a metastable two-phase microstructure results. The bcc  $\bar{\gamma}_1$  phase, ranging in composition from 18 at. percent niobium to about 34 at. percent niobium, constitutes approximately 15-20 percent of the volume of the extruded material, with the remaining volume occupied by the orthorhombic alpha phase. The x-ray diffraction pattern consists of intense, broadened alpha-phase peaks and one weak, broad, low-angle [(110) at  $37^\circ 2\theta$ ,  $\text{CuK}\alpha$  radiation]  $\bar{\gamma}_1$  phase peak partially overlapping the alpha-phase (002) peak. The  $\bar{\gamma}_1$  (110) peak has a FWHM value of  $0.4\text{-}0.5^\circ 2\theta$  and a peak height of 15-30 c/s.

The  $\bar{\gamma}_1$  lattice parameter is very sensitive to the niobium concentration which varies with changes in the metastable  $\alpha + \bar{\gamma}_1$  thermodynamic state. The analysis of the diffraction pattern requires the precise determination of the  $\bar{\gamma}_1$  (110) peak position as an aid to understanding the physical metallurgy of the extrusion process. This is carried out by first resolving the  $\bar{\gamma}_1$  (110) peak from the alpha (002) peak by a nonlinear least-squares fit to a modified Lorentz function. The resulting  $2\theta$  value is then corrected for sample displacement by using the drift correction of the alpha (002) peak calculated from a lattice parameter determination of the alpha phase. Repetitive measurements on different samples gave average standard deviations of  $0.006^\circ 2\theta$  for the  $\bar{\gamma}_1$  (100) peak position and  $6 \times 10^{-5}$  nm for the  $\bar{\gamma}_1$  lattice parameter.

Examples of this analysis carried out on alpha-phase extruded U-5.9 at. percent Nb rods as a function of extrusion variables will be presented.

<sup>1</sup>Operated for the Department of Energy by Union Carbide Corporation-Nuclear Division under Contract W-7405-eng-26.



PRECISION GUINIER X-RAY POWDER DIFFRACTION DATA

J. W. Edmonds  
 Analytical Laboratories  
 The Dow Chemical Company  
 Midland, MI 48640

The opportunity to employ microcomputers to aid in x-ray powder diffraction data acquisition/reduction by microdensitometer reading of high resolution Guinier films not only provides readily available high quality data for phase characterization [1]<sup>1</sup> and reliable pattern indexing, but indicates the accessibility of a much higher degree of precision for these systems than has previously been acknowledged.

The applications of least square fitting of profiles to diffraction data [2,3] raised questions with respect to microphotometered Guinier film data: (1) would accuracy of the determination of  $2\theta_{obs}$  be improved by the fit of an analytical profile and (2) would the type of profile yield information concerning camera and/or sample aberrations affecting peak shape.

The analytical profile chosen was the Pearson Type VII function due to the computational ease with which it can be varied in form from Cauchy to Gaussian [4]. Allowance for peak asymmetry was made to using two split profiles for each peak with a common position and height but differing breadths. Using an internal standard of size selected silicon [5], known sample preparation and film scanning techniques [1], fitting analytical profiles to digitized data from the entire Ewald sphere for  $\text{CuK}_{\alpha 1}$  radiation (front and back reflection patterns from the same sample preparation), and determining cell constants by least squares fit of only those  $2\theta_{obs}$  which lie between known Si lines, the following results were obtained:

Table 1

	a, Å	c, Å	$\sqrt{\Delta 2\theta}$	$\Delta 2\theta_{max}$	Nobs/Nposs	F <sub>N</sub>
$\alpha\text{-Al}_2\text{O}_3$ <sup>a</sup>	4.75939 (5)	12.9919 (1)	0.004°	0.015°	37/57	199
Zn <sup>0</sup> <sup>a</sup>	2.66474 (7)	4.9480 (1)	0.005°	0.010°	19/19	194
Cu <sup>0</sup> <sup>b</sup>	3.6152 (3)	--	0.013°	0.045°	8/8	77

<sup>a</sup>Crystallite size >10,000 Å.

<sup>b</sup>Crystallite size ~300 Å.

Figures in brackets indicate the literature references at the end of this paper.

Two back reflection lines for  $\text{Cu}^0$  (400 and 420) are extremely weak and one (the 400) is buried under a strong sample support line (Al foil). Peak resolution is difficult in the two extreme cases, and the corresponding  $\Delta 2\theta$  values are  $-0.037^\circ$  and  $0.045^\circ$ , respectively. Deleting these values yields for  $\text{Cu}^0$ :  $a = 3.6152$  [1] Å;  $\overline{\Delta 2\theta} = 0.004^\circ$ ,  $\Delta 2\theta_{\text{max}} = 0.006^\circ$ ,  $F_6 = 185$ .

These results represent precision of 1 to 2 parts per 100,000 except for  $\text{Cu}^0$  (1 part in 35,000), and are within  $1\sigma$  of the cell constants reported by the National Bureau of Standards.

These results give strong indications for the following conclusions:

1. Extremely high quality data is available from Guinier Cameras using high quality internal standards.

2. The inherent high quality can be extracted with simple profile fitting techniques to determine observed peak position.

3. For the fitted asymmetrical profiles, the best peak position at all values of  $2\theta$  is the profile center, a better estimation of the observed peak maximum. Instrumental aberrations which shift the observed peak maximum from the true position are negligible or at least very small.

4. Substantial peak asymmetry may be present but appears to be determined by sample rather than instrumental aberration. The asymmetry is not a simple function of  $2\theta$  as has been assumed in some applications of the Rietveld method to x-ray film data [6].

5. Profile variations in one film are a function both of background selection and line intensity due to the effects of film sensitivity in addition to the effects noted above. The profile will not easily be "quantitated" as it can be for the diffractometer [2].

6. Various effects on lattice parameters can be pronounced, especially temperature variation during data collection, and changes in chemical composition and physical state (strain, imperfections) of the sample. Even though it is possible to measure lattice parameters with this level of precision, the same level of reproducible accuracy will be more difficult to achieve due to the variation of the above parameters from laboratory to laboratory, especially during the simplest of sample preparations.

#### References

- [1] Edmonds, J. W. and Henslee, W. W., in Advances in X-ray Analysis, Vol. 22, 143-150 (Plenum, New York, 1979).
- [2] Parrish, W., Huang, T. C. and Ayers, G. L., Trans. Am. Cryst. Assoc. 12, 55-73 (1977). See also these proceedings.
- [3] See papers by Hewat, A. E., Young, R. A., Baerlocher, Ch., Cox, D. E., Albinati, A. and Prince, E., in these proceedings.
- [4] Hall, M. M., Jr., Verrarraghavan, V. G., Rubin, H. and Winchell, P. G., J. Appl. Cryst. 10, 66-68 (1977).

- 5] NBS SRM 640. Particle size reduced by suspending in isopropyl alcohol and regrinding particles which dropped out within the first half hour. Fines were vacuum dried before using.
- 6] Malmros, G. and Thomas, J. O., J. Appl. Cryst. 10, 7-11 (1977).

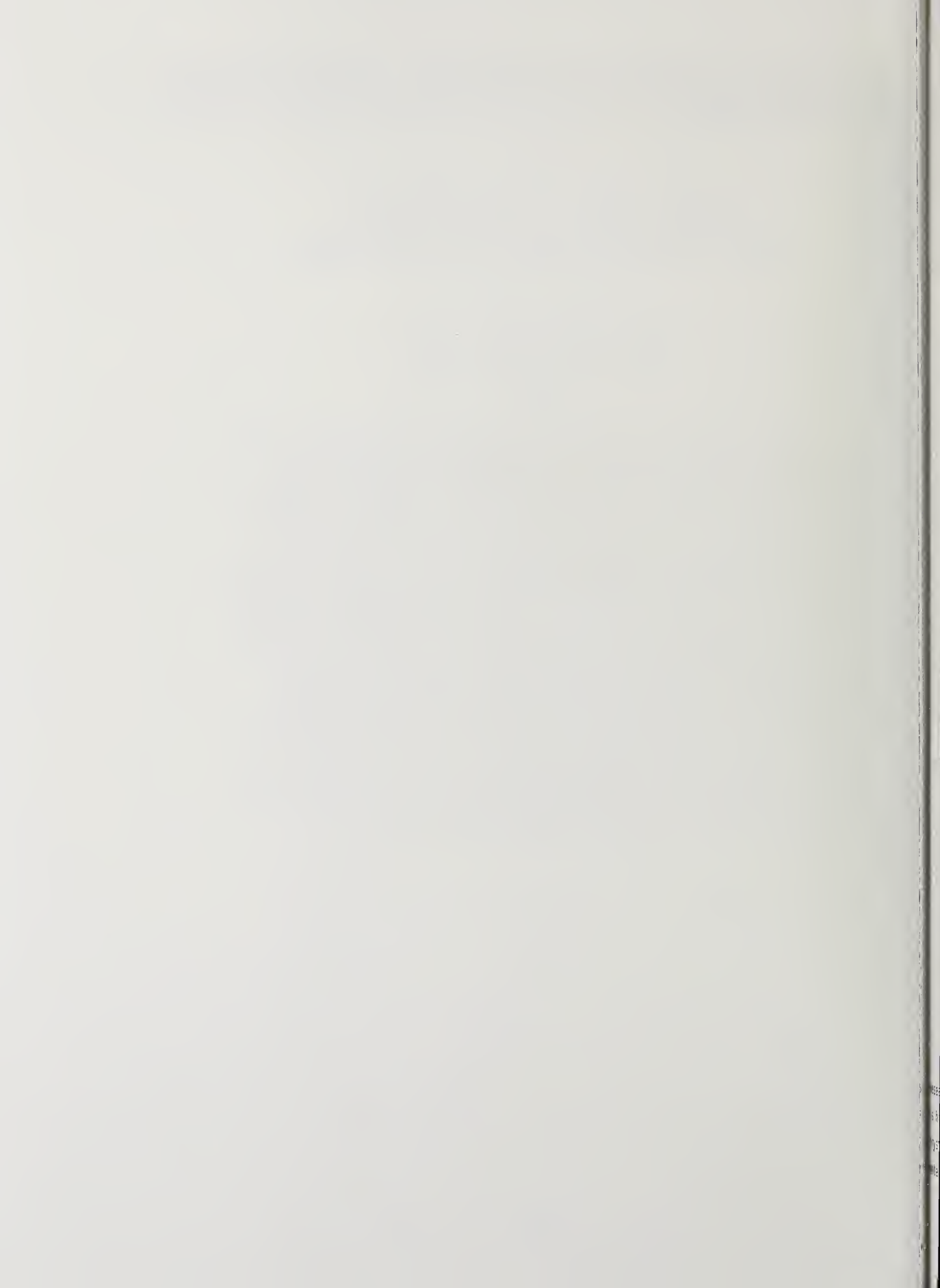


A SIMPLE GRAPHICAL METHOD FOR OBTAINING  
REASONABLY ACCURATE CELL DIMENSIONS FROM X-RAY  
POWDER PHOTOGRAPHS OF HEXAGONAL AND TETRAGONAL MINERALS

E. E. Fejer

British Museum, Natural History  
London, S. W. 7 Cromwell Road  
ENGLAND

This is essentially a graphical, high-angle extrapolation method using the Nelson-Riley function of obtaining cell dimensions from 11.46 cm diameter powder photographs of cubic, tetragonal, hexagonal, and occasionally even of orthorhombic compounds.  $\sin^2\theta$  corrected to  $\lambda K\alpha_1$  is obtained by direct measurement of  $2s = 360^\circ - 4\theta$  of suitable lines on the film and divided by  $\alpha + \beta R$  where  $\alpha$  is  $h^2 + k^2$  for tetragonal crystals,  $\beta$  is  $l^2$ , and  $R$  is  $a^2/c^2$ .  $A$  (the ratio obtained) is plotted against corresponding values of the Nelson-Riley function. A straight line drawn through the points thus obtained is extended to where it meets the axis. From the intercept at this point  $\underline{a}$  and  $\underline{c}$  can be calculated. By slight and judicious alteration of  $R$  the graph can usually be improved considerably. Erroneous indexing will also become obvious. From a final  $A$ -value, and taking into account possible errors, reproducible cell dimensions can be calculated, and these were found to be correct to about 3-4 parts in ten thousand.



## THE RELIABILITY OF POWDER INDEXING PROCEDURES

A. D. Mighell and J. K. Stalick  
Center for Materials Science  
National Bureau of Standards  
Washington, DC 20234

Recent work has proved that identification/registration of molecular materials by cell parameters is extremely effective. The NBS Crystal Data File contains unit-cell data for 60,000 substances; of these, 30,000 are molecular materials which crystallize predominantly in the monoclinic, triclinic, and orthorhombic crystal systems. If one can obtain a unit cell of a crystalline compound from a powder sample, the basis for a convenient identification procedure is established. Consequently, it is essential to determine the reliability of indexing procedures for the low-symmetry crystal systems.

In our analysis, we used a standard indexing program on fifty powder patterns measured by the JCPDS Associateship at the National Bureau of Standards. The indexing program determined the correct cell in about 50 percent of the cases and a derivative lattice in many of the remaining cases. As the quality of data decreases, the probability of obtaining either the correct lattice or a derivative lattice continually decreases. We have noted that unindexed lines often occur, not from a small amount of a second phase, but because the program has found a derivative lattice. This study has shown that the existence of geometrical ambiguities constitutes a major problem to the indexing program.

### 1. Introduction

A solid-state material can conveniently be characterized by its unit cell. Recent search with large data bases has proved that the lattice of a crystalline material is highly diagnostic; this is particularly true for molecular compounds, which usually crystallize in such lower-symmetry crystal systems as monoclinic and triclinic. Thus, a material can be registered or identified once any primitive cell which defines the lattice

has been determined. The procedure [1]<sup>1</sup> consists of the following steps (figure 1): (1) determine a primitive cell in reciprocal space; (2) convert this cell to a primitive cell in direct space; (3) reduce the cell; (4) check against the file of known materials. NBS Crystal Data File<sup>2</sup> contains unit-cell information for about 60,000 substances and is growing at the rate of about 5,000 entries per year. This represents one of the largest evaluated numerical data bases, roughly twice the size of the Powder Diffraction File. The Crystal Data File is soon to be an active component of the NIH/EPA Chemical Information System. To automate the entire registration/identification procedure, it is important to develop simple, inexpensive, and rapid methods for unit cell determination.

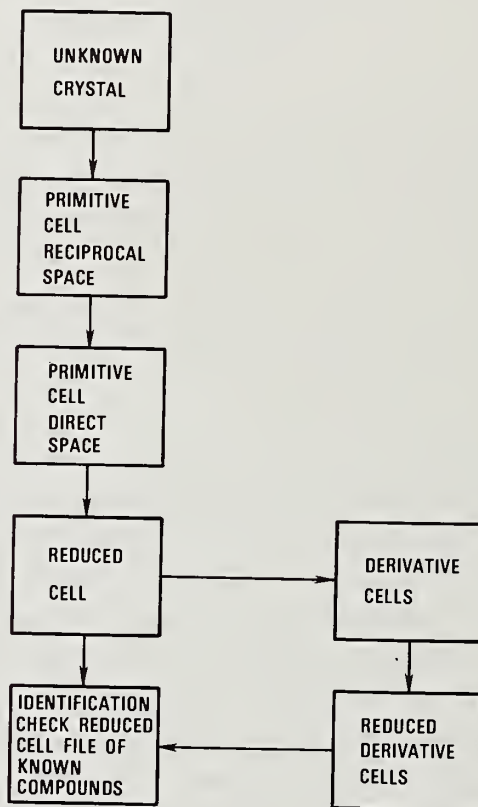


Figure 1. Outline of a crystallochemical identification procedure based on the NBS Crystal Data File reduced cells. Identification is still possible if the unknown cell defines a derivative lattice (e.g. a sub-, super-, or composite lattice).

<sup>1</sup>Figures in brackets indicate the literature references at the end of this paper.

<sup>2</sup>This file contains data that have been published in the Crystal Data Determinative [2], as well as more recent data.

<sup>3</sup>JCPDS--International Centre for Diffraction Data.

If a single crystal of suitable size can be obtained, one can determine the unit cell with an automated diffractometer or by film techniques. However, this is not always possible owing to the lack of necessary equipment or to the nature of the sample. Often a highly crystalline sample may be available but with crystals too small for the single-crystal method. This is frequently true for molecular compounds such as organics and organometallics. The organic component of the file has more than 30,000 entries and contains many compounds of industrial importance. For these materials, one potential approach is to take a powder pattern, and to index the pattern to obtain a unit cell. Once a cell has been obtained, the Crystal Data File can be checked for identification.

If powder indexing procedures are to be successful for molecular substances, they must work well in the lower-symmetry crystal systems. Figure 2 shows the space-group distribution for organic and organometallic compounds. The most common space groups are  $P2_1/c$  and  $P\bar{1}$ . In fact, 75 percent of the materials fall into five space groups, the first four of which are primitive. Figure 3 shows a classification of these materials by reduced form. A few reduced forms dominate; they correspond to the primitive orthorhombic, monoclinic, and triclinic Bravais lattices. Consequently, in our analysis of powder indexing procedures we have concentrated on the indexing of powder patterns for substances that crystallize in the lower-symmetry crystal systems. An earlier analysis by G. G. Johnson and J. W. Visser [3] has shown that Visser's indexing program [4] is indeed a valuable tool for obtaining unit cells from powder data. In our study special emphasis has been placed on analyzing the geometrical problems associated with the indexing of powder data.

## 2. Experimental

We used a sample of fifty powder patterns in the indexing study. The data were selected from "Standard X-ray Diffraction Patterns" taken by the JCPDS Associateship at the National Bureau of Standards [5]. These patterns are of high quality with an average error of slightly more than  $0.01^\circ$  in  $2\theta$  for the lines in the powder pattern. An automatic program for finding the unit cell from powder data [4] was used. The following five types of test problems were used as input to the indexing program: (1) the first 20 observed powder lines with the observed  $2\theta$  values; (2) the first 20 observed powder lines with calculated  $2\theta$  values; (3) the first 20 calculated lines (whether observed or not) with calculated  $2\theta$  values; (4) 20 lines obtained by selecting every other calculated line with calculated  $2\theta$  values; (5) 20 lines obtained by selecting every third calculated line with calculated  $2\theta$  values. The first option gave us a test of the indexing program on actual data. The other options, all of which used exact data, gave us insight on the interaction of the indexing program with geometrical problems associated with indexing.

When using actual data, the program found a cell defining the correct lattice in 50 percent of the cases. In the remaining cases, the program found either a cell defining a derivative lattice or a cell defining a lattice that bore no simple relationship to the correct lattice. Test problems (2)...(5) repeatedly illustrated the troublesome nature of geometrical problems associated with the indexing of powder data. No matter how reliable

## Space-Group Frequency (Organic)

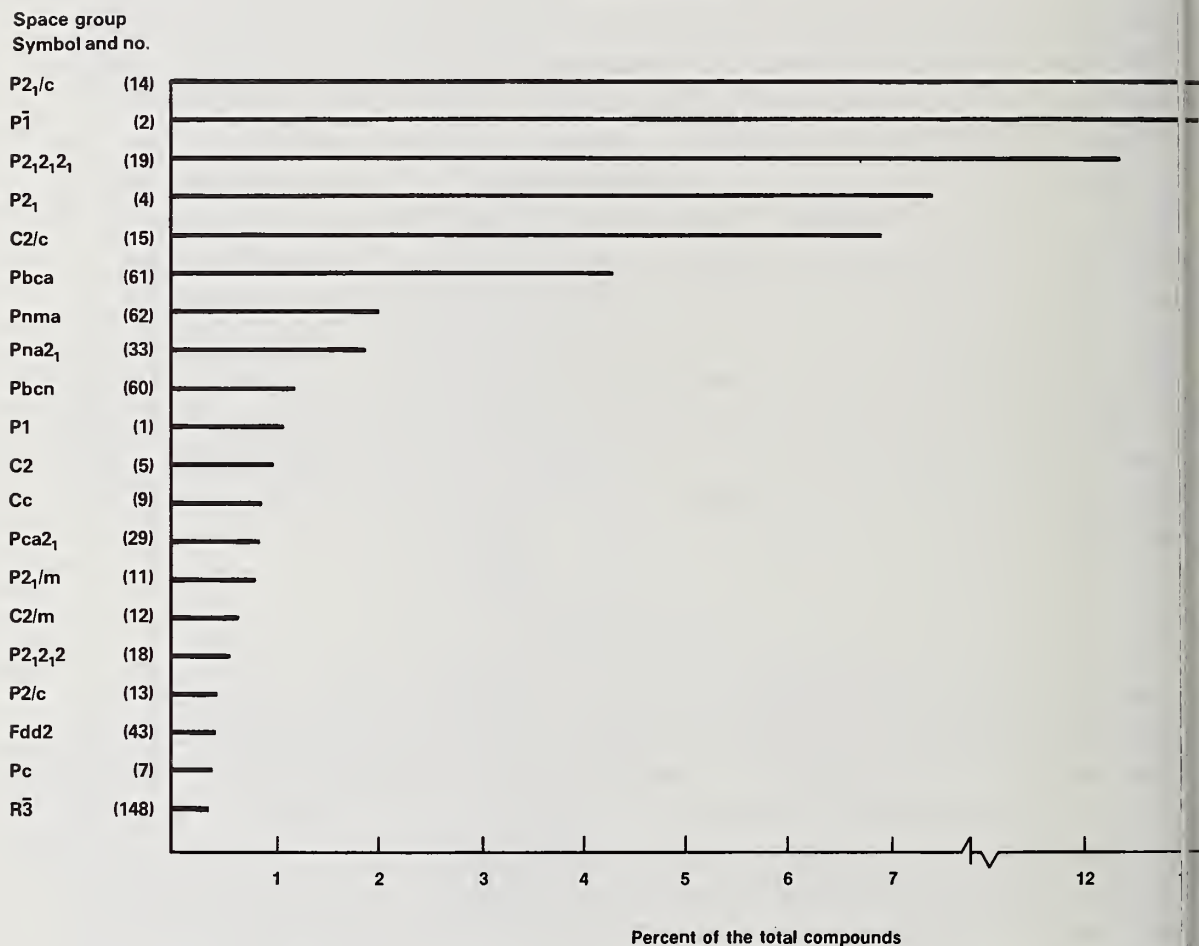
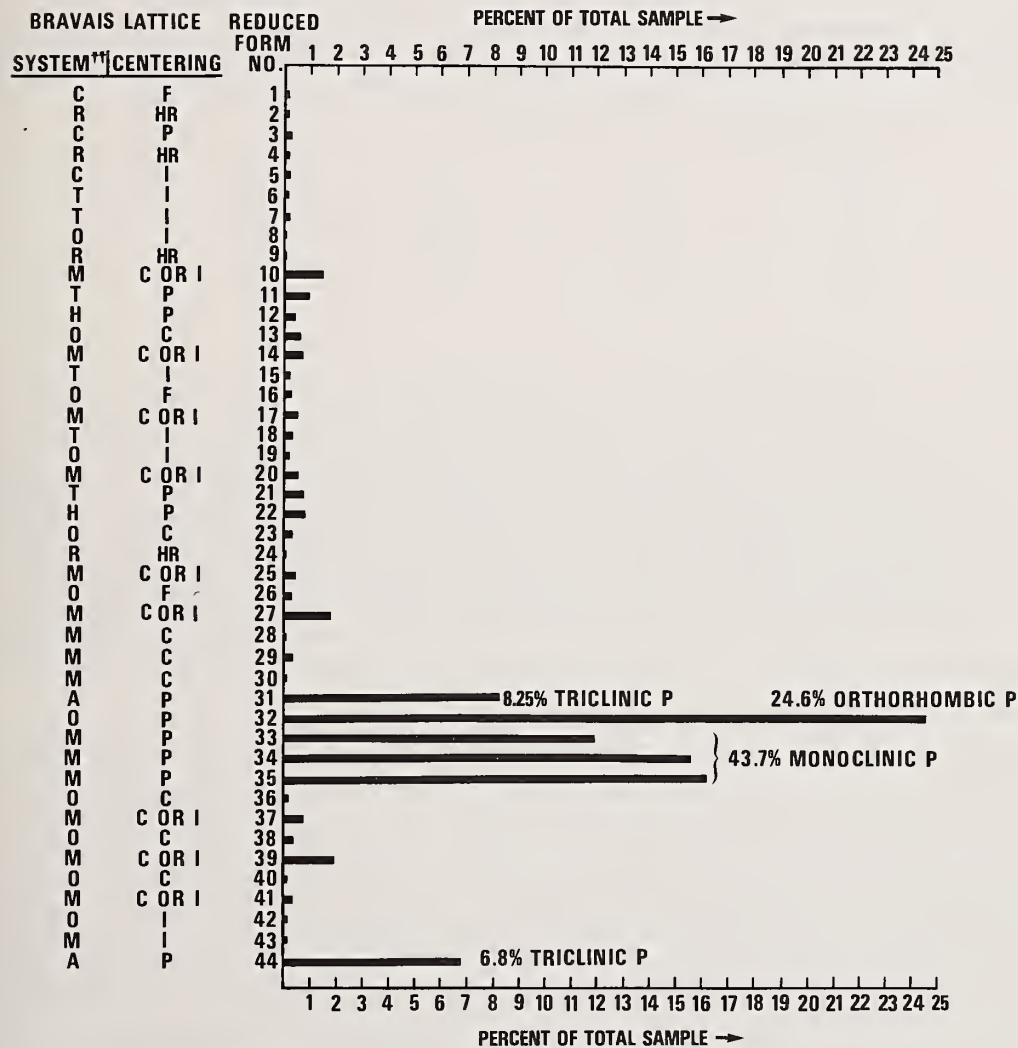


Figure 2. Relative frequency of space group occurrence for 21,051 organic and organometallic crystalline compounds. The data are from Volumes 1 and 3 of Crystal Data Determinative Tables and from the structural entries in the Cambridge Data Bank.

the observed  $2\theta$  values are, one often does not obtain the true lattice. Furthermore, a found the indexing program extremely sensitive to the quality of the data. Thus, when using the first 20 observed powder lines with calculated  $2\theta$  values, we obtained the correct solution in 75 percent of the cases. In the remaining cases, we usually obtained a derivative lattice as one of the solutions.

## REDUCED FORM FREQUENCY (21051 ORGANIC COMPOUNDS)



††KEY: A/M/O/R/T/H/C FOR TRICLINIC/MONOCLINIC/ORTHORHOMBIC/  
RHOMBOHEDRAL/TETRAGONAL/HEXAGONAL/CUBIC.

Figure 3. Classification of organic materials by reduced form number (see reference [6]). The figure shows the relative frequency of occurrence for each of the 44 reduced forms. The compounds are the same as those in figure 2. These statistics were obtained in collaboration with John Rodgers of the Cambridge Crystallographic Data Centre.

### 3. Discussion

#### 3.1. Theoretical background

Because we have data that correspond only to the lengths of reciprocal lattice vectors, two or more lattices are often consistent with large regions of the powder pattern. Indexing problems of a geometrical nature can best be understood in the framework of derivative lattices. In a paper by Santoro and Mighell [7] derivative lattices were defined and divided into three types that are specified by the nature of the transformation matrix  $\xi$  that relates the original lattice and the derivative lattice. A derivative lattice is defined in [7] as follows:

$$b_i = \sum_j S_{ij} a_j \quad (i, j = 1, 2, 3)$$

The original lattice is specified by  $a_j$  (three noncoplanar translations); the derivative lattice is specified by  $b_i$  (three noncoplanar translations that can be regarded as the edges of a primitive cell); and  $\xi$  is the transformation matrix relating the two lattices. A derivative lattice is a superlattice if the elements  $S_{ij}$  of matrix  $\xi$  are integers and if the determinant  $|\xi|$  is greater than one. A derivative lattice is a sublattice if the elements  $T_{ij}$  of matrix  $\tau$  (where  $\tau = \xi^{-1}$ ) are integers and if the determinant  $|\tau|$  is greater than one. Finally, a derivative lattice is a composite lattice if one or more of the elements  $S_{ij}$  of matrix  $\xi$  and one or more of the elements  $T_{ij}$  of matrix  $\tau$  are fractional.

Derivative lattices have features in common. Thus all nodes of a superlattice are nodes of the original lattice, but the reverse is not so; likewise all nodes of the original lattice are nodes of the sublattice but not all nodes of the sublattice are in the original lattice. A composite lattice is neither a sublattice nor a superlattice but it partakes of the two. Of particular interest to the indexing problem is the fact that derivative lattices have a certain number of d-spacings in common. With the indexing program we commonly obtained superlattices of twice the volume of the true lattice, sublattices of one-half the volume, and composite lattices of the same volume. Also, we obtained more complex derivative lattices with nonintegral volume relationships to the correct lattice.

#### 3.2. Total geometrical ambiguities

A total geometrical ambiguity occurs if two or more different lattices have exactly the same set of d-spacings. These ambiguities have been discussed in detail in a paper Mighell and Santoro [8]. Figure 4 shows a schematic example of a four-fold total geometrical ambiguity. The same set of d-spacings is consistent with four different

GEOMETRICAL AMBIGUITY

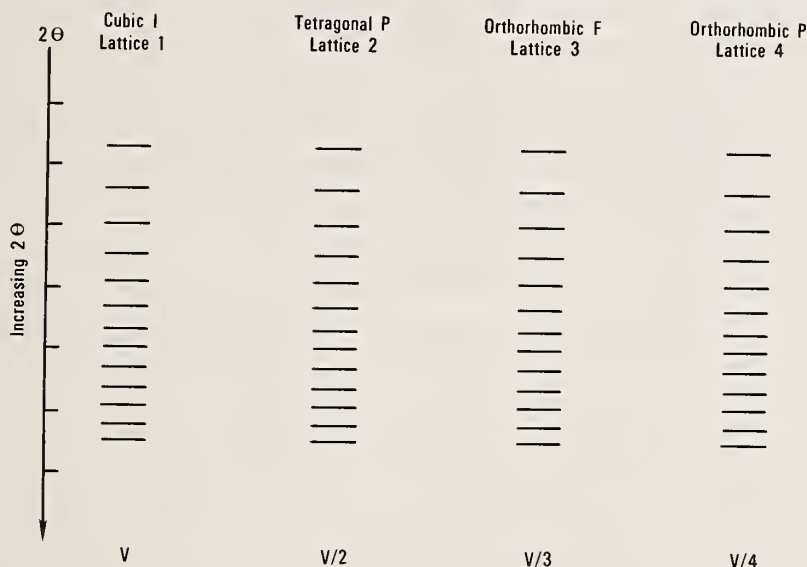


Figure 4. Total geometrical ambiguities. From any cubic I lattice, one can calculate a tetragonal P, an orthorhombic F and an orthorhombic P lattice all of which have exactly the same d-spacings (ref. [8]) as depicted schematically. The transformation matrices required to produce this four-fold ambiguity are:

$$\begin{aligned}
 \text{cubic I} \rightarrow \text{tetragonal P} & \quad \left( 0 \frac{1}{2} \frac{1}{2} / 0 \frac{1}{2} \frac{1}{2} / \frac{1}{2} 0 0 \right) \\
 \text{cubic I} \rightarrow \text{orthorhombic F} & \quad \left( \frac{1}{3} \frac{1}{3} 0 / 0 0 \bar{1} / 1 \bar{1} 0 \right) \\
 \text{cubic I} \rightarrow \text{orthorhombic P} & \quad \left( \frac{1}{4} \frac{1}{4} 0 / 0 0 \frac{1}{2} / \frac{1}{2} \frac{1}{2} 0 \right)
 \end{aligned}$$

All four lattices are represented by different reduced cells with primitive cell volumes in the ratios:  $1 : \frac{1}{2} : \frac{1}{3} : \frac{1}{4}$  as shown.

lattices, characterized by four different reduced cells with four different volumes. Although total geometrical ambiguities are probably restricted principally to the higher symmetry systems, their existence is proof that indexing is by no means simple and sometimes more than one lattice is consistent with a given set of d-spacings.

3.3. Partial geometrical ambiguities

A partial geometrical ambiguity occurs if two or more different lattices have some but not all d-spacings in common. Sometimes two different lattices are consistent with

large regions of the same powder pattern (hence the importance of using all the observed data in the indexing program). The indexing program is always confronted by partial geometrical ambiguities because every lattice has associated derivative lattices and derivative lattices have d-spacings in common. A schematic example of this is shown in figure 5. In this figure, lattices (1) and (2) have many d-spacings in common. These two lattices are in a composite relationship with each other as they have a common superlattice (they may be likened to siblings). If one allows for accidental absences, it is quite possible that more than one consistent solution exists (hence the importance of using all possible weak lines as well as strong lines).

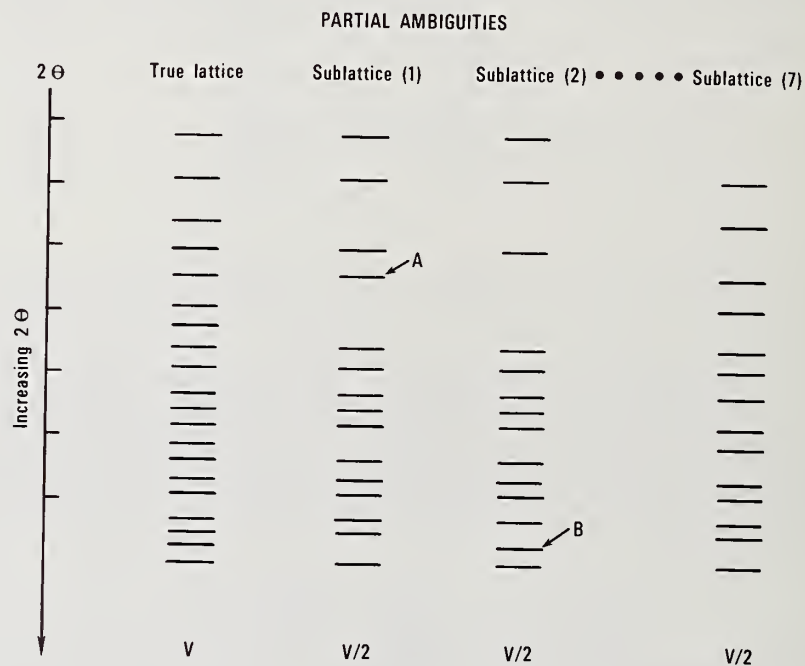


Figure 5. Partial geometrical ambiguities. Composite lattices often have many d-spacings in common and sometimes the d-spacings can be identical over a large region in  $2\theta$ . For example, the seven sublattices of  $V/2$  (i.e. those with defining primitive unit cells of  $1/2$  the volume of the unit cell defining the original lattice) that are associated with any given original lattice are in a composite relationship to one another. For a procedure to generate such derivative lattices see Santoro and Mighell [7,9], and for a listing of the transformation matrices see Mighell [1]. All d-spacings in each of the sublattices are in the original lattice. Also each sublattice has d-spacings in common with the other sublattices. Here sublattices (1) and (2) have d-spacings in common except for line 'A' which is not in sublattice 2, and 'B' which is not in sublattice (1). Usually such a close match does not occur over the entire powder pattern but it is not uncommon for such close agreement to occur over large regions of  $2\theta$ . Accidental absences will compound the problem.

### 3.4. Misrefinements

The concept of the existence of partial geometrical ambiguities allows us to explain certain deceptive types of solutions that occur in the indexing of powder patterns. The indexing program often finds a solution that indexes the powder pattern except for a few lines. In many cases unindexed lines may result not from a second phase but rather from the fact that one has determined a derivative lattice. This is illustrated in figure 6. Here, cells (1) and (2) of the same volume define lattices that are in a composite relationship with one another. Let us suppose that the indexing program finds cell (2) and then refines this cell with the data that really are from cell (1). Since cell (1) and cell (2) have a common superlattice, many d-spacings are in common. Two things can happen: first, if one is fortunate, such a refinement will use only the lines in common to both lattices

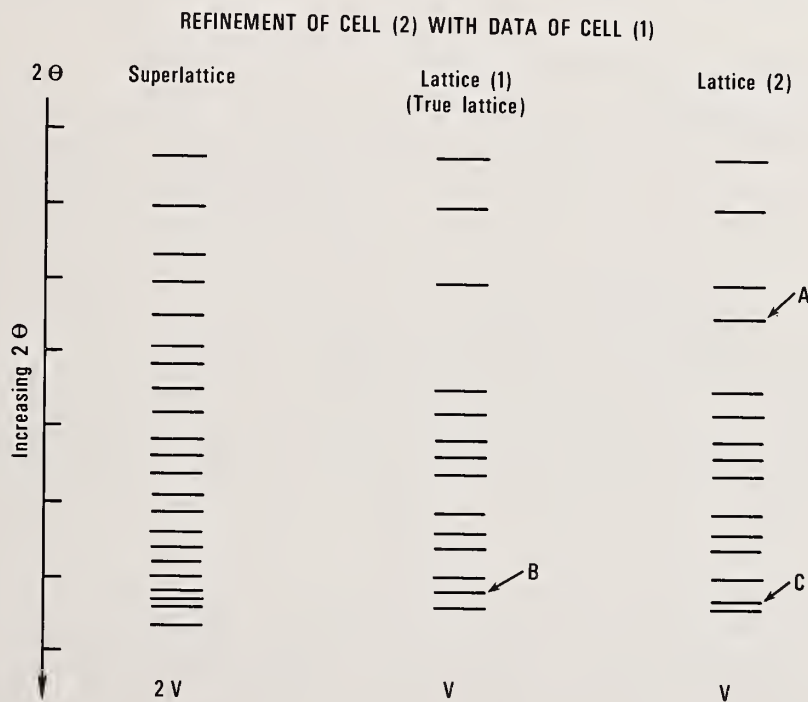


Figure 6. Schematic example of how a misrefinement can occur. Here the true lattice (1) and lattice (2) of volume  $V$  ( $V$  = volume of the primitive unit cell defining the lattice) have common superlattices of  $2V$ . Hence all lines in lattice (1) and lattice (2) are in the superlattice. Lattices (1) and (2) are in a composite relationship with each other and have many lines in common. The indexing program mistakenly tries to refine cell (2) with the data for cell (1). The line marked 'A' will not cause a problem as it will be considered an accidental absence. Line 'B' will cause a problem because it is observed but is not present in lattice (2). As 'B' is very close to line 'C', the program will use line 'B' for 'C' which will result in a misrefinement. Such misrefinements are not uncommon especially with data of poor quality.

and several lines will remain unindexed. Such cases occur and it is theoretically possible to transform cell (2) to cell (1) with a transformation matrix  $\xi$  as defined earlier for a composite lattice. Thus, although one has not obtained the correct lattice, one has obtained a correct derivative lattice. Second, if one is "unlucky" the refinement will use lines common to both lattices and some of the lines that do not belong (but are close) to allowed d-spacings for lattice (2). This results in a misrefinement and one obtains an answer that is neither the correct lattice nor a derivative lattice. Misrefinements become more and more common as the quality of the data decreases. Thus, the chance of a misrefinement can be minimized by taking good data and by adjusting parameters of the indexing program so that it will use only observed data in the refinement that are close to calculated values. The data must be good and the program must be told so.

#### 4. Conclusions

The major conclusion of this study is that automated indexing programs have great potential for finding cells suitable for identification and for characterization. However, the data must be of high quality. If single crystals of appropriate size cannot be obtained, an attractive alternative is to measure a powder pattern and to employ an indexing program to obtain a unit cell. As indicated earlier, if one has a correct primitive cell of the lattice, identification against the Crystal Data File is almost 100 percent certain, especially if one has some chemical information. Also, recent work with the Crystal Data File and with new lattice identification techniques indicates that identification is still likely if one has determined a simple derivative lattice.

Our study has revealed several considerations in using an indexing program: (1) as many lines as possible should be used, including small peaks; (2) the observed data must be of high quality (see also [10]); (3) peaks in the low  $2\theta$  region of the powder pattern are especially important; (4) unindexed peaks can occur either from a second phase or from a derivative lattice; (5) figures of merit should be interpreted with caution because in certain cases derivative lattices can give high figures of merit; (6) sometimes more than one solution exists (i.e. two or more lattices that are consistent with the same set of d-spacings). Finally, the study has shown that the power of the indexing program can be significantly augmented by devising new algorithms that take into account the existence of derivative lattices and will find the transformation matrix  $\xi$  that relates a derivative lattice to the true lattice.

---

We wish to thank Antonio Santoro for many helpful discussions in connection with this work and Timothy Blizzard for his assistance with the many computer runs required for the survey.

## References

- [1] Mighell, A. D., *J. Appl. Cryst.* 9, 491-498 (1976).
- [2] Crystal Data Determinative Tables, Third Edition: Volumes 1 and 2, J. D. H. Donnay, H. M. Ondik, S. Samson, Q. Johnson, M. H. Mueller, E. R. Ryba, G. M. Wolten, M. E. Mrose, O. Kennard, D. G. Watson, and M. V. King, eds. (1972,1973); Volume 3, O. Kennard, D. G. Watson, J. R. Rodgers, S. M. Weeds, A. Doubleday, and B. Hummelink-Peters, eds. (1978); Volume 4, H. M. Ondik, A. D. Mighell, M. E. Mrose, C. R. Robbins, and J. K. Stalick, eds. (1978). U.S. Department of Commerce, National Bureau of Standards and the JCPDS-International Centre for Diffraction Data, Swarthmore, PA.
- [3] Johnson, G. G. and Visser, J. W., Paper F10, American Crystallographic Association Spring Meeting, University of Virginia, Charlottesville, Virginia (1975).
- [4] Visser, J. W., *J. Appl. Cryst.* 2, 89-95 (1969).
- [5] Standard X-ray Diffraction Patterns published in Powder Diffraction Data from the Joint Committee on Powder Diffraction Standards Associateship at the National Bureau of Standards, JCPDS--International Centre for Diffraction Data, 1601 Park Lane, Swarthmore, PA, 19801 (1976).
- [6] International Tables for X-ray Crystallography, Vol. 1 (Kynoch Press, Birmingham, 1969), pp. 530-535.
- [7] Santoro, A. and Mighell, A. D., *Acta Cryst.* A28, 284-287 (1972).
- [8] Mighell, A. D. and Santoro, A., *J. Appl. Cryst.* 8, 372-374 (1975).
- [9] Santoro, A. and Mighell, A. D., *Acta Cryst.* A29, 171-175 (1973) (See appendix).
- [10] Shirley, R., "Data Accuracy for Powder Indexing," Symposium on Accuracy in Powder Diffraction, National Bureau of Standards, Gaithersburg, Maryland (1979).

## Discussion

Comment (Girgis): You showed a slide with four "correct" solutions of indexing. One of them is cubic, others are orthorhombic P, orthorhombic F, and tetragonal P. I would use optical measurements which would give me a clear differentiation between these crystal systems giving the right solution.

Response (Mighell and Stalick): In our study, we analyzed the reliability of indexing procedures assuming that only a set of d-spacings is available. In actual practice, however, optical measurements should routinely be carried out. We completely agree with your statement that such measurements are often invaluable in distinguishing between several possible cells that could index a powder pattern.



X-RAY POWDER DIFFRACTION IDENTIFICATION OR CRYSTAL PHASES WITH SUPERIMPOSED LINES BY THEIR SELECTIVE CRYSTALLIZATION

I. Mayer

Department of Inorganic and Analytical Chemistry

I. Gedalia and B. Laufer

Preventive Dentistry

Dental Morphology

Hadassah School of Dental Medicine

Hebrew University, Jerusalem, Israel

The identification of chemical compounds by x-ray powder diffraction is based on the  $d$  values of the three strongest lines of their x-ray powder pattern. This method is seriously handicapped when two phases coexist in the system and the strongest lines of one of them are superimposed by the lines of the other. This problem and its possible solution by selective crystallization is demonstrated in the following example:

The fluorination of  $\text{Ca}_5(\text{PO}_4)_3\text{OH}$ , the main mineral constituent of dentin, was studied. When  $\text{Ca}_5(\text{PO}_4)_3\text{OH}$  is treated by a NaF solution in acid media,  $\text{CaF}_2$  can form.  $\text{CaF}_2$  has its three strongest lines at  $d$  values of 1.93<sub>x</sub>, 3.15<sub>y</sub> and 1.65<sub>z</sub>, and the first two were found to be superimposed by the (222) and (102) reflections of  $\text{Ca}_5(\text{PO}_4)_3\text{OH}$ . As a result of this,  $\text{CaF}_2$  could not be detected in the system, because even if present, its relatively small amounts cannot change the intensity of the (222) and (102) reflections. These difficulties have been overcome when the samples were heated to about 600 °C. After this heat treatment, the intensity of the lines at  $d$  values 1.93 and 3.15 relative to the intensity of other reflections of the pattern has increased to such an extent that leaves no doubt that the origin of the increased intensity has to be attributed to the presence of  $\text{CaF}_2$ . The above results seem to indicate that at 600 °C the crystallization of  $\text{CaF}_2$  in the hydroxyapatite is significantly improved. Consequently, sharp increase in the intensity of the reflections of  $\text{CaF}_2$  takes place relative to that of  $\text{Ca}_5(\text{PO}_4)_3\text{OH}$ .



COMPARISON BETWEEN DEBYE-SCHERRER, TRANSMISSION  
AND REFLECTION MEASURING MODES

E. Woelfel  
Stoe  
Darmstadt, W. Germany

An automated powder counter diffractometer for Debye Scherrer capillaries, powder plates and thin powder layers has been developed on which transmission and reflection measuring modes can be utilized. The instrument is also suitable for low angle scattering experiments.

Curved graphite or silicon monochromators are used in Seemann-Bohlin geometry. For reduction of fluorescence radiation a secondary monochromator between specimen and counter is available.

The instrument will be described in details and examples will be discussed which show advantages and disadvantages of the different measuring modes.



STATISTICAL ANALYSIS OF THE MEASUREMENT OF GRAIN  
AND PARTICLE SIZE WITH X-RAYS

J. Hilliard

Department of Materials Science and Engineering  
Northwestern University  
Evanston, IL 60201

In collaboration with J. B. Cohen and C. Rinik, a comparison has been made of the determination of grain size in commercial steel samples by optical microscopy and by the variation in the intensity of the x-ray beam diffracted from different areas of the specimen. By using a ratio of two of the moments of the optically measured intercept-length distribution, an exact comparison could be made of the average grain size yielded by the two methods. Good agreement was found, provided the grains were reasonably equiaxed.

The x-ray method is not only non-destructive, but it is also sufficiently rapid that it could be used for the continuous monitoring of grain size during the rolling of sheet steel. The application of the procedure to the sizing of loose powders will also be discussed.



## ANALYSIS AND TOPOGRAPHY OF LATTICE DEFECTS IN POWDER DIFFRACTION PATTERNS

S. Weissmann  
College of Engineering  
Rutgers University  
Piscataway, NJ 08854

An x-ray method is described which enables the investigator to analyze quantitatively the defect structure of individual crystallites in a polycrystalline specimen, and which provides him also with x-ray topographic images of the analyzed crystallites. The analysis of the defect structure is based on the principle of the double-crystal diffractometer. The specimen is irradiated by a crystal-monochromated beam and each reflecting crystallite is considered to function independently as the test crystal of a double-crystal diffractometer. By carrying out discrete, angular specimen rotations and appropriate film shifts, to separate the spot reflections corresponding to successive rotation positions, one obtains an array of spots for each reflecting crystallite. These spot arrays, with their intensity dependence on the angular position, represent rocking curves. On the basis of the rocking-curve parameters, the excess dislocation density of the crystallite can be determined. If a resolvable substructure exists within the crystallite, the rocking curve exhibits a multimodal intensity distribution, the analysis of which gives the excess dislocation density in the subgrain boundary and in the subgrain. The topographic imaging of the reflecting crystallites is obtained by taking reflection topographs at the specimen surface. The correlation of these surface images and the analyzed spot reflections along the Debye arcs on the cylindrical film is accomplished by outward tracing of the reflection images. Using an exposure method which employs a superposition technique of unfiltered and crystal-monochromated radiation, the location of the imaged crystallites on a flat specimen is established. In this way, the morphology of the crystallites studied by the x-ray methods can be

linked to that analyzed by other imaging methods, such as light microscopy, transmission and scanning electron microscopy. Applications of the x-ray method to important technological problems in metallurgy are given.

Key Words: Double-crystal diffractometer; excess dislocation density; lattice defects; rocking curves; subgrain structure; x-ray topography.

## 1. Introduction

Research work in materials science during the last decades has clearly shown that many physical properties of solid materials, such as the self-diffusion, strength and plastic properties of metals and alloys, are structure-sensitive and are, therefore, intricately linked to faults and lattice inhomogeneities in crystal structure. Consequently, it is not surprising that an increased effort has been made in recent years to elucidate the interrelationship of the crystalline fine-structure of a solid with the observed structure-sensitive properties.

Metallographic and x-ray methods are usually employed for the study of lattice inhomogeneities. If single crystals are studied, no particular difficulty is encountered in correlating the metallographic and x-ray observations, although the correlation in fine-structural details, as revealed by both methods, may sometimes pose a serious problem. The problem becomes much more difficult if one wishes to investigate the substructure characteristics of fine-grained polycrystalline materials, *viz.* metals, alloys, or ceramic materials. In such instances, the observations made by metallography and x-ray methods cannot usually be directly correlated to the individual grain or crystallite and one has to rely on statistical sampling procedures. A correlation, however, between metallographic and x-ray observations with respect to the identical crystallites of the specimen becomes increasingly more important, particularly if structural changes that result from chemical or physical processes are to be studied. Problems of this sort arise in the study of deformation, creep, fatigue, recovery, recrystallization, precipitation and solution-hardening, to mention only a few. Such correlation of observations has been accomplished by a method combining light microscopy with x-ray reflection microscopy and diffraction analysis and will presently be described.

## 2. Diffraction Method

### 2.1. X-ray reflection microscopy

An unfiltered, divergent x-ray beam  $P$  passing through the collimator  $C$  is made to impinge at a small grazing angle on the surface of the polycrystalline test specimen  $S$  located at the center of a Debye-Scherrer camera  $E$  (fig. 1). A fine-grained photograph

plate D is placed at a distance of about 0.5 mm from the specimen surface. Owing to the divergence and spread of wavelengths of the beam, a great many crystallites, on the specimen surface satisfy the Bragg conditions of reflection and are, therefore, recorded on the photographic plate in the form of an x-ray reflection micrograph (Berg-Barrett topograph). This x-ray micrograph reveals the topographical relationship of the crystallites and can, therefore, be directly compared to the corresponding light micrograph. A correlation of the observations made of each crystallite by light and x-ray reflection microscopy is thus achieved.

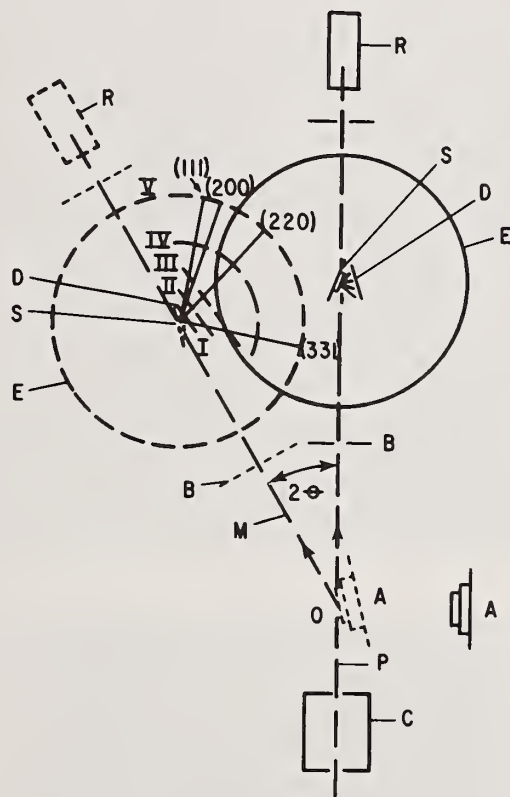


Figure 1. Experimental arrangement for taking reflection x-ray micrographs and tracing of reflecting images. Solid lines with crystal A retracted indicate arrangement for use of heterogeneous radiation. Dashed lines with crystal A in reflecting position indicate arrangement for use of crystal-monochromated radiation. The successive positions of the films for the outward tracing of reflections are given by Roman numerals.

For the diffraction analysis of lattice imperfections of the crystallites, additional experimental steps have to be carried out. First of all, there are usually too many reflection images recorded and the number of reflecting crystallites has to be drastically restricted. This is conveniently accomplished by interposing a single crystal A into the path of the beam P and adjusting the crystal so as to reflect the incident beam. The (111) reflection of a silicon or germanium crystal, possessing a high degree of lattice perfection, is preferred. The reflected, monochromated beam M thus subtends an angle of  $2\theta$  with the primary beam P, where  $\theta$  is the Bragg angle of the reflecting (hk $\ell$ ) planes of the monochromator. By rotating the entire assembly, consisting of specimen S, photographic plate D, cylindrical camera E, radiation detector R and slit system B, by the exact angle of  $2\theta$  around an axis O coincident with the vertical axis of rotation of the monochromating crystal, the identical area of the specimen S is now irradiated with crystal-monochromated radiation M. This experimental arrangement is schematically represented in figure 1 by dashed lines. Because of the stringent reflecting condition imposed by the monochromatization of the beam, fewer crystallites will now be recorded on the x-ray micrograph. The interposition of the monochromator may, therefore, be likened to the use of a high-power objective in a light microscope, except that in the x-ray analogue the selectivity of the image is achieved by restricting the orientation rather than the size of the crystallites in the field of view [1,2]<sup>1</sup>. If the specimen, however, consists of well-annealed grains and has an appropriate size distribution, the x-ray reflection micrograph, taken with a monochromated beam, may frequently suffice to establish the identity of the grains with those on the corresponding light micrograph. Figures 2a and 2b show the metallograph and x-ray reflection micrograph of an annealed 304 stainless steel sample, respectively. The identity of a few grains is given by numbers.

## 2.2. Tracing of reflection images

The individual reflection images can be traced outward in space by recording the images photographically at increasing distances from the specimen surface. The successive positions of the photographic plates are schematically indicated in figure 1 by Roman numerals, whereby V represents the circumference of the Debye-Scherrer camera. By means of this tracing technique, there is established a direct correlation between the spot reflections on the Debye-Scherrer lines and the crystallites on the specimen surface giving rise to these reflections [1]. Figures 3a and 3b show the spatial tracing of the grain reflections of figure 2b. Selected reflection micrographs at distances of 2.5 and 27.5 mm from the specimen surface are shown. For the sake of clarity only three image reflections, marked by numbers 1, 2, and 3, are shown. These images were selected not only for the purpose of illustrating the image tracing technique, but also to demonstrate a special versatility of the combination method, which will be described in a unique application of this method to stress-corrosion studies (Section 5). It is perhaps

---

<sup>1</sup>Figures in brackets indicate the literature references at the end of this paper.

orthwhile noting that, due to different crystal orientation, images that appeared in topographic proximity at the surface ended up at different (hkl) reflections on the circumference of the Debye-Scherrer camera (compare figure 2b to figure 4a).

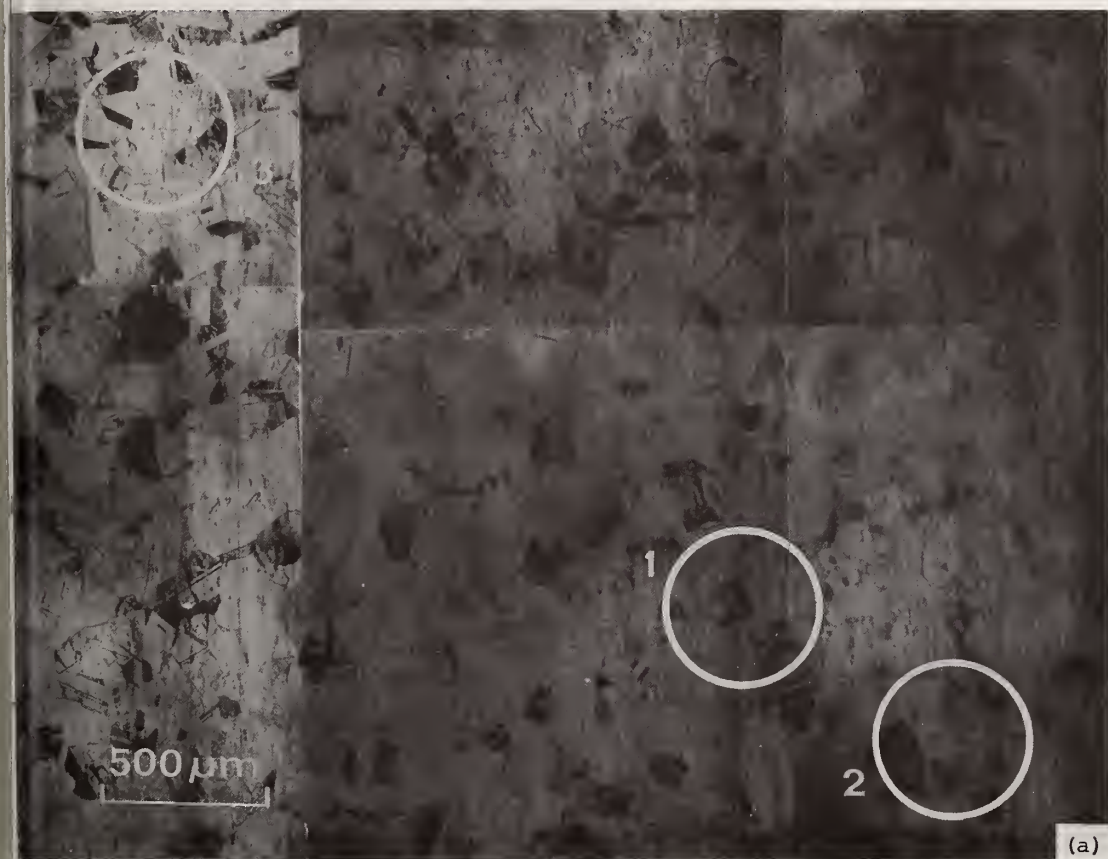


Figure 2. Identification of grains of 304 stainless steel. (a) Metallograph. (b) X-Ray reflection micrograph. Crystal-monochromated  $\text{CrK}_{\alpha_1}$  radiation.

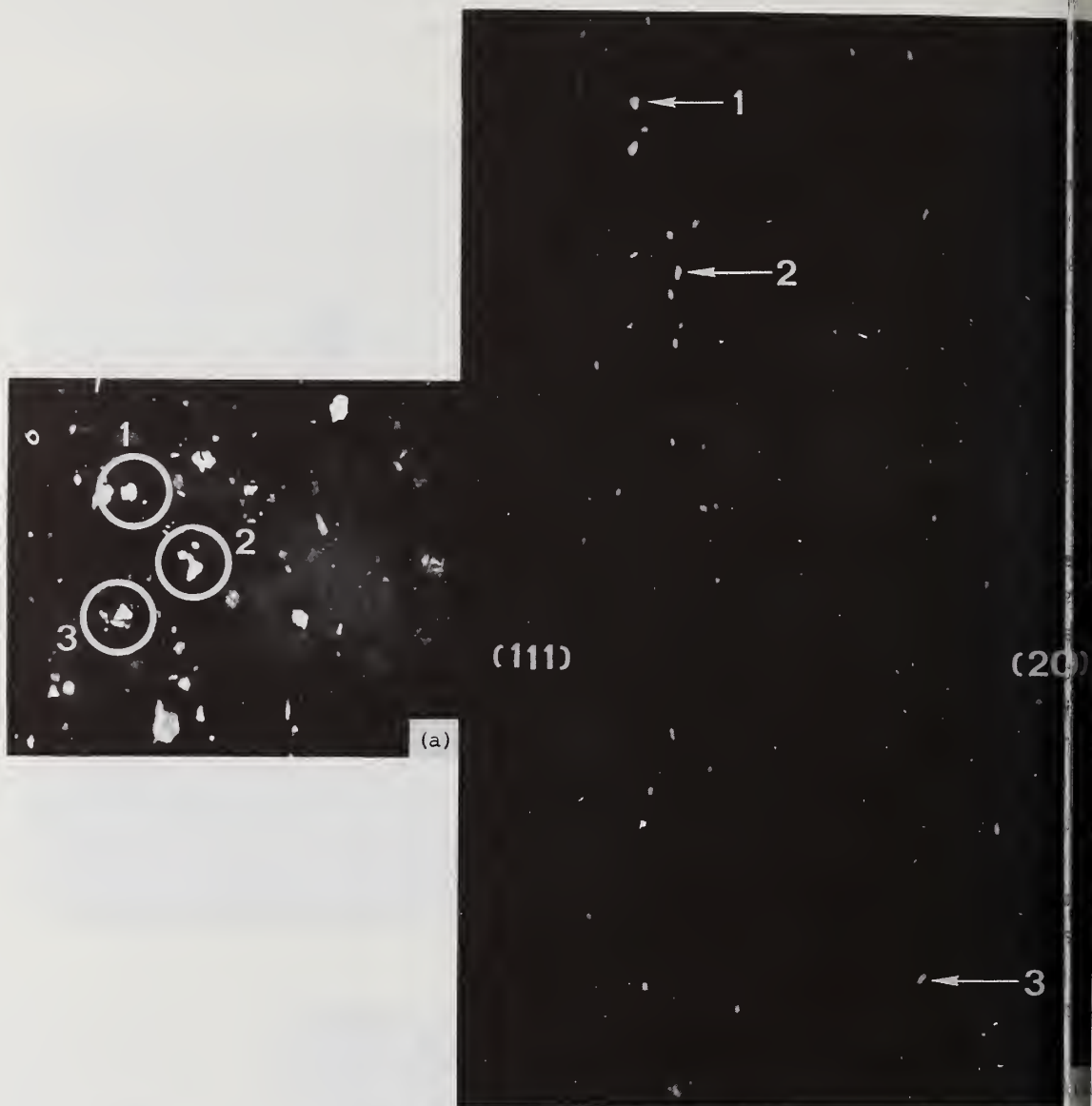


Figure 3. Outward tracing of reflection images of Fig. 2b. (a) 2.5 mm from specimen surface. (b) 27.5 mm from specimen surface.

### 2.3. Quantitative diffraction analysis of lattice defects

After the spot reflections along the Debye-Scherrer arcs have been correlated by the spatial image tracing technique to the topography of the grains at the surface, and via x-ray topography to light metallography, a quantitative analysis of the spot reflections is undertaken. This analysis is based on the principle of the double-crystal diffractometer. Each reflecting crystallite of the polycrystalline test specimen functions independently as the second crystal (test crystal) of a double-crystal

diffractometer. Consequently, by carrying out discrete, angular specimen rotations and appropriate film shifts between each specimen rotation to separate the spot reflections corresponding to successive rotation positions, one obtains arrays of spots for each reflecting crystallite, such as those shown in figures 4a and 4b. These spot arrays represent rocking curves, or rather angular samplings of the rocking curves, of the crystallites, since the intensity variation as a function of discrete specimen rotation is being recorded. The angular specimen rotation of the 304 stainless steel sample of figures 4a and 4b was carried out in intervals of 3 minutes of arc. The type of diagram obtained is conveniently referred to as multiple-exposure diagram.

### 3. Photometric Transformation of Crystallite Rocking Curves [3,4]

The arrays of spots at the equatorial reflection of the cylindrical camera, with their intensity dependence on specimen rotation, are analogous to the rocking curves of the conventional double-crystal diffractometer, because for equatorial reflections the crystallites have their plane normals parallel to the plane normal of the monochromating crystal, regardless whether they reflect in the parallel ( $m, -n$ ) or antiparallel ( $m, +n$ ) arrangement relative to the monochromating crystal. Because the reflecting crystallites contain lattice defects, *viz.* dislocations, one may conceive the picture that the reciprocal lattice point of a ( $hkl$ ) reflection of a perfect crystal is now replaced by a reciprocal lattice volume. The change of shape and intensity of the diffracted spots in the sequence of the array depends now on the extension of the contact of this reciprocal lattice volume with the Ewald sphere. For equatorial reflections, the Ewald sphere in the double-crystal diffractometer arrangement is sharply defined by virtue of the monochromating property of the first crystal. The horizontal convergence of the monochromated beam irradiating the crystallites is controlled by the rocking curve half-width of the monochromatizer and amounts typically to only about 10-15 seconds of arc. The vertical convergence for equatorial reflections is zero.

If one analyzes, however, the rocking curves of perfect crystallites for non-equatorial reflections, one will observe a systematic increase of the rocking curves with increase of azimuthal elevation  $\psi$ . The apparent increase is due to two factors, namely the velocity factor associated with the rotation of the crystallites, and the increased contribution of the vertical convergence of the beam, which remains unaltered after reflection from the monochromating, first crystal. For crystallites containing lattice defects, the non-equatorial reflections exhibit still larger increases of the rocking curves, and represent the transform of the convolution of lattice defects with the horizontal and vertical convergence of the beam. Although for many experiments there may be a sufficiently large number of equatorial reflections available to extract a statistical half-width parameter of the analyzed rocking curves,  $\bar{\beta}$ , which can be regarded as representative of the defect structure of the entire crystallite population, it is nevertheless desirable to utilize, also, non-equatorial reflections so as to increase the confidence level of statistical sampling. What follows now is an analysis of the

photometric transformation of the rocking curves of the crystallites, with the aim of utilizing all reflections on the Debye-Scherrer arcs and extracting from them statistical parameters representative of the defect structure of the entire crystallite population

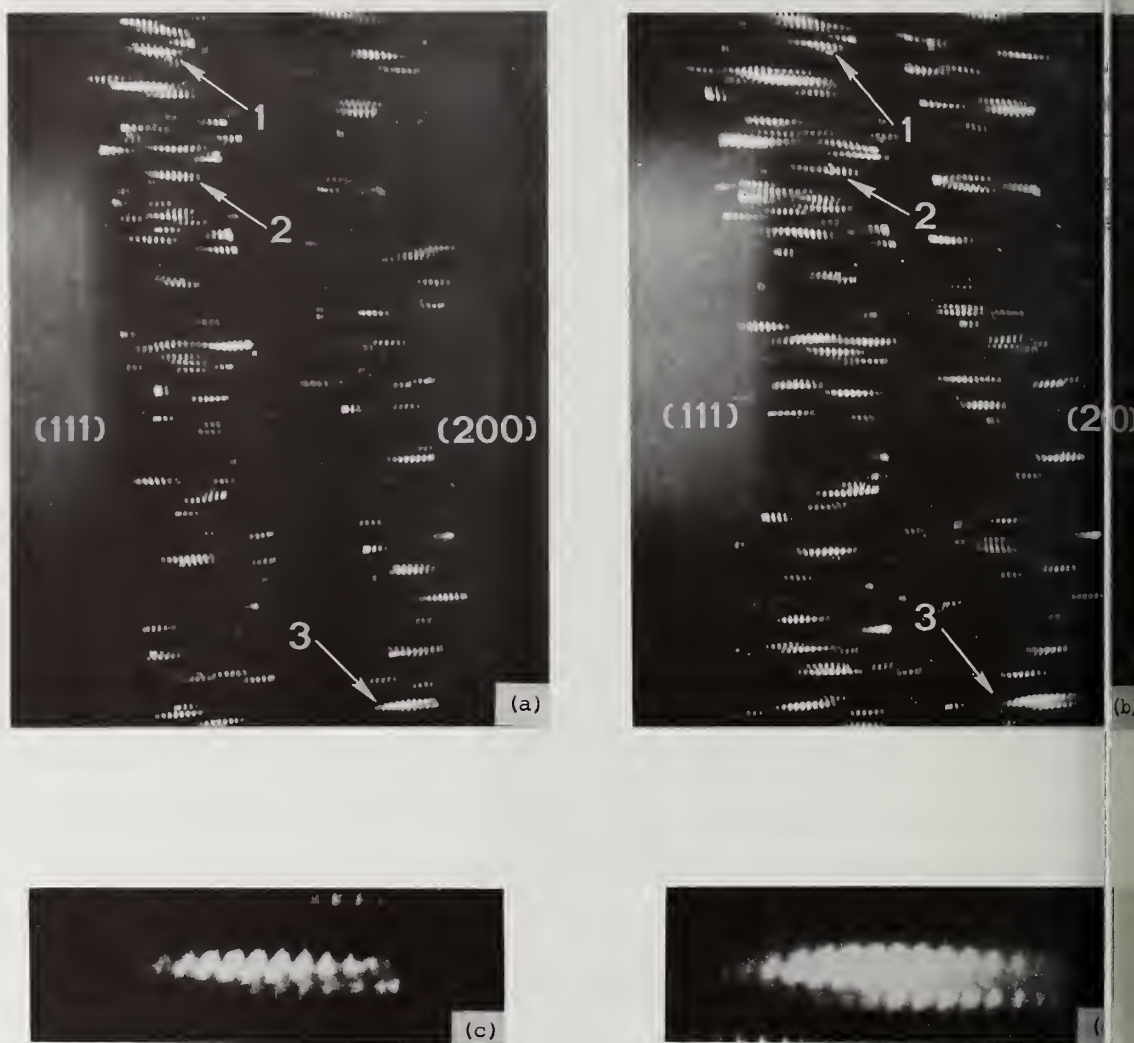


Figure 4. Detail of multiple-exposure diagram of 304 stainless steel. Array of spots represents samplings of the rocking curve of each reflecting grain. Discrete, angular specimen-rotation 3 minutes of arc.  $\text{CrK}_{\alpha_1}$  radiation. (a) Annealed. (b) Subjected to stress-corrosion. (c) Enlarged detail of rocking curve of annealed grain 3. (d) Enlarged detail of rocking curve of grain 3 after SC. (Note increase of rocking curves after SC.)

Figure 5 represents the unit sphere with center at the specimen  $S$ . The vector  $\vec{r}$  represents a ray of the pencil that converges to the specimen. With this ray and the Bragg angle  $\theta$  is associated the Debye-Scherrer cone of which a typical element is the ray  $\vec{p}_1$ . With the converging pencil is associated a two-parameter family of conjugate cones with vertices at  $S$  that intersect the unit sphere in a zone  $B$ , which will be called the reflecting zone. A configuration such as this will be associated with each point of the small, but finite, irradiated area. For the purpose of the present investigation, however, all such points may be considered to be concentrated at  $S$ , since only the integrated photographic intensities will be required.

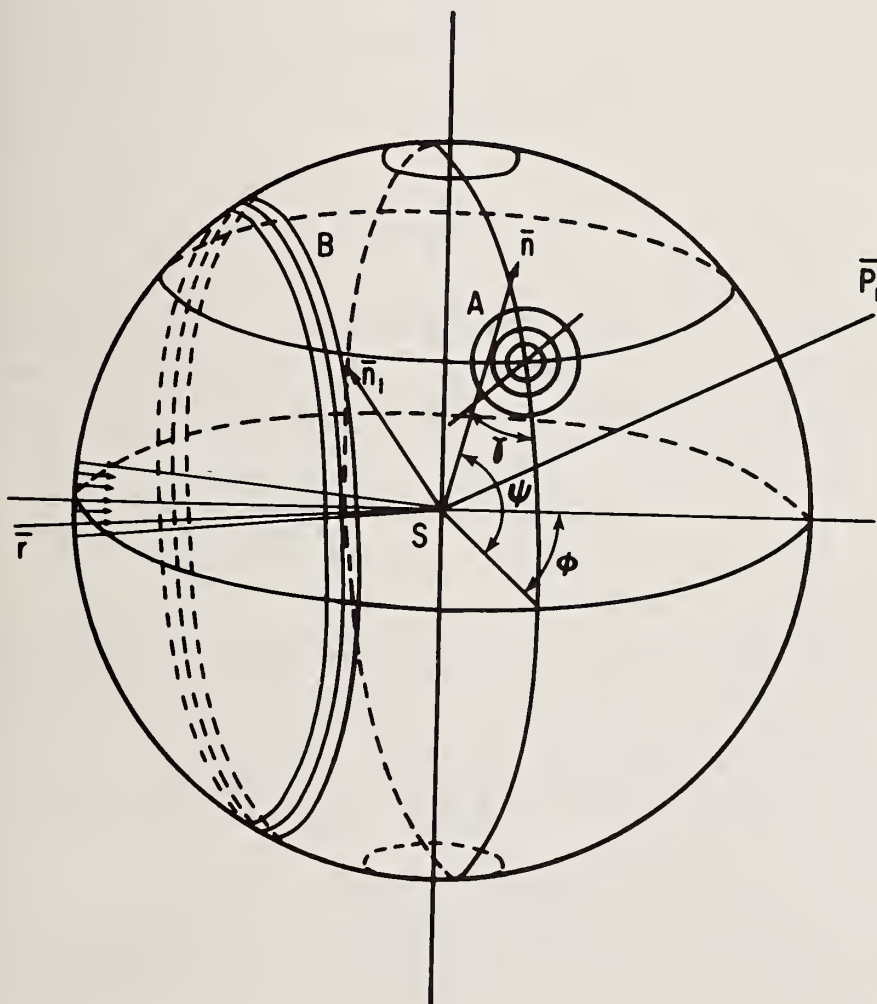


Figure 5. Reflecting zone and coordinate system.

The region A represents an area on the surface of the unit sphere pierced by the misaligned normals of a crystallite, one of which is marked  $\bar{n}$ . When the specimen is rotated about the vertical axis, reflection from this facet will occur when  $\bar{n}$  coincides with one of the typical vectors  $\bar{n}_1$ . That is, reflection occurs when the area A intersects the reflecting zone B, and the intensity of the resulting photographic spot will depend, among other things, on the amount of this intersection.

Let  $U(\xi)$ ,  $V(\eta)$  be the normalized x-ray intensity distributions in the horizontal and vertical directions of the converging beam. Since the maximum angle subtended by the beam is small, there will be values of  $(\xi, \eta)$  say  $(a, b)$  such that  $a^2, b^2 \approx 0$  and  $U(\xi), V(\eta) \approx 0$ , when  $|\xi| > a, |\eta| > b$ .

With every element  $dA$  of the area A will be associated a reflecting power  $w(A)dA$  which  $w(A)$  is a two-dimensional point function. Let  $x$  be the angular measure along a great circle passing through the centroid of the distribution and making the angle  $\gamma$  to the circle of longitude through this centroid. If  $y$  is the geodetic measure in the direction perpendicular to the  $x$ -circle and

$$W(x) = \int w(A)dy,$$

then  $W(x)dx$  is the one-dimensional reflecting power of the strip of width  $dx$  shown in figure 6, and  $W(x)$  is the true rocking curve of the crystallite in the direction of  $x$ . In terms of a rotation  $\phi$  of the specimen,  $x$  may be written

$$x = \phi \cos \psi \sin \gamma$$

as shown in figure 7.

It should be noted that, if  $\phi$  is the general coordinate shown in figure 5, a rotation of the specimen is given by the difference  $\phi_2 - \phi_1$  of two locations of the normal  $\bar{n}$ . The origin of  $\phi$  is immaterial. For general relations on the surface of the sphere,  $\phi$  is taken to be the angle shown in figure 5, but when referring to rotations of the specimen,  $\phi$  is measured as shown in figures 7 and 8. In what follows, the origin of  $\phi$  is always specified.

In particular, let the origin of  $\phi$  be the point of intersection of the circle of latitude and the conjugate cone determined by the ray  $(1,0,0)$ , and let  $\phi_1$  be the coordinate of the intersection of this circle and the cone determined by the ray  $(1, \xi, \eta)$ , as shown in figure 8. Using eq. (2), we have

$$W(x)dx = \cos \psi \sin \gamma W[(\phi - \phi_1)\cos \psi \sin \gamma]d\phi.$$

The intensity of the x-rays associated with a point of the reflecting zone is the sum of the intensities associated with the conjugate cones that intersect at this point and is, therefore,  $\int_c U(\xi)V(\eta)dc$  where  $c$  is the arc of the circle with center at the point and geodetic radius equal to  $\pi/(2 - \theta)$ . Since the extremes of  $(\xi,\eta)$  at which the irradiation is measurable are extremely small, the maximum angles of intersection of relevant conjugate cones are very small except for  $\theta$  nearly equal to  $90^\circ$ . Hence, locally the irradiation may be considered constant in the direction of the circle determined by the cone  $(1,0,0)$ , the gradient of x-ray intensities being perpendicular to this direction (except, possibly, in cases of extreme back-reflection).

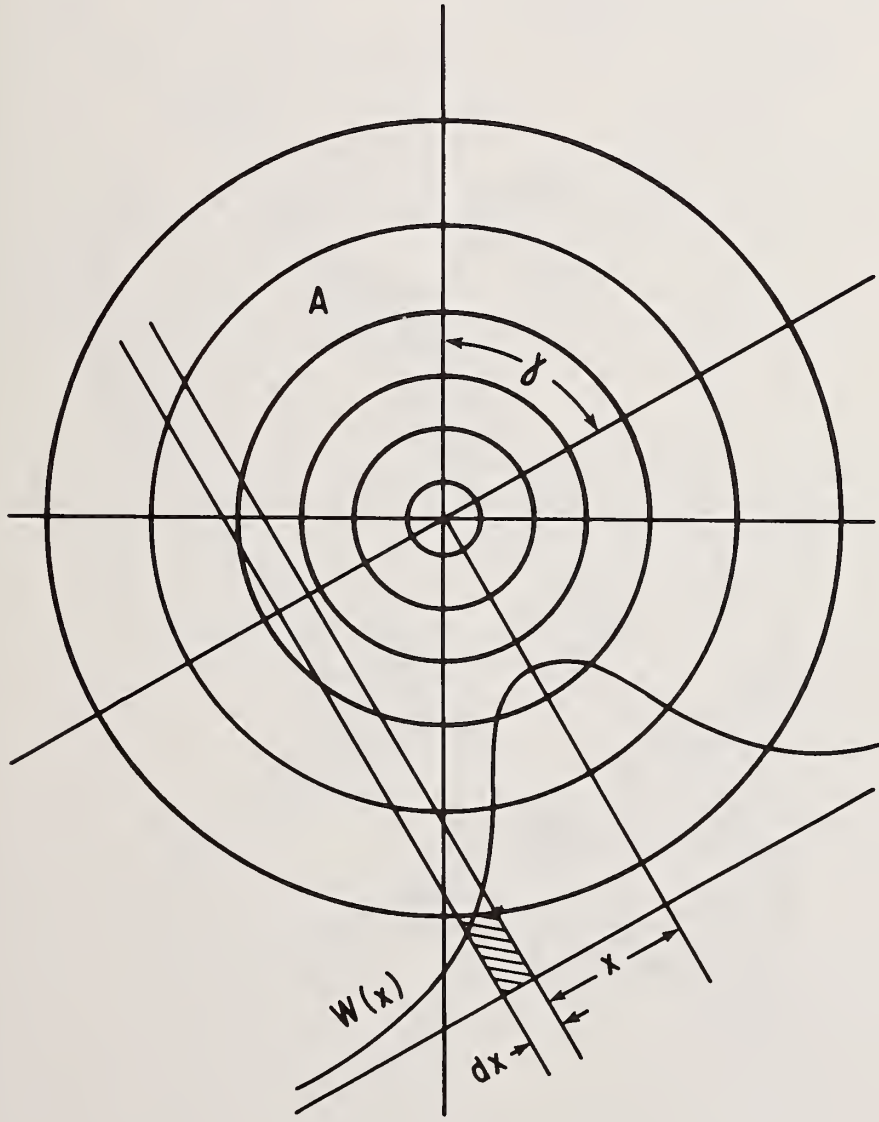


Figure 6. Distribution of misaligned normals.

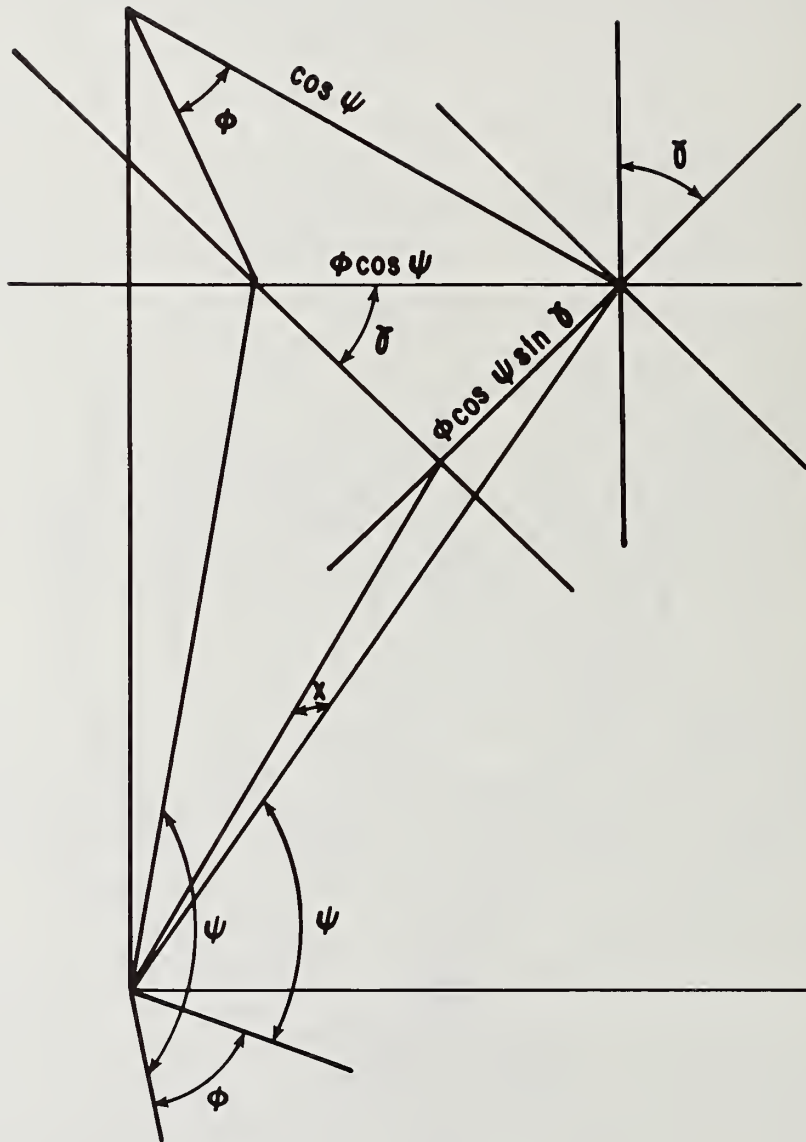


Figure 7. Great circle measure  $X$ .

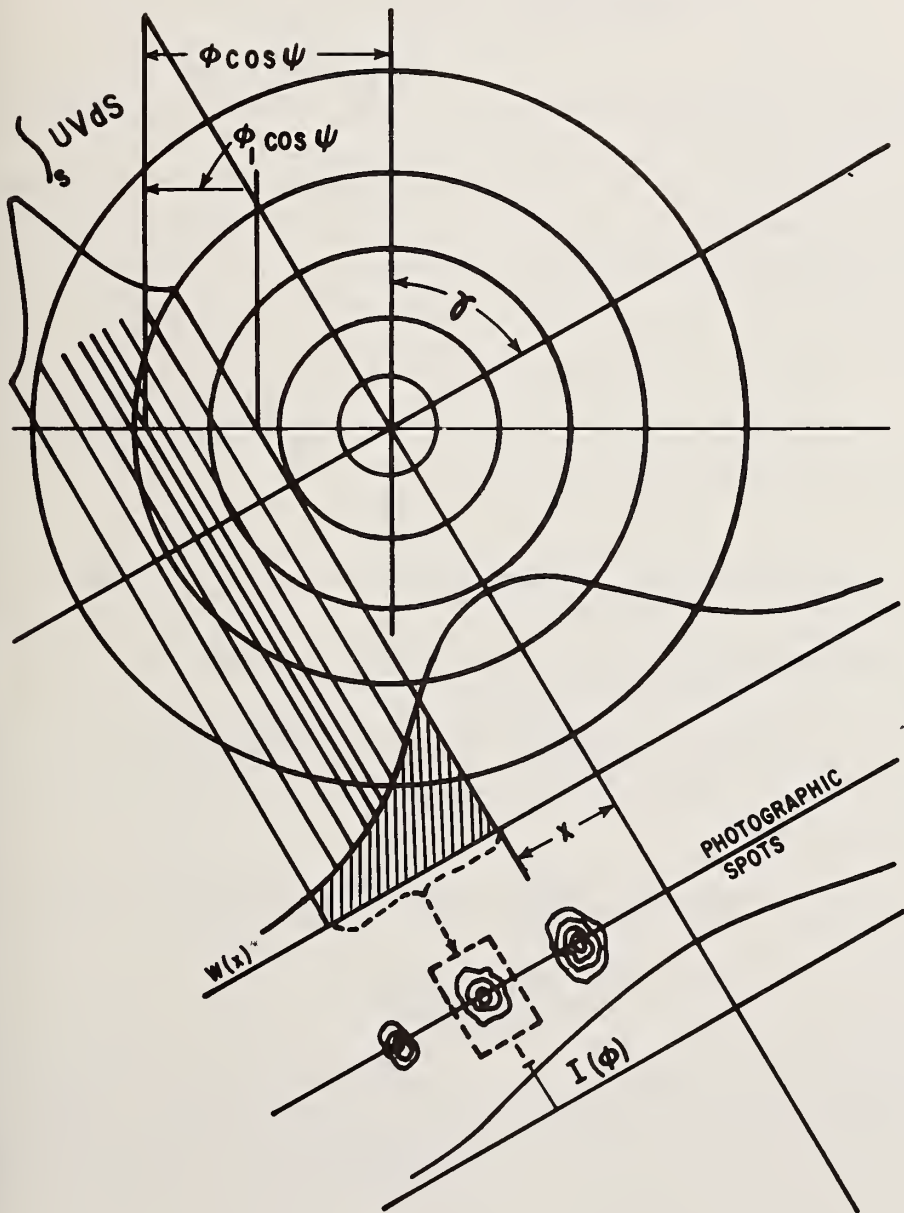


Figure 8. Photometric transformation.

Letting  $\gamma$  be the angle the circle  $(1,0,0)$  makes with the circle of latitude, the total intensity that reaches the photographic film from the misaligned region at this setting is

$$I(\phi) = \cos \psi \sin \gamma \int \int U(\xi)V(\eta)W(\phi - \phi_1)\cos \psi \sin \gamma]d\xi d\eta \quad (4)$$

where the double integration extends over all values of  $(\xi, \eta)$ . This is shown schematically in figure 8.

We may obtain  $\phi_1$  and  $\sin \gamma$  in terms of  $\xi, \eta, \psi$  and  $\theta$  in the following manner: let  $\phi$  be the general longitudinal coordinate of  $\bar{n}$  as shown in figure 5. The equation of the conjugate cone associated with the ray  $(1,0,0)$  is

$$\cos \psi \cos \phi + \sin \theta = 0 \quad (5)$$

and that of the cone associated with the ray  $(1, \xi, \eta)$  is

$$\cos \psi \cos(\phi + \phi_1) + \eta \cos \psi \sin(\phi + \phi_1) + \xi \sin \psi + \sin \theta = 0. \quad (6)$$

From these two equations and the relations  $\xi^2, \eta^2, \phi^2 \approx 0$ , we find

$$\phi_1 = \eta + \frac{\xi \sin \psi}{\sin \phi \cos \psi} = \eta + \frac{\xi \sin \psi}{(\cos^2 \psi - \sin^2 \theta)^{\frac{1}{2}}}. \quad (7)$$

Also,

$$\begin{aligned} \tan \gamma &= \frac{d\psi}{\cos \psi d\phi} = \frac{\tan \phi}{\sin \psi} \text{ (from eq. (5))} \\ &= \frac{(\cos^2 \psi - \sin^2 \theta)^{\frac{1}{2}}}{\sin \theta \sin \psi}. \end{aligned}$$

Therefore,

$$\sin \gamma = \frac{(\cos^2 \psi - \sin^2 \theta)^{\frac{1}{2}}}{\cos \theta \cos \psi}. \quad (8)$$

Let  $\sigma_\xi^2, \sigma_\eta^2, \sigma^2$  be the variances of  $U(\xi), V(\eta), W(x)$ . If  $\Sigma^2$  is the variance of the photometric intensities, then

$$\begin{aligned} \Sigma^2 &= \int \phi^2 I(\phi) d\phi = \cos \psi \sin \gamma \\ &\times \iiint \phi^2 U(\xi) V(\eta) W[(\phi - \phi_1) \cos \psi \sin \gamma] d\xi d\eta d\phi \\ &= \frac{\sigma^2}{\cos^2 \psi \sin^2 \gamma} + \sigma_\eta^2 + \frac{\sigma_\xi^2 \sin^2 \psi}{\cos^2 \psi - \sin^2 \theta} \end{aligned} \quad (9)$$

This relation between the four variances is independent of the analytical forms of  $U, V, W$ . Generally, the half-width is a more convenient parameter than the variance, but a relation between half-widths may be obtained from eq. (9) only when the analytical forms of the distribution functions are given.

A reasonable hypothesis is

$$\begin{aligned} U(\xi) &= 1/K, \quad |\xi| < K/2 \\ &= 0, \quad |\xi| > K/2 \\ V(\eta) &= \frac{1}{(2\pi)^{\frac{1}{2}} \sigma_\eta} \exp[-\eta^2/2\sigma_\eta^2] \\ W(x) &= \frac{1}{(2\pi)^{\frac{1}{2}} \sigma} \exp[-x^2/2\sigma^2] \end{aligned} \quad (10)$$

For these forms of the distributions, it is readily found that

$$\sigma_\xi^2 = K^2/12, \quad L = 2.36\sigma_\eta, \quad \beta = 2.36\sigma$$

where  $L$  is the half-width of the horizontal intensities of the irradiating beam and  $\beta$  is the half-width of the true rocking curve of the crystallite in the  $x$ -direction. Substituting these values in eq. (9), we obtain

$$\beta = (5.57\Sigma^2 - L^2 - 0.46\Delta\phi_2^2)^{\frac{1}{2}} \cos \psi \sin \gamma \quad (11)$$

where

$$\Delta\phi_2 = K \sin \psi / (\cos^2 \psi - \sin^2 \theta)^{\frac{1}{2}} \quad (12)$$

#### 4. Determination of Specific Lattice Defects from Rocking-Curve Parameters

##### 4.1. Determination of excess dislocation density of crystallite

Using eqs. (11) and (12), the half-width of the true rocking curve of the reflecting crystallite is obtained. In order to apply these equations, one has to determine the rocking-curve half-width of the monochromating crystal,  $L$ , and the vertical convergence of the beam,  $K$ . Typical values for the experimental arrangement employed, using the (111) reflection of silicon, are:  $L = 15$  seconds of arc,  $K = 10.8'$ . These values are then used for all calculations based on eqs. (11) and (12) to obtain the corrected half-width value of the crystallites,  $\beta$ . Next, the azimuthal elevation of the spot reflection,  $\psi$ , is determined by the relation

$$\sin \psi = \frac{Y/R}{2 \sin \theta [1 + (Y/R)^2]^{\frac{1}{2}}} \quad (3)$$

where  $Y$  is the vertical distance of the spot reflection measured from the equator and  $R$  is the camera radius. Using the  $\psi$  and  $\theta$  values for the reflection,  $\gamma$  is calculated from eq. (8) and  $\Delta\phi_2$  from eq. (12). Thus, when the half-width of the uncorrected rocking curve,  $2.36\Sigma$ , is experimentally determined, all parameters are now given to compute by eq. (11) the half-width of the corrected rocking curve,  $\beta$ . It will be seen that for equatorial reflections, where  $\psi$  and  $\gamma$  are  $0$  and  $90^\circ$ , respectively, eq. (11) reduces to  $\beta^2 = 5.57\Sigma^2 - L^2$ , which is the difference between the square of the half-width of the observed rocking curve of the crystallite and that of the monochromating crystal.

The  $\beta$ -values obtained do not give information about groupings of adjacent dislocations of opposite sign. The specific species of lattice defects measured by  $\beta$ , however, is the excess dislocation density,  $D$ , which can be obtained from the relation given by Hirsch [5]:

$$D = \beta^2/9b^2 \quad (4)$$

where  $b$  is the magnitude of the Burgers vector. It is the excess dislocation density which has been shown to be a most significant indicator of microplasticity [6].

If the angular lattice misalignment of the crystallite is large, the total excess dislocation density can also be assessed from the vertical spread of the spot reflections  $\Delta\psi$ . Indeed, for gross lattice defects, the measurements of the  $\Delta\psi$  spread, in conjunction with the horizontal  $\Delta\phi$  measurements, can be very effective in characterizing the overall excess dislocation density of the crystallite.

#### 4.2. Determination of substructure characteristics

If the crystallites have a substructure, then the rocking curves are no longer unimodal but multimodal; i.e., more than one peak is recorded in an array of spot of a multi-exposure diagram [7]. From the intensity data and known specimen settings, statistical parameters can be computed which are a measure of the angular tilt between two adjacent subgrains and also the angular misalignment within the subgrain. If the means  $\bar{\phi}_1$  and  $\bar{\phi}_2$  of two neighboring individual components of the multi-peaked rocking curve are determined, then the angle,  $\Delta\phi$ , subtended by the means is the projected tilt of two adjacent subgrains. Figure 9 may serve to illustrate this point. From the tilt or misorientation angle,  $\Delta\phi$ , the excess dislocation density in the subgrain boundary,  $D_{SB}$ , can be computed. Since the dislocation arrangement in the subgrain boundaries is not random but exhibits a preferred alignment, the following relation given by Hirsch [5] is used to calculate  $D_{SB}$ :

$$D_{SB} = \beta/3bt \quad (15)$$

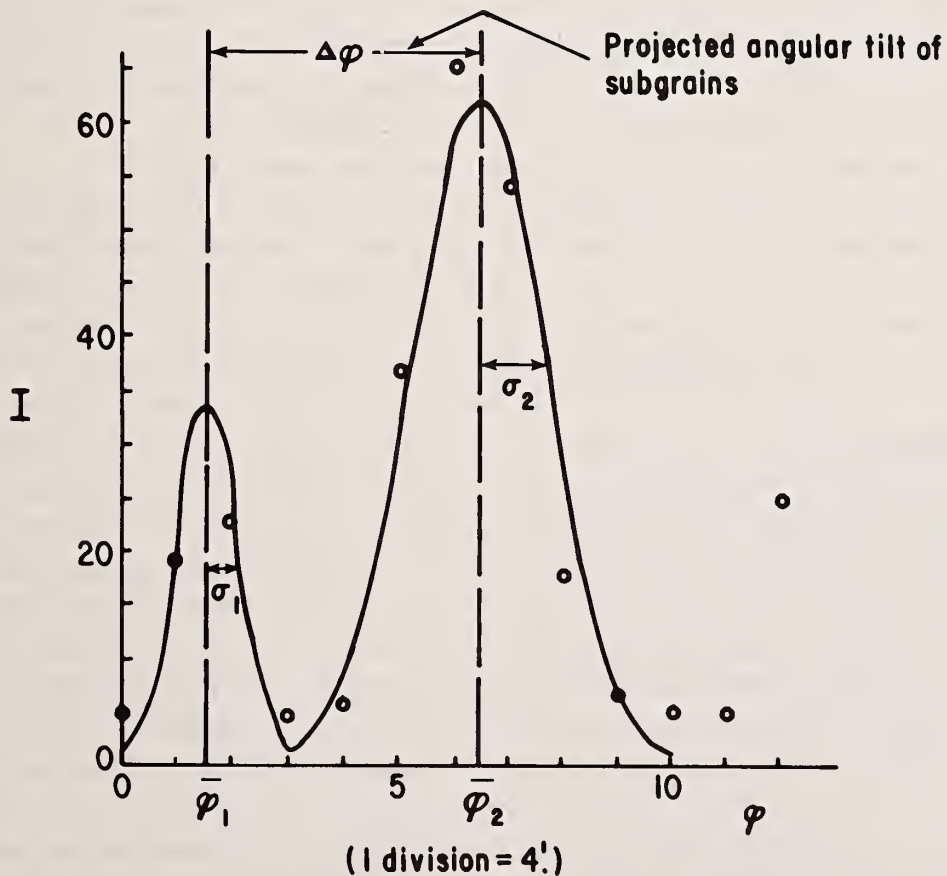


Figure 9. Comparison of the experimental data and theoretical Gaussian intensity distributions for equatorial reflection of Al 96% cold-rolled, annealed 1 hr at 300 °C, (222) line, (1, +1) position. Circles: experimental data; full line: theoretical curve [7].

where  $t$  is the subgrain size, which can be determined from the corresponding image of the reflection micrograph.

In order to determine the angular lattice misalignment existing within a subgrain, the half-width values of the individual components of the multipeaked rocking curves,  $\beta_S$  are measured. If detailed experimental data can be obtained, such as those shown in figure 9, the standard deviation,  $\sigma$ , of the individual components of the distribution curve can be determined, using the relation  $\sigma^2 = \overline{\phi^2} - \bar{\phi}^2$ . For the illustrative array, the computation of  $\sigma$  was particularly simple, since reflections occurred near the equator and the contribution of the vertical convergence of the beam to the rocking curve of the grain reflection was negligible.

Assuming the dislocation density within the subgrain to be random (*viz.* cell structure), the excess dislocation density in the subgrain,  $D_S$ , is computed again by eq. (14), substituting  $\beta_S$  for  $\beta$ .

### 5. Applications and Versatility of the Combination Method

Perhaps the versatility of the combination method can best be demonstrated by citing some of the successful applications of the method to problems in materials science. The method was applied to such diverse problems as the determination of the deformation substructure of nickel and its correlation to mechanical properties [8], growth processes in the recrystallization of aluminum [9,10], substructure formation in iron during creep [11], and residual stress and grain deformation in BeO ceramics [12].

The combination method also proved to be very useful in a recent study of a precipitation-hardening alloy of the Ti-Al-Mo system. High-temperature strength and ductility increases were obtained for this alloy by applying a step-aging program based on principles of particle-dislocation interactions [13]. Thus, precipitation of ordered  $Ti_3Al$  particles in the high-temperature beta titanium phase field induced the moving dislocations to bypass the particles. Consequently, the slip became dispersed in the hard  $\beta$ -phase and in this way increased the ductility of the alloy. Small alpha titanium and  $Ti_3Al$  particles which were precipitated in the low-temperature phase field during the step-aging program were cut by the moving dislocations, thereby increasing the yield strength of the alloy. The materials science problem involving the x-ray analysis was to elucidate and verify the effect of  $Ti_3Al$  particles as efficient agents of slip dispersal in the high-temperature  $\beta$ -field. To achieve this objective, the x-ray combination method was employed [14]. Since the  $\beta$  and  $Ti_3Al$  reflections were clearly separated on the Debye-Scherrer film, the rocking curves of the grains of the respective phases could be identified easily. It was noted that after deformation of 2 percent, the angular range of reflection for the  $Ti_3Al$  particles did not exceed 12 minutes of arc, while that for the  $\beta$ -grains exceeded more than  $1^\circ$ . Hence, the lattice misalignment in the  $\beta$ -matrix became at least five times as large as that in the  $Ti_3Al$  particles. It could be concluded, therefore, that room-temperature deformation of the  $\beta + Ti_3Al$  phase caused the  $\beta$ -matrix to undergo preferentially plastic deformation by homogeneous slip, while the undeformed, ordered  $Ti_3Al$  particles functioned as hard particles controlling the slip distribution.

In a recent application of the diffraction method to determine the prefracture damage in fatigued and stress-corroded materials [15], the analysis of the excess dislocation density in surface and bulk led to the prediction of the lifetime of the fatigued and stress-corroded materials. Such predictions are of great importance to technology. It should be pointed out that single-crystal studies of stress-corroded metals and alloys have been notoriously unsuccessful in the past. This led many investigators to believe that the phenomenon of stress corrosion is not applicable to single crystals. By applying, however, the combination diffraction method to stress-corroded polycrystalline materials, one analyzes and characterizes in essence the defect structure of small single crystals in a polycrystalline aggregate. In the stress-corrosion (SC) study of 304 stainless steel (figs. 2-4), a very low stress, i.e., 55 percent of the yield stress, was applied and the stressed alloy was subjected to a corrosive medium of  $MgCl_2-H_2O$  solution at 154 °C. Neither the applied stress nor the solution alone had any deleterious effect on the alloy; only the combined effect caused the SC attack. Because the applied stress was very low, grain (crystallite) rotation did not occur and it was possible, therefore, to analyze the identical grains for the induced defect structure as a function of stress-corrosion time. Comparison of figures 4a and 4b will show that as a result of SC attack only specific grain reflections showed an increase in the rocking-curve half-width, such as those marked by the numbers 1, 2, and 3, while the rocking curves of other grains remained invariant. For the grains 1, 2, and 3,  $\beta$  was about 14' in the annealed state and increased to about 20' after the alloy was subjected to SC for 75 percent of its lifetime. Compare the enlarged rocking-curve details of annealed grain 3 in figure 4c with those after SC in figure 4d. Thus, in analyzing the defect structure of the grains in slow, creeping SC attack, the method proved to be capable of specific selectivity.

## 6. Advantages and Limitations of the Diffraction Method

Although the essential features of the combination method of reflection topography and rocking-curve analysis were developed by the author some 25 years ago, and although the method was applied successfully to a number of problems of technological importance, the execution of the method was tedious and time-consuming. The drawback, however, did not lie in the method per se, but was principally due to the inefficient x-ray tubes which were available at that time. However, with the great efficiency of today's x-ray tubes, the availability of powerful rotating anodes and the advent of Synchrotron radiation, the method has experienced a new renaissance and has assumed new significance. Experiments that used to take weeks of exposure can now be performed in a few hours' time.

The great advantages which the method offers can be stated as follows:

- (a) It combines the topographic and analytical analyses of the defect structure of the individual crystallites of a polycrystalline specimen without surrendering the ability of statistical sampling and group representation which the study of a polycrystalline material usually offers.

- (b) If the defect structure of crystallites becomes pronounced in certain crystallographic directions, as a result of physical operations, viz. magnetization plastic deformation or diffusion, there will be pronounced changes in the rocking-curve characteristics of corresponding (hkl) reflections. Such changes frequently become self-evident by mere inspection of the spot arrays in a multi-exposure diagram. Such was the case, for example, when the deformation characteristics of a silicon powder was investigated and the rocking curves (111) reflections corresponding to the active slip planes exhibited conspicuously larger values [3].
- (c) By correlating the quantitative analysis of the defect structure to surface topography; a bridge is formed which permits subsequent detailed structural analysis and characterization of the identical crystallites by light microscopy, scanning and transmission microscopy.

The limitations of the method are rather obvious. If the crystallite size is small, i.e., of the order of a few micrometers, the spatial tracing of the reflections from specimen surface to the circumference of the Debye-Scherrer camera is difficult to carry out. Consequently, the topographic relationship between the analyzed rocking curves at the surface sites of the crystallites cannot be established unequivocally. Finally, if either as a result of a special growth or severe deformation process, the crystallites are so small and numerous that even by application of a microfocus tube and use of nuclear track plates the reflecting crystallites cannot be resolved (size limit about 1.5  $\mu\text{m}$ ), then neither topographic mapping nor rocking-curve analysis of the crystallites can be performed.

#### References

- [1] Weissmann, S., Method for the study of lattice inhomogeneities combining x-ray microscopy and diffraction analysis, *J. Appl. Phys.* 27, 389-395 (1956).
- [2] Weissmann, S., Substructure characteristics of fine-grained metals and alloys disclosed by x-ray reflection microscopy and diffraction analysis, *Trans. ASM*, 52, 599-614 (1960).
- [3] Reis, A. J., Slade, J. J., Jr., and Weissmann, S., A new x-ray diffraction method for studying imperfections of crystal structure in polycrystalline specimens, *J. Appl. Phys.* 22, 665-672 (1951).
- [4] Slade, J. J., Jr. and Weissmann, S., Study of imperfections of crystal structure in polycrystalline materials, *J. Appl. Phys.* 23, 323-329 (1952).
- [5] Hirsch, P. B., Mosaic structure, in *Progress Met. Phys.* 6, 283 (Pergamon Press, Ltd., New York, 1956).
- [6] Tsunekawa, Y. and Weissmann, S., Importance of microplasticity in the fracture of silicon, *Met. Trans.* 5, 1583-1593 (1974).
- [7] Weissmann, S. and Evans, D. L., An x-ray study of the substructure of fine-grained aluminum, *Acta Cryst.* 7, 733-737 (1954).

- [8] Weissmann, S., Quantitative study of substructure characteristics and correlation to tensile property of nickel and nickel alloy, J. Appl. Phys. 27, 1335-1344 (1956).
- [9] Weissmann, S., Growth process in recrystallization of aluminum, Trans. ASM, 53, 265-281 (1961).
- [10] Weissmann, S., Imura, T., and Hosokawa, N., Recrystallization and grain growth of aluminum, in Recovery and Recrystallization of Metals, L. Himmel, ed. (Interscience, New York, 1963), pp. 241-267.
- [11] Garofalo, F., Zwell, L., Keh, A. S., and Weissmann, S., Substructure formation in iron during creep at 600°C, Acta Met. 9, 721-729 (1961).
- [12] Smith, D. K. and Weissmann, S., Residual stress and grain deformation in extruded polycrystalline BeO ceramics, J. Am. Ceram. Soc. 51, 330-336 (1968).
- [13] Hida, M. and Weissmann, S., High-temperature strength and ductility increases of Ti-Mo-Al alloys by step-aging, Met. Trans. 6A, 1541-1546 (1975).
- [14] Hamajima, T. and Weissmann, S., Thermal equilibria and mechanical stability of Ti<sub>3</sub>Al phase in Ti-Mo-Al alloys, Met. Trans. 6A, 1535-1539 (1975).
- [15] Pangborn, R. N., Yazici, R., Tsakalakos, T., Weissmann, S., and Kramer, I. R., Determination of prefracture damage in fatigued and stress-corroded materials by x-ray double crystal diffractometry, this volume .



DETERMINATION OF PREFRACTURE DAMAGE IN FATIGUED AND  
STRESS-CORRODED MATERIALS BY X-RAY DOUBLE CRYSTAL DIFFRACTOMETRY

R. N. Pangborn, R. Yazici, T. Tsakalakos, S. Weissmann  
College of Engineering  
Rutgers University  
Piscataway, NJ 08854

and

I. R. Kramer  
David W. Taylor Naval Ship R & D Center  
Annapolis, MD 21402

The lattice defects induced in fatigued aluminum alloys and in austenitic stainless steel and titanium-aluminum alloys subjected to stress corrosion were investigated by a method based on x-ray double crystal diffractometry combined with x-ray topography. X-ray rocking curves of the grain reflections from the surface layer and bulk material of the specimens were obtained, and a statistical halfwidth value for the rocking curves,  $\bar{\beta}$ , was determined from the population of grain reflections. This parameter characterized the excess dislocation density of the analyzed grains. It was shown that a defect structure was rapidly produced in the surface layer for both the fatigue cycled and stress corroded specimens. In addition, for both deformation processes, gross mechanical instability and fracture occurred when a critical value,  $\bar{\beta}^*$ , was attained. Investigation of the induced excess dislocations in depth by incremental surface removal showed that there exists a dynamical interplay between the buildup of excess dislocations in the surface and bulk. By measuring the progressive buildup of excess dislocations in depth as a function of the number of cycles for fatigue, or the elapsed exposure time for stress corrosion, the induced damage to the material could be assessed. Consequently, the remaining lifetime of the materials could be predicted by the nondestructive x-ray method at various stages of their lives.

Key Words: Excess dislocation density; failure prediction; fatigue; stress corrosion; x-ray double crystal diffractometer; x-ray topography.

## 1. Introduction

The ability to predict the failure of materials subjected to static stressing in aggressive environments, or to dynamic or repeated loading, is of great technological importance, both for mechanical and structural applications. Since the physical properties of solid materials, such as their strength and plastic response to deformation, are structure sensitive, the prefracture damage may also be related to changes in the defect structure and lattice misalignment. For deformation processes which are known to be highly surface sensitive, the evaluation of these structural changes with respect to depth from the surface is equally important to the comprehensive characterization of deformation induced damage. Because x-ray diffraction methods are nondestructive, they represent an ideal tool with which to elucidate structural changes, and the degradation in mechanical performance they represent.

### 1.1. Stress corrosion

Stress corrosion cracking is the phenomenon of metal disintegration under the combined action of chemical corrosion and mechanical stress. Although a number of theories have been proposed to explain the stress corrosion (SC) process, no single theory has received general acceptance. Indeed, some investigators [1]<sup>1</sup> maintain that no general mechanism is applicable to SC, but rather that different mechanisms may be operative for different metals and environments. Thus, some studies [2,3] evoked a "dissolution" theory, which interpreted SC as a preferential dissolution process at the crack tip. Other investigators [4,5] attributed SC to a decrease in the surface energy by absorption. A "brittle film" model was first proposed by Logan [6], and this concept was pursued further by a number of investigators [7,8]. This latter proposal suggested that the crack propagation rate could be attributed to the dissolution of the substrate at cracked sites in the film, and was controlled by a repassivation process which prevents dissolution. Several investigators [9,10] also gathered evidence in the particular case of austenitic stainless steel, that hydrogen is evolved at the tip of the advancing crack during SC, causing local embrittlement.

Kramer [11,12] has ascribed the formation of a surface debris layer or film to the surface stresses set up in deformed metals and alloys. His preliminary studies [13,14] of uniaxially strained metals revealed that the surface layer is work hardened preferentially compared to the bulk material. Other scientists [15-17] have made etch pit density measurements, TEM analyses, and x-ray diffraction studies of tensile deformed metals to provide evidence that the dislocation density is higher at the surface than in the bulk. It would be expected that the application of static loads less than that required to produce macroscopic yield or creep will, under the influence of a corrosive environment, produce substantial multiplication and accumulation of dislocations in the

---

<sup>1</sup>Figures in brackets indicate the literature references at the end of this paper.

surface layer. Indeed, Fourier analysis of the x-ray diffraction line broadening in austenitic stainless steels revealed an increase in dislocation density due to SC, despite the small amount of plastic deformation observed to result from the testing [18]. In addition, crack initiation was associated with a critical value of the stored energy, estimated from the broadening of the diffraction lines, which was approximately the same for all specimens tested.

## 1.2. Fatigue cycling

Like stress corrosion cracking, failure under repeated stressing, employing loads in the elastic range, is both difficult to explain and to predict. Many studies [19-22] have been made in the past to relate the defect structure induced by fatigue cycling to the slip morphology exhibited on the surface. The topological features of the surface, such as persistent slip bands, intrusions and extrusions, developed during cycling have also been related to subsequent crack initiation and eventual failure [23-26]. Despite the considerable effort expended to understand the fundamental mechanisms governing crack initiation and propagation, no real consensus on what constitutes fatigue damage prior to these phenomena has yet emerged. Previous investigations employing x-ray diffraction analysis techniques have been unsuccessful in forecasting ultimate failure on the basis of changes in the patterns. Increased asterism or x-ray line broadening occurred either at very early stages of the cycling, remaining invariant thereafter [27,28], or were restricted to that period which follows the initiation of catastrophic, macroscopic failure [29,30]. Consequently, these parameters could not be associated with a marked, linear accrument of fatigue "damage" or the amount of reduction in the lifetime.

The propensity for surface layer work hardening during uniaxial straining, noted previously, may be extrapolated to fatigue by viewing a simple tensile test as the first half-cycle of push-pull fatigue. Kramer [31-33] has obtained evidence that such a surface layer is, in fact, formed during cycling of single crystals and commercial alloys. The preferential work hardening, disclosed by the enhancement of the surface layer flow stress, increased linearly during the life to a critical value at fracture which was independent of the stress amplitude [34]. It was proposed that the surface layer represents a barrier to dislocation migration from the bulk, and that fracture is initiated if the accumulation or pileup of excess dislocations at the surface produces local stresses in excess of the fracture strength.

## 1.3. Direct examination of the induced defect structure

The first objective of this study was to evaluate the structural changes in stress corroded and fatigue cycled metals and alloys as a function of their lifetimes, measured in terms of the exposure time, or number of cycles, respectively. Particular attention was focused on elucidating the distribution of structural defects from the surface to bulk induced by these deformation processes. X-ray double crystal diffractometry and

reflection topography represented sensitive, yet powerful research tools by which to analyze the prefracture damage. Thus, through a better understanding of the fundamental mechanisms leading to material failure by SC or fatigue, a new approach for predicting the onset of failure was sought.

## 2. Experimental Procedure

### 2.1. Material selection and specimen preparation

Three model materials were chosen for the preliminary investigation of tensile deformed single crystals: silicon, a low stacking fault energy, brittle material which is ductile when deformed at elevated temperature, and for which dislocations are virtually immobile after cooling to ambient temperature; aluminum, a high stacking fault energy material with microstructure typical of ductile fcc metals; and gold which exhibits little propensity for oxide layer formation. Flat test specimens were prepared from the crystals with tensile axis and surface orientations which would insure single or multiple glide and symmetric x-ray diffraction conditions, respectively.

Two types of alloys were selected for the stress corrosion investigation: austenitic stainless steel of 304 commercial grade with composition Fe-18Cr-8Ni-2Mn-1Si-0.8C; and alpha-titanium with nominal composition Ti-10Al. Flat, pin-loading specimens were cut from sheet stock with tensile axis parallel to the rolling direction.

The fatigue studies were carried out for aluminum single crystals of  $\langle 100 \rangle$  tensile axis orientation, and Al 2024 alloy with nominal composition Al-4Cu-1.4Mg-0.5Mn. Cylindrical, thread-mounting specimens were fabricated from rod stock.

All the specimens were heat treated in vacuum or in argon atmosphere, and water quenched. Suitable annealing times were determined to stress-relieve the specimens and to obtain grain sizes appropriate for the x-ray diffraction analysis. Prior to testing, the specimens were chemically or electrolytically polished to insure damage- and contamination-free surfaces.

### 2.2. Mechanical testing

The tensile tests of single crystals were performed on an Instron universal testing machine under conditions indicated in the results section. The SC tests were carried out at constant tensile loads employing the Instron equipment and a cantilever-type, dead load machine. The corrosive medium for austenitic stainless steel was a boiling  $\text{MgCl}_2\text{-H}_2\text{O}$  solution, maintained at 154 °C by controlled heating and water flow. The  $\alpha$ -Ti alloy was tested at room temperature in two types of corrosive media: a 0.5 molar, aqueous solution of NaCl, and a solution consisting of 0.5 percent HCl, 1 percent  $\text{H}_2\text{O}$  and 98.5 percent  $\text{CH}_3\text{OH}$ . A wide range of cell potentials was applied during the testing.

The fatigue cycling was performed in the push-pull mode with zero mean stress, using a Tatnell-Krause apparatus and Instron servohydraulic equipment (Model 1350). The constant applied loads for SC, and applied stress amplitudes for fatigue cycling, represented chosen fractions of the yield stress or proportional limit, respectively, predetermined from static tensile tests.

### 2.3. X-ray diffraction analysis

The principal research tool for structural characterization was the x-ray double crystal diffractometer method, in combination with Berg-Barrett topography to afford a visualization of the lattice inhomogeneity [35,36]. The application of this technique and a detailed discussion of the information it yields, both qualitative and quantitative, are presented in an invited contribution to this symposium [37]. Briefly, however, the lattice misorientation and configuration of crystal defects can be evaluated from the x-ray microscopy. The density of excess dislocations of one sign is calculated from the breadth of the diffraction peak, or rocking curve halfwidth. Since practical interest in SC required investigation of commercial alloys, an adaptation of double crystal diffractometry to polycrystalline materials was employed in this study. Debye patterns of the reflections from favorably oriented grains in the sample are recorded photographically. By carrying out incremental specimen rotations and corresponding film shifts, each grain's rocking curve can be analyzed as if it functions independently as a small single crystal. The most remarkable aspect of this special x-ray method is that the progressive change in selected grains can be followed during the deformation process. This is especially useful in the study of SC, since only particular grains are affected by the deformation, while others remain virtually unchanged. Thus, the double crystal diffractometer technique facilitated identification and analysis of only those grains which were critically affected by SC, so that by these direct measurements the computational averaging procedures, applied in conventional x-ray line broadening analysis to characterize the defect density, were avoided. For the fatigued alloy, on the other hand, the microplasticity was more uniformly distributed among the grains, and could therefore be treated statistically. The defect concentration in this case was characterized simply by taking the average rocking curve halfwidth for the analyzed grain population.

## 3. Results and Discussion

### 3.1. Change in the surface layer defect structure induced by SC or fatigue

SC experiments were performed on austenitic stainless steel at three constant stress levels corresponding to 95, 75 and 55 percent of the static yield stress at 154 °C. From the dependence of fracture time on the applied stress, shown in figure 1a, it can be seen that the fracture time increased rapidly when the applied stress dropped below the proportional limit, equal to about 75 percent of the yield stress. Scanning electron microscopy revealed a transcrystalline fracture mode for all the specimens tested. The broken curve in figure 2 illustrates the time dependence of the strain for the specimen loaded to 55 percent of the yield stress. A small initial increase was observed due to the elastic loading, and virtually no subsequent deformation, caused either by corrosion or creep, was observed for 19.5 hours, or about 80 percent of the total lifetime,  $t_f$ . After this critical exposure time,  $t_c$ , however, development of a large central crack and concomitant

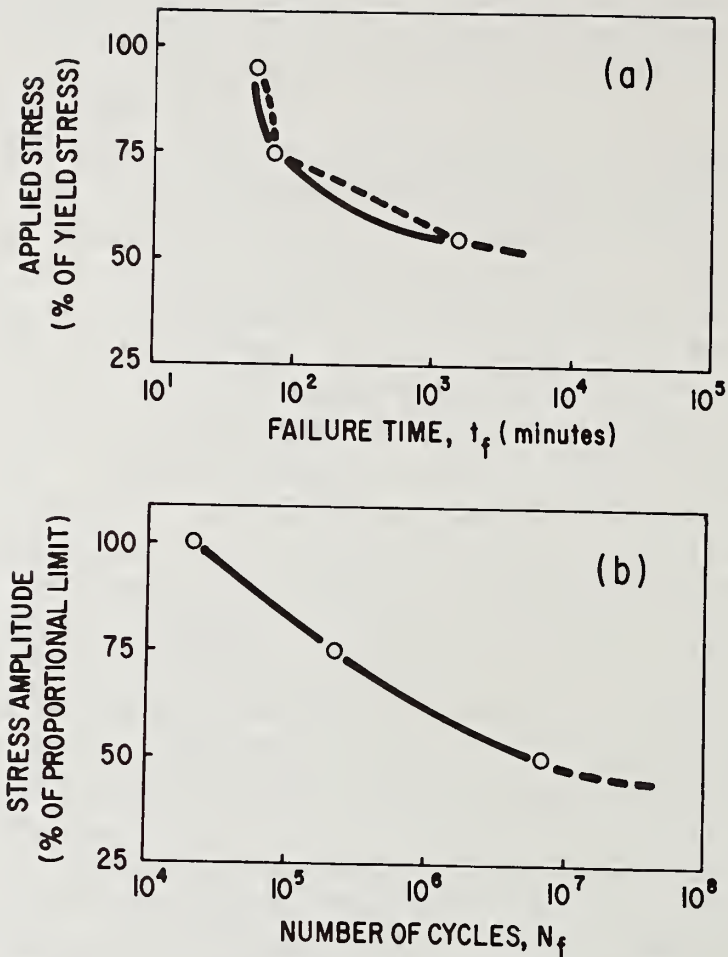


Figure 1. Dependence of specimen lifetime on stress condition: (a) failure time for SC as a function of applied static stress; (b) cycles to failure as a function of stress amplitude (S-N curve) for fatigue.

reduction of the cross-sectional area produced obvious mechanical instability. The rocking curve halfwidths for the reflecting grains, measured during SC, varied in a similar fashion with the exposure time. The solid curves in figure 2 depict the dependence of the ratio of measured-to-intrinsic (undeformed) halfwidths during the lifetime. The lower curve, denoted A, refers to the average  $\beta/\beta_0$  value for all the grains analyzed, while the upper curve, labeled B, represents the change in halfwidth for specific grains which showed a preferential or persistent broadening as a result of SC. (The selectivity of grain attack by SC is shown by the details of the multi-exposure diagram in figures 4a and 4b of reference [37]). Both curves ascend to maximum values during the first 67 percent of  $t_f$ , after which they decline conspicuously to lower values at the critical time  $t_c$ . Finally, the macroscopic mechanical instability occurring between  $t_c$  and  $t_f$  is reflected on a microscopic scale by the rapid rise of  $\beta/\beta_0$  from 80 to 100 percent of  $t_f$ .

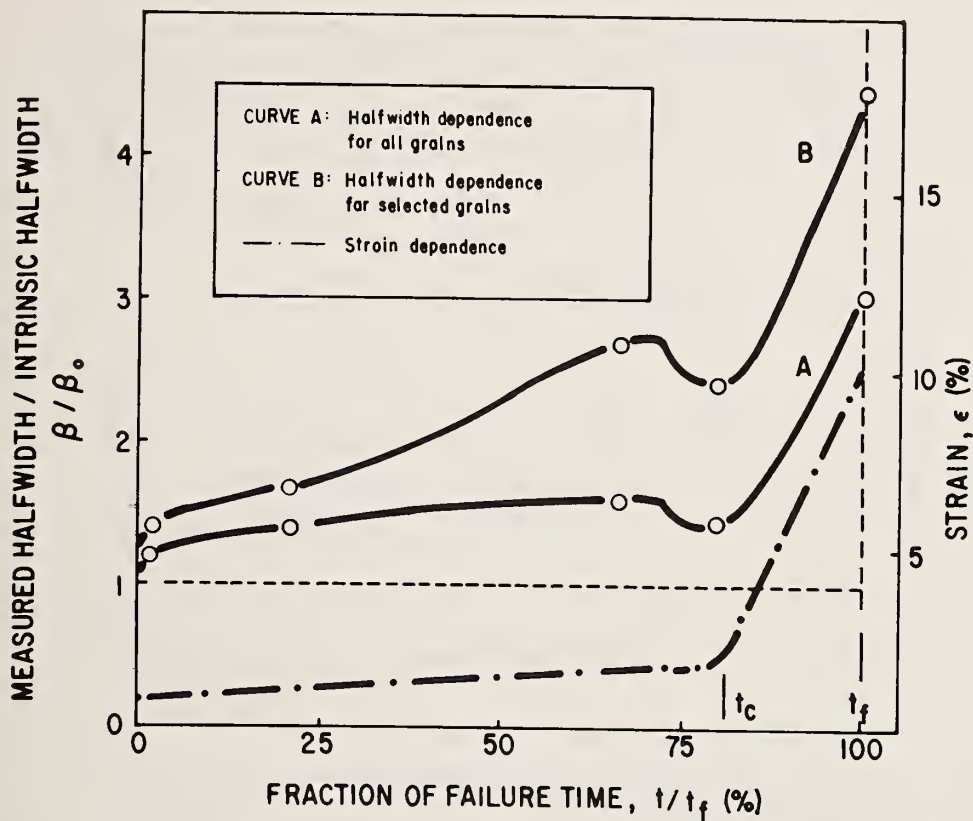


Figure 2. Changes in the strain and x-ray rocking curve halfwidths during progressive exposure to SC.

Fatigue tests were carried out on Al 2024 specimens to generate an S-N curve typical for tension-compression cycling. As shown by figure 1b, there exists a distinct similarity between the dependence of  $N_f$  on stress amplitude and the dependence of  $t_c$  on applied stress for SC in figure 1a. Three stress amplitudes corresponding to 50, 75 and 100 percent of the proportional limit for static tension were chosen for the x-ray investigation. Figure 3 shows the cyclic dependence of the halfwidths,  $\bar{\beta}$ , corrected for the average intrinsic, or undeformed halfwidth,  $\bar{\beta}_0$ .  $\bar{\beta}$  is computed according to the relation:  $\bar{\beta} = (\beta^2 - \beta_0^2)^{1/2}$ , where  $\beta$  is the average halfwidth measured after deformation. The curve, generated by using shallow-penetrating Cu radiation to analyze only the surface layer, reveals many similarities to the progressive changes in the rocking curves induced by SC, depicted in figure 2. After an initial period of rapid halfwidth expansion comprising the first 20 percent of the life (Stage I), a markedly decreased slope was obtained for the long cycling duration extending to 95 percent of the total number of cycles to failure,  $N_f$ . As in the case of SC, the macroscopic mechanical instability during the final Stage III caused another rapid enhancement of the rocking curve breadths. Remarkably, the progressive changes in the halfwidths, as well as the critical halfwidth at failure,  $\bar{\beta}^*$ , were nearly identical for cycling at all three stress levels.

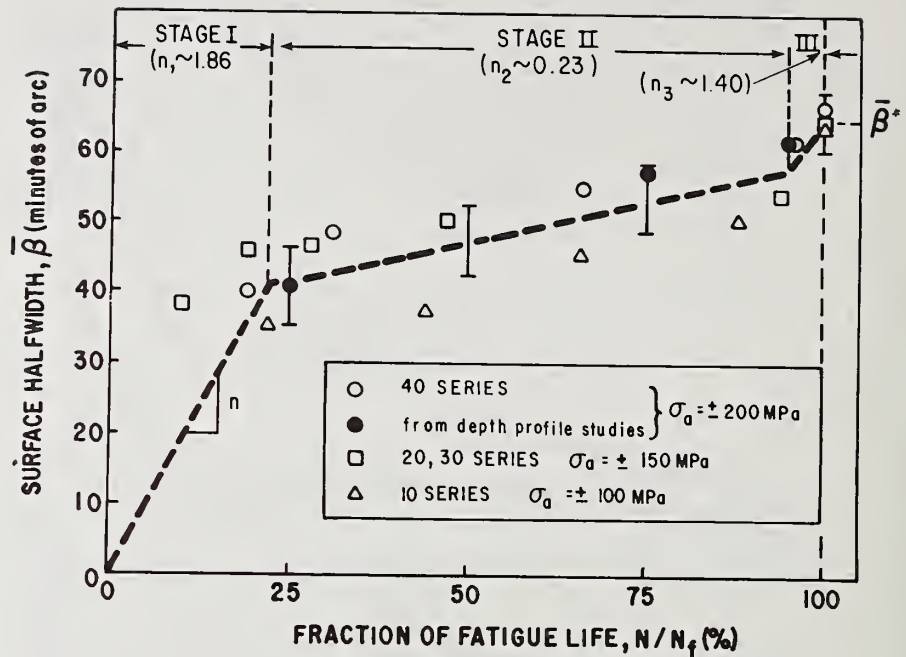


Figure 3. Change in the rocking curve halfwidths at the specimen surface during progressive fatigue cycling at selected stress amplitudes.

### 3.2. Depth distribution of the lattice defects

A preliminary study involved tensile deformed Si, Al and Au monocrystals. The distribution of excess dislocations in depth was determined by rocking curve measurement [37] after discrete surface layer removals, effected by chemical or electrolytic polishing. As shown in figure 4, a decreasing gradient in the excess dislocation density was obtained from surface to bulk for all three specimens. Significant declines from a high surface density to a constant density at about 150  $\mu\text{m}$  into the interior were measured, even for the gold crystal deformed to only 3 percent plastic strain. Thus oxide formation is presumably not a necessary prerequisite for preferential accumulation of excess dislocations in the surface layer.

Using a similar procedure, the depth dependence of the rocking curve breadths after SC and fatigue was analyzed. Figure 5 shows profiles of  $\beta/\beta_0$  as a function of depth distance from the surface,  $x$ , for austenitic stainless steel, subjected to SC at 55 percent of the yield stress. After an exposure time corresponding to only one-tenth of  $t_c$ , a notable decrease from surface to bulk for the halfwidths of grains selectively affected by the SC was obtained. These high surface halfwidths, analyzed with Cu radiation which penetrates only 1  $\mu\text{m}$  into depth, indicate that the plastic deformation occurs principally in the surface layer. Like the profiles for tensile deformed single

ystals, x-ray diffraction analysis of SC specimens after surface layer removals revealed that a constant minimum value for the halfwidths is established in depth. By contrast, when  $\beta/\beta_0$  was measured in depth after SC to the critical exposure time,  $t_c$ , the bulk  $\beta/\beta_0$  values were equivalent to those of the surface layer. An identical behavior is obtained for the  $\alpha$ -Ti for SC at 60 percent of the yield stress and an impressed cell potential of -200 mV (rest potential = -230 mV).

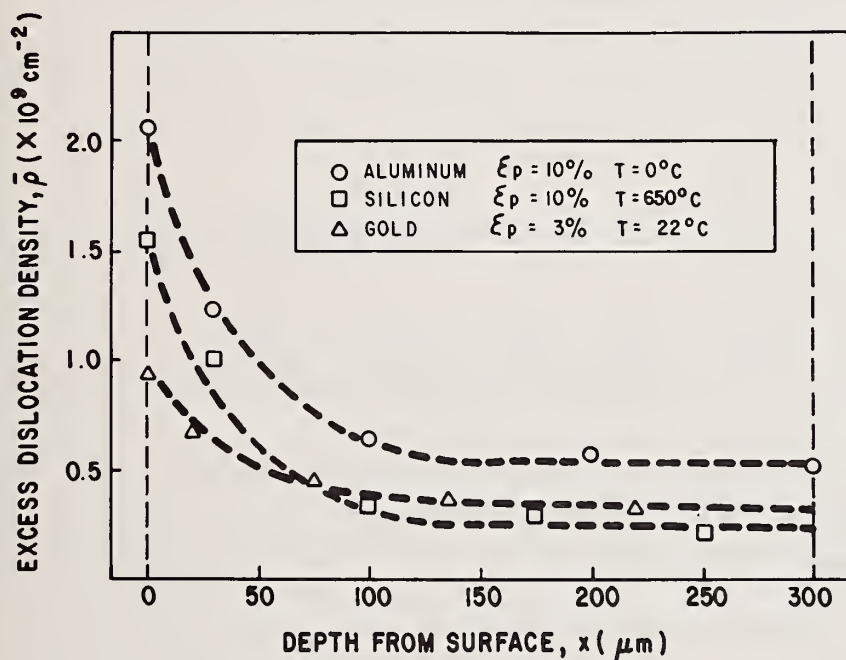


Figure 4. Experimental gradients of the excess dislocation density with depth from the surface for tensile deformed monocrystals.

[Aluminum:  $\langle 100 \rangle$  tensile axis, (100) reflection; Silicon:  $\langle 110 \rangle$  tensile axis, (112) reflection; Gold:  $\langle 123 \rangle$  tensile axis, (113) reflection.]

Al 2024 specimens subjected to fatigue cycling also exhibited surface layer halfwidth enhancements analogous to those for the tensile and SC tests. Figure 6 shows profiles obtained for alloy specimens fatigued to various stages of the fatigue life. After only 0.15 percent of the life a simple decreasing gradient typical of that for monotonic deformation was obtained. After cycling to 25 percent of  $N_f$ , however, the profile conformation exhibits an additional salient feature. After declining to a minimum value at 100  $\mu\text{m}$  in depth, the halfwidths increase again further into depth to a plateau level at about 250  $\mu\text{m}$  from the surface. The figure also shows that the halfwidth expansion at the surface occurs early in the life while the halfwidths for the bulk increase more gradually and never exceed the surface value.

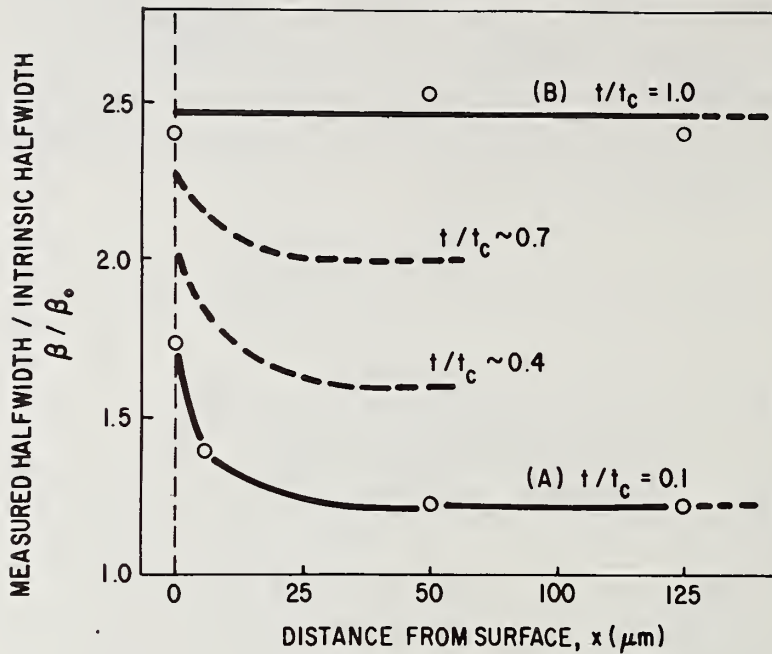


Figure 5. Depth profiles, showing the halfwidth dependence on distance from the surface of austenitic stainless steel, for various stages of SC.

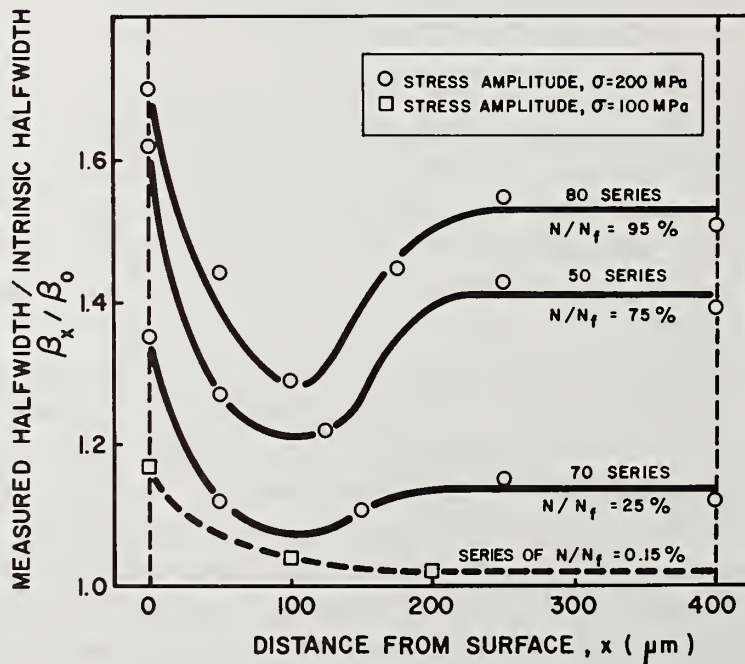


Figure 6. Depth profiles for Al 2024 specimens after various amounts of push-pull fatigue.

For both the stress corroded and fatigue cycled specimens, x-ray reflection topography [37] disclosed significant differences between the defect structures of the surface layer and bulk material. The spot reflections from the surface grains displayed substantial breakup in the azimuthal direction, along the tangent to the Debye arcs. In the radial direction, incremental specimen rotations in the parallel incident radiation produced a broad range of reflection, featuring sequential intensity maxima and minima. Both of these observations are indicative of the introduction of a deformation sub-structure [37], increases in the defect density, and concomitant work hardening of the surface layer. The reflections from grains located in the bulk, on the other hand, were well-resolved and unimodal. The reduced plastic deformation in the core region of the specimens was manifested by the short angular duration of the reflection range of the grains.

### 3.3. Influence of the surface layer on prefracture mechanical behavior

The surface layer of stress corroded or fatigue cycled specimens clearly plays a similar role in the two respective deformation processes. In both cases, the rocking curve halfwidths, representative of the induced excess dislocation densities, increased preferentially in the surface layer early in the lifetime. A long period of rocking curve invariance was exhibited during intermediate life fractions, before a final expansion stage occurred just prior to failure. The rapid saturation of the surface layer halfwidths and decreasing gradients in depth suggest that a barrier effect is created at the surface, which restricts the egression of excess dislocations generated in the bulk. As a result, a more gradual but steady accumulation of defects occurs in the interior throughout the lifetime.

In SC, the electrochemical attack was initiated at the surface by preferential deformation of the surface layer between  $t = 0$  and  $t = 0.1 t_c$ . The surface corrosion was sustained during the period from  $0.1 t_c$  to  $t_c$  by progressive deformation of the surface layer with exposure time. The corrosion process may be conceived in terms of a galvanic cell, with the plastically deformed, film-free metal grains functioning as an anode, and the undistorted grains serving as the cathode. The diffusion of the chemical species is presumably assisted by the dislocation activity in the surface layer. At the same time, this effective work hardening of the surface layer confers to it the property of a barrier to dislocation egression, and induces a dynamical interplay between surface and bulk. Thus, the effects of corrosive embrittlement of the surface layer and dislocation accumulation due to deformation under the applied load are superimposed, so that microcracks advance by a combination of electrochemical and mechanical action. The resistance to failure is therefore substantially reduced, compared to that of a material stressed in a non-corrosive medium. The approach toward a critical value,  $(\beta/\beta_0)^*$ , at which macroscopic mechanical instability at  $t_c$ , and then brittle failure at  $t_f$ , occur is accelerated in the aggressive environment.

An analogous barrier aspect of the surface layer is illustrated by the results for fatigue cycling. Preferential work hardening of the surface layer occurs during the first 20 to 25 percent of the fatigue life and impedes the outward migration of internally generated defects. The mutual interplay between the defect structure in the surface layer and the plastic deformation introduced to the bulk sustains the strengthening of this barrier. According to the model proposed by Kramer [33], microcracks are initiated at the surface when the local stress fields associated with dislocation pileups exceed the fracture strength. The rate of inward propagation of the cracks is controlled by the dislocation accumulation in depth, produced by continued cycling.

To test the surface barrier model for fatigue, a further experimental sequence was devised and carried out, as depicted by the composite diagram in figure 7. Part A of the figure presents typical depth profiles for Al 2024 specimens cycled to 75 and 95 percent of their fatigue lives. These curves were obtained by incrementally removing the surface layers by electropolishing and performing x-ray rocking curve analyses at each depth. After a total thickness of 400  $\mu\text{m}$  was removed from the original surfaces of the specimens, the fatiguing was continued at the same stress amplitude. The curves in Part B, obtained by analysis after short cycling increments, demonstrate a conspicuous decline in the  $\beta/\beta_0$  values on the initial recycling. The dislocation structure and arrangement in the bulk is obviously very unstable during cycling when the blocking effect inherent to the deformed surface layer is absent. After reaching a minimum at 1 to 2 percent of the life, the halfwidths increased again since a new, work hardened surface layer was being formed. When the recycling process was interrupted after 5 percent to obtain a second depth profile, as exhibited in Part C, the  $\beta/\beta_0$  values throughout the cross section of the specimen given 75 percent prior cycling were significantly less than that induced by the original fatigue, as shown by reference to the plateau level in Part A. Indeed the halfwidths were comparable to the value for an undeformed, virgin specimen. Furthermore, uninterrupted recycling of the specimen previously fatigued to 95 percent of its life and polished to 400  $\mu\text{m}$  in depth produced a 75 percent net increase in the normal fatigue life. These experiments not only provide a dramatic demonstration of the blocking effect of the work hardened surface layer, but also explain the remarkable extensions of fatigue life afforded by judicious, periodic surface layer removal [32,38]. Though the improvement in the lifetime has been ascribed in the past to the elimination of microcracks, persistent slip bands, and other surface relief, it may actually derive primarily from the instability of the bulk defect structure in the absence of the work hardened surface layer.

### 3.4. Nondestructive prediction of failure

The results of the x-ray diffraction studies imply that the critical accumulation of excess dislocations in the surface layer, experimentally determined by  $(\beta/\beta_0)^*$ , governs the fracture of the material. For SC of both austenitic stainless steel and alpha-titanium, mechanical instability set in when the critical halfwidth value was approached, regardless of the particular conditions employed in the tests; routes to failure

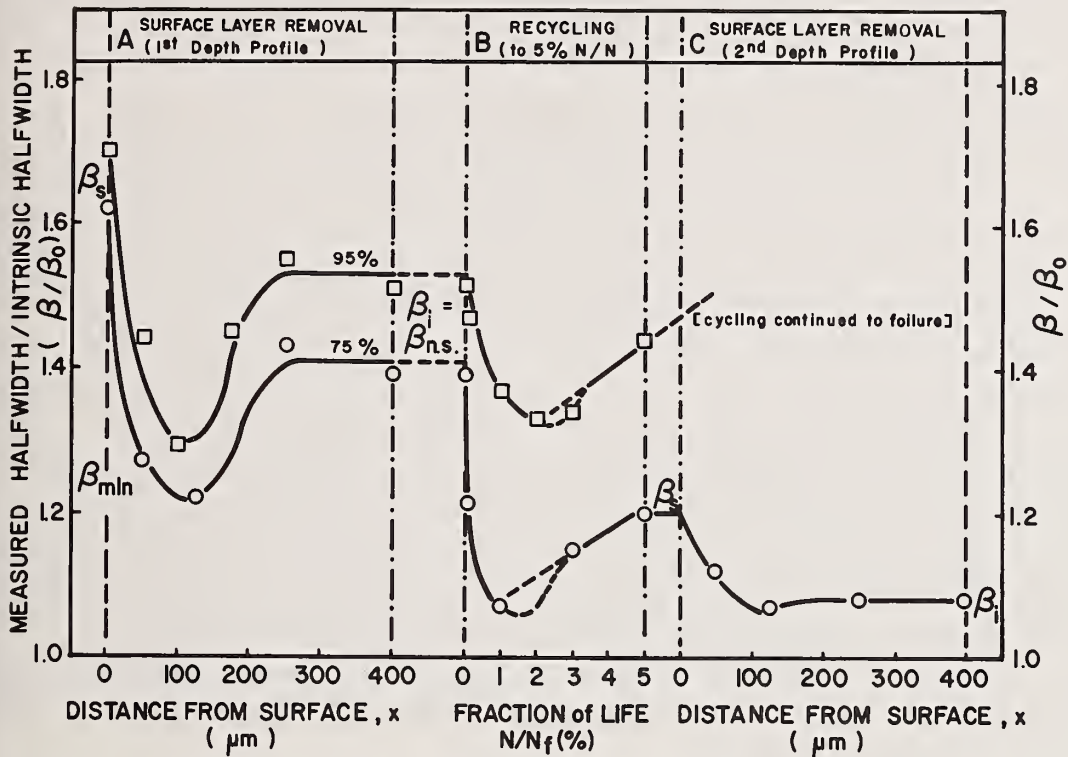


Figure 7. Composite diagram for Al 2024 specimens given prior fatigue cycling to 75 and 95 percent of their fatigue lives at  $\pm 200$  MPa, followed by surface removal and recycling treatment (A & B), and either continued recycling or a second depth profile analysis (C).

volving application of high stress and short SC exposure time or low stress and long SC exposure time produced a consistent value for  $(\beta/\beta_0)^*$ . Similarly, fatigue failure occurred at a critical corrected halfwidth value,  $\beta^*$ , which was independent of the stress amplitude. The recognition of the importance of the critical value of the halfwidth to these modes of mechanical deformation opens up an exciting vista with regard to prediction of a material's lifetime.

For SC, it may be seen from figure 2 that the dependence of the measured halfwidths on exposure time is much steeper when only selected grains are considered (Curve B), than when an average for all the grains is taken (Curve A). The enhanced potential for predicting the failure time from any intermediate point along Curve B derives from the unique capability of double crystal diffractometry to distinguish those grains exhibiting pronounced susceptibility to SC. An alternative method for predicting the remaining life of a stress corroded material resides with the disparity in the rates of change of the surface and bulk halfwidth values. As shown in figure 5, about half of the total change in the surface  $\beta$  value occurred during the first 10 percent of the critical exposure time. The plastic deformation in the bulk during this period was very minimal. Nevertheless, at the critical time,  $t_c$ , the surface layer and bulk material halfwidths

exhibit near parity. Thus, the rate of halfwidth expansion of bulk grains must be greater than that for grains at the surface during intermediate stage of the life. The broken curves shown in the figure indicate speculative conformations of the profiles for times  $t \sim 0.4 t_c$  and  $0.7 t_c$ , which would provide a nearly linear dependence of the bulk halfwidths on exposure time.

Reference to figure 6 shows that such a linear dependence, in fact, occurs for fatigue. While the surface halfwidths again exhibit an early-life saturation behavior (as shown by figure 3, and by the nearly equivalent values for  $\beta/\beta_0$  at  $x = 0$  for 25 and 95 percent of the life in figure 6), the bulk plateau values show nearly equal increases for each 25 percent increment in the expended life. The in-depth study demonstrated why in the past the x-ray patterns, which analyzed only the surface grains of cycled specimens, were inconclusive in predicting fatigue failure. Because the work hardening at the surface occurs so early in the life, it cannot be used to predict the onset of failure, nor can it even be interpreted as a true indication of fatigue damage. This latter conclusion, first suggested by Barrett [39], was also demonstrated by corresponding studies of fatigued Al monocrystals. The profile in figure 8, obtained for a crystal fatigued in the high cycle range ( $\pm 1.03$  MPa,  $2 \times 10^5$  cycles), shows that despite the surface work hardening, at sufficiently low stress amplitudes, no change in the bulk halfwidths occurred. It may be seen that the interior plateau level remained at essentially the same value as for the undeformed crystal,  $\beta_0$ , and the subsurface region extending from 50 to 150  $\mu\text{m}$  actually displayed  $\beta$  values lower than the intrinsic halfwidth of the virgin crystal.

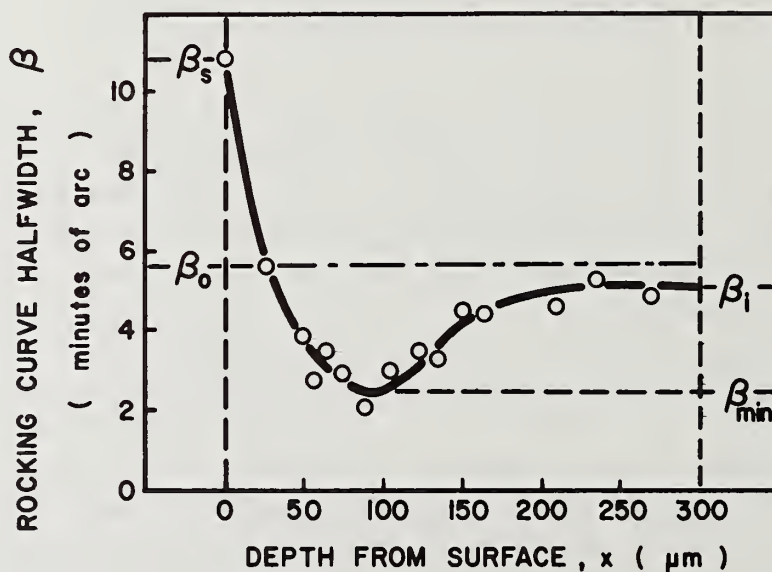


Figure 8. Profile of the measured halfwidth dependence on depth from the surface for a fatigued Al single crystal. [ $\langle 100 \rangle$  axis, (100) reflection.]

The Al 2024 depth profiles revealed how a more accurate determination of the failure life could be achieved. Figure 9 shows the dependence of the rocking curve halfwidth on the fraction of life for analysis with copper, molybdenum, and chromium radiation. The penetration produced by these three target materials provides a spectrum of penetration depths in the Al alloy of about two orders of magnitude. Chromium radiation which penetrates a maximum of 12  $\mu\text{m}$  from the surface produces very little change in  $\bar{\beta}$  from 5 to 95 percent of the life. Copper radiation which penetrates up to 37  $\mu\text{m}$ , or about one grain diameter, exhibits little more of an incline during this period (the absolute values of  $\bar{\beta}$  differ from those in figure 3 due to the smaller average grain size of the alloy stock used in the experiment). By contrast, molybdenum radiation which penetrates a depth of up to 350  $\mu\text{m}$  ascends steeply from about 5 minutes of arc at about 5 percent of the life, to 35 minutes of arc at 95 percent of the life, coinciding with the critical halfwidth value measured using copper radiation. The steep, nearly single-stage curve is attributed from the added contribution of the defect structure in the bulk to the x-ray analysis. A new criterion for fatigue life and failure prediction has therefore emerged: re-establishing the critical halfwidth value,  $\bar{\beta}^*$ , and comparing it to the  $\bar{\beta}$  value measured in depth at any stage in the fatigue process, the remaining fraction of the life can be estimated. By determining the degree of prefracture fatigue damage in this way, fatigue life, and probably the life for other deformation processes as well, may be assessed easily, accurately, and nondestructively.

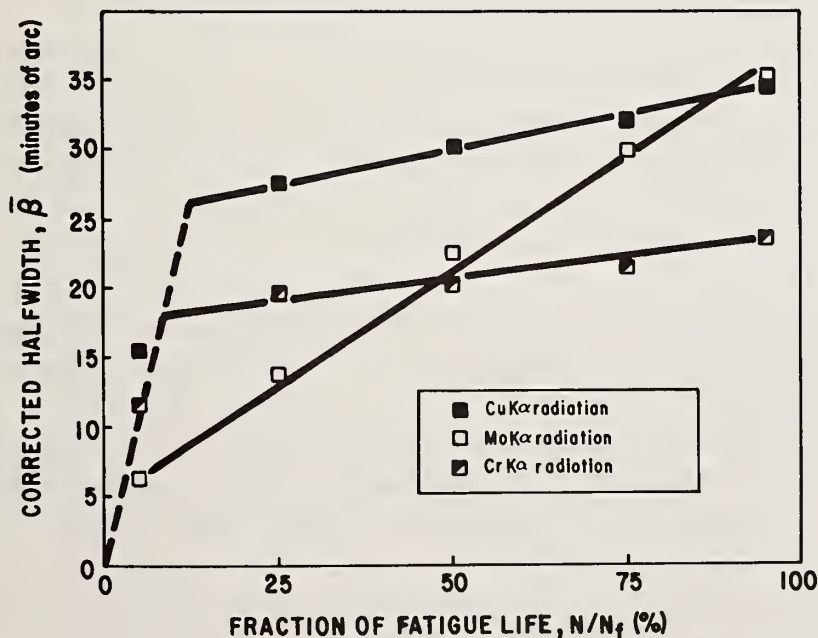


Figure 9. Comparative dependences of the rocking curve halfwidths on the fraction of fatigue life for analyses employing incident radiation from chromium, copper and molybdenum x-ray targets.

#### 4. Conclusions

1. Austenitic stainless steel and alpha-titanium were subjected to stress corrosion, and Al 2024 was cycled in the push-pull fatigue mode. Selected grains at the surface of SC specimens, and the grains located in the surface layer of fatigued specimens exhibited a higher density of excess dislocations than the bulk material, as determined by x-ray diffraction analysis. It was proposed, therefore, that the surface layer functions as a barrier to the egression of dislocations generated in the bulk, and that prefracture damage is accrued as a result of a dynamical interplay between the work hardened surface layer and the induced defect structure of the bulk material.

2. For both SC and fatigue, the x-ray rocking curve halfwidths for the surface layer increased rapidly early in the life. By contrast, the bulk material revealed a steep, linear enhancement of the measured halfwidths throughout the life, to a critical value at the onset of failure. By application of deeply-penetrating radiation to sample x-ray rocking curves in depth at various stages of the life, the measured halfwidths could be compared to this critical value. Thus, for fatigue, the remaining fraction of life prior to failure could be accurately and nondestructively estimated by this experimental technique. A similar approach for prediction of failure due to SC is currently under investigation.

---

The authors wish to express their gratitude to the Office of Naval Research (Metallurgy Program) for the support of the stress corrosion studies, and to the David W. Taylor Naval Ship R & D Center for their sponsorship of the fatigue investigation.

#### References

- [1] Pugh, E. N., On the mechanism(s) of stress-corrosion cracking, in Environment-Sensitive Mechanical Behavior, A. R. C. Westwood and N. S. Stoloff, eds. (Gordon Breach, New York, 1965), pp. 351-401.
- [2] Hines, J. G. and Hoar, T. P., The stress corrosion cracking of austenitic stainless steels. II. Fully softened, strain hardened and refrigerated materials, *J. Iron Steel Inst. (London)* 184, 166-172 (1956); *ibid.* 182, 124-143 (1955); *ibid.* 177, 248 (1954).
- [3] Sanderson, G. and Scully, J. C., Stress corrosion of titanium alloys in methanolic solutions, *Corrosion Sci.* 8 [7], 541-548 (1968).
- [4] Coleman, E. G., Weinstein, D., and Rostocker, W., On the surface energy mechanism for stress-corrosion cracking, *Acta Met.* 9 [5], 491-496 (1961).
- [5] Powell, D. T. and Scully, J. C., Fractographic observations of the stress corrosion cracking of titanium alloys in methanolic environments, *Corrosion*, 25 [12], 483-492 (1969).

- Logan, H. L., Film-rupture mechanism of stress-corrosion, J. Res. NBS, 48 [2], 99-105 (1952).
- Forty, A. J. and Humble, P., The influence of surface tarnish on the stress-corrosion of  $\alpha$ -brass, Phil. Mag. 8 [86], 247-264 (1963).
- McEvelly, A. J., Jr. and Bond, A. P., Initiation and growth of stress-corrosion cracks in tarnished brass, J. Electrochem. Soc. 112 [2], 131-138 (1965).
- Mehta, M. L. and Burke, J., Role of hydrogen in stress corrosion cracking of austenitic stainless steels, Corrosion, 31 [3], 108-110 (1975).
- Sudarshan, T. S., Louthan, M. R., Jr., and McNitt, R. P., Hydrogen induced suppression of yield point in A-106 steel, Scripta Met. 12 [9], 799-803 (1978).
- Kramer, I. R. and Podlasek, S., Stress-strain behavior of aluminum crystals at low pressures, Acta Met. 11 [1], 70-71 (1963).
- Kramer, I. R., Correlation of the surface layer stress coefficient and stress corrosion cracking, Corrosion, 31 [11], 383-391 (1975), *ibid.* 391-394.
- Kramer, I. R. and Demer, L. J., Effect of surface removal on the plastic behavior of aluminum single crystals, TSM-AIME 221 [4], 780-786 (1961).
- Kramer, I. R., Influence of the surface layer on the plastic flow deformation of aluminum single crystals, TMS-AIME 233 [7] 1462-1467 (1965).
- Kitajima, S., Tanaka, H., and Kaieda, H., Dislocation distribution near the surface of weakly deformed copper crystals, Trans. Jap. Inst. Met. 10 [1], 12-16 (1969).
- Tabata, T. and Fujita, H., An electron microscope study of dislocation arrangement in the surface layer of aluminum single crystals, J. Phys. Soc. Jap. 32 [6], 1536-1544 (1972).
- Sumino, K. and Yamamoto, M., Preferential plastic deformation in the surface region of Al and  $\alpha$ -Fe single crystals, J. Phys. Soc. Jap. 16 [1], 131 (1961).
- Kamachi, K., Otsu, T., and Obayashi, S., A study of mechanical behavior of austenitic stainless steels in the process of corrosion testing, J. Jap. Inst. Met. 35 [1], 64-70 (1971).
- Segall, R. L., Partridge, P. G., and Hirsch, P. B., The dislocation distribution of face-centered cubic metals after fatigue, Phil. Mag. 6 [72], 1493-1513 (1961).
- McGrath, J. T. and Waldron, G. W. J., An electron microscope study of dislocation arrangements in fatigued Al-1% Mg crystals, Phil Mag. 9 [98], 249-259 (1964).
- Laufer, E. E. and Roberts, W. N., Dislocations and persistent slip bands in fatigued copper, Phil. Mag. 14 [127], 65-78 (1966).
- Levine, E. and Weissmann, S., The structure and development of fatigue striations in Al, Trans. Quar. ASM 61 [1], 128-138 (1968).
- Thompson, N. and Wadsworth, N. J., Metal fatigue, Adv. in Physics (Phil. Mag. Suppl.) 7 [25], 72-170 (1958).
- Forsyth, P. J. E. and Stubbington, C. A., The mechanism of fatigue failure in some binary and ternary aluminum alloys, J. Inst. Met. 85, 339-343 (1956-7).
- Cottrell, A. H. and Hull, D., Extrusion and intrusion by cyclic slip in copper, Proc. Roy. Soc. (London) A242 [1229], 211-213 (1957).

- [26] Alden, T. H. and Backofen, W. A., The formation of fatigue cracks in aluminum single crystals, *Acta Met.* 9 [4], 352-366 (1961).
- [27] Bennett, J. A., A study of fatigue in metals by means of x-ray strain measurement, *J. Res. NBS* 46 [6], 457-461 (1951).
- [28] Taira, S. and Hayashi, K., X-ray investigation on fatigue fracture of notched steel specimen, *Bull. JSME* 9 [36], 627-637 (1966).
- [29] Gough, H. J. and Wood, W. A., A new attack upon the problem of fatigue of metals, using x-ray methods of precision, *Proc. Roy. Soc. (London)* A154 [883], 510-539 (1936).
- [30] Spencer, R. G. and Marshall, J. W., An x-ray study of changes that occur in aluminum during the process of fatiguing, *J. Appl. Phys.* 12 [3], 191-196 (1941).
- [31] Kramer, I. R., Work hardening and creep of aluminum and copper during alternate stressing, *Trans. ASM* 62 [1], 521-536 (1969).
- [32] Kramer, I. R. and Kumar, A., Relaxation and cyclic hardening of the surface layer of copper, *Met. Trans.* 3 [5], 1223-1227 (1972).
- [33] Kramer, I. R., Prediction of fatigue damage, 2nd Int. Conf. on Mech. Beh. Mat., Boston, Mass., 812-816 (Aug. 1976).
- [34] Kramer, I. R., A mechanism of fatigue failure, *Met Trans.* 5 [8], 1735-1742 (1974).
- [35] Intrater, J. and Weissmann, S., An x-ray diffraction method for the study of substructure of crystals, *Acta Cryst.* 7 [11], 729-732 (1954).
- [36] Weissmann, S. and Evans, D. L., An x-ray study of the substructure of fine-grained aluminum, *Acta Cryst.* 7, [11], 733-737 (1954).
- [37] Weissmann, S., Analysis and topography of lattice defects in powder diffraction patterns, this volume.
- [38] Thompson, N., Wadsworth, N. and Louat, N., The origin of fatigue fracture in copper, *Phil. Mag.* 1 [2], 113-126 (1956).
- [39] Barrett, C. S., The structure of cold-worked metal, Chap. XVII, Structure of Metals; Crystallogr. Methods, Principles and Data, 1st ed. (McGraw Hill, New York, 1943), pp. 377-380.

HIGH RESOLUTION POWDER DIFFRACTION AT ARGONNE'S  
ZING-P' PROTOTYPE PULSED NEUTRON SOURCE

J. D. Jorgensen, F. J. Rotella and M. H. Mueller  
Argonne National Laboratory  
Argonne, IL 60439

Argonne National Laboratory has actively pursued the development of pulsed spallation neutron sources as a viable alternative to reactors since 1974 when the first prototype spallation source, called ZING-P, was operated [1]<sup>1</sup>. The basic principles of spallation neutron sources for slow neutron scattering have recently been reviewed by Carpenter [2]. A full scale pulsed neutron source, called IPNS-I, has now been funded for construction at Argonne and is expected to be operational in 1981. The present prototype source, called ZING-P', began operation in November 1977 and will continue until IPNS-I comes on line.

The ZING-P' facility consists of an H<sup>-</sup> source, 50 MeV linear accelerator, electron stripper, and a 500 MeV proton synchrotron. The 500 MeV protons are projected in short pulses of up to 10<sup>12</sup> protons per pulse at a rate of 10-30 Hz onto a heavy metal target where neutrons are produced by spallation. Both tungsten and uranium have been used as target materials. The present uranium target yields 20-25 neutrons per proton. The high energy neutrons are then slowed to thermal energies in hydrogenous moderators of nominal dimension 10x5 cm.

A high resolution time-of-flight powder diffractometer has been constructed on an 18.3 meter flight path viewing one of these moderators. Large time-focused [3] detector banks are positioned 1 meter from the sample at  $2\theta = \pm 160^\circ$  and 1.5 meters from the sample at  $2\theta = 0^\circ$ . The time-averaged flux at the sample position is presently about  $3 \times 10^3$  n/cm<sup>2</sup>-sec for a beam size of 1x5 cm. In spite of this relatively low flux, useful count rates are achieved because of the large detector areas. The 160° banks cover 0.08 steradians and achieve  $\Delta d/d = 0.003$  (FWHM), while the 90° banks cover 0.03 steradians and achieve  $\Delta d/d = 0.05$ . The resolution of a pulsed source diffractometer remains nominally constant over a wide range of d because of the moderator characteristics.

Profile analysis techniques have been used to analyze several sets of data from this instrument. The resolution function used to fit the asymmetric, non-Gaussian peaks is a three-part stepwise-continuous function made up of a rising Gaussian, decaying Gaussian and decaying exponential. The wavelength dependence of the four peak shape parameters has been accurately determined by fitting individual peaks in a set of Fe powder data. A standard

<sup>1</sup> Figures in brackets indicate the literature references at the end of this paper.

$\text{Al}_2\text{O}_3$  sample has been studied in order to make comparisons with conventional two-axis diffractometers. The profile analysis of this data in a hexagonal lattice setting included 235 reflections where  $0.5 \text{ \AA} \leq d \leq 2.2 \text{ \AA}$ . The effectiveness of a pulsed-source diffraction for collection of low-d data, stemming from the enhanced epithermal neutron flux, is dramatically illustrated by this data. For a total counting time of 160 hours the 113 reflections have an integrated intensity of 55,000 counts and a signal to noise ratio of 90.

#### References

- [1] Carpenter, J. M., Mueller, M. H., Beyerlein, R. A., Worlton, T. G., Jorgensen, J. Burn, T. O., Sköld, K., Pelizzari, C. A., Peterson, S. W., Watanabe, N., Kimura, and Gunning, J. E., Proc. Neutron Diffraction Conf., Petten, August 5-6, 1975, Re Centrum Nederland, RCN-234, 192 (1975)
- [2] Carpenter, J. M., Nucl. Instrum. Methods 145, 91 (1977).
- [3] Carpenter, J. M., Nucl. Instrum. Methods 47, 179 (1967).

## STRESS ANALYSIS FROM POWDER DIFFRACTION PATTERNS

J. B. Cohen and H. Dölle<sup>1</sup>

Department of Materials Science and Engineering  
The Technological Institute  
Northwestern University  
Evanston, IL 60201

and

M. R. James  
Science Center  
Rockwell International  
Thousand Oaks, CA 91360

A brief review of the method of measuring residual stresses in polycrystalline materials with x-rays is given. The effect of counting statistics on precision is discussed as well as factors that affect accuracy. Beam penetration, stress gradients, and the form of the stress tensor can each seriously affect accuracy, if traditional methods are employed, and practical procedures to deal with such situations are outlined.

### 1. Introduction

Knowledge of stresses (applied or residual) is quite important in an industrial environment. Crack initiation and propagation in static or fatigue loading, or in stress corrosion, can be impeded by compressive stresses normal to the crack, and greatly accelerated by tensile stresses. Residual stresses can be produced during quenching (because of the different cooling rates of the surface and the interior and any volume changes due to transformations), during manufacturing (due to the difference in deformation of the surface and the interior--as in straightening, machining, rolling or shot peening), or due to the different response of particles and matrix in a multiphase material. During welding, the resistance of the cold base metal to the solidifying (and

---

<sup>1</sup> B. Cohen is Frank C. Engelhart, Professor of Materials Science and Engineering, and H. Dölle is a Post-Doctoral Visiting Scholar.

shrinking weld pool will produce stresses in both regions. These stress patterns can also change in service, and there is increased interest in monitoring these. For a recent overview, see reference [1]<sup>2</sup>.

Apart from deliberately induced residual stresses, the measured stresses can develop due to applied loads, or even in a quasi-uniform stress field, from differences in response of the surface and the interior, one grain with respect to another, or one phase with respect to another. In the case of residual stresses, the tensile and compressive components must balance across a section, but to see this it may be necessary to examine values in different phases. This is possible with x-rays, but it has not often been of sufficient interest; only the stresses in the major constituent are usually examined. Also, even in a single phase material there may be situations where it is not possible to remove material to examine gradients because of the geometry of the piece.

Actually, a variety of non-destructive techniques, based on the acoustic and magnetic response of a material to stresses, is being evaluated for this purpose, but so far they have proved to be too sensitive to microstructural variations such as changes in texture [2]. The x-ray method, which was first proposed in the 1920's by Lester and Aborn [3], has withstood the test of time in industry; it is the subject of this review, in which we shall examine not only the method, but its limitations, accuracy and precision, as well as the latest developments which have made it of considerable use in field situations. While there are a number of ways of examining strains with x-rays, we shall concentrate only on those that are widely employed in industry. To prove their validity, these approaches have been compared to measurements of distortion after mechanical dissection [1].

The basic principle that is employed is quite simple: An interplanar spacing ( $d$ ) in the material serves as an internal strain gage. As shown in figure 1a, in a polycrystalline specimen in the normal position on a diffractometer, only those grains with planes nearly parallel to the surface form a diffraction peak. If there are compressive stresses in the near-surface regions, the " $d$ " spacing is increased for these planes due to the effect of Poisson's ratio. When the specimen is tilted with respect to the x-ray beam (or the beam to the specimen), figure 1b, the diffracting grains have their planes more nearly perpendicular to the stresses in the surface and their increased spacing is less, or even decreased. (Components of the surface stress parallel and perpendicular to the planes now affect this spacing.) The  $2\theta$  positions of diffracting peaks from such planes and Bragg's law are all that are required to examine the strain tensor, from which the surface stresses may be determined.

---

<sup>2</sup>Figures in brackets refer to the literature references listed at the end of this paper.

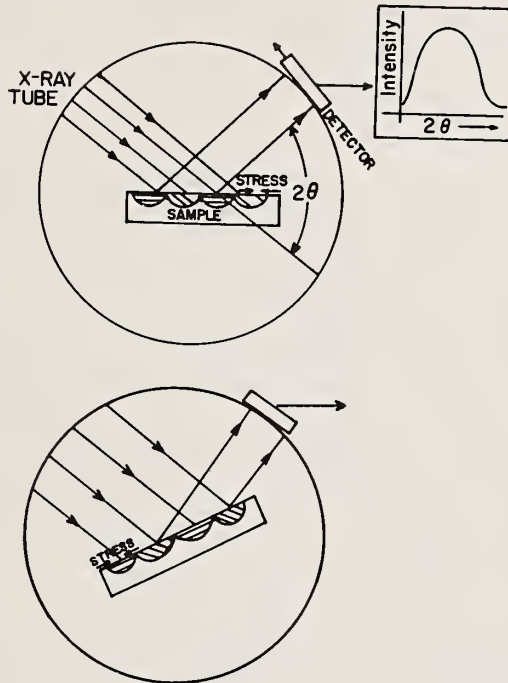


Figure 1. Top: Schematic of a diffractometer. The incident beam diffracts from planes that satisfy Bragg's law, in grains with these planes parallel to the sample's surface. If regions near the surface are in compression, with the stress parallel to the surface, because of Poisson's ratio, these planes are further apart than in the stress-free state. The "d" spacing is obtained from the peak in intensity vs. scattering angle  $2\theta$  (insert), and Bragg's law. Bottom: after the specimen is tilted, diffraction occurs from other grains, but from the same planes, and these are less separated than in (a), because there is a component of the residual stress normal to the planes.

## 2. The Basic Equation

In what follows, we shall employ the axial system,  $L_i$ , for the measurements (a "laboratory" system) and axes  $P_i$  for the specimen, as shown in figure 2. Primed quantities will refer to measurements in the laboratory system, unprimed in the sample system. With  $d_{\phi\psi}$ , the interplanar spacing at tilts  $\phi$ ,  $\psi$ , and  $d_0$ , the value for the strain from material, the strain along  $L_3$  can be written [4]:

$$\epsilon'_{33} = \frac{d_{\phi\psi} - d_0}{d_0} = \epsilon_{11} \cos^2\phi \sin^2\psi + \epsilon_{12} \sin 2\phi \sin^2\psi + \epsilon_{13} \cos\phi \sin 2\psi + \epsilon_{22} \sin^2\phi \sin^2\psi + \epsilon_{23} \sin\phi \sin 2\psi + \epsilon_{33} \cos^2\psi. \quad (1)$$

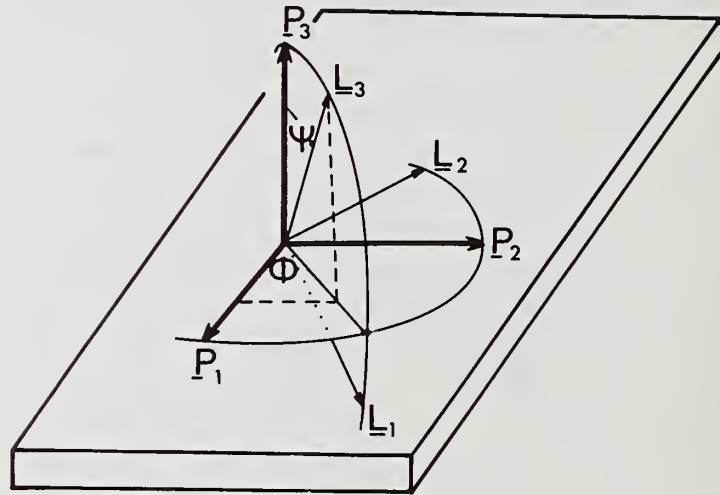


Figure 2. The axial system. The  $L_i$  are the laboratory system and measurements of  $\Delta d/d$  are made along  $L_3$ . The  $P_i$  describe the specimen.

Once the strains are determined (by the procedures to be described below), the stresses,  $\sigma_{ij}$ , can be calculated from:

$$\sigma_{ij} = \frac{1}{\frac{1}{2}S_2(hkl)} \left[ \epsilon_{ij} - \delta_{ij} \frac{S_1(hkl)}{\frac{1}{2}S_2(hkl) + 3S_1(hkl)} (\epsilon_{11} + \epsilon_{22} + \epsilon_{33}) \right]. \quad (2)$$

The term  $\delta_{ij}$  is the Kronecker delta function, and since  $\delta_{ij} = 0, i \neq j$ , the shear strain alone determine the shear stresses.

The  $S_i$  are x-ray elastic constants for a particular  $hkl$  reflection. For an elastically isotropic solid,

$$\frac{1}{2} S_2(hkl) = \frac{(1+\mu)}{E}, \quad S_1(hkl) = \left(-\frac{\mu}{E}\right),$$

where  $\mu$  is Poisson's ratio and  $E$  is Young's modulus. Theory exists to calculate the constants (for each  $hkl$  reflection) for an anisotropic crystal coupled to an isotropic matrix, and this theory shows that the values are within a few percent of the average

the well-known Reuss and Voigt formulae, which assume, respectively, constant average stress and constant average strain for all grains in the material. In addition, theory is developing for an elastically anisotropic material with severe texture. (This entire area has recently been reviewed by one of us, reference [5].) In the latter case, the elastic constants associated with a particular hkl reflection may vary with  $\phi$  and  $\psi$  tilt. It has also been well established that the x-ray elastic constants can vary appreciably with amount of plastic deformation; changes as large as 20-40 pct. have been reported. This phenomenon is not understood at the moment and can obviously severely affect the accuracy of any stress measurement if calculated values are assumed to be independent of plastic strain. Fortunately, it is possible to test for this problem, and, in many cases, to measure the effective constants. We discuss this further below. In addition, it is often the relative change in stress with some change in condition that is important, in which case the constants employed are not as important.

We turn now to the various methods, after which we will discuss other errors that affect accuracy, and also precision.

### 3. Surface Stresses Only

As a free surface cannot support a stress normal to it ( $\sigma_{33} = \sigma_{13} = \sigma_{23} = 0$ ), the stress tensor in the sample system shown in figure 2 is:

$$\begin{pmatrix} \sigma_{11} & \sigma_{12} & 0 \\ \sigma_{12} & \sigma_{22} & 0 \\ 0 & 0 & 0 \end{pmatrix} \quad (3a)$$

Of course, this tensor may be written in terms of principal axes in a rotated axial system:

$$\begin{pmatrix} \sigma_1 & 0 & 0 \\ 0 & \sigma_2 & 0 \\ 0 & 0 & 0 \end{pmatrix} \quad (3b)$$

hence, it can be shown that:

$$\epsilon'_{33} = \frac{d_{\phi\psi} - d_0}{d_0} = \frac{1}{2} S_2(hkl)[\sigma_1 \cos^2 \phi + \sigma_2 \sin^2 \phi] \sin^2 \psi + S_1(hkl)[\sigma_1 + \sigma_2]. \quad (4)$$

that at  $\psi = 0^\circ$ , a comparison of  $d_{\phi\psi}$  to  $d_0$  immediately indicates whether the sum of the principal stresses is positive or negative.

Subtracting the value for  $\psi = 0^\circ$ :

$$\begin{aligned} \left( \frac{d_{\phi\psi} - d_0}{d_0} \right) - \frac{d_{\phi, \psi=90^\circ} - d_0}{d_0} &\cong \frac{d_{\phi\psi} - d_{\phi, \psi=0}}{d_{\phi, \psi=0}} \\ &= \frac{1}{2} S_2(hkl) \sigma_\phi \sin^2 \psi. \end{aligned} \quad (5)$$

The stress in any direction,  $\phi$ , on the surface can be determined simply from the slope of  $d$  vs  $\sin^2 \psi$ . The stress-free value,  $d_0$ , is not needed. A typical plot is shown in figure 3. The principal stresses and their directions can be obtained [6], although their  $\phi$  directions are often known from the nature of the applied stress system. By application of known elastic stresses on an identical specimen, the effective elastic constants can be obtained from eqs. (4) or (5).

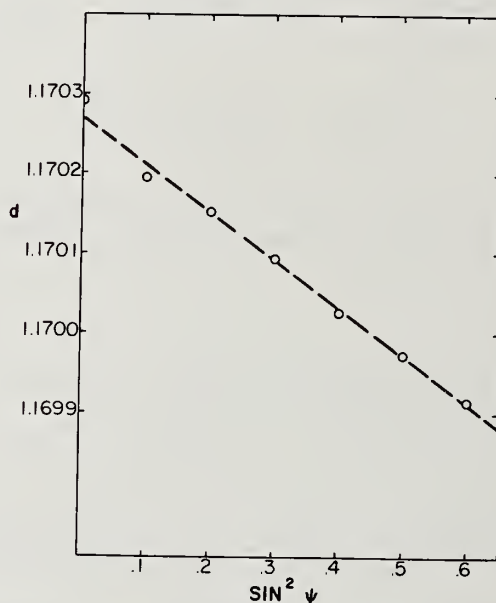


Figure 3. Interplanar spacing, "d", vs.  $\sin^2 \psi$ , normalized AISI-1010 steel, deformed in tension along  $P_1$  to a true strain of 8 pct. 211 peak,  $\text{CrK}_\alpha$  radiation;  $\sigma_{\phi=0^\circ} = -107.1$  MPa (-15,303 psi). From reference [22].

It cannot be emphasized too strongly that the linearity of "d" vs  $\sin^2 \psi$  must be confirmed in each situation, but if this is the case, the equation can be further simplified, with the aid of Bragg's law, to involve only two tilts,  $\psi = 0^\circ$  and, typically,  $\psi = 45^\circ$  or  $60^\circ$ :

$$\sigma_\phi = K \Delta 2\theta \quad (\text{in degrees}), \quad (6)$$

with:

$$K = \frac{\pi}{180} \frac{1}{S_2(hkl) \sin^2 \psi} \cot \left[ \frac{1}{2} (\theta_{\psi=0^\circ} + \theta_{\psi=\psi}) \right]. \quad (6)$$

In this "two exposure method," a high angle peak is chosen, and the  $\psi$  tilt is made as large as possible, to minimize  $K$  and hence maximize the sensitivity of the peak shift to the stress. For example, for steel,  $\text{CrK}_\alpha$  radiation, the 211 reflection at  $\approx 156^\circ 2\theta$ , and a  $\psi$ -tilt of  $45^\circ$ , a  $+ 0.1^\circ 2\theta$  shift corresponds to a stress of  $\approx -60$  MPa ( $-8600$  psi). Shifts as small as  $0.01 - 0.02^\circ 2\theta$  can be detected. If it has been verified that  $d$  vs  $\sin^2\psi$  is indeed linear, it is possible to develop simple portable equipment (for use in the field or in a factory environment) which can measure the surface stress in seconds. An example of this equipment is shown in figure 4 [7]. It is even possible to use only one incident beam direction and examine, simultaneously with two detectors, two points on the diffraction cone which come from grains tilted at different  $\psi$  values [8]. However, it has been shown [1] that in this case the stress constant,  $K$ , is much larger, which implies a larger error in stress from a given uncertainty in  $2\theta$ . (Film equipment employing this "single exposure" technique is still sometimes used for very large pieces.)

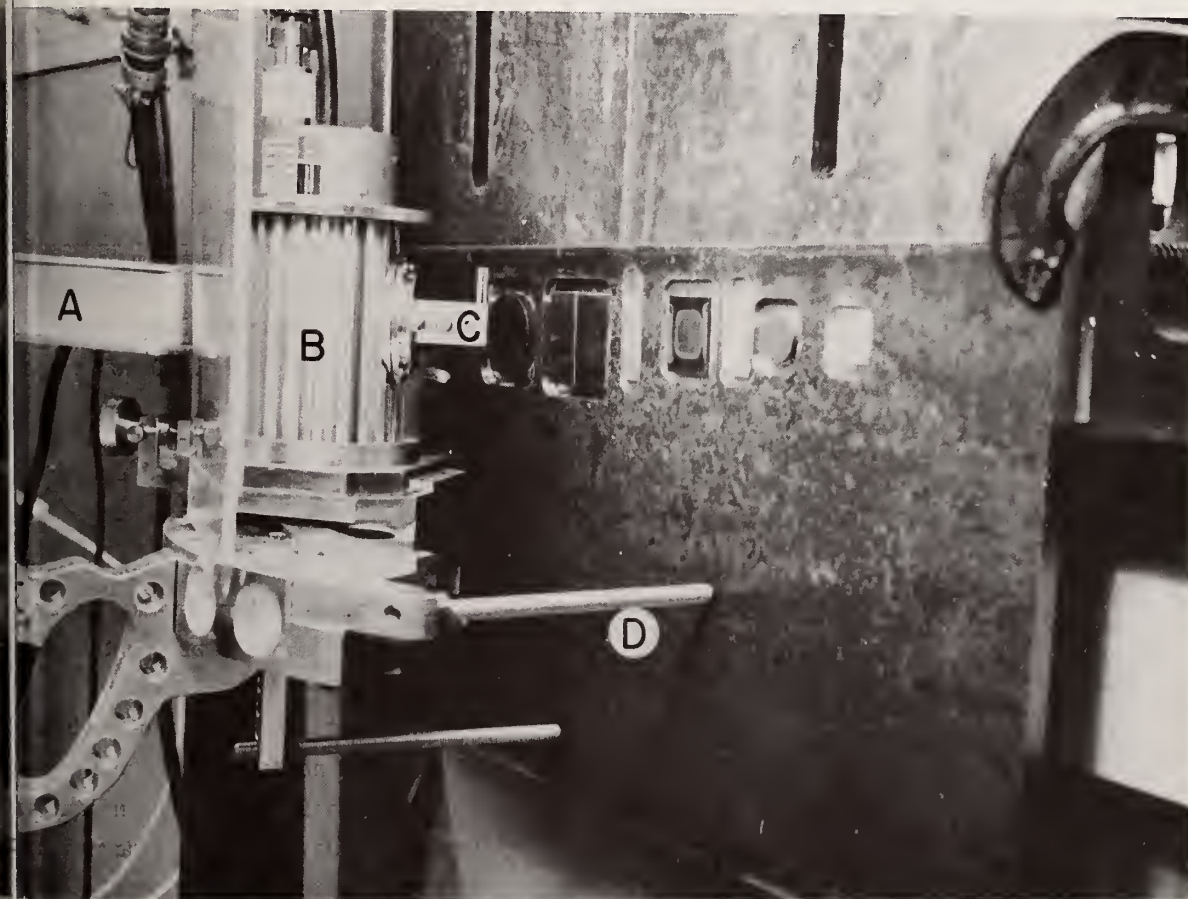


Figure 4. The PARS system [7]--a portable (x-ray) analyzer for residual stresses. (A) linear position sensitive detector to record the entire diffraction profile without detector motion; (B) air-cooled miniature x-ray tube (50 kV, 2 mA); (C) exit soller slits; (D) rods to position unit with respect to a specimen; (E) one (of two) handles.

Because of the simple form of eq. (6a), it is particularly easy to measure K by applying a series of known elastic loads to a specimen. Tensile or bending loads are commonly employed [9,10].

#### 4. The General Stress State

Because the measured stresses are averages over a finite depth of beam penetration we should consider the general stress tensor:

$$\begin{pmatrix} \sigma_{11} & \sigma_{12} & \sigma_{13} \\ \sigma_{12} & \sigma_{22} & \sigma_{23} \\ \sigma_{13} & \sigma_{23} & \sigma_{33} \end{pmatrix} . \quad (7)$$

Referring to eq. 1, the presence of  $\varepsilon_{13}$  and  $\varepsilon_{23}$  leads to curvature in the  $d$  vs  $\sin^2\psi$  relationship, as their contribution depends on  $\sin 2\psi$ . Such terms can be important in machining, or in wear; that is, when there are strong components of the deforming force tangential to their surface, and strong gradients (since the strains  $\varepsilon_{13}$ ,  $\varepsilon_{23}$ ,  $\varepsilon_{33}$  must vanish at the surface). Examples of this effect (from reference [11]) are shown in figures 5 and 6. The principal effect of the shear stresses is to cause " $d$ " vs  $\sin^2\psi$  to be non-linear in opposite senses for positive and negative  $\psi$  tilts. This  $\psi$  splitting at large curvature near  $\psi = 0$  are distinguishing features of this phenomenon. The actual stress tensors are given in the captions to the figures, and the small value of the shear stress to cause the " $\psi$  splitting" is particularly noteworthy. Also, the curves for positive and negative  $\psi$  (or by changing  $\phi$  by  $180^\circ$ ) reverse when the sign of the shear stress reverses (fig. 6). This curvature and its cause were first reported by Walbuge [12], and a simple method of analysis of the data was suggested by Dölle and Hauk [12]. It was employed in an extensive study for the first time by Dölle and Cohen [11], introducing the terms  $a_1$  and  $a_2$ , employing eq. (1) and using carats to indicate average over the depth of penetration:

$$a_1 \equiv \frac{1}{2}[\varepsilon_{\phi\psi+} + \varepsilon_{\phi\psi-}] = \langle \varepsilon_{33} \rangle + [(\langle \varepsilon_{11} \rangle \cos^2\phi + \langle \varepsilon_{12} \rangle \sin 2\phi + \langle \varepsilon_{22} \rangle \sin^2\phi - \langle \varepsilon_{33} \rangle] \sin^2\psi, \quad (8)$$

$$a_2 \equiv \frac{1}{2}[\varepsilon_{\phi\psi+} - \varepsilon_{\phi\psi-}] = [\langle \varepsilon_{13} \rangle \cos\phi + \langle \varepsilon_{23} \rangle \sin\phi] \sin |2\psi|. \quad (8)$$

Thus,  $\langle \varepsilon_{33} \rangle$  can be obtained from the intercept of  $a_1$  vs  $\sin^2\psi$ ; this value is independent of  $\phi$ , and so it can be verified by measurements at different  $\phi$  tilts. The components  $\varepsilon_{11}$ ,  $\varepsilon_{12}$ ,  $\varepsilon_{22}$  can be obtained from  $\partial a_1 / \partial \sin^2\psi$ . At  $\phi = 0^\circ$ ,  $\varepsilon_{11} - \varepsilon_{33}$ , and hence,  $\varepsilon_{11}$ , is obtained, whereas for  $\phi = 90^\circ$ ,  $\varepsilon_{22}$  can be measured. The  $\varepsilon_{11}$  component is then determined from

$$\left[ \frac{\partial a_1}{\partial \sin^2\psi} \right]_{\phi=45^\circ}.$$

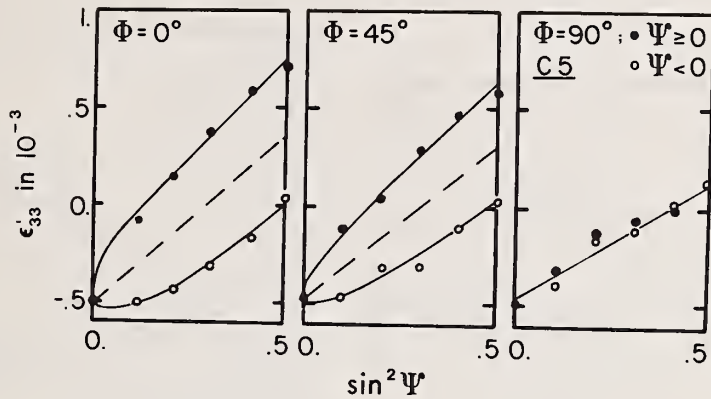


Figure 5. Normalized plain carbon steel strip (0.6 wt pct carbon) ground under flowing water to remove 5  $\mu\text{m}$  per pass [11]. Various  $\phi$  tilts shown. The curves are fits to the data points with eq. (1). The stress tensor in MPa is:

$$\begin{pmatrix} 390 & 14 & 63 \\ 14 & 306 & -1 \\ 63 & -1 & 92 \end{pmatrix}$$

211 peak,  $\text{CrK}_\alpha$  radiation.

$$\frac{\partial a_2}{\partial \sin 2\Psi},$$

is calculated for  $\phi = 0^\circ$ ,  $\varepsilon_{23}$  for  $\phi = 90^\circ$ . The curves in figures 5 and 6 are the fit to the data points with eq. (1).

The stresses are then obtained from eq. (2).

In this procedure, it is necessary to know " $d_0$ ." For steels, measurements generally yield a value for the lattice parameter of 2.8665(1)  $\text{\AA}$ . The uncertainty leads to a range of  $\approx \pm 30$  MPa in the normal stresses and hardly any variation in the shear stresses. Measurements with a well annealed powder of Cr indicate that the precision is 10 MPa for  $\sigma_{11}$ ,  $\sigma_{12}$ ,  $\sigma_{22}$ ,  $\sigma_{33}$  and better than 8 MPa for  $\sigma_{13}$ ,  $\sigma_{23}$ . This uncertainty is ten times less than the variation of the actual stresses from point to point in a specimen.

Another way of examining the stress in three dimensions is with high-energy x-rays or neutrons, isolating the volume element to be examined by suitably narrowing the slits and refining the incident and diffracted beams. The feasibility of such a procedure is considered in the next paper.

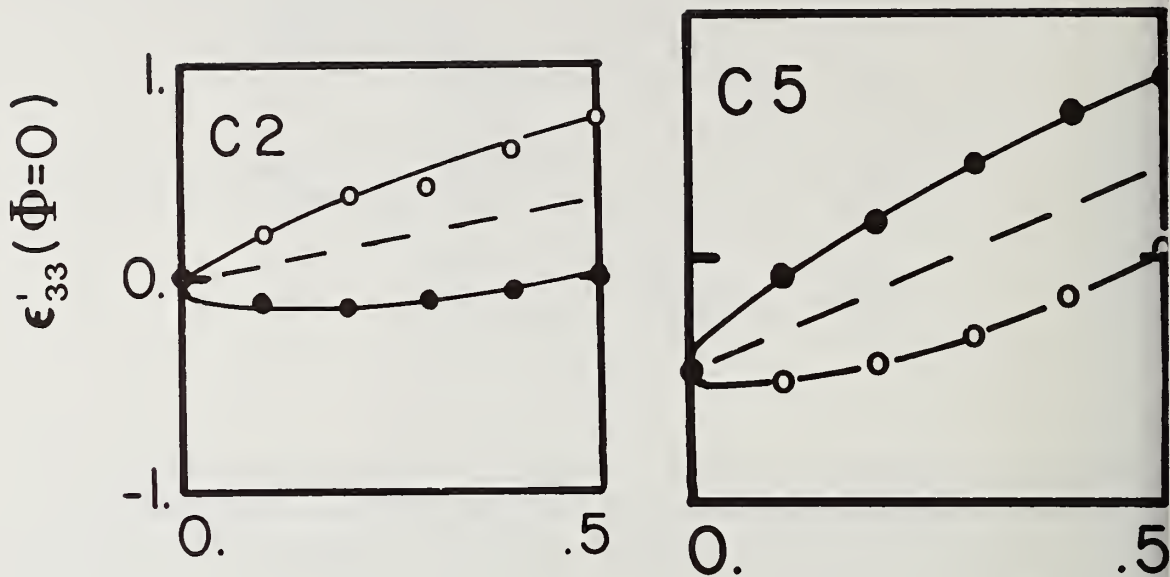


Figure 6.  $\langle \epsilon'_{33} \rangle$  vs.  $\sin^2 \psi$ . Normalized plain carbon steel strip (0.6 wt pct carbon) ground to remove 5  $\mu\text{m}$  per pass under flowing water [11].  $\phi = 0^\circ$ . Strain in units of  $10^{-3}$ . For specimen C5, the direction of grinding was reversed each pass with the final pass opposite to that for C2 (in the  $-P_1$  direction). The stress tensor for C5 is given in figure 5. For C2 (in MPa) it is:

$$\begin{pmatrix} 199 & -10 & -63 \\ -10 & 86 & 5 \\ -63 & 5 & 84 \end{pmatrix}$$

Note that the curvature for  $\psi > 0$ ,  $\psi < 0$  reverses when  $\sigma_{13}$  reverses. The curves are the fits to the data points with the stress tensors and eq. (1). 0:  $\psi < 0$ ; ●  $\psi > 0$ . 211 peak,  $\text{CrK}_\alpha$  radiation.

Except for materials with appreciable content of a second phase (such as a steel with more than  $\approx 0.4$  wt pct C), some kinds of deformation may produce strong texture at modest strains. In such cases, oscillations have been observed in  $d$  vs  $\sin^2 \psi$  as shown in figure 7. The precise interpretation for this effect is still uncertain; it may be due to elastic or plastic anisotropy [1,5]. Tests are currently underway to decide which factor is most important, after which procedures may be possible to minimize this problem. For example, any contributions from elastic anisotropy can be minimized (for any material) by employing hoo or hhh reflections [5].

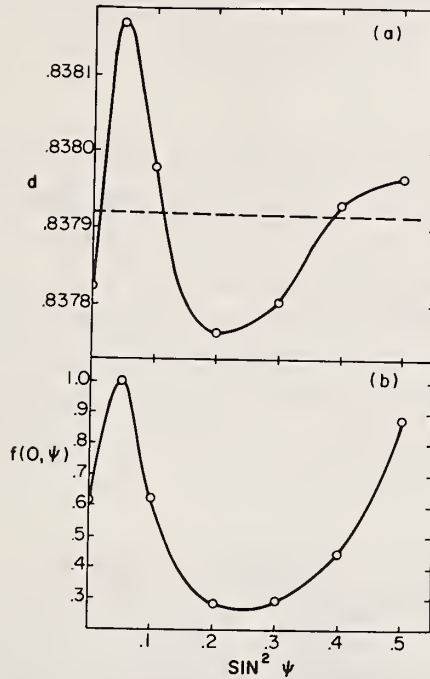


Figure 7. Interplanar spacing, "d", vs.  $\sin^2\psi$  for a  $\text{Cu}_3\text{Au}$  specimen pulled in tension along  $P_1$  to a true strain of 35 pct [22], 420 peak,  $\text{CuK}_\alpha$  radiation. The term  $f(0,\psi)$  is the area under the Bragg peak at each  $\psi$  position.

## 5. Gradients

The ability to detect stresses normal to the surface, as was discussed in the previous section, is based on the presence of gradients, and the fact that the x-ray beam averages over its penetration ( $D$ ). Therefore, it is appropriate to examine the effects of such gradients because, even in the absence of stresses normal to the surface, there will be effects on  $\langle\sigma_{11}\rangle$ ,  $\langle\sigma_{22}\rangle$ ,  $\langle\sigma_{12}\rangle$ . Corrections are available for this [1,5], and also for stress relief due to layer removal [1], if the gradients are examined in this fashion. But the presence of steep gradients can also be detected and examined from the form of "d" vs  $\sin^2\psi$  without layer removal, as illustrated in figure 8. For this figure, the stresses were obtained from an assumed stress profile (in the z-direction) [5]:

$$\langle\sigma_{ij}\rangle = \sigma_{ij}(z=0) + \int_0^D \exp(-z/\tau) g_{ij}(z) dz . \quad (9)$$

Here, with  $\mu$  the linear absorption coefficient:

$$\tau = \frac{\sin^2\theta - \sin^2\psi}{2\mu\sin\theta \cos\psi} \quad (10a)$$

for  $\psi$  tilts around the  $\theta$  axis, and:

$$\tau = \frac{\sin\theta \cos\psi}{2\mu}, \quad (10b)$$

for tilts around an axis parallel to the plane of the diffractometer. The term  $g_{ij}(z)$  describes the variation of stress with depth ( $z$ ) below the surface. (Once these average stresses are evaluated for a particular strain distribution,  $\langle \epsilon_{33}^I \rangle$  can be calculated at each  $\psi$  and  $d$  vs.  $\sin^2\psi$  obtained as will be shown below.)

Note particularly the difference in curvature near  $\psi = 0$  between this effect (if shear stress  $\langle \sigma_{13} \rangle$ ,  $\langle \sigma_{23} \rangle = 0$ ) and for  $\psi$  splitting (compare figure 8 with figures 5 or 6). Also, the values of  $d$  at  $\pm\psi$  should be identical in this case, so the effect is readily distinguished from  $\psi$  splitting.

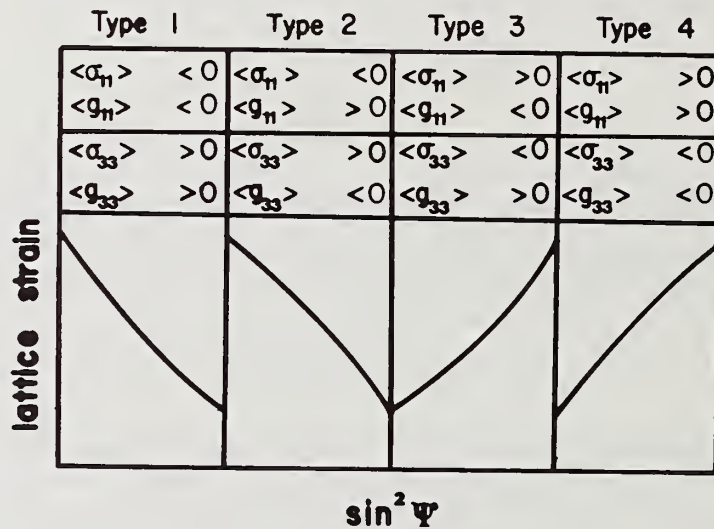


Figure 8. The effect of various gradients on "d" vs  $\sin^2\psi$ . The gradient is assumed to be linear over the x-ray beam's depth of penetration, with slope  $g_{ij}$ . Typical values were assumed (for  $\sigma_{11}$ , 200-600 MPa over 20  $\mu\text{m}$ , for  $\sigma_{33}$ , 100 MPa per  $\mu\text{m}$  (zero at the surface)).

This curvature can be employed to obtain information about gradients, and we now present a concrete example of how this can be done, with data from a SAE 1040 steel, normalized and shot peened. We make the following assumptions (all of which could be checked in a more thorough investigation):

- the x-ray elastic constants  $S_1$  and  $S_2$  do not vary with depth,  $z$ ;
- $\sigma_{ij}$  varies with  $z$  only;
- $\phi = 0^\circ$  (by definition)

- d)  $\sigma_{11}(z) = \sigma_{22}(z)$  (due to shot peening normal to the surface);  
 e)  $\sigma_{ij}(z)$ ,  $i \neq j = 0$  (no appreciable shear deformation).

Then:

$$\langle \varepsilon'_{33} \rangle_{\phi=0} = \frac{1}{2} S_2(hkl) [\sin^2 \psi \langle \sigma_{11} \rangle + (1 - \sin^2 \psi) \langle \sigma_{33} \rangle] + S_1(hkl) [2 \langle \sigma_{11} \rangle + \langle \sigma_{33} \rangle]. \quad (11)$$

From this equation:

$$\langle \varepsilon'_{22} \rangle_{\phi, \psi=0} = 2 S_1(hkl) \langle \sigma_{11} \rangle + \langle \sigma_{33} \rangle \left[ \frac{1}{2} S_2(hkl) + S_1(hkl) \right], \quad (12a)$$

$$\frac{\partial \langle \varepsilon'_{33} \rangle_{\phi=0}}{\partial \sin^2 \psi} = \frac{1}{2} S_2(hkl) [\langle \sigma_{11} \rangle - \langle \sigma_{33} \rangle]. \quad (12b)$$

With eqs. (12a,b), first estimate of  $\langle \sigma_{11} \rangle$  and  $\langle \sigma_{33} \rangle$  can be obtained, fitting a straight line to the data. Typical data is shown in figure 9. From this figure, these first estimates are:  $\langle \sigma_{11} \rangle = -309$  MPa,  $\langle \sigma_{33} \rangle = 140$  MPa. Comparison of figure 9 with figure 8 assuming the gradients are linear indicates that either  $g_{11} < 0$  or  $g_{33} > 0$ , or both.

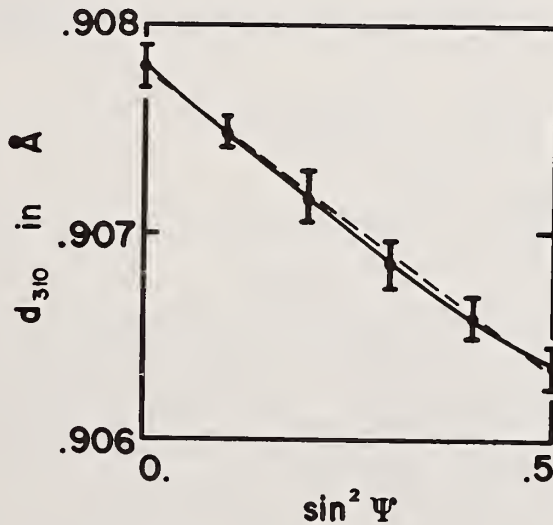


Figure 9. Measured "d" vs.  $\sin^2 \psi$ , shot peened (normalized) AISI 1040 steel; data averaged over nine specimens. Error bars from observed variation in  $2\theta$  in repeated measurements.  $\text{CoK}_\alpha$ , 310 reflection.

The measured macroscopic gradient is illustrated in figure 10a. It can be seen that the stresses vanish at  $\approx 500 \mu\text{m}$ . A simple representation of this figure was taken to be figure 10b. The terms  $z_2$  and  $g_{ij}$  were varied to give the best fit to the data:  $\langle \sigma_{11} \rangle$ ,  $\langle \sigma_{33} \rangle$ , and the measured slopes of "d" versus  $\sin^2 \psi$  at various  $\psi$  angles.

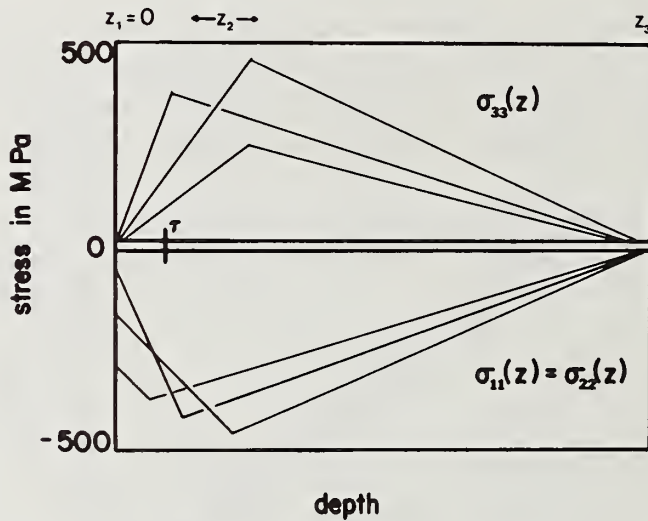
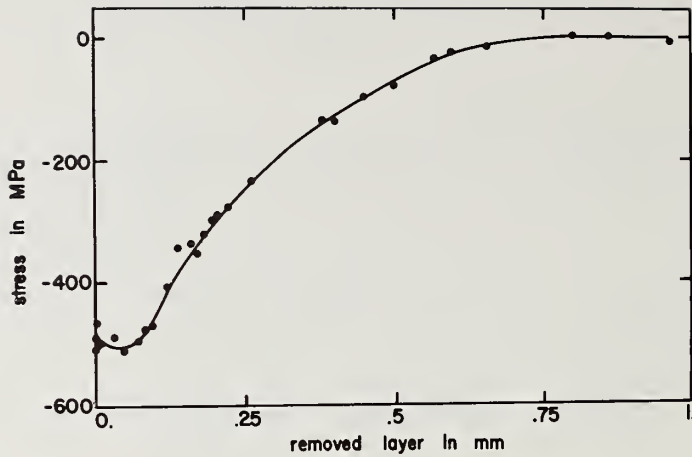


Figure 10. (a) The gradient measured by layer removal for one of the specimens in figure 9. (Etchant: 100 parts 30 pct  $H_2O$ , 10 parts 48 pct HF). Data uncorrected for layer removal and depth of penetration. 310 peak,  $CoK_{\alpha}$  radiation. (b) Assumed gradients for calculations described in text to fit data in (a).

From the average  $\langle \sigma_{33} \rangle = 140$  MPa and the penetration depth,  $\tau = 10 \mu m$ ,  $g_{33}$  was the order of  $15 \text{ MPa}/\mu m$ . From the curvature of "d" vs.  $\sin^2 \psi$ , it could be concluded that  $g_{11}$  -10 to -15  $\text{MPa}/\mu m$ . These values were actually obtained simply by choosing various  $z_2$  values and surface stresses. Of course, more sophisticated least-squares approaches are possible. This procedure might be particularly fruitful when many similar samples have to be examined for their gradients, and the gradient in one specimen has been measured by layer removal.

Finally, it is worth noting that peak shapes, as well as positions have been employed by Murakami [14] to obtain information on gradients in thin foils. While his assumptions as to the stress tensor are too restrictive for general use, his procedure could be expanded.

## 6. Factors Affecting Accuracy

We have already mentioned one possible source of inaccuracy, the elastic constants. The actual error in stress from the effects to be discussed below can be evaluated through the stress constant  $K$  and eqs. (6a,b), or by employing experimental x-ray elastic constants  $S_1$  and  $S_2$ . A particular error in  $2\theta$ , when multiplied by  $K$  for the chosen material, gives a first estimate of the error in stress.

All data should be corrected for the variation in scattering factor and Debye-Waller factor if the peak is very broad ( $> \approx 5^\circ$  in half breadth). Corrections for the Lorentz polarization and absorption factors (LPA) can be written for each position,  $2\theta$ , across a peak. Assuming filtered radiation:

$$\text{LPA} = \frac{1 + \cos^2 2\theta}{\sin^2 \theta} (1 - \tan \psi \cot \theta), \quad (13a)$$

for tilts around around the  $2\theta$  axis, and:

$$\text{LPA} = \frac{1 + \cos^2 2\theta}{\sin^2 \theta}, \quad (13b)$$

for tilts around an axis parallel to the goniometer. The latter method [15,16] is increasingly employed in Europe. It is not limited to  $|\psi| \leq \theta$ , as is a tilt around the  $\theta$  axis. Furthermore, the path lengths of the incident and diffracted beams within the specimen are equal, so absorption corrections are not involved (eq. (13b) vs. eq. (13a)). It is a helpful technique for measurements in difficult locations such as on gear teeth, where the incident or diffracted beam can be blocked by the gear itself.

Because these corrections are small and straightforward, there is no need to avoid them, and therefore no need to estimate errors from these sources.

Locating the specimen over the center of rotation can be particularly troublesome especially when the geometry of the specimen is complicated, and this is one of the largest sources of inaccuracy. There are two ways of achieving this location. The lattice parameter for two or more different reflections (widely separated in  $2\theta$ ) can be plotted vs.  $\cos^2 \theta / \sin \theta$ . Then (for  $\psi=0^\circ$ ), with "a" the lattice parameter [17]:

$$\frac{\Delta a}{a} = - \frac{2\delta}{R} \frac{\cos^2 \theta}{\sin \theta}, \quad (14)$$

with  $\delta$  the sample displacement and  $R$  the goniometer radius. The displacement can therefore be calculated from the slope of such a plot, and the sample displaced appropriately.

Another way, particularly important when  $\psi$  splitting is suspected, is to examine the peak position of a stress free powder (painted in a thin layer on the specimen in an acetone solution) at a fixed  $2\theta$  (close to the reflection angle of the specimen), and the varying  $\psi$ . An example of such a method is shown in figure 11.

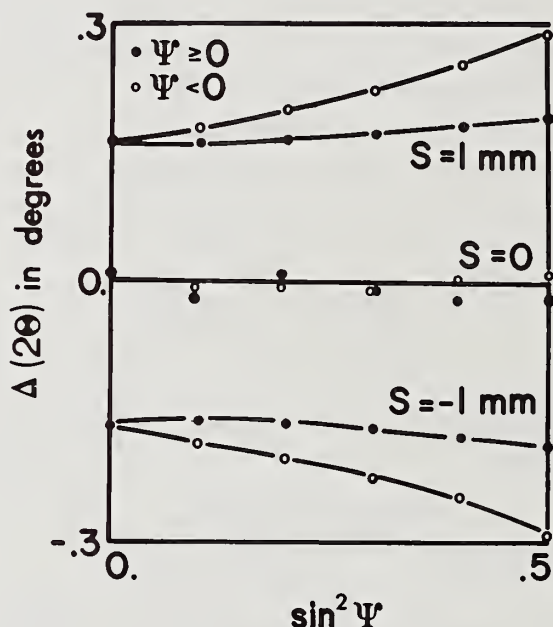


Figure 11. The effect of sample displacement on " $d$ " vs.  $\sin^2\psi$ .

Measurements made with an annealed Cr powder painted on a steel specimen in an acetone solution. 211 reflection,  $\text{CrK}_\alpha$  radiation.

In Japan, a parallel beam method is employed [18], to eliminate the sensitivity to sample position. In figure 12, a comparison of the peak shift due to sample displacement is made between this method, the parafoocusing method (for which, the receiving slits are moved to the correct focus at each  $\psi$ ), and a stationary slit, divergent beam. The parallel beam technique is obviously least sensitive. However, the peak is broadest in this case and the time for data analysis is  $\approx 1/3$  longer for the same statistical error (Section 7) than parafoocusing, and the reproducibility twice as poor for sharp profiles [19]. The stationary slit method appears to be the best compromise. However, in this case (but not in parafoocusing), the shape of the peak may vary with  $\psi$  tilt. How this alters various methods for peak location is illustrated in figure 13. Bias corrections may be taken from this plot.

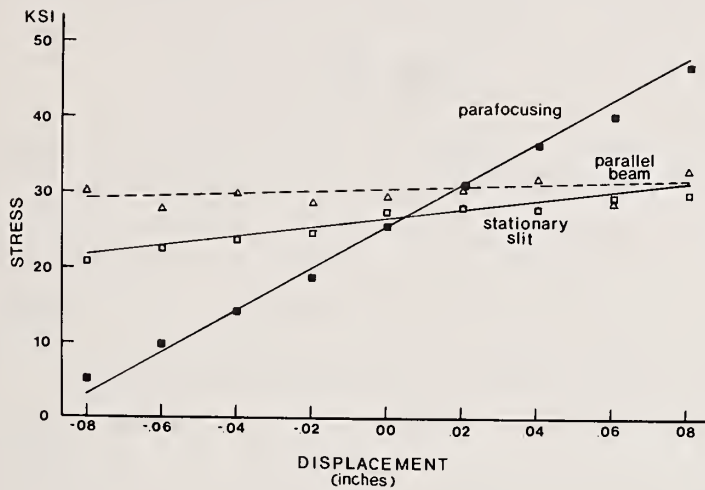


Figure 12. Measured effects of sample displacement, for various focussing techniques employed in stress measurements. Normalized 1045 steel, 211 reflection,  $\text{CrK}_\alpha$  radiation.

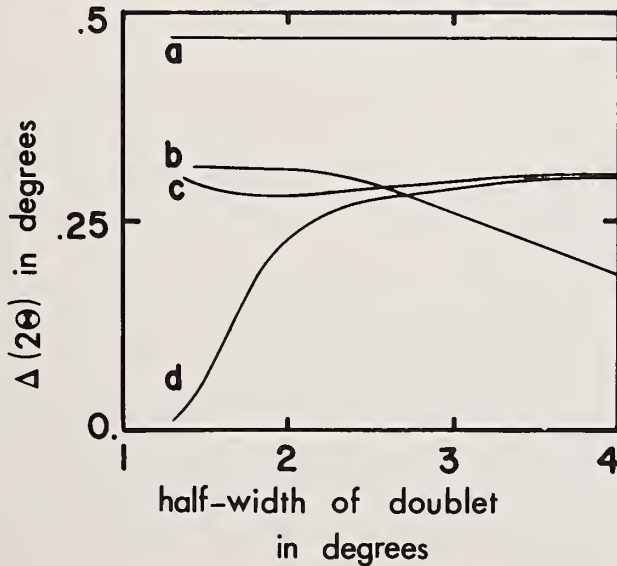


Figure 13. Calculated peak shift due to  $\text{K}_{\alpha_1} - \alpha_2$  doublet for various definitions of the peak. (a) Special slits to symmetrize peak (Wolfstieg, U., Die Symmetrisierung unsymmetrischer Interferenzlinien mit Hilfe von Spezial Henden, Härtereitechn. Mit. 31, 23-26 (1978)). (b) Center of gravity. (c) Middle of half-width. (d) Parabolic fit to top 15 pct. The same Gaussian functions were assumed for the  $\alpha_1, \alpha_2$  components. 211 reflection,  $\text{CrK}_\alpha$  radiation.

(If parafofocussing is employed, and the sample has a strong texture, it is important to introduce a permanently fixed slit, defining the beam along the  $\theta$  axis; it is not moved when the scanning slit is moved to the correct focus. This assures that the same portion of the diffraction cone is seen at all  $\psi$  tilts [20].)

An excellent presentation of the bias from various instrumental misalignments can be found in reference [2]; while the equations in this reference are based on the center of gravity of a peak, they can be used as a guide for any definition of the peak. Another source of analytical approximations to the errors is reference [22]. For this paper, we have made computer calculations of the peak shifts by a ray-tracing method. The intensity of the beam was assumed to be uniform across its cross section. This over-emphasizes the error and the resultant shifts were multiplied by 1/3, in agreement with the findings in similar comparisons by Zantopoulos and Jatczak [13]. The errors summarized in table 1 are the shift in  $2\theta$  for a  $\psi$  tilt from  $+45^\circ$  to  $-45^\circ$ . If only  $+\psi$  is employed, the errors are reduced by an additional factor of 1/2. This table can serve as a quick guide to the important aspects in alignment of the diffractometer for stress determinations. Table 2 gives some typical errors for the two-tilt method and parafofocussing, with tilt around the  $\theta$  axis. Clearly, the bias due to geometric errors can be held to quite small values, with good alignment and a judicious choice of slits.

Table 1. The influence of various mis-alignments on the accuracy of stress analysis

+ = large error (0.07° or more)

- = small error (0.01° or less)

m = medium error

type of error	$\psi$ tilt around $\theta$ axis	$\psi$ tilt around axis in diffraction plane
centers of $\theta$ , $\psi$ rotation not coincident ( $\Delta = 0.1$ mm)	-	-
4° horizontal divergence	-	m
4° vertical divergence	m	-
1° horizontal tilt of beam to the zero direction	-	+
1° vertical tilt of beam to true zero direction	+	-
tube mis-alignment ( $\Delta x, \Delta y, \Delta z$ 1 mm)	- + -	- - +
displacement of sample from the tilt axis (0.2 mm)	+	m to +
sample curvature (beam much smaller)	- to m	- to m

Table 2. Typical bias in peak location for  $2\theta = 156^\circ$   
(approximately the  $211 \text{ CrK}_\alpha$  peak from iron).

cause	peak shift between $\psi = 0^\circ$ and $\psi = 45^\circ$		peak shift between $\psi = 0^\circ$ and $\psi = 60^\circ$	
	$^\circ 2\theta$	MPa	$^\circ 2\theta$	MPa
peak location $\pm 0.01^\circ 2\theta$	+ .02	11.9	$\pm .02$	$\pm 1700$
total horizontal beam divergence of $1^\circ$	- .0006 $^\circ$	-0.35	- .0025	-215
vertical beam divergence <sup>[28]</sup> (assuming strong texture using divergent Soller slit; no receiving Soller slit)	$\pm .002$	$\pm 1.20$	$\pm .002$	$\pm 170$
sample displacement, $X' = \pm 0.025 \text{ mm}$	$\pm .0034$	$\pm 2.1$	$\pm .0088$	$\pm 760$
tilt axis displacement, $X' = \pm 0.025 \text{ mm}$	$\pm .002$	$\pm 1.2$	$\pm .0068$	$\pm 585$
maximum total errors <sup>a,b</sup>				
) in $-2\theta$ direction	- .008	-4.8	- .0201	-1150
) in $+2\theta$ direction	+ .0068	+4.1	+ .0149	+860

Note: Maximum error is either on of these but not the total range.

Calculated for steel from  $\sigma_\phi = K_\psi (2\theta - 2\theta_\psi)$  where  $K_{45} = 602 \text{ MPa}/^\circ 2\theta$  and  $K_{60} = 408.1 \text{ MPa}/^\circ 2\theta$ . Does not include error in peak location as it is dependent on time of data collection.

## 7. Factors Affecting Precision

Automation of stress measurements has been achieved in several locations. One such program, for example, includes sample alignment over the tilt axis, and preliminary scans to locate the peak and to determine the time to achieve an operator-specified precision [9,24]. Such on-line controls allow studies to be made of factors affecting reproducibility.

As shown in table 2, the error in determining a peak's location is one of the largest sources of uncertainty in the results. A number of methods have been presented to define the angle of diffraction,  $2\theta$ , from the diffraction profile, including the apex of a parabola or cubic polynomial fit to the upper portion of the profile [25], the centroid [26] and the half value breadth [18]. Comparisons between these methods indicate that the apex of a least squares parabola fit to that portion of the profile above 85 percent of the maximum intensity usually provides the most reproducible

procedure for defining the diffraction profile when determining peak shifts [19,24]. This is shown in table 3.

Table 3. Precision of various measures of profile position (10 measurements)

Sample	Time (sec)	FWHM <sup>a</sup> (°2θ)	Half-Value Breadth (°2θ)	Centroid (°2θ)	Parabola (°2θ)
AISI 1090-1	50	.45	156.149 (± .021) <sup>b</sup>	156.096 (± .011)	156.186 (± .011)
AISI 1045-2	100	3.45	155.336 (± .064)	155.396 (± .085)	155.413 (± .085)

<sup>a</sup>FWHM is the full width at half of the maximum intensity.

<sup>b</sup>The term in ( ) represents one standard deviation from the average position over the 10 measurements.

If the intensity  $I_j$  accumulated at each  $j$ th interval in  $2\theta$  is taken at  $2n+1$  observation points (the center point being defined as the working origin  $2\theta_0$ ) in equal increments,  $\delta$ , of  $2\theta$ , the peak location in a parabolic fit is given by [24].

$$2\theta_p = 2\theta_0 - (n^2 - n_0 n_4) \delta^2 M_1 / 2n_2 (n_2 \delta^2 M_0 - n_0 M_2), \quad (1)$$

where:

$$n_i = \sum_{j=-n}^n J^i \quad \text{and} \quad M_i = \delta^{i+1} \sum_{j=-n}^n J^i I_j. \quad (1)$$

(Angular intensity corrections such as the Lorentz polarization and absorption factors must be performed on the raw data before determining the peak position.)

Scatter in the peak position arises from statistical fluctuations in the x-ray intensities and the precision of the measured value is properly evaluated by its standard deviation due to counting statistics. The standard deviation in peak location (eq. (15) due to random counting errors is [19,24]:

$$S(2\theta_p) = \left[ \frac{\delta^4 (n^2 - n_0 n_4)^2}{4n_2^2 (n_2 \delta^2 M_0 - n_0 M_2)^4} \sum_{j=-n}^n (n_0 \delta^3 M_1 j^2 + (n_2 \delta^2 M_0 - n_0 M_2) \delta^2 j - n_2 \delta^3 M_1)^2 S^2(I_j) \right]^{1/2}, \quad (1)$$

where the variance in the power,  $S^2(I_j)$  depends on the method of data accumulation and given by:

$$S_{FT}^2(I_j) = I_j/t \quad \text{for fixed time, } t, \quad (17a)$$

$$S_{FC}^2(I_j) = I_j^2/c \quad \text{for fixed counts, } c. \quad (17b)$$

The error,  $S(2\theta_p)$ , introduces an error in the calculated interplanar spacing given by:

$$S(d) = \left[ \frac{\lambda \cos \theta}{2 \sin^2 \theta} \right] \frac{S(2\theta_p)}{\sqrt{2}} \left( \frac{\pi}{180} \right), \quad (18)$$

where  $\lambda$  represents the characteristic wavelength and  $S(2r)$  is in degrees  $2\theta$ .

The subsequent statistical counting error in measured residual stress is:

$$S(\sigma_\phi) = \left[ \frac{\sum_{\psi} (\sin^2 \psi - \overline{\sin^2 \psi})^2 \cdot S^2(d\psi)}{[\sum_{\psi} (\sin^2 \psi - \overline{\sin^2 \psi})^2]^2} \right]^{1/2} / [d_0 \cdot S_{2/2}^{(hkl)}], \quad (19)$$

for the  $\sin^2 \psi$  technique (eq. (5)) and:

$$S(\sigma_\phi) = K [S^2(2\theta_0) + S^2(2\theta_\psi)]^{1/2}, \quad (20)$$

for the two-tilt method (eq. (6)).

Figure 14a shows the distribution of errors in a large number of actual measurements when  $0.01^\circ 2\theta$  was chosen as the desired statistical precision for each peak in a control program employing the above equations. The half-width of the distribution is only  $2.4 \cdot 10^{-3} 2\theta$ . But when the distribution of errors in repeated measurements on the same specimens was examined (without moving it), the results in figure 14b were obtained. Clearly, the scatter is greater than the statistical error. In a series of experiments [19,24], the factors required to achieve reproducibility equivalent to the statistical error were examined. The results can be summarized as follows:

(a) Unless the peak is very sharp, at least 7 points should be employed in a parabolic fit, if the two-tilt method is employed not the three points usually taken. (The total measuring time can be kept fixed.)

(b) If the peak-to-background ratio is low (2:1) or the peak is broad ( $2^\circ$  or more), background subtraction is required, at least in the first scan to determine the region of fit. (This was not done for the data in figure 14, and this is the main reason for the poorer than expected precision.)

Even with (a) and (b) the scatter may be twice that predicted by the above statistical analysis for the two-tilt procedure. But:

c) With the total time kept fixed, the  $\sin^2\psi$  method, with at least a three point parabolic fit and background subtraction will achieve the expected error.

d) An alternative to (c) is to employ a position sensitive detector (PSD) and 30 or more points in the region of fit. In this case, background subtraction is not necessary.

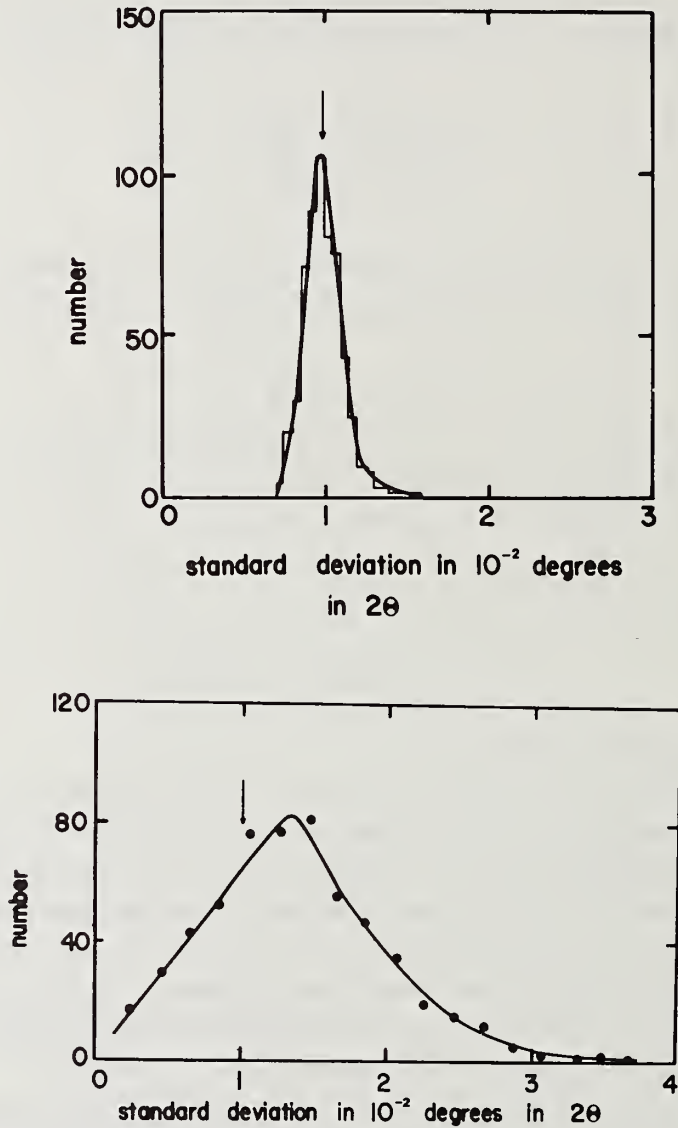


Figure 14. (a) Precision of peak location (parabolic fit, top 15 pct). 572 peaks; actual standard deviations when the indicated precision was requested. (b) 440 peaks each examined 4 times; indicating the spread in each of these 4 repeated measurements. Armco iron and steels, 211 reflection,  $\text{CrK}_\alpha$  radiation. 7 point parabolic fit for peak positions.

Automation alone will reduce the time of measurement by  $\approx 2$ . A PSD will result in time saving of a factor of 5 or more [24,27]. Indeed, if an error of 34 MPa (5 ksi) is acceptable, it has been shown that in some cases, measurements can be completed with the two tilt method with 2 seconds for each tilt [7] with the instrument in figure 4.

Finally, it is instructive to consider the total error possible in a residual stress measurement due to all the factors discussed. Samples circulated to many investigators can give perhaps the best view of the combined accuracy and precision to be expected. The following data is taken from reference [28]. The two tilt method was employed, with steel specimens.

1. SAE Round Robin No. 3 (11 laboratories reported, 1959)
  - a. flat specimen (broad peak)  
stress level: 14 MPa  
standard deviation among laboratories:  $\pm 10.3$  MPa
  - b. 1010 annealed flat steel (sharp peak)  
stress level: -5 MPa  
standard deviation:  $\pm 16.5$  MPa
2. SAE Round Robin No. 4 (25 laboratories, including many with little or no experience in residual stress measurements)
  - a. flat, shot-peened ( $R_c$  63)  
stress level: 593 MPa  
standard deviation:  $\pm 41$  MPa
  - b. 1045 Round bar, 6.22 cm diameter ( $R_c$  61/62)  
stress level: 910 MPa  
standard deviation (axial direction):  $\pm 56.5$  MPa  
standard deviation (longitudinal direction):  $\pm 72$  MPa

---

We are grateful to ONR for their continued support of our efforts in this area. Many of the experiments were carried out in Northwestern University's Long-Term X-ray facility supported (in part) by the NSF-MRL program through grant No. DMR 76-80847. We thank M. McClinton for the data on his shot-peened steels employed by us to examine gradients. One of us (H.D.) also thanks the Council for the International Exchange of Scholars for a travel grant from the Fulbright-Hays Program.

#### References

- 1] James, M. R. and Cohen, J. B., The measurement of residual stresses by x-ray diffraction techniques, in Experimental Methods in Materials Science, Vol. 1, H. Herman, ed. (Academic Press, in press).
- 2] James, M. R. and Buck, O., Quantitative nondestructive measurements of residual stresses, in Critical Reviews in Solid State and Materials Science (in press).

- [3] Lester, H. H. and Aborn, R. H., Behavior under stress of the iron crystals in steel, Army Ordnance, 6, 120-127, 200-207, 283-287, 364-369 (1925).
- [4] Evenschor, P. D. and Hauk, V., Uber nichtlineare Metalbenenabstandsverteilungen bei röntgenographischen Dehnungsmessungen, Z. Metallkde. 66 [3], 167-168 (1975).
- [5] Dölle, H., Influence of multiaxial stress states, stress gradients and elastic anisotropy on the evaluation of (residual) stresses by x-rays, J. Appl. Cryst., in press.
- [6] Nye, J. F., Physical Properties of Crystals (Clarendon Press, Oxford, 1975).
- [7] James, M. R. and Cohen, J. B., PARS - a portable x-ray analyzer for residual stresses, J. of Testing and Evaluation, 6 [2], 91-97 (1978).
- [8] Steffen, D. A. and Ruud, C. O., A versatile position sensitive xray detector, in Advances in X-ray Analysis, Vol. 21, H. F. McMurdie, C. S. Barrett, J. B. Newkirk, and C. O. Ruud, eds. (Plenum Press, New York, 1978), pp. 309-315.
- [9] Marion, R. H. and Cohen, J. B., The need for experimentally determined x-ray elastic constants, in Advances in X-ray Analysis, Vol. 20, H. F. McMurdie, C. S. Barrett, J. B. Newkirk, and C. O. Ruud, eds. (Plenum Press, New York, 1977), pp. 355-367.
- [10] Prevey, P. S., A method of determining the elastic properties of alloys in selected crystallographic directions for x-ray diffraction residual stress measurements, in Advances in X-ray Analysis, Vol. 20, H. F. McMurdie, C. S., Barrett, J. B. Newkirk, and C. O. Ruud, eds. (Plenum Press, New York, 1977), pp. 345-354.
- [11] Dölle, H. and Cohen, J. B., Residual stresses in ground steels, submitted for publication.
- [12] Walburger, H., Conference on Residual Stress Analysis, Plättig, Germany, May 3-4 (1973).
- [13] Dölle, H. and Hauk, V., Röntgenographische Spannungsermittlung für Eigenspannungssysteme allgemeiner Orientierung, Härtereitechn. Mitt. 31, [3], 165-169 (1976).
- [14] Murakami, M., Residual strains of Pb thin films deposited onto Si substrates, Acta Met. 26, 175-183 (1978).
- [15] Wolfsteig, U., Röntgenographische Spannungsmessungen mit breiten Linien, Arch. Eisenhüttenwes, 30, 447-450 (1959).
- [16] Macherauch, E. and Wolfstieig, U., A modified diffractometer for x-ray stress measurements, in Advances in X-ray Analysis, Vol. 20, H. F. McMurdie, C. S. Barrett, J. B. Newkirk, and C. O. Ruud, eds. (Plenum Press, New York 1977), pp. 369-378.
- [17] Schwartz, L. H. and Cohen, J. B., Diffraction from Materials (Academic Press, New York, 1977).
- [18] Chrenko, R. H., X-ray residual stress measurements using parallel beam optics, in Advances in X-ray Analysis, Vol. 20, H. F. McMurdie, C. S. Barrett, J. B. Newkirk, and C. O. Ruud, eds. (Plenum Press, New York, 1977), pp. 393-402.
- [19] James, M. R., An Examination of Experimental Techniques in X-ray Residual Stress Analysis, Ph.D. Thesis (Northwestern University, Evanston, IL, 1977).

- 0] Marion, R. H. and Cohen, J. B., Anomalies in measurement of residual stress by x-ray diffraction, in Advances in X-ray Analysis, Vol. 18, W. L. Pickles, C. S. Barrett, J. B. Newkirk, and C. O. Ruud, eds. (Plenum Publ. Co., New York, 1975), pp. 446-501.
- 1] Lecroisey, F., Miège, B. and Saint-Étienne, A., La Mesure de Constraints Résiduelles: Method de Détermination par Rayons X (Centre Techniques de Industries Mechaniques, B.P. 67, 60304 Senlis, France, 1978).
- 2] Marion, R. H., X-ray Stress Analysis of Plastically Deformed Metals, Ph.D. Thesis (Northwestern University, Evanston, IL, 1972).
- 3] Zantopoulos, H. and Jatczak, C. F., Systematic errors in x-ray diffractometer stress measurements due to specimen geometry and beam divergence; in Advances in X-ray Analysis, Vol. 14, C. S. Barrett, J. B. Newkirk, and C. O. Ruud, eds. (Plenum Press, New York, 1971), pp. 360-376.
- 4] James M. R. and Cohen, J. B., Study of the precision of x-ray stress analysis, in Advances in X-ray Analysis, Vol. 20, H. F. McMurdie, C. S. Barrett, J. B. Newkirk, and C. O. Ruud, eds. (Plenum Press, New York, 1977), pp. 291-309.
- 5] Koistinen, D. P. and Marburger, R. E., A simplified procedure for calculating peak position in x-ray residual stress measurements on hardened steel, Trans. of the ASM, 51, 537-555 (1959).
- 5] Singh, A. K. and Balasingh, C., Effect of x-ray diffractometer geometrical factors on the centroid shift of a diffraction line for stress measurement, J. Appl. Phys. 42 [13], 5254-5260 (1971).
- 7] James, M. R. and Cohen, J. B., The application of a position sensitive x-ray detector to the measurement of residual stresses, in Advances in X-ray Analysis, Vo. 19, R. W. Gould, C. S. Barrett, J. B. Newkirk, and C. O. Ruud, eds. (Kendall/Hunt Publ. Co., Dubuque, Iowa, 1976), pp. 695-708.
- 8] Residual Stress Measurement by X-ray Diffraction - SAEJ784a, M. E. Hilley, J. A. Larson, C. F. Jatczak, and R. E. Ricklefs, eds. (Society of Automotive Engineers, Inc., Warrendale, PA., 1971).



## X-RAY RESIDUAL STRESS EVALUATION BY AN ENERGY DISPERSIVE SYSTEM

Masao Kuriyama, William J. Boettinger and Harold E. Burdette  
National Bureau of Standards  
Washington, DC 20234

In place of traditional Bragg diffractometers, energy dispersive systems are now employed more increasingly as a tool for crystallography. These systems are not only suitable for rapid data collection and processing, but also are simple and compact, since no elaborate x-ray optical alignments, nor delicate moving parts are required. In addition, the energy of x-ray photons can be extended to considerably higher values, hence, permitting better penetration into materials.

Currently, improved quality control of industrial components demands quantitative information concerning the stress distribution near cracks and residual stress distributions after different types of cold working and heat treating or under various conditions of load. These demands naturally lead to the necessity of measuring residual strains in the interior of materials. With a little extra precaution on the divergence of an incoming x-ray beam and the opening of the detector window, energy dispersive systems will respond to these demands. Furthermore, the curve fitting of each diffraction peak will provide sufficient precision for the determination of strains in materials. The use of these systems makes it possible to determine the strain tensor in predetermined volumes in the interior of materials. Mapping of strains will become possible throughout the material.

### 1. Introduction

One of the nondestructive methods currently used for measurements of residual stresses in industrial materials involves the application of x-ray analysis for stress measurement. X-ray diffraction phenomena are used to determine macroscopic residual stresses in engineering components. The methodology of analysis and its basic principles are well known. Briefly, when materials are under stress, x-rays are diffracted with a Bragg angle which is slightly different from the Bragg angle expected in unstressed materials. The change in the Bragg angle is related to the alteration of atomic interplanar

spacings when the crystal lattice of the materials is strained. As a measurement system, the essential part of this x-ray technique is the accurate measurement of lattice constants (or their changes) in materials by use of well-refined Bragg diffractometry. The surface residual stress can be evaluated from the strains measured by x-ray diffractometry using a set of assumptions regarding material elasticity and homogeneity. Although the accuracy obtained by this technique is, in principle, superior to any other methods, an obvious shortcoming lies in its incapability of detecting strains (or stresses) in the interior of bulk materials.

Currently, improved quality control of industrial components demands quantitative information concerning the stress distribution near cracks and residual stress distribution after different types of cold working and heat treating. These demands naturally lead to the necessity of measuring residual strains in the interior of materials. Ordinary Bragg diffractometry will not be sufficient to respond to these demands. There is an entirely different approach to the x-ray evaluation of residual strains although it uses the principles of x-ray diffraction. This approach involves the use of energy dispersive solid state detectors with high energy x-ray photons. The use of solid state detectors has been introduced very effectively in the fields of scanning electron microscopy (microanalysis) and x-ray fluorescence analysis of materials in the past ten years. It is called energy dispersive spectroscopy. Unlike these successful applications, this technique has not been applied to the residual stress (strain) measurements of materials. Extremely high resolution and accuracy are required for strain measurements in comparison with the other applications. If one can improve the resolution sufficiently and overcome other important technical problems, this new system would be ideal for residual stress measurement in industry; the equipment will be compact, results will be displayed visually and almost instantaneously, and analysis of the data will be made on site by a computer. Also this system, in general, works better for high energy photons. High energy photons also make practical the use of the transmission geometry, since the x-ray absorption coefficient of materials is approximately inversely proportional to the third power of the energy of x-rays.

The use of an energy dispersive system for possible residual stress evaluation was first tested in 1973 by Leonard [1]<sup>1</sup>, who concluded, however, that this system did not have sufficient accuracy for this purpose. In this paper, we will prove that his conclusion was premature and it is still too soon to dismiss the possible industrial use of this technique for the evaluation of residual stresses. In Section 2, we will propose [2] a method for determining a strain tensor in predetermined volumes in the interior of a material, and discuss the principles involved, although they are trivial. In Section 3, we will present some data showing the attained accuracy in this system, and discuss what kind of precautions should be taken to make this system workable in practical use. Although this system should be used ultimately with high energy photons up to 300 keV, the data shown in this paper have been obtained with an ordinary laboratory x-ray source up to 50 keV. It should be noted, however, that the use of low energy photons for the test of resolution

---

<sup>1</sup>Figures in brackets indicate the literature references at the end of this paper.

accuracy does not negate the conclusion of this paper for high energy photons, since the resolution usually improves for those high energy regions. In other words, the demonstration of the sufficient accuracy for low energy photons certainly guarantees the effectiveness and accuracy of this technique when one uses more penetrating high energy photons for residual stress evaluation.

## 2. Method

In energy dispersive spectroscopy, one is concerned with the energy spectral profiles of peak positions at different energy values, instead of Bragg angles which play a key role in Bragg diffractometry. Lattice constants will be measured in energy dispersive spectroscopy by the energies of diffracted photons:

$$d(A) = \left( \frac{6.199}{\sin\theta} \right) \frac{1}{E(\text{keV})} , \quad (1)$$

where  $d$  is an atomic interplanar spacing related to lattice constants,  $E$  is the energy of diffracted photons measured from peak positions of the spectra, and the coefficient including the scattering angle  $\theta$  is constant for a given scattering geometry. Figure 1 shows a schematic diagram of an energy dispersive diffractometry system. Usually, each Soller slit consists of a vertical and a horizontal slit. Often Soller slits can be replaced by a Weycomb slit originally used as medical filters. For the present purpose, these slits will be replaced by a special slit system which improves the spatial resolution to a desired degree as described later. A solid state detector is mounted at a fixed scattering angle. For our purpose, the scattering angle should be smaller than  $30^\circ$  to ensure complete transmission geometry. The geometrical orientation of a sample is indicated by the unit vector  $\hat{n}$ , the role of which will become obvious later.

For a given sample geometry, one obtains an energy spectrum which contains many Bragg peaks obtained from  $hkl$  planes which are perpendicular to  $\hat{n}$ . From a set of interplanar spacings for different  $(hkl)$ , one can define the "stretch" in the  $\hat{n}$  direction as

$$\lambda_{\hat{n}} = \left( \frac{\Delta d}{d} \right)_{\hat{n}} = \frac{d_{hkl}^{\hat{n}} - d_{hkl}^{\circ}}{d_{hkl}^{\circ}} , \quad (2)$$

where  $d_{hkl}^{\circ}$  is the interplanar spacing for  $hkl$  diffraction obtained either from a reference unstrained material, or from an arbitrarily chosen reference part of the sample. This quantity is related to the strain tensor by

$$\lambda_{\hat{n}} = \sum_{ij} \varepsilon_{ij} n_i n_j , \quad (3)$$

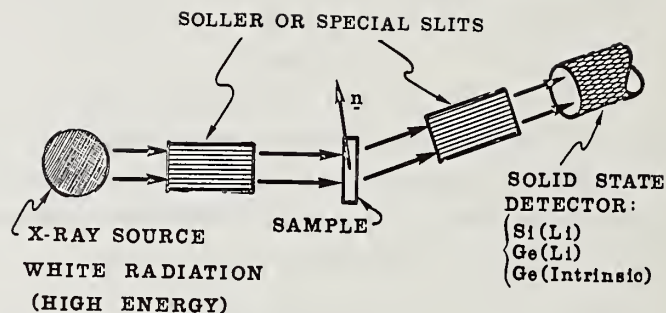


Figure 1. A schematic diagram of an energy dispersive system for powder diffractometry. The geometrical orientation of a sample is indicated by vector  $n$ , the role of which is significant for residual stress determination.

where  $\epsilon_{ij}$  is the  $i, j$  component of the strain tensor and  $n_i$  is the  $i$  component of the vector  $n$  in a frame imbedded in the sample. Since the strain tensor has, in general, six independent components  $\epsilon_{11}$ ,  $\epsilon_{12}$ ,  $\epsilon_{13}$ ,  $\epsilon_{22}$ ,  $\epsilon_{23}$ , and  $\epsilon_{33}$ , one must have a set of six simultaneous equations which can be obtained using (3) for independent measurements performed in six different orientations.

There are many ways to perform six independent experiments. Here we mention one such way that the same predetermined volume in the interior of the sample is viewed by the detector for all these six measurements. As shown in figure 2, the sample is rotated around the incident x-ray beam three times using two detectors to obtain six independent measurements. (If the incident beam direction is used as a rotational axis, one cannot obtain six independent sets if the same scattering angle is used.) As the sample is translated up and down and in other ways, one can essentially map the entire volume of the sample. The incident beam must be prepared to have a very small cross section by a slit system and also to be extremely narrow (no angular divergence). In addition, the detector must receive the scattered beam within an extremely narrow angular range so that the scattered beam should be originated from a predetermined volume inside the sample. This simple geometrical argument on the scattering is justified as long as the scattering (Bragg diffraction) is kinematical.

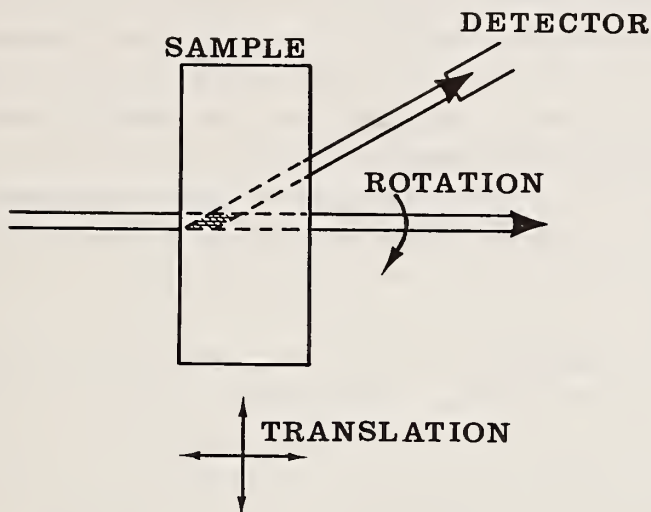


Figure 2. An example of the geometrical arrangements for the evaluation of residual strains in a predetermined volume inside materials. The sample is rotated three times around an x-ray beam to give six independent sets of measurements with two detectors. The mapping of strains throughout the volume of the sample is achieved by translations.

### 3. Accuracy

In the application to residual stress measurements, a strain ( $\Delta d/d$ ) of less than  $10^{-4}$  ( $10^{-2}$  percent) should be detected; in other words, the effective resolution of the energy dispersive system is required to be smaller than  $10^{-2}$  percent. In 1967, Giessen and Gordon demonstrated a resolution of 0.18 percent with the use of a lithium drifted Si detector [3]. Later, Laheemaki and Kantola claimed in 1971 the resolution of 0.05 percent [4]. A year later, Fukamachi, Hosoya and Terasaki used a lithium drifted Ge detector with Soller slits in their x-ray optical scattering system and estimated the resolution of slightly larger than 0.01 percent [5].

Bragg's law states that a measure for resolution is given by

$$\frac{\Delta d}{d} = - \frac{\Delta E}{E} - \cot \theta \Delta \theta, \quad (4)$$

where  $\Delta E$  is the energy resolution of a detector and  $\Delta \theta$  is the angular divergence created by the incident beam divergence and the receiving angle of the detector. For intermediate energy photons, the first term is of order of  $10^{-2}$  for the resolution of two energies. This term becomes smaller as the photon energy increases. The second term is purely controlled by the x-ray optical arrangement. Therefore, it should be kept smaller than the first term by introducing appropriate slit systems before and after a sample. As described before, it is necessary to limit the physical spatial size of the incident x-ray beam in order to measure the spatial variation of strains. The reduction of the second term should, therefore, be achieved anyway.

One may claim then that the energy resolution of current solid state detectors is not small enough to reduce the value in (4) for the evaluation of residual strains. It has been known fortunately that each diffraction profile in the energy spectrum obtained from a solid state detector is very close to a Gaussian. If the mathematical shape is known for a diffraction spectral profile, then the claim mentioned above can be circumvented: mathematically fitting the observed peaks with Gaussian functions, one can determine the centroids (or centers) of the peaks far more accurately than the  $\Delta E/E$  value stated above would indicate. As shown below, one can improve by a factor of 100 in the accuracy of determining the centroid positions.

Figure 3 shows the energy spectra obtained from a commercial material, 304 Stainless Steel. The scattering angle was set at  $2\theta = 30.00^\circ$ , with the incident beam divergence  $4.6 \times 10^{-4}$  rad ( $0.026^\circ = 1.6'$ ) and the receiving divergence much less than  $10^{-3}$  rad. The spatial size of the beam on the sample is less than  $0.5 \times 0.5 \text{ mm}^2$ . Under the present receiving slit condition, the predetermined volume is roughly  $0.5 \times 0.5 \times 0.6 \text{ mm}^3$ . It should be noted in the figure that the spectrum shows reflections of quite high order in the well-controlled background scattering. In principle, the higher order reflections should be used for the evaluation of strains, as the relative error decreases in the high energy range.

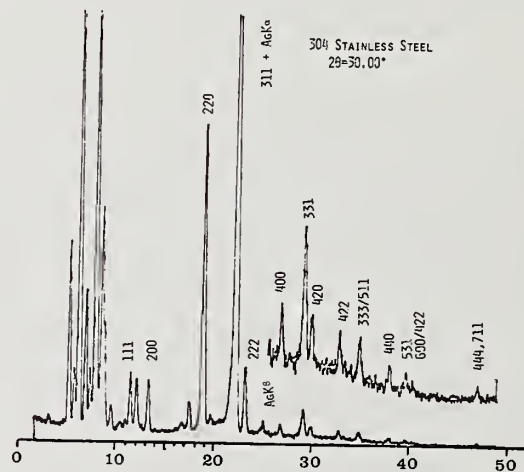


Figure 3. A Bragg diffraction energy spectrum obtained from a commercial 304 stainless steel sample. The scattering angle is  $30.00^\circ$ , ensuring a transmission geometry. The incident beam divergence is less than  $5 \times 10^{-4}$  rad ( $0.027^\circ = 1.6'$ ); and the receiving divergence is much less than  $10^{-3}$  rad. The spatial size of the beam on the sample is less than  $0.5 \times 0.5 \text{ mm}^2$ .

Figure 4 shows as example of the observed spectral profile which has been fitted by Gaussian curve with a linear background. The accuracy of determining the centroid (or peak) positions has been found to depend simply upon the counting statistics. The reproducibility of those positions has also been tested; as long as the same predetermined volume is viewed, the centroid position remains identical within the statistical error, as shown in table 1. As a reference to possible instrumental instability, Ag K $\alpha$  line spectrum in each run has been fitted with a Gaussian curve. (White radiation was obtained using a Ag target tube.) The Ag K $\alpha$  line result indicates that the instability, if any, is not significant to jeopardize the accuracy in the determination of diffraction peak positions. Table 1 demonstrates that strains of  $5 \times 10^{-5}$  can be detected with reliable reproducibility, if sufficient counting statistics is established, and strains of  $1 \times 10^{-4}$  can be detected even with moderate counting statistics.

Table 1

220			200			AgK $\alpha$ (22.2 kev)		
Peak Height	Peak Position	FWHM	Peak Height	Peak Position	FWHM	Peak Height	Peak Position	FWHM
1307.66 $\pm 7.88$	840.07 $\pm 0.04$	12.9	174.08 $\pm 4.51$	592.31 $\pm 0.18$	12.3	6046.04 $\pm 35.14$	986.870 $\pm 0.047$	13.56
1526.20 $\pm 8.67$	840.02 $\pm 0.04$	12.9	485.71 $\pm 6.59$	593.51 $\pm 0.09$	11.8	6267.04 $\pm 33.70$	986.900 $\pm 0.044$	13.61
410.79 $\pm 6.02$	840.70 $\pm 0.010$	13.2	100.03 $\pm 3.36$	592.13 $\pm 0.21$	11.9	1868.17 $\pm 19.34$	986.935 $\pm 0.086$	13.95

In conclusion, an energy dispersive diffraction system has demonstrated its capability as a useful tool for the determination of residual stresses inside materials, when the curve fitting technique is used simultaneously. The present demonstration has been carried out with low energy photons. The use of high energy photons certainly makes more practical the use of these energy dispersive systems for residual stress evaluation. More penetration and increased energy resolution of detectors will improve the resultant accuracy and detectability of strains. Since the energy dispersive system can be made simple and compact, without any delicate moving parts, the system is quite ideal for an industrial use on site, particularly when data are handled by a mini-computer. By no means, an energy dispersive system such as used here has reached the ultimate resolution; further improvements on x-ray optics and detectors should be made, in particular, with high energy photons. To demonstrate the x-ray optical quality of the energy dispersive system used in this paper, a diffraction spectrum obtained from a commercial NiP amorphous metal is shown in figure 5.

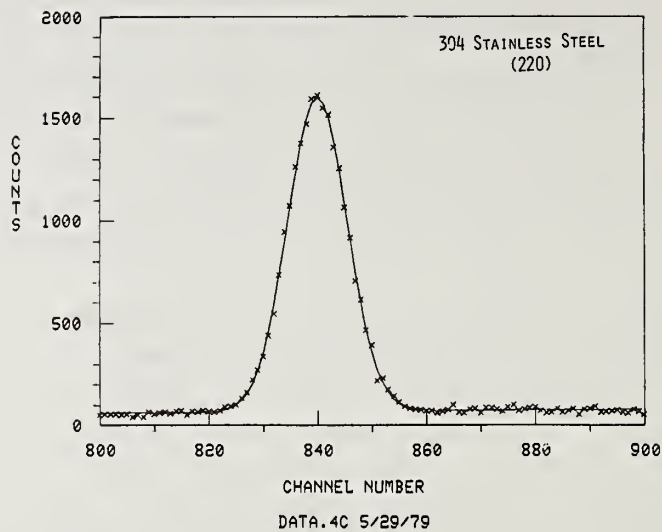


Figure 4. (a) An example of the observed diffraction profile fitted with a Gaussian curve with linear background.

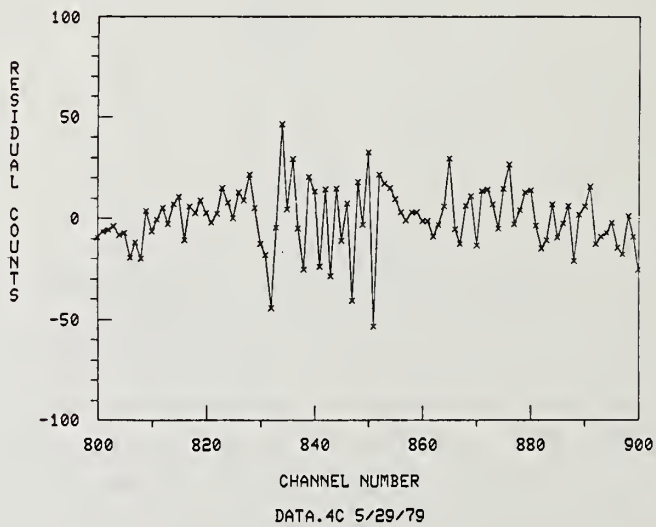


Figure 4. (b) The residuals from the Gaussian fit which are well within limits expected from counting statistics.

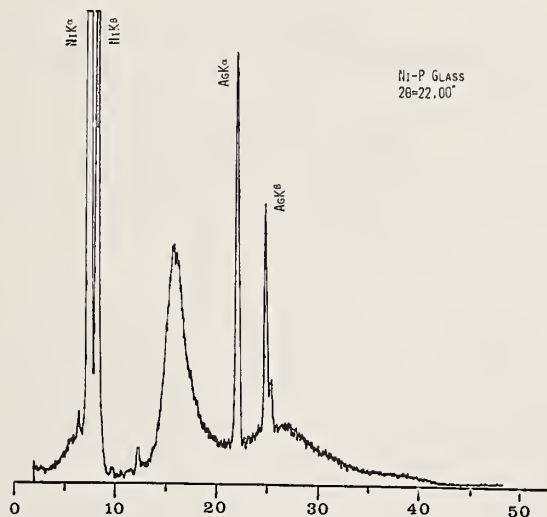


Figure 5. A diffraction energy spectrum obtained from a commercial NiP amorphous alloy, demonstrating the x-ray optical quality of the energy dispersive system used in this paper.

#### References

- 1 Leonard, L., Franklin Institute Research Lab (Philadelphia) Report F-C3454 (July 1973).
- 2 Kuriyama, M., Boettinger, W. J., and Burdette, H. E., ASNT National Fall Conference, October, Denver, CO, p. 49 (1978).
- 3 Giessen, B. C. and Gordon, G. E., *Science*, 159, 973 (1968).
- 4 Laine, E., Lahteenmaki, I., and Kantola, M., *X-ray Spectrometry*, 1, 93 (1972).
- 5 Fukamachi, T., Hosoya, S., and Terasaki, D., *J. Appl. Cryst.* 6, 117 (1973).



## STANDARD REFERENCE MATERIALS FOR QUANTITATIVE ANALYSIS AND d-SPACING MEASUREMENT

Camden R. Hubbard  
Ceramics, Glass, and Solid State Science Division  
National Bureau of Standards  
Washington, DC 20234

The National Bureau of Standards has an on going program in x-ray powder diffraction to provide Standard Reference Materials (SRMs) to the diffraction community. The first product of this program was SRM-640 Si Powder, certified in 1974 as a d-spacing standard. While this material has become widely used it is not a universal reference material. In particular, the large d-spacing region ( $>4 \text{ \AA}$ ), accessible to most diffraction apparatus is not covered. To fill this need we are reviewing materials as candidates for a large d-spacing SRM. Candidate materials currently include molybdenum disulfide, arsenic trioxide, sodalite, fluorophlogopite, muscovite, and thallos acid phthalate.

Intensity SRMs for quantitative analysis will soon be certified. The five materials ( $\alpha\text{-Al}_2\text{O}_3$ ,  $\text{TiO}_2$ -rutile,  $\text{ZnO}$ ,  $\text{Cr}_2\text{O}_3$  and  $\text{CeO}_2$ ) were selected to cover the range of linear absorption coefficients encountered in practical samples. By matching approximately the linear absorption coefficients, errors in analysis due to microabsorption can be minimized. The relative intensities and the reference intensity ratio for each material are being measured on Bragg-Brentano focusing diffractometers. The results are compared with values obtained from calculated powder patterns. The use of the reference intensity ratio as a basis for tabulation of the calibration constants needed in internal standard methods of quantitative analysis will be reviewed.

### 1. Introduction

Standard Reference Materials (SRM's) have been produced, certified and issued by NBS since 1905. NBS now issues in 70 major categories, approximately 37,000 SRM units each year to over 12,000 customers. Nearly 900 different SRM's are currently available [1]<sup>1</sup>. In general SRM's are well-characterized, stable materials (or artifacts) which are produced in quantity and have one or more physical or chemical properties measured and certified by NBS. SRM's are used to: calibrate instruments and measurement system; facilitate

<sup>1</sup>Figures in brackets indicate the literature references at the end of this paper.

the exchange of goods; maintain quality control in industry; assure the development and enforcement of equitable regulations; and assure the long term accuracy and compatibility of measurements.

In the field of x-ray powder diffraction there are a wide range of possible classes of SRM's including standards for instrument calibration and quantitative analysis. A standard for either purpose can be mixed with the sample to be studied (an internal standard) or used independently (an external standard). It is possible that the same material can be used for a variety of purposes. However, as we will see below, the requirements for each class of standards are somewhat different.

## 2. External Instrument Standards

Materials that are used to aid and/or check instrument alignment, to evaluate resolution, to determine an instrument systems stability and to intercompare various instruments are usually a stable briquette or a disk. Some instrument manufacturers have provided powdered silicon as a bonded disk or fine grain quartz slabs. Materials that have been used to test resolution include  $\text{BaSO}_4$  (1% Sr) [2], tungsten [3] and quartz [4].

The use of an external instrument standard to calibrate the  $2\theta$  scale, however, has limited accuracy. The accuracy is limited ultimately by the knowledge concerning the standard itself to about 1 part in  $10^5$ . However, errors due to systematic displacement of the Bragg peaks usually dominate. The displacements arise from geometrical properties such as axial divergence, physical factors such as sample position, and penetration of the beam into the sample. The peak displacement effects for the standard, and separately for a sample, combine to limit accuracy in cell parameter determination to between 1 and 10 parts in  $10^4$  in routine work.

## 3. Internal Instruments Standards

One of the easiest methods to obtain improved accuracy in lattice parameter determinations is to intimately mix a powdered internal instrument standard (also known as a d-spacing or  $2\theta$  standard) with the powdered phase to be characterized. In this case, displacement of Bragg profiles due to sample displacement and beam penetration affect the standard and sample reflections almost identically. The location of the standard lines are then used to generate a calibration curve (see section "Calibration Methods").

The historical development of internal instrument standards is not well documented. Their use likely began as early as the beginning of x-ray diffraction itself. During the 1940's, and probably earlier, NaCl and quartz [5] were used as internal standards. It became apparent that reference sample preparation methods and lack of homogeneity limited the usefulness of these materials. This was further accentuated by the fact that no single source or institution provided well characterized reference materials. The first major improvements in internal standards came in the 1960's.

The IUCr Commission on Apparatus and Standards headed by W. Parrish organized a round robin on cell parameter measurement. Three materials (diamond, silicon and

ingsten) were carefully selected and distributed to a number of laboratories. While the discrepancy between the results of the various laboratories was larger than expected (1 part in  $10^4$ ), mean lattice parameters with  $\sigma/a \approx 3 \times 10^{-5}$  were obtained [6]. The distributed samples and "best" lattice parameters became de facto standards. They were often used to calibrate secondary standards for routine laboratory use [7]. At NBS, the lattice parameters of high purity tungsten, silver and cadmium oxide [8] were determined to better than one part in  $10^5$ . These standards have been used for nearly 15 years by the NBS in collaboration with the Research Associateship of the International Centre for Diffraction Data - JCPDS. Approximately 1000 reference patterns have been carefully recorded using one or the other of these internal instrument standards. However, these reference materials were not made publically available. To overcome this deficiency, NBS produced SRM 640 Si powder [9]. The lattice parameters of the high purity Si were measured relative to that of NBS tungsten by powder diffractometry and measured directly by the single crystal Bond technique. The absolute uncertainty in  $a$  is reported to be within parts in  $10^5$ . Since its issuance in 1974, over 550 units have been sold to laboratories throughout the world.

A few comments on the limitations of this material are required. First, the grinding of the single crystal boules probably introduced some strain. Thus, the sample should not be used directly to define the true instrumental profile. Second, the SRM sample contains some particles up to 20  $\mu\text{m}$  in length. These small single crystals can produce undesirable spikes on the side of a recorded powder diffraction line. The effects of the spikes can be minimized by careful interpretation of the strip chart. However, for automated systems employing computer analysis of the digital data a spike can cause a serious error in determining the peak position. To overcome this problem some laboratories have further sieved the Si powder (<400 mesh). It is possible, though highly unlikely, that such a procedure could produce a powder with lattice parameters shifted by as much as 10 ppm. No definitive tests have been performed at NBS. The third, and probably far more important, limitation of the use of SRM 640 is that for  $\text{CuK}\alpha$  x-radiation the lowest Si diffraction peak occurs at  $2\theta = 44.3^\circ$ . This leaves the region between  $28^\circ$  and  $0^\circ 2\theta$  calibrated only through extrapolation.

The value of using a d-spacing internal instrument standard was demonstrated in a recent Round Robin on Search/Match Procedures, [10]. One of the test problems was a mixture containing three phases and the Si standard. One-half of the participants were told that the sample contained SRM 640 Si powder, and they were provided with the expected  $2\theta$ 's for  $\text{CuK}\alpha_1$  radiation for the Si. The other half of the participants did not receive this information. All respondents measured the d-spacings and attempted to identify the phases present in the mixture. To ascertain the quality of the observed d-spacings six lines with d-values between 4.4 and 1.54  $\text{\AA}$  ( $20^\circ$  and  $60^\circ 2\theta$  for  $\text{CuK}\alpha_1$ ) were selected and the average of the magnitude of the relative error in d-spacing (d-quality) was calculated. Results provided by the respondents fell into three categories as shown in table 1. The accuracy measured by d-quality improved significantly when the standard was used for calibration purposes. The success rate (rating) in phase identification (5 points for each correct

phase, 20 maximum) also improved as the quality of data improved. However, the d-quality of 1 part in  $10^3$  is a factor of 10 below that expected. It must be remembered, however that the purpose of the exercise was phase identification and not accurate d-spacing measurements. Significant improvement of the success in identifying phases in multiphase mixtures due to high quality data have been reported by Edmonds and Henslee [2].

Table 1. Round robin d-quality.

Use of Standard	# of Response	d-Quality	Rating
None	26	0.0018	16.1
Visual check on 2 $\theta$ values	6	0.0016	17.0
Corrected 2 $\theta$ values	7	0.0009	18.0

#### 4. Large d-Spacing Standards

To improve on the calibration of the low 2 $\theta$  range NBS is currently examining several candidates for use as a large d-spacing reference material. The criteria for a large d-spacing standard are:

- (1) that the powdered material is stable in the atmosphere, in x-rays and in mixtures with other powders;
- (2) that it is available in homogeneous quantities of 1 to 20 kg;
- (3) that the diffraction pattern exhibits a few sharp well spaced strong lines with at least one d-value  $>6 \text{ \AA}$ .

Besides receiving suggestions from co-workers and colleagues, we have searched the Handbook of the Frequently Encountered Phases Search Manual [11] for possible materials. The candidate materials are given in table 2 along with the value of the largest d-spacing, the relative intensity of that line and pertinent notes. The materials described as "ply" exhibit extreme preferred orientation. This can be used to advantage with diffractometry where only the 00 $l$  reflections will appear (fig. 1). However, the preferred orientation is a disadvantage to their use as a standard for Guinier cameras. Both sodalite [12] and thallic acid phthalate [13] have desirable characteristics except that above 30° 2 $\theta$  (Cu) there are many interfering reflections and a second sample mixed with Si would likely be required to calibrate the 2 $\theta$  scale above 30° 2 $\theta$ . We intend to accurately measure the d-spacing of one or two of the candidate materials by both powder diffractometry and the Bond single crystal method, as was done for Si SRM 640.

Table 2. Candidate large d-spacing standards

Phase	$d_{\max}$	$I^{\text{rel}}$	Notes
MoS <sub>2</sub>	6.15 Å	100	platy
Sodalite (Na <sub>8</sub> Si <sub>6</sub> Al <sub>6</sub> O <sub>24</sub> Cl <sub>2</sub> )	6.27	40	cubic
As <sub>2</sub> O <sub>3</sub>	6.39	60	Used at Dow Chemical Corp.
fluoro-phlogopite (KMg <sub>3</sub> (Si <sub>3</sub> Al <sub>10</sub> )F <sub>2</sub> )	9.96	100	platy
muscovite (KA <sub>2</sub> Si <sub>3</sub> Al <sub>10</sub> )F <sub>2</sub> )	10.0	100	platy
thallous hydrogen phthalate (TlC <sub>8</sub> H <sub>5</sub> O <sub>4</sub> )	12.9	100	mono. xtal

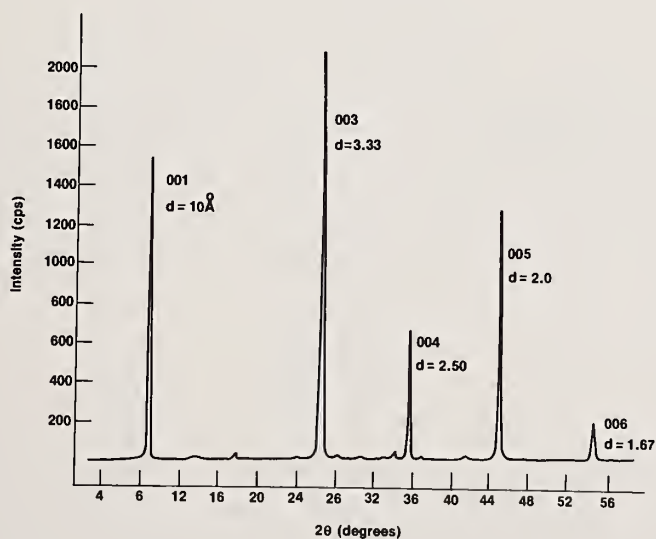


Figure 1. X-ray powder diffraction pattern of highly oriented phlogopite measured on a diffractometer with CuK $\alpha$  radiation and  $\theta$ -compensating slits. The peaks are labeled by their Miller indices and d-spacings.

## 5. Calibration Methods

There are several ways to use a d-spacing standard to correct the observed  $2\theta$  values. The simplest method which is generally used for strip chart recorded patterns is to calculate the correction factors ( $\Delta = 2\theta_{\text{true}} - 2\theta_{\text{obs}}$ ) and then for each  $2\theta$  of the sample to perform a linear interpolation between adjacent standard lines. In table 3, seven calibration points were obtained using Si and W internal standards in an  $\alpha\text{-Al}_2\text{O}_3$  sample. The mid-arc position at 80 percent height of each peak was determined from a strip chart recording measured to  $\pm 0.01^\circ$  ( $2\theta$ ). The plotted data (fig. 2) shows that linear interpolation will provide corrections which are probably as accurate as the measurements. Applying corrections with a  $\sigma_{\text{std}} = 0.01^\circ$  to data measured with a  $\sigma_{\text{obs}} = 0.01^\circ$  leads to corrected data with  $\sigma_{\text{cor}} = \sqrt{2} \times 0.01^\circ$ . Fitting a low order polynomial to the indicated corrections reduces the uncertainty in the correction factor and hence reduces  $\sigma_{\text{cor}}$ . In Guinier films, Sonneveld and Visser recommend using a second order polynomial [14]. In his paper on alignment and calibration of Guinier cameras, uses a smooth curve through the plotted points [15]. A more fundamentally sound method is to remove the aberrations due to line shape and instrumental aberrations and then perform a least-squares refinement of values for  $2\theta$ -zero, sample displacement and sample transparency [16].

Table 3.  $2\theta$  correction data.

Sample :  $\alpha\text{-Al}_2\text{O}_3$   
Standard : Si and W

Radiation: Cu  $K\alpha$  (Ni filtered)

Standard	$2\theta_{\text{true}}$	$2\theta_{\text{obs}}$	$\Delta$
Si	28.443°	28.46°	-0.02°
W	40.262	40.26	0.00
Si	47.303	47.30	0.00
Si	56.123	56.11	+0.01
W	58.251	58.22	+0.03
Si	69.131	69.11	+0.02
W	73.184	73.14	+0.04

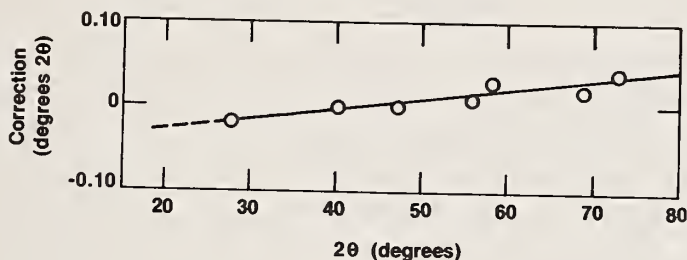


Figure 2. Correction curve based on Si and W internal Standards in  $\alpha\text{-Al}_2\text{O}_3$ .

#### 6. Intensity Standards

An external instrument standard for calibrating or checking an instrument's intensity response should be a powder formed into a disk or briquette. Two examples are pressed Ni disks [17] and a fine grained quartz mineral sample such as novaculite. Generally, for highest accuracy, each sample must be independently calibrated because of sample inhomogeneity and variable preferred orientation. Another more common use of intensity standards is for quantitative analysis. Before discussing standards for quantitative analysis it is necessary to review the basis of quantitative phase analysis [18]. The fundamental equation used throughout all methods of quantitative analysis is:

$$I_{iJ} = \frac{K_{iJ} X_J}{\rho_J \mu^*_T} \quad (1)$$

where  $I_{iJ}$  is the intensity of the  $i^{\text{th}}$  line of the  $J$ -th phase,  $K_{iJ}$  is an instrument sensitivity constant,  $X_J$  is the weight fraction of phase  $J$  in the mixture  $\rho_J$  is the density of phase  $J$ , and  $\mu^*_T$  is the mass absorption coefficient of the mixture.

The absolute intensity method of quantitative analysis works particularly well for microgram quantities such as quartz on a filter. The basic assumption involved is that

a monolayer or less of sample is deposited. In this case,  $\mu^*_T$  for the quartz grains is  $\mu^*$  of quartz and is independent of the matrix or amount of quartz. With these assumptions, eq. (1) simplifies to  $I_{iJ} = k X_J$ . A method which requires calculation of  $\mu^*_T$  is the multisample - multiphase method of Zevin [19]. For this method, all phases in the mixture (including amorphous phases) need to be included in the analysis since the constraint  $\sum X_J = 1$  is imposed. Zevin's method requires that one set of phases ( $m$ ) be present in all samples ( $n$ ) and that  $m \leq n$ . Furthermore, for reasonable precision the weight fraction of each phase should vary significantly throughout the set of samples. More general methods for quantitative analysis are based on the addition of a phase to a mixture in order to eliminate  $\mu^*_T$ . The three possible methods are dilution [20], doping with the analyte [21,22,23] and addition of an internal standard [24]. The dilution method has low precision of analysis and will not be considered further. Doping with the analyte is most sensitive when the analyte weight fraction is low. The internal standard method yields the greatest precision in most other cases. This method is also the most generally applicable since for a preselected standard a table of constants can be prepared (discussed below). NBS is preparing intensity SRM's for the internal standard method.

Before we can discuss the internal intensity standards we need to examine the internal standard method in detail. The basic equation is derived directly from eq. (1) by evaluating the ratio of intensities of the  $i^{\text{th}}$  line of the analyte J to the  $k^{\text{th}}$  line of the standard:

$$\frac{I_{iJ}}{I_{kS}} = \left( \frac{K_{iJ} X_J}{\rho_J \mu^*_T} \right) \left( \frac{\rho_S \mu^*_T}{K_{kS} X_S} \right) = \frac{k'_{JS} X_J}{X_S} \quad (2)$$

Since  $K_{iJ} = c I_{iJ}^{\text{rel}}$ , where  $c$  is a combination of a instrument sensitivity factor and numerical constants, the factor  $k'_{JS}$  is independent of the instrument. Simply,  $k'_{JS}$  is the ratio of the intensity  $I_{iJ}$  to  $I_{kS}$  for a 1:1 mixture by weight. Provided that sample factors such as strain or degree of extinction are not important, the factor  $k'_{JS}$  may be measured at one laboratory and used at any other laboratory.

In cases when all phases in a mixture are crystalline their weight fractions can be determined without addition of the standard. Applying the assumed constraint that  $\sum X_J = 1$ , eq. (2) can be transformed into [25,26]

$$X_J = \left\{ \frac{k'_{JS}}{I_J} \sum_{L=1}^n \frac{I_L}{k'_{LS}} \right\}^{-1} \quad (3)$$

Only ratios of intensities of all the phases and the constants  $k'_{LS}$  are required. An example of application of this equation is given in table 4 for a 50-50 rutile-anatase mixture.

Table 4

phase	hkl	k'	I(cps)	$X_{\text{calc}}$	$X_{\text{known}}$
TiO <sub>2</sub> -rutile	110	3.4	200	0.50 <sub>4</sub>	0.50
TiO <sub>2</sub> -anatase	101	4.3	156	0.49 <sub>6</sub>	0.50

is example is undoubtedly optimum for analysis by this method since, (1)  $\mu^*_T$  is independent of the weight fractions, and (2) as a laboratory example the weight fraction constraint is likely valid. The accuracy of analysis is limited by the accuracy of the intensity measurements and that of the quantitative constants  $k'$ . When  $\sum X_j = 1$  does not hold, ratios of weight fractions can still be determined without adding a standard. For phases J and L in a multiphase mixture if  $k'_{JL}$  is known and  $I_{iJ}$  and  $I_{kL}$  are measured then (2) yields  $X_J/X_L$ .

To avoid the necessity of determining the constants  $k'$  for each analysis, de Wolff and Visser [27] proposed tabulating  $k'$  for the strongest line of the sample and a fixed standard. In addition to de Wolff and Visser, Swanson [28] and Scott [29] recommended  $\text{Al}_2\text{O}_3$  (corundum) as the reference standard. This particular ratio has become known as the Reference Intensity Ratio and is abbreviated as  $I/I_c$ . Values of  $I/I_c$  for about 1000 phases are published in the Powder Diffraction File [30]. The NBS Monograph 25 series [31] also gives  $I/I_c$  values. The majority of these  $I/I_c$  values were determined by direct application of the definition. That is, the ratio of the strongest line ( $I^{\text{rel}} = 100$ ) of the sample and of  $\alpha\text{-Al}_2\text{O}_3$  ( $I_{113}^{\text{rel}} = 100$ ) were measured for a 1:1 mixture by weight. Generally, ratios of peak height intensities are used as an approximation to ratios of integrated intensities. Providing that the two phases have approximately equal diffraction line breadths and that the two measured lines are within  $10^\circ 2\theta$  this approximation introduces an error of probably less than 5 percent in  $I/I_c$ . Errors due to preferred orientation, microabsorption and counting statistics further limit the accuracy of  $I/I_c$  values measured to between 5 and 10 percent. Unfortunately, error estimates were not reported until recently.

A new procedure has been adopted at NBS to reduce the errors due to preferred orientation and counting statistics and an error estimate is now given. A mixture of known weight fraction ratio  $X/X_c$  is prepared which yields approximately equal intensities of the strongest line of each phase within the constraint that  $0.20 < X/X_c < 5$  in order to avoid errors due to particle statistics. Multiple lines of the sample and corundum are measured. Lines are paired which are close in  $2\theta$  and the  $I/I_c$  value is calculated for each pair using:

$$I/I_c = \frac{xx}{yy} \cdot \frac{X_c}{X} \cdot \frac{I^{yy}}{I_c^{xx}}$$

where  $I^{yy}$  is the observed intensity of a sample line with relative intensity  $yy$  and  $I_c^{xx}$  is the observed intensity of a corundum line with relative intensity  $xx$ . The relative intensities  $yy$  and  $xx$  must have been determined independently in order that errors due to preferred orientation effects are reduced. An example of application of this approach is shown in table 5. In this case, the intensity of the 113 line of  $\alpha\text{-Al}_2\text{O}_3$  could not be measured due to an interfering line overlap. The average  $I/I_c$  is 5.18 with a rms deviation from the average of 0.12 (~2 percent). Repeating these measurements at another value of  $X/X_c$  would then be performed to further reduce systematic errors due to preferred orientation

in a given mounting and to reduce random errors due to counting statistics. Typical measurements yield an internal consistency ranging between approximately 2 and 10 percent. We expect to further reduce this by application of automation and calibration of secondary reference standards.

Table 5. Determination of I/I<sub>c</sub> for ZnO.  
(X/X<sub>c</sub> = 4.57)

hkl	ZnO		$\alpha\text{-Al}_2\text{O}_3$		I/I <sub>c</sub>
	I <sup>rel</sup>	I(cps)	hkl	I <sup>rel</sup>	
100	59	249	012	61	4.99
002	46	191	104	92	5.24
101	100	413	104	92	5.21
110	31	128	116	83	5.29

Because of the increasing accuracy in Reference Intensity Ratios, we need to be clearer as to what sample volume and experimental conditions are employed in the measurements. First, relative intensities and I/I<sub>c</sub> values should be representative of a constant diffracting volume of the sample. If variable slits are employed in the measurements which lead to changing sample volume, then conversion of the observed data is required. Second, the intensities should be recorded with CuK $\alpha$  radiation. Hubbard and Smith [32] have discussed conversion to alternate wavelengths and the effect of anomalous scattering. Finally, I/I<sub>c</sub> values should be corrected for polarization effects of a monochromator if one was used [32]. (Reference Intensity Ratios should not be published unless they meet these criteria).

Although the reference standard has been chosen to be  $\alpha\text{-Al}_2\text{O}_3$  this does not imply that  $\alpha\text{-Al}_2\text{O}_3$  must be used as the internal standard in application. For example, if another reference standard eliminated peak overlap, the quantitative constant k' of eq. (2) for analyte A relative to standard S is given by:

$$k'_{AS} = \frac{I_A}{I_S} = \frac{I_A/I_C}{I_S/I_C}$$

Thus, tabulating accurate Reference Intensity Ratios will enable rapid quantitative analysis by the internal standard method even when  $\alpha\text{-Al}_2\text{O}_3$  is not the appropriate standard. Further, if all the phases in the mixture are known and if  $\sum X_j = 1$  is a good approximation, then a standard need not be added. In both cases all that is required is accurate knowledge of Reference Intensity Ratios.

Besides derivation through experimental measurements, the Reference Intensity Ratio may be calculated along with a simulated powder pattern from knowledge of the atomic positions and thermal motion [33]. These simulated patterns are free from extinction and preferred orientation. The accuracy of calculated Reference Intensity Ratios is limited by the accuracy of the structural information of the analyte and of corundum. Errors in atomic positions and thermal parameters can easily introduce significant errors. As a general rule, a single crystal R-factor below 0.08 appears adequate. Typographical errors in structural data must be detected by careful analysis of the published structure. The atomic parameters of  $\alpha\text{-Al}_2\text{O}_3$  are well known but the aspherical charge density is not yet well known [34] limiting the accuracy in calculated Reference Intensity Ratios to about 5 percent. If the powder sample of the analyte exhibits extinction or microabsorption the error in the calculated I/Ic can be as large as 100 percent. Tests on the accuracy of analyses using I/Ic values from various sources have been reported previously [26,33]. When I/Ic values have been determined from the same sample from which the test mixtures have been prepared, one can expect errors to be less than  $\pm 1$  weight percent. When values from the PDF or from calculations are used, errors of 1 to 10 percent by weight are not uncommon. This indicates that preferred orientation, extinction and/or microabsorption were present in one or more of the measurements.

To improve the accuracy of routine quantitative analysis, NBS is in the process of certifying five intensity standards. The five materials (table 6) were selected to cover the range of linear absorption coefficients likely to be encountered in analysis. By approximately matching  $\mu$  of the standard to that of the analyte as well as grinding the sample to  $< 10 \mu\text{m}$ , microabsorption can be minimized [35].

Table 6. Proposed x-ray diffraction intensity standards.

Phase	$\mu(\text{cm}^{-1})$	I/Ic(calc)
$\alpha\text{-Al}_2\text{O}_3$	124.9	1.00
ZnO	288.0	5.43
TiO <sub>2</sub> (rutile)	549.5	3.44
Cr <sub>2</sub> O <sub>3</sub>	952.1	2.16
CeO <sub>2</sub>	2082.9	14.1

These five materials will be certified for relative intensities and Reference Intensity Ratios. Currently, measurements have yielded relative intensities reproducible to 2-4 percent without rotating the samples. When a sample rotator is employed, we expect to lower the uncertainty in the relative intensity of the strongest lines to 1-2 percent. These future SRM's will generally be used for rapid, fairly accurate quantitative analysis.

They can also be used to check instrumental response and to compare the performance of various instruments. The cell parameters of these materials have been determined with uncertainty of approximately  $\pm 5$  parts in  $10^5$ .

## 7. Summary

The x-ray powder diffraction Standard Reference Materials program at NBS will soon certify five intensity standards for use as internal standards for quantitative analysis. Coupled with tables of Reference Intensity Ratios they can provide quantitative information with minimal experimental effort. Following the intensity standards we plan to certify one or two large d-spacing standards to complement SRM 640 Si powder. Possibilities for other SRMs exist including a particle size standard and respirable quartz, cristobalite and tridymite. Which future standards will be prepared, if any, depends on input from the user community. Letters recommending needed standards are welcome.

## References

- [1] NBS Standard Reference Materials Catalog, NBS Special Publication 260, 1979-80 Edition, National Bureau of Standards, Washington, D.C. 20234.
- [2] Edmonds, J. W. and Henslee, W. W., Application of Guinier camera, microcomputer controlled film densitometry, and pattern search-match procedures to rapid routine x-ray powder diffraction analysis, *Advances in X-ray Analysis*, 22, 143-150 (Plenum Press, New York, 1979).
- [3] Klug, H. P. and Alexander, L. E., X-ray Diffraction Procedures, 2nd Edition (John Wiley & Sons, New York, 1974), p. 284.
- [4] Jenkins, R. private communication.
- [5] Klug, H. P. and Alexander, L. E., *ibid.*, p. 581.
- [6] Parrish, W., Results of the IUCr precision lattice-parameter project, *Acta. Cryst.* 13, 838-850 (1960).
- [7] Calvert, L. E., private communication.
- [8] Swanson, H. E., McMurdie, H. F., Morris, M. C., and Evans, E. H., Standard x-ray diffraction powder patterns, *Nat. Bur. Stand. U.S. Monograph* 25 Sec. 4, p. 3-4 (1966), National Bureau of Standard, Washington, D.C. 20234.
- [9] Hubbard, C. R., Swanson, H. E., and Mauer, F. A., A silicon powder diffraction standard reference material, *J. Appl. Cryst.* 8, 45-48 (1975).
- [10] Jenkins R. and Hubbard, C. R., A preliminary report on the design and results of the second round robin to evaluate search/match methods for qualitative powder diffractometry, *Advances in X-ray Analysis*, Vol. 22, p. 133-142 (Plenum Press, New York, 1979)

- [11] Powder Diffraction File Search Manual for Frequently Encountered Phases publication FEP-28, International Centre for Diffraction Data, 1601 Park Lane, Swarthmore, PA 19081.
- [12] Smith, D. K., private communication.
- [13] Jenkins, R. private communication.
- [14] Sonneveld, E. J. and Visser, J. W., Automatic collection of powder data from photographs, *J. Appl. Cryst.* 8, 1-7 (1975).
- [15] Brown, A., Optimal calibration curves for Guinier-type focusing cameras, *Advances in X-ray Analysis*, 21, 289 (Plenum Press, New York, 1978).
- [16] Parrish, W., private communication.
- [17] Suortti, P. IUCr commission on crystallographic apparatus-accuracy of structure factors from x-ray powder intensity measurements, *Acta Cryst.* A33, 1012 (1977).
- [18] Klug, H. P. and Alexander, L. E., *ibid.*, 531-562.
- [19] Zevin, L. S., A method of quantitative phase analysis without standards, *J. Appl. Cryst.* 10, 147 (1977).
- [20] Clark, N. H. and Preston, R. J., Dilution methods in quantitative x-ray diffraction analysis, *X-ray Spectrometry*, 3, 21 (1974).
- [21] Copeland, L. E. and Bragg, R. H., Quantitative x-ray diffraction analysis, *Anal. Chem.* 30, 196 (1958).
- [22] Bezjak, A. and Jelenic, I., The application of the doping method in quantitative x-ray diffraction analysis, *Croat. Chem. Acta*, 43, 193 (1971).
- [23] Popovic, S. and Grzeta-Plenkovic, G., The doping method in quantitative x-ray diffraction phase analysis, *J. Appl. Cryst.* 12, 205 (1979).
- [24] Klug, H. P. and Alexander, L. E., *ibid.* p. 549.
- [25] Bezjak, A., *Croat. Chem. Acta*. 33, 197 (1961) as referenced in Karlak, R. F. and Burnett, D. S., Quantitative phase analysis by x-ray diffraction, *Anal. Chem.* 38 1741 (1979).
- [26] Chung, F. H., Quantitative interpretation of x-ray diffraction patterns of mixtures-II, *J. Appl. Cryst.* 7, 526 (1974).
- [27] de Wolff, P. M. and Visser, J. W., Absolute intensities-outline of a recommended practice, Report #641.109 Technisch Physische Dienst T.N.O. (1964).
- [28] Swanson, H., private communication.
- [29] Scott, R. F., The case for a universal x-ray diffraction intensity scale, Fifty Years of Progress in Metallographic Techniques, ASTM STP 430, Am. Soc. Testing Matls., p. 201-203 (1968).
- [30] Powder Diffraction File, Alphabetical Index, Inorganic Compounds 1978 SMA-28, JCPDS, 1601 Park Lane, Swarthmore, PA 19081.
- [31] Standard X-ray Diffraction Powder Pattern, NBS Mongograph 25, Sec. 7-15, National Bureau of Standards, Washington, D.C. 20234 (1969-1978).
- [32] Hubbard, C. R. and Smith, D. K., Experimental and calculated standards for quantitative analysis by powder diffraction, *Advances in X-ray Analysis*, 20, 27 (1977).

- [33] Hubbard, C. R., Evans, E. H., and Smith, D. K., The reference intensity ratio,  $I/I_0$  for computer simulated powder patterns, J. Appl. Cryst. 9, 169 (1976).
- [34] Calvert, L. D., private communication.
- [35] Brindley, G. W., The effect of grain or particle size on x-ray reflections from mixed powders and alloys..., Phil. Mag. 36, 347 (1945).

#### Discussion

Comment (Mortier): In your abstract, zeolite A is mentioned as a possible standard. Generally, for all zeolite types, there are a number of problems such as the Si:Al ratio the extent of the ion exchange and the proton content, and the crater content which depends on the humidity of the environment. All of these factors do influence the unit cell parameters in a rather sensitive way. If mixed with salts, ion exchange is probabl

Response (Hubbard): Comments received during and following the meeting indicate that zeolites, thallos salts and  $As_2O_3$  would be poor choices for an SRM for a variety of reasons. I do not intend to consider these materials any further.

## STRUCTURE ANALYSIS FROM GUINIER FILM DATA

P.-E. Werner

Department of Structural Chemistry  
Arrhenius Laboratory, University of Stockholm  
Fack S-106 91 Stockholm, Sweden

Experiences from more than ten investigations at this Institute during the last four years have shown that structures containing up to about 50 structural parameters can be successfully studied by use of Guinier-Hägg powder diffraction data. Photographs have been taken in a focusing camera of the Guinier-Hägg type, with strictly monochromatized  $\text{CuK}\alpha_1$  radiation, single coated films and internal standard technique. A SAAB drum film scanner [1] and a software system for Guinier films [2] have been used to extract the intensity data available on the photographs. The basic principles for determination of peak positions from transmission data (-not from optical densities-), derivation of background curves, correction procedures for non-linearity versus exposure and a method for parabolic least-squares fit of internal standard lines are described in reference [2].

The drum film scanner system will now be replaced by a minicomputer controlled scanner with semiconductor techniques and an improved software (to be published). An alphanumeric display will be used not only to control the instrument by the minicomputer, but also for direct transfer of data to a large-scale computer, where the magnetic tape version of the powder diffraction data base is available.

The Rietveld procedure [3] of profile refinement has made it possible to utilize all of the information present in a diffraction pattern. The original Rietveld program was written for single phase analysis from neutron diffraction data. The program has been revised in two steps the first of which comprised the application of profile analysis to x-ray diffraction Guinier data [4] and the second the introduction of a possibility to refine two simultaneously occurring phases in a powder pattern [5]. Examples of structure determinations from Guinier-Hägg diffraction data are given in the references [6-9].

The Rietveld procedure is primarily a refinement method, but it can be very helpful in the later steps of a structure determination as it provides the user with the possibility to calculate the distribution of the observed intensities and subsequently to find light scattering positions from Fourier maps. On the other hand, the structural information in the high angle region cannot be extracted unless the indexing problem can be solved and the Patterson function can be calculated from a low angle region with well resolved diffraction peaks (see [6] and [7]). The most important advantage of using a focusing Guinier-Hägg camera when dealing with complex structures is probably the good resolution of the diffraction lines.

<sup>1</sup> Figures in brackets indicate the literature references at the end of this paper.

The accuracy in peak positions needed for solving an indexing problem can be discussed from the minimum condition that the De Wolff figure of merit,  $M_{20}$ , should be larger than 10 for a physically plausible indexing [10]. The following approximate relation can be derived for the maximum verifiable unit cell volume for orthorhombic and lower symmetries:

$$V = \frac{3 \cdot m \cdot d_{20}^3}{4 \cdot \pi \cdot |\overline{\Delta 2\theta}|}$$

where  $m$  is the multiplicity factor for a general reflection,  $d_{20}$  is the  $d$ -value for the 20th observed line and  $|\overline{\Delta 2\theta}|$  is the average discrepancy between observed and calculated  $2\theta$  values for the first twenty lines [11]. In table 1,  $|\overline{\Delta 2\theta}|$ -values needed for solving monoclinic ( $m = 4$ ) indexing problems are calculated for some unit cell volumes and  $d_{20}$ -values.

Table 1.  
MAXIMUM VERIFIABLE UNIT CELL VOLUME  $V$ .

		$d_{20}(\text{Å})$			
		3.5	3.0	2.5	2.0
		$ \overline{\Delta 2\theta}  (^\circ)$ ( $m = 4$ )			
$V(\text{Å}^3)$	100	0.41	0.26	0.15	0.08
	500	0.08	0.05	0.03	0.015
	1000	0.041	0.026	0.015	0.008
	2000	0.021	0.013	0.008	0.004
	3000	0.014	0.009	0.005	0.0025

The  $F$ -index recently proposed by Smith and Synder [12] is probably superior to De Wolff's  $M$ -index for ranking patterns, but it has a disadvantage when estimating the plausibility of a found unit cell. The fact that the  $M$ -index increases systematically with symmetry is not a disadvantage. A cubic trial indexing of a powder pattern is more likely to be correct than a triclinic, the fraction of observed lines and accuracy being equal.

The following statements are discussed and illustrated by the indexing of three aluminum-phosphate minerals:

1. The volume of an unknown unit cell can usually not be estimated from the expression  $V = \text{const} \cdot d_{20}^3$  [13] if  $V > 1000 \text{ \AA}^3$ .
2. Although  $|\overline{\Delta 2\theta}|$  as a function of  $2\theta$  is relatively constant, a small increase with  $2\theta$  is usually observed, if the unit cell is large, and the diffraction data are accurate ( $|\overline{\Delta 2\theta}| < 0.01^\circ$ ; see fig. 1). This can be explained as overlap effects between observed lines in the high angle region. For low quality data overlap effects between observed and calculated lines are often dominating and  $|\overline{\Delta 2\theta}|$  decreases with  $2\theta$ .

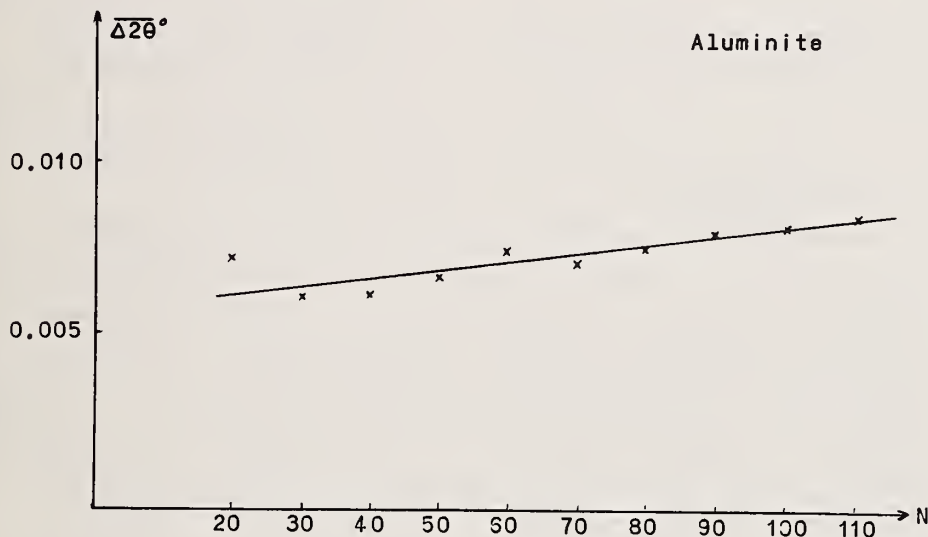


Figure 1.  $|\overline{\Delta 2\theta}|$  as function of the number of observed lines for Aluminite.

3. For large unit cells the fraction of observed lines decreases strongly with  $2\theta$ . The ready  $M_{30}$  (or  $F_{30}$ ) cannot be used to prove the correctness of the indexing of the meta-aluminite pattern (cf. table 2). It is therefore recommended that  $M_{20}$  is used in indexing programs. It is also concluded that the use of  $F_N$  (or  $M_N$ ) as data quality index can be misleading unless  $N$  is small (cf. table 2 and fig. 2).

4. The aluminite and meta-aluminite patterns have both been indexed by a trial-and-error indexing program, TREOR, written by the present author [14]. The program has also been a necessary tool for the studies [6] and [7]. All indexing programs gain in efficiency with the data quality. This is specially true for a trial-and-error program which is extremely dependent on the parameters derived from the first lines in a pattern. A multitude of non-

systematic extinctions (i.e. large unit cells) will affect the relative efficiency of various indexing programs differently. Provided that the data are accurate, relatively large unit cells may sometimes be found by trial-and-error indexing.

As an extreme example the indexing of halotrychite is discussed. Although the unit cell volume is above  $3000 \text{ \AA}^3$ , a value of  $M_{20} = 15$  was obtained for the unit cell dimensions given in table 2. If the space group is assumed to  $P2_1/c$  the value of  $M_{20}$  is increased to 18. The a-axis  $20.519 \text{ \AA}$  given in the powder diffraction file, number 26-1425, cannot be verified from the new data or from the data given in the powder file ( $M_{20} < 3$ ).

5. As a general experience of the Guinier-Hägg film measuring system described in reference [2] it can be stated that it is rare that  $|\overline{\Delta 2\theta}|$  is above  $0.01^\circ$  for the first twenty lines observed (cf. table 2). The resolution of the system is also illustrated by the fact that the number of resolved peaks in the aluminite pattern is 110, all indexed, whereas the number of d-values given in the powder diffraction file, number 8-55, is only 30.

It should be pointed out that only peak positions have been used in the calculations reported in table 2. For substances with known structures a least-squares fit of profile functions, such as the Rietveld procedure, can be used to further reduce  $|\overline{\Delta 2\theta}|$  and determine more accurate unit cell parameters.

Two methods for quantitative analysis from Guinier data have been studied. The first one is based on the extension of the Rietveld program to treat two-component problems and is described in reference [5]. The second method is based on integrated intensities of any one line from two different amounts of samples of the same material. The ratio of the absorption factors is determined from the masses and the integrated intensities. The absorption conditions are analyzed by the theoretical expression derived by Sas and De Wolff [15] for absorption in a Guinier camera. No internal standard need be added to the samples. The method has been tested on total sample amounts in the range  $0.1 - 1.5 \text{ mg}$  [16].

Table 2.

## INDEXED ALUMINUM SULPHATE MINERALS.

- I. Meta-aluminite,  $\text{Al}_2\text{SO}_4(\text{OH})_4 \cdot 5\text{H}_2\text{O}$   
 $a = 7.930(3) \text{ \AA}$ ,  $b = 16.879(4) \text{ \AA}$ ,  $c = 7.353(5) \text{ \AA}$ ,  $\beta = 106.74(7)^\circ$   
 $V = 942.4 \text{ \AA}^3$ . Ref. [11].
- II. Aluminite,  $\text{Al}_2\text{SO}_4(\text{OH})_4 \cdot 8\text{H}_2\text{O}$   
 $a = 11.444(2) \text{ \AA}$ ,  $b = 15.849(1) \text{ \AA}$ ,  $c = 7.4397(7) \text{ \AA}$ ,  $\beta = 106.85(1)^\circ$   
 $V = 1291.5 \text{ \AA}^3$ . Ref. [11]
- III. Halotrychite,  $\text{FeAl}_2(\text{SO}_4)_4 \cdot 22\text{H}_2\text{O}$   
 $a = 21.287(9) \text{ \AA}$ ,  $b = 24.291(5) \text{ \AA}$ ,  $c = 6.195(2) \text{ \AA}$ ,  $\beta = 100.27(2)^\circ$   
 $V = 3151.8 \text{ \AA}^3$ .

Compound	N	$M_N$	$F_N$	$N_{\text{poss}}$	$ \overline{\Delta 2\theta}  (^\circ)$
I	20	17	28	75	0.0097
	30	6	9	226	0.0149
	36	5	7	349	0.0144
II	20	29	67	41	0.0073
	30	27	72	68	0.0061
	110	5	13	1023	0.0084
III	20	15	35	98	0.006
	30	12	33	158	0.006

N = number of observed lines,  $N_{\text{poss}}$  = number of independent possible lines up to the Nth observed,  $M_N$  = De Wolff figure of merit [10],  $F_N$  = F-index [12],  $|\overline{\Delta 2\theta}|$  = average absolute discrepancy between observed and calculated  $2\theta$  values.

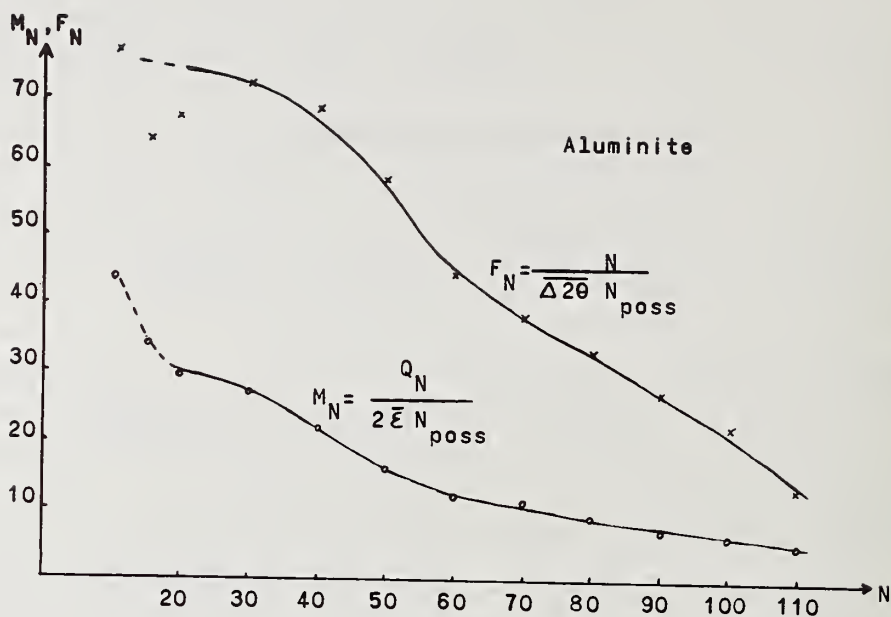


Figure 2. The figure of merits, F and M, as functions of the number of observed lines for Aluminite.

#### References

- [1] Abrahamsson, S., J. Sci. Instrum. 43, 931-933 (1966).
- [2] Malmros, G. and Werner, P. -E., Acta Chem. Scand. 27, 493-502 (1973).
- [3] Rietveld, H. M., J. Appl. Cryst. 2, 65-71 (1969).
- [4] Malmros, G. and Thomas, J. O., J. Appl. Cryst. 10, 7-11 (1977).
- [5] Werner, P. -E., Salomé, S., Malmros, G. and Thomas, J. O., J. Appl. Cryst. 12, 107-109 (1979).
- [6] Berg, J. -E. and Werner, P. -E., Z. Krist. 145, 310-320 (1977).
- [7] Waltersson, K., Werner, P. -E., and Wilhelmi, K. -A., Cryst. Struct. Comm. 6, 225-230 (1977).
- [8] Waltersson, K., Werner, P. -E. and Wilhelmi, K. -A., Cryst. Struct. Comm. 6, 231-235 (1977).
- [9] Marinder, B. -O., Chemica Scripta, 11, 97-101 (1977).
- [10] De Wolff, P. M., J. Appl. Cryst. 1, 108-113 (1968).
- [11] Farkas, L. and Werner, P. -E., Z. Krist. (to be published).
- [12] Smith, G. S. and Snyder, R. L., J. Appl. Cryst. 12, 60-65 (1979).

- [ ] Smith, G. S., J. Appl. Cryst. 10, 252-255 (1977).
- [ ] Werner, P. -E., Fortran IV program. Available on request (unpublished) (1975).
- [ ] Sas, W. H. and De Wolff, P. M., Acta Cryst. 21, 826-827 (1966).
- [ ] Werner, P. -E. and Ekström, T. (to be published).



OPTIMAL DEGREE OF AUTOMATION IN QUANTITATIVE  
X-RAY DIFFRACTION PHASE ANALYSIS

A. Griger

ALUTERV-FKI

R and D Centre of the Hungarian Aluminium  
Corporation, Budapest

During the development of an automatized hardware and software system for the quantitative x-ray diffraction phase analysis of multicomponent powder mixtures [1] the question emerged whether total automation should be aimed in all cases or not. For hydrothermal borehole samples P. Johnson [2] gave a definitely negative answer to this question. Using profile fitting evaluation techniques W. Parrish and T. C. Huang [3] assert the feasibility of straightforward complete computerization.

In our opinion two basic tasks should be differentiated:

- (1) analysis of powder mixtures of 2-3 phases with well defined real structures, producing no or little overlapping of the peaks,
- (2) analysis of powder mixtures of more than 3-4 phases exhibiting structural variability and causing serious overlappings.

The consequences of structural variability are variable line breadths, shifts of the reflections, changes in the relative intensities, uncertainties of the intensity conversion factors. Some pitfalls of unattended computer interpretation of powder patterns in the (2) group will be demonstrated and thereby the statement supported that interactive control is inevitable at some stages of data-processing corresponding to these materials.

The possibility of entirely computerized evaluation seems to be restricted to group (1), while optimal proportions between automatic and analyst-checked operations, respectively, must be established for the interpretations of the patterns relevant to group (2).

References:

- [1] Bárdossy, Gy., et al., to be published in Amer. Min. (1979).
- [2] Johnson, P. D., Adv. X-ray Anal. 21 (1977).
- [3] Parrish, W. and Huang, T. C., Conf. Appl. Cryst., Kozubnik (1978).



STANDARDS FOR THE PUBLICATION OF POWDER PATTERNS: THE  
AMERICAN CRYSTALLOGRAPHIC ASSOCIATION SUBCOMMITTEE'S FINAL REPORT

L. D. Calvert, J. L. Flippen-Anderson, C. R. Hubbard, Q. C. Johnson,  
P. G. Lenhart, M. C. Nichols, W. Parrish, D. K. Smith, G. S. Smith,  
R. L. Snyder, and R. A. Young

The American Crystallographic Association

A subcommittee of the American Crystallographic Association (ACA) was formed to recommend some guidelines the use of which could improve the overall quality of published powder diffraction data. An analysis of the Powder Diffraction File shows that many of the well-known techniques for obtaining good quality data are often not being applied, and hence there is a need for the establishment of publication standards. A major recommendation from this subcommittee is the use of a standard data-form at the author/referee level of publication. The proposed data-form is divided into five sections: sample characterization, technique, unit cell data, references, and the powder data. The information requested in these five sections represents what, in most cases, the referee and editor can reasonably expect of experimenters seeking to publish their powder data. An example of a filled-out form is shown, and instructions for completing the form are given. Another recommendation is that the ACA request that the International Union of Crystallography consider implementing these recommendations in all IUCr journals.

### 1. Introduction

Numerous analytical methods can supply elemental chemical information. What distinguishes the diffraction method is its unique capability to characterize crystalline phases. Undoubtedly, the most widely used technique in this area is x-ray powder diffraction. In this technique, diffraction data from an unknown sample are compared with a reference set of powder patterns compiled from the literature. Thus, reference patterns prepared by other crystallographers play an integral part in a typical analysis.

Regardless of its quality, it is possible for any published pattern to become a reference pattern and be used world-wide for identification purposes. If the quality is good,

the pattern is useful; if the quality is poor, the pattern can become a hindrance. In the future, this problem will become accentuated because the increasing availability and use of small computers will produce excellent-quality data for the user; then the quality of the reference patterns will become even more a limiting factor in the analysis. The situation is not satisfactory now and is expected to become worse unless corrective action is taken. Guidelines for improving the overall quality of published powder patterns are therefore deemed necessary.

In August 1977, the American Crystallographic Association (ACA), formed a subcommittee under the sponsorship of the Apparatus and Standards Committee and the Crystallographic Committee, to recommend standards for the publication of powder patterns. This subcommittee prepared a first report which was presented at the University of Oklahoma ACA meeting, March 1978. That report was modified to incorporate suggestions received during and after that meeting. A second presentation was made at the International Union of Crystallography (IUCr) meeting in Warsaw, Poland, August 1978. At about the same time, the modified report was mailed to ~150 editors of journals known to publish powder patterns. Suggestions received from those two sources were incorporated into this third and final report.

## 2. Inaccuracy of Powder-Diffraction Data

The problem is basically one of minimizing both errors in recording powder diffraction data and errors and noise introduced during the publication and archiving of the data. One might better understand these errors if we compare a powder pattern to an electromagnetic signal. In communication, a pure signal is contaminated by noise at its source and is further degraded or distorted in transmission to the point where the receiver may not recognize it. Likewise, an experimental powder pattern is contaminated by such things as instrumental errors and is further distorted in the processes of publication and archiving to the point where an analyst may not recognize it as being the same as the pattern from which it was derived.

If one works with average-quality standards having considerable noise, it is generally more difficult to identify an unknown, especially if the unknown is a mixture of several phases. This might be comparable to listening to a low-fidelity recording (e.g., an early Caruso record) on a poor AM radio during an electrical storm and trying to pick out specific words. While the communications industry has spent a great amount of research and development effort to minimize error/noise/distortion in broadcasting, transmission, and reception, it might be fair to say the powder diffraction community has concentrated primarily on the training of skillful receivers (analysts).

The ease of identifying an unknown material from its powder pattern can be related to the quality of the standards (fig. 1). While it is difficult to quantify figure 1, it is possible to assess just how significant the problem is today in powder identification, almost every analyst would agree that accurate data for both standard and unknown greatly simplify a

identification. In addition, computer search techniques using the existing data base have reached the point where further advances probably depend on higher-quality standards. Indeed, some investigators prepare their own reference-pattern libraries to enhance the ease of identification [1]<sup>1</sup>. This approach is, in general, an inefficient way for the powder diffraction community as a whole to operate.

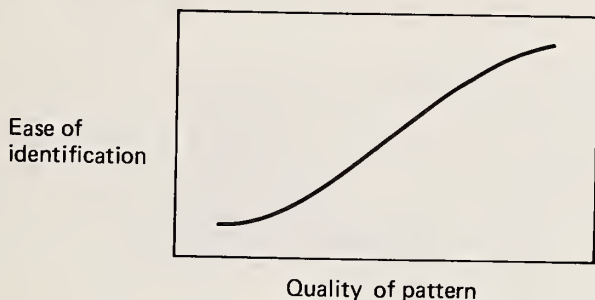


Figure 1. Schematic dependency of the ease of identification of an unknown material from its powder pattern vs quality of the pattern.

The improvement of powder diffraction analysis as a routine analytical capability has been slow. On the other hand, there have been dramatic changes in the speed, accuracy, and economy of other characterization methods during the last two decades. As examples from methods employing x-rays, x-ray fluorescence has been profoundly changed by energy-dispersive systems and structure determination by single-crystal diffraction has been equally affected by automation and direct methods. We are now at the threshold of major change in powder identification by x-rays; this change is being brought about by new techniques and instrumentation. As the signal from an unknown powder is improved by powerful methods of data processing [2-5] and as comprehensive search/matching [1,6,7] by low-cost computers becomes practical in the diffraction laboratory, the quality of the reference patterns will become the limiting factor. If the quality of both the unknown and the reference diffraction data can then be improved, the overall process can become so much more efficient that in normal cases it should be possible to characterize the phase of an unknown crystalline material in less than 10 minutes with powder diffraction methods.

How can we minimize the noise introduced into reference standards during the process of duplication and archiving? The problem is not technical--the methods for averting noise and distortion are well established and are practiced by a number of laboratories. Reports by Bliss [8] and Kennard, et al. [9] have already discussed the requirements of the publication and archiving processes. Basically, authors, editors, referees, and data compilers need an increased awareness and consistent use of already established technique.

Figures in brackets indicate the literature references at the end of this paper.

### 3. Problems with the Powder Diffraction File

A recent study [10] of the Powder Diffraction File (PDF), as distributed on magnetic tape by JCPDS-International Centre for Diffraction Data<sup>2</sup>, has revealed several points of interest to our discussion. The summary, which follows below, applies to the 20428 active inorganic patterns in sets 1 through 26 of the PDF and to those 1638 cubic and 2 triclinic patterns in sets 1 through 24, which could be indexed using the reported lattice parameters<sup>3</sup>.

The problems encountered with data on the PDF tape fall into two categories: those due to the archiving procedures and those inherent in the original published data. The less serious topic of archiving procedures will be discussed first. These problems are understandable in terms of historical development of the PDF and the uses for which it was intended.

#### 3.1. Problems in archiving procedures

##### 3.1.1. Incompleteness of the data on the magnetic tape

Each pattern on the JCPDS magnetic tape is coded with the d-I values (i.e., values of  $d$  and intensity), name, formula, quality mark, and crystal-system indicator. To date, the crystal-system indicator has only been coded on 16 percent of the patterns. The absence of space-group, lattice-parameter, and the other information that is contained on the published PDF cards severely limits the use of the tape as a research tool, especially as a tool for information retrieval.

##### 3.1.2. Incompleteness of individual patterns

Figure 2 shows the distribution of the number of d-I pairs given for each pattern in sets 1-26 of the PDF. The spikes near 20, 40, 60, and 80 pairs reflect the 20-line-per-column format of a PDF card image. These spikes indicate that many patterns have been truncated to fit the published card format. These truncations probably have little effect on phase identification, however, if the pattern is otherwise complete and is sufficiently accurate at the point of truncation.

##### 3.1.3. Rounded d values on the magnetic tape

All  $d$  values on the computer data base have been rounded to three places after the decimal. Figure 3 shows that for high-angle reflections this can cause an error of over

---

<sup>2</sup>1601 Park Lane, Swarthmore, PA, 19081, USA.

<sup>3</sup>This lattice-parameter data base was originally prepared by G. G. Johnson, Jr., of Pennsylvania State University and was updated by M. C. Nichols and B. Pimentel of Sandia Laboratories, Livermore.

$2\theta$ . Thus, the derived  $d$  values are not an adequate substitute for the experimentally measured  $2\theta$ 's, and precision is lost.

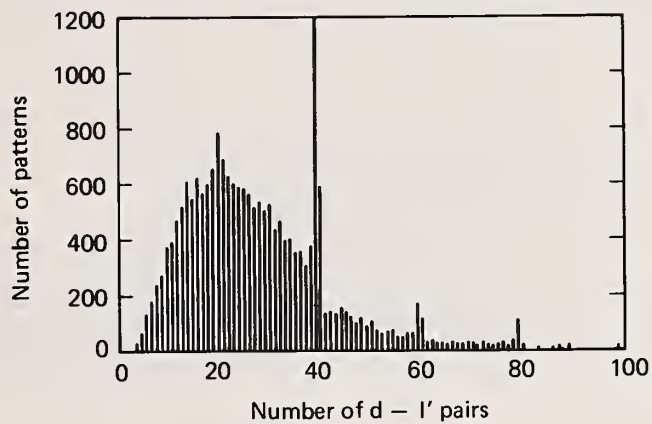


Figure 2. Distribution of  $d-l$  pairs for sets 1-26 of the Powder Diffraction File.

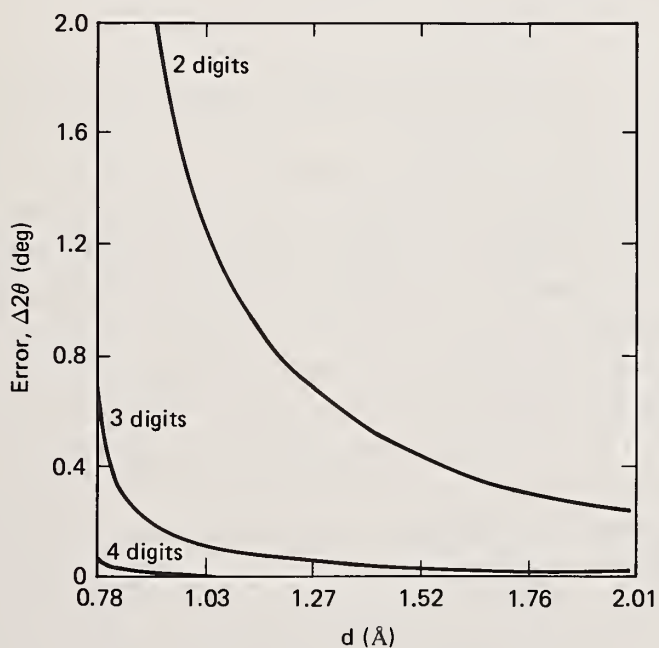


Figure 3. The error resulting from rounding off  $d$  values to four, three, and two digits after the decimal.

### 3.1.4. Editorial artifacts

Figure 4 shows the average error in  $2\theta$  up to a particular line number versus line number for the indexable cubic patterns in the PDF. The fall-off and steadying out of values above line number 40 indicate that only better-than-average data continue onto a second PDF card.

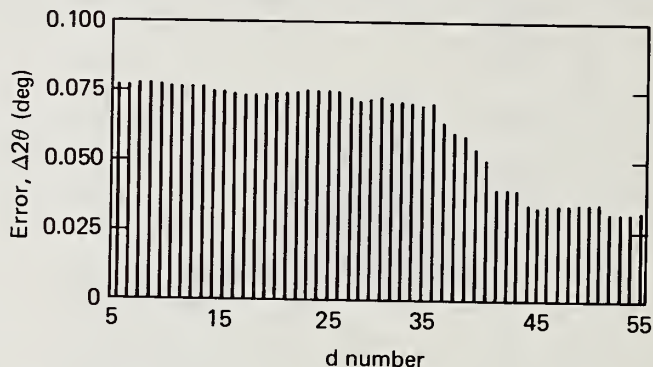


Figure 4. The effect of the 40-line PDF card format on the quality of data reported (PDF cubic patterns). Authors who measure more accurate data are more likely to continue their listing on to a second card.

### 3.1.5. Nonquantitative intensity notations

In the current version of the PDF on magnetic tape, the intensity notations,  $I < 1$  and  $I \ll 1$ , are transcribed as unity; in previous tapes these values were set to zero. These approximations were made because the symbols,  $< 1$  and  $\ll 1$  are difficult to handle in a computer format. These symbols, furthermore, are not quantitative. The present scale of 1 - 100 should be expanded so that these nonquantitative notations are no longer necessary. A recommended procedure (see below) is to report the intensities on a scale of 0 - 100.

Because the computer tape was originally compiled for the computer generation of magnetic search-manuals, which only require d's to three significant figures, it is not surprising that the current tape is not well suited for computer-assisted research. The JCPDS is currently investigating the creation of a complete data base, which will eliminate most of the above difficulties.

## 3.2. Problems with published data

### 3.2.1. Rounding or truncation of intensities

Figure 5 shows the distribution of the intensities for the cubic PDF patterns. This shows that the measured intensities of most patterns were rounded or truncated to ten parts in 100. Fewer patterns have been rounded to one part in 20. In general, the only attempts at accuracy are made for intensities between 0 and 20.

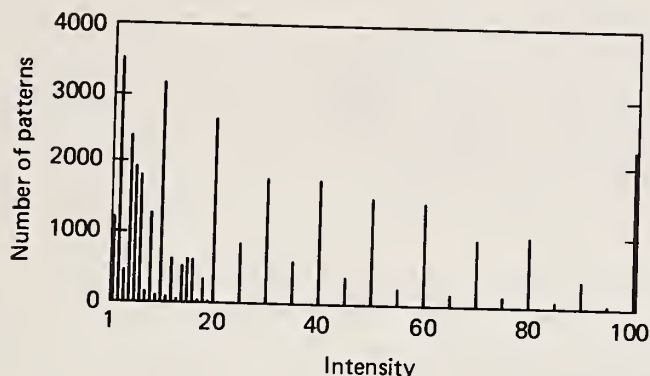


Figure 5. Distribution of reported intensities in the PDF cubic data shows significant rounding of intensities.

### 3.2.2. Inaccuracies of the intensities

Preferred orientation in the sample and conventional estimation of intensity by visual techniques are two main contributors to inaccuracies in published intensities. Diffraction techniques have developed to a level such that visual estimates of film intensities should be published in most cases. Except in rare cases, the nonnumerical descriptors (very strong, medium, very weak) have also outgrown their usefulness. (Paradoxically, some patterns using these descriptors contain very accurately measured line positions!) Preferred orientation, perhaps a more serious problem, can be minimized by special techniques [11,12]. (Most, if not all, of these techniques require careful comminution of the powder.) Comparison of the reported PDF intensities with calculated values shows [11] orientation and/or particle statistics effects which, in the best cases, are on the order of 4 to 8 percent. In the worst cases, these effects cause intensity discrepancies of several hundred percent.

### 3.2.3. Incompleteness of d's

An analysis of the pattern-completeness factor ( $N_{\text{obs}}/N_{\text{poss}}$  = number of lines observed/number that possibly could be observed for a particular space group) shows clearly that many authors only report the d spacings of the most intense reflections for a pattern. This fact becomes more noticeable as the total number of lines present increases with decreasing symmetry.

### 3.2.4. Inaccuracies of d's

We computed the average  $|\Delta 2\theta|$  ( $2\theta_{\text{obs}} - 2\theta_{\text{calc}}$ ) for each of the 1638 cubic patterns in set 1 to 24, using the reported lattice parameters. We found the average value of  $|\Delta 2\theta|$

for all these cubic patterns is  $0.091^\circ$ . For just the cubic patterns published by the National Bureau of Standards, the average value of  $|\Delta 2\theta|$  is  $0.015^\circ$ . Thus, although the technology for producing accurate  $d$  values has existed for over 20 years, it is not in routine use. A quantitative figure of merit,  $F_N$ , for evaluating powder patterns has been proposed [13] and has the form:

$$F_N = \frac{1}{|\Delta 2\theta|} \frac{N_{\text{obs}}}{N_{\text{poss}}}$$

This figure of merit combines both the accuracy of the line measurements and the pattern completeness factor mentioned above. It allows a quantitative estimate of the metric of a powder diffraction pattern. Figure 6 shows the distribution of  $F_N$  values for the PDF cubic patterns and the NBS cubic patterns. This function clearly allows a quantitative comparison of the quality of powder diffraction patterns. The use of a quantitative assessment of powder patterns is not new [13,14,15]. We only stress the need for routine use of such a measure.

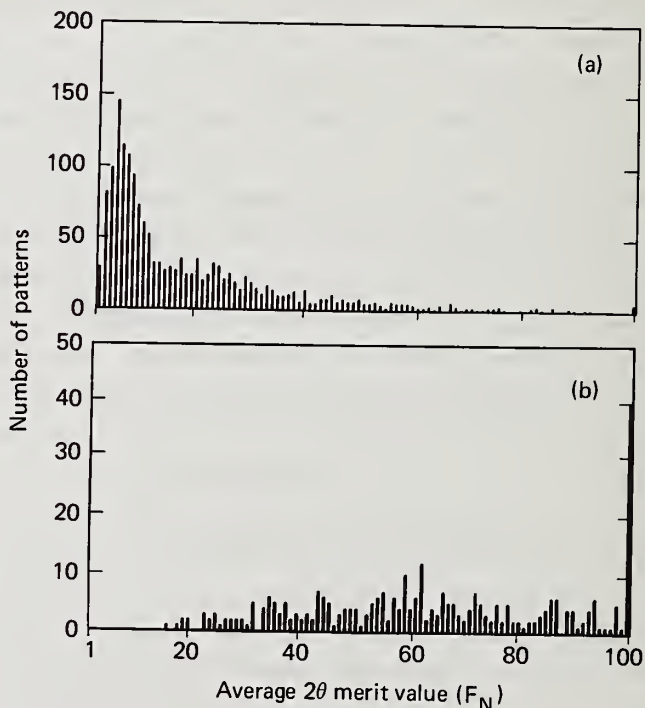


Figure 6. Quality of powder diffraction standards, (a) PDF cubic data and (b) NBS cubic data. Note that (a) includes (b), and that all patterns having  $F_N \geq 100$  are put in the  $F_N = 100$  entry.

The problems shown above indicate a need for the establishment of uniform publication standards for powder diffraction data. In the sister field of single-crystal structure determinations, there has been very marked progress over the past 20 years: experimental and computational techniques (e.g., automated diffractometers, computerized refinements, and, in many cases, computerized determinations) which were readily adopted for widespread use, the mandatory reporting of an acceptable figure of merit (the R factor), and documentation of the experimental and calculational procedures so that other investigators could, if necessary, repeat the experiment and verify the results. Such documentation is required by practically all leading journals publishing structure determinations and, as a result, is by now almost completely standardized. Today, the great bulk of published single-crystal structure determinations have an R value less than 10 percent. We assert that the same sort of "field-wide" standards can and should be achieved in the area of powder diffraction.

#### 4. Recommendations

1. We recommend the establishment of publication standards for powder diffraction data through the use of a standard data-form. We have designed such a form to be used at the author-referee level to ensure that published data are of good quality.

An example of a filled-out form is shown in Appendix A. Suggestions for filling out the data-form are given in Appendix B.

The data-form itself is divided into five sections: Sample Characterization, Technique, Unit Cell Data, References, and the Powder Data. Items on the form that are considered essential documentation are indicated by bold-face print. The other items are highly desirable information; however, it is recognized that some experimental procedures will not yield data on some of these items. Hence, omissions of data for these items should not of themselves preclude publication of the powder data.

This list of items is not all-inclusive: an all-inclusive list might be longer than the paper accompanying it. But this list does include the data most important to today's instrumentation. It represents, we believe, what the referee and editor can reasonably expect of experimenters seeking to publish their data. However, we do not intend that the list be used to stifle either new techniques in powder diffraction or the publication of powder data obtained under difficult conditions, e.g., low and high temperatures, high pressure, ultra-small quantities of materials.

We have several specific recommendations pertaining to the reporting, dissemination, and archiving of powder diffraction data:

- (a) The published powder pattern should be as complete as possible; for example, it should include weak as well as strong diffraction lines. An element of doubt often arises in phase identification when the observed strong diffraction lines match those of a particular reference pattern, but some weak lines are observed that are not listed in the reference pattern. Complete reference patterns would be a benefit in these cases and generally would make identification easier. Furthermore, the ease of computer-indexing of powder patterns depends, in most

cases, on the accuracy and completeness of the data. Ordinarily, 40 lines provide a ready characterization of the material. In the absence of 40 lines, the data should extend to (at least)  $100^\circ 2\theta$  ( $\text{Cu K}\alpha$  radiation).

- (b) Researchers should report the experimentally observed  $2\theta$  values, in degrees, corrected for systematic instrumental errors. The  $d$  values are usually not an adequate substitute for the primary data, the  $2\theta$  values. Reporting the  $2\theta$ 's does not distort information, but reporting the derived quantities,  $d$ 's and  $Q$ 's ( $1/d^2$ ), usually does. For example, even the  $d$  values reported by NBS (for the example in Appendix A) do not match exactly their observed  $2\theta$  values. We have not added additional significant figures to the reported  $d$  values (in Appendix A) to accurately accomplish an otherwise simple transformation:  $2\theta$ 's to  $d$ 's. Hence, we believe that the magnetic-tape version of the PDF should contain  $2\theta$  values which can be readily converted to  $d$ 's, if necessary, by a user program. (Authors using the magnetic-tape version, would have computer capability.) The PDF flash cards, on the other hand, should probably continue to list  $d$  values.
- (c) Intensities should be reported numerically, and on a scale from 0 to 100. This will avoid the nonquantitative notations  $I < 1$  and  $I \ll 1$  that sometimes occur with the present scale of 1-100. For example, 0.7 might be used instead of 1. This new scale will require no additional digits. The recommended scale does not preclude the use of a scale from 1-10 or 1-100, when appropriate, nor should it be understood to imply an increased accuracy for  $I < 1$ .
- (d) The reproducibility of the measured  $2\theta$ 's and  $I$ 's should be indicated. These data should be obtained by multiple mountings of the sample material.
- (e) Indexing of the powder diffraction data should be required for all but the very simple and best-defended cases. Without indexing, there is little proof that the diffraction pattern is for a single phase. Patterns can often be automatically indexed by using appropriate computer codes [4,5,16]. Authors should report a figure of merit based on accuracy of the  $2\theta$  measurements and completeness of their data. As mentioned above, a figure of merit has been proposed for this purpose.
- (f) Information concerning line breadth of the sample should be supplied. This could be full-width at half-maximum (FWHM) of a resolved  $\text{K}\alpha_1$  line in the region  $30$ - $60^\circ 2\theta$ .
- (g) Additional information of value to future users should be supplied. Such data could be standard deviations, Chemical Abstracts Service Registry number, Crystal Data index number, etc.

We believe the use of a standard data-form has a number of benefits including:

- This data-form can be used as a checklist. Authors can use the form to ensure the necessary characterization of their data. Also, familiarity with the standard form will encourage authors to record complete information on their measurements.

- The completeness of the experimental data will be easy to evaluate. Because information pertaining to the experimentation will be collected in one place in the manuscript, referees or journal editors will be able to readily judge the future usefulness of the contribution. Moreover, an editor could send the powder data to an expert in powder diffraction for refereeing and send the rest of the manuscript to another reviewer.
- The data form could be recast into a camera-ready format for direct printing in the journals. In this way, data-base managers could receive the powder data exactly as sent by the authors<sup>4</sup>.

2. This subcommittee has also given some thought as to what constitutes publishable powder diffraction data. We believe that to justify being published, powder diffraction data must be potentially useful to someone else and must constitute in some way an original contribution to the literature. To constitute an original contribution, the data must be first published for a well-characterized phase, must be a significant correction to or improvement on published data, or must relate to the phase in a previously uncharacterized condition, e.g., at elevated temperatures or pressure. A powder pattern calculated from single-crystal structure data does not in itself meet the criterion of originality. Such data, we hope, will continue to be contributed directly to the data-base managers under guidelines being established by a JCPDS committee.

3. To help gain acceptance for publication standards within the world-wide powder diffraction community, we recommend that the ACA request the International Union of Crystallography (IUCr), through the Commission on Journals, to now consider implementation of these recommendations in all IUCr journals. As a first step in that process, the Commission on Journals may elect to refer these recommendations to the Commission on Crystallographic Data for review and approval. It is envisioned that a mutually acceptable version could be included in Notes for Authors and in the Handbook for Co-Editors. If the IUCr journals enact publication standards in the near future, other journals will in time follow that lead and the quality of published powder diffraction data will improve.

---

We wish to thank our many colleagues who have taken the time to provide helpful comments during the course of this subcommittee's activities.

#### References

- [1] Frevel, L. K., Adams, C. E., and Ruhberg, L. R., A fast search-match program for powder diffraction analysis, *J. Appl. Cryst.* 9, 199-204 (1976).

---

JCPDS has recently offered to referee powder data and to receive powder data directly if they are not to be published by the journal.

- [2] Parrish, W., Huang, T. C., and Ayers, G. L., Profile fitting: a powerful method of computer x-ray instrumentation and analysis, Transactions of the American Crystallographic Association, 12, 55-73 (1976).
- [3] Goehner, R. P. and Hatfield, W. T., Automation of the Siemens D500 Powder Diffractometer, Paper I-1, Winter Meeting, American Crystallographic Association, University of Oklahoma, Norman, Oklahoma (1978).
- [4] Visser, J. W., A fully automatic program for finding the unit cell from powder data J. Appl. Cryst. 2, 89-95 (1969).
- [5] Smith, G. S. and Kahara, E., Automated computer indexing of powder patterns: the monoclinic case, J. Appl. Cryst. 8, 681-683 (1975).
- [6] Nichols, M. C., Performance of the Search Program (1966-1978-....) Past-Present-Future, Paper D6, Winter Meeting, American Crystallographic Association, University of Hawaii, Honolulu, Hawaii (1979).
- [7] Johnson, G. G., Jr., Resolution of powder patterns, in Laboratory Systems and Spectroscopy, J. S. Matson, H. B. Mark, Jr., and H. C. MacDonald, Jr., eds., pp. 45-87, ch. 3 (Marcel Dekker, New York, Basel, 1977).
- [8] Bayliss, P., X-ray diffraction powder data, Amer. Mineralogist, 61, 334-336 (1976).
- [9] Kennard, O., Hanawalt, J. D., Wilson, A. J. C., deWolff, P. M., Frank-Kamenetsky, V. A. International union of crystallography. Commission on crystallographic data. Powder data, J. Appl. Cryst. 4, 81-86 (1971).
- [10] Snyder, R. L., Johnson, Q. C., Kahara, E., Smith, G. S., and Nichols, M. C., An Analysis of the Powder Diffraction File, Lawrence Livermore Laboratory, Rept. UCRL-52505 (1977).
- [11] Smith, S. T., Snyder, R. L., and Brownell, W. E., The minimization of preferred orientation in powder diffraction patterns by spray drying, Advances in X-ray Analysis, G. J. McCarthy, C. S. Barrett, J. F. Newkirk, and C. O. Ruud, eds., Vol. 22 (Plenum, New York, 1979).
- [12] Smith, D. K. and Barrett, C. S., Sample handling problems in x-ray diffractometry, Advances in X-ray Analysis, G. J. McCarthy, C. S. Barrett, J. F. Newkirk, and C. O. Ruud, eds., Vol. 22 (Plenum, New York, 1979).
- [13] Smith, G. S. and Snyder, R. L.,  $F_N$ : a criterion for rating powder diffraction patterns and evaluating the reliability of powder pattern indexing, J. Appl. Cryst. 12, 60-65 (1979).
- [14] Donnay, G. and Donnay, J. D. H., The symmetry in the high-temperature alkali-feldspar series, Amer. J. Sci., Bowen Vol., 115-132 (1952).
- [15] deWolff, P. M., A simplified criterion for the reliability of a powder pattern indexing, J. Appl. Cryst. 1, 108 (1968).
- [16] Shirley, R., Indexing powder diagrams, Crystallographic Computing, Proceedings of 1978 Summer School (Delft University Press and Oostkoeks, 1978).

APPENDIX A: EXAMPLE OF COMPLETED DATA FORM  
POWDER DIFFRACTION DATA FOR PHASE CHARACTERIZATION

(Data from Swanson, H. E., et al. (1971). NBS Monograph No. 25, Section 9, p. 25)

BOLDFACE ITEMS ARE CONSIDERED ESSENTIAL

SAMPLE CHARACTERIZATION

NAME (CHEMICAL, MINERAL, Trivial) Magnesium Aluminum Oxide (Spinel)  
EMPIRICAL FORMULA MgAl<sub>2</sub>O<sub>4</sub>  
CHEMICAL ANALYSIS **NO**  **YES**  
SOURCE/PREPARATION Synthetic; Fusion of binary oxides  
CHEMICAL ABSTRACT REGISTRY NO. 12068-51-8 PEARSON PHASE DESIGNATION cF56  
OTHER Index of Refraction = 1.718 (isotropic)

TECHNIQUE

RADIATION TYPE, SOURCE X-rays, Cu  $\lambda$  VALUE USED 1.54056 Å  $\kappa$   $\alpha_1$   
 $\lambda$  DISCRIM. (Filters Mono, Etc.) Diffracted beam, curved LiF mono.  
 $\lambda$  DETECTOR (Film, Scint, Position Sensitive etc.) Geiger  
INSTRUMENT DESCRIPTION (Type, Slits, etc.) 17 cm Vertical Diffractometer DIV 1° REC 0.003"  
SOLLER  **Yes** No. 1 Position inc. Aperture q = 1.2  
INSTRUMENTAL PROFILE BREADTH 0.10 °2 $\theta$  TEMP (°C) 25 ± 1  
SPECIMEN FORM/PARTICLE SIZE Edge loaded powder / < 10  $\mu$ m particle size for J's, packed for 2 $\theta$ 's  
RANGE OF 2 $\theta$  FROM 5 °2 $\theta$  to 165.0 °2 $\theta$  SPECIMEN MOTION None  
INTERNAL/EXTERNAL 2 $\theta$  STD (if any) Ag (internal) LATTICE PARAMETER OF 2 $\theta$  STD 4.08641 Å  
2 $\theta$  ERROR CORRECTION PROCEDURE Linear interpolation from nearest 2 $\theta$ 's of std.  
INTENSITY MEAS. TECHNIQUE Strip chart record (peak heights) ERROR (-) 5% PEAK  **INTEGRATED**  
MINIMUM INTENSITY THRESHOLD (IN RELATIVE INTENSITY UNITS) 0.3  
INTENSITY STD USED  $\alpha$ -Al<sub>2</sub>O<sub>3</sub> hkl's OF INTENSITY STD 113  
INTENSITY RATIO I/I<sub>c</sub> 1.70 (5) CONVERSION FACTOR IF CDRUNDUM NOT USED \_\_\_\_\_  
RESOLUTION (FWHM) FOR THIS MATERIAL: 0.10 °2 $\theta$  AT 59.37 °2 $\theta$   
2 $\theta$  REPRODUCIBILITY FOR THIS MATERIAL: ± 0.02 °2 $\theta$  AT All °2 $\theta$

UNIT CELL DATA

METHOD OF CELL DETN. Cell and structure known from Ref. 1  
CELL REFINEMENT METHOD Least-squares. See Ref. 2  
a = 8.0831 (1) Å ; b = ( ) Å ; c = ( ) Å  
 $\alpha$  = ( ) (°) ;  $\beta$  = ( ) (°) ;  $\gamma$  = ( ) (°)  
Z = 8 ; O<sub>m</sub> = ( ) g cm<sup>-3</sup> ; D<sub>x</sub> = 3.578 g cm<sup>-3</sup> ; V = 528.1 Å<sup>3</sup> ; Formula Wt = 142.25  
CRYSTAL SYS. Cubic SPACE GROUP Fd3m [227] CRYSTAL DATA INDEX NO. 8.0831  
FIGURE OF MERIT TYPE F<sub>N</sub>. See Ref. 3 VALUE F<sub>29</sub> = 58(0.015, 33)

REFERENCES

1. Bragg, W. H. (1915). Nature, 95, 561.
2. Appleman, D. E., Evans, H. T. (1973). NTIS Document No. PB-216188
3. Smith, G. S., and Snyder, R. L. (1979). J. Appl. Crystallography, 12, 60.

( ) INDICATES STANDARD DEVIATION IN LEAST SIGNIFICANT DIGIT(S)

POWDER DATA

ESSENTIAL		DESIRED		
2θ EXP (DEGREES)	I/I <sub>0</sub>	d <sub>EXP</sub> (Å)	hkℓ	Δ2θ* (DEGREES)
19.02	35	4.66	111	+ .019
31.27	40	2.858	220	- .003
36.84	100	2.437	311	- .009
38.53	3	2.335	222	- .021
44.83	65	2.020	400	+ .016
55.64	9	1.650	422	- .020
59.37	45	1.5554	511	+ .008
65.24	55	1.4289	440	- .001
68.64	3	1.3662	531	+ .006
74.13	3	1.2780	620	+ .003
77.32	8	1.2330	533	- .029
78.40	1	1.2187	622	- .013
82.64	5	1.1666	444	+ .006
85.76	2	1.1320	711	- .012
90.97	5	1.0802	642	- .009
94.10	12	1.0524	731	- .005
99.34	7	1.0104	800	- .006
107.90	2	0.9527	822	- .020
111.22	8	0.93343	751	- .014
112.32	1	0.92738	662	- .035
116.91	6	0.90384	840	- .025
120.50	1	0.88722	911	+ .004
121.69	0.9	0.88203	842	- .021
126.76	0.8	0.86161	664	+ .013
130.74	8	0.84737	931	- .011
138.07	17	0.82488	844	+ .033
142.97	0.4	0.81232	933	+ .024
152.70	2	0.79266	10.2.0	- .033
160.65	11	0.78139	951	+ .025

\* 2θ<sub>EXP</sub> - 2θ<sub>CALC</sub>

Appendix B. Information to Aid in the Completion of  
the Powder Diffraction Data Form

The underlined items below correspond to each of the items on the Powder Diffraction Data-Form. Authors may not be able to complete every item, but are urged to be as complete as possible.

AMPLE CHARACTERIZATION

Chemical Name. Names should be consistent with the conventions of the journal in which the pattern is to be published. Such nomenclature is often in accord with IUPAC conventions [1-3]. This name should include polymorphic phase identification (e.g.,  $\beta$ -manganese dioxide).

Mineral Name. The mineral name should be included for all minerals or synthetic compounds known to have mineral counterparts (e.g., lead sulfide, galena).

Trivial. Common names like Rochelle salt or methylene blue, which may be of value, should be included.

Empirical Formula. The empirical or stoichiometric formula should, if possible, connote structural information such as functional groups (e.g.,  $(\text{PO}_4)_2$ ). Such stoichiometric formulas can be readily converted to strictly empirical formulas by computers. The stoichiometric formula should, however, be consistent with the conventions of the journal in which the pattern is to be published.

Chemical Analysis. The results of a partial or full chemical analysis should be communicated either on this form or in the journal article.

Source. List the source of the material. If it is a natural mineral, the location must be given. If the material is commercially obtained, state the supplier.

Preparation. State method and pertinent conditions of preparation.

Other Data. Give any other data that will help to assure that the specimen is well characterized apart from the diffraction pattern. (A high-quality diffraction pattern of an improperly identified material is of less than no use.) Such data might include: melting point or transformation temperatures, the fact that single-crystal studies were done; structure type (e.g., NaCl type), color, indices of refraction, etc.

Chemical Abstracts Service Registry Number. This number is uniquely assigned to each compound by Chemical Abstracts. It is very useful in cross correlating between various

computer data bases. This number should be included if it is known to the author. For further information see reference [4].

Pearson Phase Designation. A method for classifying structures of metals and alloys is described by W. B. Pearson [5]. The "Pearson Symbol" is quite useful and, if known, should be included (e.g.,  $\alpha$ -Se has the symbol mP32,  $\text{Al}_3\text{Zn}$  has the symbol tI16). The three parts of the Pearson symbol are: the first, lower-case letter (a, m, o, t, h, c) designating crystal system, the second, capital letter (P, C, F, I, R) designating Bravais lattice type, and a number indicating the number of atoms in the conventional unit cell: NOTE: This is not the number of formula units.

## TECHNIQUE

Radiation Type. X-rays, neutrons, electrons, etc.

Radiation Source. X-ray target material, neutron source, electron accelerating voltage, etc.

$\lambda$  Value Used. The numerical value of the wavelength used in calculating d values. List  $\lambda(K\alpha_1)$  if the  $\alpha_1$  component was fully resolved throughout the pattern or if analysis leads to  $2\theta$ 's for the  $\alpha_1$  component. List  $\lambda(K\alpha)$  if the  $K\alpha$  doublet was not resolved. If both  $\lambda(K\alpha)$  and  $\lambda(K\alpha_1)$  were used, indicate the dividing line and list both wavelengths.

$\lambda$  Discriminator (Filters, Mono, etc.). Give the method used to monochromatize the beam. State whether the monochromator or filter was used in the incident or the diffracted beam.

$\lambda$  Detector (Film, Scint., Position Sensitive, etc.). The type of radiation detector used and any unusual electronic processing should be given. (e.g., pulse-height discrimination for a scintillation or proportional detector is conventional and need not be stated.)

Instrument Description (Type, Slits, etc.). State the type and size of instrument used (e.g., 114.6-mm Debye-Scherrer camera, 17-cm diffractometer, 200-mm Guinier camera, etc.) and the conditions for the experiment. For diffractometers, state the divergence angle (Div) of the incident beam, receiving-slit width (Rec), and whether or not different or continuously varying divergence slits were used for various  $2\theta$  ranges.

Soller (Number, Position, Apertures). For diffractometers, give the number of sets of Soller slits, their positions (e.g., in incident or diffracted beam or in both) and aperture(s), because axial divergence can be a source of large profile displacement or broadening. Aperture is best characterized by  $q = R\Delta/h$ , where R is the radius of the diffractometer; h is 1/2 the axial extension of the sample, and

$$\Delta = \frac{\text{spacing between Soller foils}}{\text{length of Soller foils}}$$

Instrumental Profile Breadth. This parameter is the full width at half maximum (FWHM) of a reference sample that has minimal intrinsic broadening. It allows the instrument used to be compared with others and indicates the resolving ability. A recommended procedure is to measure the 311 reflection ( $d_{311} = 1.638 \text{ \AA}$ ) of a well-annealed Si specimen whose particle size is between 1 and 20  $\mu\text{m}$ . The FWHM of only the  $K\alpha_1$  peak should be reported (for Cu  $K\alpha_1$  radiation, this occurs at  $56.12^\circ 2\theta$ ). If another material or peak is chosen, it should be stated. If the  $\alpha_1$  and  $\alpha_2$  peaks are not resolved, report that fact along with the FWHM for the peak observed.

Temperature. State the temperature of the sample when the pattern was obtained.

Specimen Form. Indicate if the sample is a loose powder, sintered compact, metallographic mount, etc. State how the specimen was prepared for diffraction analysis (e.g., side loaded or vertically packed into a diffractometer holder, dusted onto a substrate, packed into a capillary). If different preparations were used in the measurement of d values and intensities, indicate both methods.

Particle Size. Give the average or maximum particle size in the specimen (e.g., 10  $\mu\text{m}$ , 325 mesh,  $<20 \mu\text{m}$ ).

Range of  $2\theta$ . Indicate the range of  $2\theta$  that was examined. All peaks above the stated intensity threshold (given below) in the reported  $2\theta$  range should be included under Powder data. Include a minimum of 40 peaks or all data up to  $2\theta = 100^\circ$ .

Specimen Motion. State type of sample motion during the diffraction experiment (e.g., sample spinner, rotated cylinder, Gandolfi motion, none).

Internal/External  $2\theta$  Standard (if any). If the instrument was calibrated with a known standard before or after the pattern was obtained, state "external--(material of standard)." If an internal standard was mixed with the sample to check for a specimen displacement and/or  $\theta$  zero error, state "internal--(material of standard)." A standard material recommended for both procedures is National Bureau of Standards SRM silicon [6].

Lattice Parameter of  $2\theta$  Standard. State the numerical value of the lattice parameter used in calculating the expected  $2\theta$  positions of the lines of the standard.

2 $\theta$  Error Correction Procedure. State the method used to correct the observed 2 $\theta$  values for systematic instrumental error. A recommended procedure is to use one or more external standards such as Si (ref. [6]) and determine the  $\Delta 2\theta$  ( $2\theta_{\text{exp}} - 2\theta_{\text{calc}}$ ) vs 2 $\theta$  curve. These data may be fitted using a least squares polynomial regression (e.g., a third-degree equation:  $\Delta 2\theta = a_0 + a_1 2\theta + a_2 2\theta^2 + a_3 2\theta^3$ ). If this procedure is used, state the coefficients ( $a_i$ 's) of the polynomial. A cubic standard having a large cell dimension (>10 Å) is recommended for patterns having many lines at low angles.

Intensity Measuring Technique. Indicate the method used to determine diffracted intensities: peak heights or integrated areas from a strip chart, or densitometer or step-scan data. Indicate if monochromator polarization effects have been removed from the  $I/I_0$  values reported under Powder Data.

Minimum Intensity Threshold (in Relative Intensity Units). Indicate the relative intensity (see  $I/I_0$  below) not considered to be a real peak. Typically this threshold is taken as the background reading plus 2.5 times  $\sqrt{\text{background}}$ . NOTE: Because this value will differ in regions of high and low background, limiting values should be reported.

Intensity Standard Used. Indicate the material used in determining the reference intensity ratio. Intensity standards allow for the direct comparison of intensities in different materials. Methods involving the use of corundum as an intensity standard for direct quantitative phase analysis have been described [7-9].

hkl's of Intensity Standard. Give the hkl(s) of the line(s) used for determining the  $I/I_c$  standard value.

Intensity Ratio  $I/I_c$ . Give the value of the ratio of the strongest line in the pattern to the strongest line of corundum ( $d_{113} = 2.085$  Å) in a 50-50 wt percent mixture of the two [7-9], and give the reproducibility,  $\alpha(I/I_c)$ .

Conversion Factor if Corundum not used. If  $\alpha\text{-Al}_2\text{O}_3$  is not used as the intensity standard, then the conversion factor between the standard used and corundum should be listed. This conversion factor can be used to calculate the  $I/I_c$  for the specimen.

Resolution (FWHM) for this Material. The full width at half maximum, in degrees 2 $\theta$ , of a well-resolved  $\alpha_1$  line (if possible) should be given along with the 2 $\theta$  of this line. The peak should be chosen between 30° and 60° 2 $\theta$  to avoid wavelength broadening effects. This value, of course, includes the instrumental profile breadth given above. If  $\alpha_1$  and  $\alpha_2$  are not resolved, this fact should be stated.

2 $\theta$  Reproducibility for this Material. State any measured reproducibility of the positions of the diffraction maxima; if measured for one line, state the  $2\theta$ .

#### NIT CELL DATA

Method of Cell Determination. If the unit cell was obtained from the literature, give the reference. If the unit cell was derived from the powder data, state the method or program used.

Cell Refinement Method. If the cell was refined, state the method and computer program used (if any).

Cell Parameters a, b, c,  $\alpha$ ,  $\beta$ , and  $\gamma$ . These values should be reported to the proper number of significant digits; put the standard deviations, in terms of the least significant digit, in parentheses (parameters in angstroms, angles in degrees).

$D_m$ : experimentally determined density in  $g/cm^3$

$D_x$ : calculated density; from  $D_x = Z FW/N_o V$ , where  $Z$  is the number of formula units in each unit cell,  $FW$  is formula weight,  $N_o = \text{Avogadro's number } (0.60225 \times 10^{24})$ , and  $V$  is the volume of the unit cell in  $cm^3$

Space Group. If the space group has been determined by single-crystal studies, give the Hermann-Mauguin symbol followed in brackets by the space-group number as listed in reference [10]. For space group determinations that are not your own, a reference should be given below. For unit cells determined solely from powder diffraction data, give the diffraction aspect as defined in reference [11] (pp. S-8 to S-18).

Crystal Data Index Number(s). List the axial ratios, derived from the cell parameters, that would be used to locate this material in Crystal Data Determinative Tables [11].  
Warning: these axial ratios are based on a unit cell defined by Crystal Data, which may not be the cell for which the parameters are given above. Reference [10] describes how the Crystal Data cell is obtained. These rules have been incorporated in the powder pattern evaluation program AIDS [12].

Figure of Merit Type and Value. List the type of figure of merit used (e.g.,  $M_{20}$  or  $F_N$ --see references [13] and [14]) and its value. The figure  $M_{20}$  is defined as:

$$M_{20} = \left( \frac{Q_{20}}{2 |\Delta Q|} \right) \left( \frac{1}{N_{\text{poss}}} \right),$$

where  $Q_{20}$  is the Q value ( $= 1/d^2$ ) of the 20th observed line,  $|\Delta Q|$  is the average absolute discrepancy between  $Q_{\text{obs}}$  and  $Q_{\text{calc}}$ , and  $N_{\text{poss}}$  is the number of independent diffraction lines possible up to the 20th observed line. The figure  $F_N$  is defined as:

$$F_N = \left( \frac{1}{|\Delta 2\theta|} \right) \left( \frac{N}{N_{\text{poss}}} \right),$$

where  $|\overline{\Delta 2\theta}|$  is the average absolute discrepancy between observed and calculated  $2\theta$  values and  $N_{\text{poss}}$  is the number of independent diffraction lines possible up to the Nth observed line.

With regard to the figures of merit, some guidelines for the counting of possible independent diffraction lines are in order:

Systematic absences caused by symmetry elements and lattice type are excluded in the tallying of  $N_{\text{poss}}$ .

Only one plane from the complete set of planes related by crystal symmetry is counted in  $N_{\text{poss}}$ . For example, in the cubic system, the 100 line is counted as one independent line although it is composed of diffracted intensities from all six planes of that crystallographic form.

Some forms, though not related by symmetry, have exactly the same spacing and will give rise to the same line in the powder pattern (e.g., 333 and 511 in the cubic system). Forms of this kind are also counted as one independent line. Note that this rule means that the higher-symmetry Laue group is always assumed. When a lower-symmetry Laue group is definitely known from single-crystal studies, this rule is not strictly correct for some of the diffraction lines. However, for most of these cases, the effect on the value of the figure of merit for the overall pattern should be insignificant.

For the case of accidental degeneracy (i.e., nonequivalent forms which have spacings so nearly identical that the individual lines would not be experimentally resolved), all lines in such a cluster are counted as possible independent lines; the line having the smallest  $\Delta 2\theta$  is used in the calculation of  $|\overline{\Delta 2\theta}|$  for the pattern, and the other line or lines are listed as not observed, thereby increasing  $N_{\text{poss}}$ .

The function is reported in the form

$$F_N = \text{Value} (|\overline{\Delta 2\theta}|, N_{\text{poss}}).$$

For example,

$$F_{30} = 73.5(0.012, 34).$$

We recommend that  $N$  in  $F_N$  be the 30th observed line or the last line if there are fewer than 30 lines in the pattern.

Note that if the space group or the diffraction aspect is not determined,  $N_{\text{poss}}$  can only be reported as a maximum value; i.e., no allowance would have been made for systematic absence, a fact which could appreciably reduce  $M_{20}$  or  $F_N$ .

#### REFERENCES

Cite pertinent literature references for previous x-ray or preparative studies.

#### POWDER DATA LISTING

$2\theta_{\text{exp}}$ . Report the experimentally observed  $2\theta$  values, in degrees and corrected for systematic instrumental errors. If multiple determinations of each peak were made, then the standard deviation of each  $2\theta$  value should follow in parentheses.

$I/I_0$ . List the relative intensities  $I/I_0$  of the diffraction lines on a numeric scale;  $I/I_0 = I/I_{\text{max}} \times \text{scale}$ , where  $I_{\text{max}}$  = the numeric value chosen for the most intense reflection. The scale value should be chosen such that the maximum intensity value is not greater than 100. Intensities less than 1 are reported as decimal fractions. If the standard deviation of each intensity was computed, place the value in parenthesis after each  $I/I_0$  value.

$d_{\text{exp}}$ . List the  $d$  values in angstroms, derived from the observed  $2\theta$  values using Bragg's law:  $d = \lambda/[2 \sin (\theta/2)]$ , where  $\lambda$  is the value of the wavelength stated under Technique. In reporting  $d$ 's, the number of significant figures given should be sufficient to allow recomputation of the experimental  $2\theta$ 's to their measured accuracy, i.e., the number of significant figures should be in accordance with  $\sigma(d) = (d/2) \cot \theta \sigma(2\theta)$ .

$hkl$ . List the Miller indices of the diffraction lines determined from the known unit cell. If several peaks are overlapped such that separate peak position measurements cannot be made, the  $hkl$ 's should be grouped together and given for the single intensity value. The  $hkl$ 's of all peaks can be listed, or a "+" can be post-scripted to the last one given to indicate others not listed.

$\Delta 2\theta$ . List the difference, with sign, between the experimental and calculated  $2\theta$  values:  $\Delta 2\theta = 2\theta_{\text{exp}} - 2\theta_{\text{calc}}$ . A useful rule of thumb is that, if systematic errors have been removed completely, the absolute value of each  $\Delta 2\theta$  should be less than  $3\sigma(2\theta)$ . Alternatively, a small bar-graph can be presented showing  $\Delta 2\theta$  (with sign) versus line number. The reader, if interested, could reconstruct more accurate values of  $\Delta 2\theta$  from the experimental  $2\theta$ 's and the reported lattice parameters.

## References, Appendix B

- [1] International Union of Pure and Applied Chemistry, Inorganic Chemistry Section, Definitive Rules for Nomenclature of Inorganic Chemistry 1957 (Butterworths, London, 1959).
- [2] Pure and Applied Chem. 28, 1 (1971).
- [3] Fletcher, J. H., Dermer, O. C., and Fox, R. B., Nomenclature of Organic Compounds, Principles, and Practice, Advances in Chemistry Series No. 126 (American Chemical Society, Washington, DC, 1974).
- [4] Chemical Abstracts Service Chemical Registry Structure Conventions (Chemical Abstracts Service Publishers, Columbus, Ohio, 1968).
- [5] Pearson, W. B., Handbook of Lattice Spacings and Structures of Metals and Alloys, (Pergamon Press, Oxford, 1967).
- [6] Hubbard, C. R., Swanson, H. E., and Mauer, F. A., A silicon powder diffraction standard reference material, J. Appl. Cryst. 8, 45 (1975).
- [7] Visser, J. W. and de Wolff, P. M., Absolute intensities, Report No. 641.109, Technisch-Physische Dienst., Delft, Netherlands (1964).
- [8] Chung, F. H., Quantitative Interpretation of x-ray diffraction patterns. III. Simultaneous determination of a set of reference intensities, J. Appl. Cryst. 8, 17 (1975).
- [9] Hubbard, C. R., Evans, E. H., and Smith, D. K., The reference intensity ratio,  $I/I_C$  for computer simulated powder patterns, J. Appl. Cryst. 9, 169-174 (1976).
- [10] International Tables for X-ray Crystallography, N. F. M. Henry and K. Lonsdale, eds. Vol. 1, 2nd edition (Kynoch Press, Birmingham, England, 1965).
- [11] Donnay, J. D. H. and Ondik, H. M. (eds.), Crystal Data Determinative Tables, Third Edition, Vols. 1-4 (National Bureau of Standards and Joint Committee on Powder Diffraction Standards, Publishers, 1972, 1973, 1978).
- [12] Mighell, A., et al., Single crystal and powder data evaluation and standardization program, U.S. National Bureau of Standards, to be published.
- [13] de Wolff, P. M., A simplified criterion for the reliability of a powder pattern indexing, J. Appl. Cryst. 1, 108 (1968).
- [14] Smith, G. S. and Snyder, R. L.,  $F_N$ : a criterion for rating powder diffraction patterns and evaluating the reliability of powder pattern indexing, J. Appl. Cryst. 12, 60 (1979).

## Discussion

Question (Zwell): Many analysts have asked for publication of all diffraction patterns. Wouldn't your proposal decrease the number of patterns being published and thereby reduce

information available? (Would the improvement in quality of pattern compensate for the loss of data?)

Comments (Calvert, et al.): It would be hard to predict the effect with any degree of confidence. A similar set of publication recommendations made earlier by the single-crystal community resulted in a marked improvement in the average quality of papers published in Acta and many other journals. Some journals continue to accept lower quality data but the prestige of publication in the lead crystallographic journals is such that authors generally strive to meet these standards. That result can't be bad.

Question (Zwell): It appears that it is implied that  $2\theta$  would be for Cu radiation. Wouldn't the use of such angles reduce the value of data for those persons using other radiations (chromium, cobalt, molybdenum? (d's are constant and independent of radiation.)

Comments (Calvert, et al.): Two theta would be recorded as measured. These data would not be transformed to a different wavelength since that process could potentially introduce noise.



n  
y  
x  
j  
v  
z  
o  
k  
b  
p  
c  
d  
f  
s  
u  
t  
l  
r  
m  
p  
-  
c

## SUGGESTIONS FOR A QUANTITATIVE EVALUATION OF POWDER PATTERNS

Gabrielle Donnay  
Department of Geological Sciences  
McGill University  
Montreal, P.Q. Canada H3A 2A7

The use of the residual  $D_{Nr} = \overline{|\Delta 2\theta|}$ , the mean absolute deviation (D) between  $2\theta_{obs}$  and  $2\theta_{calc}$  for all N resolved peaks (Nr), was proposed long ago [1]<sup>1</sup> for much the same reasons that it is now proposed again [2]. The observed  $2\theta$  values are the primary experimental data; they all have the same reading error, a constant for peaks of equal quality. Conversion to any wavelength-independent quantity, be it  $Q = \left| \frac{1}{d} \right|$  or  $d = 1/\left| \frac{1}{d} \right|$ , requires a function of  $\theta$  that is far from linear,  $4 \sin^2\theta/\lambda^2$  or  $\lambda/(2 \sin\theta)$ , respectively. The objection of journal editors to the inclusion of a  $\Delta 2\theta$  column must be force of habit, since the width of the table of powder data (table 1) would not have to exceed the half-page width currently used in most journals. Adding a  $\sigma d$  column corresponding to a given constant reading error in  $2\theta$ , for each observed, resolved peak would take as much space and is not nearly as informative.

A RESIDUAL (ideally, close to zero) was chosen in 1952 rather than a FIGURE OF MERIT [3,4,2] for two main reasons: (1) the residual represents a type of evaluation crystallographers are familiar with (cp. R in structure determinations); (2) the residual  $\overline{|\Delta 2\theta|}$  is directly obtained from the measurements, whereas a figure of merit requires using its reciprocal. We could not conceive of a number expressed in reciprocal units of angle as being more readily appreciated than one expressed in degrees.

The reason that only "resolved" reflections are included in the quality residual ( $D_{Nr}$ ), contrary to the proposals made in 1968 and 1969, is the following: the evaluation under discussion concerns itself only with the cell geometry, not with the calculation of peak intensities and peak shapes. Thus, peaks due to more than one possible reflection with unknown relative intensities cannot be reported with any meaningful standard deviation and thus should be excluded from the least-squares refinement of cell dimensions and from the evaluation procedure. (Peaks due to several reflections such as, for example, the cubic ones 7 1 0, 5 5 0, 5 4 3, with distinct I's but identical  $2\theta$  values are, of course, to be included in Nr.)

<sup>1</sup>Figures in brackets indicate the literature references at the end of this paper.

The resolved peaks with observed  $\Delta 2\theta$  values exceeding the  $D_{Nr}$  value by an agreed-upon factor, say 3, should be marked with a dagger in the data representation (table 1). If such reflections have reasonable high intensities, so they can be read as well as the properly interpreted ones, the pattern cannot be considered indexed in a reliable fashion. An impurity phase would have to be called on to account for the uninterpretable peak or peaks. Such patterns should certainly be eliminated from the JCPDS Powder Diffraction File if they are now included and should not be incorporated in the future.

$D_{Nr}$  and  $\Delta 2\theta$ 's  $> 3D_{Nr}$  permit us to judge the quality of experimental work that produced a given pattern. A third quantity,  $N_{poss}/N_{obs}$ , will give qualitative information on the type of crystal structure responsible for the observed pattern.  $N_{poss}$  represents the number of symmetry-independent lattice points permitted by the space group, whereas  $N_{obs}$  gives the sum of resolved and unresolved observed peaks. Note that two overlapping or nearly coincident peaks count for 2 in  $N_{poss}$  but for 1 in  $N_{obs}$ . When  $N_{poss}/N_{obs}$  is close to unity, no substructure of heavy atoms and no pseudo-repeats are present. The pattern can then be considered a reliable fingerprint of its phase. If, on the other hand, the ratio is large (values up to 60 have been observed for mineral patterns), it is clear that the powder pattern by itself does not contain sufficient data to be considered a trustworthy means of identification. It is still worth recording, but it may not be unique to the phase under study. Whenever the ratio is near unity, it is highly recommended that all possible hkl and  $d_{calc}$  values be included in the tabulation. It means very little additional length of tabulation (paper, after all, is cheaper than highly-trained brain power!) and saves a great deal of calculation time for later users: they will almost certainly notice, on their pattern additional faint lines which may or may not be accounted for by the interpretation in the literature.

Smith and Snyder [2], like De Wolff [4] before them, advocate the use of a single evaluation number,  $F_{Nobs}$ , but actually give this "Figure of Merit" always with two separate factors following it in parenthesis. The example " $F_{20} = 101 (0.009, 22)$ ," quoted from Smith and Snyder [2], means that the first 20 observed reflections on the low  $2\theta$  side give a mean absolute  $\Delta 2\theta$  of  $0.009^\circ$  and that a total of 22 reflections are possible in this  $2\theta$  range. The evaluation number 101 equals  $20/(0.009 \times 22)$ . What good is it? You are not really given a single evaluation number when three independent values must be specified for it to be meaningful. The only relation between the factors involved requires  $N_{poss}$  to be equal or greater than  $N_{obs}$  (here  $22 > 20$ ).

The sample tabulation given here (table 1) shows how little space is needed to list all three evaluation parameters:  $D_{Nr}$ , daggers to mark the seriously mismatched or unmatched resolved peaks,  $N_{poss}/N_{obs}$ . More importantly, every qualified user of powder patterns will have no problem appreciating their significance. After careful consideration it will become "crystal clear" that it is actually advantageous to work with three independent evaluation parameters rather than only one uninterpretable number. Three examples, the first two hypothetical and the third an actual case, will show how the use to which a powder pattern is put must determine whether one or another of the three parameters is to be weighted most heavily.

Table 1. Powder Pattern of Barite, BaSO<sub>4</sub> (2θ < 26.6°)

a = 7.1565, b = 8.8811, c = 5.4541 Å, Pbnm

λ = CuKα (1.54178 Å); D<sub>27</sub> = 0.009°; no Δ2θ > 3D<sub>27</sub>;

N<sub>poss</sub>/N<sub>obs</sub> = 45/31 = 1.45

Δ2θ(°)	I/I <sub>1</sub>	d <sub>obs</sub>	d <sub>calc</sub>	h k l
0.02	2	5.58	5.572	1 1 0
0.00	16	4.440	4.441	0 2 0
0.00	30	4.339	4.338	1 0 1
0.01	50	3.899	3.898	1 1 1
0	12	3.773	3.773	1 2 0
0.01	30	3.577	3.578	2 0 0
0.01	100	3.445	3.444	0 2 1
0	70	3.319	3.319	2 1 0
0	95	3.103	3.103	1 2 1
0.01	50	2.836	2.835	2 1 1
-	-	-	2.786	2 2 0
0.01	15	2.735	2.736	1 3 0
0.02	45	2.729	2.727	0 0 2
0.02	13	2.482	2.481	2 2 1
----	2	2.447	{ 2.450 2.445	{ 1 1 2 1 3 1
0.02	14	2.325	2.324	0 2 2
0.02	6	2.305	2.304	3 1 0
0.02	8	2.282	2.281	2 3 0
-	-	-	2.220	0 4 0
0.02	25	2.211	2.210	1 2 2
-	-	-	2.186	3 0 1
0	3	2.169	2.169	2 0 2
----	80	2.121	{ 2.122 2.121	{ 3 1 1 1 4 0
----	75	2.106	{ 2.107 2.104	{ 2 1 2 2 3 1
-	-	-	2.102	3 2 0
0.02	19	2.057	2.056	0 4 1
-	-	-	1.9764	1 4 1
-	-	-	1.9609	3 2 1
0.01	1	1.9486	1.9489	2 2 2
0.01	7	1.9317	1.9313	1 3 2
-	-	-	1.8866	2 4 0
0	18	1.8575	1.8575	3 3 0
0.01	4	1.7889	1.7891	4 0 0
-	-	-	1.7829	2 4 1
0.01	8	1.7617	1.7621	1 0 3
----	10	1.7584	{ 1.7599 1.7583	{ 3 1 2 3 3 1
0.00	8	1.7540	1.7539	4 1 0
-	-	-	1.7496	2 3 2
0	4	1.7284	1.7284	1 1 3
0	5	1.7239	1.7239	1 5 0
-	-	-	1.722	0 4 2

(1) A monoclinic powder pattern of  $(K,Na)AlSi_3O_8$  in the literature has a relatively high  $D_{Nr}$  value, say  $0.04^\circ$  for  $N_r = 20$ ; none of the resolved peaks, however, exceeds  $0.12^\circ$  in  $\Delta 2\theta$ ,  $N_{poss}/N_{obs}$  equals 1.23. Thus, the indexed pattern looks trustworthy on the whole. The user has obtained a similar pattern from his unknown sample; he wishes to determine a precise K to Na ratio. Uncorrected experimental errors in the literature pattern are the most likely cause of a high  $D_{Nr}$  and the user will therefore want to include a calibration standard such as quartz or calcite with his sample. The calibration-corrected measurements indexed on the basis of the literature pattern will give the user the preliminary cell dimensions needed for the least-squares refinement of his own data. His evaluation parameters turn out to be:  $D_{20} = 0.005^\circ$ , no peak with  $\Delta 2\theta \geq 0.015^\circ$  and  $N_{poss}/N_{obs} = 35/29 = 1.21$ . The user can trust his cell dimensions sufficiently to make use of the plots of cell dimensions vs K/Na ratio for alkali feldspars in the literature.

(2) An orthorhombic pattern in the Powder Data File has  $D_{30} = 0.003^\circ$  and shows one resolved peak with dagger for which  $\Delta 2\theta = 0.13^\circ$  ( $I = 30$ );  $N_{poss}/N_{obs} = 1.30$ . The user's pattern shows all the peaks with  $I > 20$  of the literature pattern, except the marked peak. There is thus little doubt that an impurity phase is to be blamed for the problematic peak in the literature pattern. The user can trust the identity of his unknown with the phase described in the literature.

(3) A new rhombohedral mineral,  $Mn_8Si_6O_{15}(OH)_8Cl_2$ ,  $Z = 23$ , gives a powder pattern extremely close to that of friedelite, a mineral with similar composition but less chlorine per formula unit. The appearance of the two minerals is different, however, and single crystal work shows the  $c$  cell dimension of the new mineral to be  $85.9 \text{ \AA}$ , four times that of friedelite. The  $a$  axes,  $13.46 \text{ \AA}$ , are the same within 0.3 percent; the space group is  $R\bar{3}m$  or  $R3m$  for both minerals. The evaluation parameters for the Debye-Scherrer pattern taken with  $FeK\alpha$  radiation are:  $D_{20} = 0.032^\circ$ ,  $\Delta 2\theta = 0.21$  at  $2\theta = 73.4^\circ$ ,  $N_{poss}/N_{obs} = 1535/26 = 59.04$ . Except for three close-in very weak reflections, all observed, resolved peaks have indices of the type  $4h \ 4k \cdot 4l$ . In the crystal structure, the Mn atoms are arranged in basal layers of the brucite type; they are situated near the nodes of a sublattice with cell dimensions  $a/4$ ,  $c/12$ . To a first approximation the Mn atoms control the powder pattern. Since the Mn sites are the same in the new mineral as in friedelite, powder pattern cannot tell the two minerals apart. The high value of  $N_{poss}/N_{obs}$  tells us that the powder pattern cannot be used as a determinative criterion.

The above examples cannot illustrate all the various problems that the user of powder patterns may encounter. They should, however, suffice to show that the revived proposals deserve serious and objective consideration. These evaluation criteria have been used routinely in our work with mineral, inorganic and organic powder patterns for over thirty years. They have proved highly satisfactory.

#### References

- [1] Donnay, Gabriell and Donnay, J. D. H., The symmetry change in the high-temperature alkali-feldspar series, Amer. J. Sci., Bowen vol., 115-132 (1952).

- [2] Smith, Gordon S. and Snyder, Robert L.,  $F_N$ : a criterion for rating powder diffraction patterns and evaluating the reliability of powder-pattern indexing, *J. Appl. Cryst.* 12, 60-65 (1979).
- [3] Wolff, P. M. de, Reliability of unit cells derived from powder diffraction patterns, *Acta Cryst.* 14, 579-582 (1961).
- [4] Wolff, P. M. de, A simplified criterion for the reliability of a powder pattern indexing, *J. Appl. Cryst.* 1, 108-113 (1968).



## X-RAY POWDER DIFFRACTION

L. D. Calvert

National Research Council of Canada  
Ottawa, Ontario, Canada, K1A 0R9

Recent years have seen rapid developments in the field of powder diffraction arising on one hand from the widespread availability of small computers and on the other hand from devices such as solid state detectors (SSD's), position sensitive detectors (PSD's), intense sources of x-radiation (synchrotrons, storage rings, flash-tubes, possible laser sources). These also, of course, make great use of on-line computers. An era of development comparable to that following the introduction of the counter-diffractometer [1]<sup>1</sup> seems probable.

The small powerful computer, cheap enough to be dedicated to a given experiment has given rise to the automation of existing standard techniques both commercially, as summarized recently at the Oklahoma meeting of the American Crystallographic Association [2] and privately [see, for example 3, 4, 5, 6 and references therein]. A key feature is the combination in a single system of the routine steps in data acquisition, data reduction and phase identification. This latter process, first programmed for big computers, is now included in routines operating on small computers [7,8,9]. The combination of x-ray fluorescence and x-ray diffraction in a single automated unit may offer advantages in some circumstances [10,11] and may be developed further. The general process can be described as an increase in the portability of sophisticated techniques which can be exported from specialist centres as a hardware plus software combination. Along these lines we may anticipate developments of combined techniques previously precluded by the excessive amount of labour required. Thus, the combination of reflection and transmission experiments on the same sample [12,13] may become routine for monitoring the often-present and vexing problem of preferred orientation in powder specimens or to obtain directly, parameters now inferred. Relatively little has been implemented so far in the area of feed-back between the experiment and the observed data. With the advent of fully-integrated software systems it will be possible to monitor the data as it is acquired and vary or repeat the data-collection as required. Similarly automatic search-and-match routines [14] tied to automatic peak-finding and profile fitting routines [15] allow the possibility of using powder diffraction methods

<sup>1</sup>Figures in brackets indicate the literature references at the end of this paper.

for on-line process control in say, fibre-making or sheet-rolling. For relatively large specimens we have the possibility of using micro-diffractometers [16] for grain-by-grain phase analysis or the possibility of automated grain-by-grain orientation analysis [17,18] with grain and particle size estimation [19] and stress analysis [20] to provide various types of process control or monitoring.

With respect to SSD's [21,22] PSD's [23,24] and intense radiation sources [25,26] there are wide-spread opportunities for applications especially in time-limited experiments. Most of these have been dealt with in this symposium so that it is unnecessary to repeat details here. The use of flash x-ray tubes to investigate shock-wave phenomena [27] is one area where laser systems are another area [28] in which future development can be expected.

Further developments in the Rietveld method [29,30,31] can be expected as can be judged from the emphasis on this topic both in the present symposium and elsewhere [32]; again it is unnecessary to repeat details already given.

Attempts to predict the future are, of course, subject to great uncertainty and the present attempt is limited to selected topics and references and also to a conservative extrapolation from present experience.

#### References

- [1] Friedman, H., Geiger counter spectrometer for industrial research, *Electronics*, 18, 132-137 (1945).
- [2] Session I. Hubbard, C. R., Chairman, Winter meeting, American Crystallographic Association, March 19-24, 1978. Program and Abstracts, Vol. 6, No. 1, p. 21.
- [3] Richesson, M., Morrison, L., Cohen, J. B., and Paavola, K., An inexpensive computer control for an x-ray diffraction laboratory, *J. Appl. Cryst.* 4, 524-527 (1971).
- [4] Slaughter, M., A Modular automatic x-ray analysis system, *Advances in X-Ray Analysis* 13, 135-147 (1972).
- [5] Segmuller, A., Automated x-ray diffraction laboratory system, *Advances in X-ray Analysis*, 15, 114-122 (1972).
- [6] King, P. J. and Smith, W. L., A computer-controlled x-ray powder diffractometer, *J. Appl. Cryst.* 7, 603-608 (1974).
- [7] Jenkins, R., Hahn, Y., Pearlman, S. and Schreinar, W. N., The APD, a new dimension in qualitative and quantitative x-ray powder diffraction, *Norelco Reporter* 26, 1-15 (1979) (This version includes the entire PDF on one disc.)
- [8] Johnson, G. G., A search-match program for the PDP-11 (Private communication).
- [9] Edmonds, J. W. and Henslee, W. W., A rapid search-match technique on a small computer, *J. Appl. Cryst.* (1979) to be published.
- [10] Jenkins, R., The role of the energy dispersive detector in x-ray diffraction, *Trans. Amer. Cryst. Ass.* 12, 43-54 (1976).
- [11] Mantler, M. and Parrish, W., *Advances in X-ray Analysis*, 20, 171-186 (1976).

- 2] Ladell, J. and Nicolosi, J., Asymmetric texture sensitive powder diffractometer, Amer. Cryst. Assn., Winter Meeting, March 20-30, 1979, Program and abstracts, Vol. 6, No. 2, p. 54.
- 3] Huang, T. C. and Parrish, W., The transmission specimen powder diffractometry and the profile-fitting method, Amer. Cryst. Assn., Winter Meeting, March 20-30, 1979, Program and abstracts, Vol. 6, No. 2, p. 55.
- 4] Frevel, L. K., Adams, C. E., and Ruhberg, L. R., A fast search-match program for powder diffraction analysis, J. Appl. Cryst. 9, 199-204 (1976).
- 5] Ayers, G. L., Huang, T. C., and Parrish, W., High-speed x-ray analysis, J. Appl. Cryst. 11, 229-233 (1978).
- 6] Goldsmith, C. C. and Walker, G. A., X-ray microdiffractometry: new applications in phase and stress analysis, Winter meeting Amer. Cryst. Assn., March 19-24, 1978, Program and abstracts, Vol. 6, No. 1, p. 31.
- 7] Riquet, J. P. and Bonnet, R., Dépouillement par Ordinateur des Clichés de diffraction obtenus par la Méthode de Laue, J. Appl. Cryst. 12, 39-42 (1979).
- 8] Bilderback, D. H., A real-time back reflection Laue camera, J. Appl. Cryst. 12, 95-99 (1979).
- 9] Hilliard, J., Statistical analysis of the measurement of grain and particle size by x-rays, Symposium on Accuracy in Powder Diffraction, National Bureau of Standards, Washington, D.C., June 11-15, 1979.
- 10] James, M. R. and Cohen, J. B., Study of the precision of x-ray stress analysis, Advances in X-Ray Analysis 20, 291-307 (1976).
- 11] Heath, R. L., The application of high-resolution solid state detectors to x-ray spectrometry: a review, Advances in X-Ray Analysis, 15, 1-35 (1972).
- 12] Gobel, H., Fast and time-resolved XRPD using linear position sensitive detectors, Winter meeting, Amer. Cryst. Assn., March 20-30, 1979, Program and abstracts, Vol. 6, No. 2, p. 54.
- 13] Hendricks, R. W., One-and-two-dimensional position-sensitive x-ray and neutron-detectors, Trans. Amer. Cryst. Assn. 12, 103-146 (1976).
- 14] Arndt, U. W. and Gilmore, D. J., X-ray television area detectors for macromolecular structural studies with synchrotron radiation sources, J. Appl. Cryst. 12, 1-9 (1979).
- 15] Hodgson, K. O., Phillips, J. C., and Wlodawer, A., Applications of synchrotron radiation to x-ray diffraction studies of proteins, Trans. Amer. Cryst. Assn. 12, 1-10 (1976).
- 16] Hastings, J. B., Synchrotron radiation facilities: opportunities for x-ray research in the United States, Winter meeting: Amer. Cryst. Assn., March 20-30, 1979, Program and abstracts Vol. 6, No. 2, p. 56.
- 17] Johnson, Q. C. and Mitchell, A. C., Flash x-ray diffraction study of LiF to 11 mega bars, Winter meeting, Amer. Cryst. Assn., March 26-30, 1979, Program and abstracts Vol. 6, No. 2, p. 75.

- [28] Forsyth, J. M., High intensity soft x-ray pulses from laser produced plasmas, *Trans Amer. Cryst. Assn.* 12, 11-26 (1976).
- [29] Rietveld, H. M., Line profiles of neutron powder peaks for structure refinement, *Acta. Cryst.* 22, 151-152 (1967).
- [30] Young, R. A., Mackie, P. E., and von Dreele, R. B., Application of the pattern-fitting structure-refinement method to x-ray powder diffractometer patterns, *J. Appl. Cryst.* 10, 262-269 (1977).
- [31] Werner, P. E., Salome, S., Malmros, G., and Thomas, J. O., Quantitative analysis of multi component powders by the full-profile refinement of Guinier-Hagg film data, *J. Appl. Cryst.* 12, 107-109 (1979).
- [32] Conference on Diffraction Profile Analysis, Cracow, Poland, August 14-15, 1978. (At meeting it was agreed that the method be called the Rietveld method.)

## THE FUTURE OF POWDER NEUTRON DIFFRACTION

M. H. Mueller

Materials Science Division  
Argonne National Laboratory  
Argonne, IL 60439

The objective of this Symposium was to assess the current position of powder diffraction--both x-ray and neutron. A good international scientific representation was present with sixteen countries represented with a total attendance of 125. The following comments are primarily confined to neutron diffraction. During this week a number of aspects of neutron powder patterns were addressed such as: the various scattering contributions to the total pattern, the problem of profile fitting, use of special or multiple detectors and distortion of peak shape.

Although Rietveld [1,2]<sup>1</sup>, proposed a profile method for refining powder neutron patterns in two articles, it took several years before the method was extensively used. However, by 1977, Cheetham and Taylor [3], pointed out in a review article that more than 175 compounds (listing included in the article) had been treated by the profile refinement technique.

As a result of our discussions this week, indeed a number of areas of developing research which offer improved or new vistas to the field have been pointed out in neutron scattering. Some of these areas are: higher resolution, especially with pulsed neutron instruments; use of multiple detectors; refined methods of fitting profiles; a better assessment of errors; availability of generalized computer programs; use of standards such as  $Al_2O_3$  for interlaboratory comparisons; development of sample environments; a consideration and understanding of the total pattern, use of deconvolution methods and application of Fourier maps to confirm the structure and refine some features, including missing atom locations; a better experimental treatment of backgrounds and an understanding of its components and the combination of x-ray and neutron powder patterns for some applications.

The consensus of opinion expressed during the Conference is that the higher resolution: will be an advantage for Fourier applications; should make possible solutions of structures involving 200 variables; will make possible an examination of scattering in the vicinity of the Bragg peaks. The high resolution powder diffractometer (HRPD) designed for the SNS project will provide resolutions of  $\Delta d/d = 3 \times 10^{-4}$ . Multiple detectors are indeed an advantage and a must for both steady state and pulsed neutron sources. The problem of profile fitting to the diffraction peaks has been given

---

Figures in brackets indicate the literature references at the end of this paper.

considerable attention the past several years so that generalized computer programs are becoming available for both the steady state and pulsed neutron techniques. Although there is some disagreement on assessment of errors associated with profile refinements, the use of the program SCRAP by M. Cooper may assist in the evaluation.

It is quite an accepted fact that environmental changes can be made with the required neutron scattering instrumentation so that temperatures from 0.1 to 2500 K are possible and pressure up to 40 K bars are within range. For example, a recent study was carried out at ILL by Aldebert and Traverse [4], on high temperature structures of  $\text{La}_2\text{O}_3$  and  $\text{Nd}_2\text{O}_3$  at temperatures up to 2225 °C.

It is apparent that the use of standards for comparison between various installations and instruments is very important. You may recall that the IUCr had a project in progress during the early 70's to collect powder pattern results from a standard  $\text{Al}_2\text{O}_3$  sample which was furnished to the several laboratories. It was not intended that the investigation be a competition between the different laboratories but rather a means for everyone... "to decide whether in their particular case optimum conditions have been achieved; or whether they should spend more time trying to improve the situation," Andresen and Sabine [5]. The results of least squares treatment of the  $\text{Al}_2\text{O}_3$  data was presented at the Cracow, Poland IUCr satellite meeting last summer and will be published in J. Appl. Cryst. in the near future. It may also be desirable to use other materials as standards of comparison which may have a more complex structure or may be a material such as MgO where it is possible to calculate and account for the total scattering.

Development and understanding of high resolution neutron powder patterns not only offer possibilities in the solution of certain atom site locations in the structure, but also may be used to better assign physical characteristics to many of the materials. For example, it should be possible to detect and characterize: stacking faults; particle size broadening; lattice strains, including anisotropic characteristics; short range order; partial site occupation, displacement disorder; thermal diffuse scattering; extinction effects; incoherent scattering; diffuse scattering; and paramagnetic scattering.

The general conclusion of the Conference was that: (1) considerable progress has been made in the past five years in the application of neutron diffraction powder patterns (2) future plans look promising and exciting; (3) contributions can be made to structure analysis to a characterization of many materials where single crystals are not available; and that future meetings should be held covering the topical area of neutron diffraction powder patterns. It has been tentatively proposed and accepted to have a satellite topical meeting at Argonne National Laboratory on neutron scattering with emphasis on powder techniques in conjunction with the next IUCr Congress and Assembly to be held in Ottawa, Canada, August 1981. It was evident in the meeting as recently stated by Dr. Pehka Suortti, "powder diffraction as a method of structure analysis has been rediscovered in the last few years... ." This has certainly been possible for the neutron case because of increased flux, improved resolution and introduction and refinement of Rietveld profile analysis methods and techniques as well as the use of x-ray and neutron results in combination.

We are indeed indebted to the organizers of this Symposium for the stimulating program and the fine arrangements which included a tour of the NBS Reactor. We look forward to an early appearance of the Symposium Proceedings.

#### References

- 1] Rietveld, H. M., Line profiles of neutron-powder diffraction peaks for structure refinement, *Acta Cryst.* 22, 151-152 (1967).
- 2] Rietveld, H. M., A profile refinement method for nuclear and magnetic structures, *J. Appl. Cryst.* 2, 65-71 (1969).
- 3] Cheetham, A. K. and Taylor, J. C., Profile analysis of powder neutron diffraction data: its scope, limitations, and applications, in solid state chemistry, *J. Solid State Chem.* 21, 253-275 (1977).
- 4] Aldebert, P. and Traverse, J. P., Etude par diffraction neutronique des structures de haute temperature de  $\text{La}_2\text{O}_3$  et  $\text{Nd}_2\text{O}_3$  (Study by neutron diffraction of the structures of  $\text{La}_2\text{O}_3$  and  $\text{Nd}_2\text{O}_3$  at high temperature), *Mat. Res. Bull.* 14, 303-323 (1979).
- 5] Andresen, A. F. and Sabine, T. M., An intercomparison of neutron powder diffraction instruments, *J. Appl. Cryst.* 10, 497-501 (1977).



JCPDS - INTERNATIONAL CENTRE FOR DIFFRACTION DATA:  
PRESENT AND FUTURE ACTIVITIES

G. J. McCarthy<sup>1</sup> and D. K. Smith<sup>2</sup>  
Materials Research Laboratory  
The Pennsylvania State University  
University Park, PA 16802

Highlights of recent and current activities of the JCPDS-ICDD subcommittees, grants-in-aid and NBS Associateship are presented. Future areas of emphasis will include new subfiles and computer databases, interaction in the Chemical Information System, topical reviews and generation of new powder data and assessment of the potential merging of the single crystal and powder databases.

1. Introduction

While some diffractionists may not be familiar with the name "JCPDS -International Centre for Diffraction Data" (JCPDS - ICDD), they will recognize its main publication, the Powder Diffraction File (PDF). For almost four decades, the JCPDS - ICDD has collected (from the literature, from contributions, or from grant research), edited and published powder data on card, magnetic tape and book form, along with search manuals and computer search/match programs for accessing this data. We present here an overview of recent past, present, and future activities of the JCPDS - ICDD.

2. Subcommittee Activities

Like many scientific organizations, the JCPDS - ICDD operates both as a professional society having volunteer members drawn from industry, universities, and government laboratories and as a publishing house. Both functions have expanded several-fold in the last decade. Technical activities are carried out primarily by subcommittees of the Technical Committee, with support from the headquarters staff as required. Some of the highlights of these activities can be cited:

---

<sup>1</sup>Chairman, Technical Committee, JCPDS - ICDD; address after September 1, 1979: Departments of Chemistry and Geology, North Dakota State University, Fargo, ND 58102.

<sup>2</sup>Chairman, JCPDS - ICDD; also a member of the Department of Geosciences.

## 2.1. Mineral subcommittee

Founded in 1971. Members of this group reviewed and upgraded all existing powder data for minerals and prepared the Mineral Subfile consisting of a data book and search manual. The group has just completed work on an update to be published in 1980. A very high percentage of all known minerals will be represented in this update.

## 2.2. Computer subcommittee

Since 1974, this group has been largely responsible for improvements in the format, documentation and quality control of the magnetic tape database. The complexity and cost of establishing the database and search/match programs at users' sites has been greatly reduced by tailoring these for three of the major computer types. The computer subcommittee has been instrumental in keeping the JCPDS - ICDD current in computer hardware and software advances.

## 2.3. Education subcommittee

The obvious need for a JCPDS - ICDD role in primary and continuing education in diffraction analysis and identification led to the formation of this group in 1972. Since then approximately a dozen symposia on these topics have been conducted at conferences. Workshops on the use of the PDF have been developed and total attendance at these is approaching 1000. Some 20 members of the JCPDS - ICDD have volunteered their time as instructors in these workshops. The workbook designed for the PDF Workshop is available also for other groups teaching powder diffraction methods.

A joint undertaking of the education and computer subcommittees was the recent set of "round robins" aimed at assessing the effectiveness and relative merits of the manual and computer search/routines and the importance of input data quality on successful identification. Current joint efforts include development of a computer search/match workshop and an American Chemical Society Audio Course.

## 2.4. Search procedures subcommittee

One of the oldest of the subcommittees, this group has concentrated on the concepts of pattern searching, especially by manual methods, in a continuing evaluation of present and alternative versions of JCPDS - ICDD Search Manuals. The subcommittee has had a long time of concern with the effect of a growing PDF (~35,000 patterns; 2000 added per year) on the accuracy and effectiveness of these manuals. Realizing that certain crystalline phases occur as answers in a high percentage of searches, the group has sought to define a set of "Frequently Encountered Phases" (FEP). A FEP Search Manual incorporating Hanawalt, Fink, and Alphabetical sections has been available for several years. Approximately 2300 phases are included in the FEP list. Continuing definition of the list and upgrading of the powder data of phases on the list are performed by the JCPDS - ICDD Associateship at the National Bureau of Standards.

## 2.5. Metals and alloys subcommittee

Recently, members of this group performed an extensive review and update of all available data on metals and alloys. This effort resulted in publication of the Metals and Alloys Subfile in 1978. Included in the subfile were a number of calculated patterns of phases for which powder data were not available. Work is underway on a supplement to be published in the early 1980's.

As the PDF continues to grow, the importance of high quality data for well-characterized phases and of smaller sets of data--subfiles--will increase. Other subcommittees (organic, inorganic, forensic, ceramic, etc.) are at work defining subfiles, reviewing the quality of data that fall within these subfiles and taking steps to calculate, solicit or otherwise obtain missing data. These groups will be generating the new products of the 1980's.

## 3. Grants-in-Aid and the JCPDS - ICDD Associateship at the NBS

While the major historical source of data for the PDF has been the scientific literature, the JCPDS - ICDD has long recognized that these data appear in rather random fashion and are of quite variable quality. Thus, for three decades, it has allocated a portion of its budget to the generation of high quality data for well-characterized materials.

The first effort of this type was an Associateship at the NBS that still operates today as the Crystallography Section. Since 1951, nearly 1200 experimental patterns of high purity materials, along with hundreds of calculated patterns, have been generated by the Associateship. A collection of these data through 1976 has been published in book form and a book of Handbook, Fink, and Alphabetical search manuals has been prepared. Most of these data are of common laboratory chemicals, minerals and other frequently encountered phases. These books constitute the JCPDS - ICDD educational package for universities and industrial continuing education programs.

In a typical year, the JCPDS - ICDD awards 15 to 18 grants-in-aid to universities and non-profit institutes for determination of powder data or for other powder diffraction activities. Current grantees are located in Japan, the United Kingdom, France, The Netherlands, Germany, and Israel as well as the U.S. Grants are often focussed on groups of materials on which the grantees are specialists. For example, current grantees are determining powder data for common crystalline organic substances, hydrous and anhydrous cement phases, rare earth-containing intermetallics, homogeneous catalysts, agricultural chemicals and phosphate minerals. Other grants calculate powder data for phases not represented in the PDF. One such grant provides calculated patterns for all metals and alloys being entered into Structure Reports.

The fact that 30-35 percent of all data issued in recent sets comes from grants-in-aid from the Associateship is evidence of their importance to the PDF.

#### 4. Future Activities

In addition to the continuing subfile and data review activities described above, the JCPDS - ICDD is increasing its efforts in several related areas. The interaction of computers in all aspects of preparation and utilization of powder data is the center of these efforts. The editorial activities have been streamlined by computer storage and analysis of the data which are employed by the editor when the pattern evaluation procedures are initiated. The computerized data will then be transferred via phone lines to the office and other editors and will ultimately be used to compose the master database and the PDF products in either hard or computer readable format. This approach will help minimize data handling and consequent errors as well as allow an expansion of the present database to include considerably more information than is presently incorporated.

The expansion of the database is part of the effort to maintain a state-of-the-art status with the PDF. Recent incorporation of the PDF in the Chemical Information System CIS, is one of several projected uses of the database. The particular advantage of the network is its ability to cross index with the other databases on the system through the compound codes, the chemical abstracts registry number. Thus, one database can augment information contained in another database. A more direct link is being established between the PDF and the Crystal Data file that will allow cross indexing through several data channels including the crystal cell. This close correlation is possible because of the similarity of information in the two databases, and coordination is especially important because of possible partial or total merging of the two databases in the future. The JCPDS - ICDD is already the publisher for Crystal Data in the four volume book form, and plans to continue in this role with future volumes.

With the projected increase in the usage of automatic powder diffractometer, APD, systems, the PDF will become even more important in computer readable form. Currently, one manufacturer has incorporated the complete PDF as part of its system. Other manufacturers have included or are contemplating provisions for using "mini" PDF files tailored to the special needs of the user. The everchanging hardware requirements and desires of the users have resulted in the addition of a computer specialist to the JCPDS - ICDD permanent staff who will be responsible for implementing these activities. Major efforts are directed towards simplifying the preparation of mini files on hard media that are compatible with the many instruments in use. The acquisition by the JCPDS - ICDD of an in-house computer will facilitate these efforts.

Although the powder diffraction method is one of the oldest instrumental analytical techniques available to the chemist, geologist, and materials scientist, it is still seeing increasing usage in research and industry. Improvements in accuracy and sophistication of instrumentation, the ever expanding scope of compounds being studied and types of information desired, such as precise cell constants, have placed very high demands on the database in completeness of coverage and in accuracy of the data itself. The demands necessitate

constant review and change of the PDF, and no diminishing of the activities is foreseen in near future. In fact, the bibliographic searches are still uncovering about the same number of published powder data each year which, along with Grant-in-Aid generated data, continues to keep the editorial flow of patterns very active.

In conclusion, the JCPDS - ICDD looks forward to continued employment of diffraction methods of identification for the coming decade and views its chief role as providing quality data of wide coverage among all crystalline substances and in the various forms necessary for efficient manual and computer utilization. It also looks forward to increased cooperation and compatibility with other organizations and databases.



DESIGN OF A HIGH-ACCURACY GONIOMETER FOR X-RAY  
POWDER DIFFRACTOMETRY AT CONTROLLED TEMPERATURE

J. F. Berar, G. Calvarin, J. Chevreul, M. Gramond and D. Weigel  
Laboratoire de Chimie-Physique du Solide  
Ecole Centrale des Arts et Manufactures  
Grande Voie des Vignes  
92290 Chatenay-Malabry, France

Precise measurements of lattice parameters, at numerous temperatures, by means of x-rays powder diffractometry give valuable information about thermal expansion coefficients and phases transitions of a material. In this purpose, we have designed in our laboratory a goniometer, easy to use, and efficient to measure diffraction angles with an accuracy of  $10^{-3}$  ( $^{\circ} \theta$ ), even if the sample is attached into a large and heavy device (cryostat, furnace...).

Owing to an original mechanical design, rotation angle ( $2\theta$ ) of the detector is exactly measured by means of an incremental photoelectric angle encoder connected to the goniometer axis.  $\theta$  and  $2\theta$  rotations are independently executed by means of step by step motors electronically operated. So, by means of the variable angular positions "zero" for  $\theta$  and  $2\theta$ , the different adjustments are executed quickly and easily with a very good reproductibility.

Another important particularity of this goniometer is its variable radius. So, in using a large radius (500 mm) and a set of high efficiency undivergent slits, angular resolution is drastically improved, principally for  $\theta < 20^{\circ}$ . Nevertheless, use of a 12 kw rotating anode x-rays generator permits to hold an appreciable intensity for diffraction peaks.

Lots of diagrams have been recorded in continuous scanning ( $0.06^{\circ} \theta/\text{min}$ ) with  $\text{Pb}(\text{NO}_3)_2$  and  $\text{Pb}_3\text{O}_4$  samples at room temperature. In the usable angular range ( $-130 < 2\theta < +160$ ), reproductibility of measurements is of  $\pm 10^{-3}$  ( $^{\circ} \theta$ ); moreover for the same diffraction peak, the difference between the negative and positive  $2\theta$  values does not exceed  $\pm 2 \times 10^{-3}$  ( $^{\circ} \theta$ ). Lattice parameters refinements, made in taking account of a simple correction function, show the differences  $\theta_{\text{theo}} - \theta_{\text{exp}}$  are less than  $\pm 10^{-3}$  ( $^{\circ} \theta$ ).

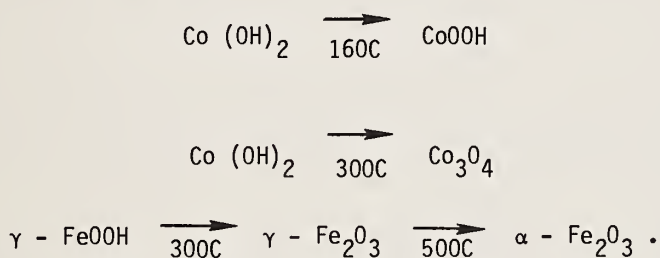
Such a high-accuracy goniometer, owing to its easy and quick working up and its competitive price, is a new and very efficient unit for all x-rays powder diffraction studies.

THE EFFECT OF TWINNING ON PARTICLE SIZE BROADENING IN SOME  
OXIDES DERIVED BY DEHYDRATION REACTIONS

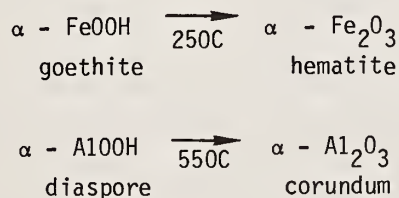
Fumio Watari  
Department of Physics  
Arizona State University  
Tempe, AZ 85281<sup>1</sup>

1. Results

Dehydration products generally consist of small crystallites, which causes peak broadening in x-ray diffraction. In most cases the reflection peaks of the decomposition products have more or less the same width, except for the gradual increase with diffraction angle. This is the case for the reactions:



the other hand, the reflection peaks are classified into two groups, sharp and broad peaks for the products of the following reactions:



The investigation of the goethite-hematite system [1]<sup>2</sup> was performed at the University of Antwerp, RUCA, B2020 Antwerp, Belgium.

Figures in brackets indicate the literature references at the end of this paper.

For these cases it was revealed by high resolution electron microscopy that the product oxides are composed of highly oriented twinned crystallites as a result of the equal possibilities of two iron atom configurations in the hexagonal close packed oxygen lattice. This results in the appearance in electron diffraction patterns among crystallites [2]. The same hexagonal unit cell can be used to describe the structure of the two twinned variants of the rhombohedral oxides [3]. Sharp powder line peaks appear for the reflection with  $l, h-k = 3n$ , which are common to both components of twin. Broad peaks occur for the reflections with  $l, h-k \neq 3n$ , for which, in the powder diffraction pattern, there is an overlapping of the particular reflections contributed from only one component and forbidden for the other.

Figure 1 shows the half peak widths of synthetic goethite and its decomposition product hematite for various dehydration temperatures.

The peak widths of goethite appears uniform, although the shape of an individual particle is a needle in synthetic goethite and usually a cleavage plate in mineral goethite [2].

Diffraction peaks common to both twin components of hematite, represented by the (110) peak, have almost the same widths as for goethite and they do not vary with the dehydration temperature. Non-common reflections, represented by the (104) peak, are much broader and they become sharper, approaching the width of the (110) reflections, as the dehydration temperature increases. The corundum formed by decomposition of mineral diasporite [4,5], involving isomorphs of phases in the goethite-hematite system, shows the same behavior except that the decomposition temperatures are higher.

## 2. Explanation

Careful examination of electron diffraction patterns had revealed the different intensity behavior of the common and non-common spots of hematite. This was interpreted using the concept of a mosaic spread in electron diffraction [2]. The same figure used to explain the above would apply for the present case. The configuration of the scatterers giving rise to the different types of reflections in figure 1 is schematically represented in figure 2.

Before decomposition, each individual particle constituting the powder sample is a single crystal, typically with the size of  $200 \times 1000 \times 10^4 \text{ \AA}^3$  in the case of synthetic goethite (fig. 2a).

After transformation, twinned oxide crystallites and voids are formed in a topotactic way [6] by loss of compositional water. As revealed by high resolution electron microscopy [2], the lattices are coherent between twins and the two different components cannot be distinguished when imaged using the common diffraction peaks (fig. 2b). Non-common reflections are produced by only one component of crystallites and so come from distinct regions separated in the specimen by the existence of other components (fig. 2c). This situation is clearly illustrated in the dark field image of hematite in [151]

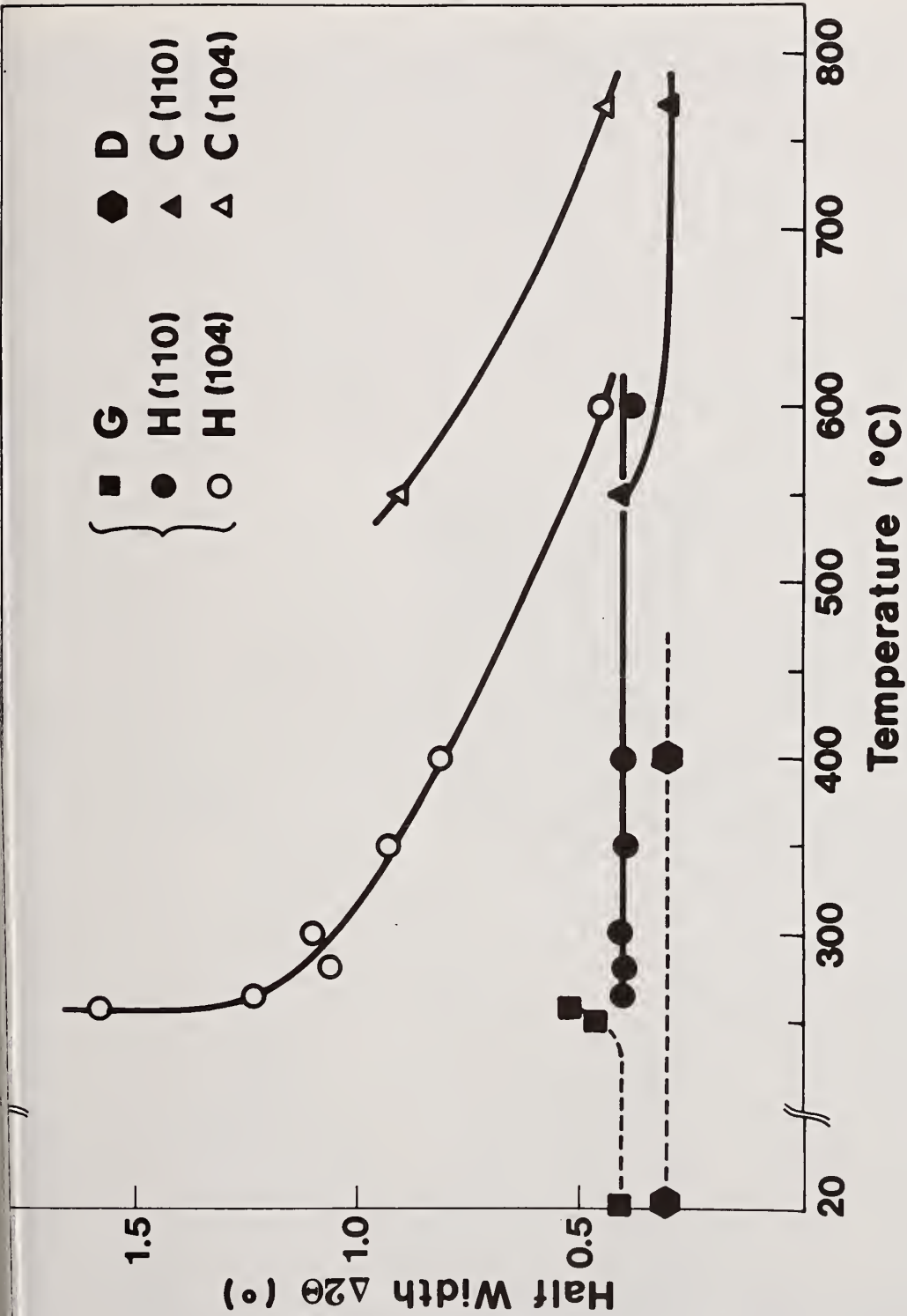


Figure 1. Change of half peak widths with dehydration temperature. (G: goethite, H: hematite, D: diaspore, C: corundum). FeK $\alpha$  for goethite-hematite and CuK $\alpha$  for diaspore-corundum were used respectively.

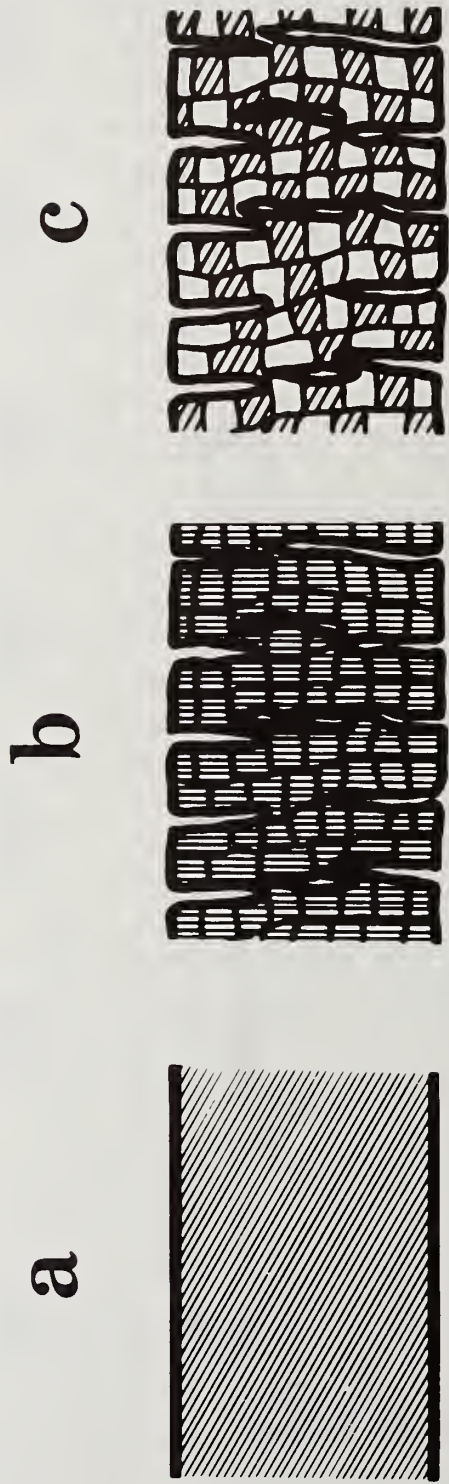


Figure 2. Schematic representation of the configuration of the scatterers for starting materials (a), common reflections (b), and non-common reflections (c) of dehydration product oxides.



Figure 3. High resolution dark field image of hematite in its [151] orientation. The black parts indicated such as 1, 2 correspond to voids formed by loss of compositional water. The crystallites with lattice fringes can be distinguished from those without fringes. The inset shows the natures of diffraction spots. (■ common spots, ○ spots belonging to reverse crystallites [3]).

orientation (fig. 3). Because non-common spots in this orientation are allowed only from one component but not from the other, the lattice fringes appear in the one component of crystallites which is responsible for these spots [2].

The decrease of the widths for the non-common diffraction peaks with dehydration temperature, shown in figure 1, results from a grain growth process among the twin crystallites during heat treatment. The size of the crystallites of hematite estimated from non-common reflections is about 50 Å just after transformation near 250 °C. For higher temperatures it approaches about 300 Å, the size estimated for synthetic goethite single crystals and for aggregates of twinned crystallites of hematite. These values are consistent with the observation by electron microscopy [2] and the results by other methods [7,8], which supports the model of figure 2.

Thus, these product oxides show different natures depending on the reflections used to study them. They behave like single crystals with voids in them for the common reflections and like well-oriented polycrystals for the non-common reflections.

#### References

- [1] Watari, F., Van Landuyt, J., and Amelinckx, S., to be published.
- [2] Watari, F., Van Landuyt, J., Delavignette, P., and Amelinckx, S., Electron microscopic study of dehydration transformations, part 1. Twin formation and mosaic structure in hematite derived from goethite, *J. Sol. Stat. Chem.* (1979), in press.
- [3] Henry, N. F. M. and Lonsdale, K., *International tables for x-ray crystallography*, Vol. 1, p. 20 (Kynoch Press, Birmingham, 1969).
- [4] Watari, F., Delavignette, P., and Amelinckx, S., Electron microscopic study of dehydration transformations, part II. The formation of "super-structures" on the dehydration of goethite and diasporite, *J. Sol. Stat. Chem.* (1979), in press.
- [5] Watari, F., Periodic regular texture of oxides derived from oxyhydroxide minerals by dehydration reaction, *Modulated Structures 1979* (Kailua Kona, Hawaii), J. M. Cowley, ed. (American Institute of Physics, New York, 1979), in press.
- [6] Günte, J. R. and Oswald, H.-R., Attempt to a systematic classification of topotactic reactions, *Bull. Inst. Chem. Res. Kyoto Univ.*, 53, 249 (1975).
- [7] Shinjo, T., Mössbauer effect in antiferromagnetic fine particles, *J. Phys. Soc. Japan*, 21, 917 (1966).
- [8] Szytula, A., Buréwicz, A., Dimitrijević, Z., Drasnicki, S., Rżany, H., Todorovic, J., Wanic, A., and Wolski, W., Neutron diffraction studies of  $\alpha$ -FeOOH, *Phys. Stat. Sol.*, 26, 429 (1968).

List of Participants

Alberto Albinati  
Institute of Chemistry - Polytechnic  
32, P.za L. Da Vinci  
20133 Milano  
ITALY

Joseph Angilello  
IBM Research Center  
Yorktown Heights, NY 10598

Christian Baerlocher  
Institut für Kristallographie und  
Petrographie, ETH  
Sonnegshasse 5  
CH-8092 Zurich  
SWITZERLAND

James H. Baird  
W. R. Grace & Co.  
7379 Route 32  
Columbia, MD 21044

D. W. Beard  
Siemens Corp.  
2 Pin Oak Lane  
Cherry Hill, NJ 08034

Stanley Block  
Center for Materials Science  
National Bureau of Standards  
Washington, DC 20234

William Boettinger  
National Bureau of Standards  
Washington, DC 20234

Robert W. Broach  
UOP Inc.  
10 UOP Plaza  
Des Plaines, IL 60016

H. Burdette  
National Bureau of Standards  
Washington, DC 20234

L. D. Calvert  
National Research Council of Canada  
Ottawa, Ont. K1A0R9  
CANADA

Donald A. Carpenter  
Union Carbide Corp.-Nuclear Div.  
Oak Ridge Y-12 Plant  
P.O. Box Y, Bldg. 9203 MS 1  
Oak Ridge, TN 37830

John A. Carrabine  
John Carroll University  
University Heights  
Cleveland, OH 44118

Odis B. Cavin  
Oak Ridge National Lab  
P. O. Box X  
Oak Ridge, TN 37830

J. B. Cohen  
Materials Science & Engineering Dept.  
The Technological Institute  
Northwestern University  
Evanston, IL 60201

M. J. Cooper  
U.K.A.E.A.  
Materials Physics Division  
AERE, Harwell  
ENGLAND OX110RA

D. E. Cox  
Brookhaven National Lab  
Physics Dept.  
Upton, NY 11973

R. Deslattes  
National Bureau of Standards  
Washington, DC 20234

L. G. Dowell  
Union Carbide Corp.  
Old Sawmill River Rd.  
Tarrytown, NY 10591

James W. Edmonds  
Dow Chemical Co.  
Bldg. 1602 1  
Midland, MI 48640

Eloise H. Evans  
JCPDS  
1621 Gruenther Avenue  
Rockville, MD 20851

Eva E. Fejer  
British Museum (Natural History)  
Dept. of Mineralogy  
Cromwell Rd.  
London SW7  
UNITED KINGDOM, GREAT BRITAIN

C. M. Foris  
E. I. du Pont de Nemours & Co.  
Central Research & Development Dept.  
Experimental Station Bldg. 356  
Wilmington, DE 19898

Alfred D. French  
U.S.D.A. Southern Regional Research Center  
P.O. Box 19687  
New Orleans, LA 70179

Kenn Gardner  
DuPont  
Experimental Station  
Wilmington, DE 19898

Ross Giese  
State University of New York  
Geology Dept. 14240 Ridge Lea  
Amherst, NY 14226

K. Girgis  
Inst. f. Krist. ETHZ  
Sonneggstr. 5  
8092 Zurich  
SWITZERLAND

Charles Goldsmith  
IBM - Route 52  
13/300-41C  
Hopewell Junction, NY 12533

Ortwin Greis  
Texas A & M University  
Chemistry Department  
College Station, TX 77843

Agnes Griger  
R & D Centre of the Hungarian  
Aluminum Corp.  
H - 1116 Fehérvári út 144  
Budapest  
HUNGARY

Alfried Haase  
Rich. Seifert & Co.  
Postfach 1280  
2070 Ahrensburg  
WEST GERMANY

J. D. Hanawalt  
University of Michigan  
Mat. & Met. Eng. Dept.  
Ann Arbor, MI 48109

Richard Harlow  
Central Research & Development Dept.  
E. I. du Pont de Nemours & Co.  
Experimental Station, Bldg. 356  
Wilmington, DE 19898

R. W. Hendricks  
Oak Ridge National Laboratory  
P.O. Box X  
Oak Ridge, TN 37830

A. W. Hewat  
I.L.L. (Institute Max von Lane -  
Paul Langevin)  
B.P. 156X  
Grenoble  
FRANCE 38042

John E. Hilliard  
Northwestern University  
Dept. Materials Science & Eng.  
Evanston, IL 60201

Hans J. Holland  
Corning Glassworks  
Tech. Staffs Div.  
Corning, NY 14830

Camden R. Hubbard  
Center for Matls. Science  
National Bureau of Standards  
Washington, DC 20234

Robert A. Jacobson  
AMES Laboratory -  
Iowa State University  
42 Spedding Hall  
Ames, IA 50011

L. D. Jennings  
Army Research Center  
Watertown, MA 02172

Q. C. Johnson  
University of California  
Box 808  
Lawrence Radiation Lab. L-404  
Livermore, CA 94550

James D. Jorgensen  
Solid State Science Division  
Argonne National Laboratory  
9700 S. Cass Ave.  
Argonne, IL 60439

TH.H.De Keijser  
Laboratory of Metallurgy  
Delft University of Technology  
Rotterdamseweg 137  
Delft 2628 AL  
THE NETHERLANDS

Hae Soo Kim  
Bldg. 21. Technical Center  
Owens-Corning Fiberglas Co.  
Granville, OH 43023

John Krc, Jr.  
Warner Lambert Pharmaceutical Res. Div.  
Joseph Campau at the River  
Detroit, MI 48232

M. Kuriyama  
National Bureau of Standards  
Washington, DC 20234

Joshua Ladell  
Philips Laboratories  
345 Scarborough Road  
Briarcliff Manor, NY 10510

J. I. Langford  
Dept. of Physics  
University of Birmingham  
Birmingham B15 2TT  
ENGLAND

Samuel Lawhorne  
IBM Corp.  
Route 52  
Hopewell Hct., NY 12533

Martin Lefkowitz  
U.S. Steel Research Laboratory  
125 Jamison Lane  
Monroeville, PA 15146

Michael E. Leonowicz  
Exxon Research & Eng. Co.  
P. O. Box 121  
Linden, NJ 07036

Ray Loghry  
Haltiburton Services - CRD  
Drawer 1431  
Duncan, OK 73533

Daniel Louër  
Université de Rennes -  
Laboratoire de Cristallochimie  
Avenue du Maréchal Leclerc  
35042 Rennes  
FRANCE

Paul Lublin  
GTE Laboratories, Inc.  
40 Sylvan Road  
Waltham, MA 02154

Greg McCarthy  
Penn State University  
205 Materials Research Lab.  
University Park, PA 16802

W. Frank McClune  
JCPDS--International Centre for  
Diffraction Data  
1601 Park Lane  
Swarthmore, PA 19081

Howard F. McMurdie  
National Bureau of Standards  
Washington, DC 20234

Chester Mallory  
NY State College of Ceramics  
Alfred University  
Alfred, NY 14802

John Mandel  
National Bureau of Standards  
Washington, DC 20234

K. Dieter Markert  
Seifert X-Ray Corporation  
2551 Industry Lane  
Fairview Village, PA 19409

Orin W. Marks  
Hercules Incorporated  
Research Center  
Wilmington, DE 19899

Garland N. Martin, Jr.  
National Institute of Dental Research  
Laboratory of Biological Structure  
National Institutes of Health  
Bldg. 30, Room 211  
Bethesda, MD 20205

Floyd Mauer  
Center for Matls. Science  
National Bureau of Standards  
Washington, DC 20234

I. P. Mayer  
Hebrew University  
Jerusalem, ISRAEL

R. C. Medrud  
Chevron Research Company  
576 Standard Avenue  
Richmond, CA 94802

Henri Merigoux  
Universite de Besancon  
Route de Gray  
Besancon  
FRANCE 25000

Julian Messick  
UCPDS--International Centre for  
Diffraction Data  
1601 Park Lane  
Swarthmore, PA 19081

Joan Mishara  
Conservation Analytical Laboratory  
Smithsonian Institution  
Washington, DC 20560

E. Y. Mittemeijer  
Laboratory of Metallurgy  
Delft University of Technology  
Rotterdamseweg 137  
2628 AL Delft  
THE NETHERLANDS

Marlene Morris  
National Bureau of Standards  
CPDS  
Washington, DC 20234

Wilfried J. Mortier  
K.U.L-Centrum Oppervlaktescheikunde  
De Croylaan 42  
B-3030 Heverlee  
BELGIUM

Melvin H. Mueller  
Argonne National Lab.  
9700 S. Cass Ave.  
Argonne, IL 60439

Robert M North  
New Mexico Bureau of Mines  
and Mineral Resources  
Campus Station  
Socorro, NM 87801

Thomas L. Nunes  
IBM East Fishkill Facility  
D/875 B/300-41C  
Route 52  
Hopewell Jct, NY 12533

Brian Osgood  
NY State College of Ceramics  
Alfred University  
Alfred, NY 14802

Robert Pangborn  
Department of Mechanics &  
Materials Science  
College of Engineering  
Rutgers University  
P. O. Box 909  
Piscataway, NJ 08854

William Parrish  
IBM Research Laboratory K41/281  
5600 Cottle Road  
San Jose, CA 95193

Joseph Perel  
Israel Fiber Institute  
Jerusalem, ISRAEL

Robert O. Pichulo  
AC Spark Plug  
1300 N. Dort Highway  
Flint, MI

Sidney S. Pollack  
DOE/PET C  
4800 Forbes Ave  
Pittsburgh, PA 15213

Benjamin Post  
Polytechnic Institute of  
New York  
333 Jay Street  
Brooklyn, NY 11201

Edward Prince  
Reactor Division  
National Bureau of Standards  
Washington, DC 20234

A. C. Roberts  
Geological Survey of Canada  
761-601 Booth Street  
Ottawa, Ontario K1A 0E8  
CANADA

Paul Rognlie  
Blake Industries  
660 Jerusalem Rd.  
Scotch Plains, NJ 07076

Wayne J. Rohrbaugh  
Mobil Research and Development  
Corporation  
Billingsport Road  
Paulsboro, NJ 08066

Frank J. Rotella  
Argonne National Laboratory  
9700 S. Cass Avenue  
Argonne, IL 60439

J. J. Rush  
National Bureau of Standards  
Building 235, A106  
Washington, DC 20234

T. M. Sabine  
New South Wales Institute  
of Technology  
Sydney, New South Wales 2007  
AUSTRALIA

S. Salome  
University of Stockholm  
Kameralsektionen  
10691 Stockholm  
SWEDEN

A. Santoro  
National Bureau of Standards  
Building 235, A106  
Washington, DC 20234

Walter Schreiner  
Philips Laboratories  
345 Scarborough Road  
Briarcliff Manor, NY 10510

R. Shirley  
University of Surrey  
Chemical Physics Department  
Surrey  
ENGLAND

John M. Sholes  
Bendix Field Engineering  
Corporation  
Department of Energy Compound  
P.O. Box 1569  
Grand Junction, CO 81501

Deane K. Smith  
Penn State University - JCPDS  
239 Deike Building  
University Park, PA 16802

Robert L. Snyder  
N.Y.S. College of Ceramics at  
Alfred University  
Alfred, NY 14802

Robert A. Sparks  
California Scientific Systems  
P. O. Box 2053  
Sunnyvale, CA 94087

Lincoln R. Spaulding  
Eastman Kodak Company  
Research Laboratories  
Building 82, Lake Avenue  
Rochester, NY 14650

Pekka H. Suortti  
Department Physics,  
University Helsinki  
Siltavuorenpenger 20 D  
Helsinki, 00170  
FINLAND

Gunter Teufer  
E. I. du Pont de Nemours & Co.  
Chemicals, Dyes & Pigments Dept.  
Jackson Laboratory  
Wilmington, DE 19898

M. W. Thomas  
A.E.R.E. Harwell  
MPD Bldg. 521.2  
Harwell, OX11 0RA  
ENGLAND

Ryosei Uno  
College of Humanities and  
Sciences  
Nihon University  
3-25-40, Sakurajosui, Setagaya-ku  
Tokyo 156  
JAPAN

Jorgen Villadsen  
Haldor Topsøe A/S  
Nymollevvej 55, P. O. Box 213  
DK-2800 Lyngby  
DENMARK

John B. Wachtman  
National Bureau of Standards  
Center for Materials Science  
Washington, DC 20234

Christian N. J. Wagner  
University of California  
Materials Department  
6531 Boelter Hall  
Los Angeles, CA 90024

G. A. Walker  
IBM Corporation  
D/875, B/300-41C  
Rt 52  
Hopewell Jct, NY 12533

Fumio Watari  
Department of Physics  
Arizona State University  
Tempe, AZ 85281

D. J. J. Weigel  
Ecole Centrale des Arts et  
Manufactures de Paris  
2 rue Pierre et Marie Curie  
Paris, 75005  
FRANCE

Rahmi Yazici  
Rutgers University  
Dept. of Mechanics & Materials  
Science  
P. O. Box 909  
Piscataway, NJ 08854

Sigmund Weissmann  
College of Engineering  
Rutgers University  
Dept. Mechanics & Materials  
Science  
P. O. Box 909  
Piscataway, NJ 08854

R. A. Young  
Georgia Institute of Technology  
School of Physics  
Atlanta, GA 30332

P. E. Werner  
University of Stockholm  
Kameralsektionen  
10691 Stockholm  
SWEDEN

Leo Zwell  
JCPDS--International Centre for  
Diffraction Data  
1601 Park Lane  
Swarthmore, PA 19081

Dennis B. Wiles  
Georgia Tech  
Atlanta, GA 30332

A. J. C. Wilson  
Department of Physics  
University of Birmingham  
Birmingham, B15 2TT  
ENGLAND

Erich Wölfel  
Stoe, c/o California Scientific  
Systems  
P. O. Box 2053  
Sunnyvale, CA 94087

Robert C. Wnuk  
IBM DSD  
Dept. 875, Bldg. 300/41C  
Hopewell Jct, NY 12533

U.S. DEPT. OF COMM. BIBLIOGRAPHIC DATA SHEET		1. PUBLICATION OR REPORT NO. SP 567	2. Gov't. Accession No.	3. Recipient's Accession No.
TITLE AND SUBTITLE ACCURACY IN POWDER DIFFRACTION (Proc. of Symp. on Accuracy in Powder Diffraction, NBS, Gaithersburg, MD, June 11-15, 1979)			5. Publication Date February 1980	
			6. Performing Organization Code	
AUTHOR(S) S. Block and C.R. Hubbard, Editors			8. Performing Organ. Report No.	
PERFORMING ORGANIZATION NAME AND ADDRESS  NATIONAL BUREAU OF STANDARDS DEPARTMENT OF COMMERCE WASHINGTON, DC 20234			10. Project/Task/Work Unit No.	
			11. Contract/Grant No.	
SPONSORING ORGANIZATION NAME AND COMPLETE ADDRESS (Street, City, State, ZIP) International Union of Crystallography, 5 Abbey Square, Chester, CHI 2HU England; Chemistry Division of the National Research Council of Canada, Ottawa, Canada K1A0R6, and the National Bureau of Standards, Washington, DC 20234			13. Type of Report & Period Covered Final	
			14. Sponsoring Agency Code	
SUPPLEMENTARY NOTES Library of Congress Catalog Card Number: 80-60010  <input type="checkbox"/> Document describes a computer program; SF-185, FIPS Software Summary, is attached.				
ABSTRACT (A 200-word or less factual summary of most significant information. If document includes a significant bibliography or literature survey, mention it here.) The proceeding of the Symposium on Accuracy in Powder Diffraction presents the papers, abstracts and discussions of the symposium held at the NBS, Gaithersburg, Maryland, on June 11-15, 1979. The symposium was jointly sponsored by the NBS, the National Research Council of Canada, and the International Union of Crystallography. These proceedings contain a total of 24 invited and contributed abstracts. Many papers are followed by an edited discussion. The proceedings are divided into the following topics: Total Pattern, Instrumentation and Automation, Profile Fitting, Analysis of Peak Shape, Lattice Parameters and Indexing, Applications, and Future Opportunities in Powder Diffraction.				
KEY WORDS (six to twelve entries; alphabetical order; capitalize only the first letter of the first key word unless a proper name; separated by semicolons) Applications; lattice parameters; peak shape; powder diffraction; profile fitting; X-ray neutron.				
AVAILABILITY <input checked="" type="checkbox"/> Unlimited  <input type="checkbox"/> For Official Distribution. Do Not Release to NTIS		19. SECURITY CLASS (THIS REPORT)  UNCLASSIFIED		21. NO. OF PRINTED PAGES  553
<input checked="" type="checkbox"/> Order From Sup. of Doc., U.S. Government Printing Office, Washington, DC 20402, SD Stock No. SN003-003-02153-9  <input type="checkbox"/> Order From National Technical Information Service (NTIS), Springfield, VA, 22161		20. SECURITY CLASS (THIS PAGE)  UNCLASSIFIED		22. Price  \$9.00

USCOMM-DC



# NBS TECHNICAL PUBLICATIONS

## PERIODICALS

**JOURNAL OF RESEARCH**—The Journal of Research of the National Bureau of Standards reports NBS research and development in those disciplines of the physical and engineering sciences in which the Bureau is active. These include physics, chemistry, engineering, mathematics, and computer sciences. Papers cover a broad range of subjects, with major emphasis on measurement methodology and the basic technology underlying standardization. Also included from time to time are survey articles on topics closely related to the Bureau's technical and scientific programs. As a special service to subscribers each issue contains complete citations to all recent Bureau publications in both NBS and non-NBS media. Issued six times a year. Annual subscription: domestic \$17; foreign \$21.25. Single copy, \$3 domestic; \$3.75 foreign.

NOTE: The Journal was formerly published in two sections: Section A "Physics and Chemistry" and Section B "Mathematical Sciences."

**DIMENSIONS/NBS**—This monthly magazine is published to inform scientists, engineers, business and industry leaders, teachers, students, and consumers of the latest advances in science and technology, with primary emphasis on work at NBS. The magazine highlights and reviews such issues as energy research, fire protection, building technology, metric conversion, pollution abatement, health and safety, and consumer product performance. In addition, it reports the results of Bureau programs in measurement standards and techniques, properties of matter and materials, engineering standards and services, instrumentation, and automatic data processing. Annual subscription: domestic \$11; foreign \$13.75.

## NONPERIODICALS

**Monographs**—Major contributions to the technical literature on various subjects related to the Bureau's scientific and technical activities.

**Handbooks**—Recommended codes of engineering and industrial practice (including safety codes) developed in cooperation with interested industries, professional organizations, and regulatory bodies.

**Special Publications**—Include proceedings of conferences sponsored by NBS, NBS annual reports, and other special publications appropriate to this grouping such as wall charts, pocket cards, and bibliographies.

**Applied Mathematics Series**—Mathematical tables, manuals, and studies of special interest to physicists, engineers, chemists, biologists, mathematicians, computer programmers, and others engaged in scientific and technical work.

**National Standard Reference Data Series**—Provides quantitative data on the physical and chemical properties of materials, compiled from the world's literature and critically evaluated. Developed under a worldwide program coordinated by NBS under the authority of the National Standard Data Act (Public Law 90-396).

NOTE: The principal publication outlet for the foregoing data is the Journal of Physical and Chemical Reference Data (JPCRD) published quarterly for NBS by the American Chemical Society (ACS) and the American Institute of Physics (AIP). Subscriptions, reprints, and supplements available from ACS, 1155 Sixteenth St., NW, Washington, DC 20056.

**Building Science Series**—Disseminates technical information developed at the Bureau on building materials, components, systems, and whole structures. The series presents research results, test methods, and performance criteria related to the structural and environmental functions and the durability and safety characteristics of building elements and systems.

**Technical Notes**—Studies or reports which are complete in themselves but restrictive in their treatment of a subject. Analogous to monographs but not so comprehensive in scope or definitive in treatment of the subject area. Often serve as a vehicle for final reports of work performed at NBS under the sponsorship of other government agencies.

**Voluntary Product Standards**—Developed under procedures published by the Department of Commerce in Part 10, Title 15, of the Code of Federal Regulations. The standards establish nationally recognized requirements for products, and provide all concerned interests with a basis for common understanding of the characteristics of the products. NBS administers this program as a supplement to the activities of the private sector standardizing organizations.

**Consumer Information Series**—Practical information, based on NBS research and experience, covering areas of interest to the consumer. Easily understandable language and illustrations provide useful background knowledge for shopping in today's technological marketplace.

*Order the above NBS publications from: Superintendent of Documents, Government Printing Office, Washington, DC 20402.*

*Order the following NBS publications—FIPS and NBSIR's—from the National Technical Information Services, Springfield, VA 22161.*

**Federal Information Processing Standards Publications (FIPS PUB)**—Publications in this series collectively constitute the Federal Information Processing Standards Register. The Register serves as the official source of information in the Federal Government regarding standards issued by NBS pursuant to the Federal Property and Administrative Services Act of 1949 as amended, Public Law 89-306 (79 Stat. 1127), and as implemented by Executive Order 11717 (38 FR 12315, dated May 11, 1973) and Part 6 of Title 15 CFR (Code of Federal Regulations).

**NBS Interagency Reports (NBSIR)**—A special series of interim or final reports on work performed by NBS for outside sponsors (both government and non-government). In general, initial distribution is handled by the sponsor; public distribution is by the National Technical Information Services, Springfield, VA 22161, in paper copy or microfiche form.

## BIBLIOGRAPHIC SUBSCRIPTION SERVICES

The following current-awareness and literature-survey bibliographies are issued periodically by the Bureau:

**Cryogenic Data Center Current Awareness Service.** A literature survey issued biweekly. Annual subscription: domestic \$25; foreign \$30.

**Liquefied Natural Gas.** A literature survey issued quarterly. Annual subscription: \$20.

**Superconducting Devices and Materials.** A literature survey issued quarterly. Annual subscription: \$30. Please send subscription orders and remittances for the preceding bibliographic services to the National Bureau of Standards, Cryogenic Data Center (736) Boulder, CO 80303.

**U.S. DEPARTMENT OF COMMERCE**  
**National Bureau of Standards**  
Washington, D.C. 20234

OFFICIAL BUSINESS

Penalty for Private Use, \$300

POSTAGE AND FEES PAID  
U.S. DEPARTMENT OF COMMERCE  
COM-215



SPECIAL FOURTH-CLASS RATE  
BOOK

---

9721











